UNIVERSITÉ DE STRASBOURG

ÉCOLE DOCTORALE de Physique et Chimie Physique (ED182)

Institut de Physique et Chimie des Matériaux de Strasbourg

(UMR 7504 CNRS – Unistra)

THÈSE

présentée par :

Geoffrey COTIN

soutenue le : **24 novembre 2017**

pour obtenir le grade de : **Docteur de l'université de Strasbourg**

Discipline/ Spécialité : Chimie-Physique des Matériaux

Nouvelles Stratégies vers la synthèse de nanoparticules magnétiques multifonctionnelles innovantes combinant imagerie par IRM et/ou thérapie par hyperthermie magnétique

THÈSE dirigée par :

Mme Bégin-Colin Sylvie	Professeur, IPCMS, ECPM, Université de Strasbourg

RAPPORTEURS :

Mme Motte Laurence	Professeur, Laboratoire CSPBAT, Bobigny
Mme Delville Marie-Helène	Directrice de recherche, ICMCB, Bordeaux

---

EXAMINATEURS :

M Viau Guillaume	Professeur, LPCNO, Toulouse
M Frisch Benoît	Directeur de recherche, LCAMB, Strasbourg
M Meyer Florent	PU-PH, Faculté de chirurgie dentaire, INSERM UMR 1121, Strasbourg

A ma maman

Remerciements

« Seul on va plus vite, ensemble on va plus loin ». C'est pendant ces trois années de thèse que j'aurais pu prendre la mesure de ce proverbe africain tant les collaborations menée pendant ces trois ans se sont révélées enrichissantes. C'est pour cela que je tiens à remercier tous ceux et celles qui ont contribué de près ou de loin à ce projet.

Je remercie M. Stefan Haacke, directeur de l'IPCMS de m'avoir permis d'effectuer ma thèse à l'institut, ainsi que M. Pierre Rabu et Mme Nathalie Viart pour leur accueil au sein du Département de Chimie des Matériaux Inorganiques.

Je remercie les membres de mon jury de thèse, Mme Laurence Motte, Professeur à l'université de Paris, Mme Marie-Helène Delville, Directrice de recherche à l'université de Bordeaux, M Guillaume Viau, Professeur à l'université de Toulouse, M Benoit Frisch, Directeur de recherche à l'université de Strasbourg.

Comment ne pas commencer ces remerciements par celle qui m'a fait confiance dès le départ, ma directrice de thèse, Sylvie Bégin Colin. Ces trois années furent riche en émotions et je pense qu'autant l'un que l'autre nous nous ne sommes pas ennuyé un instant. Merci Sylvie d'avoir eu la patiente de m'encadrer, en me canalisant sans brimer toutes ces idées que j'ai pu avoir même si tu savais d'avance ce qui allait marcher ou pas. Malgré tes occupations tu as toujours été présente quand j'avais besoin de discuter et je t'en remercie. Pendant ces trois années tu m'as fait grandir tant scientifiquement qu'humainement, tu m'as permis de voyager et je n'aurais pas pu espérer mieux. Mais ces trois années n'ont pas comptées que des moments heureux, et là encore tu étais présente et tu m'as soutenu. Je pense que peu de directeurs de thèse ont tes qualités humaines et peu de doctorants ont la chance d'être soutenu comme je l'ai été. Encore une fois merci.

Ce travail n'aurait pas la même allure sans le travail conséquent de Céline Kiefer. Merci à toi pour ta motivation, ton intérêt pour la synthèse de nanoparticules. Ta rigueur et ton travail m'ont permis d'explorer des chemins que je n'aurais pas eu le temps de faire autrement. Cette thèse c'est aussi la tienne. Merci aussi pour les cours d'alsacien et bien sûr Unis pour vaincre !

J'ai trouvé un de mes soutient les plus solide pendant cette thèse chez le plus jeune des ~~post-docs~~ chargés de recherche Damien Mertz. Merci à toi d'avoir toujours pris le temps de répondre à mes questions et surtout d'avoir pris le temps d'imager toutes ces nanoparticules (et aussi d'avoir relu ma thèse).

Dans un équipe chacun à son rôle, et dans la nôtre j'ai toujours pu compter sur Benoit Pichon pour ses remarques scientifiques pertinentes.

Trois ans c'est long mais ça passe plus vite quand on s'amuse. C'est pour cela que je voudrais remercier mon binôme de labo/frère de chloroforme Mathias Dolci, mais aussi mon binôme de bureau Quentin Evrard qui ont eu à me supporter pendant ces trois années (qui ont dû paraitres longues pour eux). Merci à vous d'avoir rendu la vie plus drôle. Merci au « Bibele » Elodie Martin, à Florian Gellé, Francis Perton et la princesse Kubra pour ces pauses gâteaux.

Pendant cette thèse j'ai pu découvrir le monde de la biologie à l'INSERM grâce à Florent Meyer, merci pour ton encadrement. Un énorme merci à ma maman de l'INSERM, Christine Affolter qui m'a prise sous son aile pour me montrer toutes les ficelles de la culture cellulaire.

Je tiens à remercier toutes les personnes avec qui j'ai eu la chance de travailler : Corinne Petit et Secou Sall de l'ICPEES pour l'étude IR en température, Benoit Heinrich de l'IPCMS pour l'étude SAXS, Béatrice Uring-Lambert du Nouvel Hôpital Civil de Strasbourg pour la cytométrie de flux ma première supportrice dans le concours ma thèse en 180 secondes, Jean Marc Greneche de l'université du Maine pour tout le Mössbauer, Anne Boos et Pascale Ronot de la plateforme analytique du DSA pour les dosages, Gregory Francius pour l'AFM phase liquide, Christophe Lefevre pour L'affinement des RX,Fadi Choueikani pour les mesures synchrotron, Jesus de la Fuente et Laura Asin pour l'étude *in vivo* de mes particules, Dris Ihiawakrim, Simona Moldovan et Ovidiu Ersen de l'IPCMS pour les manips TEM in situ, toute l'équipe de Sophie Laurent à L'université de Mons pour leur accueil et toutes les mesures de relaxométrie. Un grand merci également à l'équipe de Delphine Felder-Flesch, Catalina Bordeianu, Audret Parrat, Sebastien Piant pour la synthèse de la molécule dendron sans qui je n'aurais pas pu explorer les propriétés théranostiques de mes objets.

Merci tout plein à Cedric Leuvrey de l'IPCMS pour le temps qu'il a passé a imager mes premières nanoparticules (et qui a passé des après-midi à imager des particules qu'aucun microscopiste ne devrait imager) mais aussi à la fée de l'administration Sylvie Maingé qui est la seule personne à ma connaissance qui comprenne toute la paperasse.

Merci au DCMI pour la bonne humeur, les conseils et les barbeucs avec mention spécial à Anne Carton et Emilie Delahaye pour toutes ces fois où j'ai bloqué la porte du diffracto.

Merci aux anciens doctorants et post docs de l'équipe Walid Baaziz, Xiaojie Liu, Yu liu et Aurélie Walter qui m'a tout appris sur la synthèse et la fonctionnalisation des nanoparticules. Merci aux stagiaires que j'ai eu la chance d'encadrer et qui ont participé aux travaux présentés dans ce manuscrit : Emilie Hailin, Elodie Schunder et Valentin Begin. Merci à mon successeur, mon petit ~~frère~~ frach Francis Perton pour l'aide que tu m'as apporté pendant la rédaction. Je finis cette thèse l'esprit tranquille en sachant que tu feras évoluer et progresser ce sujet.

J'ai eu la chance pendant cette thèse de participer à l'aventure ma thèse en 180 secondes, et je voudrais remercier l'équipe du jardin des sciences de Strasbourg pour leur accompagnement dans ce projet.

Un dernier merci à ceux qui m'ont permis de m'évader ce cette thèse de temps en temps : Nelson, Adrien, Maeva, Noémie, Colombine, Marion et Jean Marc. Sans vous je n'aurais peut-être pas tenu ces trois ans. Et bien sûr, merci à mes parents, ma sœur et ma mamie pour votre soutient toutes ces années malgré que je n'ai pas toujours su bien vous expliquer ce que je faisais.

Table of abbreviations

Introduction

Table of abbreviations

ACAC	Actetylacetonate
AFM	Atomic force microscopy
AFM	Antiferromagnetic
AMF	Alternative Magnetic field
Bp	Boiling point
CA	Contrast Agent
Col	Columnar
D2-2P	Dendron molecule
DBE	Dibenzylether
DLS	Dynamic Light Scattering
DMSO	Dimethylsulfoxyde
DSC	Differential Scanning Calorimetry
DTG	Differential Thermogravimetric
EELS	
EHC	Enhancement Contrast Ratio
EPR	Electronic Paramagnetic Resonance
F(i)M	Ferro(i)magnetic
FACS	Fluorescence-Activated Cell Sorting
FBS	Fetal Bovine Serum
FC	Field Cooling
FSC	Forward-Scattered Light
ADF	Annular dark-field
HDD	Hexadecanodiol
HSt	Stearic Acid
ICA	Independent component analysis
ICP-MS	Induced Coupled Plasma - Mass Spectrometry
IONPS	Iron oxide nanoparticles
IR	Infrared
IS	Isomere Shift
Iso	Isotropic liquid
Lam	Lamellar
MH	Magnetic Hyperthermia
MRI	Magnetic Resonance Imaging
Ms	Saturation Magnetisation
NaOl	Sodium Oleate
NaSt	Sodium Stearate
NC	Nanocubes
NMRD	Nuclear Magnetic Resonance Dispersion
NO	Nanooctopods
NPl	Nanoplates
NPs	Nanoparticles
NS	Nanosphere
OA	Oleic acid

Oam	oleyamine
OD	Octadecene
OE	dioctylether
Ol	Oleate
PBS	Phosphate Buffer Saline
PCA	Principal component analysis
PEG	Polyethyleneglycol
QS	Quadripolar Displacement
RBF	Round bottom flask
ROI	Region Of Interest
SAR	Specific Absorption Rate
SAXS	Small Angle X-ray Scattering
SEM	Scanning Electron Microscopy
Si	Signal Intensity
SSC	Side-Scattered Light
St	Stearate
TD	Thermal Decomposition
TEM	Transmission Electron Microscopy
TGA	Thermogravimetric Analysis
USPION	Ultra small paramagnetic iron oxide nanoparticles
WHO	World Health Organisation
XRD	X-ray diffraction
ZFC	Zero field cooling

Introduction

Cancer is one of major causes of death in the world with 8.8 million deaths in 2015 according to WHO. Surgery, chemotherapy, and radiotherapy are the most common conventional therapies currently applied. However although much progress has been made in cancer treatment this last decade, new approaches are necessary at the same time for improving existing therapies or developing new techniques of treatment in order to minimise deleterious side effects and to increase the patient survival rates. Multifunctional biocompatible nano-objects represent the most challenging innovation in medicine able to revolutionise the field of diagnosis and therapy, named *theranostic*, for targeted treatment of cancer. Therefore there is currently a medical need to develop efficient nano-objects for cancer treatment. Image-guided therapy will be also crucial for the development of new treatments. Thus, the design of such nano-objects will allow real progress to achieve temporal and spatial site local therapy and imaging. Thus the future of nanomedicine lays in the development of multifunctional nanoplatforms which combine both therapeutic and multimodality imaging components and which also act locally in tumors to avoid side-effects.

Such theranostic nano-objects combining therapeutic action to multimodal imaging and providing image guided therapy (to monitor the effect of therapy by imaging) may get a boost with the emerging nanotechnology. Indeed the explosive growth of nanotechnology has brought challenging innovations in the synthesis of multifunctional nano-objects for medicine, able to revolutionize the field of diagnosis and therapy. The new or optimized synthesis methods actually developed pave the way towards materials design which will allow real progress to achieve local therapy with high resolution imaging.

Among attractive nano-objects, iron oxide based nanoparticles are promising thanks to their outstanding balance between magnetic properties, surface-to-volume ratio suitable for efficient functionalisation and proven biocompatibility. Indeed ultra small iron oxide nanoparticles are already commercially used as T_2 contrast agent for magnetic resonance imaging (MRI) and are of particular interest as biodegradable and non toxic nano-objects compared to other contrast agents families. The saturation magnetization of nanoparticles, their agregation state and the ability of the coating to diffuse water molecules are important parameters to provide a good MRI contrast. Iron oxide nanoparticles are also now developed for therapy by magnetic hyperthermia. When exposed to alternating magnetic fields of appropriate intensity and frequency, these nanoparticles release heat locally (where they are concentrated), which reduces the viability of cancer cells. The magnetic hyperthermia potential is demonstrated with the favorable recent results of the "nanothermotherapy" study in clinical phase II led by a German company *MagForce Nanotechnology* **(**hospital Charité in Berlin) and with its use to enhance the sensitivity of tumor cells towards chemio or radio-therapy, to trigger a thermally-induced release of drugs or to act on cell membranes. However, one of magnetic hyperthermia limitations is the low power heating of usual magnetic nanoparticles, requiring a local injection of large quantities of nanoparticles. There is thus currently a challenge for optimizing the heating power of magnetic nanoparticles. The amount of heat generated by nanoparticles is highly dependent on their structural and magnetic properties (high saturation magnetization and high magnetocristalline anisotropy). Given the clinical importance of the magnetic hyperthermia results, it is important to synthesise nanoparticles with improved performance in magnetic hyperthermia. However, optimisation is not yet well-understood and experimental results from nanoparticles systems vary significantly. As such, the constant improvement and development for better and more reliable nanomaterials is of key importance.

Today the chemical methods are the only ones able to address properly the challenges in the elaboration of multifunctional nanoparticles. The ability of tuning the different structural parameters of nanoparticles makes them the methods of choice for designing nanoparticles for the different biomedical fields. Among currently promising iron oxide based nanoparticles synthesized by such chemical methods are those displaying higher anisotropy through their doping or their anisotropic shape. Indeed by playing on the NPs shape *e.g.* via the synthesis of cubic iron oxide NPs or flower-shaped nanostructures which enable cooperative magnetism the heating power was recently considerably improved. Thus synthesis methods are now optimized towards the tuning of the nanoparticle shape and composition.

Among current developed chemical methods, the thermal decomposition method which consists in the decomposition of a metal precursor at high temperature in a high boiling point organic solvent in presence of ligands have been shown to be among the most suitable to modulate the composition and the shape of nanoparticles. Decades of research have been devoted to investigate the role of the ligand or the solvent over the control of the nanoparticles size while the precursor has been considered as a metal atoms reservoir. Then nanoparticles with different shapes have been synthesized and especially cubic shaped nanoparticles which have been shown to display enhanced heating properties. However if the main parameters controlling the size are quite identified, those triggering the shape are not well understood as well as the shape formation mechanism. Another grey area is the thermal decomposition itself. Understanding the thermal decomposition process would also lead to major breakthroughs in the understanding on the formation mechanism of the NPs in order to be able to properly design NPs (shape/size/composition) to meet the challenges set by nanomedicine.

Finally, this field is now confronting also to another problem as large amount of nanoparticles are more and more needed for *in vitro* and *in vivo* trials. The yield and the scale up of the synthesis methods are under scrutiny and the current challenges of the area.

In this context, the challenge of this PhD work was to identify and understand the relevant parameters in the thermal decomposition for the synthesis of anisotropic shaped iron oxide nanoparticles in order to get efficient heat mediators for therapy by magnetic hyperthermia combining contrast enhancement properties for imaging by MRI. During the first synthesis experiments by thermal decomposition, among important parameters to control the shape, we identify/discover one parameter which has been poorly investigated: the precursor. Indeed, the way the precursors decompose (kinetic, monomer nature …) is often left out and certainly because it can be very complex to investigate (as we will see later). Therefore we decide to synthesize our own precursor and to investigate the role of the precursor, which is poorly known/studied, in the synthesis mechanism.

In this work, the precursor studied will be iron stearate. Iron oleate is rather used in most of the reports but studies anterior to this PhD in our group showed that iron oleate was unstable with time contrarily to iron stearate. The iron stearate synthesis and study will be a large part of this work aiming at determining its role in the outcome of the synthesis. The role of the precursor will be studied in regard of the synthesis condition to identify the major parameters for the synthesis of anisotropic iron oxide nanoparticles. This has led us to analyse the proper mechanism of the formation of the nanoparticles which has yet to be unravelled. Therefore, the thermal decomposition method will also be looked at thanks to cutting edge characterisation techniques. To complete our knowledge, the synthesis of iron stearate will be extended to manganese and cobalt in order to determine if our synthesis method is generalizable. Part of this work will be also devoted to identify promising tracks for the scaled up production of iron oxide NPs.

Finally the better control of synthesis parameters allowed us to synthesize different anisotropic nanoparticles. They will be finely characterized and functionalized with dendron molecules which have been already shown suitable for in vitro and in vivo applications. Their efficiency for the diagnosis by MRI and therapy by magnetic hyperthermia will be then assessed.

This PhD work is divided into four parts that compose nine chapters.

The first part was logically devoted to establish a picture of the synthesis and characterisation of iron oxide nanoparticles for the targeted applications.

- In Chapter I, generalities on iron oxide nanoparticles and their magnetic properties will be presented. Their functionalization for biomedical applications and the challenges for MRI and magnetic hyperthermia will be introduced.
- In Chapter II, the main methods for iron oxide nanoparticles characterization will be described as well as the main characterization techniques used in this work.

The second part was centred on the precursor and the thermal decomposition process.

- In Chapter III, the *in house* synthesis of the iron stearate precursor will be presented as well as a comprehensive study of its structure and thermal decomposition according to its structure and hydration degree. Experimental and modelling will be combined in order to define what in the precursor matter for its decomposition.
- Chapter IV will focus on the *in-situ* investigation of the first steps of thermal decomposition. Various fine characterisation methods such as liquid AFM or TEM in liquid cell will be combined to begin the unveiling of the NPs formation mechanisms. The role of the structure of the precursor will be central in this chapter as well.

The third part was devoted to the optimization of the syntheses processes and the expansion to other metals.

- Chapter V, will at first present the scale up of our precursor synthesis method and then will explore various route to improve the thermal decomposition process in an industrialization perspective. The synthesis of iron stearate will be then expanded to that of manganese and cobalt stearates. Their decomposition into nanoparticles will be realized and the resulting nanoparticles will be compared to the literature.

Finally, the fourth part will investigate the synthesis and characterization of anisotropic nanoparticles, their functionalization and their potential for MRI and magnetic hyperthermia.

- In Chapter VI, the role of the precursor structure and hydration degree in regard of the synthesis conditions will be screened in order to synthesize anisotropic irons oxide NPs.
- Chapter VII will focus on the fine characterization of the structural and magnetic properties of the anisotropic shaped obtained in chapter VI before and after their dendronization.
- Chapter VIII will demonstrate the potential of our shaped nanoparticles in diagnosis with MRI. The link between shape – properties for the MRI contrast agent application will be discussed. The *in vivo* bio distribution will be presented.
- Chapter IX will assess the heating power of the previous anisotropic NPs with magnetic hyperthermia. The cell internalisation regarding the shape of the NP will be addressed and flow cytometry will check the cell internalisation. *In vitro* and preliminary *in vivo* magnetic hyperthermia experiments will be discussed.

After the bibliography in chapter I and material and methods in chapter II, the chapters III to IX have been structured on the model of publications, including a state of the art of each topic in the introduction of each chapter, to favour their fast submission.

Chapter I

Introduction to functionalized iron oxide nanoparticles for magnetic resonance imaging and magnetic hyperthermia

I Introduction to functionalized iron oxide nanoparticles for magnetic resonance imaging and magnetic hyperthermia

I.1 Generalities

I.1.1 The iron oxide spinel structures

Iron oxide is a general term as it exists various phases of iron oxide. As the applications often demanded high magnetic properties, the choice of the community went on the magnetite Fe_3O_4 phase as it presents the highest saturation magnetisation (92 emu/g)[1]. Nevertheless, magnetite is easily oxidized at the nanoscale in maghemite γFe_2O_3 that presents a lower saturation magnetisation (74 emu/g). This means that the iron oxide phases have to be closely monitored in order to control/understand their magnetic properties.

The most studied iron oxide phases are the magnetite and maghemite phases. Magnetite is an inverse spinel: $Fe^{3+}_A[Fe^{2+}Fe^{3+}]_BO_4^{2-}$. Magnetite and maghemite crystallize in the same inverse spinel structure (Figure I.1) with the general formula AB_2X_4 with the associate space group Fd-3m. The iron cations get in the different interstitial sites with an eighth of the tetrahedral sites A and half of the octahedral sites B occupied. With iron cations inside a FCC lattice formed by the O^{2-}. The primitive cell is made of 8 AB_2X_4 units.

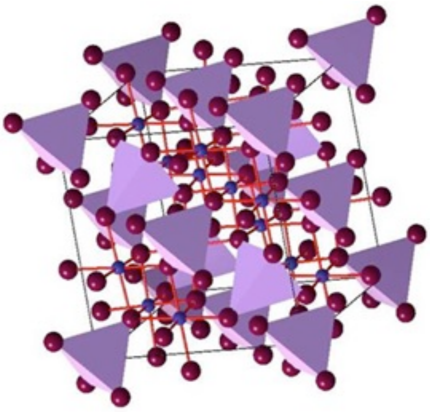

Figure I.1 - The inverse spinel crystallographic structure

However at the nanoscale, the Fe^{2+} ions at the surface of magnetite are very sensitive to oxidation[2–10]. The oxidation of Fe^{2+} into Fe^{3+} is accompanied by vacancy formation ($\square$), giving the general formula $Fe^{3+}_A[Fe^{2.5+}_{2-6\delta}Fe^{3+}_{5\delta}\square_\delta]_BO_4^{2-}$. The complete oxidation corresponds to $\delta = 1/3$ and leads to maghemite γ–Fe_2O_3. The XRD patterns of magnetite and maghemite are very similar and the lattice parameter are very close which makes it difficult to discriminate between magnetite and maghemite. Magnetite displays conductive properties and a saturation magnetization larger than that of maghemite.

As the maghemite is the oxidized form of the magnetite, all the iron cations are present under the Fe^{3+} form. This generates the formation of cationic vacancies in order to have a charge balance. The developed equation is written as follows $Fe^{3+}_A[Fe^{3+}_{5/3}\square_{1/3}]_BO_4$. Depending on the condition of maghemite formation, the vacancies can be organized in the lattice resulting in a reduction of the symmetry (cubic $P4_332$ or tetragonal $P4_32_12$), or completely disorganized[11–13]. In the latter case there won't be symmetry change and the maghemite will remain in the Fd-3m space group.

Altough the maghemite X-Ray diffraction (XRD) pattern presents surstructure peaks (210) and (211) when vacancies ordering occurs (cf. Chapter II, Figure II.4), their low intensity can make them hard to observe due to the background noise that can be important with nanosized iron oxide. In such a case and in the case of completely disorganized maghemite, a problem arises when it comes to its differentiation with magnetite. Indeed, as they belong to the same space group, the X-ray diffractograms present the same peaks slightly shifted due to the small lattice parameter difference (Table I.1).

Table I.1 - Lattice parameter of magnetite and maghemite

	Maghemite	Magnetite
Lattice parameter (Å)	8,351	8,396
JCPDS file number	39-1346	19-629

Infrared spectroscopy allows a better distinction of these two phases as the chemical environment of the Fe-O bond is different between magnetite and maghemite. Indeed the IR spectra of stoichiometric magnetite display one peak at around 570 cm^{-1}, whereas the IR spectra of maghemite displays several bands between 800-400 cm^{-1} which number and resolutions depends on the structural order of vacancies in maghemite (cf. Chapter II, Figure II.5)[7,14,15]. But this is most of the time not enough to characterise each phase. Indeed, to measure the stoichiometric deviation δ of the magnetite $Fe_{3-\xi}O_4$ other techniques must be employed. Mössbauer spectroscopy is a priori the most adapted method to evaluate the exact deviation from stoichiometry δ in $Fe_{3-\delta}O_4$.[16] This technique is sensitive to the oxidation degree, chemical environment of iron and can determine the ratio Fe^{2+}/Fe^{3+}.
All the main characterisation techniques of the iron oxide NPs are discussed in detail in chapter II.

I.1.2 Magnetism of iron oxide

I.1.2.1 Notions of magnetism

Magnetism can be described at three levels:

- The formation of a magnetic moment at the atomic level (atomic moments)
- The apparition of a magnetic order from the interaction between the atomic moments
- Interactions with the crystal field that induce a magneto-crystalline anisotropy, i.e. the magnetic moment tend to align along a specific crystallographic direction.

The magnetic moment μ can be described as a dipole that will tend to align itself in a defined direction under the influence of an external magnetic field. This phenomenon generates a magnetisation M defined as the magnetic moment per unit volume. The maximum of magnetisation named magnetisation saturation M_s is an essential characteristic of a magnetic material. Another parameter is the magnetic susceptibility χ that defines the inclination of the material to align its magnetisation with an applied magnetic field H.

Three magnetic behaviours are observed:

- Diamagnetism, present in any substances, that presents a χ weak and negative, no spontaneous magnetic organisation.
- Paramagnetism is defined by systems presenting non paired spins and for which χ is positive, no spontaneous magnetic organisation.
- Ferromagnetic, defines a system with a spontaneous magnetic organisation even without an external magnetic field.

I.1.2.2 The ferromagnetic class

As described before, the ferromagnetic class presents a spontaneous magnetic organisation. This comes from the alignment of magnetic moments owing to a strong interaction named exchange. Three kinds of alignments can occur under a critical temperature giving rise to three classes:

- Ferromagnetism: parallel alignment that occurs below Curie temperature (T_C).
- Ferrimagnetism: non compensated anti parallel alignment that occurs below Curie temperature.
- Antiferromagnetism: compensated anti parallel alignment that occurs below Neel temperature (T_N).

Above Curie and Neel temperatures, thermal fluctuations remove the magnetic order. The material will lose its spontaneous magnetisation and will be seen as paramagnetic.

I.1.2.3 Magnetism of magnetite

In magnetite, magnetism comes from the the presence of both Fe^{2+} and Fe^{3+} in the same site (octahedric). An electronic transfer from Fe^{3+} site to Fe^{2+}site is then possible du to the unpaired electron in the t_{2g} orbital of one of the Fe^{2+}. This electron is able to jump in a same symmetry orbital of its Fe^{3+} neighbour. This delocalisation favours a ferrimagnetic order. Fe^{3+} ions carry a total moment of 5 μ_B and 4 μ_B for the Fe^{2+} ions. The magnetic structure of magnetite can be represented as the following Figure I.2.

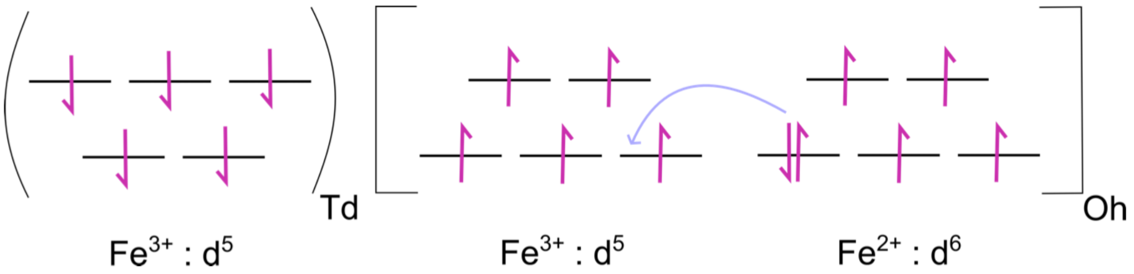

Figure I.2 – Representation of exchange interactions between iron cations in octahedral sites (Oh) and tetrahedral sites (Td) for magnetite[17].

The ions in the tetrahedral site are not involved in this transfer because the energy of their orbitals doesn't allow their hybridation. We observe an antiferromagnetic coupling between the total moment of the octahedral and tetrahedral sites. The moment of $\mathrm{Fe}^{3+}_{\mathrm{Octa}}$and $\mathrm{Fe}^{3+}_{\mathrm{Tetra}}$ will compensate. The total moment of the magnetite unit will be determined by the moment of the Fe^{2+} ions thus 4 μ_B. The remaining magnetisation is proportional to this total moment and is 92 emu/g for the bulk magnetite.

For the maghemite, the interactions between tetrahedral site and octahedral sites are predominant over the coupling intra site. The overall moment is then $({}^{5}/_{3} * 5\mu_B)$ - $5\mu_B = 3.33\ \mu_B$ leading thus to a saturation magnetisation of 74 emu/g for the bulk.

I.1.3 The superparamagnetic behaviour

I.1.3.1 Origin of superparamagnetism

At the bulk scale, magnetic materials display a structure made of magnetic domains called Weiss domains separated by walls named Bloch walls. This structuration minimizes the internal energy of the material. When the size of the sample decreases (Figure I.3[18]), the number of domains decreases to a single domain under a critical radius R_C. Below R_c the creation of Bloch walls becomes unfavourited as its creation requires an energy γ.S with γ the surface energy and S the surface of the wall. This energy becomes too important for small particles when the ratio S/V becomes too high (V being the volume of the NP). The NP is then made of a single magnetic domain and is called "monodomain".

Monodomain NPs present a magnetisation oriented along a specific direction (named easy magnetisation axis) stable through time at room temperature. The magnetisation hysteresis is opened with a coercitive field H_C and a residual magnetisation M_R (Figure I.3 a[19]). R_C for magnetite and maghemite is around 30 nm[20,21] but will vary with the synthesis process.

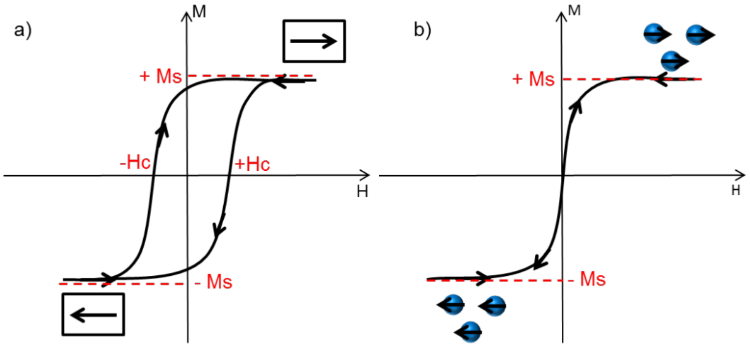

Figure I.3 - Evolution of magnetic properties with size decrease: a) ferrimagnetic behaviour, b) superparamagnetic behaviour

Now if we focus on a monodomain magnetic particle with an uniaxial anisotropy. If no external field is applied, the two possible direction of the magnetisation along the easy magnetisation axis will have the same energy. They are separated by an energy barrier E_B = KV with K the effective anisotropy constant and V the volume of the particle (Figure I.4[17]).

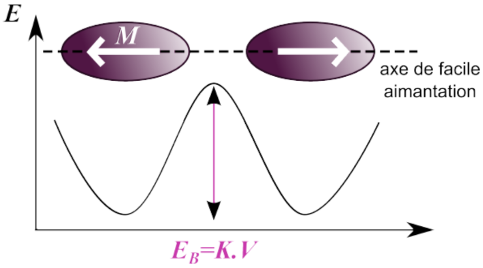

Figure I.4 - Representation of the two possible orientations of the magnetisation along the easy magnetisation axis and of the energy barrier that separates the two states

At low temperature, the thermal energy E_T (E_T = kT, with k the Boltzman constant and T the temperature) doesn't allow to overcome this barrier. The magnetisation is frozen in one direction. The particle is seen as ferrimagnetic.

But if the size of the particle decreases, the volume will then decrease and at a precise radius $R_{S,}$ the thermal energy will be higher than the barrier energy. The magnetisation can then flip randomly because of the thermal energy at room temperature and no permanent magnetisation can be measured. This phenomenon is called superparamagnetism. The magnetisation cycle will be closed without H_C or M_R (Figure I.3 b).

The values of saturation magnetisation of magnetite are reported in litterature between 30 and 68 emu/g (against 92 emu/g for the bulk) depending on the size and NPs synthesis methods. These variations can be explained by the nanosize and/or defects induced by oxidation and/or surface and/or volume spin canting in the NPs [22–26] and will be explained later on.

I.1.3.2 Magnetisation dynamics

We've seen that, for superparamagnetic NPs, the magnetisation is flipping because of the thermal energy. The characteristic duration of the barrier overcome is given by the Neel-Brown equation (Eq. I.1). This equation doesn't take into account the NP-NP interaction and give the time of relaxation τ named Neel relaxation.

$$\tau_N = \tau_0 exp^{\left(\frac{KV}{k_B T}\right)}$$ *Equation I.1*

With $\tau_0 \approx 10^{-9} - 10^{-11}$ s, K the effective anisotropy constant, V the volume of the NP and T the temperature.

Equation I.1 shows that τ_N increases with temperature or with the size of the NP. Then a superparamagnetic NP magnetisation can be frozen below a specific temperature T_B. This value depends on the acquisition time τ_m. Thus from equation I.1, T_B can be expressed as follows:

$$T_B = \frac{KV}{k_B ln\frac{\tau_m}{\tau_0}}$$ *Equation I.2*

This means that the effective anisotropy constant can be calculated from T_B and τ_m. As τ_m is typically 100 s for a squid measurement $ln\frac{\tau_m}{\tau_0} = 25$. Thus

$$KV = 25 k_B T_B$$ *Equation I.3*

This equation can only be used in the case of superparamagnetic NPs without dipolar interactions. Indeed, T_B is function of the material nature and the NPs parameter but also from dipolar interaction between NPs. Dipolar interactions between two NPs is a long range, anisotropic interaction that depends on the magnetisation of each NP and their distance. The more the dipolar interactions are important, the higher T_B is shifted towards high temperatures[27]. Nevertheless, in order to compare two types of NPs, the approximation that T_B is the maxima of the ZFC (Zero Field Cool) curve is made.

The magnetic measurements are detailed in chapter II.

I.1.4 The magnetic anisotropy

Several parameters of the material can induce magnetic anisotropy. Its energy tends to align the magnetic moments along a specific direction. Thus the anisotropy energy (E_A) can be written as the sum of the different contributions. The most common are the magneto-crystalline energy (E_{MC}), the shape energy (E_{Sh}). The surface energy (E_S) becomes non negligible at the nanoscale.

$$E_A = E_{MC} + E_{Sh} + E_S$$ Equation I.4

- Magneto-crystalline anisotropy finds its origin in the crystallographic structure of the material. More precisely from the crystal field that pairs the magnetic orbitals moments to the crystal lattice. It expresses the dependence of a monocrystal magnetisation to the direction of the applied magnetic field in relation to the crystallographic directions of this crystal. These directions along which the magnetisation of the material is eased are named easy magnetisation axis[28]. It can be written as a free energy with the following equation:

$$E_{MC} = K_1 V sin^2\theta + K_2 V sin^2\theta + \cdots$$ Equation I.5

With K_1 and K_2 the first and second order anisotropy constants, V the volume and θ the angle between the magnetisation and the eased magnetisation axis. The values of K_1 and K_2 for magnetite and maghemite are given in the table I.2.

Table I.2: Magnetocrystalline anisotropy constant of magnetite and maghemite

	K_1 (J.m^{-3})	K_2 (J.m^{-3})
Magnetite	-1.35.10^4	0,28.10^4
Maghemite	-2,5.10^4	Negligible

The MC energy is minimal when the field is aligned with eased magnetisation axis. The eased magnetisation axes are given by the sign of K_1 and the ratio $K_2/|K_1|$. For magnetite, the eased magnetisation axis are found along the $\langle 111 \rangle$ directions.

The equation I-IV can be simplified for a monodomain NPs with the first order term as follows.

$$E_{MC} = K_V V sin^2\theta \qquad \text{Equation I.6}$$

With K_V the effective anisotropic constant.

- Shape anisotropy: This anisotropy comes from the demagnetic field that is inhomogeneous in the anisotropic shaped samples. The magnetisation depends then on the orientation of the magnetisation with respect to the shape of the sample. The energy associated will be minimized is the magnetisation of the system aligns with the longest dimension of the sample. The expression of the energy is given in equation I.7.

$$\mathrm{E}_{Sh} = \frac{1}{2}\,\mu_0 \mathrm{V}\left(N_x M_x^2 + N_y M_y^2 + N_z M_z^2\right) \qquad \text{Equation I.7}$$

This anisotropy if is often dominant over the other ones as it commands the direction of the magnetisation at equilibrium without an external field.

- Surface anisotropy: This contribution occurs for nanosized system where the surface is no negligible anymore. It originates in a symmetry rupture of the surface atoms compared to the core atoms. Surface atoms have less close neighbours favouring an orientation of the magnetic moment perpendicular to the surface. The associated energy is given in equation I.A-VIII.

$$E_S = K_S V sin^2\alpha \qquad \text{Equation I.8}$$

With K_S the surface anisotropy, and α the angle between the magnetisation and the surface normal. This interaction increases with the ratio $Atoms_{surface}/Atoms_{core}$ thus with a decreasing size of the NPs.

From these points it's easy to understand that the magnetism of NPs will be driven by the equilibrium of these energies. Moreover, each energy will vary with temperature, applied field, shape and size of the NPs. All these will influence the magnetic properties of the NPs but also the dynamics of the magnetization reversal.

I.1.5 Role of structural defects on magnetic properties

I.1.5.1 Surface

When working at the nanoscale, surface of the object becomes non negligible as percentage of surface atoms increases for decreasing size. The Fe^{2+} ions on the surface are more sensitive to the oxidation leading to a surface layer of maghemite on the surface of the NP. This sensitivity towards oxidation will increase with decreasing size of the NP[4,9,10,29,30]. The combination of complementary characterisation methods (XRD, IR, Magnetic measurement, Mössbauer) done on various size NPs synthesized through thermal decomposition showed that for a diameter below 8 nm the composition of the whole NP is close to the one of maghemite (non stoichiometric over the whole volume). Above 12 nm, the NPs are made of a core of magnetite and an oxidized layer on the surface[4,9–11]. This oxidized layer has been estimated to few nm whatever the size of the NP[4,10,29,30]. For sizes between 8 and 12 nm, NPs show an important gradient of composition (Figure I.5). Similar results have been observed on NPs synthesized through coprecipitation[3].

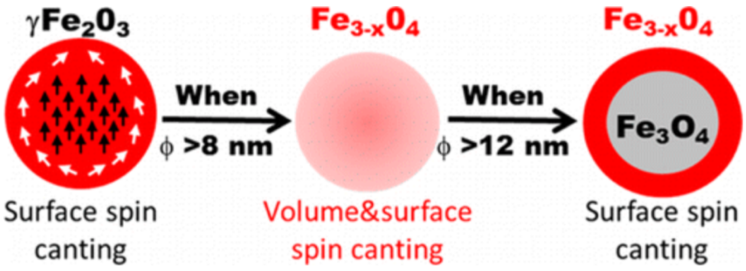

Figure I.5 - Evolution of magnetite NPs composition with the NP size[9]

Another effect of the surface is spin canting. It comes from the reduced coordination of surface atoms generating a local anisotropy. The magnetic moments tend to align perpendicularly to the surface[31–33] instead of along the applied magnetic field or along the eased magnetisation axis (when no field is applied). This will cause a decrease of the global magnetisation of the NP. This layer has been named “dead layer” as it doesn’t participate in the magnetisation of the NP. This layer has been experimentally seen with Mössbauer spectroscopy or with magnetic measurements with temperature[25,34,35]. Recently, Unni and al.[36] showed that introducing O_2 in the synthesis allows reducing this dead layer thus improving the magnetic properties.

I.1.5.2 Volume

Defects in the volume of the NP (vacancies, impurities or dislocations) will also have a detrimental effect on the NP magnetism. It has been reported that low temperature synthesis tends to generate NPs with magnetic properties more apart from bulk than synthesis at high temperature[22,37–39]. This difference is believed to come from the presence of crystalline defect more easily obtained at low temperature. Aside crystallographic defects, the composition disorder (meaning the distribution of Fe^{2+} and Fe^{3+} in the sites) is a major parameter. Indeed, changing the distribution of the magnetic ions will have an effect on the strength of the exchange interaction leading to lower magnetic properties[40,41].

The defects whether they are on the surface or in the volume have a major role on the magnetic properties. Thus they have to be identified and monitored. Chapter II will present with more details on the characterisation methods.

I.1.6 Conclusion

The inverse spinel phase of iron oxide, magnetite and maghemite are ferrimagnetic. Working at the nanoscale induces original superparamagnetic properties interesting for several applications. But the magnestism at the nanoscale is complex as magnetite tends to be oxidized at the surface and different defects may have a detrimental effect on the magnetic properties. These defects may depend on the synthesis conditions.

To improve magnetic properties of iron oxide NPs, shape and composition anisotropies are an interesting level that will be explored in this PhD project. NPs with different shape will be synthesized in order to enhance their magnetic properties. The next part will then focus on the main synthesis methods of iron oxide NPs.

I.2 The synthesis of iron oxide NPs

Remark : Parts of the next paragraphes have been published in two book chapters (Chapter 2 in Iron oxide nanoparticles for biomedical applications: synthesis, functionalization and applications, ed. Morteza Mahmoudi & Sophie Laurent, METAL OXIDE SERIES, Elsevier, 2018 and Chapter 4 in "Contrast agents for MRI", Serie: New Developments in NMR, Ed. Matthew J. Allen and Valérie C. Pierre, Royal Society of Chemistry, 2018) or in a paper (*Nanomedicine (Future Medicine) 2016,* Vol. 11, No. 14, Pages 1889-1910) to which I have contributed.

I.2.1 Overview

Iron oxide nanoparticles (NPs) generated a tremendous enthusiasm towards their synthesis among the years. The challenge is being addressed by chemist, physicist and biologist with more or less success. The most reported methods and their importance are represented in Figure I.6.

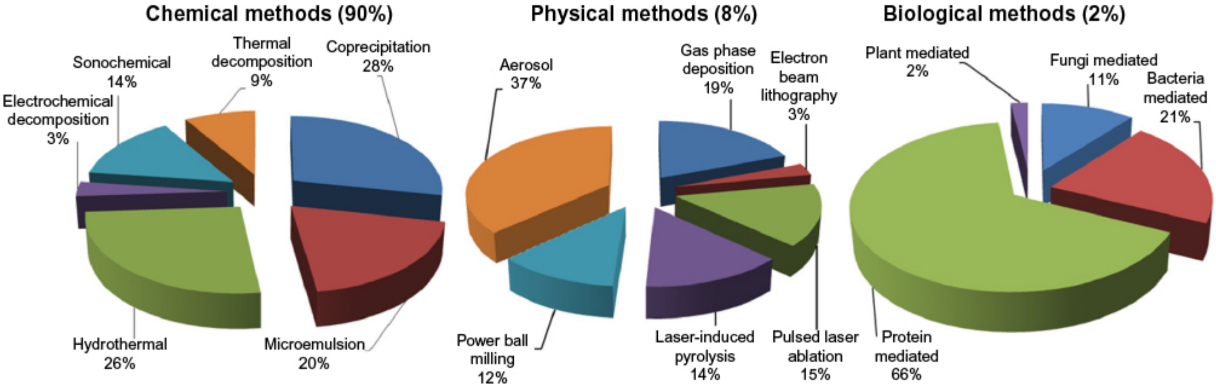

Figure I.6 - Most reported iron oxide NPs synthesis methods[42]

- Biological methods are a growing domain as the synthesis is completely green and already biocompatible after synthesis Nevertheless these methods are limited by the slow rate of formation of the NPs.
- Physical methods are also poorly represented as they require expansive equipments with weak control over the final product.
- Chemical methods are the most used nowadays. This area is more mature as it is the oldest.

Many methods have been created over the years but only few are now commonly used. These methods are with few exceptions based on a bottom up approach. Meaning that the iron oxide is assembled from atoms. This provides many possibilities toward the phase but also the shapes that can be synthesized.

Today the chemical methods are the only ones able to address properly the challenges in the elaboration of multifunctional NPs. The ability of tuning the different parameters of the nano object is making them the choice methods for designing NPs for the different biomedical fields. Yet this field is now confronted to another problem as large amounts of NPs are needed for *in vitro* and *in vivo* trials. The yield and the scale up of these methods is under scrutiny and the current challenge of the area.

I.2.2 The wet chemical synthesis methods

Many techniques have been developed to synthesize iron oxide NPs[43–47]. The advantages and drawbacks of the most reported techniques are presented in the table I.3.

Table I.3- Advantages and drawbacks of the most reported methods[47]

Method	Condition	T(°C)	Reaction Time	Solvent	Size (nm)	Size dispersity	Shape control	Yield
Coprecipitation	Very simple	20-90	Minutes	Water	< 20	Average	Average	High
Micoremulsion	Complex	20-50	Dozen of minutes	Water/Organic	< 50	Relatively narrow	Good	Poor
Polyol	Very simple	>180	Dozen of minutes	Organic	< 10	Relatively narrow	Really good	Average
Hydrothermal	Simple but high pressure	>200	Hours	Water – Water/ethanol	< 1000	Relatively narrow	Really good	Average
Thermal decomposition	Complicated	200-400	Hours	Organic	< 20	Narrow	Really good	High

The synthesis by coprecipitation is the easiest and most used method. NPs are formed with the addition of a base in acid aqueous solution of iron salts Fe^{2+} and Fe^{3+}. Those ions are soluble in acidic medium but precipitate when the basicity increases. This method main advantage is to produce a large amount of powder in water. Nevertheless, sized dispersity is not well controlled and the NPs tend to aggregate as they are « naked » as synthesized (no molecule on their surface to provide colloidal stability) in water.

Other methods have been developed in order to improve the control of the shape and size of the NPs such as microemulsion synthesis[48–50], hydrothermal synthesis[51] and the polyol synthesis[52–54] among many other. Since the 2000s[11,55,56], the synthesis through thermal decomposition quickly developed for the synthesis of iron oxide NPs. This method allows the synthesis of monodisperse NPs with a narrow size distribution and a good morphology control. Furthermore, the NPs are stable in organic solvents thanks to their *in situ* organic coverage during the synthesis. Therefore this synthesis method has been choosen for this PhD work and is thus more detailed below.

I.2.3 The thermal decomposition method

Thermal decomposition synthesis method (TD) for iron oxide NPs is based on the synthesis method of quantum-dots or semi conductor nanocrystals that have been developed and popularized in the 2000s[57,58]. It consists in the decomposition of a metallic complex in a high boiling point organic solvent (Figure I.7) with surfactants that will stabilize the as formed NPs. This method favours the formation of well crystallized NPs[59] functionalized with organic molecules providing colloidal stability in organic solvent. The TD is the most appropriate method to synthesize high quality NPs as it eases to the separation of nucleation and growth which is the key factor for obtaining NPs with a narrow size distribution.

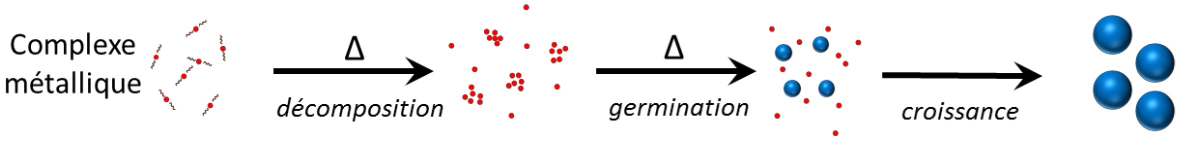

Figure I.7 Schematic representation of the TD synthesis[19]

Few precursors are commonly used for the TD, among them Fe(acac)n (acac = acetylacetonate)[55,56,60], iron oleate[10,11,61–65] or carbonyls Fe(CO)x[66,67]. There are two ways to do the TD of an iron complex. The first one is called « hot injection » and consists in the injection of the precursor in a solution of surfactant in a solvent at high temperature. This will abruptly decompose the metallic complex[59]. It is quite complicated to be reproducible with the hot injection method and it is not well adapted for scale up synthesis[68]. The second one is named « heating up » method. The precursor is solubilized at room temperature with the surfactant. Then the solution is heated till the solvent boiling point. With the increasing temperature, the precursor will decompose and release iron-based monomer leading to the sursaturation of the solution and thus to the nucleation of NPs.

The TD synthesis with the variety of variables offers a proper freedom towards the design of NPs to tune the size, morphology and composition. Nevertheless, this freedom comes with an increasing difficulty to understand and master the process. One must imagine the thermal decomposition as a spider web where each string is a parameter of the synthesis or of the NPs. As all are entangled it is quite difficult to tune one without having an influence on another. Yet for the ones that overcome these difficulties the TD synthesis limits to the imagination of the experimenter as described after.

I.2.3.1 Understanding NPs formation with thermal decomposition

I.2.3.1.1 General principle

The thermal decomposition method principle is quite simple. An iron source commonly called precursor is decomposed in a high boiling point solvent with the presence of a ligand. The role of the ligand is crucial as it will stabilize the NPs preventing their aggregation due to Van der waals and dipolar interactions. The precursor decomposition is induced through a stimulus which is heat for TD but other methods have been developed using different stimuli (ultrasound, microwaves …). The general scheme of NPs formation synthesis is shown in figure I.B-3.

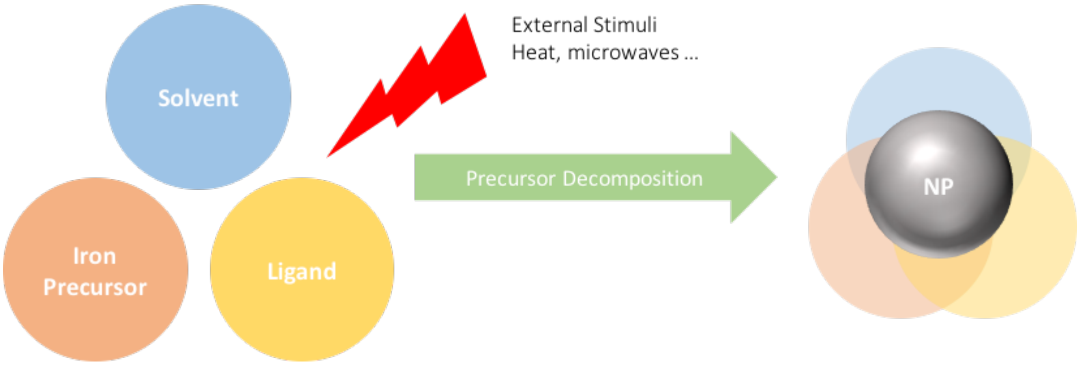

Figure I.8 - General principle of NPs formation in wet chemical synthesis in organic solvent

The steps between the beginning of precursor decomposition and the NPs formation are described by the nucleation/growth theory reported by LaMer[69] in 1950.

I.2.3.1.2 Lamer's Theory

LaMer theory[69] describes the nucleation/growth steps in solution. It has been successfully applied to the TD to understand the mechanism of formation of the NPs. Three major stages are observed (Figure I.9) during the NPs formation:

- Monomers generation.
- Nucleation after a critical nucleation concentration (C_{min}^{nu}) in monomer is reached.
- Growth after the monomer concentration goes below C_{min}^{nu} and stays above the saturation.

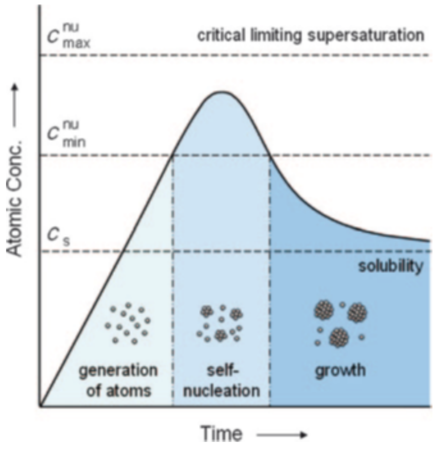

Figure I.9 - Variation of monomer concentration during nucleation-growth process. From Xia[70]

Most of the following paragraph are detailling the excellent work by Van Embden *et al*[68] and their theoretical calculation about the thermal decomposition processes.

i. Thermodynamics of the nucleation phenomenon

To understand how the NPs can be formed, it is necessary to understand the nucleation process. LaMer was the first to explain that in a closed system the nucleation becomes thermodynamically allowed if the free monomer concentration gets above a critical nucleation concentration. At this concentration the system is supersaturated and nuclei can start to form. Homogeneous nucleation begins with the formation of a new surface in solution. The free energy of the formation of a spherical NP is written as the sum of the bulk and the surface contribution. The surface contribution ΔG_S increases the free energy of the system: $\Delta G_S = 4\pi r^2\gamma$ with γ the surface energy and r the radius of the nucleus.

On the opposite the bulk term ΔG_B will reduce the total free energy: $\Delta G_B = \left(\frac{4\pi r^3}{3}\right)\Delta G_V$

With ΔG_V the Gibbs free energy per unit volume and is expressed as follows: $\Delta G_V = -\left(\frac{RT}{V_M}\right) ln\ S$ with R the gas constant, T the temperature, V_M the molar volume of the monomer and S the level of supersaturation defined as the ratio between the monomer concentration and the concentration of monomer in equilibrium with a flat surface.

Then the total free energy ΔG_T can be written as: $\Delta G_T = -\frac{4\pi r^3 RT \ln S}{3V_M} + 4\pi r^2\gamma$

The different energies can be plotted as function of the radius of the nuclei as shown in Figure I.10. This plot can be decomposed in two times. At the beginning for small nuclei when the surface to volume ratio is high the surface contribution is dominant and ΔG_T increases. It will rise up to a maximum with increasing radius and then decreases. This means that after the maximum the bulk term is predominant. When the surface energy is driving the system the nuclei formed are not stable and will dissolve into monomers.

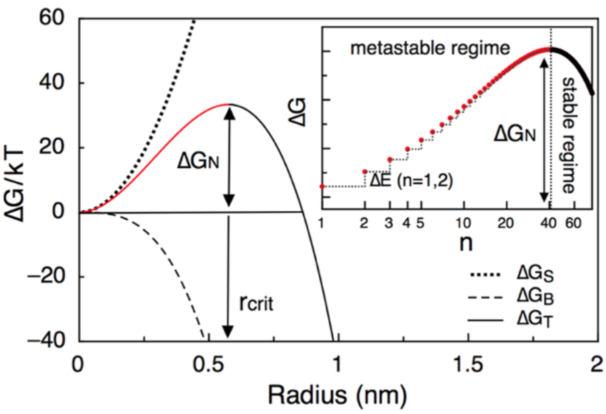

Figure I.10- Energy of the nucleation with the radius of the nucleus[68]

To get a stable nucleus an energy barrier needs to be jumped over to get to a bulk energy driven system. This energy barrier ΔG_N can be calculated as being the derivative of ΔG_T with r equals to 0.

$$\Delta G_N = \frac{16\pi\gamma^3 V_M^2}{3R^2T^2(\ln S)^2}$$

This expression can be used to calculate the critical radius r_C corresponding to the smallest stable nucleus.

$$r_c = \frac{2\gamma V_M}{RT\ln S}$$

ii. The conversion of the precursor into monomer

As explained before, the metallic complex decomposes and generates monomer during the first step of the NP formation. The monomer represents the basic unit to build the iron oxide lattice. Those species have been ascribed to intermediate “poly-ironoxo” clusters[2,71].

But, during the thermal decomposition synthesis, the conversion of the precursor (P) into monomer (M) is not instantaneous or total from the beginning. The rate of monomer formation has been expressed by Van Embden *et* al.[68] They assumed the conversion phenomenon as a first order reaction.

$$P \overset{k_f}{\rightarrow} M \qquad \text{with } k_f \text{ the formation rate}$$

The monomer formation rate is then defined as follows:

$$\frac{d[M]}{dt} = -\frac{d[P]}{dt} = A\exp\left\{\frac{-E_A}{RT_V}\right\}[P]$$

with A the prefactor, E_A the activation energy (related to the magnitude of the ligand binding coefficient) for the precursor decomposition or disassociation and T_V the solution temperature at a given time.

This equation gives precious information that is that the precursor to monomer conversion increases exponentially with temperature.

iii. The nucleation of nanoparticles

To explain the nucleation, LaMer considered that when the monomer concentration rose above a minimal nucleation concentration C_{nuc}^{min}, germination could occur. This step would stop when the monomer concentration after being consumed in the formation of nuclei go under this concentration. This is a fundamental step as it will dictate the size of the NPs and their size distribution. The nucleation has been observed around 250 °C for iron carboxylate complexes such as iron oleate and stearate[2,9]. This temperature matches with the first weight loss observed on the thermogravimetric (TGA) curves realized on these complexes. The separation between the nucleation and growth phases is the key point for the formation of NPs with a monodisperse size.

The separation of the germination and growth phase allows to generate a large amount of germs that is followed with the homogeneous growth without the creation of new germs [9,71]. This leads to a narrow size distribution. The expression of Van Embden nucleation rate is given in the following equation:

$$\frac{d[N]}{dt} = 8\pi r_m D N_A S^{pu+1}[M_\infty]^2 \exp\left\{\frac{-\left(4\pi r_m^2 p^{2/3}\gamma\right)}{k_b T_V}\right\}$$

Thanks to this equation, they've been able to look at the influence of the major variables on the nucleation (Figure I.11).

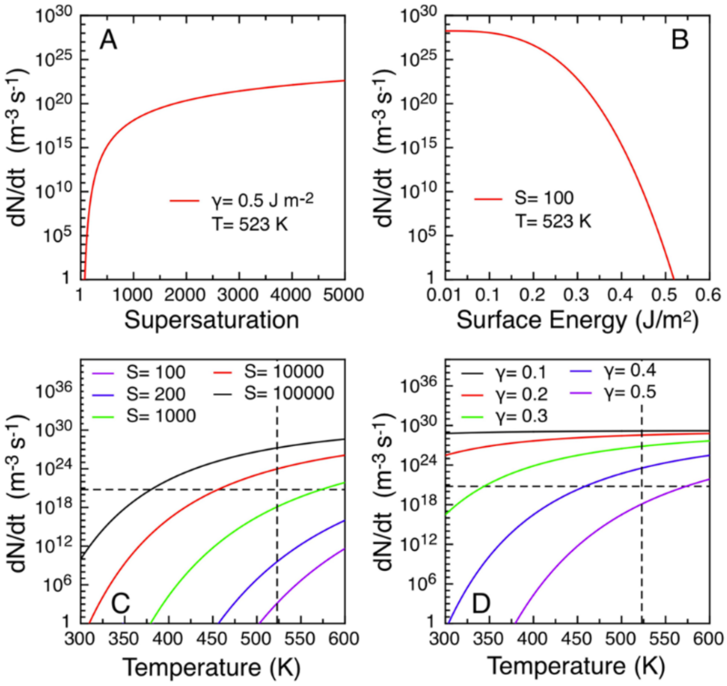

Figure I.11- Influence of various parameters on the nucleation rate of the NPs. A) Supersaturation, B) surface energy, C) Temperature and surpersaturation, D) Temperature and surface energy

Those simulations show several valuable inputs.

- Nucleation rate increases rapidly with the sursaturation level. Meaning that for highly supersaturated systems more nuclei will be formed leading to smaller NPs size after growth.
- Nucleation for a given sursaturation is unfavoured for increasing surface energy value. This means that some materials will be harder to synthesis but mostly that some crystallographic planes could be favoured if their surface energy is lower. Also stabilizing the surface by reducing its energy will promote the formation of nuclei.
- Temperature does have a central role but its influence can be diminished due to small surface energy. As it can be imagined low sursaturation is harmful for the nucleation despite using high temperature. This means in a first time that at low precursor concentration nucleation could not occur at all. In a second time it is clear that a precursor that converts more easily in monomer will (at a given temperature) generate more nuclei than a very stable precursor.

Monomer concentration is as shown before function of the precursor stability. Its stability relies on the ligands nature, their amount, the solvent nature and the temperature treatment applied[9]. On top of that the ligand and solvent can also interact with the surface of the nuclei modifying their surface energy influencing the process.

iv. The growth of the NPs

The growth of NPs is quite simple compared to the nucleation phenomenon. The remaining monomer after nucleation or still forming will diffuse towards the surface and get incorporated in the bulk of the NP. As this phenomenon is an equilibrium, the NP can also dissolve and release monomer. This case is not favoured as long as enough monomer keeps forming. But at the point when no or few monomer is formed, the smaller NPs will dissolve and the monomer will depose on the bigger NPs leading to a narrowing of size distribution. This phenomenon called Ostwald ripening allows obtaining a NPs good size distribution. The whole phenomenon of NP formation is summarized in Figure I.12.

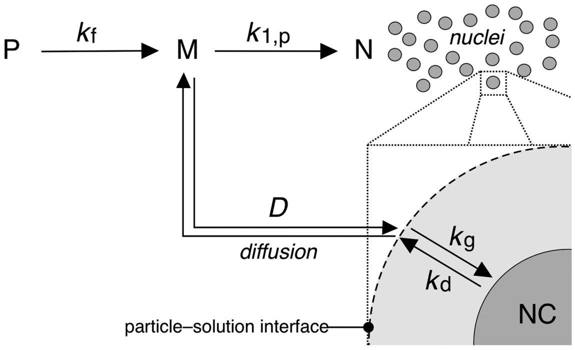

Figure I.12- Representation of the formation of NPs in TD

I.2.3.2 Controlled synthesis of NP with TD

I.2.3.2.1 Size and size distribution control

i. Size control

As discussed before, the final size of the NPs is determined by the nucleation step and the number of germs formed. As the system is closed, once nucleation occurred, the remaining monomers will act as a reservoir for the growth phase. It has been shown with theory that the key point for nucleation is the conversion of the precursor into monomer. As the rate of monomer formation (RMF) is increasing exponentially with the temperature, the temperature is a major parameter and is bounded to the solvent. Usually the solvents used in the TD are chosen among alkenes as they offer a large range of boiling point depending on the length of their chain and are considered as more “inert”. The higher the temperature, the more efficient the decomposition of the precursor will be. This means that, at high temperature, monomer will keep forming during the growth phase leading to bigger NPs this has been confirmed by constant monomer supply experiments[72]. The temperature is thus the first lever for the size control. This has been experimentally observed for iron oleate or iron stearate. The NPs size increases with the solvent boiling point[9–11]. As the iron precursor is decomposing on a large range of temperature[9,71], at the highest temperature the most monomers are formed then the NPs are bigger. But the final size depends also on the solvent nature and not solely on its boiling point[9]. The nature of the solvent might not be the first parameter that comes to mind but, depending on its chemical properties, it will be able to interact with the precursor hence affects the RMF. A polar solvent such as hexadecanol stabilizes more likely the complex that decomposes at higher temperature and leads to smaller NPs. On the opposite, octylether (that has about the same boiling point as hexadecanol) stabilizes less likely the complex leading to bigger NPs.

The heating rate to reach the growth temperature is probably more important than the boiling temperature[68]. If this rate is chosen slow (typically 1°C/min), the RMF will be slow as well. Once enough monomer is formed nucleation will occur as precursor keeps converting slowly. This case will give fewer nuclei but could also lead to a second nucleation during the heating. With a high rate (10 °C/min) lot of monomers will be formed quickly exceeding the minimal amount of monomers needed for the nucleation. More nuclei will be formed compared to the slow rate and less monomer will remain for the growth. Also the nucleation is quicker for high heating rates (all the monomer needed is available) the size distribution will be smaller.

The second parameter that has been extensively studied concerns the ligand. Experimentally the ratio ligand/precursor influence has not clearly been established and seems to depend on the precursor nature. Demortiere et al. have observed an increase of the size with with an increasing ratio for the iron oleate[10]. While Bronstein *et al.*[73] observed a decrease then an increase and again a decrease of the NPs size with an increasing amount of oleic acid with the same precursor. Vargas *et al.*[74] reported a decrease of the size for the synthesis with $Fe(acac)_3$ when Meledandri *et al.*[75] observed an increase of the size in the same condition. The influence of this ratio is still not well understood and is investigated.

The nature of the ligand is another example. While the carboxylic acid ligand has non evident effect on the size, amines reduce the size significantly. In fact, amines would ease the decomplexation of the oleate and stearate coordinated on the iron by reacting with the carboxylate[76]. This helps the decomposition thus the formation of monomers and the germination[9]. Actually the carboxylic acid ligand influence could be quite complex as it can stabilize the precursor thus having an effect on the RMF. But it can also interact with the newly formed nucleus stabilizing its surface and thus favouring the nucleation. This implies that a ligand can have at the same time a harmful and a beneficial effect on the nucleation and hence on the NP size.

Nonetheless what has to be underlined is that all these parameters will mostly have an effect on the RMF. Thus one parameter that has to be taken into account is the stability of the iron precursor itself. Bronstein et al.[77] showed that the decomposition temperature of the precursor is a major parameter for the size control and that iron oleate decomposition can be different depending on its synthesis and purification conditions. The purification and the drying have been identified as major parameters[64,77]. The decomposition mechanism is also quite sensitive to the amount of molecules coordinated to iron atoms: the nature and quantity of ligands in the reaction have an effect on the precursor. Germination and growth are modified leading to different size NPs[64,77].

Not to forget the simplest way: increasing the duration of the growth step[67,78]. That can be explained by two mechanisms. The first one being that the longer the reflux the more monomer will form (of course this point is valid in the sole case where non decomposed precursor is still present in the reaction). The second one is named “Ostwald ripening”, in this mechanism the smallest NPs (that present the higher surface/volume ratio and hence the higher surface energy) dissolve and the monomer created will participate to the growth of bigger NPs. One has to be careful though as the shape of the NP can evolve through time but this point will be addressed later on.

ii. Size distribution control

The size distribution of NP is a parameter that has to be carefully monitored. As shown in the previous paragraph the inhomogeneity can come from multiple nucleation steps or if the nucleation step is not quick enough.

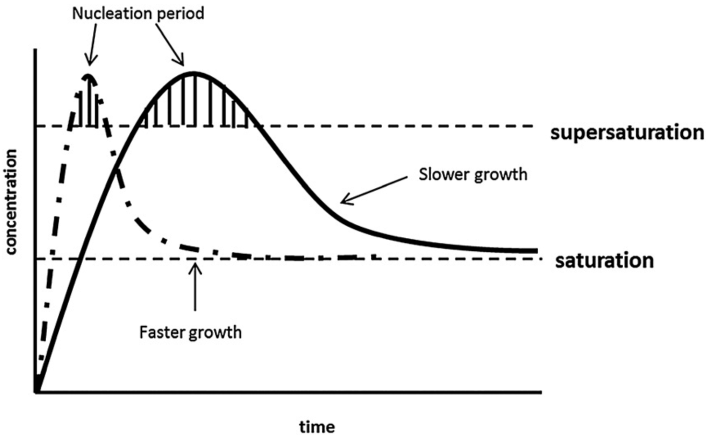

Figure I.13- Representation of the nucleation length effect on the growth of NPs[79]

Experimental parameters have then to be precisely controlled. For example, one has to be careful that the temperature inhomogeneity inside the reactional volume is minimal. Indeed, the presence of hot spots can lead to local nucleation ahead of the general nucleation in the whole volume.
Another inhomogeneity to be controlled is found in the precursor especially for carboxylate complexes. As iron oxidation degree can vary, one can imagine that a product thought to be homogeneous be in fact a combination of several complexes. This distribution in complexes each with specific thermal stability will favour several nucleation steps (depending if the stabilities are different enough). Lastly the Ostwald ripening is also a way to narrow the size distribution.

I.2.3.2.2 Composition control

The composition control can relate to two different situations:

i) The NPs oxidize during its formation: the main example of this problem concerns oxidation of magnetite ($Fe_{3-x}O_4$) when the composition might change due to the size of the NP. A layer of magnetite partially oxidized on the surface[10,27,77,78] can be observed and this point has been discussed in I.A.5.1.

In other experimental conditions, it has been observed that NPs can be composed of a core of wüstite FeO with an oxidized shell[61,62,64,73]. Actually, the thermal decomposition of iron (III) oleate with sodium oleate and oleic acid gives rise to reducing conditions favouring the formation of $Fe_{1-x}O$[80]. The formation of a shell of $Fe_{3-x}O_4$ is caused by the oxidation of the $Fe_{1-x}O$ core with time. It has been reported that oleate species favour a reducing environment explaining the $Fe_{1-x}O$ core. The reducinf environment is also ascribed to alkenes at high temperature.

ii) The inhomogeneous composition in doping elements in NPs that can be observed sometimes when one tries to elaborate mixed ferrites MFe_2O_4 (M= Zn, Mn, Co, Ni …).

Mixed ferrites are of a grand interest as replacing some Fe cations with another transition metal can improve the magnetic properties of the NP. For example, Mn and Zn have been identified as increasing the M_S value[81,82] while Co increases the H_C due to the spin-orbit coupling effect that will increase the magnetocrystalline anisotropy[82]. In both cases doping is efficient up to a limit amount of doping element that will hinder magnetic properties. Then it is easy to understand how doping can be a crucial point in the design of tailored NPs. Previous works have been realised[55,56,83–85] by combining two precursors (often $M(acac)_n$[55,56,60]) with the desired elements wanted. Nevertheless, work still needs to be done for better mastering the doping of ferrite with TD.

TD is not the best method choice for doping because of one simple point: the temperature of decomposition of the precursors which may be different. It has been explained that during the TD process, the nuclei form using available monomer. If during germination only one monomer (of one metal) is present, it is most likely that the nuclei will be made of the oxide of this sole element. Then depending on the temperature of formation of the monomers of the other elements two outcomes are possible:

i) If the decomposition T difference is small → a gradient of composition with an elemental ferrite at core and an increase of the % of the doping element along the diameter[40,86].

ii) If the T difference is large → a core-shell structure made of two different oxides with an interfacial doped layer.

The second case is yet interesting. As the combination of two different materials can lead to original magnetic properties, core-shell NPs may be synthesized by a method named « seed mediated growth ». The NPs synthesis is split in two times. First NPs of the core material are synthesized and then the growth of the second material at the surface of the core is started. The use for the shell of a precursor with a higher thermal stability than that of the core favours its growth at the surface of NPs and limites the risk of inducing the nucleation of NPs of the shell material. The method is represented in Figure I.13. This method has permitted the synthesis of different types of core-shell structures such as $MFe_2O_4@MFe_2O_4$[87] with M=Co, Mn, $Fe_3O_4@MnO$[88–91]. Interestingly this method can also be used to increase the size of NPs by growing a shell of the same material on the core.

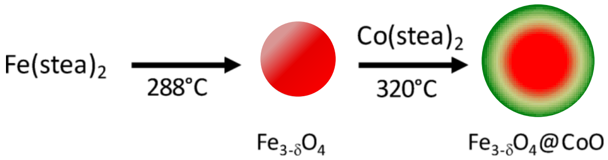

Figure I.13 - Schematic representation of the seed mediated growth method for the synthesis of core-shell $Fe_{3-x}O_4@CoO$ *NPs*[92]

This method allows to go further with the synthesis of onion like NPs with several layers of different materials to tune the magnetic properties[88]. This approach, while being an interesting tool for the design of NPs, does not solve the problem of heterogeneous doping. To remedy that, it is needed to use two precursors that form monomers around the same temperature[68]. Using precursors of different nature is an idea but it could be problematic for shape control as the ligands liberated during the reaction will affect the shape at it will be discussed in the following part. Nevertheless Bazziz *et al.* succeeded in synthesizing cobalt ferrite NPs with a more homogeneous Co distribution by replacing oleic acid ligand by hexadecylamine which has helped to decompose the cobalt stearate precursor which presented a higher thermal stability that the iron stearate one[93]. Another idea is to work on a "family" of precursor to tune their decomposition temperature.

I.2.3.2.3 Shape control

To improve the magnetic properties, i.e. the saturation magnetization or magnetic anisotropy by keeping a superparamagnetism behavior, the NPs size increase is limited as the supermagnetiism behaviour will disappear above a given limited nanometric size in the range 20-30 nm for iron oxide NPs. Then to improve the magnetic properties while keeping the superparamagnetic behaviour increasing the anisotropy energy is a strategy. So synthetizing anisotropic shapes should lead to superparamagnetic NPs with higher magnetic properties. One of the principal advantage of the TD synthesis is that the control of the shape is "eased". Many parameters have been studied and several shapes have already been obtained. Cubes (Table I.4), truncated octahedra[94], tetrapods[95] or platelets[96,97] have been reported. Nevertheless, the shape control is not trivial and the protocols reported are often poorly reproducible.

i. Theory

Shape of the nucleus: to understand how to form anisotropic shapes, the nucleation theory detailed above has to be completed. It has been discussed that nucleation can be tuned in many ways (nature of solvent, precursor and ligands, their amount, heating rate, temperature..) and that has a major influence on the NPs size. However these parameters may also affect the shape of the nucleus. Different kinds of nuclei can be obtained depending if they are formed with thermodynamic or kinetic conditions.

In the case of a thermodynamic control, the nucleus is going to favour the formation of lowest energy planes. For a fcc structure the following sequence is determined $\gamma_{\{111\}} < \gamma_{\{100\}} < \gamma_{\{110\}} < \gamma_{\{hkl\}}$ (with h,k or l >1)[98]. This means that the thermodynamic nucleus should be enclosed by {111} planes thus an octahedron. But the thermodynamics also state that the nuclei have to reduce their surface compared to their volume in order to be stable. Actually the shape enclosed by {100} planes, which is a cube, has a lower surface than an octahedron of the same volume. Thus the thermodynamic nucleus is a compromise, enclosed by both {111} and {100} planes. This shape is a Wulff polyhedron is named truncated octahedron can be assimilated to a faceted sphere.

In the kinetic control, the RMF has to be considerably slow, the atoms tend to form nuclei with the inclusion of stacking faults or twin defects[70]. The nuclei take then shape that deviated from those favoured by thermodynamics (i.e, a higher energy structure). If twin defects are present in the nuclei in the form of a (111) mirror plane, single or multiple twinned nuclei are obtained. To reduce its energy that is increased by the strain du to the twin defect, the nucleus will increase its coverage with either (111) or (100) planes. This case is quite rare for iron oxide NP and mostly observed for metal NPs.

An extreme case is the inclusion of stacking faults and/or twin planes that will lead to plate like seeds covered with {111} facets at the top and the bottom surfaces. This shape is highly energetic despite {111} planes because of its high surface area and lattice strain. Figure I.14 represents different nuclei shapes and the associated NP shape after their growth.

It looks like the kinetic control allows to get to anisotropic shapes while thermodynamics give nuclei close to spherical shapes. But the growth of the nuclei is also important as it will be exposed below.

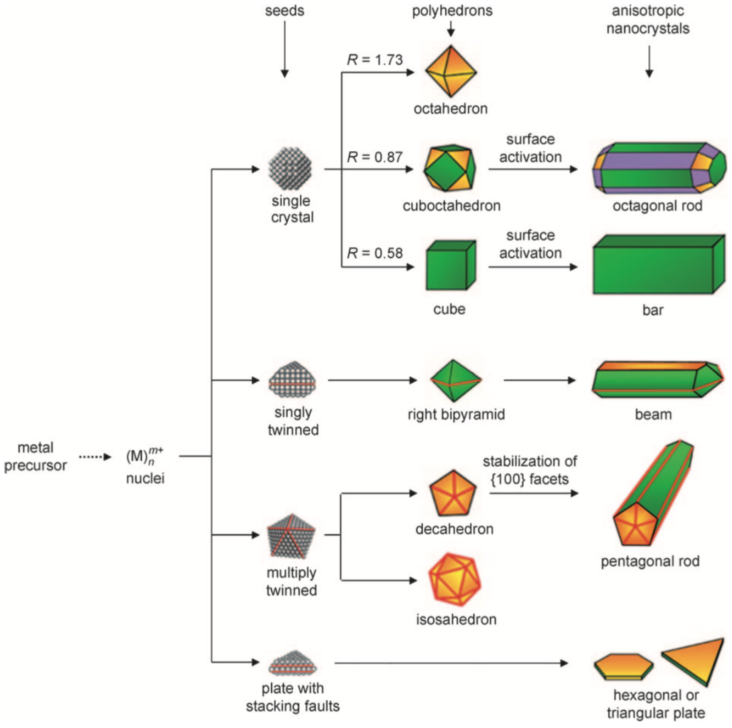

Figure I.14- Different nuclei shapes and the NPs obtained after their growth[70]

Anisotropic growth: the nucleus can take several shapes depending on the nucleation process. Even if it has a major influence on the final shape, the growth that takes place afterwards can be a game changer. This will be detailed in the following paragraphs.

As discussed before, growth is the accretion of monomers units on the formed nuclei. But depending on the shape hence on the crystallographic planes exposed on the nuclei, growth can be directed towards specific shapes. Let's take the (common) case of the single crystal nuclei. The nucleus is assimilated to an isotropic sphere as enclosed with {111} and {100} planes. The energy of each plane family being different if the growth rate of one family is faster than the other the final shape will be completely different as represented in figure I.15. The idea being if the growth rate of a plane family is greatly superior the one of the other plane family, the faster growing family will end up disappearing leaving a NP only enclosed by the slowest growing plane family.

The control of the growth rate is commonly made through the addition of specific ligand. This ligand is supposed to interact with the plane family that is desired in the final shape blocking its growth. The most used ligands in literature are sodium carboxylate (e.g. sodium oleate), amines (e.g. oleyamine) and sometimes the solvent is also used as active specie (e.g. dibenzyl ether). The role of the type of ligand on the shape control will be more detailed with a practical example in the following part.

The ligand is not the only parameter to consider the tuning of the heating rate[85,99], the reaction time[85,100] and the system temperature[11] also have to be adjudsted in order to get the desired morphology.

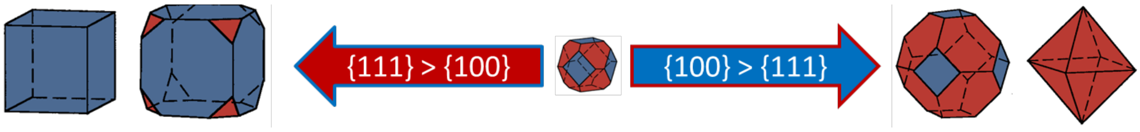

Figure I.15- Evolution of the shape of the nucleus depending on the growth rate of a specific plane family

A specific attention has to be given to the stability of these non-thermodynamic shapes. For example, the energy of a crystallographic direction increases with its length. For instance, in the cubic system the diagonals (<111> directions) are longer than the normal to the faces (<100> directions). The positions at the end of the <111> directions are then more energetic than the one on the faces. This implies that the atoms that will depose on the <111> will try to lower the energy of the system by diffusing towards a face. This phenomenon can be tuned by controlling the speed of the deposition[101]. If it is larger than the diffusion, the control is kinetic. Ramification can be observed leading to a pods shape. On the opposite thermodynamic control will favour diffusion, promoting the growth of {100} faces and leading to an increase in the {111} coverage changing the morphology to octahedra. Many cases can be found in-between as shown in Figure I.16.

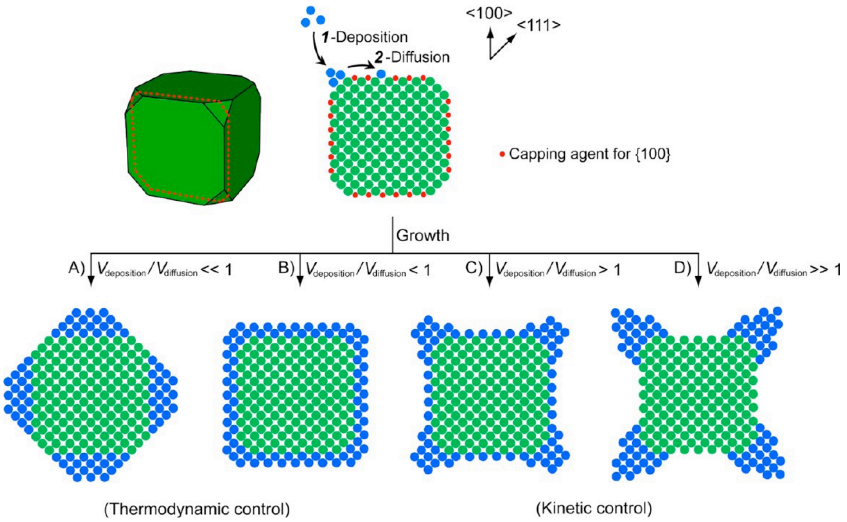

Figure I.16- Representation of the shape evolution depending on the kinetic conditions[101]

This example is in the case of still converting monomer. But the shape can also evolve with time if not stabilized enough. The corner of cubes can dissolve and the as released monomer will deposite on the facets to lower the energy of the system changing the shape.

Simulation work tries to elucidate the best conditions for the synthesis of a specific shape. Bealing and al.[102] simulated the influence of the coverage of the {111} and {100} planes on the shape of PbSe nanocrystals. As shown in figure I.17, there are areas of existence of those defined shapes that are bigger or smaller depending if the shape is thermodynamically favoured.

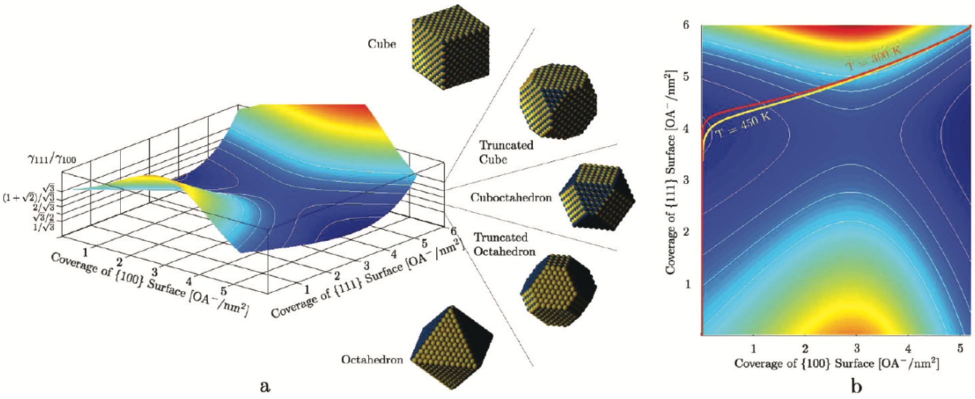

Figure I.17 – Influence of the coverage of {111} and {100} planes on the shape[102]

I.2.3.2.3 Nanocube synthesis

Lot of efforts have been done towards the controlled synthesis of iron oxide nanocubes. Several ligands have been screened along the synthesis parameters. Sodium oleate (combined with oleic acid) is the most reported growth controlling agent to get to cubic NPs[64,80,96,103,104]. According to Shavel[103] oleate would be responsible of the shape control with a strong interaction towards the (111) planes. Rath[104] showed through simulation that the {111} planes of magnetite the most active surface for adsorption but this kind of demonstration have to be treated cautiously as the {111} planes of magnetite can have 6 different terminations[105].

Several protocols report the synthesis of cubes with different oleate salts. Xu et al.[106] explained the formation of cubic NPs from iron chloride thanks to the strong interaction of planes by the chloride ions. Guardia et al.[99,107] presented a different method starting from Fe(acac)$_3$ with decanoic acid and benzylether. Table I.5 summarizes different cubes synthesis found in literature.

Table I.5 – Experimental conditions of cubes synthesis

	Precursor	Solvent	Ligand	Reflux T and duration	Heating rate	Observations
[108]	$Fe(acac)_3$	DBE	OA	290 °C / 30'	20 °C/min	Size and shape control with time and quantity of DBE
	$Fe(acac)_3$	DBE	OA / 4-Bisphenyl carboxilic acid	290 °C / 30'	20 °C/min	Smaller cubes
[96]	$Fe(Ol)_3$	OD or TOA	OA	340°C / 4h	10-15 °C/min	Size controled with T
[109]	$Fe(acac)_3$	DBE	OA / 4-Bisphenyl carboxilic acid	290 °C / 30'	ND	
[103,110]	$Fe(Ol)_3$	Squalane	NaOl / OA	315 °C / 2h	20 °C/min	Coreshell
[111]	$Fe(acac)_3$	DBE	OA / HDD /OAm	290 °C / 1h	15 °C/min	If heating rate increase along shoter reflux bigger NPs on the opposite smaller NPs
[61]	$Fe(Ol)_3$	eicosane	NaOl / OA	350 °C / 30'	3.3 °C/min	Coreshell
[106]	$Fe(Ol)_3$ in situ	OD	NaOl	315 °C/ 2h	ND	Shape control through amount of NaOl
[112]	$Fe(Ol)_?$	OD	OA	320 °C / 30 '	5.5 °C/min	
[80]	$Fe(Ol)_3$	OD	NaOl / OA or DBAOL	315 °C / 30'	3.3 °/min	
[64]	$Fe(Ol)_3$	OD	NaOl /OA	315 °C / 30 '	4 °C/min	Ratio Fe(Ol)/NaOl control the size
[113]	$Fe(St)_2$	OA	NaOl /OA	380 °C / 2h	5 °C/min	
[114]	$Fe(acac)_3$	Squalane	Decanoic acid / DBE	310 °C / 1h	7 °C /min	Size controled with ratio squalane/DBE

AO: oleic acid, NaOL: sodium oleate, OAm: oleylamine, DBAOL: dibutylammonium oleate, DBE: Dibenzylether, TOA: tri-n-octylamine, OD: octadecene, acac: acetylacetonate, Ol: oleate, St: stearate

This table shows that there are many ways to get cubes. The first point one can notice is that it needs two ligands to make cubes. The combination of a ligand with different interactions with the nucleus surface (e.g. carboxylate/carboxylic acid, carboxylic acid/amine …). This could be explained as the strong ligand influences the nucleation step by stabilizing the precursor. Concerning temperature, cubes require a high reflux temperature (>300°C) except for high heating rates (≥ 10 °C/min). This is expected as the cube not being a thermodynamic shape it would appear for higher energy synthesis. The solvent nature tends to control the composition of the NP. In alkenes core-shell NPs are produced with a core of FeO (wüstite) and a shell of magnetite attributed to the highly reducing environment generated with alkenes at high temperature. Moreover, this raises the question of the nuclei composition. In ethers (mostly DBE) the cubes are homogeneous magnetite. Guardia[114] then reported that it is actually the decomposition products of the DBE that control the synthesis of homogenous cubes but the decomposition of DBE could create an oxidizing environment that favours magnetite over wüstite.

The last point concerns the precursor. Most of the syntheses are made with iron oleate, a non commercial product that has to be synthesized in house. Many papers don't bother presenting the characterisations of this product. Bronstein et al.[77] are the only one to have studied the influence of the structure of the precursor on the morphology of the NPs. They have shown that, depending the number of oleate chains coordinated to the iron, the shape of the NPs can tune from spheres to cubes. This means that the structure of the precursor is not a detail and should be investigated in order to conclude on set of synthesis conditions.

From this, no general rule can be drawn for the synthesis of cubes. Yet few points can be kept in mind as the association strong/weak ligand, the high temperature and the influence of the precursor structure. The difficulty of this synthesis is that for a chosen system, getting cubes comes down to finding the fragile equilibrium between all of the parameters.

I.2.3.3 Conclusion

Among all the methods developed to synthesize iron oxide NPs, thermal decomposition is actually the one that allows the most freedom in the design of original NPs. The catch is that this method can be quite difficult to master and requires good understanding of the phenomenon occurring during the reaction. Looking at the thermodynamics allows to identify key points that will be of use for the design of NPs. The interrogation that comes out of this literature study is “does the precursor structure have an effect on the outcome of the synthesis?”. This matter has not been investigated contrary to the effect of ligands and temperature and no general rule can be established. Could this point be one of the keys to master the shape control? This question will be addressed in this manuscript.

I.3 NPs for biomedical applications

I.3.1 Some challenges with iron oxide NPs

Multifunctional biocompatible nano-objects represent the most challenging innovation in medicine able to revolutionise the field of diagnosis and therapy, named *theranostic*, for targeted treatment of cancer[115–126]. Such theranostic nanoparticles, which bear both imaging and therapeutic functions on the same nanoparticle, can simultaneously identify disease states and deliver therapy and allow thus following the effect of therapy by imaging. The possibility of combining a therapeutic action with image guided diagnosis while avoiding side-effects may boost the emerging market of nanotechnology in biomedicine. Indeed, the explosive growth of nanotechnology has brought smart innovations in the synthesis of multifunctional nano-objects and paves the way towards designing materials that will allow real progress to achieve local therapy with high resolution imaging. The combination of conventional cancer therapies with nanotechnology bears an enormous potential for tailored treatments according to the patient needs.

To design such theranostic nano-objects (Figure I.18), several challenges need to be overcome: (i) the creation/design of NPs which will allow, **in one nano-object**, combining high contrast imaging by MRI and/or optical imaging and an efficient therapeutic action such as magnetic hyperthermia, photoablation, radiotherapy or drug delivery; (ii) to obtain multifunctional organic coatings bearing different functionalities allowing optical imaging, stealthiness, biodistribution, targeting and drug delivery; (iii) to validate the efficiency of this unique nano-object bearing all these functions *in vitro* and *in vivo*.

Iron oxide nanoparticles (IONPs) are of special interest for biomedical applications thanks to their outstanding balance between magnetic properties, surface-to-volume ratio for functionalisation and proven biocompatibility. Commercial formulations are already available as contrast agents in MRI (e.g. Feridex, Resovist) and as heating vectors in magnetic hyperthermia (MH) (Nanotherm^{TM}). The development of MRI contrast agents (CAs) represents a valuable market. Ultra-small IONPs are of particular interest due to their superior biodegradability and non-toxicity[43,44] compared to other CA families such as Gd-based agents. To be used as T_2-CAs, NPs should exhibit high saturation magnetisation and be functionalised with ligands ensuring optimal diffusion of water molecules around the magnetic core. Moreover, biocompatible stable suspensions in physiological media with an average hydrodynamic size smaller than 100 nm are essential to achieve good *in vivo* biodistribution.

At the same time, there is a growing interest in the development of heating vectors for MH due to the potential of this therapy as a stand-alone treatment or adjacent therapy for cancer. This was shown by the recent favourable results of the “*nanothermotherapy*” study in phase II clinical trials led by *MagForce Nanotechnology* (Hospital Charité, Berlin) on patients suffering from glioblastoma multiforme leading to an improvement on patient survival from 6.2 to 13.4 months[127,128]. Moreover, the combination of the “*nanothermotherapy*” with conventional radiotherapy led to a European market authorisation[127–129], also including prostate cancer and the treatment of local residual pancreas and oesophagus tumours in combination with chemotherapy. The positive impact of MH in cancer therapy will allow us to expect great breakthroughs in biomedical science. However, one of the limitations of MH is the low heating power of conventional magnetic NPs, requiring local injection of NPs in large quantities. Given the clinical importance of the MH results, it is important to synthesise NPs with improved performance in MH[86,87,130]. However, optimisation is not yet well-understood and experimental results from NPs systems vary significantly.

As today, the follow-up of therapy by imaging is reported of paramount importance to provide real-time information of its efficacy. To achieve that aim, there is a crucial need to design innovative multifunctional NPs combining imaging and therapeutic action for nanomedecine applications. Magnetic IO-based NPs are among the most promising NPs which would allow combining efficiently imaging by MRI and therapy by MH. The main parameters controlling the imaging and hyperthermia properties of IO-based NPs are discussed in this part.

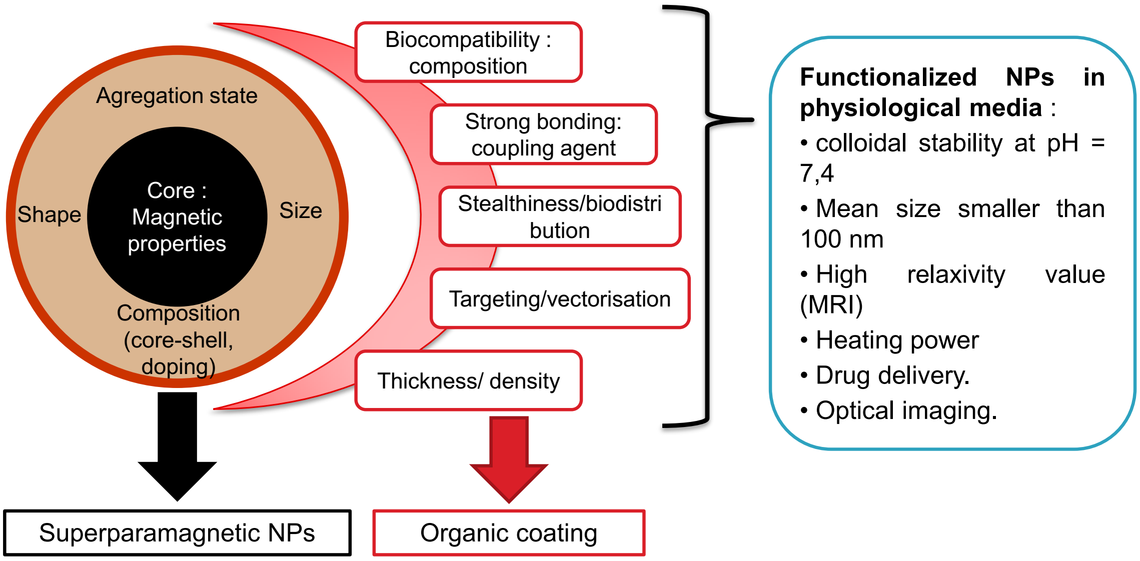

Figure I.18 - Design of functionalised IO-based NPs for biomedical applications

I.3.2 Fonctionnalisation of NPs for biomedical applications

Superparamagnetic iron oxide nanoparticles (NPs) with appropriate surface coating are widely used for numerous biomedical applications. One challenge is the design and the grafting of the organic coating which should favour ideal biodistribution, ensuring multifunctionalization (targeting, optical imaging…) and preserving a small size distribution of coated NPs in physiological media[131]. The grafting strategy is therfore an important step for biomedical applications as the mean hydrodynamic size of functionnalized NPs has to stay below 100 nm for *in vivo* injection and it must be able to preserve the properties of both the coating and the NP[15,132,133]. The functionnalization strategy depends mainly on the NPs and molecule nature and synthesis method.

I.3.2.1 Main organic coating

The main molecules which have been used to coat superparamagnetic iron oxide nanoparticles (IO NPs) are natural or synthetic polymers. Besides, other molecules have been developped such as non polymeric coating, dendrimer, dendron and silanes based molecules which have the potential to create an advanced biocompatible contrast agent for biomedical applications, including *in vivo* diagnostic imaging. Dendrimer-based organic/inorganic hybrids represent highly advanced pharmaceutical tools, able to target a specific type of cell or organ, be tracked while doing it and deliver a specific drug *in situ*.
Besides organic coatings, silica based coatings have been also widely reported. The coating of a non-porous silica shell around IO NPs but also around other type of inorganic NPs was widely developed these three last decennia with the aim to form a protective shell around the inorganic NPs[134]. The possibility to coat or to encapsulate plasmonic, magnetic or luminescent inorganic NPs by mesoporous silica shells[135–137] generated also a strong interest for range of applications such as catalysis, energy and drug delivery. Mesoporous silica capped at the surface of magnetic NPs appeared as particularly attractive coatings because of the advantages brought by the association of the porous silica (pore ordered arrangement, high surface area, drug loading capacity) and the magnetic NPs (magnetic guidance, MRI and magnetic hyperthermia). A silica coating is particularly advantageous as it ensures chemical stability of the inorganic core, high dispersibility in aqueous solutions and high biocompatibility of the resulting core-shell nanocomposites. Moreover, the silica surface can be easily modified by grafting alkoxysilanes with various end-groups functions to afford a versatile chemical functionalization.

In this PhD work, dendron molecules will be used to coat the synthesized IONPs. S. Begin-Colin, D. Felder-Flesch and co-workers demonstrated the great interest of dendronized iron oxide NPs obtained through direct grafting of small sized hydrophilic dendrons, through a phosphonate anchoring on NPs, for the development of efficient MRI contrast agents[138–140]. Indeed, such nano-objects were shown to display very good colloidal properties and higher relaxivity values than commercial polymer-functionalized NPs. The choice of phosphonic acid as coupling agent was justified by previous studies that have evidenced a significantly higher grafting rate and a stronger binding than those obtained with carboxylate anchors[29,141]. A clear input was brought by the small-sized dendrons as they are discrete and monodisperse entities, and relevant characteristics like their size, hydrophilicity, molecular weight and biocompatibility can easily be tuned as a function of their generation[142–145].

I.3.2.2 Functionalization strategies

The interaction of molecules with NPs depends on the nature molecules and on the synthesis way of NPs. The NPs may be encapsulated within polymers or proteins without (pure encapsulation) or with weak (electrostatic..) or strong (anchoring group) interactions between NPs and molecules (Figure I.19). For NPs in situ coated with surfactants during the synthesis, the surfactants may be exchange with the bioactive molecules by ligand exchange processes described below but also if an excess of surfactants is added, hydrophobic interactions may be generated leading to water soluble NPs (Figure I.19). However, such hydrophobic interactions do not induce enough strong interactions with the NPs surface for biomedical applications. Therefore, the most used functionalization strategy aimed currently at inducing a strong bonding between the molecules and NPs.

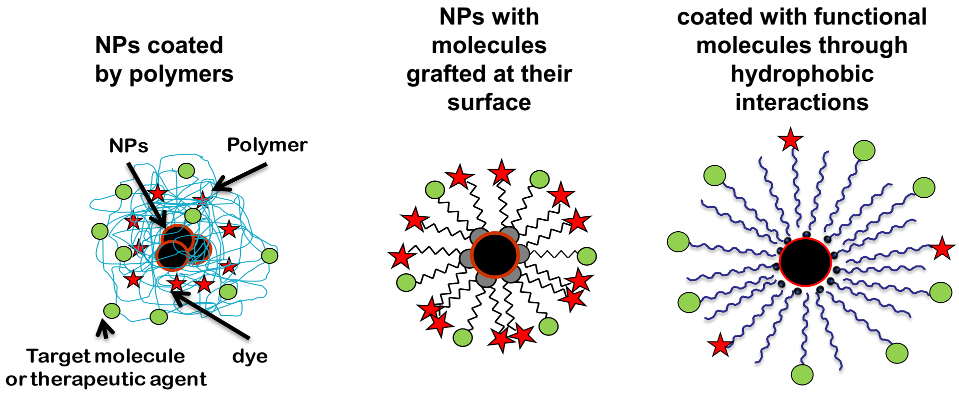

Figure I.19 - Schematic representation of NPs: a) coated by polymers b) with molecules grafted at their surface and c) coated with functional molecules through hydrophobic interactions

To coat the NPs by bioactive molecules, the NPs may be synthesized in the presence of biocompatible ligands[146–148] but more and more often the functionalization step occurs after the NPs synthesis step[149,150].

In the post synthetic coating process, first, the magnetic cores are synthesised, and depending on the synthesis method, their surface is “free” (naked NPs) (as in co-precipitation) or capped by surfactants protecting against agglomeration (in situ coated NPs). The functionalization takes then place by direct grafting (naked NPs) or by grafting by ligand exchange (in situ coated NPs) or by ligand exchange and phase transfer (in situ coated NPs) (Figures I.20)[138].

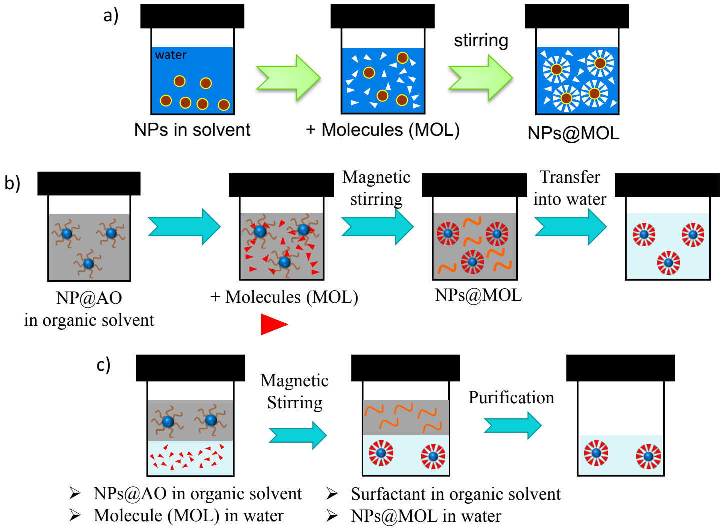

Figure I.20 - a) Direct grafting of uncoated NPs by molecules (MOL = white triangle), b) direct grafting of NPs coated by oleic acid (OA) (NPs@OA) by ligand exchange of oleic acid with molecules (MOL = red triangle). and c) ligand exchange and phase transfer process

When naked NPs are obtained as with coprecipitation or polyol approaches, the molecules are introduced in the NPs water suspension at suitable pH depending on anchoring and functional groups at their surface[138,139] and direct grafting occurs. When NPs are *in situ* coated during their synthesis step as with the more and more used decomposition methods of metal precursor in organic solvants in controlled conditions, direct ligand exchange may be realized by just introducing the molecules in the organic solvant. The molecules have to be soluble in the organic solvent which is generally quite polar. They present generally an anchoring group displaying a high affinity with the surface to be functionalized and replace the former ligand. Then the coated NPs are transfered in water.

Otherwise a ligand exchange and phase transfer process may be realized. Molecules are dissolved in the aqueous phase and the NPs are dispersed in a non-water-miscible organic solvent. Then the water suspension of molecules is put into contact with the NPs suspension in a hydrophobic solvant. Under stirring, the two phases come into contact and the NPs transfer from the organic phase to the aqueous phase is observed due to the molecule grafting at the NPs surface.

One may notice that both processes are based on the higher affinity of the new ligand anchoring group towards the iron oxide surface compared to the original one (often oleic acid or oleylamine). Indeed, the nature of the coating interactions with the surface of NPs is a key point as this coating may encapsulate the NPs or may be physisorbed (electrostatic interactions, hydrophobic interactions), or chemisorbed at the surface of NPs (through anchoring groups). Current studies suggest that a strong binding of molecules at the surface of NPs is important for the colloidal stability in physiological media and thus for increasing the longevity of NPs in the blood (the biodistribution)[149]. The anchoring group used depends primarily on the chemical nature of the NP and on the nature of the surfactant present on the surface prior to functionalization and which will be exchanged[151].

I.3.2.3 The importance of the anchoring group

As for all oxides, the surface of iron oxide is covered by hydroxyl groups due to water chimisorption (Figure I.21)[15,132,152]. Part of these surface -OH groups are amphoteric and the surface charge can be changed by varying the pH. Thus depending on the pH of the solution, the surface of the iron oxide NPs can be positively or negatively charged (Figure I.21). The isoelectric point (IEP) is the pH at which the surface has as many positive charges as negative charges. IEP for iron oxides is around 6.8[153]. At acidic pH, the NPs are positively charged and at basic pH, negatively charged (Figure I.21).

Thus if molecules bear functional groups such as carboxylate or ammonium groups, they can be physisorbed at the iron oxide surface in water suspension: the functional groups interact through electrostatic interactions with the protonated or deprotonated OH groups at the surface of the NPs. However, molecules can also react with the -OH groups of the NP surface to form a chemical bond between the surface and the molecule. Purely electrostatic interactions are not strong enough for applications in the biomedical field. Indeed, it is important that the molecule does not desorbed during injection or over time. A weak bond between molecules and the iron oxide surface makes that the molecules may be replaced by blood proteins and causes NPs capture by the RES. Therefore, grafting methods promoting a strong bond with the surface of the NPs were developed using anchoring group presents on the molecules.

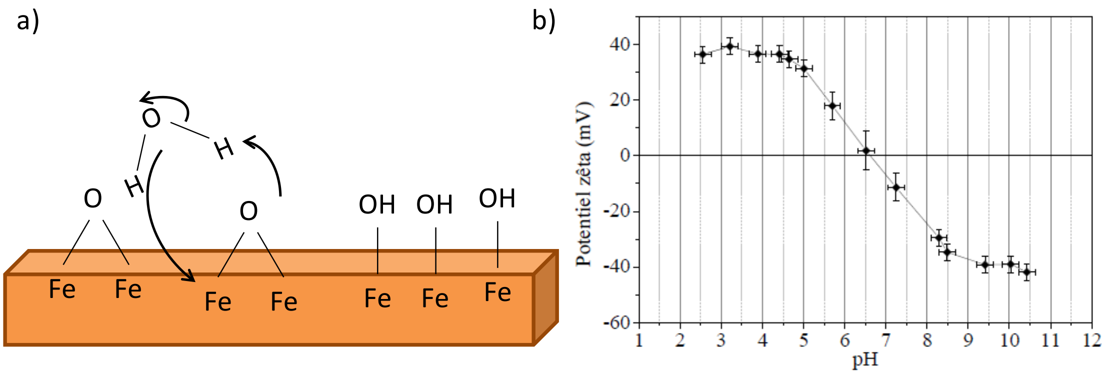

Figure I.21 - a) schematic representation of the iron oxide surface b) surface charge and zeta potential evolution according to the pH in the case of "naked" iron oxide NPs synthesized by the coprecipitation method[152]

To ensure a strong anchoring of molecules at the NPs surface, various anchoring groups including carboxylates[154–158], catechol[159,160], phosphonate[15,138,140,161–166] based ligands have been developed[132].

More or less strong interactions between these groups and the surface of iron oxides (OH surface) have been reported and such discrepancies on the strength of the bond were due to the fact that depending on the NPs synthesis method, the nature of molecules and the grafting method, different types of complex may be observed. For example with carboxylate anchoring group: three surface complexes may be formed: monodentate, bidentate chelate or bidendate bridging complexes. The strength of the anchoring influences further the NPs stability in physiological media.

The most used molecules were silane molecules. The silanization process is based on the formation of a covalent network of silane molecules at the surface of the NPs. The silane groups are covalently bound to the NP by reaction between the surface hydroxyl groups and the alkoxysilane function (-Si-OR). Aminosilanes are mainly used for the silanization of iron oxide NPs[167–170] but organosilanes, namely aminopropyltriethoxysilane (APTS) or aminopropyltrimethoxysilane (APTMS), do not lead to stable iron oxide NPs in water at pH 7 (the pH has to be decreased down to pH 5 to protonate the amine moieties). Therefore, these aminosilanes are most useful as intermediate groups for further coupling of other (bioactive) molecules. The alkaline hydrolysis of tetraethyl orthosilicate (TEOS) known as the Stöber synthesis is widely used for the formation of silica shell on the particles[171–173]. This method allows to obtain iron oxide NPs very stable in water as the silica isoelectric point is around 2-3 with is much lower than the physiologic pH. This shell presents a high density of –OH reactive groups on their surface which can be used to couple other bioactive molecules. The silica shell can also be further silanized with functional organosilanes[174].

Among anchoring on iron oxide, the phosphonate moiety was introduced as an effective anchoring agent because of the high ability of $-PO(OH)_2$ groups to complex metal ions and to form complexes which are stable even at elevated temperature[161,175–177]. A significantly higher grafting rate and stronger binding than those obtained with carboxylate anchors have been evidenced[8,29,164]. Previous works on iron oxide NPs fonctionnalized with dendrons bearing phosphonate anchoring groups demonstrated a good colloidal stability in water and osmolar media and very high enhancement contrast ratio (EHC) values at high magnetic field[140,165].

I.3.3 Design of iron oxide NPs for MRI

I.3.3.1 MRI and contrast agent principles

Magnetic Resonance Imaging (MRI) is based on the physical phenomenon of nuclear magnetic resonance of hydrogen atoms. As the human body is mainly constituted by water and fat, hydrogen atoms account approximately 63% of its mass. In a permanent magnetic field B_0, the hydrogen nuclear spins align with (parallel) or against (antiparallel) the external magnetic field. The difference in populations of parallel and antiparallel protons is determined by the energy difference between the two states, ΔE. Under irradiation by a resonant radiofrequency wave B_1, the nuclei absorb the electromagnetic energy and the antiparallel spin population increases. Thus, the longitudinal magnetisation M_{xy} (parallel to the external magnetic field) decreases and the transverse magnetisation M_z (perpendicular to the external magnetic field) increases.

As B_1 excitation stops, the nuclear spins return to their initial state (M parallel to B_0), which is known as relaxation. This process is depicted in Figure I.22 and consists of i) the longitudinal relaxation, T_1 relaxation, where M_z returns to its initial state and ii) the transverse relaxation, T_2 relaxation, which is the return of M_{xy} to zero. In these processes, T_1 is the time required for the longitudinal magnetisation to recover 63% of the equilibrium value (Figure I.22a), whereas T_2 is the time required for the transverse magnetisation to drop to 37% of its magnitude (Figure I.22b). From these relaxation processes, it is possible to reconstruct magnetic resonance images, either using T_1 or T_2, which contrasts strongly depends on the relaxivity values.

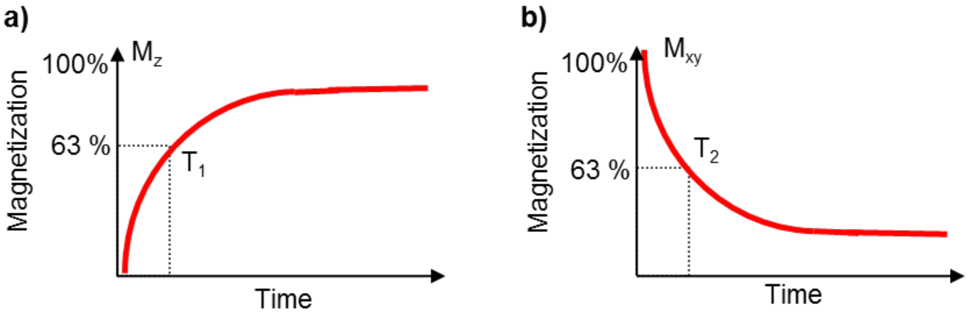

Figure I.22 - Schematic representation of the nuclear spin relaxation process. a) Longitudinal relaxation: T1 is the time required for longitudinal magnetization to recover to 63% of its equilibrium and b) Transversal relaxation: T2 is the time required for transverse magnetization to drop to 37% of its initial magnitude.

However, in most tissues the intrinsic contrast is not sufficient to provide relevant structural information and external agents are used to enhance it. These agents, known as contrast agents (CAs), are used to improve the visibility of tissues by changing the relaxation time around them. On one hand, paramagnetic CAs, such as gadolinium (Gd^{3+}) or manganese (Mn^{2+}), change contrast by inducing large fluctuating magnetic fields experienced by nearby protons. On the other hand, ferri or ferromagnetic CAs, such as iron oxide, change contrast by inducing a local magnetic field gradient. In the presence of a CA, proton relaxation rate increases because it results from the addition of the intrinsic proton relaxation rate and that of the CA relaxivity contribution. The observed relaxivity is then expressed as:

$$R_{i,obs} = R_{i,p} + r_{i,ca}C = \frac{1}{T_i} + r_{i,ca}C$$

where $R_{i,obs}$ is the observed relaxation rate (in s^{-1}), $R_{i,p}$ the intrinsic proton relaxation rate (in s^{-1}) or the relaxation rate in absence of CA, $r_{i,ca}$ the contrast agent relaxivity (in $mM^{-1}.s^{-1}$), C the CA concentration in $mmol^{-1}.L^{-1}$, T_i the relaxation time.

However, it is important to note that the effect of T_1 and T_2 relaxation times on signal intensity depends on repetition time (time interval between perpendicular radiofrequency pulses, T_R) and echo time (time between radiofrequency pulse measurements, T_E). Thus, in a T_1-weighted image, T_R is set short (typically T_R < 500 ms) in order to allow substances with short T_1 to recover sufficient magnetisation between repetitions. Consequently, T_1 CAs led to bright T_1-weighted images. Whereas, in T_2-weighted images, T_E is set long (typically T_E > 60 ms) and the areas with short T_2 lose their transverse magnetisation and appear black.

In this way, T_1 CAs, so-called positive CAs, reduce the longitudinal relaxation time T_1 increasing signal intensity in T_1-weighted images while, T_2 CAs, so-called negative CAs, reduce transverse T_2 relaxation time and reduce the signal intensity in T_2-weighted images. The efficacy of a CA is evaluated in terms of relaxivity (r_i) but the ratio r_2/r_1 should also be considered in order to determine whether to use a material as T_1 or T_2 CA. Therefore, T_1 agents present high relaxivity r_1 and low r_2/r_1 ratio (< 2), Whereas T_2 agents are characterised by a high r_2 relaxivity and a high r_2/r_1 ratio.

The diffusion of water molecules around CAs or the interaction of water with CAs is also an important parameter for T_1 or T_2-based CAs and inner and outer-sphere relaxation processes need to be considered. The inner sphere relaxation consists in the direct energy exchange between protons and electrons located in the first hydratation sphere of the paramagnetic ions. It requires close interaction between the paramagnetic agent and the surrounding water molecules and is strongly influenced by the ability of the agent to rapidly exchange water molecules (retention time τ) (Figure I.23)[178,179]. T_1-CAs are mainly based on paramagnetic ions such as Gd^{3+}, Mn^{2+}, Dy^{3+} in the form of ion complexes. In order to experience fast relaxation, water protons need to be in close proximity to the paramagnetic ions. Thus, inner-sphere relaxation contribution dominates the T_1-constrasting effect. While T_2-CAs are mainly based on superparamagnetic NPs, for which the inner sphere contribution to relaxation is minor as compared to the dominant outer-sphere contribution[43]. This relaxation is due to the movement of water protons near the local magnetic field gradients generated by the superparamagnetic NPs. (Figure I.23b). Therefore, the nature of the organic coating at the surface of CAs is very important and would strongly influence the interaction of water molecules with CAs. As this work is focused on iron oxide-based NP systems, in the following, our discussion will be mainly dedicated to T_2-CAs.

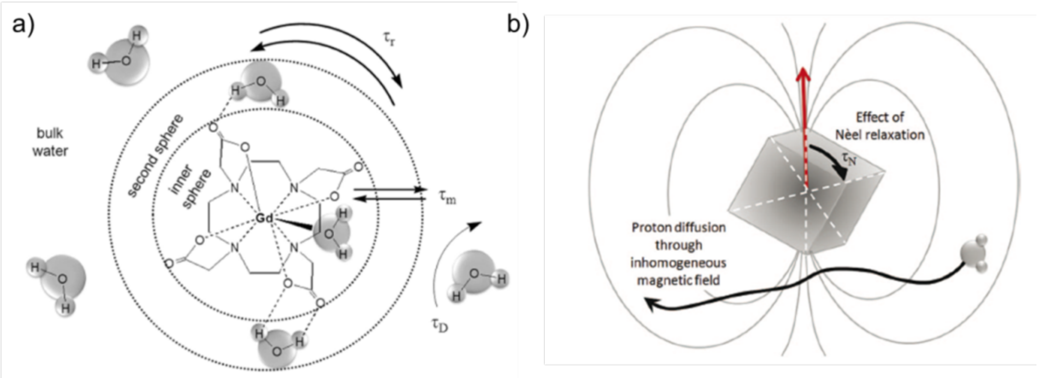

Figure I.23 - Relaxation mechanisms. a) “Internal sphere model” for paramagnetic ions, b) “External sphere model” for superparamagnetic NPs[145]

The magnetic interaction of superparamagnetic NPs with water protons was described by a model of external sphere, the relaxation rate in this model can be written as:

$$\boldsymbol{R_2} = \frac{\left(\frac{64\pi}{135000}\right)\gamma^2 N_A M \mu_c^2}{rD}$$

where N_A, is the Avogadro constant, M, the NPs molarity, μ_c, the cluster magnetic moment, r, the effective particle radius and D the diffusion constant of water molecules. If this equation deals with aggregates of NPs and r is the effective aggregate size.

Most iron oxide based NPs in suspension are under the form of aggregates of NPs: the mean hydrodynamic diameter D_H (the diameter of functionalized particles in water suspensions) which includes the organic coating is larger than the diameter of the NPs given by D_{TEM}. From above equation, it is clear that the intrinsic properties of the CA and the nature of its organic coating, which at the same time would has an influence on water diffusion, directly affect the transverse relaxation rate R_2 ($1/T_2$).

Therefore, the magnetic properties of the NPs such as the magnetic moment (μ_c) or the saturation magnetisation, the effective or aggregate size (r) and the water diffusion constant around the magnetic core, which is mainly related to the nature of the organic coating, are key parameters to control in order to design highly contrasting T_2-CA. These different aspects will be discussed in the following section.

I.3.3.2 Important parameters controlling contrast enhancement

I.3.3.2.1 Influence of the NPs magnetic properties

The magnetic properties of NPs have a strong influence on their contrasting effect as R_2 relaxation rate is proportional to the square of the magnetic moment of the NPs. But saturation magnetisation itself depends on many factors such size, composition and particle shape. Thus, these different aspects have been investigated in order to tune the contrasting effect of the magnetic/superparamagnetic NPs.

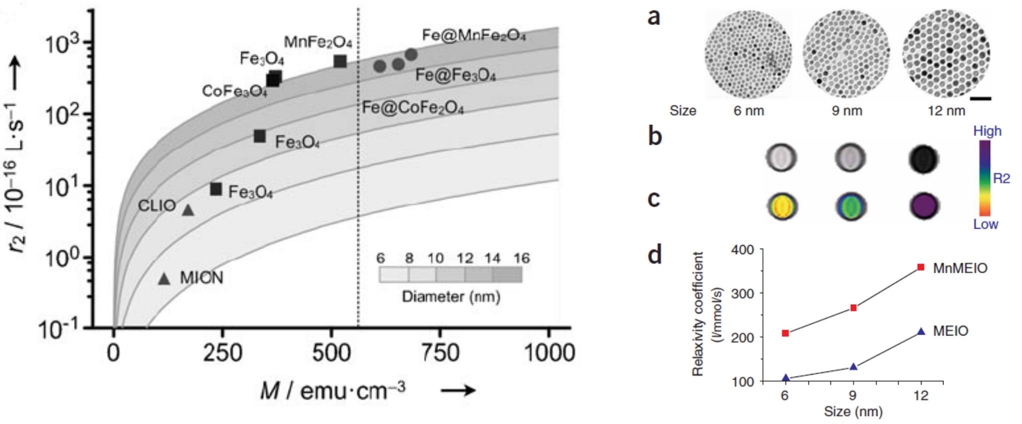

Figure I.24- Left: Transverse relaxivity values (r2) of various magnetic NPs as a function of size and saturation magnetisation, measured at 20 MHz (0.47 Tesla)[180]; right: Influence of size on relaxivity values. a) TEM images, b) T2w-weighted MRI images and c) colour maps for 6 , 9 and 12 nm MnMEIO nanoparticles (MnMEIO : manganese magnetism-engineered iron oxide) d) nanoparticle size versus R2[181]

Firstly, the effect of NP size on relaxivity has been studied by many groups (Figure I.24)[166,181,182]. When the size of IONPs is reduced under 5 nm, the magnetic moment strongly decreases and surface spin disorder is accentuated. As a result, these NPs, commonly known as ultra small IONPs, can be used as T_1-CAs[183,184]. Otherwise, according to above equations, the R_2 relaxation rate is proportional to the square of the magnetic moment of the NP (related to the saturation magnetisation of the synthesised NPs) and inversely proportional to its radius. Since the magnetic moment of a NP is proportional to its volume, R_2 increases with the size of the NP (Figure I.24). In the case of spherical iron oxide NPs, a maximum transverse relaxivity was obtained for magnetite and maghemite NPs with a mean diameter of 27 and 25 nm, respectively[185]. However, with the current synthesis methods, it is difficult to prepare oxide NPs with homogeneous diameter larger than 20 nm[4]. Furthermore, in this size range, NPs are at the limit of the blocked single domain size / superparamagnetic regime, thus dipolar interactions often induce agregation which consequently increases their relaxivity (see below section NPs agregation state) and affect their colloidal stability. As such, it is important to note that relaxivity values are to be related to the mean hydrodynamic size in water suspensions and not to the core size. Thus, establishing the optimal size value is not straightforward as it would strongly depend on the colloid stability and aggretation state.

On the other hand, tuning the composition of the NPs can be used as an alternative strategy to increase M_s[186]. Yoon *et al.*[180] established the diagram shown in Figure I.24 which gives the transverse relaxivity of different NPs according to their size, composition and saturation magnetisation. On that same line, Lee *et al.*[181] studied the effect of the composition of different ferrites MFe_2O_4 (with M = Fe, Co, Ni, Mn) on the relaxivity values, leading to high relaxivities for manganese ferrite NPs due to higher M_s (r_2 = 358 mM^{-1}.s^{-1} at 1.5 T) (Figure I.24 right). The highest M_s values were obtained for metal NPs with a natural oxide layer shell. For instance, r_2 values of 220 and 324 mM^{-1}.s^{-1}, were exhibited by Fe@Fe_3O_4 NPs with bcc-Fe and α-Fe cores, respectively[187–189]. Alternatively, the Fe-core was coated with a manganese ferrite layer leading to similar relaxivity values (M_s = 149 emu.g^{-1} and r_2 = 356 mM^{-1}.s^{-1})[180]. Thus, the size and composition of the NPs are important parameters that control the relaxivity values (Table I.6).

Finally, relaxivity values can be optimised by varying NP shape[166,182,190]. Saturation magnetisation is directly influenced by the effective particle anisotropy, which will vary by the addition of shape anisotropy. This was observed by Joshi *et al.*[182] and Smolenski *et al.*[166] when they compared spherical and faceted NPs, leading in both cases to higher values of relaxivity for faceted NPs. Similarly, cubic iron

oxide NPs (r_2 = 761 $mM^{-1}.s^{-1}$ at 3 T)[191], as well as octapod IONPs (edge length of 30 nm) (r_2 = 679.3 ± 30 $mM^{-1}.s^{-1}$ at 7 T) exhibited significant transverse relaxivity values (Table 1)[192]. At the same time, shape and composition can be simultaneously tuned to achieve an enhanced effect on relaxivity. This was recently reported with single core and core-shell cobalt ferrite nanocubes -exhibiting spring magnet behaviour- with maximum relaxivity found with concave-like nanocubes- (r_2 = 958 $mM^{-1}.s^{-1}$ at 1.5 T)[193].
Some recent values of transverse relaxivity recorded at 0.47-9.4 T are gathered in Table I.6. It is important to note that the external magnetic fields used in clinical MRI are mainly 1.5 and 3 T, but 7 T instruments are also available.

I.3.3.2.2 Influence of the NPs aggregation state

The aggregation state of iron oxide NPs, which may be evidenced by the comparison of D_{TEM} and D_H (Table I.6), has also an influence on the performance of CAs, as T_2 strongly depends on the aggregation state or cluster size of magnetic NPs (cf equation above). This effect has led to a new strategy consisting in the formation/synthesis of size controlled aggregates or clusters[185,194–198]. These agregates or structures can be considered as magnetic spheres in which the interactions between NPs produce a strong magnetic field gradient and thus a predominant r_2 effect. According to the aggregation state, the transverse relaxation rate, R_2, and the relaxivity r_2 are affected differently depending on the NP aggregation state and thus three different regimes can be distinguished[185,195,199,200]. Figure I.25 left describes the evolution of R_2 and r_2 with NP aggregate size through the three different regimes. First, for small clusters, r_2 is given by the theory of the outer sphere. NPs are homogeneously dispersed and water protons diffuse between the magnetic cores before being completely out-of-phase. At this point, r_2 increases with the size of the cluster. This regime is called the « *motional average regime* » (MAR). Then, up to a size limit, r_2 no longer increases with size. The size is so large that water molecules *feel* a constant magnetic field during their relaxation. Particles are then in a "static dephasing regime" (SDR), which determines the relaxivity limit. Finally, if the size further increases, r_2 decreases with increasing size. The decrease rate of r_2 depends on the echo time (*echo limited regime*, ELR).

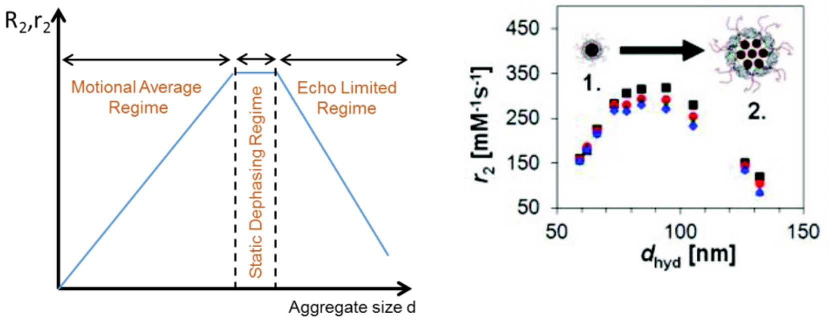

Figure I.25 - left) Schematic view of the relaxation rate and transverse relaxivity (respectively R2 and r2) evolution as a function of the aggregation state; right) Evolution of transverse relaxation (r2) as a function of the aggregation state[185].

In contrast, longitudinal relaxivity tends to decrease as the cluster size increases. As previously discussed, the key mechanisms for T_1 relaxation are different from that governing T_2 relaxation, thus the aggregation effect on r_1 relaxivity differs. In an internal sphere model, when the aggregate size increases, the surface accessibility and the proton exchange rate are reduced[43,200] leading to a decrease on r_1 relaxivity.

Table I.6 - Relaxivity values reported in the literature for ferrite particles. Note that the composition of the magnetic core has been stated as iron oxide when the crystalline phase was not specified.

Type	Magnetic core	Coating	D_{TEM} (nm)	D_H (nm)	M_s (emu.g^{-1})	r_2 (mM^{-1}.s^{-1})	B (T)	Ref.
IONPs	Ferridex	dextran	5	160	75	120	1.5	201
	Fe_3O_4	dextran	4.6	20	68	34.8	0.47	202
	Fe_3O_4	DMSA	12		120	218	1.5	203
	Fe_3O_4	DSPE-mPEG1000	13.8	28.6	ND	385	0.47	204
	Fe_3O_4	DSPE-mPEG1000	13.8	28.6	ND	385	0.47	
	Fe_3O_4	DSPE-mPEG1000	4.8	14.8	ND	130	0.47	138
	Fe_3O_4	phosphonate dendron	10	50	70	272	1.5	
Doped ferrite	$Zn_{0.4}Mn_{0.6}Fe_2O_4$	DMSA			175	860	4.5	205
Core-shell	$Fe/MnFe_2O_4$	DMSA	16	45	146	356	0.47	180
	$Fe/CoFe_2O_4$	DMSA	16	45	133	243	0.47	
	$Fe/NiFe_2O_4$	DMSA	16	45	142	260	0.47	
	Bcc Fe/Fe_3O_4	PEG	15	40-45	164	220	3	188
	α-Fe/Fe_2O_4	DMSA	16		140	324	9.4	187
NPs Clusters/ aggregates	Fe_3O_4	PVP	7.6 -0.3	30-20	ND	174-249	7	206
	Fe_3O_4	pH-sensitive hydrogel	45-79	53-94	62	245-416	3	195
	Fe_3O_4	PEI-PCL-PEG polymer	9.1	51-41	ND	256-289	1.41	185
	Fe_3O_4	DMSA	3.8-0.2	50-70	32-82	84-204	1.5	196
	Fe_3O_4	citrate	19.7-28.8	11-15.6	65.4-81.8	365	9.25	197
Nano-cubes	Iron oxide	PEG phospholipid	57.8		132.1	324	1.5	207
	Iron oxide	PEG phospholipid	22	43	5	761	3	191
	$Co_{0.5}Fe_{1.5}O_4$	PMAO	20		~ 60	958	1.5	193
Octopods	Iron oxide	HDA-G2	30	58	71	679	7	192

**ND: not disclosed in the reference; PEG; polyethylene glycol; PMAO, poly maleic anhydride 1-octadecene; HDA-G2, 1-hexadecylamine.*

Thus the CA contrasting effect is not only dictated by the intrinsic magnetic properties of the magnetic core but also by the diffusion of water molecules in the magnetic field gradient around the magnetic NPs. The nature of the functionalisation of the magnetic NPs can then affect the movement of water molecules. In fact, due to the nature and structure of the organic molecules around the NPs, water molecules can be excluded of the magnetic core, their approach slowed or on the contrary, the organic coating can increase the residence time close to the magnetic core. As a result it is important to understand and control the effect of the ligand in the relaxivity values.

I.3.3.2.3 Influence of water diffusion and NPs coating

As mentioned before, T_1-constrating effect is mainly dominated by inner sphere mechanisms while T_2-constrasting effect is more influenced by outer sphere mechanisms. In both cases, the contrasting effect is strongly dependent on the circulation of water molecules close to the CA. In the case of functionalised NPs, the coating should allow the circulation of water molecules. Polyethylene glycol (PEG) chains are often used to functionalise IO NPs as they fulfil this requirement. PEG chains are usually associated with two or three water molecules and this strong association slows down the diffusion of water molecules, leading to an increase on r_2 relaxivity[205]. On the contrary, coating consisting of hydrophobic polymers decrease the transverse relaxivity[179]. Consequently, the optimum coating should ensure a compromise between achieving sufficient diffusion to affect the relaxivity of water protons and, at the same time, allowing an exchange fast enough to allocate the maximum number of water molecules near the CA[43,208].

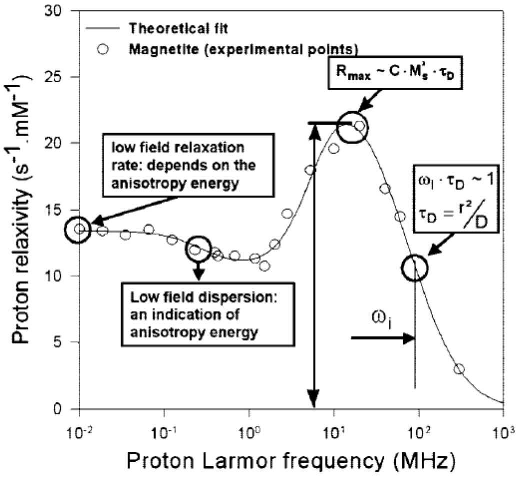

Figure I.26 - Example of Nuclear Magnetic Resonance Dispersion (NMRD) profile for a colloidal suspension of superparamagnetic NPs. This profile is presenting the evolution of the r1 proton relaxivity with the applied external magnetic field. The various parameter extracted from the profile are: R_{max}, the maximal relaxivity; M_s, the saturation magnetisation of NPs; τ_D, the diffusion correlation time; r is the NP radius and D the water diffusion coefficient[43]

Coating thickness can thus also influence the NP MRI properties. Increasing the polymer chain length[209] or the thickness of a silica shell[210], may cause a decrease in r_2 relaxivity. In contrast, in the case of IONPs coated with a pH-sensitive hydrogel[195], it has been shown that increasing the thickness of the hydrogel layer can increase r_2 relaxivity. Depending on the pH value, the hydrogel layer swells and more water molecules diffuse close to the magnetic core.

The determination of the nuclear magnetic resonance dispersion (NMRD) profile allows to assess the diffusion of water molecules around the CA according to the coating properties[210–213]. Determining the NMRD profile of a CA consists in measuring the relaxivity r_1 versus a range of frequencies/external magnetic fields. Obtained by a method of rapid cycling field, it allows a quick analysis of the properties of a CA and to determine at which frequency range / magnetic field it will be most effective. A NMRD profile of magnetite NPs is presented in Figure I.26. The fitting of the curve allows obtaining the mean relaxometric radius (r), specific magnetisation (M_s), crystal anisotropy energy (E_a) and the Néel relaxation time (τ_N) of the colloid.

I.3.4 Design of iron oxide NPs for magnetic hyperthermia

I.3.3.1 Magnetic hyperthermia principles

The medical term *hyperthermia* is used to refer to a therapeutic approach in which a region of interest is subjected to a heat treatment above normal physiological temperature (*ca.* 37 °C in humans). The success of this approach steams from the difference in heat tolerance between healthy tissue and tumour cells. Due to the intrinsic rapid growth of tumour tissue and the resulting defective architecture of the vascular supply, these cells are more sensitive to increased temperatures, with values over 42° C being sufficient to affect their viability. Nowadays, this method is considered as an alternative and/or complementary method for cancer treatment[127,214]. A moderate temperature increase (41 - 46°C) causes the modification of cellular function, cell degradation and may finally lead to controlled cell death or apoptosis. On the other hand, if the applied temperature exceeds 50 °C, cell death occurs rapidly causing tissue necrosis. In that case, the treatment is known as *thermoablation*.

In conventional hyperthermia, heating may be induced by different sources such as microwaves, ultrasounds or radiofrequency waves. Magnetic particle hyperthermia, also known as magnetic hyperthermia (MH), takes advantage of the heat produced by the exposure of MNPs to an alternating current (AC) magnetic field. This technique was firstly introduced by Gilchrist *et al.*, with his pioneering work in 1957 locally heating lymph nodes loaded with MNPs[215],. Since then, researchers have put much interest in the development of MH and MNPs as heating mediators as attested by the growing number of publications and reviews constantly published in the field (see refs. for some recent reviews[86,214,216,217])

The capacity of a material to generate heat under the influence of an AC magnetic field is characterised by its *specific absorption rate* (SAR) or *specific loss power* (SLP), expressed in W/g : $\boldsymbol{SAR} = \frac{\boldsymbol{\Delta T}}{\boldsymbol{\Delta t}} \frac{\boldsymbol{C}}{\boldsymbol{m_{Fe}}}$.

where c is the heat capacity of the fluid per unit mass, m_{Fe} the concentration of the colloidal solution studied (g.L^{-1} of iron) and $\Delta T/\Delta t$ the measured temperature increase with time. The SAR value is widely used to characterise the heat generation capability of a system; however, the SAR value for a given sample depends on the strength and frequency of the used magnetic field and the results cannot be directly compared between different experimental setups[218]. Consequently, the use of an alternative parameter, the *intrinsic loss power* (ILP), was proposed to normalise the SAR value:[219] $ILP = \frac{P}{\rho H^2 f} = \frac{SAR}{H^2 f}$

where P is the volumetric power dissipation $P = \mu_0 \pi \chi''(f) f H^2$, $\chi''(f)$ the imaginary part of the magnetic susceptibility, ρ the density of the magnetic material, H the strength of the magnetic field and f the frequency. This parameter allows for a direct comparison between results from different groups as it is independent of the AC field strength and frequency conditions. However, it is important to consider that this is a low-field approximation and the results will only be valid when the magnetic response of the NPs is linear with the applied field (the used field is below the magnetic saturation field of the NPs).

Two main mechanisms are responsible for the heat dissipated by magnetic NPs under the effect of an AC magnetic field: hysteresis and relaxation losses. For multi-domain ferro or ferrimagnetic nanoparticles, heat loss is generated when exposed to a magnetic field due to a phenomenon known as *domain wall displacement*[220]. When particles are exposed to a time varying magnetic field, a hysteretic magnetic behaviour will be observed. The dissipated energy per cycle P can be obtained from the area, A, of the hysteresis loop multiplied by the frequency: $\mathbf{P} = \mu_0 \mathbf{f} \oint \mathbf{HdM} = \mathbf{Af}$. The area A is determined by the NP coercivity and remanent magnetisation.

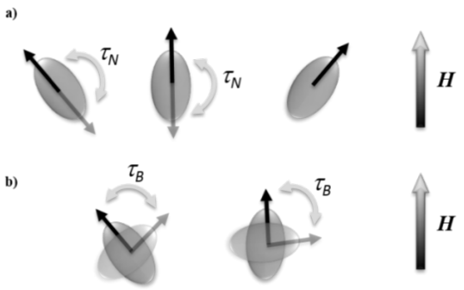

Figure I.27- a) Néel and b) Brown relaxation mechanisms

When superparamagnetic particles are exposed to a dc magnetic field, no hysteresis is observed and therefore, no heat loss can be generated by this mechanism. The applied AC field supplies the energy for the NPs to overcome the rotation energy barrier and allows for energy losses. Thus, for superparamagnetic NPs, heating losses by relaxation mechanisms are predominant. There are two types of relaxation processes; Néel and Brownian relaxation (Figure I.27).

Néel relaxation corresponds to the magnetic relaxation process of the magnetic moments upon exposure to an external magnetic field. The characteristic time of return to equilibrium depends on the effective anisotropy of the crystal (which takes into account different contributions such us the magnetocrystalline energy, shape anisotropy or surface effects, among others) and is defined by the Néel equation (cf. § I.1.3). Simultaneously, the magnetic moment of the NPs interacts with the externally applied AC magnetic field leading to the physical rotation of the NPs by Brownian motion. Rotational friction is generated as a result of the interaction with the surrounding liquid, which is dependent on its viscosity, η, and the hydrodynamic diameter of the NP, V_H. The characteristic relaxation time by Brownian motion is defined as $\boldsymbol{\tau_B} = \frac{3\eta \mathrm{V_H}}{\boldsymbol{kT}}$.

Both relaxation mechanisms may occur simultaneously and the overall effective relaxation time, τ_{eff}, of the ferrofluid will be the result of the effect of both relaxation phenomena: $\tau_{eff} = \frac{\tau_B \tau_N}{\tau_B + \tau_N}$.

As discussed above, the size of the NPs, or more precisely whether the nanoparticles are SPM or not, determines the main mechanism whereby heat will be dissipated under non-zero field conditions. Brown relaxation dominates for large NPs in settings with low viscosity while Néel relaxation dominates for smaller NP systems in viscous solutions. However, the predominance of either relaxation phenomenon is also highly dependent on the anisotropy of the NP itself, mainly its magnetocrystalline anisotropy and the exhibited shape effects. As NPs are exposed to increased magnetic fields, the magnetisation will reverse when the supplied energy allows overcoming the anisotropy barrier. Moreover, dipolar interactions may increase the energy barrier for rotation in NP systems due to hindered spin rotation, which at the same time increases particle relaxation time and thus vary the effective heat loss[221–223].

As a result, when rationalising the design of NPs for MH, it is important to take into account the different parameters governing the relaxation mechanisms, hence the expected heat dissipation of the system. These various parameters are discussed in the next section diving between intrinsic and extrinsic parameters influencing the generated heat by NPs.

I.3.3.2 Key parameters controlling the generated heat

I.3.3.2.1 Extrinsic parameters

Magnetic field amplitude and frequency: As previously discussed, heating efficiency is characterised by the SAR value of the ferrofluid. The dissipated heat; however, does not only depend on the structure and composition of NPs but also on the frequency and amplitude of the magnetic field (*H*) applied[224]. SAR values typically increase with increasing frequencies and/or field amplitudes. Currently, most SAR values reported in the literature are measured at a frequency range of 300 – 700 kHz and a field range of 10 – 30 kA.m^{-1}. Nonetheless, it is still unclear if these values are safe at a clinical level. Brezovich established a safety limit for magnetic hyperthermia where the product $H \cdot f$ should be less than 4.85 x 10^{8} A.m^{-1}.s^{-1} to avoid eddy current effects[107]. In other words, the safety limit was fixed to avoid non-specific heating or damage to the human body. However, this threshold was obtained from the discomfort/tolerance feedback given by healthy patients upon a one hour MH treatment on the whole torso. No further remarks were done to this limit under other treatment conditions, i.e. smaller treated area, shorter treatment time, etc. More importantly, this study has not been repeated. As a result, this value remains as a reference and not a limit until further studies are done.

Viscosity of the fluid: as we saw from Brown based equation, Brown relaxation time is proportional to the viscosity of the fluid. Thus, in very viscous media, Brown relaxation time is longer and heating by Néel relaxation is predominant. Fortin *et al.* were able to optimise the SAR value of a suspension of γ-Fe_2O_3 by varying the ratio of glycerol : water in solution, hence varying the viscosity of the medium[225]. Similarly, De la Presa *et al.* compared the behaviour of NPs with various sizes in agar and water[226]. They observed that for large NPs, the heating power decreases when the viscosity increases while it remains stable for smaller NPs in both media. Thus empirically confirming that the reigning mechanism for heat loss in small NPs is Néel relaxation while for larger NP systems, Brown motion plays an important role.

I.3.3.2.2 Intrinsic parameters

The NP heating power primarily depends on their magnetic properties. Previously, we saw that the NPs MRI properties are strongly influenced by the saturation magnetisation. Magnetic hyperthermia, in turn, is governed by the particle anisotropy, the blocking temperature and the Néel and Brownian relaxation times. But other parameters such as particle size or the nature of the surface coating also influence the heating power of NPs. The different effects observed by each of these parameters will be discussed in the following section.

NP size: As previously stated when we discussed the different mechanisms of heat loss, the size of the NP core, and more precisely, whether the NP is monodomain or not, is of key importance. For large blocked particles of more than 100 nm, hysteresis losses are predominant. Conversely, for smaller particles, relaxation mechanisms prevail. At the same time, the main mechanism of relaxation, whether Néel or Brown, depends on the anisotropy of the NP (Figure I.27). The increase in anisotropy reduces the critical size transition between Néel and Brown mechanisms. This is a parameter to consider when assessing the heating capability of a system in a biological environment as Brown mechanism might become blocked upon cell internalisation. At the same time, the surface coating may also influence the heating ability of NPs by varying Brownian relaxation and the consequent heat transfer into the medium.

The influence of core size on SAR values has been the subject of many recent studies[225,228]. It seems that NPs with a size at the limit between a SPM single domain behaviour and a blocked domain would be optimal for MH treatments. In spite of that, due to the variation in the physical properties of synthesised NPs, the experimental values range between 12 and 25 nm[107,181,229]. Firstly, the magnetic properties of iron oxide NPs strongly depend on the synthesis method[138,230]. Beyond the mean size, particle size distribution can have a very significant effect on the value of SAR. A very small increase in polydispersity has been shown to decrease greatly the efficiency of NPs heating (Table I.7)[231,232].

Among the highest published SAR values measured under conditions compatible with clinical use ($Hf <$ 4.85 x 10^{8} A.m^{-1}.s^{-1}), 30 nm Fe_3O_4 NPs synthesised by chemical methods followed by a size selection process exhibited an outstanding performance (600 W.g^{-1} at 400 kHz and 10.3 kA.m^{-1}, ILP = 14.0

$nH.m^2.kg^{-1}$). However, the obtained heat loss remains far from that of Fe_3O_4 NPs produced by magnetotactic bacteria (magnetosomes 960 $W.g^{-1}$ at 410 kHz, 9.9 $kA.m^{-1}$, ILP = 23.7 $nH.m^2.kg^{-1}$), which has since not been achieved by chemically synthesised particles in the laboratory[233].

Particle Anisotropy: the effective anisotropy of a NP system has a strong impact on heat dissipation as we saw from its exponential dependence in Néel relaxation time. As such, changes in NPs anisotropy may allow varying the heating power of a NP system. The effective anisotropy of a NP is mainly the sum of the crystal or magnetocrystalline anisotropy, the shape anisotropy and surface effects. In the absence of an applied magnetic field, the magnetisation of the system will be pointing in the direction of minimum energy or *easy axis*. Under non-zero field conditions, the spin of the domains will try to orientate with the direction of the field. The energy required, known as crystal anisotropy, is primarily due to *spin-orbit* coupling hence it is the result of the intrinsic structure of the material (Figure I.28). Two main strategies can be adopted to increase the effective particle anisotropy hence the heating efficiency of NPs:

i) Varying the crystalline anisotropy of the material
ii) Varying shape

As stated above, the crystal anisotropy of a material is an intrinsic parameter hence, it will depend on the structure and composition of the system. Magnetite has the highest anisotropy among iron oxides, 11-14 $kJ.m^{-3}$, while that of maghemite is ~ 4.6 $kJ.m^{-3}$. Nonetheless, the anisotropy value may be increased by inserting other transition metals in the inverse spinel structure such as cobalt, manganese or nickel. Doping of iron oxide with Co or Mn has been proposed as a way to improve SAR[214]. Lee *et al.*[87] have shown that manganese or cobalt ferrites have higher SAR than magnetite NPs for identical sizes. However, up to now most publications have been devoted to IONPs because of their proven biocompatibility, ease of synthesis and tuning of their size with narrow size distribution. Despite their potential, the development of doped ferrites was thus limited because of their reduced biocompatibility and the complexity of their synthesis, which commonly leads to core-shell NPs or chemical heterogeneities[92,93,193].

Nevertheless core@shell NPs with a ferrite core of low magnetocrystalline anisotropy and a shell of ferrite with high magnetocrystalline anisotropy, have been synthesised leading to higher SAR values than NPs having homogeneous composition of the same materials[87]. The elevated SAR values were related to the magnetic exchange interaction between the core and shell materials of the NP. This increase in anisotropy is mainly due to the coupling between two interfaces of different magnetic nature, such as that between ferromagnetic and antiferromagnetic materials[234]. The core-shell structure is a promising approach to enhance the properties of NPs in hyperthermia[212,214].

On the other hand, the modification of NPs shape may also lead to an increase in the effective anisotropy and surface effects become more important. At the nanoparticle surface, changes in neighbouring atoms and in crystal orientation lead to changes in the local magnetisation with respect to the surface. For faceted particles, under non-zero field conditions, domain wall motion will be oriented towards forming flat domains to minimise energy thus increasing surface anisotropy[220]. At the same time, it seems that cubic morphology leads to a decrease in spin canting compared to spherical particles[107]. Faceted[182] or cubic-shaped[107,235,236] NPs have been found to display higher SAR values than their spherical counterparts (Table I.7). Nanocubes with an optimal size of 19 nm were found to have one of the highest SAR values published to date (2453 Wg^{-1} at 29 $kA.m^{-1}$ and 520 kHz, ILP = 5.6 $nH.m^2.kg^{-1}$)[107].

From this discussion, it may be obvious that an increase in particle anisotropy increases Néel relaxation time, hence, the heat dissipated by the system. However, this is not always the case. As shown by Habib *et al.*[237] the obtained SAR value for core@shell NPs increases along with anisotropy until reaching an maximum value upon which SAR no further increases or even falls. The influence of anisotropy is even more difficult to predict when the distance between NPs decreases (i.e. at high concentration) as SAR theory accounts only for individual NPs. The collective behaviour and its effect on the system anisotropy and heating capacity will be discussed in the following section.

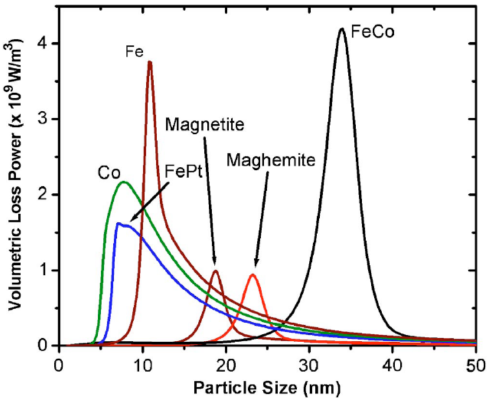

Figure I.28- SLP (or SAR) evolution as a function of size for various NP systems at 300 kHz and 39.8 kA.m^{-1}.[237]

I.3.3.2.3 Magnetic NPs concentration or collective behaviour

It is generally agreed that nanoparticle concentration has a direct effect on heat loss under MH due to dipolar interactions[235,238]. At the same time, to achieve a therapeutic effect upon MH treatment, high concentrations of NPs may be required in a delimited area, leading to high interacting systems. It is, therefore, crucial to understand the collective magnetic behaviour of NPs in order to control its influence on the achieved heating power. When the concentration in solution increases, inter-particle distance decreases leading to increased dipole interactions which modify the magnetic properties of the fluid. The stabilisation of NPs may occur as independent entities (single cores) or forming aggregates of several NPs. The latter leading to inter-core and inter-aggregate interactions. At inter-core distances, the exchange interactions start to contribute to the overall magnetic energy. Flower-shaped nanostructures which consist of controlled aggregates of NPs with coherent crystallographic orientation have been reported to exhibit cooperative behaviour with the consequent improvement on the obtained SAR values[197,239]. Conversely, independent cores stabilised in solution as aggregated suspensions have shown decreased SAR with increasing inter-particle interactions due to a collective spin rotation, which increases the energy barrier for rotation[240].

The effect of NP concentration in heat loss is somehow a controversial topic (see recent review by Deatsch *et al.*[86]). In general, when Néel relaxation is dominant, SAR decreases with increasing concentration whereas when Brownian relaxation predominates the opposite is observed. For instance, De la Presa *et al.*[241] reported no concentration effect on heating power when conducting SAR measurements on aggregated NPs for concentrations ranging from 6 to 300 mg.mL^{-1} Fe. They suggested that changes in concentration were only affecting inter-aggregate distances preserving the aggregate structure hence inter-particle distances. As such, interactions between aggregates should have little effect on the heating power. Conversely, Dennis *et al.*[242] observed a direct correlation between concentration and heating power. Dennis *et al.* reported high SAR values at high concentrations due to chain formation. As the distance between particles decreases, dipolar interactions increase and the formation of aggregates such as chains is favoured[242–244]. These chains present uniaxial anisotropy along their structure, which prevents them from rotating freely increasing their heating power, as observed for magnetosomes[233]. However, when the concentration is too high, the chains collapse and form larger aggregates, which causes the reduction of SAR[242]. The observed spatial arrangement of NPs can be also favoured by the morphology NPs. Martinez-Boubeta *et al.* showed that chain arrangement is particularly favoured for cubic NPs thanks to face-to-face arrangement[235]. When magnetosomes extracted from AMB-1 magnetotactic bacteria were used, NP chain formation was also observed with a maximum SAR *in vivo* of 875 W.g^{-1} for chains of ~300 nm in length[245].

Table I.7 - SAR values for ferrite nanoparticles from literature.

Type	Magnetic core	Core size (nm)	Coating	H (kA.m^{-1})	f (kHz)	Solvent	SAR (W.g^{-1})	ILP[a] (nHm^{2}kg^{-1})	ref.
Mono-domain	γ-Fe_2O_3	10-12	dextran	7.2	880	PM	210	4.6	231
	γ-Fe_2O_3	6-12	dextran	7.2	880	PM	90	2.0	
	Fe_3O_4	8	naked	14	300	H_2O	97	1.6	
	γ-Fe_2O_3	3	dextran	12.5	500	H_2O	106	1.4	228
	γ-Fe_2O_3	5	dextran	12.5	500	H_2O	524	6.7	
	γ-Fe_2O_3	7	dextran	12.5	500	H_2O	625	8.0	
Cubes	Fe_3O_4	45	sulphate ions	8	260	H_2O	63	3.8	236
	Iron oxide	19	PEG	29	520	H_2O	2452	5.6	107
	$CoFe_2O_4$	20	PMAO	32	105	H_2O	915	8.5	193
Chains	Magnetosomes	38		10	410	H_2O	960	23.4	233
	Magnetosomes	30		10	410	H_2O	530	12.9	
	Magnetosomes	45		31.8	183	gel	390	2.1	245
	Iron oxide	20	DMSO	23.9	765	H_2O	500	1.1	235
		40	DMSO	23.9	765	H_2O	205	0.5	
	Fe_3O_4	44	dextran	48	160	H_2O	81	0.2	242
	Iron oxide	44	-	23.9	765	agar 5%	1200	2.7	244
Clusters/multi-core	γ-Fe_2O_3 (nanoflowers)	11	citrate	21.5	700	H_2O	1944	6.0	239
	γ-Fe_2O_3	10.5	citrate	25	520	H_2O	1500	4.6	197
Core@shell	$CoFe_2O_4$	9	DMSA	37.4	500	H_2O	443	0.6	87
	$MnFe_2O_4$	15	DMSA	37.4	500	H_2O	411	0.6	
	$MnFe_2O_4$@$CoFe_2O_4$	15	DMSA	37.4	500	H_2O	3034	4.3	
	$CoFe_2O_4$@$Zn_{0.4}Fe_{2.6}O_4$	60	TMAOH	37.4	500	H_2O	10600	15.2	246

[a] *ILP values are shown for comparison. Note that at high field amplitudes ILP is no longer valid as it is a low-field approximation not applicable if the magnetic response of the ferrofluid is not linear with the field.*

Note: PM, physiological media; PEG, polyethylene glycol; PMAO, poly maleic anhydride 1–octadecene; DMSO,dimethyl sulfoxide ;DMSA, dimercaptosuccinic acid ; TMAOH, tetramethylammonium hydroxide.

I.3.3.2.4 Heat loss in biological environments

The use of MH as a stand-alone or an adjacent therapy for the treatment of cancer holds great possibilities. The number of publications on the development of new materials constantly increases with new systems exhibiting better and more robust heating properties. Nonetheless, to stablish the basis of a reliable therapy it is important to understand how the properties of the nanoheating vectors change upon exposure to a biological environment. We already discussed that the heat dissipation achieved by MNPs depends on the viscosity of the media. SAR values obtained in glycerol : water mixtures or in agar gel were significantly lower compared to water suspensions[241,247]. This trend was also found in a cell environment with SAR values decreasing at least 50 % and even 90 % depending on the size, shape and composition of the MNPs[248]. These results were observed both when MNPs were associated to the cell membrane and when internalised. This effect was attributed to Brownian mobility restriction. On the other hand, Etheridge *et al.* demonstrated that changes in heat loss were mainly associated with particle aggregation even if viscosity also had a detrimental effect on the obtained SAR[249].

Due to the increasing interest in the field, the number of *in vitro* studies concerning cytotoxicity, cell internalisation pathways or even MH response is increasing. The initial works were focused on proving the feasibility of the therapy achieving complete cell death upon MH treatment[107]; or even, targeted-treatment upon decoration of the NPs with cell membrane factors, such as EGF[250]. Due to the limitations of the available instruments to run MH experiments *in vitro*, most commonly, the experiments are carried out on cell suspensions. The translation of these results into an *in vivo* model is not always clear as cell responses may be altered compared to cells in tissues. More recently, some groups have started working on systems that allow applying MH on cell monolayers. In that case, cells can be kept under normal incubation conditions permitting studying their response to the treatment in a more realistic scenario. Dual therapies combining MH and chemotherapy have shown to achieve a synergistic effect significantly decreasing cell viability[251,252]. The initial studies, as previously stated, were focused on proving the outcome of the treatment, i.e. whether cells could be eliminated by MH. Nonetheless, the translation of this technique into a medical therapy requires understanding the mechanism of cell death as to avoid causing tissue necrosis and the subsequent side effects. Very recently, Yunok et al. have used chitosan- $MnFe_2O_4$ to control the main mechanism of cell death on MDA-MB-231 cells by tuning the conditions of the applied field[253]. Nonetheless, most commonly the analysis of the effect of the treatment is done by *post hoc* techniques leaving uncertain the direct response of cells to the treatment. On that basis, Connord *et al.* developed an MH system combined with a confocal microscope allowing real-time analysis of MH experiments on live cells. Immediate cell response and lysosomal membrane changes were investigated[254]. But more recently, Blanco-Andujar et al. reported a real-time tracking of cell response upon MH treatment showing an induced apoptotic death after a 2 h treatment under a field of amplitude 10.5 kA/m and frequency of 950 kHz[255]. Some of the most relevant references on *in vitro* MH experiments are gathered in Table I.8.

Table I.8 - Comparison of in vitro magnetic hyperthermia treatments reported in the literature

Cell support	NPs	*Cell line*	*H* *(kA.m^{-1})*	*f* *(kHz)*	*SAR* *(W.g^{-1})*	*ILP* (nHm^{2}kg^{-1})	*Dose*	*notes*	*ref.*
Suspension	ATAP-PEI-$ZnFe_2O_4$@Au	MCF7/U87	5	300	-	-	45 min	peptide-MH synergistic therapy. Viability down to ~40%	256
	PLGA-Fe_3O_4	MCF7/L929/ G1	18	305	-	-	1-2 h	chemo-MH synergistic therapy (Cur/5-FU) improved with targeted uptake (F + Tf)	257
	EGF- Fe_3O_4	MDA-MB-	37.5	233	78^a	0.8	2 h	Targeted particle uptake (EGFR)	250
	pluronic-Fe_3O_4 agg	A549	6	386	-	-	15 min	Cell death by autophagy via ROS generation	258
	PEG-IO	KB	20	110	509^b	5.6	1 h	Complete cell death but no detail on the mechanism	107
	dextran-Fe_3O_4	DC	12.7	260	-	-	5-15	Controlled cell death. Necrotic population after 10 min	259
Monolayer	GM-$Zn_{0.4}Fe_{2.6}O_4$	MDA-MB-	37.4	500	-	-	80 min	Chemo-MH synergistic effect. Cell death via apoptosis	251
	MG-IO	INR1G9-CCK2R	41.4	275	-	-	2 h	Specific targeting by CCK2 receptor. Viability down to ~35%	260
	Chi-$MnFe_2O_4$	MDA-MB-	20-50	307	209^c	0.3	30 min	Death by necrosis or apoptosis obtained depending on MH conditions. Viability down to ~20%	253
	$(Zn_{0.4}Co_{0.6})Fe_2O_4$@$(Zn_{0.4}Mn_{0.6})Fe_2O_4$	HeLa	60	200	1343	1.9	20 min	chemo-MH synergistic therapy (DOX). Viability down to ~20%	252
	MG-IO	INR1G9-CCK2R	42.2	300	-	-	2 h	Real-time analysis of lysosome membrane permeabilisation.	254
	CA-IO	DX3	10.8	950	-	4.1	2 h	Real-time monitoring of apoptosis on adherent cells.	255

Note: ATAP, mitochondria-targeting pro-apoptotic amphipathic tail-anchoring peptide; IO, iron oxide; Chi, chitosan; CA, citric acid, PEG, polyethylene glycol; agg, aggregates, FU, fluorouracil; Cur, curcumin; PLGA, poly(D,L-lactic-co-

glycolic acid; MG, synthetic replicate of gastrin; F, folate; Tf, transferrin; EGF, epidermal growth factor; EGFR, EGF receptor, GM, geldanamycin (antitumor antibiotic); MA, magnetic actuation.

[a] *Measurement conditions: 233kHz@20.7 kA/m^{-1}*

[b] *Measurement conditions: 320 kHz@15 kA/m^{-1}*

[c] *Measurement conditions: 307 kHz@50 kA.m^{-1}*

Conversely, the number of MH studies *in vivo* is rather limited due to the intrinsic challenges found when translating this therapy into a live system: (i) heat is dissipated by the vascular system, (ii) NPs penetration within the tumour is hampered by its microenvironment and finally (iii) particle accumulation in the targeted area may be limited. Cancer cell growth occurs in a chaotic manner, which leads to fast tissue vascularisation or angiogenesis. As a consequence of the overgrowth, tumours are subjected to low pH, energy deprivation and hypoxia, factors that decrease the efficiency of therapies such as radiotherapy or chemotherapy[261,262]. Moreover, this effect is enhanced by the tumour microenvironment that limits the permeation of any drugs into the tumour[263]. This is also the case for MNPs, as histological studies have repeatedly found their accumulation on the edge of tumours. However, as observed by Kolosnjaj-Tabi, *et al.*[130], this architecture can be altered with MH. They observed that PEG-Fe_3O_4 cubes successfully penetrated within the tumour tissue after a 3-dose MH cycle treatment thanks to the alteration of the collagen structure. Most commonly, *in vivo* MH experiments are faced with this problem as MNPs are directly injected subcutaneously into the tumour area. Total remission by local MH upon direct injection (DI) has been reported in the literature by different groups; however, most commonly even though this approach leads to a decrease in tumour growth, a delayed recurrence after the treatment is observed (Table I.C-5). Most recently, Gao *et.al.*[264], combined the use of MH with chemotherapy using DOX/PLGA-Fe_3O_4 NPs leading to total eradication of the tumour after 5 days. Similarly, Matsuoka *et al.*[265], achieved complete regression of osteoblastoma xenografs by direct injection of magnetic cationic liposomes after 15 days upon a 30 min MH treatment. From the published data it is clear that DI stands as an interesting option from a prognosis perspective. More importantly, intratumoral application could be a reality in a clinical environment as MNPs may be injected using the established protocols for tumour biopsy. Yet the possibility of achieving a therapeutic targeted effect in deep tissues with a minimally invasive approach remains linked to intravenous injection (IV), especially if considering non-solid tumours. Problems such as targeted MNP accumulation or limited tumour retention are known limiting factors[266]. On that basis, Moroz *et al.* compared IA injection against DI to target a liver tumour model in rabbits. Particle distribution and the obtained necrotic pattern in the tumour tissue was superior by IA injection with tumour size reduction observed in nearly 80% of animals[267]. Total regression was not achieved upon treatment as observed in other cases upon IV injection (Table I.9). Remarkably, Huang *et al.* reported complete regression of tumours upon IV injection in ~80% of animals using a very short 2 min dose treatment of MH (980 kHz, 38 kA.m^{-1})[268]. Due to the limited accumulation and distribution of MNPs in tumours, the variation in the obtained results by different groups is not surprising as the experimental MH conditions are established on the basis of total accumulation without a clear answer to whether the conditions are optimal for the MNP accumulation level. On that basis, Dähring *et al.,* recently developed a micro-CT guided system to map the distribution of MNPs *in vivo* upon tumour injection. This allowed modulating the MH treatment depending on the local concentration of NPs leading to an enhanced MH effect, which improved tumour regression[269]. This technique could be potentially adapted to tumour models upon IV injection allowing to readjust the administrated MH treatment.

Table I.9 - Comparison of in vivo magnetic hyperhetmia treatments reported in the literature by intravenous or direct tumour injection.

NPs	***Injection***	***H ($kA.m^{-1}$)***	***f (kHz)***	***SAR ($W.g^{-1}$)***	***Treatment***	***notes***	***ref.***
PEG-Fe_3O_4	DI	23.8	111	137	3 x 30 min	observed changes on tumour microenvironment	130
MCL	DI	-	118	-	30 min	complete regression	265
Magnetosome chains	DI	31.8	183	875	3 x 20 min	chain formation, total remission	245
DOX/PLGA-Fe_3O_4	DI	1	626	77	110 s	chemo-MH synergistic therapy, total elimination of tumours after 5 days	264
OA-IO-OA	DI	-	265	-	-	apoptotic mechanism identified in growth inhibition	270
DOX/PPy- Fe_3O_4	DI	8	230	487	20 min	total remission without recurrence	271
DMSA-Fe_3O_4	DI	15.4	435	658 / 900	60 min	tumour growth remission	230
PVP-Au@Fe_3O_4 multicore	DI	19.9	110	634	5 x 5 min	photo-MH synergistic therapy. Growth regression compared to control over 5 days.	272
GM- $Zn_{0.4}Fe_{2.6}O_4$	DI	37.4	500	-	30 min	chemo-MH synergistic effect. Tumours elimination after 8 days.	251
$CoFe_2O_4$@$MnFe_2O_4$	DI	37.3	500		10 min	complete tumour elimination	87
FA-PEG-IO clusters	IV	8	230	248	20 min	Life-spam increased 4 weeks	273
Fe@Fe_3O_4	IP[a]	39.8	145		15 – 20 min	Life-spam increased by 31%	274
Fe_2O_3 μm-beads	IA/DI	30 - 45	53		20 min	IA achieved better results; tumours reduced in 79% of animals	267
PEG-Fe_3O_4	IV	38	980	754	2	78% mice tumour free after 160 days	268
PEG-dextran-Fe_3O_4	IV	56 - 104	153	62-78	20 min	14% targeting efficiency; inhomogeneous distribution in the tumour; HS showed necrosis but no apoptosis. Tumour growth delayed but no survivors.	275
PEG PL-(Mn-Zn)Fe_2O_4	IV		390	324	8 x 30 min	Delayed tumour growth but no eradication.	276

Note: DI, direct injection; IP, intraperitoneal injection; IV, intravenous injection; IA, interarterial injection; PEI; polyethyleneimine; mSi, mesoporous silica; PPy. polypyrrole, PEG, polyethylene glycol; MCL, Magnetite Cationic Liposomes; FA, folic acid; PLGA, poly(lactic-co-glycolic acid); PEG-PL, PEG-phospholipid (1,2-distearoyl-sn-glycero-3-

phosphoethanolamine-N-[methoxy(polyethylene glycol copolymers, DSPE-PEG2000); HS, histology studies; GM, geldanamycin (antitumor antibiotic).

[a] *Cells loaded with MNPs were administrated to the animal model.*

I.3.4 Conclusion

The rational design of IONPs for MRI and MH is of key importance to target the actual needs on the development of better performing systems for nanomedecine. In the case of T_2-CAs for MRI, magnetic iron oxide based NPs must be designed to have the highest relaxivity r2 value along with a high r2/r1 ratio. We have seen that intrinsic parameters such as saturation magnetisation, NPs size, chemical composition and shape or the aggregation state have a direct effect on relaxivity. However, besides the design of the NP core, the organic coating is also a key component as it allows to control water diffusion and residence time close to the magnetic core.

Similarly for the design of IONPs as heating mediators in MH, intrinsic parameters such as NP size, particle anisotropy or collective magnetic behaviour were shown to directly affect heat loss.

There have been various IONP formulations brought to the market within the last years for MRI applications, such as Feridex or Resovist, but only one formulation has been granted approval for clinical use in MH. Nanotherm^{TM} is a ferrofluid used by MagForce^{TM}(Berlin) constituted by aminosilane-coated spherical IO NPs of *ca*. 15 nm size. Besides the apparently simple formulation of this ferrofluid, the results of the clinical trials carried out by MagForce^{TM} are very encouraging. However, the intratumoral injected dose required to achieve a therapeutic effect is very high (112 mg.mL^{-1}). As such, optimising the design of the heating mediator nanoagents for MH while keeping an efficient heating power has become a truly important challenge. As we have seen in this review, this could be achieved by tuning the various parameters evoked in the above paragraphs: size, shape, magnetocrystaline anisotropy and collective behaviour.

Additionally, one major future perspectives of such IO NPs will be also towards the combination of targeted MRI and MH. Current progress in synthesis methods allows now synthesizing NPs with different shapes and/or core@shell structures that are highly promising to improve the heat efficacy. Such NPs designed for magnetic hyperthermia display very good MRI properties as they are also related to NPs magnetic properties. Simply : the heating efficacity is greatly improved by increasing the NPs anisotropy and that contributes also to enhance relaxivity values.

However the heat released by magnetic NPs does not depend only on their intrinsec properties in suspensions but also on the magnetic interaction between individual NPs. The aggregation state of NPs have a direct impact both on relaxivity (they increase) and heating (more complex) values. The degree of interaction will vary with concentration upon internalisation and accumulation but also, it is important to consider that the potential of a ferrofluid to dissipate heat may be affected by the constrictions of the biological environment (fixation to cell membranes, interaction with biological molecules, etc.). Therefore, besides the challenge to optimise the synthesis of NPs for their therapeutic use in MH and imaging, there is a need to ensure that their performance is maintained upon exposure to biological environments. The adoption of a remote MH therapy either as a stand-alone or a reliable adjunct therapy is still far from being a reality due to the variable performance found in many NP systems, and to the limited understanding of the mechanisms and signalling pathways involved in tumour cell destruction. As we discussed previously, magnetosome chains have been found to exhibit yet the best performance under MH measurements; however, it is still unclear if and under which conditions, aggregation or chain formation occurs in living cells. It is clear that the understanding of MH at the cell level is far from complete. A better knowledge about magnetic particle interactions in living tissue is thus of foremost importance to achieve a better understanding of MH and heat transfer inside tumour cells.

I.4 General conclusion

Iron oxide NPs are fascinating as the nano size leads to very suitable properties at the origin of plenty of biomedical applications. Nevertheless, to be used as theranostic agents, their magnetic properties need to be enhanced in order to reduce to dose needed for an efficient treatment.

Magnetic properties are mostly dependent on the NPs characteristics’s (size, shape, composition, defects …). To improve their properties work has to be done on their synthesis to control these parameters. Thermal decomposition is the most appropriate way to design NPs with specific shapes but some knowledge on the synthesis is required in order to develop new protocols. Literature shows that many parameters (solvent, ligand, temperature …) have a role on the outcome of the synthesis but despite few hints at a relation between the precursor structure and the NPs this point has never been properly studied. Cubic shape has been quite studied and has shown better efficiency in theranostic application than sphere. Anisotropic synthesis is a real challenge but that worth the time spent on it.

Altough synthetizing anisotropic shapes is capital for the application, for an *in vivo* use, NPs need to be functionalized with organic molecules providing colloidal stability and biocompatibility. For a good biodistribution and bioelemination, functionalized NPs needs to present a hydrodynamic diameter under 100 nm while keeping the NPs properties. The molecules on the surface on the NPs need to provide biocompatibility but also need to remain strongly anchored on the surface of the NP withouth desorbing with time or in vivo. Colloidal stability is not only capital for in vivo injection but it also plays a role on the theranostic application as aggregation state can have a (nefaste) effect on the properties.

In that context, my PhD work dealt with the synthesis of dendronized iron oxide based NPs displaying anisotropic shape to improve their properties as heating agent for magnetic hyperthermia whilealways checking their properties as contrast agent for MRI. It has conducted me to synthesize and characterize structurally and thermally an *in house* precursor. The *in house* synthesis is an attempt to contribute to a better understanding of the synthesis parameters controlling the shape during the thermal decomposition method. IONPs with different shapes have been thus synthesized and characterized; they have been then coated with dendron molecules which have been found suitable as contrast agent for *in vitro* and *in vivo* MRI. Their magnetic and colloidal properties have been investigated and their potential as contrast agent for MRI and as heating agent by magnetic hyperthermia has been evaluated in water suspension, *in vitro* through cell studies and some preliminary *in vivo* studies have been conducted.

REFERENCES

1. Han, D. H., Wang, J. P. & Luo, H. L. Crystallite size effect on saturation magnetization of fine ferrimagnetic particles. *J. Magn. Magn. Mater.* **136,** 176–182 (1994).
2. Hyeon, T., Lee, S. S., Park, J., Chung, Y. & Na, H. B. Synthesis of highly crystalline and monodisperse maghemite nanocrystallites without a size-selection process. *J. Am. Chem. Soc.* **123,** 12798–12801 (2001).
3. Santoyo Salazar, J. *et al.* Magnetic Iron Oxide Nanoparticles in 10−40 nm Range: Composition in Terms of Magnetite/Maghemite Ratio and Effect on the Magnetic Properties. *Chem. Mater.* **23,** 1379–1386 (2011).
4. Daou, T. J. *et al.* Hydrothermal Synthesis of Monodisperse Magnetite Nanoparticles. *Chem. Mater.* **18,** 4399–4404 (2006).
5. Belin, T., Guigue-Millot, N., Caillot, T., Aymes, D. & Niepce, J. C. Influence of Grain Size, Oxygen Stoichiometry, and Synthesis Conditions on the γ-Fe2O3 Vacancies Ordering and Lattice Parameters. *J. Solid State Chem.* **163,** 459–465 (2002).
6. Guigue-Millot, N. *et al.* Chemical Heterogeneities in Nanometric Titanomagnetites Prepared by Soft Chemistry and Studied Ex Situ: Evidence for Fe-Segregation and Oxidation Kinetics. *J. Phys. Chem. B* **105,** 7125–7132 (2001).
7. Jolivet, J.-P. & Tronc, E. Interfacial electron transfer in colloidal spinel iron oxide. Conversion of Fe3O4-γFe2O3 in aqueous medium. *J. Colloid Interface Sci.* **125,** 688–701 (1988).
8. Daou, T. J. *et al.* Phosphate Adsorption Properties of Magnetite-Based Nanoparticles. *Chem. Mater.* **19,** 4494–4505 (2007).
9. Baaziz, W. *et al.* Magnetic Iron Oxide Nanoparticles: Reproducible Tuning of the Size and Nanosized-Dependent Composition, Defects, and Spin Canting. *J. Phys. Chem. C* **118,** 3795–3810 (2014).
10. Demortière, A. *et al.* Size-dependent properties of magnetic iron oxide nanocrystals. *Nanoscale* **3,** 225–232 (2011).
11. Park, J. *et al.* Ultra-large-scale syntheses of monodisperse nanocrystals. *Nat. Mater.* **3,** 891–895 (2004).
12. Bronstein, L. M. *et al.* Influence of Iron Oleate Complex Structure on Iron Oxide Nanoparticle Formation. *Chem. Mater.* **19,** 3624–3632 (2007).
13. Farrell, D., Cheng, Y., McCallum, R. W., Sachan, M. & Majetich, S. A. Magnetic interactions of iron nanoparticles in arrays and dilute dispersions. *J. Phys. Chem. B* **109,** 13409–13419 (2005).
14. Tartaj, P., Morales, M. del P., Veintemillas-Verdaguer, S., González-Carreño, T. & Serna, C. J. The preparation of magnetic nanoparticles for applications in biomedicine. *J. Phys. Appl. Phys.* **36,** R182 (2003).
15. Walter, A. *et al.* Modulation of Relaxivity, Suspension Stability, and Biodistribution of Dendronized Iron Oxide Nanoparticles as a Function of the Organic Shell Design. *Part. Part. Syst. Charact.* **32,** 552–560 (2015).
16. Billotey, C. *et al.* Cell internalization of anionic maghemite nanoparticles: quantitative effect on magnetic resonance imaging. *Magn. Reson. Med.* **49,** 646–654 (2003).
17. Vichery, C. *Procédé de recuit protégé appliqué à des nanoparticules d'oxyde de fer : étude des relations structure / propriétés magnétiques*. (Palaiseau, Ecole polytechnique, 2012).
18. Mody, V. V., Singh, A. & Wesley, B. Basics of magnetic nanoparticles for their application in the field of magnetic fluid hyperthermia. *Eur. J. Nanomedicine* **5,** 11–21 (2013).
19. Walter, A. *Élaboration de nano-objets magnétiques dendronisés à vocation théranostic*. (Strasbourg, 2014).
20. Brice-Profeta, S. *Etude de l'ordre chimique et magnétique d'oxydes spinelles de taille nanométrique par dichroïsme magnétique circulaire des rayons X.* (Paris 6, 2004).
21. Zijlstra, H. Chapter 2 Permanent magnets; theory. *Handb. Ferromagn. Mater.* **3,** 37–105 (1982).
22. Roca, A. G. *et al.* Magnetite nanoparticles with no surface spin canting. *J. Appl. Phys.* **105,** 114309 (2009).
23. Morales, M. P., Serna, C. J., Bødker, F. & Mørup, S. Spin canting due to structural disorder in maghemite. *J. Phys. Condens. Matter* **9,** 5461 (1997).
24. Tronc, E., Prené, P., Jolivet, J. P., Dormann, J. L. & Grenèche, J. M. Spin Canting in γ-Fe2O3 Nanoparticles. *Hyperfine Interact.* **112,** 97–100 (1998).
25. Tronc, E. *et al.* Surface-related properties of γ-Fe2O3 nanoparticles. *J. Magn. Magn. Mater.* **221,** 63–79 (2000).
26. Dormann, J. L., Fiorani, D. & Tronc, E. Magnetic Relaxation in Fine-Particle Systems. in *Advances in Chemical Physics* (eds. Prigogine, I. & Rice, S. A.) 283–494 (John Wiley & Sons, Inc., 1997).
27. Pauly, M. *Structuration de nanoparticules magnétiques d'oxyde de fer en films et étude de leurs propriétés magnétiques et de magnétotransport*. (Strasbourg, 2010).
28. Skumryev, V., Blythe, H. J., Cullen, J. & Coey, J. M. D. AC susceptibility of a magnetite crystal. *J. Magn. Magn. Mater.* **196,** 515–517 (1999).
29. Daou, T. J. *et al.* Coupling Agent Effect on Magnetic Properties of Functionalized Magnetite-Based Nanoparticles. *Chem. Mater.* **20,** 5869–5875 (2008).
30. Park, J. *et al.* One-Nanometer-Scale Size-Controlled Synthesis of Monodisperse Magnetic Iron Oxide Nanoparticles. *Angew. Chem. Int. Ed.* **44,** 2872–2877 (2005).
31. Kachkachi, H., Ezzir, A., Noguès, M. & Tronc, E. Surface effects in nanoparticles: application to maghemite -Fe O. *Eur. Phys. J. B* **14,** 681–689 (2000).
32. Iglesias, Ò. & Labarta, A. Role of surface disorder on the magnetic properties and hysteresis of nanoparticles. *Phys. B Condens. Matter* **343,** 286–292 (2004).
33. Kodama, R. H. & Berkowitz, A. E. Atomic-scale magnetic modeling of oxide nanoparticles. *Phys. Rev. B* **59,** 6321–6336 (1999).
34. Millan, A. *et al.* Surface effects in maghemite nanoparticles. *J. Magn. Magn. Mater.* **312,** L5–L9 (2007).
35. Shendruk, T. N., Desautels, R. D., Southern, B. W. & Lierop, J. van. The effect of surface spin disorder on the magnetism of γ-Fe 2 O 3 nanoparticle dispersions. *Nanotechnology* **18,** 455704 (2007).
36. Unni, M. *et al.* Thermal Decomposition Synthesis of Iron Oxide Nanoparticles with Diminished Magnetic Dead Layer by Controlled Addition of Oxygen. *ACS Nano* **11,** 2284–2303 (2017).
37. Dutta, P., Manivannan, A., Seehra, M. S., Shah, N. & Huffman, G. P. Magnetic properties of nearly defect-free

maghemite nanocrystals. *Phys. Rev. B* **70,** 174428 (2004).

38. Morales, M. P. *et al.* Surface and Internal Spin Canting in γ-Fe2O3 Nanoparticles. *Chem. Mater.* **11,** 3058–3064 (1999).

39. Mürbe, J., Rechtenbach, A. & Töpfer, J. Synthesis and physical characterization of magnetite nanoparticles for biomedical applications. *Mater. Chem. Phys.* **110,** 426–433 (2008).

40. Peddis, D. *et al.* Cationic distribution and spin canting in $CoFe_2O_4$ nanoparticles. *J. Phys. Condens. Matter* **23,** 426004 (2011).

41. Sawatzky, G. A., Van Der Woude, F. & Morrish, A. H. M"ossbauer Study of Several Ferrimagnetic Spinels. *Phys. Rev.* **187,** 747–757 (1969).

42. Ali, A. *et al.* Synthesis, characterization, applications, and challenges of iron oxide nanoparticles. *Nanotechnol. Sci. Appl.* **9,** 49–67 (2016).

43. Laurent, S. *et al.* Magnetic Iron Oxide Nanoparticles: Synthesis, Stabilization, Vectorization, Physicochemical Characterizations, and Biological Applications. *Chem. Rev.* **108,** 2064–2110 (2008).

44. Gupta, A. K. & Gupta, M. Synthesis and surface engineering of iron oxide nanoparticles for biomedical applications. *Biomaterials* **26,** 3995–4021 (2005).

45. Figuerola, A., Di Corato, R., Manna, L. & Pellegrino, T. From iron oxide nanoparticles towards advanced iron-based inorganic materials designed for biomedical applications. *Pharmacol. Res.* **62,** 126–143 (2010).

46. Mornet, S., Vasseur, S., Grasset, F. & Duguet, E. Magnetic nanoparticle design for medical diagnosis and therapy. *J. Mater. Chem.* **14,** 2161–2175 (2004).

47. Colombo, M. *et al.* Biological applications of magnetic nanoparticles. *Chem. Soc. Rev.* **41,** 4306–4334 (2012).

48. Lu, A.-H., Salabas, E. L. & Schüth, F. Magnetic Nanoparticles: Synthesis, Protection, Functionalization, and Application. *Angew. Chem. Int. Ed.* **46,** 1222–1244 (2007).

49. Gutiérrez, L. *et al.* Synthesis methods to prepare single- and multi-core iron oxide nanoparticles for biomedical applications. *Dalton Trans* **44,** 2943–2952 (2015).

50. Lopez-Perez, J. A., Lopez-Quintela, M. A., Mira, J. & Rivas, J. Preparation of magnetic fluids with particles obtained in microemulsions. *IEEE Trans. Magn.* **33,** 4359–4362 (1997).

51. Chen, D. & Xu, R. Hydrothermal synthesis and characterization of nanocrystalline Fe3O4 powders. *Mater. Res. Bull.* **33,** 1015–1021 (1998).

52. Wan, J., Cai, W., Meng, X. & Liu, E. Monodisperse water-soluble magnetite nanoparticles prepared by polyol process for high-performance magnetic resonance imaging. *Chem. Commun.* 5004–5006 (2007). doi:10.1039/B712795B

53. Dong, H., Chen, Y.-C. & Feldmann, C. Polyol synthesis of nanoparticles: status and options regarding metals, oxides, chalcogenides, and non-metal elements. *Green Chem.* **17,** 4107–4132 (2015).

54. Chakroune, N., Viau, G., Ricolleau, C., Fiévet-Vincent, F. & Fiévet, F. Cobalt-based anisotropic particles prepared by the polyol process. *J. Mater. Chem.* **13,** 312–318 (2003).

55. Sun, S. *et al.* Monodisperse MFe2O4 (M = Fe, Co, Mn) nanoparticles. *J. Am. Chem. Soc.* **126,** 273–279 (2004).

56. Sun, S. & Zeng, H. Size-Controlled Synthesis of Magnetite Nanoparticles. *J. Am. Chem. Soc.* **124,** 8204–8205 (2002).

57. Murray, C. B., Norris, D. J. & Bawendi, M. G. Synthesis and characterization of nearly monodisperse CdE (E = sulfur, selenium, tellurium) semiconductor nanocrystallites. *J. Am. Chem. Soc.* **115,** 8706–8715 (1993).

58. Peng, X., Wickham, J. & Alivisatos, A. P. Kinetics of II-VI and III-V Colloidal Semiconductor Nanocrystal Growth: 'Focusing' of Size Distributions. *J. Am. Chem. Soc.* **120,** 5343–5344 (1998).

59. Jeong, U., Teng, X., Wang, Y., Yang, H. & Xia, Y. Superparamagnetic Colloids: Controlled Synthesis and Niche Applications. *Adv. Mater.* **19,** 33–60 (2007).

60. Redl, F. X. *et al.* Magnetic, electronic, and structural characterization of nonstoichiometric iron oxides at the nanoscale. *J. Am. Chem. Soc.* **126,** 14583–14599 (2004).

61. Wetterskog, E., Tai, C.-W., Grins, J., Bergström, L. & Salazar-Alvarez, G. Anomalous Magnetic Properties of Nanoparticles Arising from Defect Structures: Topotaxial Oxidation of $Fe_{1-x}O|Fe_{3-\delta}O_4$ Core|Shell Nanocubes to Single-Phase Particles. *ACS Nano* **7,** 7132–7144 (2013).

62. Lak, A. *et al.* Size dependent structural and magnetic properties of FeO–Fe3O4 nanoparticles. *Nanoscale* **5,** 12286 (2013).

63. Pichon, B. P. *et al.* Microstructural and Magnetic Investigations of Wüstite-Spinel Core-Shell Cubic-Shaped Nanoparticles. *Chem. Mater.* **23,** 2886–2900 (2011).

64. Hai, H. T. *et al.* Size control and characterization of wustite (core)/spinel (shell) nanocubes obtained by decomposition of iron oleate complex. *J. Colloid Interface Sci.* **346,** 37–42 (2010).

65. Sun, X., Frey Huls, N., Sigdel, A. & Sun, S. Tuning Exchange Bias in Core/Shell FeO/Fe_3O_4 Nanoparticles. *Nano Lett.* **12,** 246–251 (2012).

66. Shipway, A. N., Katz, E. & Willner, I. Nanoparticle arrays on surfaces for electronic, optical, and sensor applications. *Chemphyschem Eur. J. Chem. Phys. Phys. Chem.* **1,** 18–52 (2000).

67. Herman, D. A. J. *et al.* How to choose a precursor for decomposition solution-phase synthesis: the case of iron nanoparticles. *Nanoscale* **7,** 5951–5954 (2015).

68. van Embden, J., Chesman, A. S. R. & Jasieniak, J. J. The Heat-Up Synthesis of Colloidal Nanocrystals. *Chem. Mater.* **27,** 2246–2285 (2015).

69. LaMer, V. K. & Dinegar, R. H. Theory, Production and Mechanism of Formation of Monodispersed Hydrosols. *J. Am. Chem. Soc.* **72,** 4847–4854 (1950).

70. Xia, Y., Xiong, Y., Lim, B. & Skrabalak, S. E. Shape-controlled synthesis of metal nanocrystals: simple chemistry meets complex physics? *Angew. Chem. Int. Ed Engl.* **48,** 60–103 (2009).

71. Kwon, S. G. *et al.* Kinetics of monodisperse iron oxide nanocrystal formation by 'heating-up' process. *J. Am. Chem. Soc.* **129,** 12571–12584 (2007).

72. Nozawa, K., Delville, M.-H., Ushiki, H., Panizza, P. & Delville, J.-P. Growth of monodisperse mesoscopic metal-oxide

colloids under constant monomer supply. *Phys. Rev. E Stat. Nonlin. Soft Matter Phys.* **72,** 011404 (2005).

73. Bronstein, L. M. *et al.* Nanoparticles by Decomposition of Long Chain Iron Carboxylates: From Spheres to Stars and Cubes. *Langmuir* **27,** 3044–3050 (2011).

74. Vargas, J. M. & Zysler, R. D. Tailoring the size in colloidal iron oxide magnetic nanoparticles. *Nanotechnology* **16,** 1474–1476 (2005).

75. Meledandri, C. J., Stolarczyk, J. K., Ghosh, S. & Brougham, D. F. Nonaqueous Magnetic Nanoparticle Suspensions with Controlled Particle Size and Nuclear Magnetic Resonance Properties. *Langmuir* **24,** 14159–14165 (2008).

76. Mourdikoudis, S. & Liz-Marzán, L. M. Oleylamine in Nanoparticle Synthesis. *Chem. Mater.* **25,** 1465–1476 (2013).

77. Bronstein, L. M. *et al.* Influence of Iron Oleate Complex Structure on Iron Oxide Nanoparticle Formation. *Chem. Mater.* **19,** 3624–3632 (2007).

78. Baaziz, W. *Synthèse et caractérisation des nanoparticules spinelles et coeur-coquille à base d'oxyde de fer et de cobalt*. (Strasbourg, 2011).

79. Keating, M., Chen, Y., Larmour, I. A., Faulds, K. & Graham, D. Growth and surface-enhanced Raman scattering of Ag nanoparticle assembly in agarose gel. *Meas. Sci. Technol.* **23,** 084006 (2012).

80. Kovalenko, M. V. *et al.* Fatty Acid Salts as Stabilizers in Size- and Shape-Controlled Nanocrystal Synthesis: The Case of Inverse Spinel Iron Oxide. *J. Am. Chem. Soc.* **129,** 6352–6353 (2007).

81. Bárcena, C. *et al.* Zinc ferrite nanoparticles as MRI contrast agents. *Chem. Commun.* 2224–2226 (2008). doi:10.1039/B801041B

82. Li, D. *et al.* Synthesis and Size-Selective Precipitation of Monodisperse Nonstoichiometric MxFe3–xO4 (M = Mn, Co) Nanocrystals and Their DC and AC Magnetic Properties. *Chem. Mater.* **28,** 480–489 (2016).

83. Bao, N. *et al.* Formation Mechanism and Shape Control of Monodisperse Magnetic $CoFe_2O_4$ Nanocrystals. *Chem. Mater.* **21,** 3458–3468 (2009).

84. Zeng, H., Rice, P. M., Wang, S. X. & Sun, S. Shape-Controlled Synthesis and Shape-Induced Texture of $MnFe_2O_4$ Nanoparticles. *J. Am. Chem. Soc.* **126,** 11458–11459 (2004).

85. Song, Q. & Zhang, Z. J. Shape Control and Associated Magnetic Properties of Spinel Cobalt Ferrite Nanocrystals. *J. Am. Chem. Soc.* **126,** 6164–6168 (2004).

86. Deatsch, A. E. & Evans, B. A. Heating efficiency in magnetic nanoparticle hyperthermia. *J. Magn. Magn. Mater.* **354,** 163–172 (2014).

87. Lee, J.-H. *et al.* Exchange-coupled magnetic nanoparticles for efficient heat induction. *Nat. Nanotechnol.* **6,** 418–422 (2011).

88. Salazar-Alvarez, G. *et al.* Two-, Three-, and Four-Component Magnetic Multilayer Onion Nanoparticles Based on Iron Oxides and Manganese Oxides. *J. Am. Chem. Soc.* **133,** 16738–16741 (2011).

89. Masala, O. & Seshadri, R. Spinel Ferrite/MnO Core/Shell Nanoparticles: Chemical Synthesis of All-Oxide Exchange Biased Architectures. *J. Am. Chem. Soc.* **127,** 9354–9355 (2005).

90. Im, G. H. *et al.* Fe3O4/MnO hybrid nanocrystals as a dual contrast agent for both T1- and T2-weighted liver MRI. *Biomaterials* **34,** 2069–2076 (2013).

91. Lee, K. S. *et al.* Seed Size-Dependent Formation of Fe_3O_4/MnO Hybrid Nanocrystals: Selective, Magnetically Recyclable Catalyst Systems. *Chem. Mater.* **24,** 682–687 (2012).

92. Baaziz, W. *et al.* High Exchange Bias in Fe3−δO4@CoO Core Shell Nanoparticles Synthesized by a One-Pot Seed-Mediated Growth Method. *J. Phys. Chem. C* **117,** 11436–11443 (2013).

93. Baaziz, W. *et al.* Tuning of Synthesis Conditions by Thermal Decomposition toward Core–Shell $Co_xFe_{1-x}O$@$Co_yFe_{3-y}O_4$ and $CoFe_2O_4$ Nanoparticles with Spherical and Cubic Shapes. *Chem. Mater.* **26,** 5063–5073 (2014).

94. Zhang, L., Wu, J., Liao, H., Hou, Y. & Gao, S. Octahedral Fe3O4nanoparticles and their assembled structures. *Chem. Commun.* 4378–4380 (2009). doi:10.1039/B906636E

95. Zitoun, D., Pinna, N., Frolet, N. & Belin, C. Single Crystal Manganese Oxide Multipods by Oriented Attachment. *J. Am. Chem. Soc.* **127,** 15034–15035 (2005).

96. Zhou, Z. *et al.* Anisotropic Shaped Iron Oxide Nanostructures: Controlled Synthesis and Proton Relaxation Shortening Effects. *Chem. Mater.* **27,** 3505–3515 (2015).

97. Wang, H. *et al.* Hexagonal magnetite nanoprisms: preparation, characterization and cellular uptake. *J Mater Chem B* **3,** 4647–4653 (2015).

98. Yang, C., Wu, J. & Hou, Y. Fe3O4 nanostructures: synthesis, growth mechanism, properties and applications. *Chem. Commun.* **47,** 5130 (2011).

99. Guardia, P., Pérez-Juste, J., Labarta, A., Batlle, X. & Liz-Marzán, L. M. Heating rate influence on the synthesis of iron oxide nanoparticles: the case of decanoic acid. *Chem. Commun.* **46,** 6108–6110 (2010).

100. Gao, G. *et al.* Shape-Controlled Synthesis and Magnetic Properties of Monodisperse Fe_3O_4 Nanocubes. *Cryst. Growth Des.* **10,** 2888–2894 (2010).

101. Xia, Y., Xia, X. & Peng, H.-C. Shape-Controlled Synthesis of Colloidal Metal Nanocrystals: Thermodynamic versus Kinetic Products. *J. Am. Chem. Soc.* **137,** 7947–7966 (2015).

102. Bealing, C. R., Baumgardner, W. J., Choi, J. J., Hanrath, T. & Hennig, R. G. Predicting Nanocrystal Shape through Consideration of Surface-Ligand Interactions. *ACS Nano* **6,** 2118–2127 (2012).

103. Shavel, A. & Liz-Marzán, L. M. Shape control of iron oxide nanoparticles. *Phys. Chem. Chem. Phys.* **11,** 3762–3766 (2009).

104. Rath, S. S., Sinha, N., Sahoo, H., Das, B. & Mishra, B. K. Molecular modeling studies of oleate adsorption on iron oxides. *Appl. Surf. Sci.* **295,** 115–122 (2014).

105. YANG, T. *et al.* Surface structures of Fe3O4 (111), (110), and (001): A density functional theory study. *J. Fuel Chem. Technol.* **38,** 121–128 (2010).

106. Xu, Z., Shen, C., Tian, Y., Shi, X. & Gao, H.-J. Organic phase synthesis of monodisperse iron oxide nanocrystals using iron chloride as precursor. *Nanoscale* **2,** 1027–1032 (2010).

107. Guardia, P. *et al.* Water-Soluble Iron Oxide Nanocubes with High Values of Specific Absorption Rate for Cancer Cell Hyperthermia Treatment. *ACS Nano* **6,** 3080–3091 (2012).
108. Kim, D. *et al.* Synthesis of Uniform Ferrimagnetic Magnetite Nanocubes. *J. Am. Chem. Soc.* **131,** 454–455 (2009).
109. Cervadoro, A. *et al.* Synthesis of Multifunctional Magnetic NanoFlakes for Magnetic Resonance Imaging, Hyperthermia, and Targeting. *ACS Appl. Mater. Interfaces* **6,** 12939–12946 (2014).
110. Shavel, A., Rodríguez-González, B., Spasova, M., Farle, M. & Liz-Marzán, L. M. Synthesis and Characterization of Iron/Iron Oxide Core/Shell Nanocubes. *Adv. Funct. Mater.* **17,** 3870–3876 (2007).
111. Yang, H., Ogawa, T., Hasegawa, D. & Takahashi, M. Synthesis and magnetic properties of monodisperse magnetite nanocubes. *J. Appl. Phys.* **103,** 07D526 (2008).
112. Yin, Y. & Alivisatos, A. P. Colloidal nanocrystal synthesis and the organic–inorganic interface. *Nature* **437,** 664–670 (2005).
113. Kim, D. *et al.* Synthesis of Hollow Iron Nanoframes. *J. Am. Chem. Soc.* **129,** 5812–5813 (2007).
114. Guardia, P. *et al.* One pot synthesis of monodisperse water soluble iron oxide nanocrystals with high values of specific absorption rate. *J. Mater. Chem. B* (2014). doi:10.1039/C4TB00061G
115. Liong, M. *et al.* Multifunctional Inorganic Nanoparticles for Imaging, Targeting, and Drug Delivery. *ACS Nano* **2,** 889–896 (2008).
116. Kim, J., Piao, Y. & Hyeon, T. Multifunctional nanostructured materials for multimodal imaging, and simultaneous imaging and therapy. *Chem. Soc. Rev.* **38,** 372–390 (2009).
117. De, M., Ghosh, P. S. & Rotello, V. M. Applications of Nanoparticles in Biology. *Adv. Mater.* **20,** 4225–4241 (2008).
118. Mornet, S., Vasseur, S., Grasset, F. & Duguet, E. Magnetic nanoparticle design for medical diagnosis and therapy. *J. Mater. Chem.* **14,** 2161–2175 (2004).
119. Yoo, D., Lee, J.-H., Shin, T.-H. & Cheon, J. Theranostic Magnetic Nanoparticles. *Acc. Chem. Res.* **44,** 863–874 (2011).
120. Colombo, M. *et al.* Biological applications of magnetic nanoparticles. *Chem. Soc. Rev.* **41,** 4306 (2012).
121. Dufort, S. *et al.* Nebulized gadolinium-based nanoparticles: a theranostic approach for lung tumor imaging and radiosensitization. *Small Weinh. Bergstr. Ger.* **11,** 215–221 (2015).
122. Richard, S. *et al.* Antioxidative Theranostic Iron Oxide Nanoparticles toward Brain Tumors Imaging and ROS Production. *ACS Chem. Biol.* **11,** 2812–2819 (2016).
123. Benyettou, F. *et al.* Toward theranostic nanoparticles: CB[7]-functionalized iron oxide for drug delivery and MRI. *J. Mater. Chem. B* **1,** 5076–5082 (2013).
124. Benyettou, F. *et al.* A multimodal magnetic resonance imaging nanoplatform for cancer theranostics. *Phys. Chem. Chem. Phys. PCCP* **13,** 10020–10027 (2011).
125. Le, T. Q., Seznec, H. & Delville, M.-H. Functionalized nanomaterials: their use as contrast agents in bioimaging: mono- and multimodal approaches. *Nanotechnol. Rev.* **2,** 125–169 (2013).
126. Duguet, E., DELVILLE, M. H. & Mornet, S. Synthesis and characterization of iron oxide ferrite nanoparticles and ferrite-based aqueous fluids. in 47–72 (2012).
127. Maier-Hauff, K. *et al.* Intracranial Thermotherapy using Magnetic Nanoparticles Combined with External Beam Radiotherapy: Results of a Feasibility Study on Patients with Glioblastoma Multiforme. *J. Neurooncol.* **81,** 53–60 (2007).
128. Maier-Hauff, K. *et al.* Efficacy and safety of intratumoral thermotherapy using magnetic iron-oxide nanoparticles combined with external beam radiotherapy on patients with recurrent glioblastoma multiforme. *J. Neurooncol.* **103,** 317–324 (2011).
129. Thiesen, B. & Jordan, A. Clinical applications of magnetic nanoparticles for hyperthermia. *Int. J. Hyperth. Off. J. Eur. Soc. Hyperthermic Oncol. North Am. Hyperth. Group* **24,** 467–474 (2008).
130. Kolosnjaj-Tabi, J. *et al.* Heat-Generating Iron Oxide Nanocubes: Subtle 'Destructurators' of the Tumoral Microenvironment. *ACS Nano* **8,** 4268–4283 (2014).
131. Milosevic, I. *et al.* Effects of coating spherical iron oxide nanoparticles. *BBA - Biochim. Biophys. Acta* (2016). doi:10.1016/j.bbagen.2016.05.016
132. Begin-Colin, S. & Felder-Flesch, D. Magnetic Nanoparticles: From Fabrication to Clinical Applications. in *Magnetic Nanoparticles: From Fabrication to Biomedical and Clinical Applications* 151–191 (Nguyen TK Thanh, 2012).
133. Walter, A. *et al.* Functionalization strategies and dendronization of iron oxide nanoparticles. *Nanotechnol. Rev.* **4,** 581–593 (2015).
134. Guerrero-Martínez, A., Pérez-Juste, J. & Liz-Marzán, L. M. Recent progress on silica coating of nanoparticles and related nanomaterials. *Adv. Mater. Deerfield Beach Fla* **22,** 1182–1195 (2010).
135. Liu, J., Qiao, S. Z., Hu, Q. H. & Lu, G. Q. M. Magnetic nanocomposites with mesoporous structures: synthesis and applications. *Small Weinh. Bergstr. Ger.* **7,** 425–443 (2011).
136. Wang, Y. & Gu, H. Core-shell-type magnetic mesoporous silica nanocomposites for bioimaging and therapeutic agent delivery. *Adv. Mater. Deerfield Beach Fla* **27,** 576–585 (2015).
137. Yang, P., Gai, S. & Lin, J. Functionalized mesoporous silica materials for controlled drug delivery. *Chem. Soc. Rev.* **41,** 3679–3698 (2012).
138. Basly, B. *et al.* Effect of the nanoparticle synthesis method on dendronized iron oxides as MRI contrast agents. *Dalton Trans.* **42,** 2146–2157 (2013).
139. Lamanna, G. *et al.* Dendronized iron oxide nanoparticles for multimodal imaging. *Biomaterials* **32,** 8562–8573 (2011).
140. Basly, B. *et al.* Dendronized iron oxide nanoparticles as contrast agents for MRI. *Chem. Commun.* **46,** 985–987 (2010).
141. Boyer, C., Bulmus, V. & Davis, T. P. Efficient Usage of Thiocarbonates for Both the Production and the Biofunctionalization of Polymers. *Macromol. Rapid Commun.* **30,** 493–497 (2009).
142. Bertin, A., Steibel, J., Michou-Gallani, A.-I., Gallani, J.-L. & Felder-Flesch, D. Development of a dendritic manganese-enhanced magnetic resonance imaging (MEMRI) contrast agent: synthesis, toxicity (in vitro) and relaxivity (in vitro, in vivo) studies. *Bioconjug. Chem.* **20,** 760–767 (2009).
143. Bertin, A., Michou-Gallani, A.-I., Steibel, J., Gallani, J.-L. & Felder-Flesch, D. Synthesis and characterization of a

highly stable dendritic catechol-tripod bearing technetium-99m. *New J. Chem.* **34,** 267–275 (2010).

144. Bertin, A., Michou-Gallani, A.-I., Gallani, J.-L. & Felder-Flesch, D. In vitro neurotoxicity of magnetic resonance imaging (MRI) contrast agents: influence of the molecular structure and paramagnetic ion. *Toxicol. Vitro Int. J. Publ. Assoc. BIBRA* **24,** 1386–1394 (2010).

145. Villaraza, A. J. L., Bumb, A. & Brechbiel, M. W. Macromolecules, Dendrimers and Nanomaterials in Magnetic Resonance Imaging: The Interplay Between Size, Function and Pharmacokinetics. *Chem. Rev.* **110,** 2921–2959 (2010).

146. Steitz, B. *et al.* Fixed Bed Reactor for Solid-Phase Surface Derivatization of Superparamagnetic Nanoparticles. *Bioconjug. Chem.* **18,** 1684–1690 (2007).

147. Tsai, Z.-T. *et al.* In situ preparation of high relaxivity iron oxide nanoparticles by coating with chitosan: A potential MRI contrast agent useful for cell tracking. *J. Magn. Magn. Mater.* **322,** 208–213 (2010).

148. Dai, L. *et al.* One-pot facile synthesis of PEGylated superparamagnetic iron oxide nanoparticles for MRI contrast enhancement. *Mater. Sci. Eng. C Mater. Biol. Appl.* **41,** 161–167 (2014).

149. Qiao, R., Yang, C. & Gao, M. Superparamagnetic iron oxide nanoparticles: from preparations to in vivo MRI applications. *J. Mater. Chem.* **19,** 6274–6293 (2009).

150. Geinguenaud, F., Banissi, C., Carpentier, A. F. & Motte, L. Iron Oxide Nanoparticles Coated with a Phosphorothioate Oligonucleotide and a Cationic Peptide: Exploring Four Different Ways of Surface Functionalization. *Nanomaterials* **5,** 1588–1609 (2015).

151. Nam, J. *et al.* Surface engineering of inorganic nanoparticles for imaging and therapy. *Adv. Drug Deliv. Rev.* **65,** 622–648 (2013).

152. Walter, A. *et al.* Functionalization strategies and dendronization of iron oxide nanoparticles. *Nanotechnol. Rev.* **4,** 581 (2015).

153. Bacri, J.-C., Perzynski, R., Salin, D., Cabuil, V. & Massart, R. Ionic ferrofluids: A crossing of chemistry and physics. *J. Magn. Magn. Mater.* **85,** 27–32 (1990).

154. Fauconnier, null, Pons, null, Roger, null & Bee, null. Thiolation of Maghemite Nanoparticles by Dimercaptosuccinic Acid. *J. Colloid Interface Sci.* **194,** 427–433 (1997).

155. Lattuada, M. & Hatton, T. A. Functionalization of monodisperse magnetic nanoparticles. *Langmuir ACS J. Surf. Colloids* **23,** 2158–2168 (2007).

156. Maurizi, L., Bisht, H., Bouyer, F. & Millot, N. Easy Route to Functionalize Iron Oxide Nanoparticles via Long-Term Stable Thiol Groups. *Langmuir* **25,** 8857–8859 (2009).

157. Miguel-Sancho, N. *et al.* Development of Stable, Water-Dispersible, and Biofunctionalizable Superparamagnetic Iron Oxide Nanoparticles. *Chem. Mater.* **23,** 2795–2802 (2011).

158. Răcuciu, M., Creangă, D. E. & Airinei, A. Citric-acid-coated magnetite nanoparticles for biological applications. *Eur. Phys. J. E* **21,** 117–121 (2006).

159. Amstad, E. *et al.* Surface functionalization of single superparamagnetic iron oxide nanoparticles for targeted magnetic resonance imaging. *Small Weinh. Bergstr. Ger.* **5,** 1334–1342 (2009).

160. Frey, N. A., Peng, S., Cheng, K. & Sun, S. Magnetic nanoparticles: synthesis, functionalization, and applications in bioimaging and magnetic energy storage. *Chem. Soc. Rev.* **38,** 2532–2542 (2009).

161. Lalatonne, Y. *et al.* Bis-phosphonates–ultra small superparamagnetic iron oxide nanoparticles: a platform towards diagnosis and therapy. *Chem. Commun.* 2553–2555 (2008). doi:10.1039/B801911H

162. Guénin, E. *et al.* Catechol versus bisphosphonate ligand exchange at the surface of iron oxide nanoparticles: towards multi-functionalization. *J. Nanoparticle Res.* **16,** 2596 (2014).

163. Daou, T. J. *et al.* Coupling Agent Effect on Magnetic Properties of Functionalized Magnetite-Based Nanoparticles. *Chem. Mater.* **20,** 5869–5875 (2008).

164. Daou, T. J. *et al.* Investigation of the grafting rate of organic molecules on the surface of magnetite nanoparticles as a function of the coupling agent. *Sens. Actuators B Chem.* **126,** 159–162 (2007).

165. Basly, B., Felder-Flesch, D., Perriat, P., Pourroy, G. & Bégin-Colin, S. Properties and suspension stability of dendronized iron oxide nanoparticles for MRI applications. *Contrast Media Mol. Imaging* **6,** 132–138 (2011).

166. Smolensky, E. D. *et al.* Scaling laws at the nanosize: the effect of particle size and shape on the magnetism and relaxivity of iron oxide nanoparticle contrast agents. *J. Mater. Chem. B* **1,** 2818 (2013).

167. Yamaura, M. *et al.* Preparation and characterization of (3-aminopropyl)triethoxysilane-coated magnetite nanoparticles. *J. Magn. Magn. Mater.* **279,** 210–217 (2004).

168. Shen, M. *et al.* Facile one-pot preparation, surface functionalization, and toxicity assay of APTS-coated iron oxide nanoparticles. *Nanotechnology* **23,** 105601 (2012).

169. Yathindranath, V. *et al.* One-Pot Synthesis of Iron Oxide Nanoparticles with Functional Silane Shells: A Versatile General Precursor for Conjugations and Biomedical Applications. *Langmuir* **29,** 10850–10858 (2013).

170. Herrmann, I. K., Grass, R. N., Mazunin, D. & Stark, W. J. Synthesis and Covalent Surface Functionalization of Nonoxidic Iron Core−Shell Nanomagnets. *Chem. Mater.* **21,** 3275–3281 (2009).

171. Lee, H. *et al.* Thermally Cross-Linked Superparamagnetic Iron Oxide Nanoparticles: Synthesis and Application as a Dual Imaging Probe for Cancer in Vivo. *J. Am. Chem. Soc.* **129,** 12739–12745 (2007).

172. Selvan, S. T., Tan, T. T. Y., Yi, D. K. & Jana, N. R. Functional and multifunctional nanoparticles for bioimaging and biosensing. *Langmuir ACS J. Surf. Colloids* **26,** 11631–11641 (2010).

173. Piao, Y., Burns, A., Kim, J., Wiesner, U. & Hyeon, T. Designed Fabrication of Silica-Based Nanostructured Particle Systems for Nanomedicine Applications. *Adv. Funct. Mater.* **18,** 3745–3758 (2008).

174. Zhang, C. *et al.* Silica- and Alkoxysilane-Coated Ultrasmall Superparamagnetic Iron Oxide Particles: A Promising Tool To Label Cells for Magnetic Resonance Imaging. *Langmuir* **23,** 1427–1434 (2007).

175. Smolensky, E. D., Park, H.-Y. E., Berquó, T. S. & Pierre, V. C. Surface Functionalization of Magnetic Iron Oxide Nanoparticles for MRI Applications – Effect of Anchoring Group and Ligand Exchange Protocol. *Contrast Media Mol. Imaging* **6,** 189–199 (2011).

176. Sahoo, Y. *et al.* Alkyl Phosphonate/Phosphate Coating on Magnetite Nanoparticles: A Comparison with Fatty Acids. *Langmuir* **17,** 7907–7911 (2001).

177. Lalatonne, Y. *et al.* Characterization of magnetic labels for bioassays. *J. Magn. Magn. Mater.* **321,** 1653–1657 (2009).

178. Jaszberenyi, Z., Sour, A., Toth, E., Benmelouka, M. & Merbach, A. E. Fine-tuning water exchange on GdIII poly(amino carboxylates) by modulation of steric crowding. *Dalton Trans.* 2713–2719 (2005).

179. Duan, H. *et al.* Reexamining the Effects of Particle Size and Surface Chemistry on the Magnetic Properties of Iron Oxide Nanocrystals: New Insights into Spin Disorder and Proton Relaxivity. *J. Phys. Chem. C* **112,** 8127–8131 (2008).

180. Yoon, T.-J., Lee, H., Shao, H. & Weissleder, R. Highly magnetic core-shell nanoparticles with unique magnetization mechanism. *Angew. Chem. Int. Ed Engl.* **50,** 4663–4666 (2011).

181. Lee, J.-H. *et al.* Artificially engineered magnetic nanoparticles for ultra-sensitive molecular imaging. *Nat. Med.* **13,** 95–99 (2007).

182. Joshi, H. M. *et al.* Effects of shape and size of cobalt ferrite nanostructures on their MRI contrast and thermal activation. *J. Phys. Chem. C Nanomater. Interfaces* **113,** 17761–17767 (2009).

183. Zeng, L., Ren, W., Zheng, J., Cui, P. & Wu, A. Ultrasmall water-soluble metal-iron oxide nanoparticles as T1-weighted contrast agents for magnetic resonance imaging. *Phys. Chem. Chem. Phys. PCCP* **14,** 2631–2636 (2012).

184. Kim, B. H. *et al.* Large-scale synthesis of uniform and extremely small-sized iron oxide nanoparticles for high-resolution T1 magnetic resonance imaging contrast agents. *J. Am. Chem. Soc.* **133,** 12624–12631 (2011).

185. Pöselt, E. *et al.* Relaxivity optimization of a PEGylated iron-oxide-based negative magnetic resonance contrast agent for T_2-weighted spin-echo imaging. *ACS Nano* **6,** 1619–1624 (2012).

186. Wang, W. *et al.* Size and Compositional Effects on Contrast Efficiency of Functionalized Superparamagnetic Nanoparticles at Ultralow and Ultrahigh Magnetic Fields. *J. Phys. Chem. C* **116,** 17880–17884 (2012).

187. Cheong, S. *et al.* Simple Synthesis and Functionalization of Iron Nanoparticles for Magnetic Resonance Imaging. *Angew. Chem. Int. Ed.* **50,** 4206–4209 (2011).

188. Lacroix, L.-M. *et al.* Stable single-crystalline body centered cubic Fe nanoparticles. *Nano Lett.* **11,** 1641–1645 (2011).

189. Khurshid, H. *et al.* Core/shell structured iron/iron-oxide nanoparticles as excellent MRI contrast enhancement agents. *J. Magn. Magn. Mater.* **331,** 17–20 (2013).

190. de Montferrand, C. *et al.* Iron oxide nanoparticles with sizes, shapes and compositions resulting in different magnetization signatures as potential labels for multiparametric detection. *Acta Biomater.* **9,** 6150–6157 (2013).

191. Lee, N. *et al.* Water-Dispersible Ferrimagnetic Iron Oxide Nanocubes with Extremely High r_2 Relaxivity for Highly Sensitive in Vivo MRI of Tumors. *Nano Lett.* **12,** 3127–3131 (2012).

192. Zhao, Z. *et al.* Octapod iron oxide nanoparticles as high-performance T2 contrast agents for magnetic resonance imaging. *Nat. Commun.* **4,** 2266 (2013).

193. Sathya, A. *et al.* CoxFe3–xO4 Nanocubes for Theranostic Applications: Effect of Cobalt Content and Particle Size. *Chem. Mater.* **28,** 1769–1780 (2016).

194. Saha, I. *et al.* pH-Sensitive MR Responses Induced by Dendron-Functionalized SPIONs. *J. Phys. Chem. C Nanomater. Interfaces* **117,** 1893–1903 (2013).

195. Paquet, C. *et al.* Clusters of Superparamagnetic Iron Oxide Nanoparticles Encapsulated in a Hydrogel: A Particle Architecture Generating a Synergistic Enhancement of the T2 Relaxation. *ACS Nano* **5,** 3104–3112 (2011).

196. Roca, A. G. *et al.* Effect of Nanoparticle and Aggregate Size on the Relaxometric Properties of MR Contrast Agents Based on High Quality Magnetite Nanoparticles. *J. Phys. Chem. B* **113,** 7033–7039 (2009).

197. Lartigue, L. *et al.* Cooperative Organization in Iron Oxide Multi-Core Nanoparticles Potentiates Their Efficiency as Heating Mediators and MRI Contrast Agents. *ACS Nano* 121129155806007 (2012). doi:10.1021/nn304477s

198. Kostopoulou, A. *et al.* Colloidal Assemblies of Oriented Maghemite Nanocrystals and their NMR Relaxometric Properties. *ArXiv14035450 Cond-Mat* (2014).

199. Laurent, S., Bridot, J.-L., Elst, L. V. & Muller, R. N. Magnetic iron oxide nanoparticles for biomedical applications. *Future Med. Chem.* **2,** 427–449 (2010).

200. Roch, A., Gossuin, Y., Muller, R. N. & Gillis, P. Superparamagnetic colloid suspensions: Water magnetic relaxation and clustering. *J. Magn. Magn. Mater.* **293,** 532–539 (2005).

201. Li, W. *et al.* First-pass contrast-enhanced magnetic resonance angiography in humans using ferumoxytol, a novel ultrasmall superparamagnetic iron oxide (USPIO)-based blood pool agent. *J. Magn. Reson. Imaging JMRI* **21,** 46–52 (2005).

202. Shen, T., Weissleder, R., Papisov, M., Bogdanov, A. & Brady, T. J. Monocrystalline iron oxide nanocompounds (MION): physicochemical properties. *Magn. Reson. Med.* **29,** 599–604 (1993).

203. Jun, Y.-W. *et al.* Nanoscale size effect of magnetic nanocrystals and their utilization for cancer diagnosis via magnetic resonance imaging. *J. Am. Chem. Soc.* **127,** 5732–5733 (2005).

204. Tong, S., Hou, S., Zheng, Z., Zhou, J. & Bao, G. Coating Optimization of Superparamagnetic Iron Oxide Nanoparticles for High T2 relaxivity. *Nano Lett.* **10,** 4607–4613 (2010).

205. Jang, J. *et al.* Critical enhancements of MRI contrast and hyperthermic effects by dopant-controlled magnetic nanoparticles. *Angew. Chem. Int. Ed Engl.* **48,** 1234–1238 (2009).

206. Huang, J. *et al.* Effects of Nanoparticle Size on Cellular Uptake and Liver MRI with Polyvinylpyrrolidone-Coated Iron Oxide Nanoparticles. *ACS Nano* **4,** 7151–7160 (2010).

207. Lee, N. *et al.* Magnetosome-like ferrimagnetic iron oxide nanocubes for highly sensitive MRI of single cells and transplanted pancreatic islets. *Proc. Natl. Acad. Sci. U. S. A.* **108,** 2662–2667 (2011).

208. Walter, A. *et al.* Validation of a dendron concept to tune colloidal stability, MRI relaxivity and bioelimination of functional nanoparticles. *J. Mater. Chem. B* **3,** 1484–1494 (2015).

209. LaConte, L. E. W. *et al.* Coating thickness of magnetic iron oxide nanoparticles affects R2 relaxivity. *J. Magn. Reson. Imaging JMRI* **26,** 1634–1641 (2007).

210. Pinho, S. L. C. *et al.* Relaxometric Studies of γ-Fe2O3@SiO2 Core Shell Nanoparticles: When the Coating Matters. *J. Phys. Chem. C* **116,** 2285–2291 (2012).

211. Laurent, S. *et al.* Influence of the length of the coating molecules on the nuclear magnetic relaxivity of superparamagnetic colloids. *Phys. Status Solidi C* **1,** 3644–3650 (2004).

212. Walter, A. *et al.* Mastering the Shape and Composition of Dendronized Iron Oxide Nanoparticles To Tailor Magnetic Resonance Imaging and Hyperthermia. *Chem. Mater.* **26,** 5252–5264 (2014).

213. Bordonali, L. *et al.* NMR-D study of the local spin dynamics and magnetic anisotropy in different nearly monodispersed ferrite nanoparticles. *J. Phys. Condens. Matter* **25,** 066008 (2013).

214. Kumar, C. S. S. R. & Mohammad, F. Magnetic nanomaterials for hyperthermia-based therapy and controlled drug delivery. *Adv. Drug Deliv. Rev.* **63,** 789–808 (2011).

215. Gilchrist, R. K. *et al.* Selective inductive heating of lymph nodes. *Ann. Surg.* **146,** 596–606 (1957).

216. Laurent, S., Dutz, S., Häfeli, U. O. & Mahmoudi, M. Magnetic fluid hyperthermia: focus on superparamagnetic iron oxide nanoparticles. *Adv. Colloid Interface Sci.* **166,** 8–23 (2011).

217. Périgo, E. A. *et al.* Fundamentals and advances in magnetic hyperthermia. *Appl. Phys. Rev.* **2,** 041302 (2015).

218. Rosensweig, R. E. Heating magnetic fluid with alternating magnetic field. *J. Magn. Magn. Mater.* **252,** 370–374 (2002).

219. Kallumadil, M. *et al.* Suitability of commercial colloids for magnetic hyperthermia. *J. Magn. Magn. Mater.* **321,** 1509–1513 (2009).

220. Cullity, B. D. & Graham, C. D. *Introduction to magnetic materials*. (IEEE/Wiley, 2009).

221. Dormann, J. L., Bessais, L. & Fiorani, D. A dynamic study of small interacting particles: superparamagnetic model and spin-glass laws. *J. Phys. C Solid State Phys.* **21,** 2015 (1988).

222. El-Hilo, M., O'grady, K. & Chantrell, R. W. The ordering temperature in fine particle systems. *J. Magn. Magn. Mater.* **117,** 21–28 (1992).

223. Shtrikman, S. & Wohlfarth, E. P. The theory of the Vogel-Fulcher law of spin glasses. *Phys. Lett. A* **85,** 467–470 (1981).

224. Glöckl, G. *et al.* The effect of field parameters, nanoparticle properties and immobilization on the specific heating power in magnetic particle hyperthermia. *J. Phys. Condens. Matter* **18,** S2935–S2949 (2006).

225. Fortin, J.-P. *et al.* Size-Sorted Anionic Iron Oxide Nanomagnets as Colloidal Mediators for Magnetic Hyperthermia. *J. Am. Chem. Soc.* **129,** 2628–2635 (2007).

226. de la Presa, P. *et al.* Study of Heating Efficiency as a Function of Concentration, Size, and Applied Field in γ-Fe2O3 Nanoparticles. *J. Phys. Chem. C* **116,** 25602–25610 (2012).

227. Liu, X. L. *et al.* Optimization of surface coating on Fe3O4 nanoparticles for high performance magnetic hyperthermia agents. *J. Mater. Chem.* **22,** 8235–8244 (2012).

228. Jordan, A., Rheinländer, T., Waldöfner, N. & Scholz, R. Increase of the Specific Absorption Rate (SAR) by Magnetic Fractionation of Magnetic Fluids. *J. Nanoparticle Res.* **5,** 597–600 (2003).

229. Patsula, V., Moskvin, M., Dutz, S. & Horák, D. Size-dependent magnetic properties of iron oxide nanoparticles. *J. Phys. Chem. Solids* **88,** 24–30 (2016).

230. Kossatz, S. *et al.* High Therapeutic Efficiency of Magnetic Hyperthermia in Xenograft Models Achieved with Moderate Temperature Dosages in the Tumor Area. *Pharm. Res.* **31,** 3274–3288 (2014).

231. Brusentsov, N. A. *et al.* Evaluation of ferromagnetic fluids and suspensions for the site-specific radiofrequency-induced hyperthermia of MX11 sarcoma cells in vitro. *J. Magn. Magn. Mater.* **225,** 113–117 (2001).

232. Gazeau, F., Lévy, M. & Wilhelm, C. Optimizing magnetic nanoparticle design for nanothermotherapy. *Nanomed.* **3,** 831–844 (2008).

233. Hergt, R. *et al.* Magnetic properties of bacterial magnetosomes as potential diagnostic and therapeutic tools. *J. Magn. Magn. Mater.* **293,** 80–86 (2005).

234. Iglesias, O., Labarta, A. & Batlle, X. Exchange bias phenomenology and models of core/shell nanoparticles. *J. Nanosci. Nanotechnol.* **8,** 2761–2780 (2008).

235. Martinez-Boubeta, C. *et al.* Learning from Nature to Improve the Heat Generation of Iron-Oxide Nanoparticles for Magnetic Hyperthermia Applications. *Sci. Rep.* **3,** (2013).

236. Gonzalez-Fernandez, M. A. *et al.* Magnetic nanoparticles for power absorption: Optimizing size, shape and magnetic properties. *J. Solid State Chem.* **182,** 2779–2784 (2009).

237. Habib, A. H., Ondeck, C. L., Chaudhary, P., Bockstaller, M. R. & McHenry, M. E. Evaluation of iron-cobalt/ferrite core-shell nanoparticles for cancer thermotherapy. *J. Appl. Phys.* **103,** 07A307–07A307 (2008).

238. Mehdaoui, B. *et al.* Increase of magnetic hyperthermia efficiency due to dipolar interactions in low anisotropy magnetic nanoparticles : theoretical and experimental results. *Phys. Rev. B* **87,** (2013).

239. Hugounenq, P. *et al.* Iron Oxide Monocrystalline Nanoflowers for Highly Efficient Magnetic Hyperthermia. *J. Phys. Chem. C* **116,** 15702–15712 (2012).

240. Blanco-Andujar, C., Ortega, D., Southern, P., A. Pankhurst, Q. & K. Thanh, N. T. High performance multi-core iron oxide nanoparticles for magnetic hyperthermia: microwave synthesis, and the role of core-to-core interactions. *Nanoscale* **7,** 1768–1775 (2015).

241. de la Presa, P. *et al.* Study of Heating Efficiency as a Function of Concentration, Size, and Applied Field in γ-Fe$_2$O$_3$ Nanoparticles. *J. Phys. Chem. C* **116,** 25602–25610 (2012).

242. Dennis, C. L. *et al.* Nearly complete regression of tumors via collective behavior of magnetic nanoparticles in hyperthermia. *Nanotechnology* **20,** 395103 (2009).

243. Novakova, A. A., Smirnov, E. V. & Gendler, T. S. Magnetic anisotropy in Fe3O4—PVA nanocomposites as a result of Fe3O4-nanoparticles chains formation. *J. Magn. Magn. Mater.* **300,** e354–e358 (2006).

244. Serantes, D. *et al.* Multiplying Magnetic Hyperthermia Response by Nanoparticle Assembling. *J. Phys. Chem. C* **118,** 5927–5934 (2014).

245. Alphandéry, E., Faure, S., Seksek, O., Guyot, F. & Chebbi, I. Chains of Magnetosomes Extracted from AMB-1 Magnetotactic Bacteria for Application in Alternative Magnetic Field Cancer Therapy. *ACS Nano* **5,** 6279–6296 (2011).

246. Noh, S. *et al.* Nanoscale Magnetism Control via Surface and Exchange Anisotropy for Optimized Ferrimagnetic Hysteresis. *Nano Lett.* **12,** 3716–3721 (2012).

247. Fortin, J.-P. *et al.* Size-Sorted Anionic Iron Oxide Nanomagnets as Colloidal Mediators for Magnetic Hyperthermia. *J. Am. Chem. Soc.* **129,** 2628–2635 (2007).

248. Di Corato, R. *et al.* Magnetic hyperthermia efficiency in the cellular environment for different nanoparticle designs. *Biomaterials* doi:10.1016/j.biomaterials.2014.04.036

249. Etheridge, M. L. *et al.* Accounting for biological aggregation in heating and imaging of magnetic nanoparticles. *Technology* **2,** 214–228 (2014).

250. Creixell, M., Bohórquez, A. C., Torres-Lugo, M. & Rinaldi, C. EGFR-Targeted Magnetic Nanoparticle Heaters Kill Cancer Cells without a Perceptible Temperature Rise. *ACS Nano* **5,** 7124–7129 (2011).

251. Yoo, D., Jeong, H., Noh, S.-H., Lee, J.-H. & Cheon, J. Magnetically triggered dual functional nanoparticles for resistance-free apoptotic hyperthermia. *Angew. Chem. Int. Ed Engl.* **52,** 13047–13051 (2013).

252. Wang, L. *et al.* An integrated nanoplatform for theranostics via multifunctional core–shell ferrite nanocubes. *J. Mater. Chem. B* **4,** 1908–1914 (2016).

253. Oh, Y., Lee, N., Kang, H. W. & Oh, J. In vitro study on apoptotic cell death by effective magnetic hyperthermia with chitosan-coated MnFe 2 O 4. *Nanotechnology* **27,** 115101 (2016).

254. Connord, V. *et al.* Real-Time Analysis of Magnetic Hyperthermia Experiments on Living Cells under a Confocal Microscope. *Small Weinh. Bergstr. Ger.* **11,** 2437–2445 (2015).

255. Blanco-Andujar, C. *et al.* Real-time tracking of delayed-onset cellular apoptosis induced by intracellular magnetic hyperthermia. *Nanomed.* **11,** 121–136 (2015).

256. Shah, B. P. *et al.* Core-shell nanoparticle-based peptide therapeutics and combined hyperthermia for enhanced cancer cell apoptosis. *ACS Nano* **8,** 9379–9387 (2014).

257. Balasubramanian, S. *et al.* Curcumin and 5-fluorouracil-loaded, folate- and transferrin-decorated polymeric magnetic nanoformulation: a synergistic cancer therapeutic approach, accelerated by magnetic hyperthermia. *Int. J. Nanomedicine* **9,** 437–459 (2014).

258. Sadhukha, T., Wiedmann, T. S. & Panyama, J. Enhancing Therapeutic Efficacy through Designed Aggregation of Nanoparticles. *Biomaterials* **35,** 7860–7869 (2014).

259. Asín, L., Ibarra, M. R., Tres, A. & Goya, G. F. Controlled cell death by magnetic hyperthermia: effects of exposure time, field amplitude, and nanoparticle concentration. *Pharm. Res.* **29,** 1319–1327 (2012).

260. Sanchez, C. *et al.* Targeting a G-protein-coupled receptor overexpressed in endocrine tumors by magnetic nanoparticles to induce cell death. *ACS Nano* **8,** 1350–1363 (2014).

261. Hildebrandt, B. *et al.* The cellular and molecular basis of hyperthermia. *Crit. Rev. Oncol. Hematol.* **43,** 33–56 (2002).

262. Otte, J. Hyperthermia in cancer therapy. *Eur. J. Pediatr.* **147,** 560–569 (1988).

263. Jain, R. K. & Stylianopoulos, T. Delivering nanomedicine to solid tumors. *Nat. Rev. Clin. Oncol.* **7,** 653–664 (2010).

264. W, G. *et al.* A smart, phase transitional and injectable DOX/PLGA-Fe implant for magnetic-hyperthermia-induced synergistic tumor eradication. *Acta Biomater.* **29,** 298–306 (2016).

265. Matsuoka, F. *et al.* Hyperthermia using magnetite cationic liposomes for hamster osteosarcoma. *Biomagn. Res. Technol.* **2,** 3 (2004).

266. Hilger, I. & Kaiser, W. A. Iron oxide-based nanostructures for MRI and magnetic hyperthermia. *Nanomed.* **7,** 1443–1459 (2012).

267. Moroz, P., Jones, S. K. & Gray, B. N. Tumor response to arterial embolization hyperthermia and direct injection hyperthermia in a rabbit liver tumor model. *J. Surg. Oncol.* **80,** 149–156 (2002).

268. Huang, H. S. & Hainfeld, J. F. Intravenous magnetic nanoparticle cancer hyperthermia. *Int. J. Nanomedicine* **8,** 2521–2532 (2013).

269. Dähring, H., Grandke, J., Teichgräber, U. & Hilger, I. Improved Hyperthermia Treatment of Tumors Under Consideration of Magnetic Nanoparticle Distribution Using Micro-CT Imaging. *Mol. Imaging Biol. MIB Off. Publ. Acad. Mol. Imaging* **17,** 763–769 (2015).

270. Shetake, N. G. *et al.* Magnetic nanoparticle-mediated hyperthermia therapy induces tumour growth inhibition by apoptosis and Hsp90/AKT modulation. *Int. J. Hyperthermia* **31,** 909–919 (2015).

271. Hayashi, K. *et al.* Magnetically responsive smart nanoparticles for cancer treatment with a combination of magnetic hyperthermia and remote-control drug release. *Theranostics* **4,** 834–844 (2014).

272. Espinosa, A. *et al.* Can magneto-plasmonic nanohybrids efficiently combine photothermia with magnetic hyperthermia? *Nanoscale* **7,** 18872–18877 (2015).

273. Hayashi, K. *et al.* Superparamagnetic Nanoparticle Clusters for Cancer Theranostics Combining Magnetic Resonance Imaging and Hyperthermia Treatment. *Theranostics* **3,** 366–376 (2013).

274. Basel, M. T. *et al.* Cell-delivered magnetic nanoparticles caused hyperthermia-mediated increased survival in a murine pancreatic cancer model. *Int. J. Nanomedicine* **7,** 297–306 (2012).

275. DeNardo, S. J. *et al.* Thermal dosimetry predictive of efficacy of 111In-ChL6 nanoparticle AMF--induced thermoablative therapy for human breast cancer in mice. *J. Nucl. Med. Off. Publ. Soc. Nucl. Med.* **48,** 437–444 (2007).

276. Xie, J. *et al.* High-performance PEGylated Mn–Zn ferrite nanocrystals as a passive-targeted agent for magnetically induced cancer theranostics. *Biomaterials* **35,** 9126–9136 (2014).

Chapter II

Characterizing functionalized iron oxide nanoparticles

II Characterizing functionalized iron oxide nanoparticles

The main and usual characterization techniques which are used to characterize the shape, size, composition and magnetic properties of NPs and in particular of iron oxide nanoparticles (IONPs) are described here as well as the characterization techniques to evidence the presence of the organic coating, the type of surface complexes and the colloidal stability, i.e. hydrodynamic size distribution. A part of this chapter has been published in a book chapter (Chapter IV) in “Contrast agents for MRI”, Serie: New Developments in NMR, Ed. Matthew J. Allen and Valérie C. Pierre, Royal Society of Chemistry, 2018 to which I have contributed to.

II.1 Characterization of the iron oxide core in functionalized nanoparticles

The characterization of the size and shape of NPs is mainly performed by using transmission electron microscopy (TEM) but besides classical TEM, Energy Dispersive Spectroscopy (EDS), Electron Energy Loss Spectroscopy (EELS), high angle annular dark field in scanning TEM (HAADF-STEM) and Electron Tomography are other modes which also bring valuable information on NPs shape and composition. Other techniques, such as X-Ray diffraction (XRD), IR spectroscopy, ^{57}Fe Mössbauer spectrometry and also less usual techniques such as Raman and photoemission (XPS) spectroscopies do allow investigating the composition of IONPs.

II.1.1 Characterization of the size, size distribution and shape of nanoparticles

II.1.1.1 TEM & Electron Tomography

Transmission electron microscopy allows for a precise analysis of nano-scaled morphological features. It is recognized as an essential characterization tool in the field of NPs and contributes thus extensively to the development of nanomaterials and nanostructures[1]. As their peculiar properties originate from the control of their shape and size, the corresponding research fields require systematic and statistical studies of such structural and morphological characteristics at the atomic scale. Given the strong interaction between accelerated electrons and matter, several types of signals result from the irradiation of the NPs sample leading to various analysis modes with specific selectivities (morphological, structural, chemical etc.). The TEM technique is thus the authoritative characterization tool in the field of NPs, especially on a last generation electron microscope equipped with spherical aberration correctors, photon detector and an electron spectrometer.

When applied in one of the existing imaging modes (classical TEM, high angle annular dark field in scanning TEM –HAADF-STEM), TEM provides precise informations on the size and general shape of individual particles[2]. Such analysis approach can be easily generalized to an assembly of NPs by using appropriate image treatment tools for obtaining statistical values representative of the whole specimen[3]. The size statistics may be calculated from the size measurements of NPs in TEM images by using the free "ImageJ" program (Figure II.1)[4].

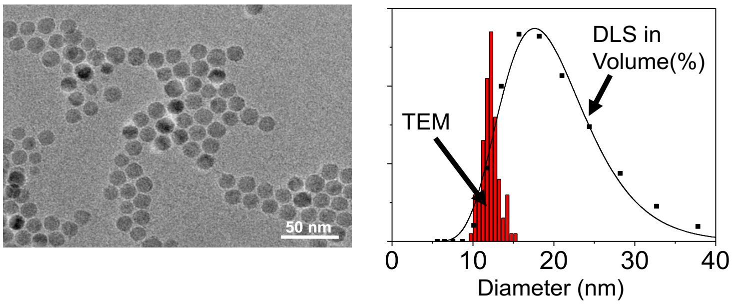

Figure II.1 - TEM image of IO NPs synthesized by thermal decomposition and coated with oleic acid molecules (left) and size distributions determined from TEM images and DLS measurements (right).

In the high resolution TEM or STEM configurations, structural parameters such as the crystallographic structure and the type and density of atomic defects can be determined[5]. In particular, the development of the incoherent HAADF-STEM imaging mode in which the image intensity is directly proportional to the mean atomic number of the nano-sized specimen, provided new capabilities of analysis allowing in particular to spatially localize various phases, with close atomic numbers, in the nanograin. A typical example is the determination of the spatial distribution of two metallic phases within the same complex particle with a bipyramidal morphology[6].

The development of specific TEM holders allowing to heat the specimen under vacuum or even in inert or reactive atmospheres opens new perspectives for the dynamical *in situ* analysis of the structural and morphological evolution of the nanosystems as well as their reactivity in controlled environments[7]. By adapting the experimental TEM conditions in order to minimize the irradiation damages, phase and reactivity diagrams can be obtained for oxide or metallic NPs as well as direct informations on their growth and formation process by nucleation, aggregation and subsequent calcination. A typical example of such an *in situ* TEM study concerns the analysis of the morphological and structural evolution of metallic NPs confined inside carbon nanotubes as a function of the temperature, in order to precisely solve in real time the dynamical evolution of the system at high temperatures (Figure II.2)[8].

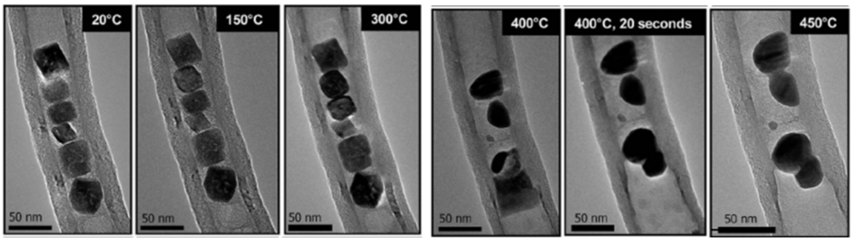

Figure II.2 - Thermal evolution of Co–CoO based nanoparticles casted inside the inner channel of a carbon nanotube investigated by in situ TEM experiments under vacuum, showing the changes in the nanoparticle and localization on the support[8].

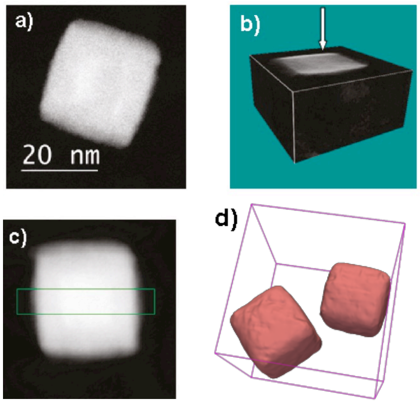

Figure II.3 - a) 2D STEM-HAADF image at 0° tilt, extracted from the tilt series used to reconstruct the volume of a core-shell NP. b) Slice of the reconstructed volume. c) Projection computed from the reconstruction in the direction indicated by the white arrow in b). d) 3D representation of the external shapes of two analysed cubic-shaped nanoparticles

In the case of NPs with a complex shape or topography due to the presence of several types of crystallographic facets, terraces and steps on the surface, as well as for particles with a porous internal structure, the classical 2D analysis consisting in the acquisition of unique images of the analyzed areas are not sufficient for unraveling their structural or morphological characteristics. To obtain a 3D reliable representation of the nano-object, the 3D imaging method by electron tomography can be used, which allows for qualitative and quantitative 3D analyses with a nanometric (even atomic) spatial resolution[9]. Electron tomography is based on recording a series of images of an object, tilted inside the electron microscope, along the widest possible angular range. The construction of a 3D matrix describing the sample directly in the real space is carried out by applying mathematical algorithms based on radon's theorem. That allows to bypass the limitations of 2D image projections and to solve the increasing complexity of synthesized NPs giving a deeper and more reliable insight into their 3D shape and architecture. To illustrate this capability of analysis as applied to NPs, the realistic 3D representation of iron oxide based NPs and the investigation of their composition were achieved by electron and STEM-HAADF tomography as schematized in Figure II.3 and allowed confirming the 3D cubic shape of NPs and their core-shell structure with a core of FeO and a shell of spinel iron oxide[2].

II.1.1.2 X-Ray diffraction (XRD)

The indexation of X-ray peaks in XRD patterns allows identifying the crystalline phase(s) present in NPs but also to determine the NPs mean crystallite size. The average crystallite size L has often been estimated using the Debye-Scherrer equation, $\Delta(2\theta) = K\lambda/(\Lambda\ \chi o\sigma(\theta))$. K is a dimensionless shape factor, with a value close to unity (a typical value of about 0.9 is often used). $\Delta(2\theta)$ is the line broadening at half the maximum intensity (FWHM), after subtracting the instrumental line broadening, in radians. λ is the X-ray wavelength. θ is the Bragg angle (in degrees). It is worth to note that the Scherrer equation is limited to nanoscale particle and it is not applicable to grains larger than about 0.1 to 0.2 µm.

The mean crystallite size is now more and more extracted from Profile matching refinements which consist in comparing experimental and simulating XRD patterns. They are often performed through the Fullprof program[10] using LeBail's method[11] with the modified Thompson-Cox-Hasting pseudo-Voigt profile function. Another approach consists in the deconvolution of the X-ray pattern using MAUD software based on the Rietveld method combined with a Fourier analysis to describe particularly the low part of the wings of the Bragg peaks: this description which can be applied to synchrotron, time of flight neutron and electrons patterns is suitable in the case of NPs and nanoarchitectures. Indeed, it allows thus to refine the microstructural parameters, i.e. size of the coherent diffraction domain assuming different shapes, the microsize-strains, the lattice parameter, as well as some instrumental parameters[12–14]. This procedure gives also rise to estimate the Rietveld texture and stress analysis in the case of thin films studied by x-ray diffraction.

When the mean crystallite size is in agreement with the TEM mean size, the NPs can be considered as being monocrystalline/single crystal.

II.1.1.3 Granulometric measurement by dynamic light scattering (DLS)

The particle size distribution in suspension is generally determined by granulometric measurements which give the mean hydrodynamic diameter of NPs functionalized or not in suspension. Dynamic light scattering (DLS) (also referred to as Photon Correlation Spectroscopy or Quasi-Elastic Light Scattering) is the technique which is used to determine the size distribution profile of NPs in suspension or polymers in solution. Fundamentally, the NPs suspension is illuminated by a laser beam and the fluctuations of the scattered light are detected at a known scattering angle θ by a fast photon detector.

NPs suspended within a liquid undergo brownian motion. The larger the particle, the slower the Brownian motion will be. DLS monitors the brownian motion with light scattering. The speed at which NPs are diffusing due to brownian motion is measured by recording the rate at which the intensity of the scattered light fluctuates. Smaller particles cause the intensity to fluctuate more rapidly than large particles. The dynamic information of the particles is derived from an autocorrelation of the intensity trace recorded during the experiment. Once the autocorrelation data have been generated, different mathematical/analysis approaches can be applied to determine information from it. DLS software of commercial instruments typically displays the particle population at different diameters. If the system is monodisperse, there should only be one population (monomodal size distribution), whereas a polydisperse system would show multiple particle populations.

The particle size is given in terms of hydrodynamic diameter which is the diameter of a hard sphere that diffuses at the same speed as the “nano-object” being measured. The hydrodynamic diameter will thus not only depend on the size of the particle core but also on the size of surface structures, particle concentration, and the type of ions in the medium. For example in Figure 1, the size distribution determined from DLS is shifted by comparison with that determined by TEM because NPs are coated with oleic acid (thickness of 1-2 nm) and are in suspension in THF. For a non-spherical particle, DLS will give the diameter of a sphere that has the same average translational diffusion coefficient as the particle being measured.

The primary size distribution obtained from a DLS measurement is the intensity-weighted distribution obtained from the chosen analysis. Volume or number size distributions are derived from the intensity distribution using Mie theory and the optical properties of the particles are required to make this transformation (particle refractive index (RI) , particle absorption (Abs)). Transformation from intensity to volume or number makes the following assumptions: all particles are spherical, all particles have a homogenous & equivalent density, the optical properties are known (RI & Abs).

An important point to notice is that among the size distributions in intensity, volume or number, the size distribution in number is not representative of the NPs suspension state. Size distributions in volume or intensity are required as they are equivalent to the mass or weight distribution.

This technique allows also measuring the zeta potential of NPs in water suspension

The colloidal stability of NPs is the result of a balance between attractive forces and repulsive forces. In the case of iron oxide NPs, the attractive forces are mainly due to van der Waals interactions and magnetic interactions between NPs acting as magnetic dipoles. These interactions depend on the nature of the material and the distance between two NPs. The Van der Waals interactions energy varies as $1/r^2$ and dipole - dipole interactions energy as $1/r^3$, where r is the distance between NPs. As iron oxide NPs are superparamagnetic, magnetic interactions can be neglected and the main attractive interactions are the van der Waals ones. To ensure a colloidal stability of NPs in suspension, repulsive forces are needed and are mainly induced by electrostatic interactions or/and steric repulsions[15].

At physiological pH, naked iron oxide NPs are not stable in suspensions and floculate. Indeed, as for all oxides, the surface of iron oxide is covered by amphoteric hydroxyl groups due to water chimisorption. Depending on the pH of the solution, the surface of the iron oxide NPs can be positively or negatively charged. The isoelectric point (IEP) is the pH at which the surface has as many positive charges as negative charges. For iron oxides, its value is about 6.8[16]. IO NPs are thus stable in suspension by electrostatic interactions only at pH far from their IEP.

Thus for applications in the biomedical field, the IO NPs have to be functionalized with molecules ensuring steric and/or electrostatic interactions. The NPs colloidal stability provided by electrostatic interactions in water is broadly assessed by zeta potential measurements[15]. From a theoretical viewpoint, the zeta potential ζ is the electric potential in the interfacial double layer at the location of the slipping plane relative to a point in the bulk fluid away from the interface. In other words, zeta potential is the potential difference between the dispersion medium and the stationary layer of fluid attached to the dispersed particle (a potential exists between the particle surface and dispersing liquid which varies according to the distance from the particle surface). The magnitude of the zeta potential indicates the degree of electrostatic repulsion between adjacent, similarly charged particles in a water dispersion. Colloids with high absolute value of zeta potential (≥ 30) are electrically stabilized while colloids with low zeta potentials tend to coagulate or flocculate (if no steric repulsion is provided).

II.1.2 Characterization of the composition of iron oxide based nanoparticles

The most studied iron oxide phases are the magnetite and maghemite phases. Magnetite is an inverse spinel: $Fe^{3+}_A[Fe^{2+}Fe^{3+}]_BO_4^{2-}$. However, at the nanoscale, the Fe^{2+} ions in octahedral (B = *Oh*) sites are very sensitive to oxidation. The oxidation of Fe^{2+} into Fe^{3+} is accompanied by vacancy formation ($\square$), giving the general formula $Fe^{3+}_A[Fe^{2.5+}_{2-6\delta}Fe^{3+}_{5\delta}\square_{\delta}]_BO_4^{2-}$. The complete oxidation corresponds to $\delta = 1/3$ and leads to maghemite γ–Fe_2O_3. The XRD patterns of magnetite and maghemite are very similar (Figure II.4) and the lattice parameter are very close which makes it difficult to discriminate between magnetite and maghemite. Magnetite displays conductive properties and a saturation magnetization larger than that of maghemite. It is now well established that the Fe^{2+} ions located at the surface of magnetite NPs are very sensitive to oxidation and that the size decrease increases their sensitivity to oxidation[17–25].

To enhance magnetic anisotropy and/or saturation magnetization of IO NPs, beside the tuning of the NPs shape, strategies were either to dope iron oxide by elements such as Zn, Co, Ni or Mn[26,27] or to synthesize core-shell NPs with two phases displaying different magnetic properties to induce exchange magnetic properties[27–29]. For example, core-shell structures with antiferromagnetic and ferrimagnetic (AFM/FIM) materials display exchange bias properties, which lead to large coercive fields and allow to shift the superparamagnetic limit towards room temperature[2,30,31]. Another strategy is the synthesis of core-shell NPs by using mixed ferrites with hard and soft anisotropy inducing exchange coupled properties which have been found very favourable to MRI and therapy by hyperthermia[32]. However it is not easy to evidence the core-shell composition of NPs and also the doping homogeneity and amount. Indeed doped iron oxide NPs display generally complex structure with chemical heterogeneities[30,33]. The main characterization techniques allowing to discriminate between magnetite and maghemite and to evidence the NPs composition of doped or core-shell NPs are described below.

II.1.2.1 X-Ray Diffraction (XRD)

The XRD patterns allow identifying the crystalline phases present in powders. For core-shell NPs, both type of phases may be indexed on XRD patterns if their weight is large enough (≥5%). For doped iron oxide NPs, the analysis of XRD patterns allow confirming that NPs have a cubic spinel structure (AB_2O_4) and the lattice parameters are compared to those of JCPDS file of the expected ferrite. However, for both core-shell or doped iron oxide NPs, XRD does not afford to evidence the possible presence of a composition gradient and the presence of two types of ferrite is difficult as the lattice parameters may be close. Other techniques such as ^{57}Fe Mössbauer spectrometry or X-ray magnetic circular dichroism (XMCD) experiments are needed to conclude.

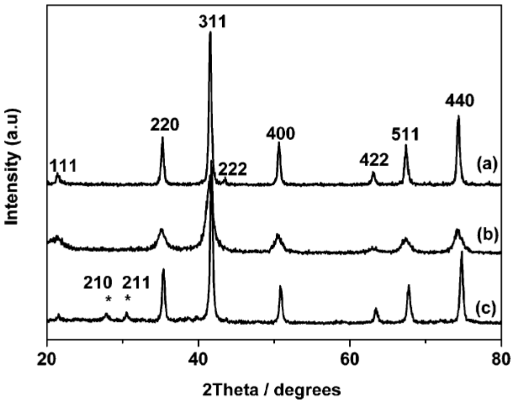

Figure II.4 - XRD patterns of $Fe_{3-x}O_4$ NPs with a mean diameter of 40 nm (a) or 12 nm(b) and of maghemite γ–Fe_2O_3 (c). The peaks marked with asterisks are additional peaks present in maghemite exhibiting vacancies ordering[19].

The magnetite phase and its corresponding oxidized phase, maghemite, have a similar structure and they display thus similar XRD patterns (Figure II.4). The refinement of the XRD pattern allows calculating the mean value of the lattice parameter and to compare it to those of stoichiometric magnetite Fe_3O_4 (0.8396 nm, JCPDS file 19-629) and maghemite γ-Fe_2O_3 (0.8346 nm, JCPDS file 39-1346) phases. A lattice parameter intermediate between those of magnetite and maghemite indicates that the composition is intermediate between these two structures. The composition of IO NPs has been demonstrated to depend on the synthesis method and on size of NPs[18,27,34]. For NPs synthesized by thermal decomposition in experimental conditions detailed in reference[27], it has been reported that the small NPs (<8 nm) are quite fully oxidized and display a composition close to that of maghemite. The NPs with sizes larger than 12 nm are constituted of a magnetite core with an oxidized shell and the amount of magnetite in the NPs increases when the size increases. For intermediate sizes (8-12 nm), the composition is found to be intermediate between those of magnetite and maghemite without a clear core-shell structure and with the occurrence of a perturbed oxidized state with defects. Similar results were noticed with NPs synthesized by coprecipitation[18], for sizes smaller than 20 nm, the composition of NPs was reported to be close to that of maghemite and for sizes higher than 20 nm, NPs were found to display a core-shell structure with a core of stoichiometric magnetite surrounded by an oxidized layer. Such a feature was consistent with the disappearance in ZFC/FC curves of the Verwey transition, which is typical of bulky magnetite, when NPs sizes are smaller than 20 nm[18].

II.1.2.2 IR spectroscopy

The magnetite and maghemite phases can be easily differentiated on symmetry grounds. Wavenumbers assigned to spinel structure are in the 800-400 cm^{-1} range. The IR spectra of stoichiometric magnetite display one peak at around 570 cm^{-1}, whereas the IR spectra of maghemite are more complicated due to the sensitivity of IR analyses to vacancies ordering (Figure II.5). Indeed, maghemite differs from magnetite by the presence of vacancies within the Oh sites, and the absence of Fe^{2+} cations. It often displays superstructure forms, which arise as a result of cationic and vacancy ordering (Figure 5). The vacancies can be randomly distributed (space group *Fdιm* as in magnetite), or partially (*P*4332) or totally ordered (*P*43212). The maghemite phase displays thus several bands between 800-400 cm^{-1} which number and resolutions depend on the structural order of vacancies in maghemite[23,35,36]. The higher the order, the larger the number of lattice absorption bands between 800 and 200 cm^{-1} (Figure II.5). The IR spectrum of NPs, with a lattice parameter close to that of magnetite and identified as a core-shell NPs with a core of magnetite surrounded by an oxidized layer with a composition close to that of a disordered maghemite, displays an intense band at around 570 cm^{-1} with a large shoulder up to 750 cm^{-1}.

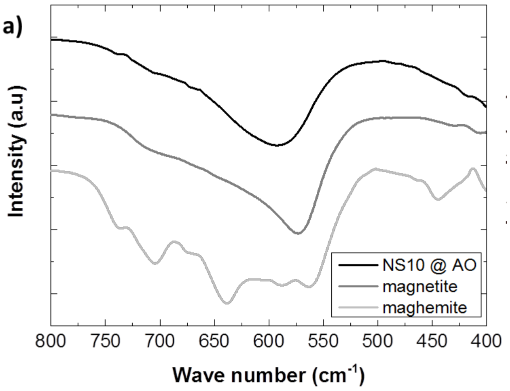

Figure II.5 - IR spectra between 800-400 cm^{-1} corresponding to the Fe-O bands of NPs of 10 nm in diameter synthesized by thermal decomposition compared to maghemite (partially disordered vacancies) and magnetite IR spectra[35].

II.1.2.3 ^{57}Fe Mössbauer spectrometry

Mössbauer spectrometry is a priori the most adapted method to evaluate the exact deviation from stoichiometry δ in $Fe_{3-\delta}O_4$. The discovery of "the recoilless nuclear resonance fluorescence of gamma radiation" by Rudolf Mössbauer in 1958[37–41] gave rise to the development of the so-called

Mössbauer spectrometry, a resonance technique giving physical parameters extremely relevant and useful in materials science. Indeed, its high sensitivity and its non-destructive behavior made this technique progressively of growing interest not only for physicists and chemists, but also geologists, metallurgists, biologists, and industrials to explore the possibility to better understand some structural, chemical, magnetic and electronic properties. Many books, chapters have yet reported on the fundamental aspects of the Mössbauer effect and the physical meaning of Mössbauer hyperfine parameters while seminars and tutorials at conferences and workshops have illustrated the wide range of interests and applications of transmission Mössbauer spectrometry (see a selection of books[24,42–47]). One does mention that this nuclear local probe technique can be easily applied to solid state materials including frozen solutions but is not suitable to liquids and gas. Let us remember that this spectroscopic technique is sensitive to three hyperfine interactions at probe nuclei which can be simultaneously evidenced and quantified in a single Mössbauer spectrum. They describe how nuclear moments interact with close electronic shells and the atomic environment. One distinguishes thus the electric monopole interaction resulting in the isomer shift (IS mm/s), the electric quadrupole interaction causing the quadrupole splitting (QS mm/s) of partially two-fold degenerate nuclear levels and the magnetic dipole interaction giving rise to magnetic splitting (hyperfine field B_{hf} T) of completely six-fold degenerate nuclear levels. The nuclear states and the typical Mössbauer spectra (single line, quadrupolar doublet and Zeeman sextets) are schematized in Figure II.6 in the case of ^{57}Fe isotope (excited nuclear state I_{ex} = 3/2).

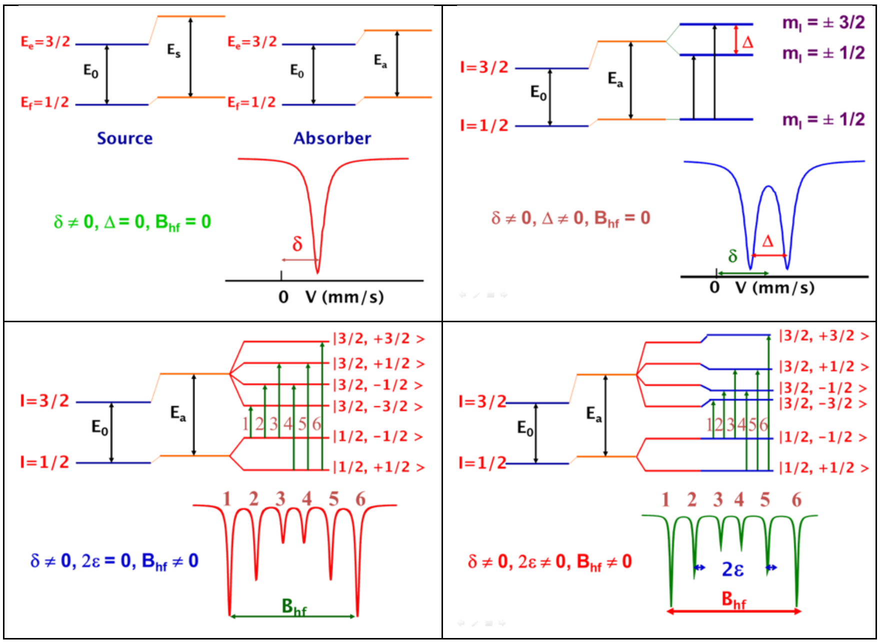

Figure II.6 - Nuclear level ground and excited states and corresponding typical Mössbauer spectra for a random powdered sample in the case of pure electric monopole interaction between electrons and protons which gives rise to isomer shift δ (top left); in the case of a non-zero electric field gradient (EFG), electric quadrupole interaction resulting from the precession of the quadrupole moment and its neighboring originating a partial degeneracy of excited levels and to quadrupolar doublet characterized by its quadrupolar splitting Δ (top right); in presence of magnetic dipolar interaction, one observes a total degeneracy of ground and excited states which gives rise to Zeeman splitting into a sextet and the hyperfine field B_{hf} *(bottom left); in presence of combined magnetic dipolar interaction, electric monopolar interaction and electric quadrupolar interaction labelled here as quadrupolar shift 2ε (bottom right).*

A specific attention has to be paid to the preparation of the Mössbauer sample and the instrumental conditions to optimize the registration time: optimal experimental conditions are based on a thin powdered layer containing 5 mg of Fe/cm^2 which corresponds to the effective absorber thickness which does not correspond to the real physical thickness but to the number of Mössbauer active atoms per surface unit. This criterion has to be well satisfied to prevent thicknesses effects which originate a non-homogeneous broadening of lines, a change of their respective intensities and a distortion of their profiles. In the case of ferrofluids, attention has to be paid to the quantity of Fe and the cooling conditions to get a homogeneous distribution of nanoparticles in the sample. It is also important to note that special care can be satisfied on nanoparticles which are sensitive to atmosphere: sample holder has to be cleaned in glove box and sealed *in situ* before its transfer to any Mössbauer device to prevent any post-synthesis oxidation. In addition, the studies of ultra-fine nanoparticles may require their insertion in a matrix to improve the registration time because of the recoil effect due to their smallness but the interface nanoparticle-matrix has to be considered when interpreting Mössbauer hyperfine structures.

A complete description of the experimental spectrum gives rise first to discriminate the number of Fe species present in the sample, to information relative to their chemical bonding and structural properties (crystalline or amorphous state, valence state, mixed valency state, spin state and spin crossover) and to estimate *a priori* their respective proportions, providing a good spectral resolution. It is also important to emphasize that the profile of the Mössbauer lines (width and shape) allow to conclude on the crystalline quality, the chemical composition, the chemical disorder (non-homogeneities, defects, vacancies), the topological nature of the Fe network (crystalline-amorphous-nanocrystalline states). The addition of temperature dependence facilities makes possible to follow *in situ* solid state reactions, electron transfer and disproportionation mechanisms, spin transition, structural phase transitions and transformations (crystallization), magnetic ordering transitions and some electron and magnetic relaxation phenomena.

It is important to emphasize also the recoilless fraction or Lamb–Mössbauer factor (so called f) and the second-order Doppler shift (SOD) which have to be taken into account in the estimation of each Fe species. Indeed, they are strongly dependent on the binding of the resonant nucleus in the lattice and vary with the chemical composition of the phase(s), their lattice structure and the environmental conditions, such as temperature or pressure. The estimate of the f factor which remains a delicate task is extrapolated from the temperature evolution of absorption areas but they are assumed to be similar within a single phase containing different Fe species in most of studies reported in literature, or within different phases.

Furthermore, the application of an external magnetic field contributes to characterize the Fe moment orientations, the sign of hyperfine field which is parallel or anti-parallel to the magnetic moment[25], the sign of the quadrupolar splitting, the magnetic structures and to follow the superparamagnetic relaxation phenomena from dynamic to blocked magnetic states in the case of magnetic confined nanostructures[48–51]. Indeed, the intensities of the intermediate lines of the Zeeman sextet are correlated to the angle between the γ–beam and the magnetic Fe moment: the area ratios of the six lines are given by 3:p:1:1:p:3, where $p = 4 \sin^2\theta/(2 - \sin^2\theta)$ where θ represents the angle between the hyperfine field held by the nucleus probe and the propagation direction of the γ–beam. Consequently, one can model theoretical in-field Mössbauer spectra as a function of ideal magnetic collinear and non-collinear magnetic structures, as illustrated in Figure II.7, assuming here that the external magnetic field is oriented parallel to the γ–beam (when the external field is applied perpendicular to the γ–beam, the respective relative ratios have to be inversed: 3:4:1:1:4:3 becomes 3:0:1:1:0:3 and *vice versa*). In addition, it is usually observed that the values of the intermediate intensities differ from 0 or 4 in the case of collinear magnetic structures as most of magnetic structures are canted. It becomes thus possible to estimate directly this angle from the in-field Mössbauer data: then, the total effective field at the nucleus results from the vectorial sum of the hyperfine field and the applied field, one can establish the following expression: $B^2_{hf} = B^2_{eff} + B^2_{app} - 2B_{eff}B_{app}\cos\theta$ which allows the hyperfine field to be accurately estimated. It is thus possible to conclude whether the hyperfine field at Fe nuclei is parallel or anti-parallel to the Fe magnetic moment.

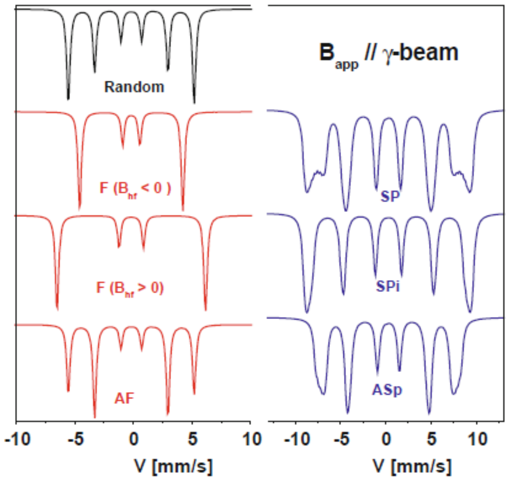

Figure II.7 - Theoretical Mössbauer spectra on linear and non collinear magnetic structures in presence of external field applied parallel to γ–beam: random powder in zero-field, ferromagnetic with magnetic moments antiparallel and parallel to the magnetic moment, and antiferromagnetic structures and non collinear magnetic structures of speromagnet, sperimagnet and asperomagnet.[51]

In the case of ferrimagnetic Fe-containing systems (as ferrites), the application of an external magnetic field allows also to discriminate accurately Fe species located in octahedral and tetrahedral sites, contrary to zero-field measurements giving rise to non-resolved or weakly resolved hyperfine structures, preventing thus a clear distinction both Fe species. The proportions have to be first discussed in terms of stoichiometry, cationic distribution including inversion, and then compared to magnetic measurements, particularly in the presence of different paramagnetic species.

The elementary applications of Mössbauer spectrometry in the case of Fe-containing materials consist in checking whether the sample under study does not contain any Fe-containing impurity phase (lower limit about 1 at.% Fe in optimal conditions). The modelling of the spectrum which consists in describing the hyperfine structure from a superimposition of elementary quadrupolar and/or magnetic components composed of lorentzian lines allow to estimate thus the number of Fe species, their respective proportions, and valence and spin states, particularly in the case of crystalline samples. But a first critical analysis of the linewidth allows to conclude on the crystalline quality: a broadening of lines is usually due to the presence of chemical non-homogeneities as vacancies, defects, atomic disorder. Studies versus temperature under controlled atmosphere have to be performed to establish the temperature dependence of the hyperfine parameters, to give evidence any structural or spin state transition, electron transfer and magnetic ordering of Fe moments. All results have to be then compared to the predictions established from X-ray diffraction: some significant disagreement (larger than the error bar) on the proportions must be considered in terms of defective chemical compositions and/or stoichiometric effects. In the case of topologically disordered systems, the broadening and the overlapping of lines have to be carefully described and modelled with discrete distributions of either quadrupolar splitting or hyperfine field, linearly correlated with that of isomer shift when the profile of the spectrum is asymmetrical. Let us emphasize that the ratio $\langle\Delta^2\rangle/\langle\Delta\rangle^2$ is a parameter quantifying the topological disorder and allows to conclude unambiguously if the material behaves as an amorphous[52].

In addition to the usual applications of ^{57}Fe Mössbauer spectrometry, the interest in the case of magnetic nanoparticles is to discriminate the surface from the volume contributions and to distinguish the static and dynamic magnetic effects[28,29,53,54,54–60]. Indeed, the comparison of zero-field and in-field

Mössbauer spectra gives rise to model the surface from structural and magnetic points of view: numerous studies have been particularly performed on maghemite and ferrite nanoparticles. Nevertheless, experiments at room temperature may be suitable to bring first information on the nature of the assembly of nanoparticles. The presence of both quadrupolar and magnetic features with broadened and/or asymmetrical lines may be *a priori* explained according to two main situations: (i) NPs with different sizes, i.e. a mixture of NPs exhibiting fast and slow superparamagnetic relaxation phenomena and static magnetic effects, or (ii) a mixture of non-interacting, weakly interacting and interacting NPs resulting well dispersed, rather close and aggregated NPs, respectively. A first alternative to identify the more realistic explanation can be obtained from Transmission Electron Micrographs illustrating some hundreds of NPs (sampling becomes quite relevant and decisive). A second one is to apply a small magnetic field (typically <0.5T produced by a simple magnet) on the sample to check how the magnetic fraction is increased, the dynamics and static effects are influenced by the external field, providing that the external magnetic field is large enough.

A deep analysis of the hyperfine structures resulting from zero-field and in-field Mössbauer spectra allowed the non-chemical homogeneity within monodisperse NPs to be characterized. A nice illustration is due to some $CoFe_2O_4$ NPs prepared by thermal decomposition route[61]: in-field Mössbauer hyperfine structures have to be modeled by means of joint distributions of canting angles and effective field for both tetrahedral and octahedral Fe sites allowing to estimate the respective hyperfine field consistent with the zero-field Mössbauer spectrum obtained at the same temperature. Such a description gives rise to a non-homogeneous cationic distribution with an excess of Co and Fe in the central and external part of nanoparticles, respectively.

Because the surface contribution is strongly enhanced in confined systems, the occurrence of an Fe-oxide layer recovering metallic NPs can be evidenced, including to identify its chemical nature and to estimate its thickness. The case of the “inverse spinel magnetite NPs”, this mixed valent phase is submitted to an immediate oxidation phenomenon giving rise to non-stoichiometric magnetite (Fe_3O_4: $Fe^{2+}Fe^{3+}{}_2O_4$) up to maghemite ($\gamma\text{–}Fe_2O_3$: $Fe^{3+}{}_2O_3$), whatever most of the chemical route and their synthesis conditions. On the contrary, magnetotactic bacteria containing stoichiometric magnetite can be perfectly obtained under microoxic conditions[62]. X-ray diffraction is not suitable to distinguish and to estimate the proportions of those two phases as the lattice parameters are not so different in the bulk state but are strongly dependent on the chemical route in the nanostate. The mean isomer shift value behaves as a crucial parameter to determine the mean valence state and consequently the mean stoichiometry or the proportions of both “ideal magnetite and maghemite” content in the frame of a core-shell model. However this naive description gives rise to an estimate of the thickness of maghemite shell (about 3 nm), which has been found rather independent of the size, the morphology of the nanoparticles and on the chemical route[18,19,23,63]. A second fitting model consists in considering two components corresponding to those of ideal magnetite and maghemite, as illustrated in Figure II.8.

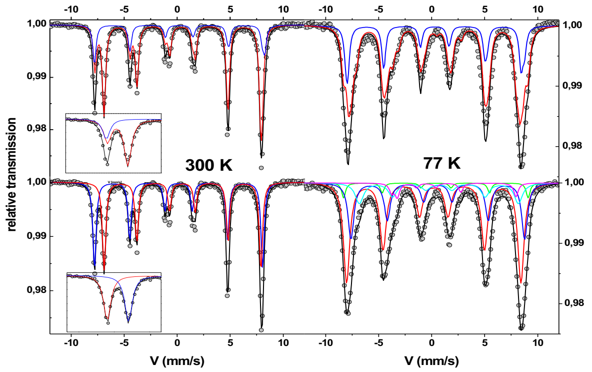

Figure II.8 - Examples of Mössbauer spectra at 300 K (left) and at 77 K (right). The bottom spectra show the decomposition into several components as generally done with a non-stoichiometric magnetite phase, while the top spectra were modeled assuming two stoichiometric phases as maghemite and magnetite (see text). The inset shows clearly the differences of the left outermost lines and the hyperfine spectra well-established for these two phases.[19].

This result justifies the Fe-oxide NPs smaller than 6 nm consist only of maghemite except those synthesized under microoxic conditions: such a feature excludes the presence of magnetite in opposite to several papers in 90's concluding that the disappearance of the Verwey transition was resulting from confined effects. In addition, the mixed analysis of hyperfine structures characteristic of non-functionalized and functionalized gives rise to the chemical linkage between the nanocarrier and the grafted molecules which can be in turn compared to some predictions established from *ab initio* calculations[23,64,65]. Figure II.9 left illustrates the Mössbauer spectra recorded at 77K on maghemite before and after grafting with dopamine: one new magnetic component allows to conclude that the dopamine is linked to the octahedral Fe unit and a partial electron transfer. Those two features are consistent with ab initio predictions (see Figure II.9 right and ref[65]).

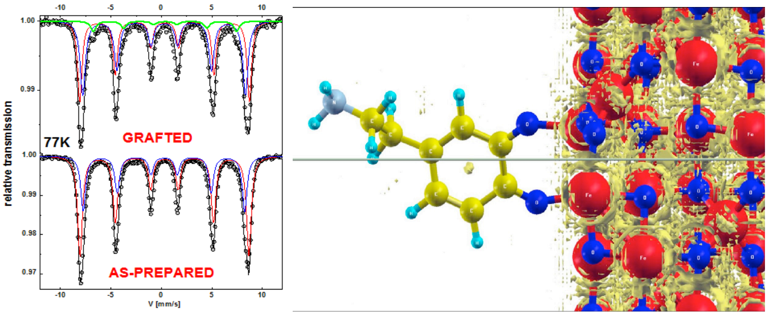

Figure II.9 - ^{57}Fe Mössbauer spectra of the as-produced maghemite particles (bottom) and their related nanohybrids resulting from DA grafting (top)recorded at 77 K (right), and ionicity of the system, estimated by 0.5 isosurface of reduced density gradient (EPLF) in LDA+U[65].

The magnetic properties characteristic of the "bulk" and the surface of the NPs can be obtained from a subtle analysis of in-field Mössbauer spectrum assuming a core-shell magnetic structure. It is important to emphasize that the external magnetic field has to be strong enough to overcome superparamagnetic relaxation phenomena and to split the zero-field hyperfine structure into a well-resolved in-field hyperfine structure, i.e. typically 8-10T. It is well established that the surface causes a symmetry breaking and thus a loss of neighbors, a distortion of the structural lattice giving rise to a change of interatomic distances, both contributing to a change of the magnetic moment. The interactions between superficial magnetic moments are modified and topological frustration plays an important role, favoring non-collinear magnetic moments. The core-shell model consists thus in assuming a shell with randomly oriented magnetic moments and a core with ideally oriented magnetic moments parallel or perpendicular to the external magnetic field, according to the nature of magnetic interactions. The in-field hyperfine structure can be thus decomposed into two magnetic components: one reflecting a random distribution of magnetic moments with lines area ratio as 3:2:1:1:2:3 and the second one typical of a saturated system as illustrated in figure II.10, attributed to the shell and core contributions, respectively. Such a model has been applied to NPs of γ–Fe_2O_3 maghemite which is a ferrimagnet[66–70].The thickness of the canted magnetic superficial layer can be estimated from $e = r/2 \sin^2\theta$ (assuming $e << r$) where r and θ represent the mean radius of the nanoparticle and the angle between the hyperfine field held by the nucleus probe and the propagation direction of the γ–beam, respectively. Figure II.10 illustrates a series of in-field Mössbauer spectra obtained on dispersed nanoparticles of maghemite, i.e. non-interacting nanoparticles, with different sizes[67]. One clearly observes that the intensities of intermediate lines increase when the size is decreasing suggesting that the canting of Fe magnetic moments increase: as the lower the size, the larger the surface/volume ratio, the canting originates clearly from the surface. It is now important to emphasize that the zero intensity of intermediate lines does not mean that there is no canting but the surface/volume ratio is too small to be clearly observed.

Those different selected examples illustrate how the zero-field and in-field transmission Mössbauer spectrometry provide relevant information to better understand the chemical, structural and magnetic properties of individual and assemblies of magnetic NPs. A particular application is the understanding of mixed magnetite and maghemite NPs. Nevertheless, those results require first an improvement of the experimental conditions and instrumental facilities and then a special attention and particular strategy in modelling the hyperfine structures which remains a very delicate task. In addition, complementary techniques as FC and ZFC (field-cooled and zero-field cooled) magnetic measurements, XMCD (X-ray magnetic circular dichroism) are necessary to compare the different results providing the samples were highly characterized by X-ray diffraction and Transmission Electron Microscopy. Finally, Monte Carlo, *ab initio* and molecular dynamics computer modeling which becomes now suitable to describe physical properties of NPs and particularly some observables as the Mössbauer hyperfine parameters, is a new alternative to study magnetic NPs.

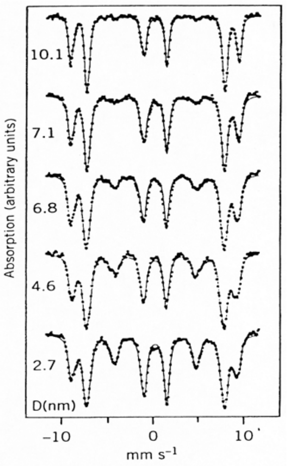

Figure II.10 - In-6T field Mössbauer spectra of maghemite nanoparticles of different size as mentioned on left[67].

II.1.2.4 STEM-HAADF, EDX and-EELS

If analytical information on the studied NPs is required, it can be obtained in a first step by using the STEM-HAADF incoherent imaging mode due to the direct dependence of the image intensity on the atomic number[71]. However, a large number of multiphase or heterogeneous particles are made out of elements with relatively close atomic numbers, which does not make the STEM-HAADF tomography so efficient. In this particular case, the chemical composition of NPs can be probed by energy dispersive X-ray spectroscopy (EDS) at the nanoscale and even at the atomic scale, depending on the spot size and intensity available in the STEM mode[72]. A significant improvement in obtaining chemically-resolved spatial resolution or in the chemical sensitivity was made possible after the generalization of Electron Energy Loss Spectroscopy (EELS) and related Energy-Filtered TEM (EFTEM) techniques. They can be implemented on state-of-the-art transmission electron microscopes equipped with electron spectrometers for the assessment of the chemical composition of NPs as well as of their electronic and optical properties. In particular, in the case of light elements such as for instance the oxygen for which the EDX analyses are not efficient, the acquisition of chemical maps by EELS is currently the best way for obtaining spatially solved compositional information[73] as well as the distribution of the oxidation degree within the particles.

II.1.3 Magnetic properties: magnetic measurements

Magnetization can be measured as function of an applied magnetic field or of temperature. In both case, magnetization can be measured after Field Cooling (FC) or Zero Field Cooling (ZFC) as well as under an alternative field for AC (Alternative Current) susceptibility measurements. Magnetic characteristics can be quantified by measuring the saturation magnetisation (Ms), the coercive field (Hc), the squareness/remnant ratio (Mr/Ms) and the blocking temperature (T_B).

Data are carefully corrected from diamagnetic contributions due to the sample holder, polymer matrix and silicon substrate. Saturation magnetization is calculated from magnetization versus applied magnetic field curves recorded at different temperatures such as 5 or 300 K (Figure II.11)[74] by dividing the magnetization at high applied field (typically at 5 T) by the mass of the inorganic core. This latter may be deduced from thermogravimetric analysis (TGA) of the powder, which allows to measure the mass ratio between the organic coating and the inorganic core. However, in samples containing magnetite, a large incertitude may be observed due to a weight gain due to the oxidation of Fe^{2+} contained in magnetite. Therefore, elemental analysis appears as a good method to evaluate the inorganic mass.

The measurement procedure for zero field cooled (ZFC) and field cooled (FC) curves (Figure II.11) are as follows: samples are magnetically demagnetized at room temperature and cooled to 5 K without applying any magnetic field. Magnetization may be then recorded from 5 K to 300 K (or 400 K) upon heating (ZFC curve) under a given applied magnetic field (below which that leads to the saturation of magnetization (e.g. H = 75 Oe)). Samples are then cooled to 5 K under the same applied field, and magnetization is recorded upon heating (FC curve). AC susceptibilty is measured under an alternating magnetic field (frequency range: 0.3-1000 Hz) upon heating after having cooled the sample in zero field (Figure II.11).

In order to facilitate comparison between different samples, hysteresis loops may be normalised to the saturation magnetization, ZFC/FC curves are normalized to the peak of the ZFC curve and AC susceptibility to the maximum value measured.

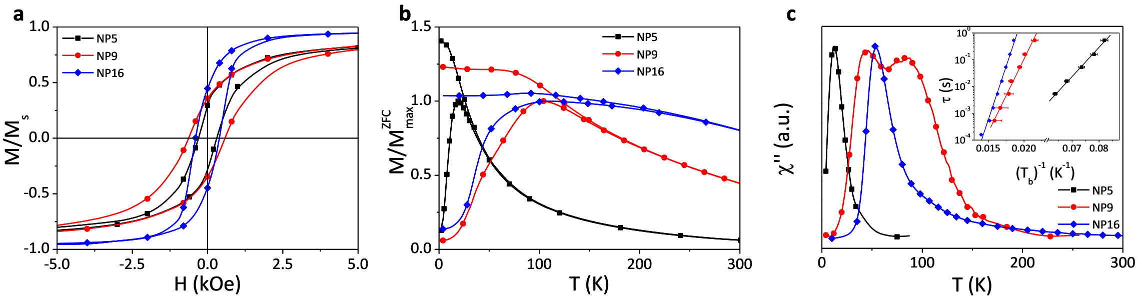

Figure II.11 - Magnetization measurements of iron oxide NPs with size of 5 nm (NP5), 9 nm (NP9) and 16 nm (NP16) dispersed in a polymer matrix: a) M(H) curves presenting an hysteresis loops at 5 K, b) ZFC/FC M(T) curves measured under a permanent field of 75 Oe and c) imaginary part of the AC susceptibility χ" measured under an alternative field at 1 Hz. Inset: inverse of the blocking temperature as function of the measurement time (dots), and fits to the Néel-Brown law (lines)[74].

If no hysteresis is observed at room temperature in magnetization curve as a function of applied field, it is characteristic of superparamagnetic NPs above their blocking temperature. Hysteresis loops are generally observed at 5 K (Figure II.11) and give access to Ms, M_r/M_s and H_C. For an ensemble of non-interacting NPs with their magnetization easy-axis oriented randomly, M_r/M_s should in theory decrease from $M_r/M_s = 0.5$ at 0 K to $M_r/M_s = 0$ at the blocking temperature[75]. The coercive field may be an indirect evaluation of the effective anisotropy of NPs. A non-linear variation of H_c with NP diameter has sometimes been observed and is a result of the competition between two contradictory "nanosize" effects[74]. Indeed, when NP size decreases, surface anisotropy becomes important[76] and the effective anisotropy increases, which explain the increase of coercive field from NP16 to NP9[74]. However, the thermal energy required to overcome the anisotropy barrier decreases when decreasing NP diameter[77], and lower fields are thus required for the magnetization reversal of the smaller NPs[34]

The saturation magnetization M_s increases with the particle size.[18,27,34] Even if some synthesis conditions have been noticed to lead to NPs with a Ms very close to bulk one, the Ms values are often lower than those of bulk magnetite and maghemite, 92 and 76 emu/g respectively. They were found to be related to the iron oxide composition evolution and to the presence of oxidation defects, surface and volume spin canting as a function of NPs diameter. Small NPs presented mainly a surface spin canting. NPs with large sizes display Ms which depends on both their oxidized shell thickness, defects and surface spin canting. NPs with intermediate sizes display a surface and in particular a volume spin canting due to a disordered structure induced by a perturbed oxidation state in these NPs[27].

The presence of spin canting in NPs may be evidenced by performing Mössbauer measurements under an applied magnetic field as described in the above paragraph but also by magnetization measurements after cooling down under a magnetic field (FC curves). To evaluate possible exchange interactions between the core of NPs and a canted layer at the surface, magnetization measurements are performed at temperatures between 5 K and 50 K after cooling down the powders under a field of 5T. Surface defects due to symmetry breaking of atoms at NPs surface and/or a disordered layer resulting from heterogeneous surface oxidation can conduct to a destabilization of the ferrimagnetic order of spins at the surface, which leads to a core-shell system similar to that of metal NPs oxidized at their surface. In the case of ferromagnetic or ferrimagnetic NPs and at low temperatures, the disordered spins at the surface can lead to the formation of spin glass like layer (assimilated for example to an antiferromagnetic layer). exhibiting a larger magnetic anisotropy. This structure results in exchange coupling of interfacial spins of the ordered core and the disordered shell which enhance softly the magnetic anisotropy energy. This behavior can be evaluated by cooling down the sample with applying an external field. It will orientate the spins in the magnetic field's direction, except those canted, which lead to a shift of hysteresis loop to the negative fields and allow calculating an exchange field H_E. Magnetic exchange effects in ferrimagnetic/antiferromagnetic F(i)M/AFM core-shell NPs such as Co/CoO, Fe_3O_4/CoO or FeO/Fe_3O_4... can be evaluated by measuring[30,33] the negative shift of the coercive field (Hc) in FC (M(H) curves which corresponds to the exchange bias field (H_E).

ZFC/FC curves, characteristic of superparamagnetic NPs, are given in Figure II.11. The maximum of the ZFC curves is often assimilated to the blocking temperature T_B i.e., the transition between ferrimagnetic (below) and superparamagnetic (above) states. However, the blocking temperature is also strongly dependent on dipolar interactions between NPs, the stronger are dipolar interactions, the higher is the shift of T_B towards larger temperature.

The broadening of the ZFC curves and the splitting of ZFC and FC curves are generally related to the largest polydispersity in size for NPs which induces a distribution of blocking temperature. The shape of FC curves can also give an indication about the strength of dipolar interactions: if FC curves do not reach a plateau as soon as T_B is reached suggests that the dipolar interactions are not prevailing in the samples (Figure II.11).

AC susceptibility measurements can be very useful to measure the blocking temperature which corresponds to the maximum of the imaginary part χ" (Figure II.13). Indeed, the variation of this maximum with the field frequency allows measuring the effective anisotropy constant K_{eff} according to the Néel-Brown law (inset of Figure II.11):

$$\tau = \frac{1}{2\pi f} = \tau_0 \exp\left[\frac{K_{eff}V}{k_B T}\right]$$

where f is the AC field frequency, K_{eff} the effective anisotropy constant and V the NP volume (determined from the NP diameter measured by TEM). The values of τ_0 obtained are close to the theoretical value ($\tau_0 = 10^{-10}$-10^{-11} s) and thus confirm that the well-dispersed NPs are non-interacting.

Thus magnetic measurements performed on dispersed NPs allow determining the intrinsic magnetic properties of individual NPs (in particular M_s, T_B and K_{eff}), without any effect of dipolar interactions which can strongly modify these properties. For interacting NPs, the variation of the blocking temperature as function of the relaxation time cannot be fitted to the Néel-Brown law as this model is not adapted for assembled interacting NPs. Other laws are used to fit the T_B curve such as the Vogel-Fulcher law or with a spin-glass like model[74].

II.2 Characterization techniques for nanoparticle coating

One important fact is to verify that the NPs are coated by organic molecules, polymers or silica shells and that a bond has been formed between the coupling/anchoring agent bore by molecules and the surface of NPs. Anchoring groups may have different binding affinities which should affect significantly the final performance of the NPs. Strong anchoring groups should favor a higher density of molecules at the surface of NPs and thus enable higher stability, anti-biofouling ability, and higher densities of bioactive molecule. For example, it has been shown both experimentally and theoretically that when the density of PEG layer reaches a given value, the unspecific adsorption of protein to the NPs may be highly prevented[78–80].

In this paragraph, the main characterization techniques confirming the grafting of molecules are detailed: IR spectroscopy, thermogravimetric analysis (TGA), dynamic light scattering (DLS), zeta potential measurements (ZPM) and elemental analysis. Elemental analysis brings valuable information on the presence of molecules and on the grafting rate when specific elements of molecules such as N, Si, P may be quantified with respect to iron. The combination of these techniques demonstrates the presence of the molecules at the surface of NPs but the major remaining difficulty is to evaluate the strength of their anchoring at the surface of IO NPs through their anchoring groups.

II.2.1 Fourier transform infrared spectroscopy (FT-IR)

FTIR is a suitable technique to characterize both IO NPs and its molecular/polymer coatings. Typically, for coated IO NPs, the presence of iron oxide is confirmed by the presence of Fe-O bands in the range 800-200 cm^{-1} which are usually not overlapped by vibrations bands of organic or polymer coatings. The magnetite (Fe_3O_4) displays one broad band located at 580-590 cm^{-1} while the maghemite (γFe_2O_3) phase displays several bands between 800-400 cm^{-1} which number and resolutions depend on the structural order of vacancies in maghemite[32,79].

A first step to confirm the presence of the coating at the surface of NPs is to compare the IR spectra of molecules and NPs coated with molecules after their purification step. The main characteristic bands of the molecules have to be identified on the IR spectra of purified functionalized NPs. The FTIR signatures of coatings depend on their nature and functional end-groups but also on the type of bonds achieved with the Fe-OH surface. Thus, the evolution of IR bands of the anchoring groups (shift of their position and/or modification of IR bands intensity) has to be carefully investigated and the nature of the surface complex determined if possible.

For molecules bearing carboxylate groups as anchoring agent, the interaction of the carboxylate with the NPs surface is confirmed by the appearance of the characteristic asymmetric and symmetric COO^- stretching bands of metal carboxylates between 1700 and 1400 cm^{-1}. These asymmetric ν_{as}(COO-) and symmetric ν_s(COO-) bands are usually observed in the range (1650-1500 cm^{-1}) and (1340-1440 cm^{-1})

respectively. The wavenumber difference ($\Delta\nu$), between the $\nu_{as}(COO^-)$ and $\nu_s(COO^-)$ IR bands, may allow identifying the type of carboxylate surface complex which can be either monodentate ($\Delta\nu$ =200–320 cm^{-1}) where one metal ion is binding with one carboxylic oxygen atom, or chelating bidentate ($\Delta\nu$ = <110 cm^{-1}) where one metal ion is binding with two carboxylate oxygens, or bridging bidentate ($\Delta\nu$ =140–190 cm^{-1}) where two metal ions are binding with two carboxylate oxygens[82]. The nature of the carboxylate complex will depend on parameters such as the coating strategy, the NPs synthesis method. Most reported surface complexes are either bridging bidentate or chelate bidentate[83].

P-OH and P=O bonds in phosphonate based molecules are characterized by the presence of bands at 900 -1000 and around 1200-1250 cm^{-1} respectively[23,81,84,85,and references herein] However the clear identification of P-O bands is mostly difficult as the bands overlap with other bands such as bands from other groups (phenyl, C=C, C-C, C-H bands). A fine IR characterization of the phosphonate based molecules at different synthetic steps may allow identifying the phosphonate bands in the 1250-800 cm^{-1} region. The comparison of the phosphonate bands zone before and after the grafting step allows mostly observing that the phosphonate bands evolved but the unambiguous identification of the surface complex is difficult. A fine IR characterization of phosphonate based dendrons at different synthetic steps allowed identifying unambiguously the P=O band around 1200 cm^{-1}, and the P-OH bands at 1020 et 999 cm^{-1} [81,86]. After the dendronisation of two types of IO NPs synthesized either by thermal decomposition or coprecipitation, the P=O band intensity strongly decreased, and the P-OH bands disappeared while new bands appeared due to a modification of the electronic density around the atoms with the formation of the Fe-O-P bond. For NPs synthesized by thermal decomposition, two bands were clearly observed at 1047 and 985 cm^{-1} and were attributed to Fe-O-P bonds. For NPs synthesized by coprecipitation, only one Fe-O-P band was clearly identified at 975 cm^{-1} whereas the second Fe-O-P band would be contained within the shoulder (around 1050 cm^{-1}) of the band at 1109 cm^{-1} which was attributed to the aromatic C-C bonds. Based on the IR results, the phosphonate surface complex was possibly at least binuclear for both types of NPs. However, hydrogen bonding may also be responsible for the shift or intensity decrease of P-OH and P=O peaks. The combination of IR with XPS spectroscopies may allow concluding as explained below.

II.2.2. Thermal Gravimetric Analysis (TGA)

TGA allows to estimate the mass fraction between the organic coating and the inorganic NPs. In TGA, the samples are heated from ambient temperature up to 1000 °C in the range of 5-20°C/min and the weight loss due to the degradation of the organic materials of the sample is recorded with temperature. The observed weight loss is a proof of the presence of the organic coating but it is also mostly used to evaluate the grafting rate. For instance, TGA was shown efficient to estimate the mass fraction of various grafted silanes at the surface of ca. 10 nm size cobalt ferrite NPs[87].

II.2.3 Dynamic Light Scattering (DLS) and Zeta Potential (ZP)

DLS and ZP measurements are well-established methods usually used concomitantly to confirm the grafting of molecules and to establish the colloidal stability of NPs dispersed in aqueous solutions. In DLS, the light scattering by NPs in solution allows to sense their brownian motion and then to provide information about their diffusion coefficient and then their dynamic size distribution in the solvent. When the size of molecules to graft is large enough, the particle size distribution of coated NPs is shifted towards larger sizes by comparison with that of NPs before their coating.

The ZP is defined as the electrical potential at the slipping plane of the double ionic layer of the coated NPs. In ZP measurements, by applying an alternative electric field, the electrophoretic mobility of the coated IO-NPs dispersed in aqueous solutions can be measured and application of the Henry equation allows to measure the ZP. In a first approximation, the ZP measurements give an indication of the surface charge of the coated NPs. When the ZP values are higher than 30 mV in absolute value, it is admitted that suspensions of NPs bearing charged groups have in general a high colloidal stability ensured by electrostatic repulsions. Nevertheless, NPs coated with non-charged polymers or molecules can have a high colloidal stability ensured by steric repulsion, even with ZP values inferior to 30 mV. The ZP measurements allow also, by varying the pH value, to evaluate the isoelectric point (IEP) of the coated IO NPs which corresponds to the pH at which the ZP is equal to 0 mV. The IEP is an important parameter ascertaining the pH range ensuring a colloidal stability of coated IONPs by electrostatic interaction in an aqueous solution. After their coating, the IEP of IO NPs is generally shifted which prove also their coating. Indeed, the IEP of IO is around 6.8-7 which makes that naked IO NPs are not stable in suspensions at physiological pH.

II.3 Conclusion

The development of iron oxide based NPs for biomedical applications is still facing several challenges that have to be overcame among which the design of the organic coating and its grafting at the surface of NPs while preserving properties of both NPs and molecules. Indeed, the molecules anchored at the surface of NPs have to be able to provide different functions such as dyes for optical imaging, targeting ligands to reach target tissue or cells, or therapeutic agents (drug delivery). However, besides the design of the bioactive molecules, their grafting has to be controlled to ensure hydrodynamic sizes be lower 100 nm to favor a good biodistribution. In addition, a strong bond between the molecules and NPs has to be confirmed to avoid their desorption after *in vivo* injection. The mean hydrodynamic size (smaller than 100 nm) of coated NPs will strongly depend on the nature of the grafted molecules to the NPs surface and on the grafting strategy. All of these parameters (size distribution, mean size, shape, composition, hydrodynamic sized of NPs, magnetic properties, coating efficiency in terms of density or anchoring strength) are important to control and requires the combination of different characterization techniques which have been described in this chapter.

II.4 Description of main characterization techniques used in this manuscript

NPs were characterized by **transmission electron microscopy (TEM)** with a TOPCON 002B microscope operating at 200 kV (point resolution 0.18 nm). The size distribution of NPs was calculated from the size measurements of more than 300 nanoparticles using ImageJ software.

Scanning electron microscopy (SEM) was performed using a Zeiss gemini SEM 500 microscope equipped with a field emission gun (SEM-FEG) operating at an accelerating voltage of 1 *kV*.

Thermogravimetric measurements were performed on dried powder samples from 20 to 600 °C at 5°C/min under air by using a SETARAM TGA 92 apparatus.

The X-ray diffraction (XRD) pattern was recorded at room temperature with a Bruker D8 Advance diffractometer equipped with a monochromatic copper radiation source (Kα = 0.154056 nm) and a Sol-X detector in the 27-65°(2θ) range with a scan step of 0.03°. High purity silicon powder (a = 0.543082 nm) was systematically used as an internal standard. Profile matching refinements were performed through the Fullprof program[10] using Le Bail's method[11] with the modified Thompson-Cox-Hasting (TCH) pseudo-Voigt profile function.

Standard Infrared spectra were recorded between 4000 and 400 cm^{-1} with a Fourier transform infrared (FTIR) spectrometer, Digilab Excalibur FTS 3000 series. Samples were gently ground and diluted in non-absorbent KBr matrixes.

^{57}Fe Mössbauer spectra were performed at 300 K and 77 K using a conventional constant acceleration transmission spectrometer with a ^{57}Co(Rh) source and a bath cryostat where the sample chamber is under He atmosphere. Further spectra have been obtained using a homemade cryofurnace where sample is maintained under vacuum, whatever the temperature ranged from 77K up to 400°C. The spectra were fitted by means of the MOSFIT program[88] involving asymmetrical and lines with lorentzian profiles and a α–Fe foil was used as the calibration sample. The values of isomer shift are quoted relative to that of α-Fe at 300 K.

Granulometry measurements were performed on a nanosize MALVERN (nano ZS) apparatus for each NP suspension.

REFERENCES

1. Carenco, S. *et al.* The core contribution of transmission electron microscopy to functional nanomaterials engineering. *Nanoscale* **8,** 1260–1279 (2016).
2. Pichon, B. P. *et al.* Microstructural and Magnetic Investigations of Wüstite-Spinel Core-Shell Cubic-Shaped Nanoparticles. *Chem. Mater.* **23,** 2886–2900 (2011).
3. Pyrz, W. D. & Buttrey, D. J. Particle size determination using TEM: a discussion of image acquisition and analysis for the novice microscopist. *Langmuir* **24,** 11350–11360 (2008).
4. Rasband, W. https://imagej.nih.gov/ij/.
5. Le Beulze, A. *et al.* New insights into the side-face structure, growth aspects, and reactivity of Ag(n) nanoprisms. *Langmuir* **30,** 1424–1434 (2014).
6. Burgin, J. *et al.* 3D morphology of Au and Au@Ag nanobipyramids. *Nanoscale* **4,** 1299–1303 (2012).
7. Takeda, S. & Yoshida, H. Atomic-resolution environmental TEM for quantitative in-situ microscopy in materials science. *Microscopy (Oxf)* **62,** 193–203 (2013).
8. Baaziz, W. *et al.* High-Density Monodispersed Cobalt Nanoparticles Filled into Multiwalled Carbon Nanotubes. *Chem. Mater.* **24,** 1549–1551 (2012).
9. Ersen, O., Florea, I., Hirlimann, C. & Pham-Huu, C. Exploring nanomaterials with 3D electron microscopy. *Materials Today* **18,** 395–408 (2015).
10. Rodríguez-Carvajal, J. Recent advances in magnetic structure determination by neutron powder diffraction. *Physica B: Condensed Matter* **192,** 55–69 (1993).
11. Le Bail, A., Duroy, H. & Fourquet, J. L. Ab Initio Structure Determination of LiSbWO6 by X ray Powder Diffraction. *Materials Research Bulletin* **23,** 447–452 (1988).
12. Lutterotti, L. & Scardi, P. Simultaneous structure and size–strain refinement by the Rietveld method. *J Appl Cryst, J Appl Crystallogr* **23,** 246–252 (1990).
13. Lutterotti, L., Matthies, S. & Wenk, H.-R. *MAUD (material analysis using diffraction): a user friendly Java program for Rietveld texture analysis and more*. **1,** (1999).
14. Ferrari, M. & Lutterotti, L. Method for the simultaneous determination of anisotropic residual stresses and texture by x-ray diffraction. *Journal of Applied Physics* **76,** 7246–7255 (1994).
15. Walter, A. *et al.* Functionalization strategies and dendronization of iron oxide nanoparticles. *Nanotechnology Reviews* **4,** 581 (2015).
16. Bacri, J.-C., Perzynski, R., Salin, D., Cabuil, V. & Massart, R. Ionic ferrofluids: A crossing of chemistry and physics. *Journal of Magnetism and Magnetic Materials* **85,** 27–32 (1990).
17. Hyeon, T., Lee, S. S., Park, J., Chung, Y. & Na, H. B. Synthesis of highly crystalline and monodisperse maghemite nanocrystallites without a size-selection process. *J. Am. Chem. Soc.* **123,** 12798–12801 (2001).
18. Santoyo Salazar, J. *et al.* Magnetic Iron Oxide Nanoparticles in 10–40 nm Range: Composition in Terms of Magnetite/Maghemite Ratio and Effect on the Magnetic Properties. *Chem. Mater.* **23,** 1379–1386 (2011).
19. Daou, T. J. *et al.* Hydrothermal Synthesis of Monodisperse Magnetite Nanoparticles. *Chemistry of Materials* **18,** 4399–4404 (2006).
20. Belin, T., Guigue-Millot, N., Caillot, T., Aymes, D. & Niepce, J. C. Influence of Grain Size, Oxygen Stoichiometry, and Synthesis Conditions on the γ-Fe2O3 Vacancies Ordering and Lattice Parameters. *Journal of Solid State Chemistry* **163,** 459–465 (2002).
21. Guigue-Millot, N. *et al.* Chemical Heterogeneities in Nanometric Titanomagnetites Prepared by Soft Chemistry and Studied Ex Situ: Evidence for Fe-Segregation and Oxidation Kinetics. *J. Phys. Chem. B* **105,** 7125–7132 (2001).
22. Jolivet, J.-P. & Tronc, E. Interfacial electron transfer in colloidal spinel iron oxide. Conversion of Fe3O4-γFe2O3 in aqueous medium. *Journal of Colloid and Interface Science* **125,** 688–701 (1988).
23. Daou, T. J. *et al.* Phosphate Adsorption Properties of Magnetite-Based Nanoparticles. *Chem. Mater.* **19,** 4494–4505 (2007).
24. Gütlich, P., Bill, E. & Trautwein, A. X. *Mössbauer Spectroscopy and Transition Metal Chemistry: Fundamentals and Applications*. (Springer, 1978).
25. Hanna, S. S., Heberle, J., Perlow, G. J., Preston, R. S. & Vincent, D. H. Direction of the Effective Magnetic Field at the Nucleus in Ferromagnetic Iron. *Phys. Rev. Lett.* **4,** 513–515 (1960).
26. Kumar, C. S. S. R. & Mohammad, F. Magnetic nanomaterials for hyperthermia-based therapy and controlled drug delivery. *Advanced Drug Delivery Reviews* **63,** 789–808 (2011).
27. Baaziz, W. *et al.* Magnetic Iron Oxide Nanoparticles: Reproducible Tuning of the Size and Nanosized-Dependent Composition, Defects, and Spin Canting. *J. Phys. Chem. C* **118,** 3795–3810 (2014).
28. Morup, S., Dumesic, J. & Topsoe, H. *Applications of Mössbauer in Spectroscopy*. **2,** (R. Cohen., 1953).
29. Dormann, J. L. Le phénomène de superparamagnétisme. *Rev. Phys. Appl. (Paris)* **16,** 275–301 (1981).
30. Baaziz, W. *et al.* High Exchange Bias in Fe3−δO4@CoO Core Shell Nanoparticles Synthesized by a One-Pot Seed-Mediated Growth Method. *J. Phys. Chem. C* **117,** 11436–11443 (2013).

31. Baaziz, W. *et al.* Tuning of Synthesis Conditions by Thermal Decomposition toward Core–Shell Co $_x$ Fe $_{1-x}$ O@Co $_y$ Fe $_{3-y}$ O $_4$ and CoFe $_2$ O $_4$ Nanoparticles with Spherical and Cubic Shapes. *Chemistry of Materials* **26,** 5063–5073 (2014).

32. Lee, J.-H. *et al.* Exchange-coupled magnetic nanoparticles for efficient heat induction. *Nat Nano* **6,** 418–422 (2011).

33. Baaziz, W. *et al.* Tuning of Synthesis Conditions by Thermal Decomposition toward Core–Shell CoxFe1–xO@CoyFe3–yO4 and CoFe2O4 Nanoparticles with Spherical and Cubic Shapes. *Chem. Mater.* **26,** 5063–5073 (2014).

34. Demortière, A. *et al.* Size-dependent properties of magnetic iron oxide nanocrystals. *Nanoscale* **3,** 225–232 (2011).

35. Tartaj, P., Morales, M. del P., Veintemillas-Verdaguer, S., González-Carreño, T. & Serna, C. J. The preparation of magnetic nanoparticles for applications in biomedicine. *J. Phys. D: Appl. Phys.* **36,** R182 (2003).

36. Walter, A. *et al.* Modulation of Relaxivity, Suspension Stability, and Biodistribution of Dendronized Iron Oxide Nanoparticles as a Function of the Organic Shell Design. *Part. Part. Syst. Charact.* **32,** 552–560 (2015).

37. Mössbauer, R. L. Kernresonanzfluoreszenz von Gammastrahlung in Ir191. *Z. Physik* **151,** 124–143 (1958).

38. Mössbauer, R. . Nuclear Resonance Absorption of Gamma Radiation in Ir191. **45,** 538 (1958).

39. Mössbauer, R. L. Kernresonanzabsorption von γ-Strahlung in Ir191. *Z.Naturforsch.* 211 (1959).

40. Mössbauer, R. L. Recoilless Nuclear Resonance Absorption of Gamma Radiation: A new principle yields gamma lines of extreme narrowness for measurements of unprecedented accuracy. *Science* **137,** 731–738 (1962).

41. Mössbauer, R. L. Nobel Lecture. (1961).

42. Greenwood, N. N. & Gibb, T. C. *Mössbauer Spectroscopy*. (1971).

43. Long, G. J. *Mössbauer Spectroscopy Applied to Inorganic Chemistry, Modern Inorganic Chemistry Series*. **1,** (Plenum Press, 1984).

44. Long, G. J. *Mössbauer Spectroscopy Applied to Inorganic Chemistry, Modern Inorganic Chemistry Series*. **2,** (Plenum Press, 1989).

45. Long, G. J. & Grandjean, F. *Mössbauer Spectroscopy Applied to Inorganic Chemistry, Modern Inorganic Chemistry Series*. **3,** (Plenum Press, 1989).

46. Long, G. J. & Grandjean, F. *Mössbauer Spectroscopy Applied to Magnetism and Materials Science,*. **1,** (Plenum Press, 1993).

47. Long, G. J. & Grandjean, F. *Mössbauer Spectroscopy Applied to Magnetism and Materials Science,*. **2,** (Plenum Press, 1996).

48. Chappert, J. *J. de Phys. C* **197,** 71

49. Chappert, J., Teillet, J. & Varret, F. Recent developments in high field Mössbauer spectroscopy. *Journal of Magnetism and Magnetic Materials* **11,** 200–207 (1979).

50. Greneche, J.-M. Noncollinear magnetic structures investigated by high-field Mossbauer spectometry. *Acta Physica Slovaca* **45,** 45 (1995).

51. Greneche, J.-M. *The Contribution of 57Fe Mössbauer Spectrometry to Investigate Magnetic Nanomaterials, in Mössbauer Spectroscopy*. (Yutaka Yoshida and Guido Langouche, 2013).

52. Lopez-Herrera, M. E., Greneche, J. M. & Varret, F. Analysis of the M"ossbauer quadrupole spectra of some amorphous fluorides. *Phys. Rev. B* **28,** 4944–4948 (1983).

53. Morup, S. *Mössbauer Spectroscopy applied to Inorganic Chemistry*. (G.J. Long, 1987).

54. Dormann, J. L., Fiorani, D. & Tronc, E. Magnetic Relaxation in Fine-Particle Systems. in *Advances in Chemical Physics* (eds. Prigogine, I. & Rice, S. A.) 283–494 (John Wiley & Sons, Inc., 1997).

55. Tronc, E. Nanoparticles. *Il Nuovo Cimento D* **18,** 163–180 (1996).

56. Morup, S., Hansen, M. . & Frandsen, C. Magnetic Properties of Nanoparticles, in The Oxford Handbook of Nanoscience and Technology: Materials, Structures, Properties and Characterization Techniques. in (A.V. Narlikar, Y.Y. Fu, 2010).

57. Papaefthymiou, G. C. Nanoparticle magnetism. *Nano Today* **4,** 438–447 (2009).

58. Mørup, S., Hansen, M. F. & Frandsen, C. Magnetic interactions between nanoparticles. *Beilstein Journal of Nanotechnology* **1,** 182–190 (2010).

59. Mørup, S., Hansen, M. F. & Frandsen, C. 1.14 - Magnetic Nanoparticles. in *Comprehensive Nanoscience and Technology* (eds. Andrews, D. L., Scholes, G. D. & Wiederrecht, G. P.) 437–491 (Academic Press, 2011).

60. Mørup, S. & Hansen, M. . Superparamagnetic Particles, in Handbook of Magnetism and Advanced Magnetic Materials. Novel Materials. in **4,** 2159–2176. (H. Kronmüller, S. Parkin, 2007).

61. Peddis, D. *et al.* Cationic distribution and spin canting in CoFe $_2$ O $_4$ nanoparticles. *Journal of Physics: Condensed Matter* **23,** 426004 (2011).

62. Faivre, D., Böttger, L. H., Matzanke, B. F. & Schüler, D. Intracellular magnetite biomineralization in bacteria proceeds by a distinct pathway involving membrane-bound ferritin and an iron(II) species. *Angew. Chem. Int. Ed. Engl.* **46,** 8495–8499 (2007).

63. Daou, T. J. *et al.* Water soluble dendronized iron oxide nanoparticles. *Dalton Trans* 4442–4449 (2009). doi:10.1039/b823187g

64. Karimi, A. *et al.* Effect of chain length and electrical charge on properties of ammonium-bearing bisphosphonate-coated superparamagnetic iron oxide nanoparticles: formulation and physicochemical studies. *Journal of Nanoparticle Research* **12,** 1239–1248 (2010).

65. Fouineau, J. *et al.* Synthesis, Mössbauer Characterization, and Ab Initio Modeling of Iron Oxide Nanoparticles of Medical Interest Functionalized by Dopamine. *J. Phys. Chem. C* **117,** 14295–14302 (2013).

66. Coey, J. M. D. Noncollinear Spin Arrangement in Ultrafine Ferrimagnetic Crystallites. *Phys. Rev. Lett.* **27,** 1140–1142 (1971).

67. Tronc, E., Prené, P., Jolivet, J. P., Dormann, J. L. & Grenèche, J. M. Spin Canting in γ-Fe2O3 Nanoparticles. *Hyperfine Interactions* **112,** 97–100 (1998).

68. Tronc, E. *et al.* Surface-related properties of γ-Fe2O3 nanoparticles. *Journal of Magnetism and Magnetic Materials* **221,** 63–79 (2000).

69. Tronc, E. *et al.* Surface effects in noninteracting and interacting γ-Fe2O3 nanoparticles. *Journal of Magnetism and Magnetic Materials* **262,** 6–14 (2003).

70. Tronc, E. *et al.* Magnetic properties of γ-Fe2O3 dispersed particles: size and matrix effects. *Journal of Magnetism and Magnetic Materials* **272,** 1474–1475 (2004).

71. Grieb, T. *et al.* Determination of the chemical composition of GaNAs using STEM HAADF imaging and STEM strain state analysis. *Ultramicroscopy* **117,** 15–23 (2012).

72. Slater, T. J. A. *et al.* STEM-EDX tomography of bimetallic nanoparticles: A methodological investigation. *Ultramicroscopy* **162,** 61–73 (2016).

73. Carenco, S. *et al.* Magnetic Core−Shell Nanoparticles from Nanoscale-Induced Phase Segregation. *Chem. Mater.* **23,** 2270–2277 (2011).

74. Pauly, M. *et al.* Size dependent dipolar interactions in iron oxide nanoparticle monolayer and multilayer Langmuir–Blodgett films. *J. Mater. Chem.* **22,** 6343–6350 (2012).

75. Bedanta, S. & Kleemann, W. Supermagnetism. *J. Phys. D: Appl. Phys.* **42,** 013001 (2009).

76. Bodker, null, Morup, null & Linderoth, null. Surface effects in metallic iron nanoparticles. *Phys. Rev. Lett.* **72,** 282–285 (1994).

77. Vázquez-Vázquez, C., López-Quintela, M. A., Buján-Núñez, M. C. & Rivas, J. Finite size and surface effects on the magnetic properties of cobalt ferrite nanoparticles. *J Nanopart Res* **13,** 1663–1676 (2011).

78. Sofia, S. J., Premnath, V. & Merrill, E. W. Poly(ethylene oxide) Grafted to Silicon Surfaces: Grafting Density and Protein Adsorption. *Macromolecules* **31,** 5059–5070 (1998).

79. Szleifer, I. Protein adsorption on surfaces with grafted polymers: a theoretical approach. *Biophys. J.* **72,** 595–612 (1997).

80. Liu, D. *et al.* Effective PEGylation of Iron Oxide Nanoparticles for High Performance In Vivo Cancer Imaging. *Adv. Funct. Mater.* **21,** 1498–1504 (2011).

81. Basly, B. *et al.* Dendronized iron oxide nanoparticles as contrast agents for MRI. *Chem. Commun.* **46,** 985–987 (2010).

82. Deacon, G. B. & Phillips, R. J. Relationships between the carbon-oxygen stretching frequencies of carboxylato complexes and the type of carboxylate coordination. *Coordination Chemistry Reviews* **33,** 227–250 (1980).

83. Hofmann, A. *et al.* Highly monodisperse water-dispersable iron oxide nanoparticles for biomedical applications. *J. Mater. Chem.* **20,** 7842–7853 (2010).

84. Lartigue, L. *et al.* Water-Soluble Rhamnose-Coated Fe3O4 Nanoparticles. *Org. Lett.* **11,** 2992–2995 (2009).

85. Borggaard, O. K., Raben-Lange, B., Gimsing, A. L. & Strobel, B. W. Influence of humic substances on phosphate adsorption by aluminium and iron oxides. *Geoderma* **127,** 270–279 (2005).

86. Lamanna, G. *et al.* Dendronized iron oxide nanoparticles for multimodal imaging. *Biomaterials* **32,** 8562–8573 (2011).

87. De Palma, R. *et al.* Silane Ligand Exchange to Make Hydrophobic Superparamagnetic Nanoparticles Water-Dispersible. *Chem. Mater.* **19,** 1821–1831 (2007).

88. Teillet, J. & Varret, F. Unpublished MOSFIT program.

Chapter III

Boosting NPs design by *in house* precursor synthesis: combined modeling and experimental approaches

III Boosting NPs design by *in house* precursor synthesis: combined modeling and experimental approaches

III.1 INTRODUCTION

Iron oxide based nanoparticles are involved in a lot of applications (magnetic data storage, MR devices, electrodes for battery or supercapacitor, nanomedecine..) and as their properties depend on their size, shape or composition, large efforts have been made to develop synthesis methods able to tune "on demand" these parameters. Among all the investigated NPs synthesis methods[1–9], the thermal decomposition method which consists in the thermal decomposition of a metal precursor in a high boiling point organic solvant in presence of surfactants has been shown very promising to vary the size[10–13] and the shape[14–16]. Different types of metal precursor have been used including organometallic compounds or metal carboxylates which are suitable precursors for the synthesis of NPs due to their reactivity and solubility. Semiconductor, catalytic and magnetic NPs have been thus synthesiszed[1–9,17,18]. The most used thermal decomposition approaches to synthesize iron oxide NPs (IONPs) are those developped by Hyeon[10] and Sun[11] which involved mainly iron oleate and iron acetyl acetonate as iron precursor respectively. However one may notice that the synthesis mechanisms are not yet well understood restricting thus a fine investigation of structure-composition-shape-properties relationships in NPs. Indeed doped iron oxide NPs displayed very interesting magnetic properties but are often not homogeneous in composition. They exhibited a composition gradient of the doping element explained sometimes by the different decomposition temperatures of metal precursors[19–21]. Several synthesis conditions have been reported for the synthesis of cubic shaped NPs : the most used Kovalenko's approach[14] involved the decomposition of iron oleate in presence of a mixture of oleic acid and sodium oleate. The sodium oleate is expected to strongly bind on specific surfaces of nuclei and to favor a cubic growth and by further playing on the heating rate and the boiling point of organic solvents, the nanocube size can be modulated. Some authors have noticed that such nanocubes are not homogeneous in composition and consisted in core-shell nanocubes with a core constituted of the wüstite FeO phase and a shell of $Fe_{3-x}O_4$[14,22]. Pelligrino et al reported also a nanocube synthesis involving iron acetyl acetonate and decanoic acid in dibenzylether[23] and then by playing on the amount of dibenzyl ether by introducing squalene, they have demonstrated that the nanocube shape was due to the decomposition products of dibenzylether during the synthesis which adsorbed on specific faces and triggered a cubic growth[24].

Due to the high potential of this synthesis approach, there is therefore a strong need in a better understanding the mechanism of the thermal decomposition for a better NPs synthesis control and design. It is now admitted that it follows the LaMer model[25] which is based on the fact that the energy barrier of the nucleation process is much higher than that of the growth process[26].

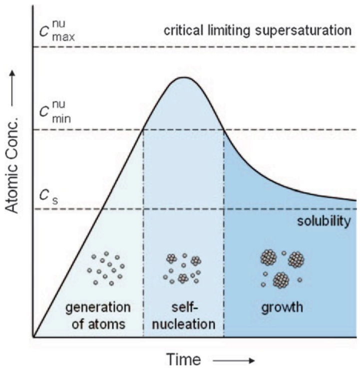

Figure III.1 - Representation of LaMer theory from Xia et al[27]

Monomers are generated upon decomposition. When the monomer concentration exceeded a given limit, the nucleation process occured with an amount of nuclei depending on the excess in monomer concentration by comparison with this concentration limit. The nucleation step decreased the monomer concentration below this concentration limit and if some monomers are always available, a grain growth is observed. The minimum radius of a stable nucleus that can grow spontaneously in the supersaturated solutions is inversely proportional to the supersaturation[2,28]. Indeed a large excess of monomer by comparison with the concentration limit leads to a burst of nucleation of nuclei, then there are less monomers available for the growth step and small NPs are obtained. If the monomer concentration is not elevated at the germination step, a small amount of nuclei formed, thus the growth step is favored and larger NPs are obtained.

A first question arised: what will drive the concentration in monomers upon decomposition ? With the oleate complex, which has been widely used[10,15,29–31], the nucleation step was reported to occur from monomers resulting from the dissociation of iron oleate[29]. Monomers, the minimum building units, of iron oxide nanocrystals, are supposed to be intermediate species such as polyironoxo clusters, which concentration increases as the reaction proceeds[31]. Baaziz *et al.* reported that the synthesis parameters affect the NPs nucleation and growth steps by modifying the stability of iron precursor (iron stearate) and thus the monomer formation[13]. The monomer formation was observed to be reaction time- and/or temperature-dependent and to vary mainly as a function of the nature of solvents and ligands. These observations showed that the monomer formation would strongly depend on the iron precursor stability. The influence of chemical/experimental conditions on the precursor stability was already evidenced by Bronstein *et al.*[30] who have underlined the effect of solvent and washing conditions on iron oleate precursor thermal behavior and thus on the nucleation and germination steps. This is confirmed also by the experimentally observed instability of iron oleate. Indeed iron oleate batches were observed not to be stable with time and from one batch to another batch, different sized/shaped NPs may be obtained which affect strongly the NPs synthesis reproducibility. For example, very nice nanocubes may be synthesized according to the Kovalenko’s method but we observed that several batches of *in house* synthesized iron oleate were necessary to obtain at least one leading to perfect nanocubes. Thus after these first experiments with iron oleate synthesized in the laboratory[10,15] and with regards to the low stability of this iron complex which is highly sensitive to the synthesis, washing and storage conditions[15,30], a commercial iron stearate complex has been used. A synthesis in standard conditions has been set and led to the reproducible synthesis of 10 nm NPs[32]. However the replacement of iron oleate by iron stearate in the synthesis conditions of nanocubes led to nanocubes but not so perfect and nice as those obtained with the good batch of iron oleate[15]. Considering a possible influence of impurities in commercial batches, we decided to synthesize our own iron stearate. It was shown to be more stable with time and to conduct to the reproducible synthesis of spherical NPs with a mean size of 10 nm. However again perfect nanocubes were difficult to obtain reproducibly. Thus we decided to investigate in depth the structure and thermal behaviors of iron (II &III) stearates. In addition, to the best of our knowledge, very few papers dealt with the influence of the iron precursor structure on the synthesis of NPs[30,33].

In this work, we will demonstrate how we have quite solved the “problems” of metal carboxylate based precursors by combining experimental and modeling studies. Both approaches demonstrated the important role of coordinated water in the chemical and thermal stabilities of iron carboxylate based precursors and how it has affected the nucleation and germination steps.

III.2 Experimental details

III.2.1 Precursor Synthesis

Iron stearate (II) and (III) were prepared by precipitation of sodium stearate and ferrous chloride or ferric chloride salts in an aqueous solution. Briefly, sodium stearate (9.8 g, 32 mmol) was transferred into a 2-necked round bottomed flask (RBF) and solubilized in distilled H_2O (dH_2O, 80 ml). The solution was heated to reflux and stirred for 30 min until complete dissolution of the stearate. Separately, $FeCl_2.4H_2O$ (3.16 g, 16 mmol) or $FeCl_3.6H_2O$ (2,88 g, 16 mmol) was dissolved in dH_2O (40 ml) and added onto the sodium stearate solution under vigorous stirring. A light orange precipitate was formed immediately. The solution was kept under stirring at this temperature 15 min. Thereafter, the solution was allowed to cool down to room temperature (RT). The obtained precipitate was washed once by centrifugation (hot dH_2O, 14000 rpm, 10 min). The product was then filtrated with a büchner funnel and oven dried at 65 °C for 24 h.

III.2.2 Standard synthesis of 10 nm sized NPs

Iron oxide nanospheres (NS) are synthesized by thermal decomposition of the as synthesized iron stearate in presence of oleic acid in dioctylether . The iron II stearate (1.38 g, 2.2 mmol) is mixed with OA (1.24 g, 4.4 mmol) in 20 ml of octylehter (OE) in a two neck RBF. The mixture is stirred and heated at 120 °C for 1 h without reflux condenser in order to dissolve the reactants and remove the water residues. The cooler is then connected to the flask and the solution is heated to the boiling temperature (≈ 290 °C) with heating rate of 5 °C/min and heated to reflux for 2h under air. After cooling to RT, a black suspension is obtained which is solubilized in 10 ml of chloroform. The NPs are then precipitated by the addition of an excess of acetone the first time and washed three times with chloroform and acetone at a ratio of 1:4 at 14000 rpm for 5 min by centrifugation. The NPs can finally be suspended in 50 ml of THF.

III.2.3 Standard synthesis of nanocubes

Iron oxide nanocubes (NC) are synthesized by thermal decomposition of the as synthesized iron stearate in presence of oleic acid and sodium oleate. 2.32 mmol of iron III stearate is mixed with 3 mmol of ligands (OA, 0.45 g 1.5 mmol and NaOl 0.45g, 1.5 mmol) in 15 mL octadecene (OD). The mixture is stirred and heated at 120 °C for 60 min without reflux condenser in order to dissolve the reactants and remove the water residues. The cooler is then connected to the flask and the solution is heated up to 200 °C for 10 min with a heating rate of 5 °C/min. The solution is then heated up to 315 °C with a heating rate of 1 °C/min and refluxed for 60 min under air. After cooling to RT, a black and viscous suspension is obtained and is treated as previously. The NPs can finally be suspended in 50 ml of THF.

III.2.4 Determination of the synthesis yield

After the synthesis, the NPs are washed once as described above. The supernatant is collected and the NPs are solubilized in 5 mL chloroform. Both solutions (200 µL for the NPs and 3 ml for the supernatant) are then digested for 48 h at room temperature with 220 µL of concentrated HNO_3. The iron solutions are then diluted to 10 mL in deionized water. The concentration is then measured on a Perkin Elmer AAS spectrometer.

III.2.5 Other characterization techniques

IR in temperature.
IR samples were prepared using dry potassium bromide (KBr). A precise mass of precalcined sample is mixed in a mortar at 3wt% with KBr. This dilution prevents saturation of signals. The powder sample is next placed in the IR reaction chamber. The chamber is closed and helium or air is introduced (5mL/min). A ramp of temperature of 2°C/min is applied until the temperature reach 140°C and the sample is conserved at this temperature during all the processus evolution (2-3 days).

^{57}Fe Mössbauer spectra were performed at 300 K and 77 K using a conventional constant acceleration transmission spectrometer with a ^{57}Co(Rh) source and a bath cryostat where the sample chamber is under He atmosphere. Further spectra have been obtained using a homemade cryofurnace where sample is maintained under vacuum, whatever the temperature ranged from 77K up to 400°C. The spectra were fitted by means of the MOSFIT program[34] involving asymmetrical and lines with lorentzian profiles and a α–Fe foil was used as the calibration sample. The values of isomer shift are quoted relative to that of α-Fe at 300 K.

Electronic paramagnetic resonance (EPR): X-band EPR spectra were recorded with a continuous-wave ESP-300-E spectrometer (Bruker Biospin GmbH, Germany). The resonator is a Bruker ER 4102ST standard rectangular cavity operating in the TE_{108} mode equipped with an ESR900 Oxford cryostat ($\nu \sim 9.3$ GHz in X-band). Temperature was measured with a Cernox sensor (accuracy: $\Delta T/T \sim 5\%$).

The spectrometer was tuned so as the settings (modulation coils, incident microwave power) do not distort the EPR signal.

III.3. RESULTS

III.3.1 Synthesis of spherical and cubic shaped iron oxide nanoparticles from iron stearate precursors

Iron oleate as precursor for the synthesis of iron oxide NPs (IONPs) by thermal decomposition is mainly synthesized by mixing a suspension of hexahydrated iron (III) chloride in water with a suspension of sodium oleate in organic solvent which lead to iron oleate precursor in the organic solvent[10]. Due to the effect of washing and drying conditions on the iron oleate stability that we have observed in earlier studies[13,15] and the influence of washing solvent, ageing and storage reported by Bronstein et al[30], among published synthesis methods of metal carboxylates[35,36], a simple, scalable and "green" approach involving "just" a co-precipitation of the iron stearate in water was chosen. As the commercial iron stearate that we used at first, was "sold" as an iron II stearate and that iron oleates are synthesized under iron (III) oleates, both iron II and iron III stearates were synthesized by this co-precipitation method.

Considering the influence of solvent and drying conditions on the decomposition of the iron oleate in earlier studies, and the reported difficulties to obtain anhydrous stearate[35], the dehydration of both iron stearates was also investigated. The thermogravimetric analysis (TGA) curves of both hydrated stearates named $FeSt_2$ and $FeSt_3$ (Figure III.2) displayed similar shapes with a first small weight loss below 200°C attributed to dehydratation of powders and a second large weight loss above 200°C attributed to the decomposition of stearates[2,29,37]. The TGA curves (Figure III.2) are similar to that reported for iron oleate[2,13,31]. Based on infrared spectroscopy and TG/DSC analyses, it was earlier inferred by Heyon and al. that, in the first step above 200°C, one oleate ligand dissociated from the iron oleate precursor in the temperature range of 200–240°C and the other two oleate moieties dissociated at ∼300◦C following a CO_2 elimination pathway[31].

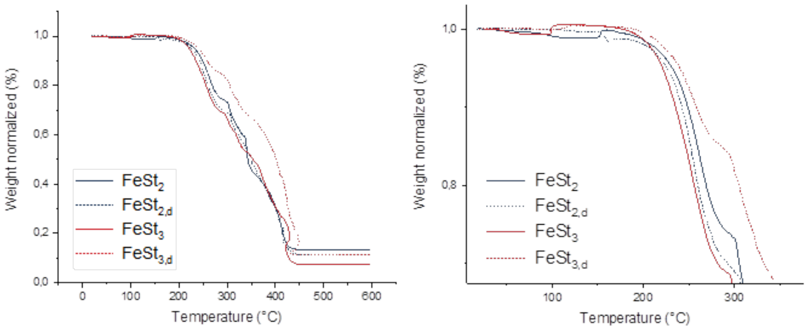

Figure III.2 - TGA curves of hydrated (plain line) and dehydrated (doted line) $FeSt_2$ (blue) and $FeSt_3$(red) *iron stearates (left) and enlargement on the region 0-350°C (right)*

From TGA curves of both iron stearates and from dehydration experiments at different temperatures by checking the IR spectra of iron stearates at each step, a dehydration treatment has been established at 140°C for 48h. Dehydration experiments are generally conducted by heating powders up to 200°C but heating treatments above 140°C or too long at 140°C have been shown to induce not only dehydration but also to affect the iron stearate (FeSt) structure. This treatment led to a mean weight loss of 20 and 12 % for $FeSt_3$ and $FeSt_2$ respectively. The dehydrated powders are named $FeSt_{2,d}$ and $FeSt_{3,d}$.

All iron stearates were then tested in standard conditions leading to the reproducible synthesis of 10 nm NPs (thermal decomposition of the commercial iron II stearate in presence of oleic acid in octylether[13]). Iron oxide NPs with a spherical shape were reproducibly synthesized with all stearates and representative TEM images of the different syntheses are given in Figure III.3. The mean NPs size with $FeSt_3$ whatever its hydration state is slightly smaller than that obtained with $FeSt_2$ (Table III.1).

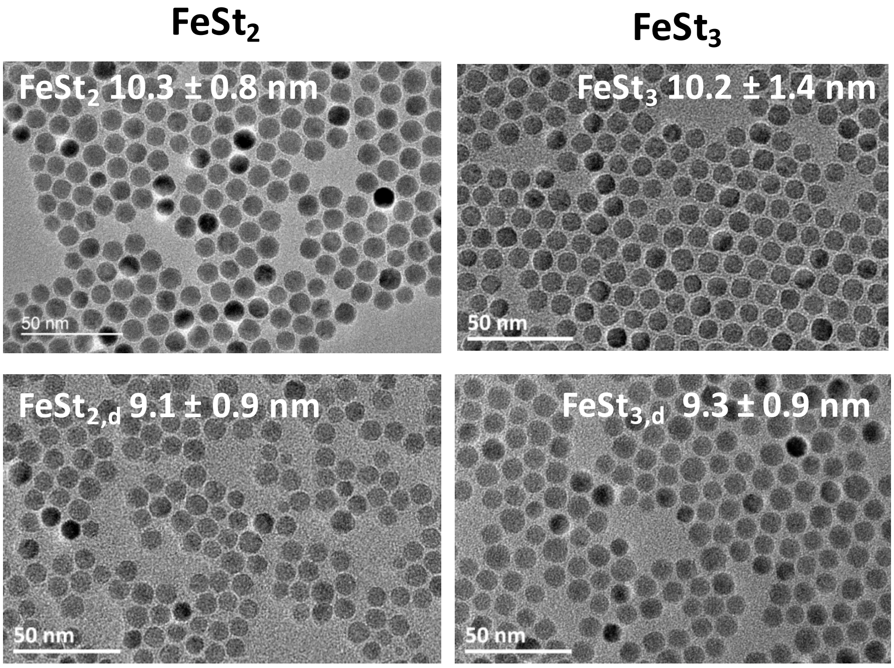

Figure III.3 - Standard synthesis of 10 nm sized NPs with iron II (a) and III (b) stearates and dehydrated iron II (c) and III (d) stearates

The nature of the iron stearate has also an influence on the synthesis yield. The NPs yield is higher with iron II than with iron III stearate and the dehydration step allowed enhancing this yield (Table III.1).

The effect of dehydration on the yield was also confirmed by a two step synthesis process with FeSt: the NPs synthesis at ~ 290°C was performed once and after cooling down to room temperature, the synthesis step was reproduced again. During the second synthesis step, the remaining precursors may contribute to the growth of NP synthesized during the first step. From Figure III.4 and Table III.1, a clear correlation is noticed between the mean size of NPs after this two synthesis steps process and the yields. An increase of the NPs mean size after the two-step process is observed with $FeSt_2$ (low yield) by comparison with dehydrated $FeSt_2$ (higher yield). That suggests that all iron precursors were not decomposed during the first synthesis step up to ~ 290°C with $FeSt_2$ by comparison with the dehydrated one. With $FeSt_3$, a slight size increase is observed with dehydrated $FeSt_3$ but there is quite no NPs size variation. These results by considering also the synthesis yield suggested that most of $FeSt_2$ precursors were decomposed in this synthesis condition at ~290 °C and that all $FeSt_3$ precursors were not decomposed at 290°C. With $FeSt_3$, some other $FeSt_3$ based precursors should be present in the reaction mixture and decomposed only above 290°C when most of $FeSt_2$ based precursors decomposed below 290°C. We would like to note that after the first synthesis step in the two steps synthesis process, the NPs are smaller than after only one synthesis step. We have also observed such smaller size during a seed mediated growth process to growth a CoO layer at the surface of IONPs[38,39]. We supposed that some growth occured during the cooling stage.

Table III.1 - TEM mean size and yield for nanoparticles synthesized in standard synthesis conditions of 10 nm sized NPs and shape and TEM mean size for nanoparticles synthesized in standard conditions of nanocubes as a function of the nature of stearates

		$FeSt_2$	$FeSt_{2,d}$	$FeSt_3$	$FeSt_{3,d}$
Standard 10 nm synthesis	*TEM mean size (nm)*	10.3 ± 0.8	10.2 ± 0.9	9.1 ± 0.9	9.3 ± 0.9
	Yield (%)	90	94	83	85
	Two synthesis steps (nm)	9.6 ± 1.2 11 ± 1.1	9.5 ± 0.9 9.2 ± 1.1	8.4 ± 0.4 8.3 ± 1.2	8.3 ± 1 8.8 ± 1
Standard nanocubes synthesis	*Shape*	Not defined shape	Quite cubic	Not defined shape	Quite cubic
	TEM mean size (nm)	13.5 ± 1.8*		11.4 ± 1.8*	15.9 ± 1.8

These first experiments demonstrated that $FeSt_2$ seems to "better" decompose below 290°C than $FeSt_3$ and that the dehydration favors the decomposition of stearates below 290°C. It would also explain the lower mean size of NPs synthesized with $FeSt_3$: the amount of produced monomer is lower and thus the nucleation and grain growth are more limited. A this point, assuming that $FeSt_3$ would have one stearate more than $FeSt_2$, after the nucleation step which is reported to occur in the same temperature range between 200-240°C by loss of one stearate chain, the further decomposition of $FeSt_2$ is easier than that of $FeSt_3$ which would bear one more stearate chain. The lower yield with $FeSt_3$ may be thus related to the decomposition kinetics which would be faster with $FeSt_2$ than with $FeSt_3$.

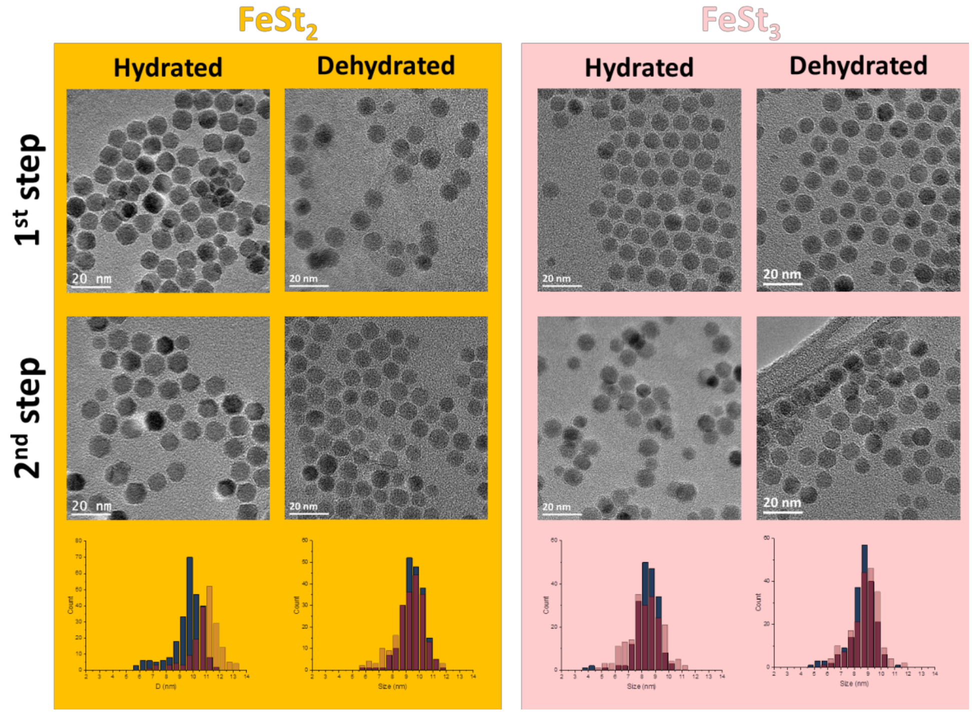

Figure III.4 - TEM images of NPs after the two step synthesis process as a function of the nature of stearates (Top : iron II stearate after one (left) and two (middle) synthesis steps and the corresponding size distribution; dehydrated iron II stearate).

The standard synthesis conditions of iron oxide nanocubes[15], which were shown to conduct to very nice nanocubes (when the iron oleate batch was considered as "optimal"), were also tested with these iron stearates. As observed in Figure III.5, without dehydration, the cubic morphology can not be obtained. Nicer nanocubes were synthesized with dehydrated iron stearates. By further optimizing the amount of sodium oleate and the heating rate, nanocubes as perfect as those obtained with iron oleate in optimal conditions were obtained (cf. Chapter VII). Thus the hydration of FeSt precursor appeared as very important to control the shape of NPs. This is in agreement with our empirical experimental observation that the dehydration time of iron oleate on $MgSO_4$ was one parameter crucial to obtain iron oleate precursor suitable for the nanocube synthesis[40].

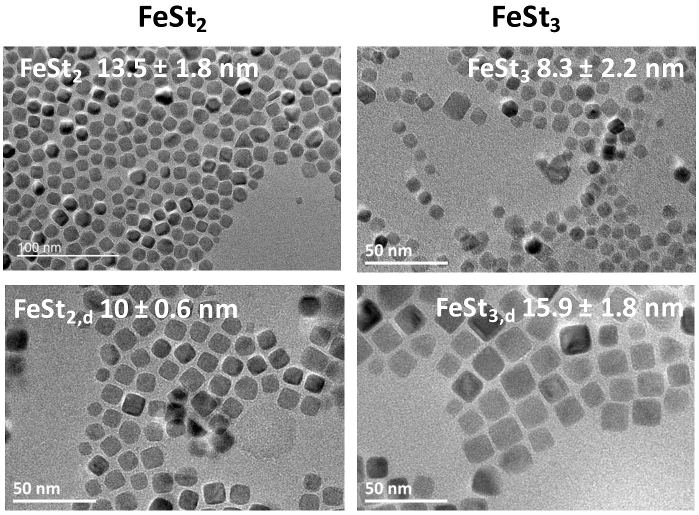

Figure III.5 - Standard synthesis of cubic shaped NPs with iron II (a) and III (b) stearates and dehydrated iron II (c) and III (d) stearates

As the iron oleate precursor was observed to be altered with ageing and storage conditions, the stability of $FeSt_2$ has been investigated as a function of ageing time. $FeSt_2$ has been stored in a vial in a desiccator under air. Then it has been decomposed in a standard synthesis of 10 nm NPs at different ageing times. The NPs size was found to be similar after one month but after six months the mean size decreased by 1 nm and by 1.5 nm finally after one year (Table III.2). The ageing time of the stearate has then a slight influence on the size of the NPs. Nevertheless, the storing conditions were not strict; a storing under vacuum or inert gas should allow a longer storage quality of the precursor. Still up to one month, simple storage conditions can be used.

Table III.2 - Mean size of NPs synthesized each month for one year with the same $FeSt_2$ stored up to 12 months.

Months	0	1	6	12
Mean size (nm)	9.7 ± 0.85	9,6 ± 0.9	8,5 ± 1.0	8.2± 1.1

The synthesis of 10 nm NPs and nanocubes by thermal decomposition of hydrated and dehydrated $FeSt_2$ and $FeSt_3$ has allowed evidencing the influence of the nature of the iron stearate and of its hydration state on the NPs yield and thus size and their shape. These results afforded understanding that nanocubes were not synthesized with iron stearates because they were more hydrated whatever their synthesis conditions (co-precipitation in water or biphasic synthesis) than the iron oleate obtained mainly by biphasic approach. Furthermore, iron oleate is generally obtained as an oily product when iron stearates are under the form of powder.

These results also demonstrated that from the point of view of the synthesis of precursor at low price, $FeSt_2$ may be used for the standard synthesis of 10 nm NPs. For a tuning of the shape, dehydrated iron stearates appear more suitable leading to more defined nanocubes and the cubic shape with iron III stearate appeared more defined than iron II stearate. That may be related to the fact that iron III stearate beard more chelating ligands than iron II stearate contributing thus to the cubic growth.

To better understand the differences between stearates and the effect of the hydration state, all stearates have been characterized and their thermal behavior studied by combining experimental and modeling approaches.

III.3.2. Characterisation and structure of iron stearates

A lot of papers dealt with the structure/composition of Zn or Cr stearates or acetates but few papers dealt with pure iron stearates[41] and even iron oleate. The structure of iron stearates has been mainly investigated by Abrahamson and al[41] while Nakamoto and al[42] studied its interaction and solvation with pyridine. The structure of $FeSt_2$ is often described with one iron II cation coordinated with two stearate molecules (Figure III.6) but the possible oxidation of iron II and the hydration should modify the structure of the complex. Some mixed-valence trinuclear iron carboxylate complexes, $[Fe^{III}_2Fe^{II}O(O_2CR)_6L_3]$ were proposed and the solvation would lead for acetate to $[Fe_3O(O_2CCH_3)_6L_3]St$.[42] Abrahamson et al. reported that commercial $FeSt_2$ was a mixed valence compound (μ-oxo trimer) $[Fe^{III}_2Fe^{II}O(St)_6(H_2O)_3]$ in agreement with Nakamoto and al. For FeSt3, Abrahamson et al reported that the commercial product consisted in a mixture of stearic acid and a trinuclear FeIII cluster (trimer) and proposed the following μ-oxo trimer : $[Fe_3O(St)_6(H_2O)_3][St]$ with $St=C_{18}H_{35}O_2$.

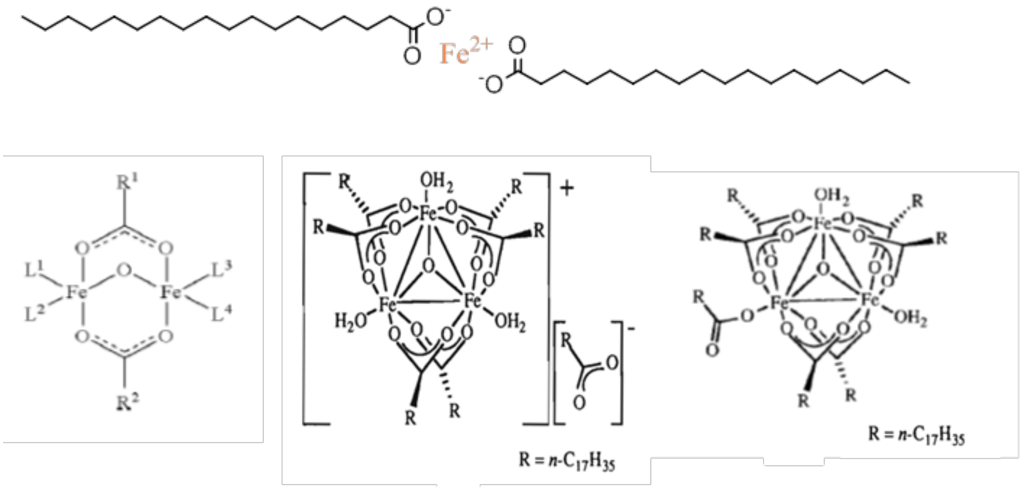

Figure III.6 - Published structures of iron stearates[41].

Consequently, we have investigated the structure of the stearates by analyzing their oxidation degree, the coordination of carboxylate with iron cations, the lamellar structure, the elemental analysis and finally the dehydration steps by TGA and IR.

III.3.2.1. Oxidation degree of iron cations

III.3.2.1.1 Mössbauer spectroscopy

Mössbauer spectra of $FeSt_3$ and $FeSt_2$ before and after dehydration at 300 and 77K are compared in Figure III.7. The spectra are better resolved at 77K than at 298 K (see relative transmission scale) that may be attributed to the molecular structure of stearates which is not so rigid at 300K but becomes when cooled down. In addition one observed clearly some broadened and symmetrical quadrupolar features at 77K while some asymmetry clearly occured at 300K. The refined values of Mössbauer parameters at 77K are summarized in Table III.3. The spectra at 77K are quite similar and can be described by at least two quadrupole split doublets (three for $FeSt_{2,d}$ to get better resolution) characteristic of Fe III cations in high spin state in all cases. The Mössbauer spectrum of $FeSt_2$ at 300K suggested the presence of Fe(+II) but its contribution is surprisingly not visible at 77K: it could be attributed to some reduction of the sample with ageing, since experiments have been done shortly after their preparation. The present results indicated that all stearates are constituted of only Fe(+III) ions with mainly two different molecular environments (except for $FeSt_{2,d}$). This oxidation degree was expected for dehydrated stearates due to the heat treatment under air while the presence of mainly Fe(+III) cation is not surprising as all $FeSt_x$ were synthesized under air. As the commercial iron stearate that we were using in our earlier syntheses was sold as a Fe(+II) stearate, its Mössbauer spectra has been recorded and the oxidation degree was determined to be also unambiguously III.

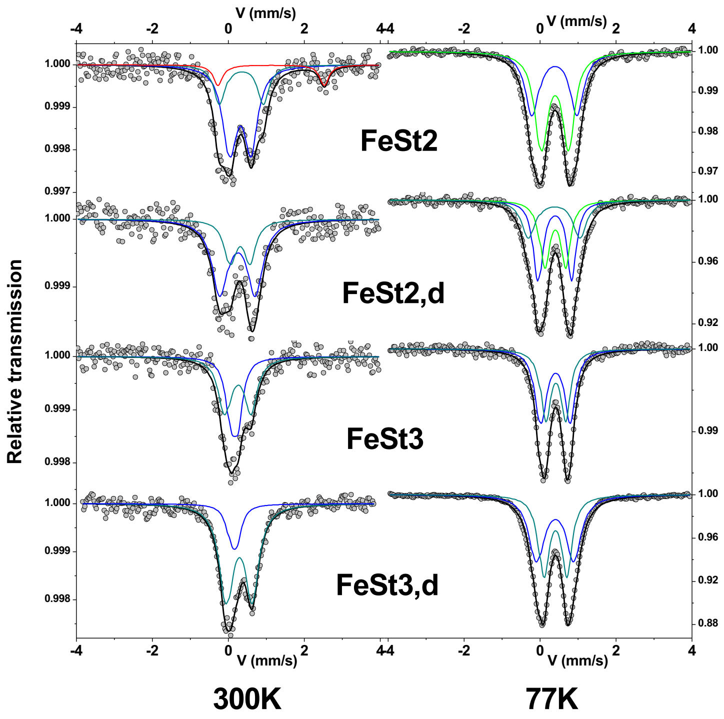

Figure III.7 - Mössbauer spectra at 300 and 77 K of iron stearates before and after dehydration

Table III.3 - Mössbauer parameters (IS: isomer shift; QS: quadrupole splitting Area: proportions assuming that they are proportional to their respective absorption areas).

T(K)	FeSt$_2$			FeSt$_{2,d}$		
	IS (mm.s^{-1}) ±0.01	QS (mm.s^{-1}) ±0.02	Area % ±2	IS (mm.s^{-1}) ±0.01	QS (mm.s^{-1}) ±0.02	Area % ±2
77K / 77K under vacuum	0.50 / 0.50	1.15 / 1.07	42 / 48	0.49 / 0.50	1.16 / 1.06	36 / 52
	0.51 / 0.50	0.70 / 0.64	58 / 52	0.51 / 0.51	0.70 / 0.66	64 / 48
77K / 77K under vacuum	0.52 / 0.53	0.76 / 0.71	55 / 56	0.52	0.96	54
	0.53 / 0.51	0.52 / 0.50	45 / 44	0.53	0.60	46

For each stearate, Fe^{3+} species with mainly two different environments are observed. For FeSt$_2$ and FeSt$_{2,d}$, both environments are similar and only their proportions varied after dehydration (Table III.3). The water molecules should contribute mainly to one of the environment or are less strongly bounded to Fe(+III) in this environment and the dehydration induced an increase of the proportion of this environment (QS = 0.7 mm.s^{-1}).

One may notice that both Mössbauer spectra of FeSt$_2$ and FeSt$_{2,d}$ recorded at 77K under vacuum displayed also very similar Mössbauer parameters and proportions. By comparison with samples at 77K without vacuum treatment, the QS values have both slightly decreased. That may suggest a low hydration degree of Fe(+II) stearates or that the water molecules are not strongly involved/bounded in the chemical structure of iron II stearates.

By contrast, both environments in FeSt$_3$ and FeSt$_{3,d}$ are different: only the QS values increased after dehydration without variation of their proportion which suggested just an effect of dehydration on these environments. Both Fe(+III) environments in $FeSt_3$ would involve water molecules more strongly bounded than in $FeSt_2$. The weak/small variation of Mössbauer parameters of $FeSt_3$ after a vacuum treatment supported this conclusion.

III.3.2.1.2 Electronic paramagnetic resonance

EPR measurements have been performed and analyzed by Dr Nathlie Parizel at the institute of chemistry of Strasbourg.

Figure III.8 shows the X-band EPR spectrum of powder sample of FeSt2 recorded at 6 K with an intense signal at g = 2.03 and a weak signal at very low field around g = 31 (black arrow).

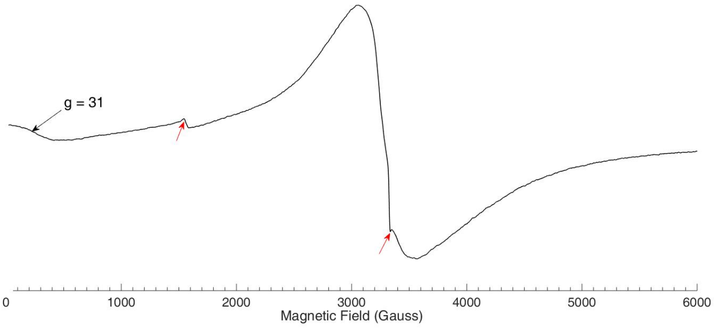

Figure III.8- X-band EPR spectrum of powder sample of $FeSt_2$ recorded at 6 K

The signal at $g_{\mathrm{eff}} \approx 31$ most likely originated from a high-spin (S=2) Fe^{II} species. Such integer spin systems (namely non-Kramers system) are expected to be EPR silent at conventional fields and frequencies (X-band, 9.31 GHz). However, in some cases of low symmetry (from axial to rhombic), transitions involving $|\Delta M_S| > 1$ (formally EPR forbidden) may become partially "EPR allowed". Such an opportunity is attributed to a spread in zero-field-splitting (ZFS) values[43–46]. The signal around g = 2 is associated with the low-spin state (S = 1/2) of Fe^{III} complexes in the rhombic symmetry crystal field. This type of signal may be described by a rhombic spin Hamiltonian including only the Zeeman interaction:

$$H = \mu_B\left(g_x B_x S_x + g_y B_y S_y + g_z B_z S_z\right)$$

The peak-to-peak line width is ΔB = 510 G and that is the result of the multiple orientations into the powder sample. The small signals at 1546 G and 3334 G (red arrows) are due to impurities coming from the cryostat and appeared here due to low level of the entire EPR signal.

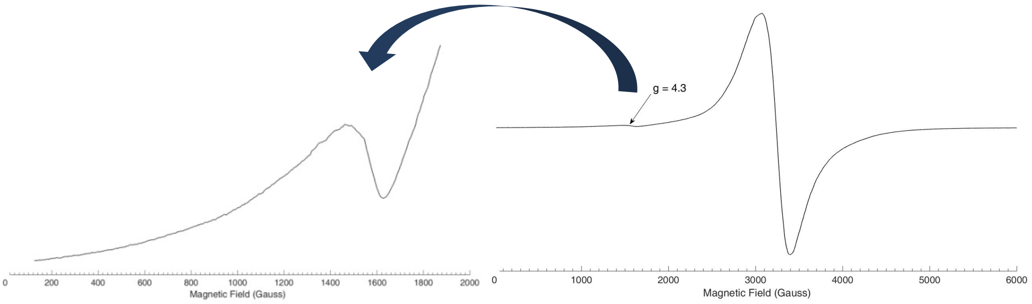

Figure III.9 - Right: X-band EPR spectrum of the powder sample of FeSt3 recorded at 6 K – left: enlargement around g = 4.3.

The spectrum of $FeSt_3$ (Figure III.9) exhibited two signals, one around g = 2 and a smaller one at g = 4.3. As previously, the first is associated with the low-spin (S = 1/2) state of Fe^{III} ion and the peak-to-peak line width is ΔB = 340 G. The last signal with g = 4.3 implied the presence in the examined compound of the high-spin (S = 5/2) ferric species in the rhombic symmetry crystal field. In this system, the ground state is split into three Kramers' doublets due to spin-orbit mixing with the excited states. These doublets are split by an applied magnetic field and the near isotropic g-factor of 4.3 is assigned to a transition within one of them. The spin Hamiltonian for a paramagnetic ion with S = 5/2 may be written as:

$$H = D\left\{S_z^2 - \frac{1}{3}S(S+1)\right\} + (E/D)\left(S_x^2 - S_y^2\right) + \frac{1}{D}\beta\, H.g.S$$

with $S^2 = S_x^2 + S_y^2 + S_z^2$; D and E are the ZFS parameters.

When $\lambda = {}^{E}/_{D} = 0.33$, it corresponds to the rhombic symmetry and, $g_{eff} = g_x = g_y = g_z = 4.3$ This signal is observed in Fe^{III} doped disordered media and it is generally assigned to Fe^{III} in a weak crystal field environment[47,48].

The X-band EPR spectra of the powder samples of $FeSt_{2,d}$ and $FeSt_{3,d}$, Figures III.10 and 11 respectively, looked very similar. For both compounds, EPR spectra contained the signatures of two particular high-spin species of Fe^{III} ion. One of them is a signal already encountered at g = 4.3 in the powder sample of $FeSt_3$ and associated with a high-spin (S = 5/2) in a rhombic symmetry. The other is made up of a low-field signal with g-factor near 6, corresponding to $g_{\perp eff}$ and a group lines around g = 2 associated to its $g_{\parallel eff}$ value. These special components of g are characteristic of a high-spin Fe^{III} ion into an axial symmetry ($\lambda = 0$).

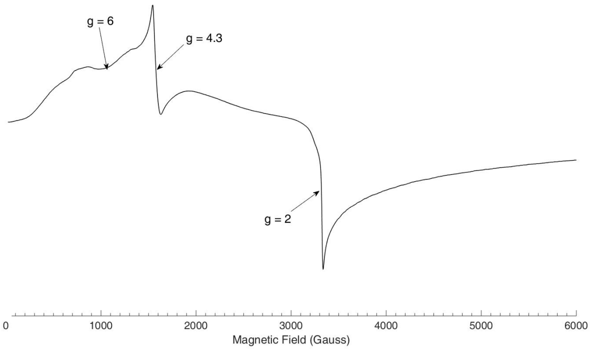

Figure III.10 - X-band EPR spectrum of the powder sample of $FeSt_{2,d}$ recorded at 6 K

In Figure III.11, the sharp peak at g = 2 that is surimposed onto the parallel component of the signal of the HS Fe^{III} ion is probably arising from a non-ferric radical impurity located, for example, on a pendant chain.

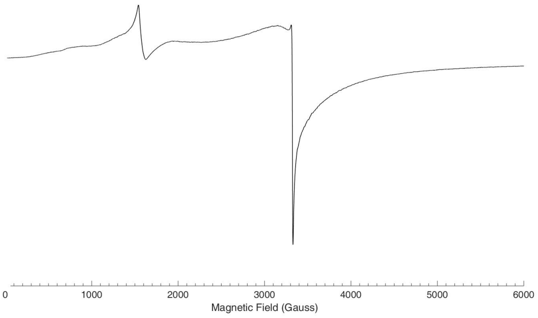

Figure III.11 - X-band EPR spectrum of the powder sample of $FeSt_{3,d}$ recorded at 6 K

Table III.4 – Summary of EPR results

	$FeSt_2$	$FeSt_3$
Hydrated	HS (S = 2) Fe^{II} LS (S = 1/2) Fe^{III}	HS (S = 5/2) Fe^{III} LS (S = 1/2) Fe^{III}
Dehydrated	HS (S = 5/2) Fe^{III} axial symmetry HS (S = 5/2) Fe^{III} rhombic symmetry	HS (S = 5/2) Fe^{III} axial symmetry HS (S = 5/2) Fe^{III} rhombic symmetry

III.3.2.1.3 Conclusion

Both EPR and Mössbauer spectroscopies evidenced the presence of small amount of Fe^{2+} in $FeSt_2$ but otherwise all stearates exhibit Fe^{3+} with two different environments and those of dehydrated iron stearates would be very close.

III.3.2.2 Carboxylate coordination in iron stearates

III.3.2.2.1 IR spectroscopy

Infrared spectroscopy is a powerful technique to identify the structural elements of molecules but it can also give precious information on the structure that the molecule is adopting. The IR spectra of different iron stearates have been realized on a powder in ATR mode and are given in Figure III.12 and IR peaks are listed in table III.5. The analysis of alkyl chain bands allowed determining their organisation and that of the carboxylate bands gave precious information on the anchoring on the metal center. One IR spectra with indexation of all bands is given in Figure III.13.

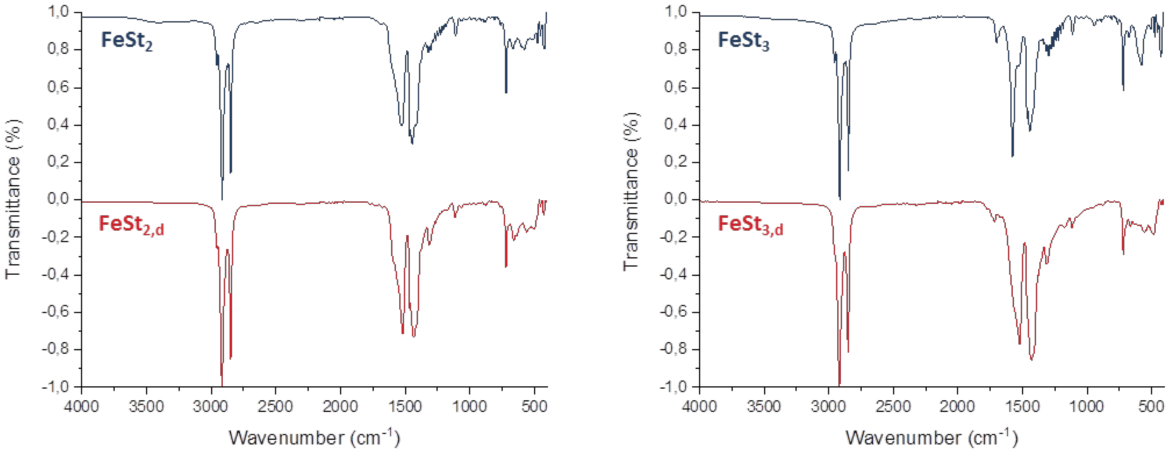

Figure III.12 - IR spectra of all iron stearates

In all IR spectra, alkyls bands are located in the high frequency region of 3000-2800 cm^{-1}. They are attributed to the symmetrical (ν_s) and asymmetrical (ν_{as}) stretching of CH_3 and CH_2 and will be discussed below in the text. In the 3800-3000 cm^{-1} range, the broad vibration band between 3600 and 3200 cm^{-1} is assigned to the OH stretching vibrations of water molecules (physisorbed molecular water) and their bending mode exhibited a band at about 1621 cm^{-1}. Another important region of interest concerned the carboxylate bands. Carboxylates presented an asymmetric stretching singlet $\nu C=O$ around 1700cm^{-1}[17,18]. When coordinated to metal ions, this carboxylate band is split into a doublet of the antisymmetric COO^- band ($\nu_{as}COO$) and the associated symmetric band (ν_sCOO). The deprotonated carboxylate group can coordinate according to several modes on the metal center as depicted in Figure III.14. The wavenumbers of these bands are highly sensitive to the structure of the carboxylate group, the nature of solvent, the nature of the ligands and the nature of the metal ion.

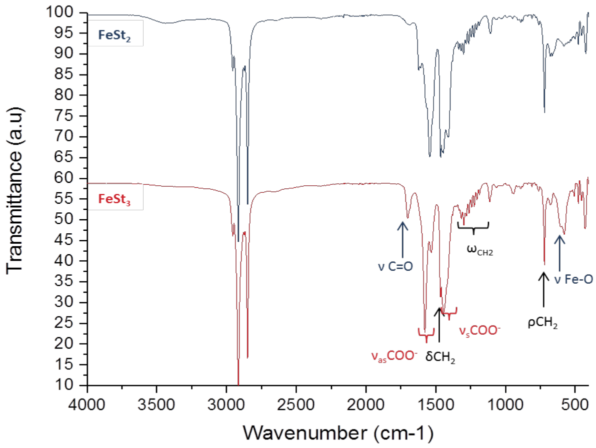

Figure III.13 - IR spectrum of iron stearate with indexation of main IR bands

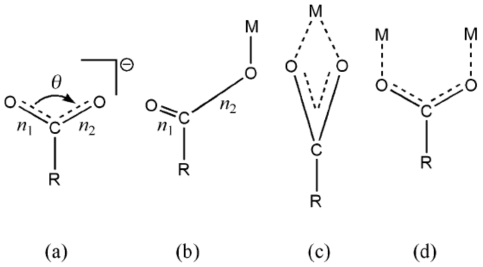

Figure III.14 - Bonding geometries and naming conventions for metal carboxylate complexes. a) Free anion in aqueous solution, where n1 and n2 are approximately equal. b) Monodentate bonding where one oxygen atom is bonded to the metal cation: n1 is the C-O bond length of the unbound oxygen (shorter) and n2 is the C-O bond length of the oxygen bonded to the metal cation (longer). c) Chelate bidentate, where one metal cation is bonded to both oxygen atoms. d) Bidentate bridging, where one metal cation is bonded to each oxygen atom[49].

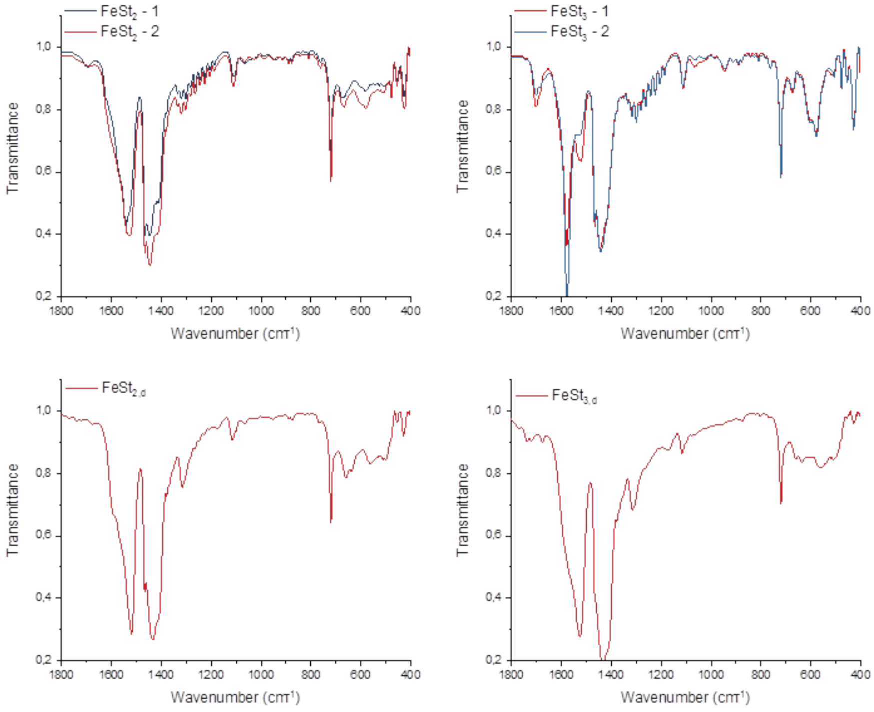

Figure III.15 - Superposition of IR spectra of FeSt from different batches in the region 1800-400 cm^{-1}

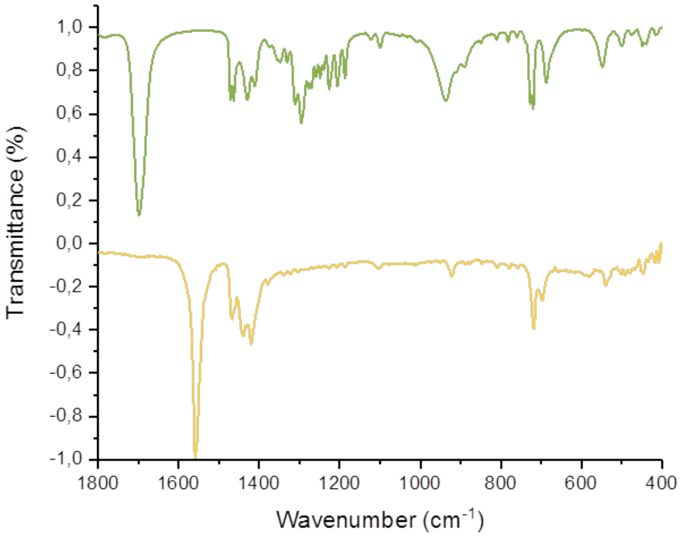

Figure III.16 - IR spectra of stearic acid (green) and sodium stearate (yellow)

The coordination mode of the carboxylate group can be determined from consideration of the antisymmetric band (ν_{as}COO) and symmetric band (ν_sCOO) in IR spectra as it will influence the difference of frequency $\Delta\nu$ with $\Delta\nu = \nu_{as}COO - \nu_sCOO$[50,51]. Beside the ionic coordination, three main coordinations are commonly observed : monodentate, bridging bidentate and chelate bidentate[50–53]. To establish the carboxyl coordination, two main approaches have been published. The ν_{as}COO and ν_sCOO bands are located at different wavenumbers relative to values for the free carboxylate ion, usually taken as those of the sodium or potatium salts[52–55]. It has thus been reported that $\Delta\nu_{chelating} < \Delta\nu_{bridging} < \Delta\nu_{ionic} < \Delta\nu_{monodentate}$[52]. Another trend for both stretching frequencies and/or band separation values $\Delta\nu$ has been also outlined as: uncoordinated acid > unidentate coordination > bidentate (bridging>chelating) coordination > free carboxylate ion[53]. In another paper on calcium stearate/oleate, the following ranking has been proposed: $\nu_{unidentate\cdot} > \nu_{bridging\cdot} > \nu_{bidentate}$[55].One may notice here a discrepancy about the free carboxylate ionic coordination.

However most of time, only the $\Delta\nu$ value is considered and compared with published range of values. In the monodentate mode, $\Delta\nu$ would be then in the range 200-400 cm^{-1} [56]. $\Delta\nu$ for bridging bidentate is observed in the 140-170 cm^{-1} range and that of chelate bidentate between 40 and 100 cm^{-1}. In-between 100 and 140 cm^{-1}, a mixed coordination, chelate/bridging, is expected as already observed for neodymium butyrate[57]. The ν_{as}COO band is generally between 1510-1650 cm^{-1} and the ν_sCOO band between 1360-1450 cm^{-1}.

Table III.5 - IR bands in the 1800-1400 cm^{-1} range of the stearates, NaSt and HSt.

HSt	NaSt	FeSt2	FeSt2,d	FeSt3	FeSt3,d	Proposed assignments
1700 vs		1700 vw	-	1700 w	1700 vw	$\nu C=O$
		1620 w	1620 vw	1620 w	1620 vw	Water
	1558 vs	1578 m	1578 m	1578 s	1578 m	$\nu_{as}COO^-$
		1527 s	1527 s	1527 m	1527 s	
1470-1462 m	1467	1462 s	1462 s	1462 s	1462 m	δCH_2
1429 s	1441 s	1443 s	1440 s	1443 s	1430 s	ν_sCOO^-
1410	1419 s	1410 s	1410 s	1410 s	1410 s	

Table III.6 – Δv calculated for HSt, NaSt and the four FeSt

	monodentate	bridging	mixed	Chelating
NaSt			117, 139	
HSt	271, 290			
$FeSt_2$ **$FeSt_{2,d}$**		168 m 168 m		84 s 84 s
$FeSt_3$ **$FeSt_{3,d}$**		168 s 168 m		84 s 97 s

IR spectra of all stearates displayed similar carboxyl bands : two $ν_{as}$COO bands and two $ν_s$COO with different intensities as a function of the nature of stearates (Table III.5). The presence of weak band at 1700 cm^{-1}, in particular for $FeSt_3$, suggested the presence of very small amount of free stearic acid which tended to disappear after the dehydration step or the presence of a monodentate compound. Similarly, the weak band at 1620 cm^{-1} is only more or less clearly observed when the broad band between 3500-3000 cm^{-1} is visible. Otherwise the foot of the peak, where carboxyl bands are present, is quite large at this position and may include this small contribution. As in IR spectra of naked oxides, a broad vibration band between 3600 and 3200 cm^{-1} and the band at 1621 cm^{-1} are assigned to the OH stretching vibrations of water molecules (physisorbed molecular water) and to their bending mode respectively, this band has been attributed to the bending mode of water molecules.

Our main difficulty is the assignment of the carboxylate bands as for all iron stearates, several $ν_{as}$COO and $ν_s$COO are observed (Figure III.12 and Table III.5). At first, we decided to consider the IR spectra of stearic acid (HSt) and sodium stearate (NaSt) and to compare them to those of iron stearates (Figure III.16 and Table III.5).

The IR spectra of HSt displayed carboxyl bands (1700, 1429, 1410 cm^{-1}) similar to those reported by Abrahamson et Lukaski[41]. The intense peak at 1700 cm^{-1} is assigned to $\nu_{C=O}$ and peaks at 1429 and 1410 cm^{-1} are assigned to group C-O-H stretches.The IR spectra of the commercial sodium stearate (NaSt) is given in Figure III.16 . One may notice that this compound displayed a lamellar structure (wagging bands in the range 1350-1200 cm^{-1}). The absence of the hydroxyl vibration in the region of 3300–3500 cm^{-1} and the replacement of the carbonyl (C=O) stretching band, at ca. 1700 cm^{-1}, by carboxyl asymmetric (νasCOO) and symmetric (νsCOO) stretching vibrations indicated that NaSt is anhydrous and free of an excess of carboxylic acid. The presence of the carboxyl bands confirmed a complete resonance in the COO moieties as a result of coordination with the metal. The position of the carboxylate bands is given in Table III.5 and three carboxyl bands are indexed. There is a strong band $ν_{as}$COO band at 1558 cm^{-1} as expected and already identified in sodium alkanoates with different length of alkyl chains[58]. The presence of two symmetric stretching frequencies meant that the $ν_s$COO band was split and indicated extensive head group intermolecular interactions. Both $ν_s$COO bands led to Δν values (Table III.6) corresponding to a mix of bridging and chelating coordination which may be related to the observed lamellar structure.

Considering FeSt IR spectra, the carboxyl band positions are compared to those of NaSt which is considered often as the ionic carboxylate; a larger splitting of the stretching frequencies is often an indication of monodentate coordination: the $ν_{as}$COO increased when the $ν_s$COO decreased due to the breakdown in equality of the carbonyl group. The asymmetric and symmetric vibrational frequencies in the monodentate carboxylate are closer to the vibrations of C=O (~1700 cm^{-1}) and C–O (~1400 cm^{-1}) in the carboxylic acid form. In our case, a weak asymmetric band at 1700 cm^{-1} is observed and could be attributed either to monodentate or free stearic acid.

For the chelating configuration, the carboxylate group has the same group symmetry as in the free ionic state. Therefore, a decrease in ν_{as}COO and an increase in ν_{s}COO frequencies are generally expected (relative to those of carboxylate in the monodentate coordination state). Thus the bands at 1527 and 1443 cm^{-1} are attributed to the presence of a chelating coordination in agreement with the calculated $\Delta\nu$ value. An asymmetrical vibration of 1550 cm^{-1} and symmetrical vibration at 1456 cm^{-1} ($\Delta\nu$ = 94 cm^{-1}) have been reported for the bidentate carboxylate, $Zn(O_2CCH_3)_2.2H_2O$[54,55].

The bridging coordination of carboxylate has similarity to the unidentate coordination because in the bridging coordination only one oxygen coordinates to one particular cation. But the group symmetry in the bridging coordination state is similar to that in the chelate coordination. However the chelate coordination of carboxylate caused the OCO angle to decrease in comparison to those of the free ionic form and the bridging coordination. Therefore, relatively higher band positions (in wavenumbers) may be expected for the carboxylate vibration in the bridging coordination mode.

In another paper, it is reported that, to differentiate between monodentate and bridging cooordination, the ν_{as}COO is generally smaller in the bridging configuration. Therefore, the ν_{as}COO band at 1578 cm^{-1} is attributed to the ν_{as}COO band of the bridging configuration. The strong band at 1443 cm^{-1} being attributed to the chelating coordination, the band at 1410 cm^{-1} is considered as the symmetric stretching frequency of the bridging configuration. Such ν_{as} and ν_{s} values are in agreement with reported values for other carboxylate compounds[53] and the so calculated $\Delta\nu$ (168) is in agreement with the $\Delta\nu$ range reported for a bridging configuration: 140-170.

One may observe that in our case, $\Delta\nu_{ionic}$ values are intermediate between those of the bridging and chelating ones and the ν_{as} evolved similarly, which is completely different from previous reported results. This may be related to the fact that these rules have been established with complexes with short alkyl chains (mainly formate and acetate). Furthermore Deacon et al.[59] by comparing their ranking with those of Manhas and Trikhas[60] established that "some complexes with symmetrically bridged carboxylates have both ν_{as}COO and ν_{s}COO at higher frequencies than the corresponding ionic values".

Thus, all stearates have a structure with carboxylates in bridging and chelate coordinations. From the carboxyl band intensities, one may advance that $FeSt_3$ displayed mainly a COO bridging coordination when $FeSt_2$ displayed mainly a chelate coordination. After dehydration, the carboxylate coordination is mainly bidentate chelate as it can be, in particular, seen when both dehydrated and hydrated $FeSt_3$ are compared (Figure III.17).

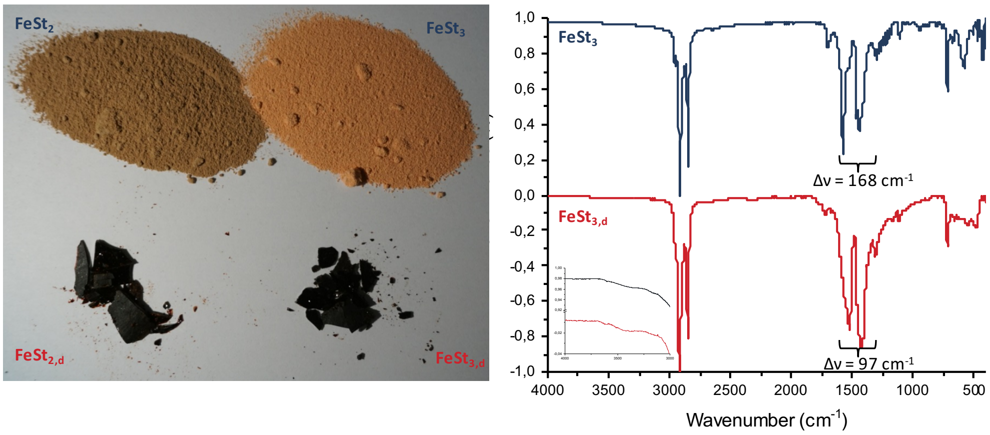

Figure III.17 - Comparison of IR spectra of hydrated and dehydrated $FeSt_3$ (right) and images of samples of hydrated and dehydrated $FeSt_3$ (left).

However, one may notice that the intensity ratio of the asymmetric and symetric stretching bands is very different when iron stearates are hydrated whereas the ratio get closer to one when dehydrated. In fact, both v_{as}COO and v_sCOO modes can be affected by the corresponding modes of coadsorbed carboxylates. In addition, the occurence of hydrogen bonding between the non coordinated oxygen atom of unidentate carboxylate ligand and a solvent molecule may lead to a reduction in the CO2 asymmetric stretching frequency. To investigate a possible interaction of carboxylate groups with water molecules, the synthesis of $FeSt_3$ and $FeSt_2$ has been conducted in D_2O. D_2O has a higher capacity to solvate polar species compared to H_2O. The IR spectra of both stearates in D_2O are given in Figure III.18: the IR spectra of $FeSt_2$ is not affected by these synthesis conditions when a clear modification of v_{as}COO bands intensities is observed for $FeSt_3$: the intensity of the band at 1527 cm^{-1} increased when that of the band at 1585 cm^{-1} has strongly decreased and is slightly shifted to higher wavenumber. The synthesis in D_2O seems to favor the chelate coordination and to affect the bridging one. Such an intensity decrease in the v_{as}COO/ v_sCOO intensity ratio was reported for strong H-bonded carboxylate groups with proton transfer and attributed to weakening of the C-O ---H-O- bonds by deuteration[61]. Such H bonds with carboxylate are thus observed with bridging coordination of carboxylate and would mean that in bridging coordination, one oxygen in carboxyl bridging is in interaction with water molecules. The fact that dehydrated $FeSt_3$ presented mainly a chelate coordination by comparison with hydrated $FeSt_3$ would suggest that the removal of water favored the chelate coordination: one important part of the bridging coordination in $FeSt_3$ involved thus H bonds with carboxylate through water and the removal of water favoured the formation of the chelate coordination.

Therefore, $FeSt_3$ consisted mainly in bridging carboxylates, with one oxygen involved in H-bonds with water molecules and chelate carboxylates. After dehydration, the bridging carboxylates with H-bonds would transform in chelate carboxylates due to the removal of water, the bridging carboxylates would not be affected as well as the chelate carboxylates.

For $FeSt_2$, the coordination is mainly chelate with some bridging coordinations. The intensities ratio v_{as}COO/ v_sCOO is smaller than 1 and get closer to one after the dehydration step. That could suggest that the quality of the carboxylate coordination is enhanced without head group interaction or H-bonds.

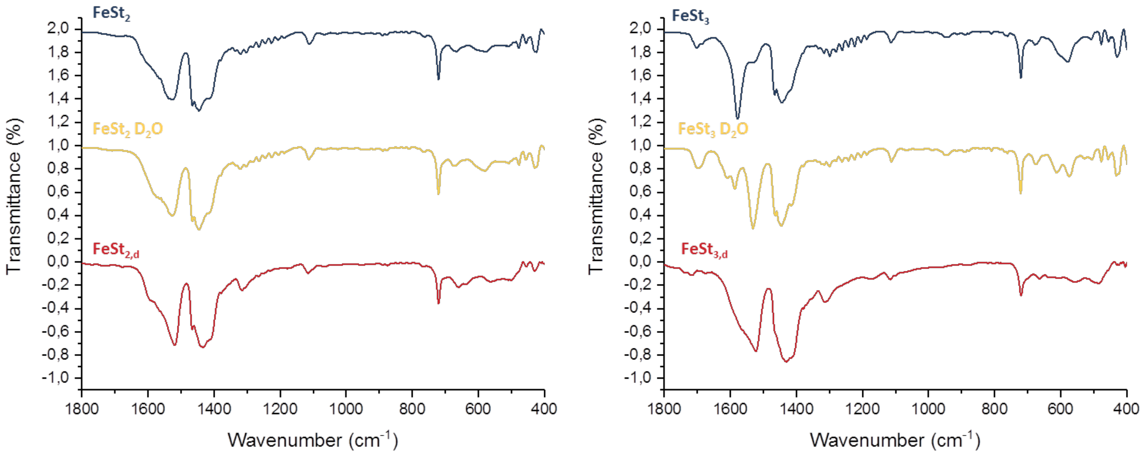

Figure III.18 - IR spectra of FeSt2 and FeSt3 synthesized in D2O.

Possible presence of Fe_3O or FeO bonds

The possible presence of Fe-O-Fe bonds has been investigated by considering bands in the range 700-400 cm^{-1}. One may notice that the bands in this wavenumber range are generally scarcely assigned in literature due certainly to their low intensity. Furthermore the bands in this wavenumbers range are more resolved after dehydration than before, where they appeared broaden. Bands positions are given in Table III.7 as well as the proposed assignements when it was possible.

The coordination of the carboxylate with the metal cations and the resulting resonance in the C-O bonds of the carbonyl group has been reported to lead to the presence of ν_{as} and ν_s bands but also bands at 950, 580 (out of plane twisting) and (rocking) ~540 cm^{-1} [62].

For iron oxides, the IR spectra of stoichiometric magnetite displayed one Fe-O-Fe peak at around 570 cm^{-1} and maghemite with vacancy disordering exhibited IR spectrum with two broad features at around 600 and 450 cm^{-1}, assigned respectively to Fe-O deformation in *Oh* and *Td* sites and Fe-O deformation in *Oh* sites[63].

Some carboxyl bands have been been clearly established: δ(OCO) = 670 cm^{-1} or 676 and 668 cm^{-1} for $FeSt_3$[41], 675 and 663 cm^{-1} for acetate analog[64]; π(COO) = 615 cm^{-1} [50].

After Abrahamson *et* al.[41] and Nakamoto *et* al.[42], .$FeSt_3$ would be an μ-oxo trimer with Fe_3O and would display bands in the 100-400 cm^{-1} range and around 600 cm^{-1}; they reported the Fe_3O band position for different type of complexes: $[Fe_3O(St)_6(H_2O)_3][St]$ at 582 cm^{-1}, $[Fe_3O(St)_6(H_2O)_3][St].8H_2O$ at 585 cm^{-1}, commercial $FeSt_2$ at 661 and 570 cm^{-1}, $[Fe_3O(St)_6(H_2O)_3]^+$ at 635 cm^{-1}, $[Fe_3O(Ac)_6(H_2O)_3]^+$ at 609 cm^{-1} [41]. Bands at 605 cm^{-1} [65] or at 594.1 cm^{-1} [42] or at 555 cm^{-1} [66] have also been attributed to Fe^{III}_3O units, $Fe^{II}Fe^{III}_2O$ was identified at 537 cm^{-1}. Band at 495 cm^{-1} would be attributed to Fe-O bond, FeO_4 at 380 cm^{-1}. From all the published data, the presence of Fe_3O would be assigned to a band around 600 cm^{-1}.

To try to identify the bands which could be attributed to a Fe_3O ou Fe-O-Fe bond, the bands of IR spectra of NaSt and/or HSt have been "removed" as well as the δ(OCO) bands at around 665-680 cm^{-1}. The remaining bands are 637/634 cm^{-1} and 567/560 cm^{-1} in dehydrated stearates, 575/580 et 600 cm^{-1} for hydrated stearates (585 weak in NaSt). The bands at 567/560 cm^{-1} in dehydrated stearates may be related to bands at 575/580 cm^{-1} in hydrated samples and the dehydration step.

From all these considerations, only the band at 600 cm^{-1} remained not clearly assigned even if some papers assigned it to πCO2 or γCOO. Considering the weak intensity of concerned bands, we propose that the presence of Fe_3O would be negligeable.

Table III.7 – Proposed assigments of bands in the region 700 – 400 for HSt, NaSt ans $FeSt_x$

HSt	NaSt	$FeSt_2$	$FeSt_3$	$FeSt_{2,d}$	$FeSt_{3,d}$	Approximate assignments	Abrahamson
687m	696m	680m,br	675m	–	–	δCOO^-	
		665m	–	660m	666m	δOCO	FeSt2 Fe3O
		–	–	637w	634w		other Fe3O
		600m,br	600 m, sh		600 w, br	πCO2 ou Fe-O ou γCOO-	
	583-588 w,br	580 m	575 s			ν_tCOO^-	582-585 Fe3O
			–	567m	560m	ν_tCOO ρCOO^- Fe-O	
548m	539 m					ρCOO 525	
502m	488wbr	500w	507w	503w	496w sh	ρCOO^-	
476w	478wbr	476m	476m	477m sh	485m		477
448w	446m	452w	458w	455w	457 w sh		456-463
439 m	436 msh						
415w	415w	424s	427s	428s	424s		426-428
411w	408w						

s: strong, m: medium, w:weak, sh: shoulder, br:broad

To check the formation of an iron stearate complex without Fe-O bonds, the elemental analysis of stearates has been considered and the results are given in Table III.8-9. Two analyses have been performed on the same sample and the slight observed weight variations could be attributed to a hydration of powders with time.

Table III.8 - Elemental analyses of $FeSt_2$

	Fe (%)	C (%)	H (%)	O (%)	Total (%)
$FeSt_2$	9.0	67.6	11.0	9.7	97.3
	9.0	67.2	11.0	10.5	97.7
Mean value	9.0	67.4±0.2	11.0	10.1±0.4	97.5±0.2
$FeSt_{2,d}$	9.0	70.7	11.5	9.2	100.4
	9.0	67.7	10.6	12.2	99.5
Mean value	9.0	69.2±1.5	11.1±0.5	10.7±1.5	100.0±0.5
Theoretical composition					
$FeSt_2$	9.0	69.5	11.3	10.3	100.1
$FeSt_{1.9}$	9.4	69.2	11.2	10.2	100.1

Table III.9 - Elemental analyses of $FeSt_3$

	Fe (%)	C (%)	H (%)	O (%)	total
$FeSt_3$	8.8	67.0	10.9	9.2	95.9
	8.8	70.7	11.5	10.4	101.4
Mean value	8.8	68.8±1.8	11.2±0.3	9.8±0.6	98.6±0.8
$FeSt_{3,d}$	7.5	67.9	10.9	11.3	97.6
	7.5	69.5	11.1	11.8	99.9
Mean value	7.5	68.7±0.8	11.0±0.1	11.6±0.3	98.8±1.1
Theoretical composition					
FeSt3	6.2	71.6	11.6	10.6	100.0
FeSt2.45	7.6	70.5	11.4	10.4	100.0
FeSt2.4	7.5	70.6	11.4	10.5	100.0
FeSt2.1	8.6	69.8	11.3	10.3	100.0
FeSt2	9.0	69.5	11.3	10.3	100.0
Abrahamson and al molecular formula					
$Fe_3O(St)_6(H_2O)_2St$	7.6	68.7	11.3	12.4	100.0
$Fe_3O(St)_6(H_2O)_3)St$	7.6	68.2	11.3	13.0	100.0

The fact that the total weight % is not 100 is due to the non consideration of water in these analyses. The elemental analyses suggested about 2.5 % of water for hydrated $FeSt_2$ which value strongly decreased in the dehydrated sample as expected. The standard deviation on elemental analyses of $FeSt_3$ and $FeSt_{3,d}$ is larger but the water weight % is observed to decrease after dehydration.

The elemental analyses of all FeSt have been compared to the theoretical elemental analyses of iron stearates with different stearate composition and of the Abrahamson'stearates. Except for $FeSt_{3,d}$, the iron weight % is different from that of the Abrahamson's stearates confirming that the molecular formula of our stearates does not correspond to these stearates. As dehydrated iron stearates are strongly suggested from all current characterizations to have a close composition, we may propose that $FeSt_{3,d}$ would have a composition of $FeSt_x$ type. For $FeSt_2$, there is a quite good agreement between theoretical $FeSt_2$ and $FeSt_{2,d}$ weight % and the slight discrepancy with hydrated $FeSt_2$ may be attributed at this stage to variation in its hydration state. By contrast, the elemental analyses suggested that $FeSt_3$ would have a composition close to that of $FeSt_2$/$FeSt_{2.1}$ and after dehydration, close to $FeSt_{2.4}$.

To check if the composition deduced from elemental analyses was correct, we have considered the total weight loss deduced from different TGA curves presented in Figure III.33 and Figure A.4 in Annexe and we have evaluated the amount of water considering that, during the thermal tratment, $FeSt_2.xH_2O$ and $FeSt_3.xH_2O$ transformed into hematite Fe_2O_3. The total weight losses obtained with different samples resulting from different TGA analyses are given in Table III.10 . The mean weight loss of $FeSt_2$ is lower than that of $FeSt_3$ which is consistent with the higher expected composition in stearate for $FeSt_3$. The weight losses of $FeSt_{2,d}$ and $FeSt_{3,d}$ are similar confirming that these dehydrated stearates displayed a very similar structure.

Table III.10 – Total weight loss measured in the TGA curves

Weight loss (%)	$FeSt_2$	$FeSt_3$	$FeSt_{2,d}$	$FeSt_{3,d}$	Theoretical $FeSt_2$	Theoretical $FeSt_3$
1 air	-84.8 %	-93%	-88.7%	-88.7%	-87.2 %	-91.2 %
2 air	-86.6 %	-92.7%				
3 air	-87.6%	-88.2%				
Mean value	- 86.3± %	- 91.3± %			-86.4	-89.5
4 argon	-91.5%	-90.1%				

The comparison of the experimental and theoretical ($FeSt_2$ and $FeSt_3$ without water molecules) weight losses suggested that $FeSt_2$ and $FeSt_3$ are either dehydrated or have a different composition. Furthermore by considering the starting/experimental $FeSt_{2-}$ or $FeSt_{2,d-}.xH_2O$ composition and a weight loss due to the formation of hematite αFe_2O_3, x values of -2.2 and 5 were respectively obtained and similarly of 0.7 and -11 for $FeSt_{3-}$ and $FeSt_{3,d-}.xH_2O$.

However previous experiments showed that $FeSt_2$ and $FeSt_3$ are hydrated. Simple considerations depicted in Figure III.19 demonstrated clearly that the number of stearate chains per atoms may vary strongly as a function of the carboxylate coordination which would affect also the number of water molecules. A mixed carboxylate coordination led to less stearate/atom ratio (5/6 Fe in the Figure III.19.Bottom) than a "mono" coordination (6/6 Fe in the Figure III.19.Top). IR analalyses have clearly demonstrated that all stearates presented a mixed coordination with "more" bridging coordination for $FeSt_3$ and "more" chelate coordination for other iron stearates. **These results and the result of elemental analyses suggested strongly that $FeSt_3$ would have a composition lower than $FeSt_3$ and closer to that of $FeSt_2$ and that also $FeSt_2$ would have a composition in stearate lower than 2.**

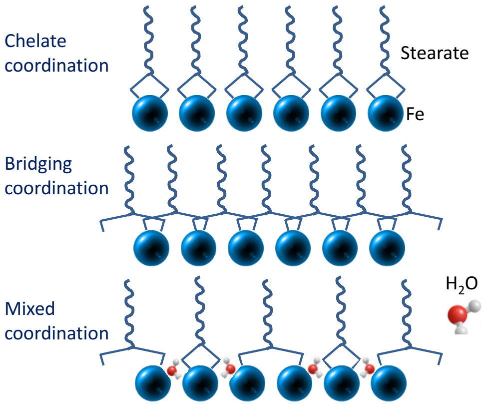

Figure III.19 – Schematic representation of the different stearates coordinations

Considering the weight loss of dehydrated stearates and assuming that they are fully dehydrated, the weight loss would lead to a molecular mass of 706.86 g/mol which would correspond to a composition close to $FeSt_{2.3}$.

By following results of elemental analyses which suggested a composition $FeSt_{2.1}$ for $FeSt_3$, the weight loss considering a $FeSt_{2.1}@xH_2O$ compound led to the final formula: $FeSt_{2.1}@15H_2O$, (to note that a composition with 2.3St would lead to $FeSt_{2.3}@12H_2O$). Considering that the dehydration step induced only a water weight loss, $FeSt_{3,d}$ would correspond to $FeSt_{2.1}@3H_2O$. During the dehydration step a weight loss of 20% is observed, which would correspond to the lost of $10H_2O$ (by considering $FeSt_{2.1}@15H_2O$) leading thus for dehydrated $FeSt_3$ to $FeSt_{2.1}$@5H2O which is quite close to $FeSt_{2.1}@3H_2O$ determined from the total weight loss.

For $FeSt_2$, a composition of $FeSt_{1.8}$ was proposed and the weight loss would suggest the presence of one water molecule: $FeSt_{1.8}@H_2O$ which seems low. A composition $FeSt_{1.5}$ would lead to 6 water molecules. The weight loss due to dehydration is about 12% leading to the lost of $4H_2O$, the composition of $FeSt_{2,d}$ would be close to $FeSt_{1.5}@2H_2O$.

These calculations allowed giving an approximate mean composition and considering also that the co-precipitation reaction leading to iron stearates occured in water; we have certainly a distribution of precursors with different composition/structure. This would be in agreement with the observation that the precursors in the thermal decomposition process decomposed on a large range of temperature[2,13,31].

III.3.2.2.2 Modeling

To get a better insight on the structure of stearates, modeling has been developped on $FeSt_2$ which appears to be the “mean” structure. This modeling, which has been at first performed during the PhD of Xiaojie Liu but better exploited in this study, has been realized by the modeling team of our department: Dr Mauro Boero, Dr Carlo Massobrio and Dr Guido Ori.

The stability of Fe stearates either in the presence or in the absence of water has been investigated via first principles molecular dynamics simulations[67] within the density functional theory framework[68]. Since the central metal atom is four-fold coordinated with oxygen atoms of the -COO moieties terminating the hydrocarbon chains, and being this coordination planar, two additional coordination sites are in principles available to complete the hydration shell of Fe[69], one above this coordination plane, and one below.

Starting from relaxed geometries at 0 K, shown in Figure III.20, one or two water molecules are inserted in the empty coordination sites along the axis orthogonal to the –COO M OOC– plane passing across Fe. As a consequence, the metal center can become either five- or six-fold coordinated.

For $FeSt_2$, in dry conditions non-planar –COO Fe OOC– coordinations may arise as a result of thermal fluctuations at finite (room) temperature. The situation at 300 K is sketched in Figure III.21.

In the case of partial (five-fold) or full (six-fold) hydration, a damped dynamics, performed to quench the structure and allow the system to find a stable local minimum, has shown that the water molecules can stabilize around the Fe center as shown in Figure III.22. This situation, however, can change significantly at 300 K. Namely, (see Figure III.22-25) when one H_2O molecule is present, it can form strong hydrogen bonds with the nearby carboxylate group of the stearate chain surrounding the iron cation. This strong interaction can even give rise to an exchange of protons between the water molecules and the carboxylate group as in a Zundel-like[70] complex. When two water molecules are present, at 300K a destabilization of the hydration shell of Fe arises. The net effect is the evaporation of one of the two water molecules, which leaves the coordination shell of Fe. At the same time large conformational changes of the hydrocarbon chains occur, summarized by the snapshot in the fourth panel of Figure III.25.

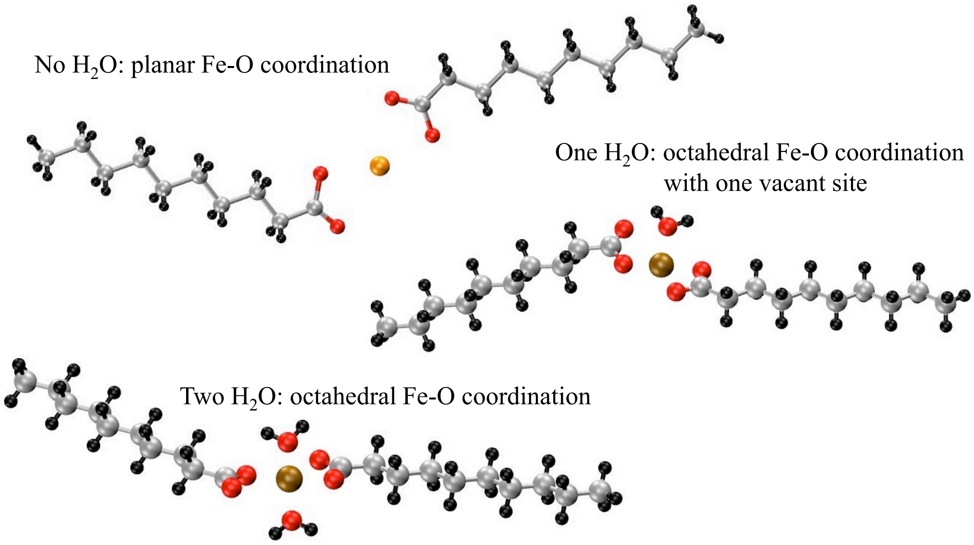

Figure III.20 - Equilibrium geometries of Fe stearates at 0 K in the absence and in presence of water.

An analysis of the Bader charges[71] of the system has shown that the three coordination shown above corresponded to a net charge on the Fe site of +1.9 in the planar Fe-O in dry conditions, whereas charges of +2.2 and +2.8 were found in the cases of a single H_2O molecule and two H_2O molecules respectively. We can thus infer that in dry conditions the metal center is basically Fe(II), while in full hydration conditions it is rather Fe(III). The case of partial hydration in which a defective octahedron with a single water molecule is realized, the situation is somehow intermediate.

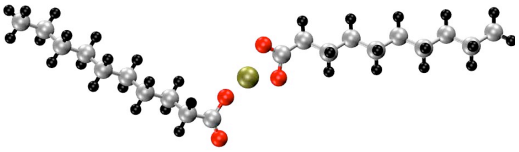

Figure III.21 - Equilibrium geometries of Fe stearates at 300 K (dry) in the absence of water.

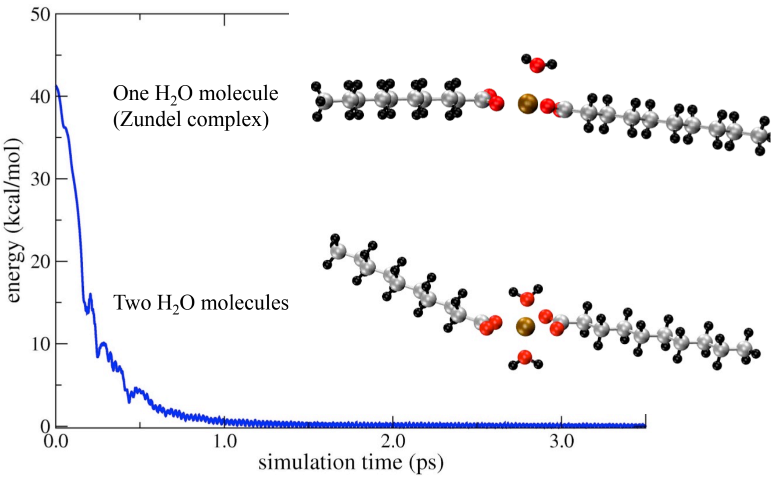

Figure III.22 - Fe-based stearates: quenched (stable) configurations in wet conditions

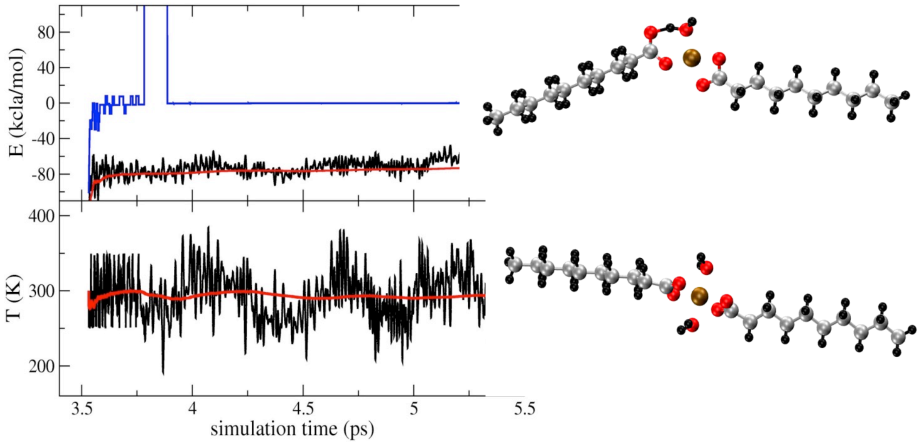

Figure III.23 - Thermal evolution of Fe stearate at 300 K in wet conditions

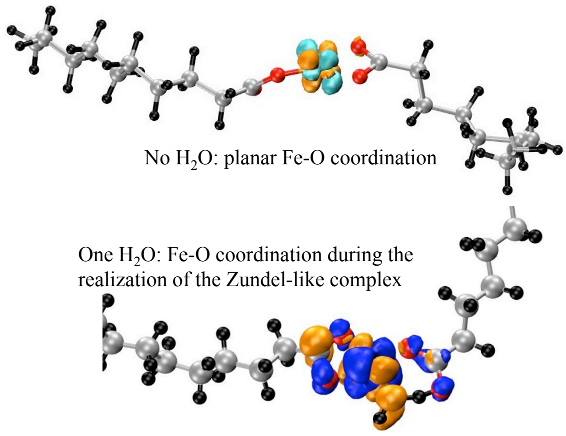

Figure III.24 - Fe-based stearates: Spin density distribution at 10^{-3} e/Å^3

	T = 0 K	**T = 300 K**
1 H_2O	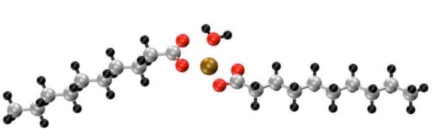	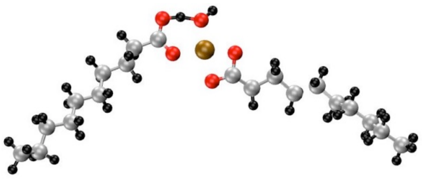
2 H_2O	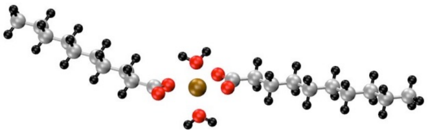	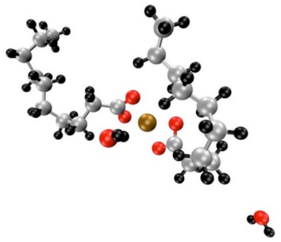

Figure III.25 – Struture of $FeSt_2$ depending on the number of water molecules interacting with Fe and temperature

The modeling experiments allowed confirming our hypotheses that the stable coordination of carboxylates with iron cations is the chelate one. When the iron stearates are hydrated, carboxylates may form bridging coordination by involving one water molecule interacting via hydrogen bonds.

Importantly, the oxidation degree in hydrated $FeSt_2$ is rather Fe^{3+} when it is close to Fe^{2+} in the dehydrated state.

III.3.2.2.3 Discussion

From IR spectra, for $FeSt_2$ whose structure is the simplest, two carboxylate coordinations are clearly established: one main chelate bidentate coordination with a small amount of bridging bidentate coordination. That would explain (cf. Figure III.19) the composition in stearate, deduced from elemental analyses, smaller than 2 (~$FeSt_{1.5}$). After dehydration, the main coordination is chelate bidentate even if some bridging coordination is always present. Such semi-quantitative evaluation may be correlated with Mössbauer results which identified two iron environments with one environment becoming majoritary after dehydration. Thus IR spectra fitted quite well with Mössbauer results and let us to advance that the environment of Fe^{3+} in $FeSt_2$ could be mainly related to the coordination of two carboxylate with a structure close to that proposed by modeling. The composition of $FeSt_2$ and $FeSt_{2,d}$ would be close to $FeSt_{1.5}@6H_2O$ and $FeSt_{1.5}@2H_2O$ respectively.

With $FeSt_3$ which is constituted of Fe^{3+}, a mixture of chelate bidentate and bridging bidentate coordinations with some bridging coordinations involving water molecules is suggested from consideration of carboxylate bands. The mixture of chelate and bridging coordinations are in agreement with a lower composition in stearate for $FeSt_3$ (~$FeSt_{2.1}$). The presence of an IR band at 1700 cm^{-1} suggested either the presence of free stearic acid or a monodentate complex. After the dehydration step, the coordination is mainly chelate but some bridging coordinations are also present. The composition of $FeSt_3$ and $FeSt_{3,d}$ would be close to $FeSt_{2.1}$@15H2O and $FeSt_{2.1}$@5H2O respectively.

III.3.2.3 The lamellar structure of iron stearates

III.3.2.3.1 IR spectroscopy

Alkyl chains are ubiquitous in biological and polymer systems and determine, in many cases, the arrangement of complex molecules. Their infrared signature may help in understanding the structure of iron stearates.

Hydrated iron stearates

The first alkyls bands to be noticed are located in the high frequency region of 3000-2800 cm^{-1}. They are attributed to the symmetrical (ν_s) and asymmetrical (ν_{as}) stretching of CH_3 and CH_2.The CH_2 bands are detected around 2915 cm^{-1} ($\nu_{as}CH_2$) and at 2848 cm^{-1} (ν_sCH_2) as observed for crystalline n-alkanes in the fully extended all trans conformation[58] indicating an order of the methylene chains. Another indicator of the order is the ratio of their intensities I_{2848}/I_{2916}[58], the higher the more organized are the chains due to Van der Waals interaction. The bands assigned to the tail CH_3 group are also indicative of intermolecular interactions. According to Nelson and al[58], as those bands are singlets no lowering of the molecular symmetry is observed. Moreover the intensity of the band ν_sCH_3 is higher than $\nu_{as}CH_3$. This is explained by Nelson et al who attributed a lower value for the asymmetrical stretching to interlayer interaction. H atom will interact with a carbon atom of the adjacent chain, the C-H bond of a methyl group will then lengthens, become weaker inducing the reduction of the $\nu_{as}CH_3$ signal. This means that for both stearates there is overlapping of neighbours layers.

In the low frequency region, scissoring, waging, twisting and rocking vibrations are detected. At 1464 cm^{-1} the CH_2 scissoring is found (δCH_2). The position of this band has been used to investigate the packing arrangement of the chains. With a triclinic packing leading to a strong, narrow and shape band at 1470-1474 cm^{-1}, an orthorhombic a doublet at 1462 and 1474 cm^{-1}, a hexagonal packing will translate as a single band at 1468-1469 cm^{-1}[58,72,73]. This can be completed with the analysis of the in plane rocking of CH_2 (ρCH_2) at 720 cm^{-1}. If this band is split an orthorhombic packing is confirmed if not (singlet) it's either triclinic or hexagonal packing[74]. In our case, a singlet is observed at 720 cm^{-1} eliminating the orthorhombic packing. The δCH_2 is observed around 1465 cm^{-1} thus a hexagonal packing.

The region between 1350 and 1150 cm^{-1} is composed of a progression of narrow regularly spaced low intensity bands assigned to the CH_2 wagging (ωCH_2) of the chain. For an even numbered chain the number of bands observed is m/2 with m the number of carbons atoms of the alkyl chain[75]. These bands are observed for an all trans conformation of the chains. The observation of 9 bands in this area is in accordance with the 18 carbon atoms of the stearate chain. The band observed around 1100 cm^{-1} is ascribed to the C-C stretching.

From the alkyl band analysis, we can conclude that both compounds adopted a hexagonal packing with an all trans conformation of the chains. That is in agreement with SEM images which showed a lamellar structure (Figure III.26 left) and XRD patterns (Figure III.26 right) which evidenced a lamellar structure. The structure will be analyzed in more detailled in the next paragraph by performing small angle X-ray scattering.

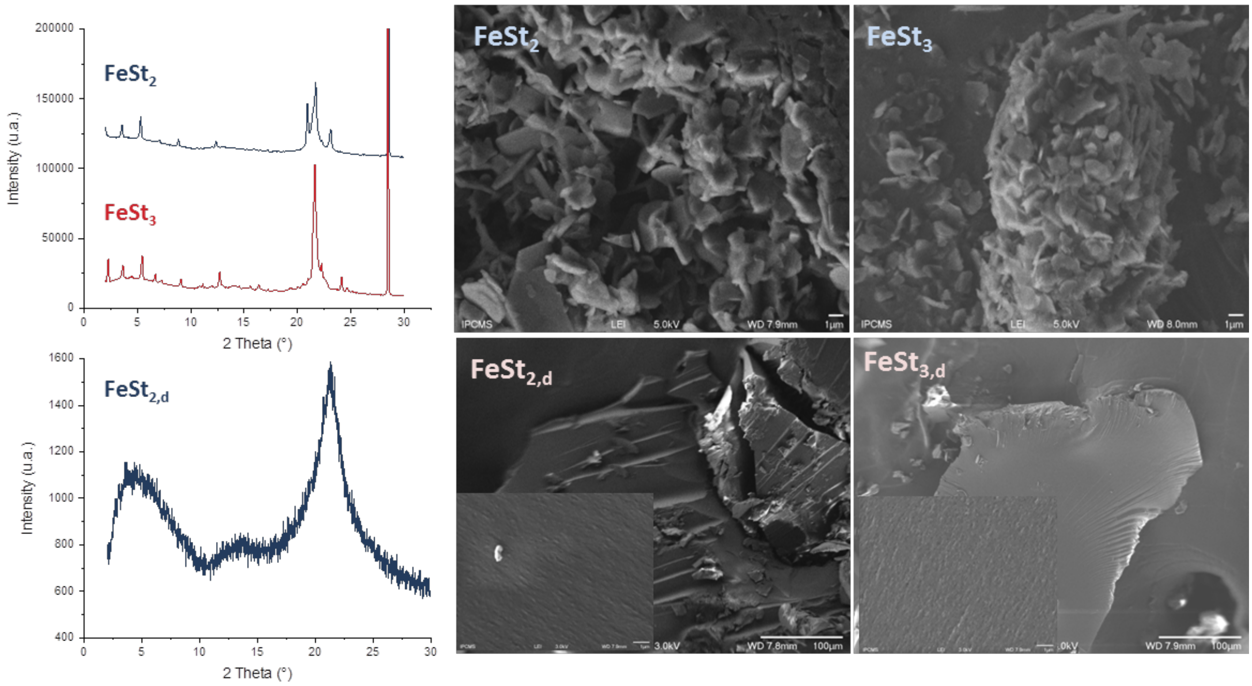

Figure III.26 - XRD pattern and SEM images of both iron stearates $FeSt_2$ and $FeSt_3$ before (top images) and after dehydration (down images, XRD pattern of $FeSt_{2,d}$)

Dehydrated stearates

In the case of dehydrated stearates, $FeSt_{2,d}$ and $FeSt_3$,d, IR spectra, in the wavenumber range 3000-2800 and 1350-1150 cm^{-1} provided also useful information on their organisation. At first, the CH_2 wagging (ωCH_2) of the chain observed between 1350-1150 cm^{-1} (Figure III.18) in hydrated stearates has disappeared showing a loss of the lamellar structure confirmed also with the loss of the CH_3 bands. That is in agreement with their morphology change observed in SEM image and with their XRD pattern which showed the disapperance of an ordered organisation of the structure.

III.3.2.3.2 Small Angle X-ray Scattering (SAXS)

SAXS patterns of $FeSt_2$ and $FeSt_3$ before and after dehydration are given in Figure III.27. $FeSt_2$ is organized in a lamellar crystal phase "Lam0" (reflections (001), periodicity d = 50.7 Å), with a lateral arrangement of the aliphatic chains in a two-dimensional hexagonal subarray of rotator type ($h_{ch,\ cr}$ = 4.12 Å; section of the chains: $S_{ch,\ cr}$ = 19.6 Å^2). $FeSt_3$ formed a classical three-dimensional lamellar crystal phase "Lam0" (reflections (001), periodicity d = 50.1 Å), in which the signals of the crystalline phase of the excess stearic acid are superimposed. Both $FeSt_{2,d}$ and $FeSt_{3,d}$ are amorphous at room temperature and are reorganized into lamellar strata on first heating to 70°C.

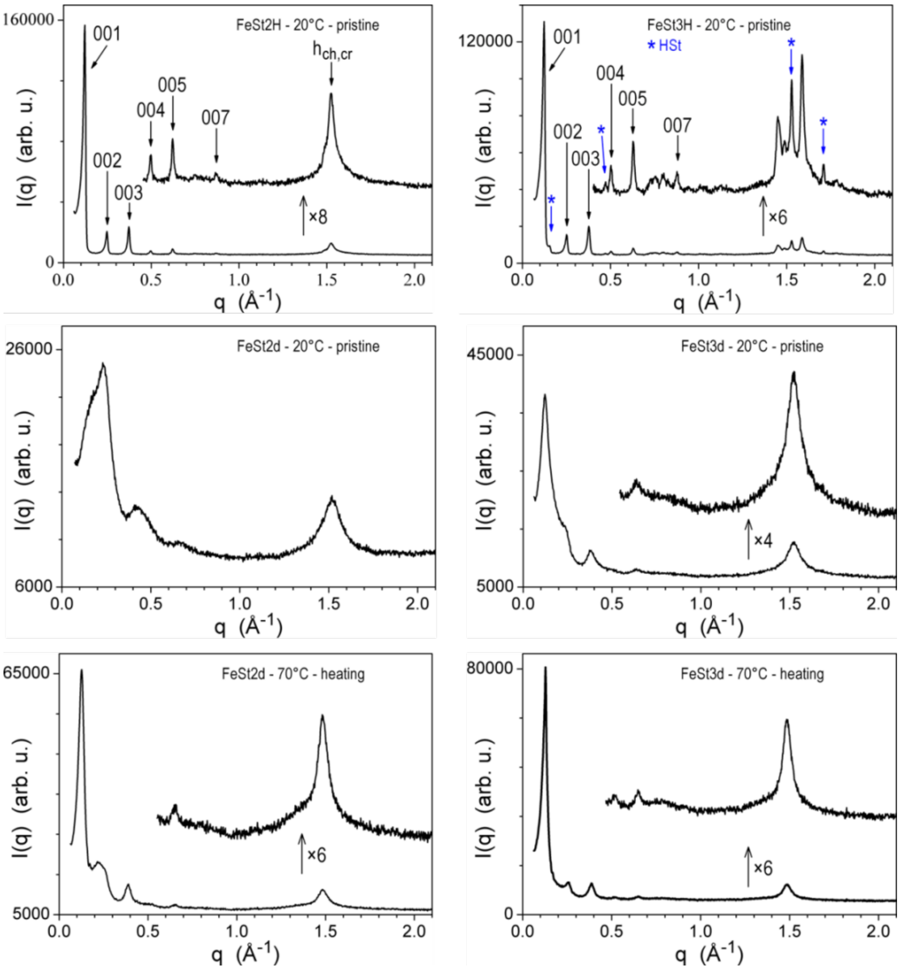

Figure III.27 - SAXS patterns

Both IR spectroscopy and SAXS confirmed the lamellar structure of hydrated FeSt and the amorphous configuration of dehydrated ones. $FeSt_3$ is shown to contain stearic acid which allowed ascribing the IR peak at 1700 cm^{-1} in IR spectra to free stearic acid and not to monodentate coordination.

III.3.2.4 Thermal behavior of iron stearates below 200°C

III.3.2.4.1 TGA/DTA/DTG curves below 200°C

The comparison of iron stearates TGA/DTA curves before and after their dehydration step should help to understand their structure and in particular the bonding of water molecules. The TGA curves are shown in Figure III.28 and the main weight losses occured, as often reported, above 200°C. As the iron stearates have been dehydrated by a heat treatment at 140°C for 48h under air, the TGA/DTG/DTA curves of hydrated stearates have been considered in the temperature range 20-300°C (Figure III.29). The main observed features are summarized in Table III.11. We may observe that the weight loss below 200°C is very low and of the order of few percent in agreement with elemental analyses. Furthermore weight loss and gain steps may be observed in the different TGA curves below 200°C. As these features concerned very small percent in weight and to be sure to consider real effects and not artefact, several

TGA curves have been compared (see Figure III.28) and TGA curves of stearates (Figure III.1) have been compared to the isothermal TGA/DTG/DTA curves which have led to dehydrated stearates. The weight loss and gain features are always observed even if they may occur at slightly shifted temperatures which is suggested to be attributed to different hydration degrees of iron stearates.

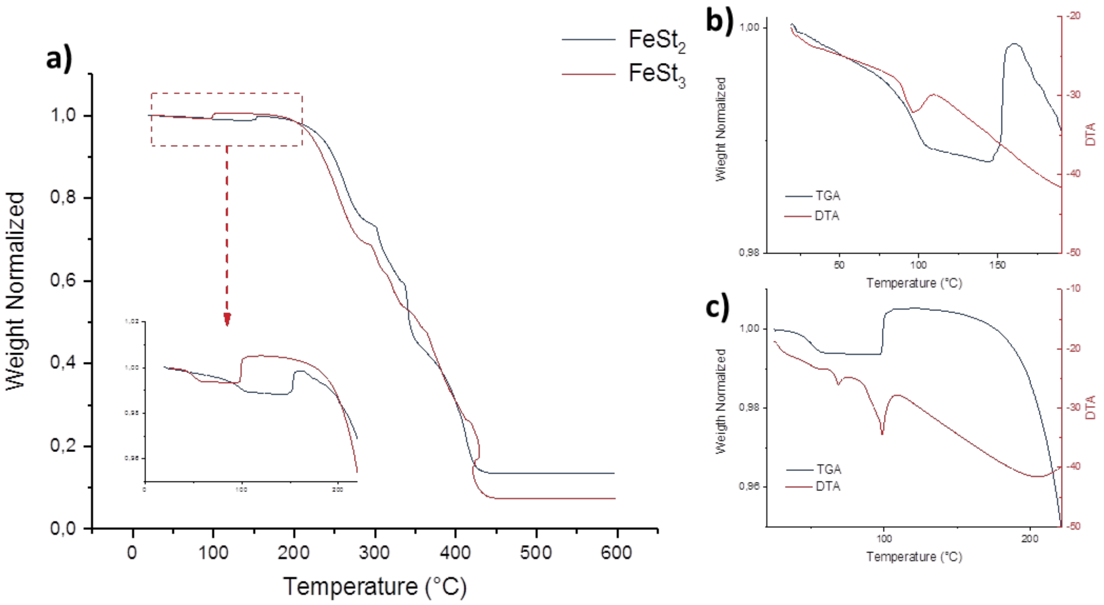

Figure II.28 - TGA curves (a) of $FeSt_2$ and $FeSt_3$ and TGA and DTA curves of $FeSt_2$ (b) and $FeSt_3$ (c) below 200°C.

Below 200°C, the TGA curves of both stearates look similar with that of $FeSt_2$ appearing enlarged and shifted to higher temperatures. Both TGA curves displayed a small weight loss at around 55-65 and 90-100°C for $FeSt_3$ and $FeSt_2$ respectively, a plate, then an abrupt weight gain at 100 and 150°C respectively and finally after a small plate, the beginning of the large weight loss around 200°C. The TGA/DTG/DTA curves of both stearates presented in Figure III.29 and also TGA/DTA/DTG curves of the isothermal treatment at 140°C where the curve below 0.4h corresponded to the heating up to 140C in Figure A.6 have helped to correlate TGA features with DTA features (Table).

$FeSt_3$: The weight loss at 50°C for $FeSt_3$ is associated with an endothermal DTA peak in Figure III.30 (clearly visible in Figure III.28.c) and may be attributed to the loss of water molecules weakly bounded to $FeSt_3$.

The weight gain observed is quite surprising but such weight gain has already been observed during TGA/DTA experiments with quite stoechiometric magnetite and was attributed to the oxidation of FeII in magnetite and the formation of maghemite[79]. Thus the observed weight gain could be due to an oxidation of Fe^{2+}. However Fe^{3+} has been demonstrated by Mössbauer spectroscopy and RPE to be the main cation in both stearates. That would suppose that a reduction of Fe^{3+} has occured before this oxydation step. From modeling experiments, we have seen that the coordination of water has an impact on the oxidation degree of iron and thus the dehydration step should induce a reduction of Fe^{3+}.

$FeSt_2$: The broad DTA endothermal peak around 100°C in Figure III.30 for $FeSt_2$ appeared under the form of two endothermal peaks in Figure III.31.d and is associated with a weight loss. Thus we may suggest that around 100°C, $FeSt_2$ is simultaneously dehydrated and reduced. The Fe^{2+} cations so formed would be further oxidized around 140-150°C leading to weight gain.

In the case of $FeSt_3$, a DTA peak without clear weight loss step is observed at around 70°C in Figure III.28.b and in Figure III.30.d, it could be included in the broad DTA peak in this temperature range (t (h): 0.24-0.31 / 72-90°C). A weight gain at 100°C is associated with this broad endothermal DTA peak in Figure III.30.d and is observed in figure III.29.c. These results would confirm that the reduction of Fe^{3+} would occur around 100°C simultanesously with the dehydration of iron stearates.

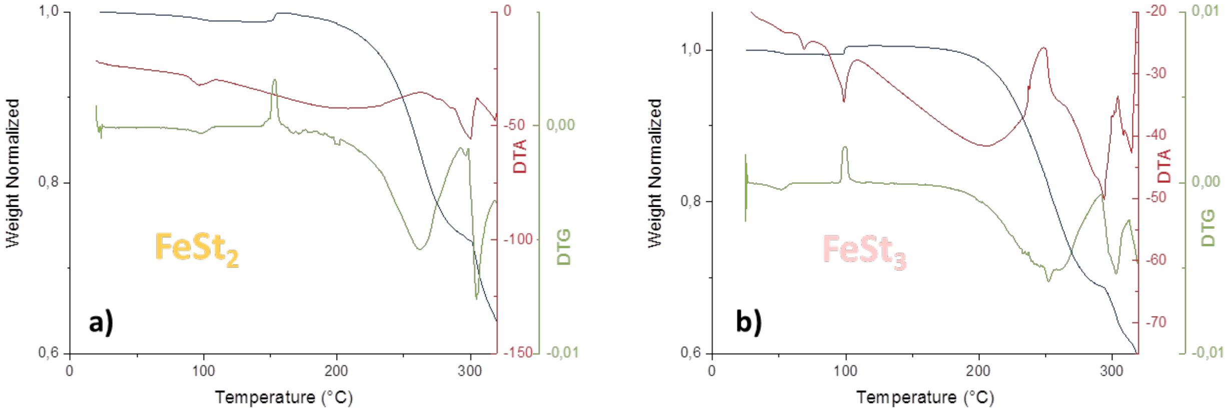

Figure III.29 - TGA/DTG/DTA curves of FeSt2 (a) and FeSt3 (b) below 300°C.

Table III.11 - Features observed in TGA/DTG/DTA curves of FeSt2 and FeSt3 below 300°C (Figures Y&Z)

Increasing T	$FeSt_2$			$FeSt_3$		
	TGA	DTG	DTA	TGA	DTG	DTA
	Low constant wl					
35-60°C				wl step	one peak	exothermal peak at 50°C
70°C				No weight loss		Endothermal peak
100°C	wl step	Perhaps a peak	Large endothermal peak = 2 peaks	90 °C no wl 100°C **wg step**	One peak	2 endothermal peaks: 90-100°C
150°C	**wg step**					
160°C	wl step		Broad endo peak			

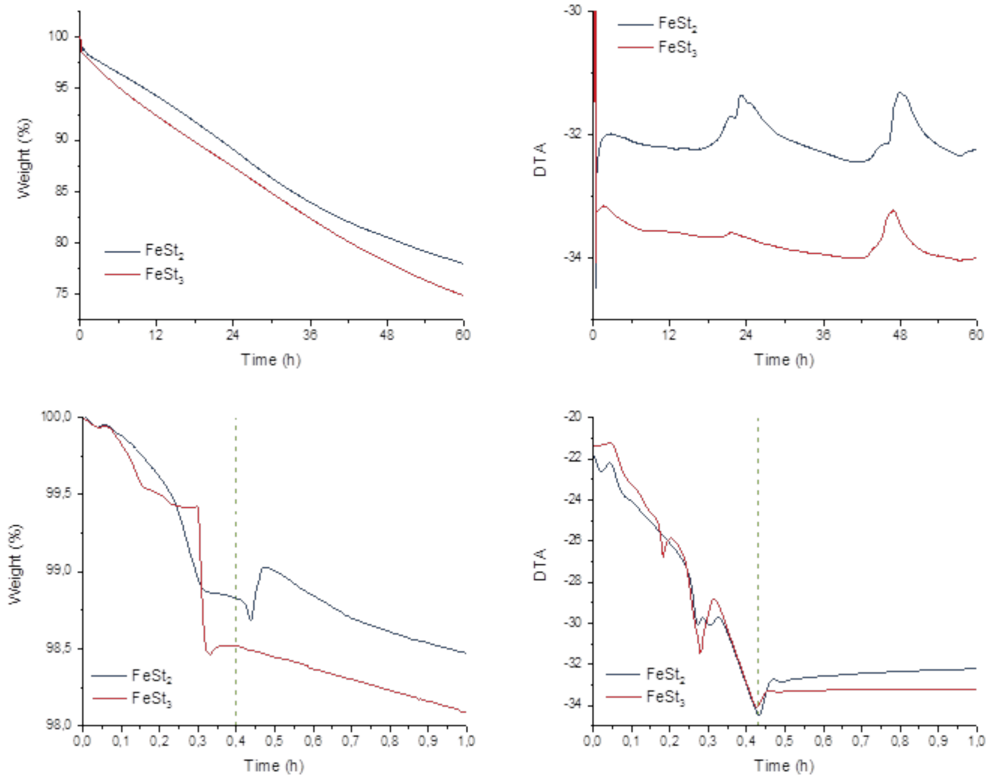

Figure III.30 - Isothermal treatments at 140°C of FeSt2 and FeSt3: TGA (a-c) and DTA (b-d) curves.

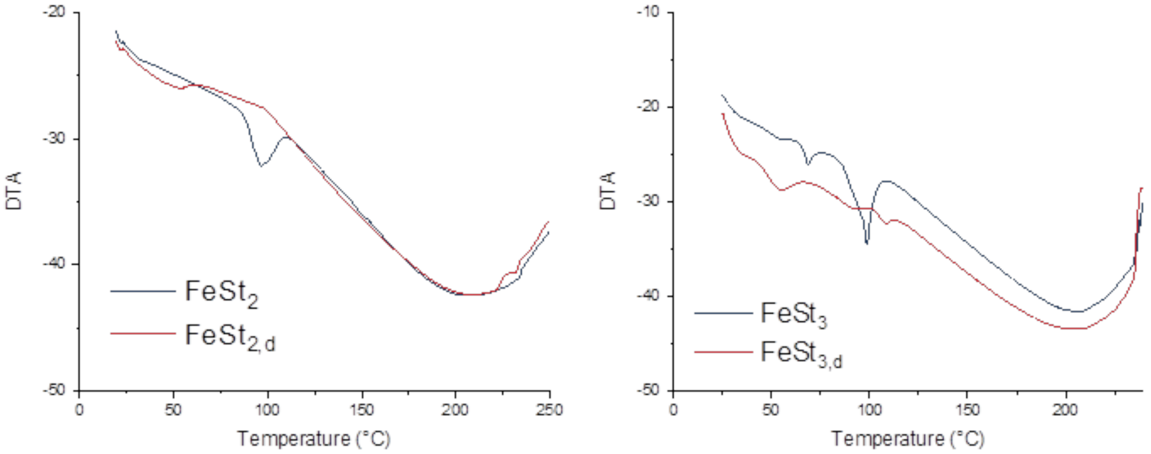

Figure III.31 - DTA curves of all stearates

TGA curves of dehydrated stearates showed no weight loss below 140°C but only a weight loss at 160°C for $FeSt_{2,d}$ and a weight gain between 110 and 120°C for $FeSt_{3,d}$.

Main differences between hydrated and dehydrated stearate in DTA curves are: a large endothermal peak at 50°C observed after dehydration which seem to be also present in hydrated stearates but less apparent/resolved and the disappearence of the endothermal peak at 100°C. In addition two endothermal peaks at around 80 and 110°C are noticed with dehydrated $FeSt_{3,d}$. For $FeSt_{3,d}$, the peak at 80°C could be due to the reduction of Fe^{3+} in Fe_{2+} and that at 110°C, which is linked to a weight gain, to its reoxidation. The reduction of Fe^{3+} would be shifted at higher temperature by comparison with hydrated $FeSt_3$.

The TGA curves are presented in Figure III.32. The weight losses of $FeSt_2$ and $FeSt_3$ at the first heating at 120 °C., followed by an isotherm of 4 min at this same temperature, are respectively 1.7% and 1.2%. Weight losses are observed around 90-100 °C for $FeSt_2$ and 55-65 and 120 °C for $FeSt_3$.

At the second heating, additional weight losses are noticed at 120°C of about 0.3% and 0.6% for $FeSt_{2Hd}$ and $FeSt_{3Hd}$ respectively. HSt began to evaporate at 110-120 °C, with a rapid weight loss above 140-150 °C. Temperatures corresponding to 5% of weight loss, with ramps of 5°C/min, are : T = 171 °C (HSt), 214 °C ($FeSt_{2,Hd}$), 220 °C ($FeSt_{2d}$), 185 °C ($FeSt_{3,Hd}$), 202 °C ($FeSt_{3d}$).

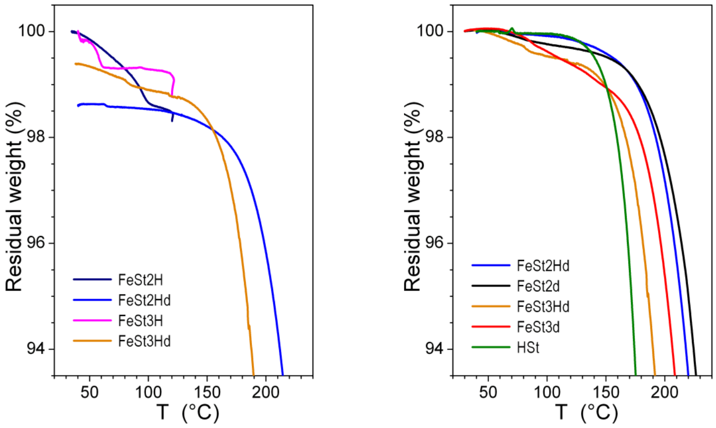

Figure III.32 - TGA curves below 200°C of $FeSt_{2H}$*=*$FeSt_2$*,* $FeSt_{3H}$*=*$FeSt_3$*,* $FeSt_{2Hd}$ *and* $FeSt_{3Hd}$ *which are respectively* $FeSt_2$ *and* $FeSt_3$ *after a heating treatment at 140°C for 4min,* $FeSt_{2,d}$*,* $FeSt_{3,d}$ *and HSt.*

III.3.2.4.2 Polymorphism by differential scanning calorimetry

The DSC curves are given in Figure III.33. $FeSt_2$ is a crystalline powder that, when the temperature increased, melted at around 90°C (ΔH = 73 J/g), towards the isotropic liquid. This phase transition is accompanied by a weight loss in TGA, due to the desorption of water molecules at the time of the collapse of the crystal lattice. The isotropic liquid crystallized when the temperature is lowered. This new crystalline phase melted at a lower temperature (T_F = 60 ° C, ΔH = 53 J/g) to a mesophase. The non-reversible transition to the isotropic liquid is between 130 and 140 ° C (ΔH = 1.0 J/g). Another thermal phenomenon, visible in the mesomorphic domain between the melting peak and about 110 °C., is attributed to a coexistence zone with a crystalline phase.

$FeSt_3$ has two melting peaks at about 66 °C. (ΔH = 10 J/g) and between 93 and 98 °C (ΔH = 93 J/g), also associated with weight losses in TGA. The first peak is probably derived from the melting of excess stearic acid (T_F = 68 °C, ΔH = 214 J/g), and the second from that of iron stearate with some stearic acid. A mesophase in equilibrium with the isotropic phase is observed by SAXS at the second heating, but the isotropization transition is not detected by DSC, probably because it is very low in energy and spreads over a very high temperature range large.

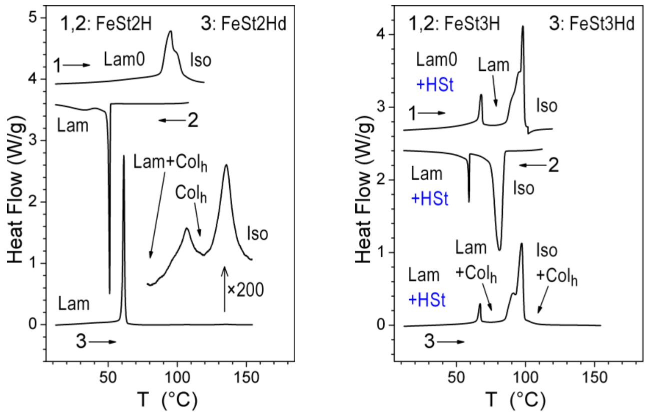

Figure III.33 - DSC curves of hydrated iron stearates and FeStxHd corresponds to $FeSt_x$ after a heating up to 120°C for 4 min.

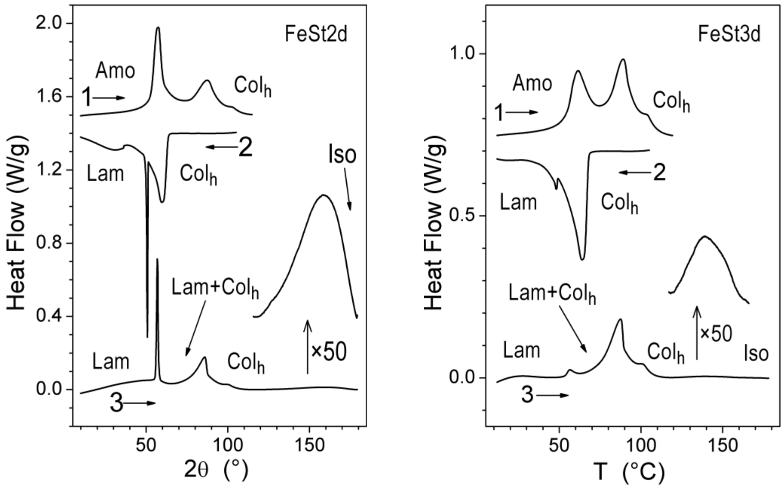

Figure III.34 - DSC curves of dehydrated iron stearates.

$FeSt_{2,d}$ and $FeSt_{3,d}$ are amorphous powders which crystallized on heating and then melted towards a mesophase around 100 °C. In both cases, the fusion phenomenon has the characteristic profile of a mixture forming an eutectic, with a fine peak, observed at about 55 °C., followed by an asymmetrical peak which extended to 90 °C, the overall melting enthalpy being about 50 J/g. These two systems are therefore mixtures. Obviously, annealing modified the iron stearate and led to the appearance of a second species, which probably coexisted with the initial one.

It is noted that this chemical transformation of the stearates stabilized the mesomorphism, since the mesophase appeared as soon as the first heating took place and since the transition to the isotropic liquid, although very broad, is delayed at 130-175 °C for $FeSt_{2d}$ and 125-160 °C for $FeSt_{3d}$, for enthalpy variations of 5 J/g and 1.1 J/g respectively.

III.3.2.4.3 IR spectroscopy in temperature

IR spectra have been recorded as a function of the temperature to evidence some structural evolutions during the dehydration step (Figure III.35). From IR spectra in Figure III.36, the main bands corresponding to CH_2 (band around 2918 cm^{-1}), CO_2 (around 2361 cm^{-1}), carboxylate (around 1545 cm^{-1} for $FeSt_2$ and 1580 cm^{-1} for $FeSt_3$) and water (around 3465 cm^{-1} for $FeSt_2$ and 3415 cm^{-1} for $FeSt_3$) fonctions have been followed as a function of temperature through a method developped by Pr Corinne Petit at the Institut of chemistry and Process for energy, environment and health. An additional band has been followed for $FeSt_3$ at about 1113 cm^{-1} ascribed to C-C stretching. In the following discussion, we considered only the thermal behavior below 150°C as the thermal decomposition process leading to NPs will be developped in the next paragraph.

These curves in Figure III.36 may be related to TGA curves: the water weight loss is clearly observed below 100°c for FeSt$_2$ and below 50°C with FeSt$_3$. That is in agreement with TGA curves where a weight loss is observed at these temperatures for hydrated stearates. Similarly the IR band at 1620 cm^{-1} in Figure III.35 disappeared above 100°C for FeSt$_2$ and above 50°C for FeSt$_3$ which confirmed that this band is correlated to water adsorption. In Figure III.36 for FeSt$_3$, an increase in the water band is observed above 50°C around 100°C together with some features in CH$_2$, COOH and C-C bands which may be related to the evaporation of freee stearic acid which has been identified in FeSt$_3$ by SAXS and IR spectroscopy.

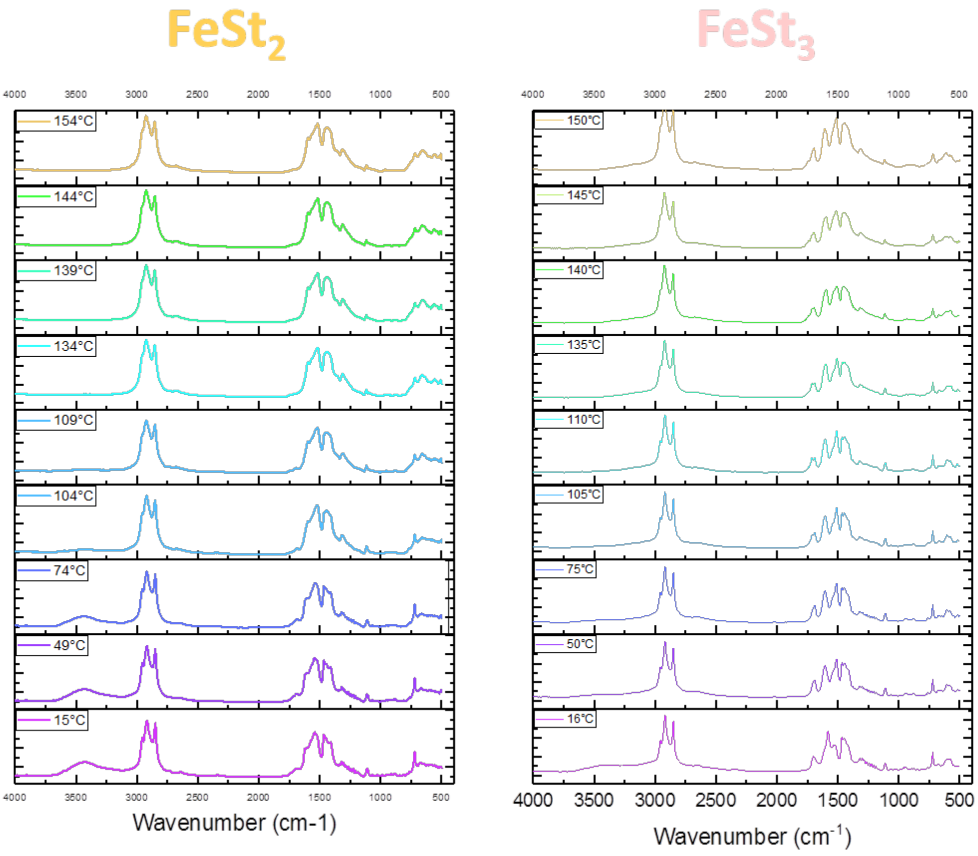

Figure III.35 - IR spectra of FeSt2 (left) and FeSt3 (right) as function of temperature

The wagging bands in Figure III.35 are strongly attenuated between 75-100°C for FeSt$_2$ and this effect is shifted up to at least 140°C for FeSt$_3$. That is certainly due to dehydratation which affected the lamellar structure of hydrated iron stearates. Indeed in Figure III.36, the evolution of the water band is often correlated to the evolution of the CH$_2$ band. It is again in agreement with TGA/DTA curves where the loss of lamellar structure is suggested above 70°C for FeSt$_2$ and around 150°C for FeSt$_3$.

In Figure III.35, the carbonyl symmetric stretching bands of both stearates did not seem affected by the temperature increase while those of FeSt$_2$ tended to not evolve but to be more resolved and those assymetric evolved strongly for FeSt$_3$ and. Indeed the intensity of the band corresponding to chelate coordination at 1515 cm^{-1} increased from 50°C for FeSt$_3$. This may be related to the COOH band evolution in Figure III.36 where the COOH band (chelate coordination) is quite not affected by the heat treatment up to 140°C for $FeSt_2$ when that of $FeSt_3$ (bridging coordination) strongly decreased from 50°C. That is in agreement with the observation that the dehydration of $FeSt_3$ favoured the chelate coordination.

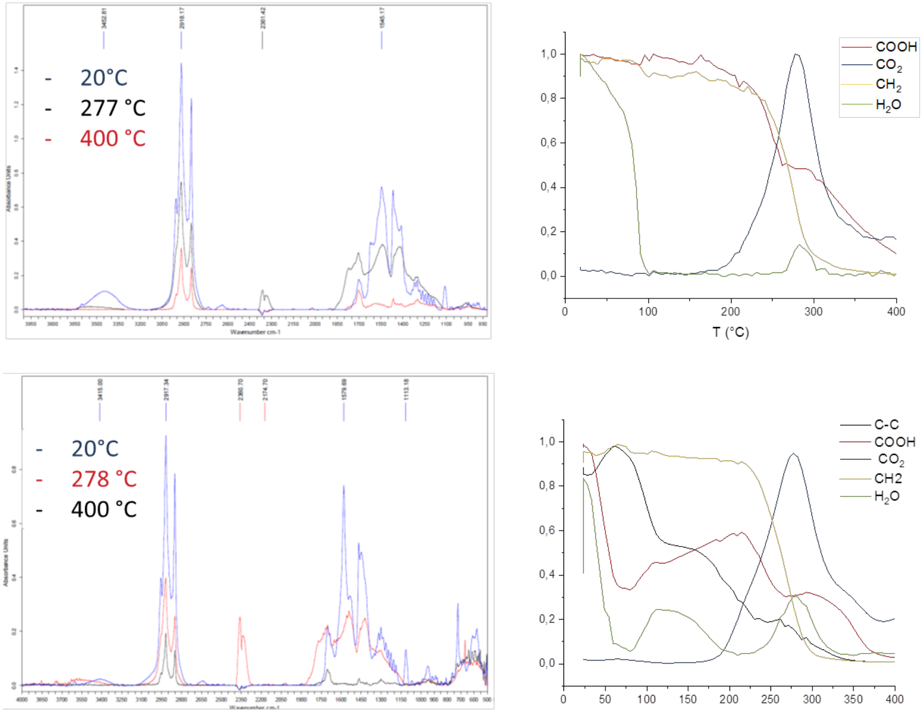

Figure III.36 - Evolution of IR bands of FeSt2 (top) and FeSt3 (down) as a function of heat treatment under air

The correlation between TGA/DTA experiments and IR spectroscopy (Table III.12) suggested that during the heat-treatment up to 140°C, $FeSt_3$ is dehydrated from 50°C [resulting in the reduction of Fe^{3+} in Fe^{2+}] which favored the modification of carboxylate coordination from bridging to chelate. One may suppose that the bridging coordination which has evolved towards the chelate one is those which involved water molecules.

Table III.12 – Events observed in DTG and IR(T)

Increasing T	**FeSt2**			**FeSt3**		
	TGA	**DTA**	**IR (T)**	**TGA**	**DTA**	**IR(T)**
	Low constant wl					
35-60°C				wl step	exothermal peak at 50°C	Disappearence of water bands
70°C			Loss of lamellar structure above 70°C	No weight loss	Endothermal peak	Intensity increase of chelate band Reduction of Fe^{2+}
100°C	wl step	Large endothermal peak = 2 peaks	Disappearence of water bands	90 °C no wl 100°C	2 endothermal peaks: 90-	Oxidation of Fe^{3+}

			Reduction of Fe^{3+}	**wg step**	100°C	
150°C	**wg step**		Oxidation of Fe^{2+}			Loss of lamellar structure
160°C	wl step	Broad endo peak				

III.3.2.5 Conclusion on the structure of iron stearates

All iron stearates have been shown to be composed of Fe^{3+} by Mössbauer spectroscopy and ERP except $FeSt_2$ which contained some Fe^{2+}. IR spectroscopy demonstrated that the carboxylates of stearates are coordinated to the iron cation through a mixture of chelate and bridging bidentate coordinations. The chelate coordination is majoritary in $FeSt_2$ and $FeSt_{2,d}$ when it is mainly bridging for $FeSt_3$ with some water molecules involved in bridging coordinations. For both hydrated stearates, the dehydration triggered the chelate coordination. These carboxylate and water coordinations have been confirmed by modeling experiments.

The combination of elemental analyses and TGA results suggested a composition lower in stearates than the expected one but it is coherent with consideration of structures involving iron stearates presenting a mixture of bridging and chelate bidentate coordinations (Figure III.19). The mean composition would be close to $FeSt_{2.1}@15H_2O$ for $FeSt_3$, $FeSt_{2.1}@5H_2O$ for $FeSt_{3,d}$, $FeSt_{1.8}@6H_2O$ for $FeSt_2$ and $FeSt_{1.5}@2H_2O$ for $FeSt_{2,d}$. Nevertheless from all characterizations, all stearates should display a distribution of iron stearates with different composition in stearates: $FeSt_x$.

III.3.3 Thermal decomposition of iron stearates

IR and Mössbauer spectroscopies as a function of temperatures, TGA analyses up to 600°C and modeling have been performed to analyze the thermal behavior of iron stearates and to try to understand the decomposition mechanism and in particular the very strong influence of the water coordination on the thermal behavior of both types of stearates.

III.3.3.1 TGA/DTG/DTA curves

TGA curves presented in Figure III.2, showed that the main weight loss occured above 200°C and several main steps were observed. The comparison of TGA curves performed on different samples (Figure III.37) showed that these features were observed in all samples but their amplitude and temperature did vary which could be attributed again to different hydration degrees of iron stearates which will affect the type of coordination and thus the decomposition kinetics.

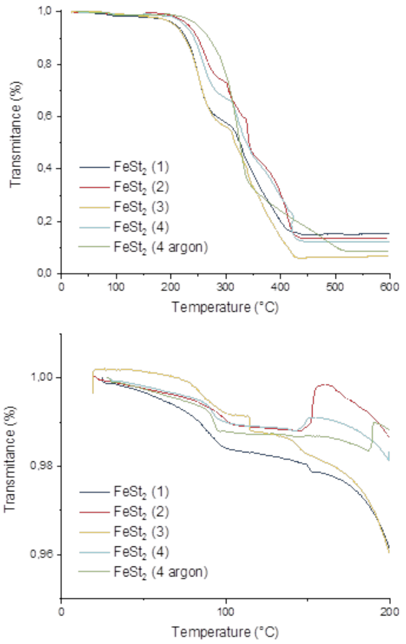

Figure III.37 - TGA curves of different samples of hydrated iron stearates.

The first weight loss occured in the temperature range 180-290°C, then the weight loss stabilized slightly and another large weight is observed from about 300±20°C which can be decomposed in at leat three steps and certainly more (see red curves in TGA curves in Figure III.38). An endothermal reaction is clearly visible in some curves between 425-450°C. The weight loss stopped at about 450°C for all iron stearates.

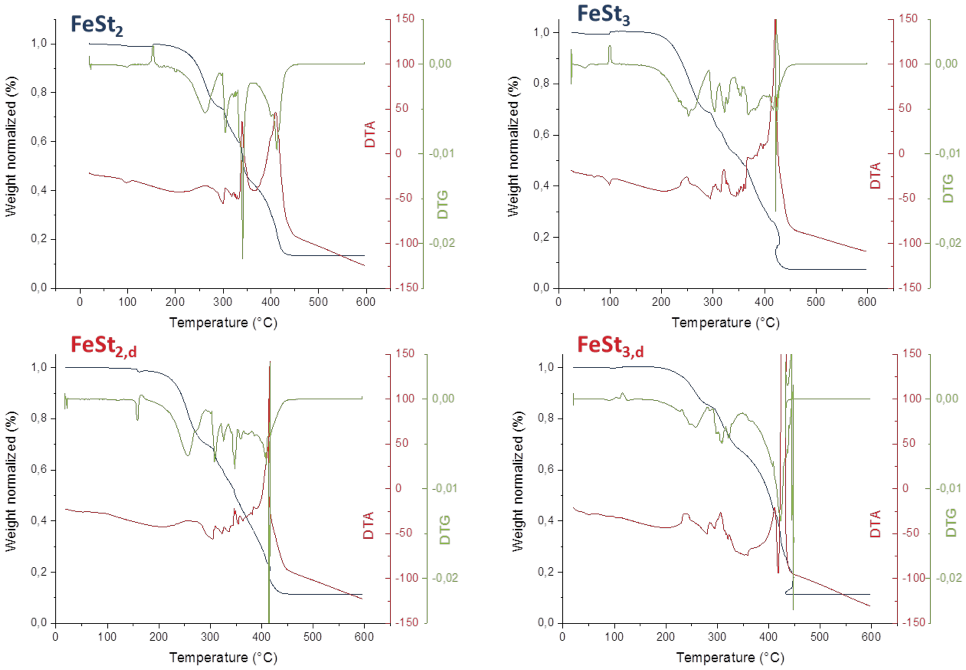

Figure III.38 – ATG (black)/DTG(green)/DTA(red) curves of all stearates

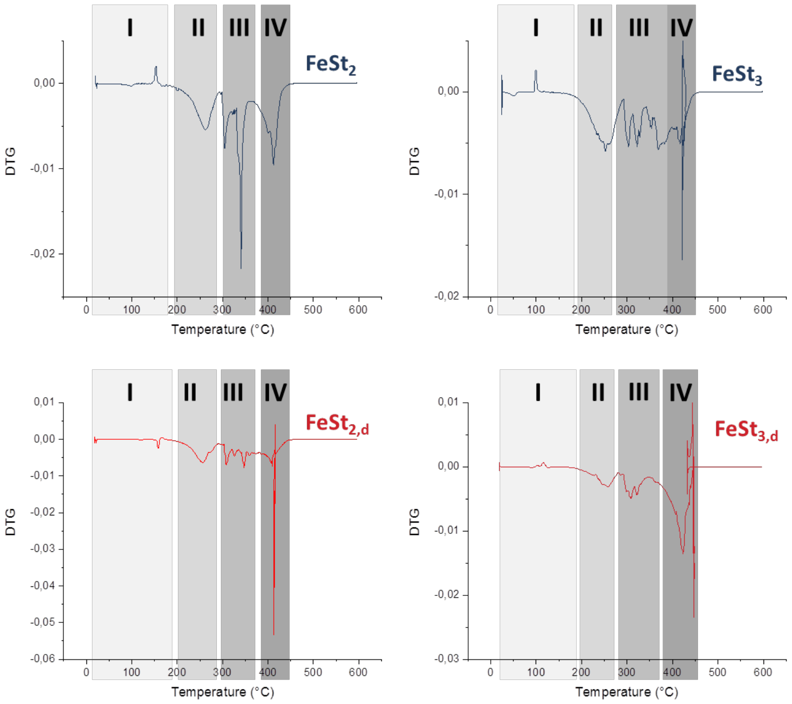

Figure III.39 - DTG curves of all FeSt

The DTG curves (Figure III.38 and Figure III.39) evidenced at least four weight losses with an important one at 340°C for FeSt$_2$. The DTG peaks for FeSt$_3$ are less resolved but at least five main features may be noticed and especially one at 420°C which should correspond to a sudden decomposition of a product. With dehydrated samples, the DTG peak intensity has strongly decreased and the peak at 250°C is always observed. A sudden weight loss is observed around 420°C for FeSt$_2$ and 450°C for FeSt$_3$ which presented also an additional weight loss before this peak at 420°C.

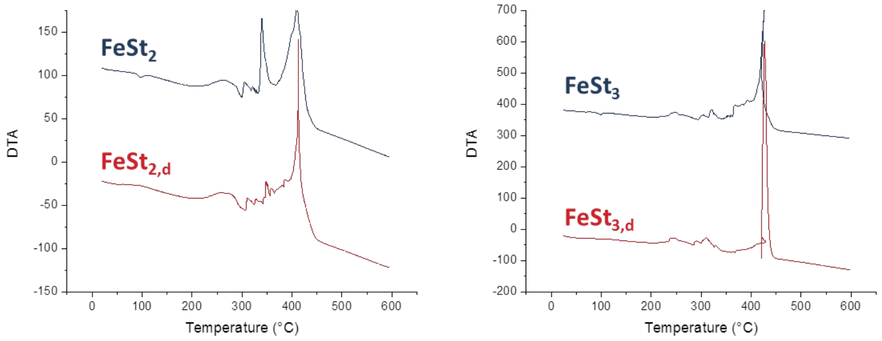

Figure III.40 - DTA curves of all stearates

The DTA curves (Figure III.38 and Figure III.40) displayed two main exothermal peaks for FeSt$_2$ at 340 and 420 °C when those of FeSt$_3$ displayed one main peak at 420°C. Both dehydrated iron stearates exhibited one exothermal peak at 440°C but an important endothermal peak is also noticed.

Table III.13 – List of the events observed on the TGA curves

FeSt$_2$		**FeSt$_3$**		**FeSt$_{2,d}$**		**FeSt$_{3,d}$**	
DTG	**DTA**	**DTG**	**DTA**	**DTG**	**DTA**	**DTG**	**DTA**
260, m	Exo, br w	250,m	Exo, Br m	260, s	Exo, br w	250 m	Exo br
300, m	Endo, w	300, m	Exo,m	310m	Exo,w	300m	
340, s	Exo, s	320, m	Exo, m	330w	Exo,w		
		350, w	Exo, w	350, m	Exo, w		
		380 s	Exo, s			380 w	Exo w
410 s	Exo, s	410,s	Exo, s	410s	Exo,s	410s	Exo,s

From earlier studies, the first weight loss would correspond to the first step leading to sufficient monomer for the germination step[10,11,13]. Bronstein et al[30] have also investigated the thermal decomposition of iron oleates by TGA and observed four main DTA peaks, one corresponding to solvant evaporation, one around 240°C corresponding to the germination, one around 300°C attributed to the growth step and the last one above 400°C due to decomposition or organic molecules. Therefore from these considerations, one may conclude that all stearates induced a germination at quite the same temperature as they all exhibited a DTA peak around 240-250°C. The two peaks at 300 and above 400°C are also observed but between 240 and 400°C, several peaks are observed depending on the iron stearates. This peak distribution may be ascribed to the presence of a distribution of iron stearates with different chemical stabilities. That would be in agreement with previous results which have strongly suggested a distribution of iron stearates with mixed chelate and bridging coordinations. One may notice that the last peak is observed around 300°C for FeSt$_2$ and FeSt$_{2,d}$ when it is at higher temperature for FeSt$_3$ and FeSt$_{3,d}$. That suggested that the decomposition of all stearates is quite finished at 340°C (all the monomers have been generated) for FeSt$_2$ and FeSt$_{2,d}$ when a higher temperature (380°C) needs to be reached to induce the decomposition of all different stearates in FeSt$_3$ and FeSt$_{3,d}$. These conclusions explained the results observed during the NPs synthesis from all stearates: the low decomposition yield of FeSt$_3$ and FeSt$_{3,d}$ by comparison with that with FeSt$_2$ and FeSt$_{2,d}$ is explained by the NPs synthesis temperature at ~290°C which allowed decomposing most of iron stearates in FeSt$_2$ and FeSt$_{2,d}$ when a higher temperature would have been necessary to decompose all stearates in FeSt$_3$ and FeSt$_{3,d}$.

The sudden weight loss observed above 400°C may be attributed to CO$_2$ departure. Indeed the decomposition of iron alcanoates has been largely investigated and is known to lead to the formation of ketones and CO$_2$[36]. That was confirmed by IR experiments in temperature: a CO$_2$ band, whose intensity increased and then decreased, is observed in this temperature range as depicted in Figure III.36.

III.3.3.2 Mössbauer spectrometry after heat treatments

To get better insight in the oxidation degree of iron cations during the thermal decomposition of FeSt$_2$ and FeSt$_3$, Mössbauer spectra at different temperatures and heating times up to 140°C have been recorded using a cryofurnace where the powdered sample remained under vacuum. The refined values of the Mössbauer parameters are given in Table III.14.

Table III.14 - Mössbauer parameters (IS: isomer shift; QS: quadrupole splitting Area: proportions assuming that they are proportional to their respective absorption areas).

T(K)	**FeSt2**			**FeSt3**		
	IS (mm.s^{-1}) ±0.01	**QS (mm.s^{-1}) ±0.02**	**Area % ±2**	**IS (mm.s^{-1}) ±0.01**	**QS (mm.s^{-1}) ±0.02**	**Area % ±2**
77K	0.50	1.15	42	*0.52*	*0.76*	*55*

	0.51	*0.70*	*57*	0.53	0.52	45
77K sous vide	0.50	1.07	48	*0.53*	*0.71*	*56*
	0.50	0.64	52	0.51	0.50	44
Heat treatments						
1h at 50°C	0.52	1.31	16	*0.53*	*0.68*	*71*
	0.51	*0.72*	*84*	0.39	0.38	29
1h at 50°C + 1h at 100°C	0.52	1.25	25	*0.52*	*0.82*	*38*
	0.52	*0.71*	*75*	0.49	0.38	62
1h at 50°C + 1h at 100°C + 1h at 140°C	0.58	1.35	22	*0.53*	*0.69*	*87*
	0.52	*0.69*	*69*	0.24	0.34	13
	1.25	3.11	9			
1h at 50°C + 1h at 100°C + 1h at 140°C + 15h-FeSt$_2$ and 20h-FeSt$_3$ at 140°C	0.74	1.06	11	*0.52*	*0.77*	*56*
	0.49	*0.77*	*75*	0.28	0.34	20
	1.24	3.01	14	1.27	2.78	24

Mössbauer spectra gave evidence for the appearance of a new quadrupolar doublet from 140°C under vacuum for iron stearate which isomer shift is attributed to Fe(+II). Thus a reduction of Fe^{3+} occured for both iron stearates. As these experiments have been conducted after heat treatments in vacuum, this reduction should take place at higher temperature during TGA experiments under air. Such a reduction of iron III in iron carboxylates has already been observed in other studies by Mössbauer spectroscopy but their Mössbauer spectra were only recorded at room temperature preventing thus the comparison to be clearly achieved[76,77]. Nevertheless it is consistent with the identification of magnetite in samples after the thermal decomposition[12,13] which supposed that Fe^{3+} cations have been reduced during the thermal process.

With FeSt$_2$, one may notice that the quadrupolar doublet (IS around 0.5 and QS around 0.7 mm.s^{-1}) is always present whatever the heat-treatment and its proportion tends to increase with heating treatment. Therefore this doublet can be attributed to Fe^{3+} without bonding to water molecules. With the second doublet, an increase in IS and QS is observed with heating and when Fe^{2+} cations appeared, its proportion decreased and its isomer shift increased up to 0.74 mm.s^{-1} showing Fe with an intermediate isomer shift value between Fe(+II) and Fe(+III). It should correspond to FeIII cations beginning to be transformed into Fe(+II). Therefore the two Fe(+III) environments in FeSt$_2$ are one environment without water molecules around Fe(+III) and one environment with water molecules whose removal induced its reduction in Fe(+II).

With FeSt$_3$, the doublet with an IS value close to 0.5 and a QS value around 0.7 has been attributed to iron with quite no bonded water. It corresponds also to a low spin Fe(+III) with an octahedral configuration too. For the other doublet, a decrease of the IS and QS values is observed down to respectively 0.28 and 0.34. Such a low value of IS with Fe(+III) ions suggested a coordination 4 and a tetrahedral configuration. The third doublet is characterized by Mössbauer parameters typical of high-spin Fe(II) in a six-coordinated environment [IS(77 K)=1.26-1.24 mms-1 and ΔE_Q = 2.68 mm s-1].

Therefore these Mössbauer spectra as a function of temperature demonstrated that Fe^{3+} cations are reduced during the thermal treatment under vacuum from 140°C, which could be extrapolated to about 250°C. $FeSt_2$ underwent a reduction before $FeSt_3$. These results demonstrated that the reduction of Fe^{3+} occurred during the germination step.

III.3.3.3 IR spectroscopy after heat treatments

IR spectra as a function of temperature have also been performed above 150°C and are presented in Figure III.36 and Figure III.41. The consideration of Fe-O bands in the range 1000-500 cm^{-1} showed that the intensity of these bands increased from 265°C for $FeSt_2$ and from 300°C for $FeSt_3$. It confirmed again that the nucleation step occured during the first weight loss in TGA curves (figure III.38) between 200 and 300°C for both precursors. The decomposition of $FeSt_2$ would be faster than that of $FeSt_3$.

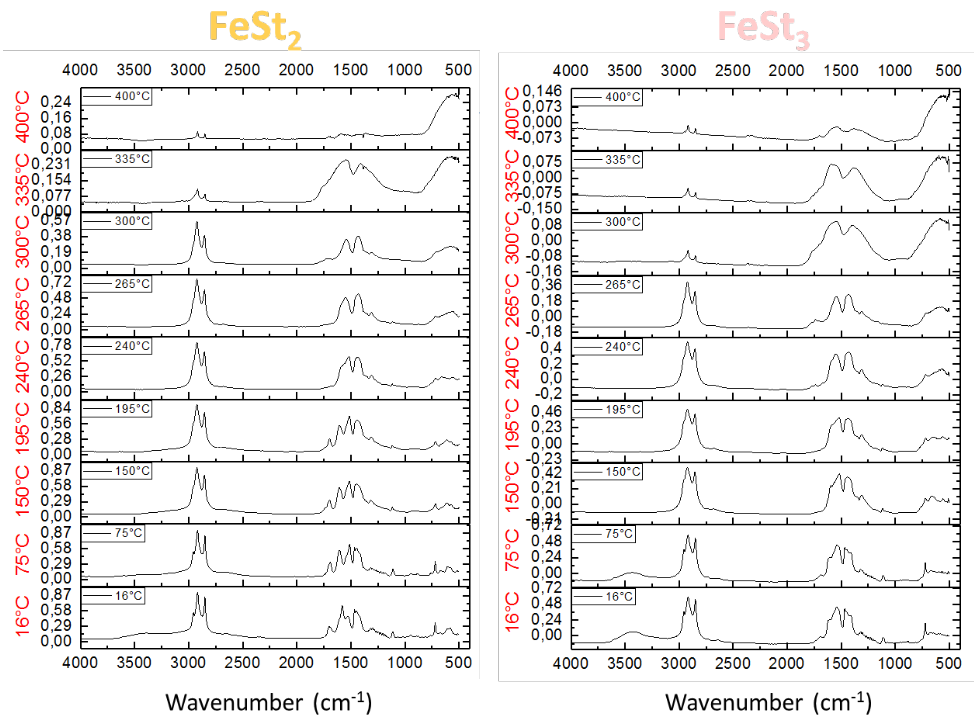

Figure III.41 – IR spectra Hydrated $FeST_x$ with T

Table III.15 – Proposed link between TD and TGA events

$FeSt_2$	**$FeSt_3$**	**$FeSt_{2,d}$**	**$FeSt_{3,d}$**	**Proposed link with TD**	**Region in DTG (Fig A.2)**
260, m	250,m	260, s	250 m	Alkyl chain desorption + Germination	**II**
300, m	300, m	310m	300m	Beginning of decomposition	**III**
340, s	320, m	330w		End of decomposition $FeSt_2$	
	350, w	350, m		End of decomposition $FeSt_2$,d	
	380 s		380 w	End of decomposition both $FeSt_3$	
410 s	410,s	410s	410s	Burning of chains + CO_2 degagement	**IV**

Description of the events noticed in TGA curves (Figure III.38) can be linked to the major events observed in TD (Table III.15).

For $FeSt_2$: Together with the appearence of Fe-O bands and thus formation of germs at 265°C, we observed a change in the carboxylate coordination (1800-1300 cm^{-1}): the band corresponding to bridging carboxylate disappeared and a new band at 1700°C characteristic of free stearates appeared.

Therefore the coordination of carboxylate is mainly chelate and should correspond to the anchoring of stearate chains at the surface of germs. At 300°C, the carboxylate bands are broaden and the intensity of the CH_2 bands in the range 3000-2600 cm^{-1} has strongly decreased as well as the IR band at 716 cm^{-1} which suggest the burning of alkyl chains.

With $FeSt_3$: at 240°C, the band at 1700 cm^{-1} disappeared and the carboxylate bands broadened. At 300°C, the coordination of carboxylates is mainly chelate and the 1700 cm^{-1} band appeared again. It corresponded to the formation of germs and coordination of stearates at the surface of germs. By contrast to $FeSt_2$, the bands of alkyl chains (3000-2600 cm^{-1}) are always present at 300°C but their intensity also decreased with the temperature increase.

At 400°C for both stearates, the intensity of Fe-O band is high but those of alkyl chains and carboxylate groups are very low showing that the stearate chains have burnt. That is confirmed by the observation of CO_2 band in this temperature range as well as water band. The thermal decomposition of stearate chains generated CO_2 and water.

III.3.3.4 Modeling

To inspect the desorption process of the stearate chain, since non-negligible activation barriers might exist and since these are beyond the reach of standard molecular dynamics simulations, we resorted on the free energy sampling technique known as Blue Moon ensemble[78]. The reaction coordinate inspected within this approach was the distance between the metal atom and the carboxylate group of one of the two stearate chain. Results in dry and wet conditions are summarized in Figure III.42 and III.43. From these simulations on iron stearate, stearate chains desorbed from iron cations, releasing iron atoms and thus the nucleation of iron oxide NPs may occur. However, the desorption seems to be easier in dry conditions, where a free energy barrier of about 15.02 kcal/mol has to be overcome, than in wet conditions, where this same activation barrier increases to larger values, thus making energetically more demanding the desorption of stearate chains.

This modeling established clearly the role of water in the stabilisation of iron stearate and explained our experimental results which have shown that $FeSt_3$ which is more hydrated than $FeSt_2$ decomposed at higher temperature than $FeSt_2$ and thus led to a nucleation at higher temperature.

It explained also how the dehydration induced a loss of the lamellar structure.

Modeling simulation on the hydrated complex showed that the dehydration caused by the temperature induced the departure of a water molecule along with the reduction of Fe^{3+} in Fe^{2+}. As it is shown in figure III.43 that is during this step a Fe-O bond is created.

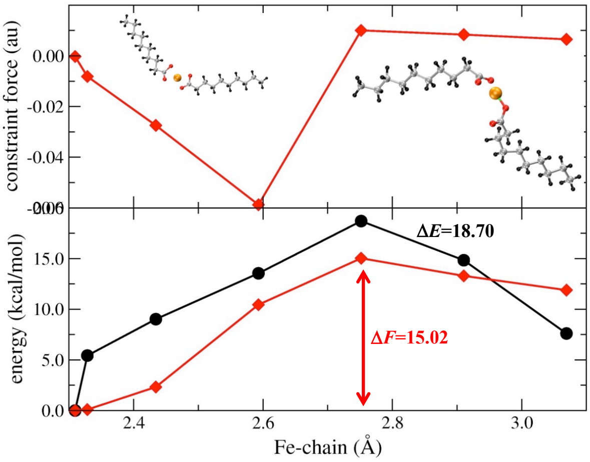

Figure III.42 - Equilibrium geometries of Fe-based stearates at 300 K in wet conditions. Constraint force (upper panel) and free and total energies (lower panel) for the desorption of the chain in Fe-based *stearates at 300 K in dry conditions. The free energy profile is shown by the red line and the total energy one by the black line. The free energy barrier to the desorption, indicated in the lower panel, amounts to 15.02 kcal/mol.*

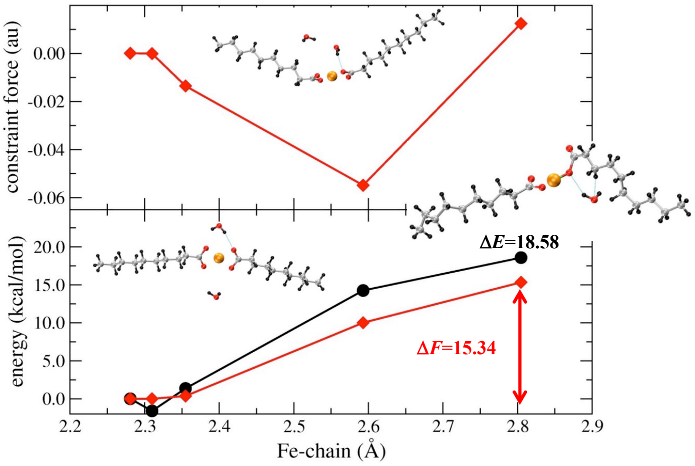

Figure III.43 - Fe-based stearates at 300 K in wet conditions. Constraint force (upper panel) and free and total energies (lower panel) for the desorption of the Fe-based stearates at 300 K in wet conditions. The free energy profile is shown by the red line and the total energy one by the black line. The free energy barrier to the desorption, indicated in the lower panel, is already larger than 15.34 kcal/mol (calculations still in progress) before the completion of the desorption process.

III.3.3.5 Conclusion on the thermal decomposition process

The different characterization techniques have shown that Fe^{3+} is reduced during the germination step, that the nucleation step occured during the first weight loss in TGA curves between 200 and 300°C. The decomposition of $FeSt_2$ is occurring at lower temperature than $FeSt_3$. The decomposition of $FeSt_2$ and $FeSt_{2,d}$ would end around 340°C when higher temperatures are needed to decompose completely $FeSt_3$ and $FeSt_{3,d.}$ Modeling confirmed that the presence of water molecules made the decomposition of stearates more difficult.

III.3.4 Conclusion

Two iron stearate precursors have been synthesized by co-precipitation of hydrated Fe(+II) and Fe(+III) chlorides and sodium stearate and they have been dehydrated. $FeSt_3$ appeared more hydrated than $FeSt_2$ and all stearates exhibited a distribution of carboxylate coordination (bridging and chelate bidentate coordination) on iron cation. The coordination is mainly bridging for $FeSt_3$ when it is mainly chelate for $FeSt_2$. After their dehydration process which has induced a higher weight loss for $FeSt_3$ than for $FeSt_2$, the coordination evolved towards the chelate one for $FeSt_3$ when it stayed mainly chelate for $FeSt_2$. The presence of a mixed coordination in these stearates explained why their composition in stearate chains is lower than the expected one. Even if a distribution of stearate compounds with different thermal stabilities existed in all iron stearates, the mean composition would be close to $FeSt_{2.1}$@$15H_2O$ for $FeSt_3$, $FeSt_{2.1}$@$5H_2O$ for $FeSt_{3,d}$, $FeSt_{1.8}$@$6H_2O$ for $FeSt_2$ and $FeSt_{1.5}$@$2H_2O$ for $FeSt_{2,d}$.

Their decomposition has been investigated by using different characterization techniques such as TGA, Mössbauer and IR spectroscopies as a function of temperature and modeling. TGA showed that all iron stearates displayed a distribution of precursors which decompose at different temperatures: up to 380°C for $FeSt_3$ and $FeSt_{3,d}$ and to 340-350°C for $FeSt_2$ and $FeSt_{2,d}$. These results are in agreement with previously published results[29,31] where the monomer formation, has been found to be reaction time- and/or temperature-dependent.

Mössbauer spectroscopy showed a reduction of Fe^{3+} during the germination step and the reduction occured at lower temperature for $FeSt_2$. From IR spectroscopy, $FeSt_2$ induced a nucleation at lower temperature than $FeSt_3$. The decomposition of $FeSt_2$ would be faster than that of $FeSt_3$. Modeling experiments confirmed that less hydrated samples would be easier to decompose than hydrated samples. It confirmed the different observed results that $FeSt_3$ which is more hydrated than $FeSt_2$ decomposed up to higher temperatures.

If we relate these results to the observed size of NPs and to the formation of nanocubes, we can explain the slightly lower size of spheres with $FeSt_3$ and $FeSt_{3,d}$ to a larger distribution of precursors by comparison with $FeSt_2$, which decompose up to higher temperature (340°C for $FeSt_2$ and 380°C for $FeSt_3$). The nucleation step occurs quite at the same temperature but the amount of nuclei and their size may be different as a function of the monomer concentration at this step. Afte rthat, the comparison of the distribution of precursors which exhibit different decomposition temperatures suggested that the kinetic of decomposition is faster with $FeSt_2$ than with $FeSt_3$. At 350°C, from DTA and DTG curves, quite all $FeSt_2$ has been decomposed when higher temperature are needed for $FeSt_3$. That may explain why the nanosphere size is slightly lower for $FeSt_3$: the amount of monomer available at the boiling point of solvent was certainly lower than that with $FeSt_2$.

The structure and hydratation degree of iron stearates were shown to have no influence on the synthesis of spherical NPs but one on that of nanocubes. That may be explained by kinetic considerations of the monomer generation. Indeed the nucleation occurs at quite the same temperature for the four stearates but the monomer concentration may be different depending on the type of stearates leading thus to different nuclei sizes and amount. The fact that a reduction of Fe^{3+} is observed during the germination step suggested that the nuclei are composed of wustite. This is supported by the fact that we know from earlier studies that the nanocubes are core-shell with a core of wustite and a shell of magnetite attributed to an oxidation of wustite. However with the nanosphere reaction mixture, spinel iron oxide NPs are formed, which means that FeO nuclei have been oxidized during the synthesis process and certainly during the growth step. Therefore considering the different reaction mixture and heating temperature, one may suggest that oleate chains should contribute to prevent nuclei from oxidation. However the nanocube shape is favored with dehydrated stearates by contrast with the hydrated ones. Several hypotheses can be made: water contributed to the oxidation of nuclei or the water destabilized the oleate shell at the nuclei surface favouring oxygen diffusion or the dehydrated stearates decomposed faster leading to a high growth kinetic inhibiting/hindering the oxidation.

After dehydration, the distribution of precursors seems less broad. After the germination step around 250°C, the weight loss is faster suggesting a faster monomer formation kinetic in agreement with modeling experiments. Thus dehydrated iron stearates favour a high growth kinetic. The cubic shape formation is thus suggested to be favour by a high growth kinetic. That would be in agreement with the fact that nanocubes are generally obtained when applying high heating rates.

There should be a competition between the kinetic of oxydation and growth of nuclei depending on the monomer generation kinetic during the increase in temperature (from 240°C up to the boiling point). Slow growth kinetic due to a slow monomer formation kinetic should favour the oxidation of NPs when the high growth rate would hamper their oxidation.

REFERENCES

1. Yin, Y. & Alivisatos, A. P. Colloidal nanocrystal synthesis and the organic–inorganic interface. *Nature* **437,** 664–670 (2005).
2. Park, J., Joo, J., Kwon, S. G., Jang, Y. & Hyeon, T. Synthesis of Monodisperse Spherical Nanocrystals. *Angewandte Chemie International Edition* **46,** 4630–4660 (2007).
3. Cushing, B. L., Kolesnichenko, V. L. & O'Connor, C. J. Recent advances in the liquid-phase syntheses of inorganic nanoparticles. *Chem. Rev.* **104,** 3893–3946 (2004).
4. de Mello Donegá, C., Liljeroth, P. & Vanmaekelbergh, D. Physicochemical Evaluation of the Hot-Injection Method, a Synthesis Route for Monodisperse Nanocrystals. *Small* **1,** 1152–1162 (2005).
5. Reiss, P., Protière, M. & Li, L. Core/Shell Semiconductor Nanocrystals. *Small* **5,** 154–168 (2009).
6. Burda, C., Chen, X., Narayanan, R. & El-Sayed, M. A. Chemistry and Properties of Nanocrystals of Different Shapes. *Chem. Rev.* **105,** 1025–1102 (2005).
7. Kumar, S. & Nann, T. Shape control of II-VI semiconductor nanomaterials. *Small* **2,** 316–329 (2006).
8. Tao, A. R., Habas, S. & Yang, P. Shape Control of Colloidal Metal Nanocrystals. *Small* **4,** 310–325 (2008).
9. Jun, Y., Choi, J. & Cheon, J. Shape control of semiconductor and metal oxide nanocrystals through nonhydrolytic colloidal routes. *Angew. Chem. Int. Ed. Engl.* **45,** 3414–3439 (2006).
10. Park, J. *et al.* Ultra-large-scale syntheses of monodisperse nanocrystals. *Nat Mater* **3,** 891–895 (2004).
11. Sun, S. *et al.* Monodisperse MFe2O4 (M = Fe, Co, Mn) nanoparticles. *J. Am. Chem. Soc.* **126,** 273–279 (2004).
12. Demortière, A. *et al.* Size-dependent properties of magnetic iron oxide nanocrystals. *Nanoscale* **3,** 225–232 (2011).
13. Baaziz, W. *et al.* Magnetic Iron Oxide Nanoparticles: Reproducible Tuning of the Size and Nanosized-Dependent Composition, Defects, and Spin Canting. *J. Phys. Chem. C* **118,** 3795–3810 (2014).
14. Kovalenko, M. V. *et al.* Fatty Acid Salts as Stabilizers in Size- and Shape-Controlled Nanocrystal Synthesis: The Case of Inverse Spinel Iron Oxide. *J. Am. Chem. Soc.* **129,** 6352–6353 (2007).
15. Pichon, B. P. *et al.* Microstructural and Magnetic Investigations of Wüstite-Spinel Core-Shell Cubic-Shaped Nanoparticles. *Chem. Mater.* **23,** 2886–2900 (2011).
16. Kim, D. *et al.* Synthesis of Uniform Ferrimagnetic Magnetite Nanocubes. *Journal of the American Chemical Society* **131,** 454–455 (2009).
17. Chaudret, B. Organometallic approach to nanoparticles synthesis and self-organization. *Comptes Rendus Physique* **6,** 117–131 (2005).
18. Dumestre, F., Chaudret, B., Amiens, C., Renaud, P. & Fejes, P. Superlattices of iron nanocubes synthesized from Fe[N(SiMe3)2]2. *Science* **303,** 821–823 (2004).
19. Peddis, D. *et al.* Cationic distribution and spin canting in CoFe2O4 nanoparticles. *J Phys Condens Matter* **23,** 426004 (2011).
20. Baaziz, W. *et al.* Tuning of Synthesis Conditions by Thermal Decomposition toward Core–Shell CoxFe1–xO@CoyFe3–yO4 and CoFe2O4 Nanoparticles with Spherical and Cubic Shapes. *Chem. Mater.* **26,** 5063–5073 (2014).
21. Deatsch, A. E. & Evans, B. A. Heating efficiency in magnetic nanoparticle hyperthermia. *Journal of Magnetism and Magnetic Materials* **354,** 163–172 (2014).
22. Wetterskog, E., Tai, C.-W., Grins, J., Bergström, L. & Salazar-Alvarez, G. Anomalous Magnetic Properties of Nanoparticles Arising from Defect Structures: Topotaxial Oxidation of $Fe_{1-x}O|Fe_{3-\delta}O_4$ Core|Shell Nanocubes to Single-Phase Particles. *ACS Nano* **7,** 7132–7144 (2013).
23. Guardia, P. *et al.* Water-Soluble Iron Oxide Nanocubes with High Values of Specific Absorption Rate for Cancer Cell Hyperthermia Treatment. *ACS Nano* **6,** 3080–3091 (2012).
24. Guardia, P. *et al.* One pot synthesis of monodisperse water soluble iron oxide nanocrystals with high values of specific absorption rate. *J. Mater. Chem. B* (2014). doi:10.1039/C4TB00061G
25. LaMer, V. K. & Dinegar, R. H. Theory, Production and Mechanism of Formation of Monodispersed Hydrosols. *J. Am. Chem. Soc.* **72,** 4847–4854 (1950).
26. Kwon, S. G. & Hyeon, T. Formation Mechanisms of Uniform Nanocrystals via Hot-Injection and Heat-Up Methods. *Small* **7,** 2685–2702 (2011).
27. Xia, Y., Xiong, Y., Lim, B. & Skrabalak, S. E. Shape-controlled synthesis of metal nanocrystals: simple chemistry meets complex physics? *Angew. Chem. Int. Ed. Engl.* **48,** 60–103 (2009).
28. Kwon, S. G. *et al.* Kinetics of Monodisperse Iron Oxide Nanocrystal Formation by 'Heating-Up' Process. *Journal of the American Chemical Society* **129,** 12571–12584 (2007).
29. Hyeon, T., Lee, S. S., Park, J., Chung, Y. & Na, H. B. Synthesis of highly crystalline and monodisperse maghemite nanocrystallites without a size-selection process. *J. Am. Chem. Soc.* **123,** 12798–12801 (2001).
30. Bronstein, L. M. *et al.* Influence of Iron Oleate Complex Structure on Iron Oxide Nanoparticle Formation. *Chemistry of Materials* **19,** 3624–3632 (2007).
31. Kwon, S. G. *et al.* Kinetics of monodisperse iron oxide nanocrystal formation by 'heating-up' process. *J. Am. Chem. Soc.* **129,** 12571–12584 (2007).
32. Baaziz, W. *et al.* Magnetic Iron Oxide Nanoparticles: Reproducible Tuning of the Size and Nanosized-Dependent Composition, Defects, and Spin Canting. *The Journal of Physical Chemistry C* **118,** 3795–3810 (2014).
33. Herman, D. A. J. *et al.* How to choose a precursor for decomposition solution-phase synthesis: the case of iron nanoparticles. *Nanoscale* **7,** 5951–5954 (2015).
34. Teillet, J. & Varret, F. Unpublished MOSFIT program.

35. Nelson, P. N. & Taylor, R. A. Theories and experimental investigations of the structural and thermotropic mesomorphic phase behaviors of metal carboxylates. *Applied Petrochemical Research* **4,** 253–285 (2014).
36. Akanni, M. S., Okoh, E. K., Burrows, H. D. & Ellis, H. A. The thermal behaviour of divalent and higher valent metal soaps: a review. *Thermochimica Acta* **208,** 1–41 (1992).
37. Kwon, S. G. *et al.* Kinetics of Monodisperse Iron Oxide Nanocrystal Formation by 'Heating-Up' Process. *Journal of the American Chemical Society* **129,** 12571–12584 (2007).
38. Baaziz, W. *et al.* Magnetic Iron Oxide Nanoparticles: Reproducible Tuning of the Size and Nanosized-Dependent Composition, Defects, and Spin Canting. *The Journal of Physical Chemistry C* **118,** 3795–3810 (2014).
39. Liu, X. *et al.* Systematic Study of Exchange Coupling in Core–Shell Fe3−δO4@CoO Nanoparticles. *Chem. Mater.* **27,** 4073–4081 (2015).
40. Pérez, N., López-Calahorra, F., Labarta, A. & Batlle, X. Reduction of iron by decarboxylation in the formation of magnetite nanoparticles. *Phys Chem Chem Phys* **13,** 19485–19489 (2011).
41. Abrahamson, H. B. & Lukaski, H. C. Synthesis and characterization of iron stearate compounds. *Journal of Inorganic Biochemistry* **54,** 115–130 (1994).
42. Nakamoto, T., Katada, M. & Sano, H. Mixed-valence states of iron long-chain carboxylate complexes. *Inorganica Chimica Acta* **291,** 127–135 (1999).
43. Bouslimani, N. *et al.* Spontaneous Reduction of High-Spin FeIII Complexes Supported by Benzoic Hydrazide Derivative Ligands. *Eur. J. Inorg. Chem.* **2009,** 3734–3741 (2009).
44. Hendrich, M. P. & Debrunner, P. G. Integer-spin electron paramagnetic resonance of iron proteins. *Biophys. J.* **56,** 489–506 (1989).
45. Kirmse, R. Electron Paramagnetic Resonance of d Transition Metal Compounds. (Reihe: Studies in Inorganic Chemistry, Vol. 16.) Von F. E. Mabbs und D. Collison. Elsevier, Amsterdam, 1992. XX, 1326 S., geb. 995.00 hfl, 622.00 $. — ISBN 0-444-89852-2. *Angewandte Chemie* **106,** 609–609 (1994).
46. Andres, H. *et al.* Planar Three-Coordinate High-Spin FeII Complexes with Large Orbital Angular Momentum: Mössbauer, Electron Paramagnetic Resonance, and Electronic Structure Studies. *J. Am. Chem. Soc.* **124,** 3012–3025 (2002).
47. Prasad, S., Shinde, R. F. & Balakrishnan, I. Electron paramagnetic resonance spectroscopic studies of calcined FAPO-11 molecular sieve. *Microporous Materials* **2,** 159–162 (1994).
48. Walker, F. A. Models of the bis-histidine-ligated electron-transferring cytochromes. Comparative geometric and electronic structure of low-spin ferro- and ferrihemes. *Chem. Rev.* **104,** 589–615 (2004).
49. Sutton, C. C. R., da Silva, G. & Franks, G. V. Modeling the IR Spectra of Aqueous Metal Carboxylate Complexes: Correlation between Bonding Geometry and Stretching Mode Wavenumber Shifts. *Chem. Eur. J.* **21,** 6801–6805 (2015).
50. Deacon, G. B. & Phillips, R. J. Relationships between the carbon-oxygen stretching frequencies of carboxylato complexes and the type of carboxylate coordination. *Coordination Chemistry Reviews* **33,** 227–250 (1980).
51. Nakamoto, K. Applications in Inorganic Chemistry. in *Infrared and Raman Spectra of Inorganic and Coordination Compounds* 149–354 (John Wiley & Sons, Inc., 2008).
52. Zelenák, V., Vargová, Z. & Györyová, K. Correlation of infrared spectra of zinc(II) carboxylates with their structures. *Spectrochim Acta A Mol Biomol Spectrosc* **66,** 262–272 (2007).
53. Palacios, E. G., Juárez-López, G. & Monhemius, A. J. Infrared spectroscopy of metal carboxylates: II. Analysis of Fe(III), Ni and Zn carboxylate solutions. *Hydrometallurgy* **72,** 139–148 (2004).
54. Mehrotra, R. C. & Bohra, R. *Metal carboxylates*. (Academic Press, 1983).
55. Lu, Y. & Miller, J. D. Carboxyl Stretching Vibrations of Spontaneously Adsorbed and LB-Transferred Calcium Carboxylates as Determined by FTIR Internal Reflection Spectroscopy. *Journal of Colloid and Interface Science* **256,** 41–52 (2002).
56. Peddis, D. *et al.* Cationic distribution and spin canting in $CoFe_2O_4$ nanoparticles. *Journal of Physics: Condensed Matter* **23,** 426004 (2011).
57. Binnemans, K., Jongen, L., Bromant, C., Hinz, D. & Meyer, G. Structure and mesomorphism of neodymium(III) alkanoates. *Inorg Chem* **39,** 5938–5945 (2000).
58. Nelson, P. N. & Ellis, H. A. Odd–even chain packing, molecular and thermal models for some long chain sodium(I) n-alkanoates. *Journal of Molecular Structure* **1075,** 299–310 (2014).
59. Deacon, G. B., Huber, F. & Phillips, R. J. Diagnosis of the nature of carboxylate coordination from the direction of shifts of carbon oxygen stretching frequencies. *Inorganica Chimica Acta* **104,** 41–45 (1985).
60. Manhas, B. S. & Trikha, A. K. *J. Indian Chem. Soc.* 315 (1982).
61. Chernyshova, I. V., Ponnurangam, S. & Somasundaran, P. Adsorption of Fatty Acids on Iron (Hydr)oxides from Aqueous Solutions. *Langmuir* **27,** 10007–10018 (2011).
62. Nelson, P. N. & Taylor, R. A. Theories and experimental investigations of the structural and thermotropic mesomorphic phase behaviors of metal carboxylates. *Appl Petrochem Res* **4,** 253–285 (2014).
63. Daou, T. J. *et al.* Phosphate Adsorption Properties of Magnetite-Based Nanoparticles. *Chem. Mater.* **19,** 4494–4505 (2007).
64. Meesuk, L., Jayasooriya, U. A. & Cannon, R. D. Vibrational spectra of carboxylate complexes. VII. Partial valence trapping in a trinuclear mixed-valence iron(III,III,II) cluster: vibrational spectra of [Fe3O(OOCCH3)6L3] and related mixed-metal complexes. *J. Am. Chem. Soc.* **109,** 2009–2016 (1987).
65. Popescu, M. *et al.* Preparation and structure of ordered films of iron carboxylate complexes. *Thin Solid Films* **274,** 143–146 (1996).

66. Meesuk, L., Jayasooriya, U. A. & Cannon, R. D. Vibrational spectra of carboxylate complexes. VII. Partial valence trapping in a trinuclear mixed-valence iron(III,III,II) cluster: vibrational spectra of [Fe3O(OOCCH3)6L3] and related mixed-metal complexes. *J. Am. Chem. Soc.* **109,** 2009–2016 (1987).
67. Car, R. & Parrinello, M. Unified Approach for Molecular Dynamics and Density-Functional Theory. *Phys. Rev. Lett.* **55,** 2471–2474 (1985).
68. Kohn, W. & Sham, L. J. Self-Consistent Equations Including Exchange and Correlation Effects. *Phys. Rev.* **140,** A1133–A1138 (1965).
69. Wagner, B., Reinen, D., Brunold, T. C. & Guedel, H. U. Iron(VI) in Tetrahedral Oxo Coordination: A Single Crystal EPR Study. *Inorg. Chem.* **34,** 1934–1942 (1995).
70. Marx, D., Tuckerman, M. E., Hutter, J. & Parrinello, M. The nature of the hydrated excess proton in water. *Nature* **397,** 601–604 (1999).
71. Henkelman, G., Arnaldsson, A. & Jónsson, H. A fast and robust algorithm for Bader decomposition of charge density. *Computational Materials Science* **36,** 354–360 (2006).
72. Weers, J. G. & Scheuing, D. R. Micellar Sphere to Rod Transitions. in *Fourier Transform Infrared Spectroscopy in Colloid and Interface Science* **447,** 87–122 (American Chemical Society, 1990).
73. Ren, Y., Iimura, K., Ogawa, A. & Kato, T. Surface Micelles of CF3(CF2)7(CH2)10COOH on Aqueous La3+ Subphase Investigated by Atomic Force Microscopy and Infrared Spectroscopy. *J. Phys. Chem. B* **105,** 4305–4312 (2001).
74. Snyder, R. G., Strauss, H. L. & Elliger, C. A. Carbon-hydrogen stretching modes and the structure of n-alkyl chains. 1. Long, disordered chains. *J. Phys. Chem.* **86,** 5145–5150 (1982).
75. Nelson, P. N., Ellis, H. A. & Taylor, R. A. Odd–even alternation in a homologous series of Zn (II) n-alkanoates. *Journal of Molecular Structure* **986,** 10–15 (2011).
76. Bassi, P. S., Randhawa, B. S. & Jamwal, H. S. Mössbauer study of the thermal decomposition of some iron(III) monocarboxylates. *Thermochimica Acta* **62,** 209–216 (1983).
77. Bassi, P. S., Randhawa, B. S. & Jamwal, H. S. Mössbauer study of the thermal decomposition of some iron(III) dicarboxylates. *Thermochimica Acta* **65,** 1–8 (1983).
78. Sprik, M. & Ciccotti, G. Free energy from constrained molecular dynamics. *The Journal of Chemical Physics* **109,** 7737–7744 (1998).
79. Daou, T. J. *et al.* Hydrothermal Synthesis of Monodisperse Magnetite Nanoparticles. *Chemistry of Materials* **18,** 4399–4404 (2006).

Chapter IV

Novel insight on the nanoparticles synthesis through the thermal decomposition process of long chain carboxylate precursors

IV Novel insight on the nanoparticles synthesis through the thermal decomposition process of long chain carboxylate precursors

IV.1 Introduction

The synthesis of nanocrystals has found to be central to meet the challenges of this century. Offering new perspectives in many areas (catalysis, energy, biomedical …) their synthesis has been at the centre of a research frenzy. The last decade developments of the synthesis methods improved the quality and range of nanoparticles (NPs). In particular, the thermal decomposition (TD) that established itself as the reference method for high quality NPs synthesis. From the pioneer work of Hyeon[1] and Sun[2], it proved to be efficient in the synthesis of iron oxide NPs with high crystallinity, controlled size and narrow size distribution. The thermal decomposition method also permitted the synthesis of shape-controlled or core-shell or doped iron oxide NPs. Yet the latters remain quite difficult to master and the synthesis reproducibility is not good enough.

Indeed doping of iron oxide with Co or Mn has been proposed as a way to improve the heating properties of ferrite NPs[3–6]. Up to now, most works were devoted to iron oxide NPs[7] because of their proven biocompatibility and ease of synthesis and to the tuning of their size with a narrow size distribution. Despite their high potential, the development of doped ferrites was thus limited, their synthesis being moreover generally more complex leading often to chemical heterogeneities (i. e. the distribution of doping element is not homogeneous in the NPs)[8–10]. Heiss and *al.* observed the formation of core-shell $FeO@CoFe_2O_4$ NPs from the decomposition of mixed Co/Fe oleates[11]. Baaziz et al[12] obtained similar results with metal stearates and demonstrated that the use of oleylamine as ligand favoured the decomposition of precursors and a less reducing medium, which allows obtaining cobalt ferrite NPs with homogeneous composition.

Concerning the tuning of the NPs shape, Kovalenko et *al.*[13] have reported the synthesis of iron oxide nanocubes from the iron oleate decomposition assisted by sodium or potassium oleates as surfactants. The cubic shape of NPs was attributed to a slower growth rate for the {100} facets due to the interaction of the surfactant on the growing surface[14]. The structure of these cubes was further reported to consist in a core-shell $FeO@Fe_{3-x}O_4$ structure[15,16]. Also, Pellegrino *et al.*[17] synthesized iron oxide nanocubes with homogeneous composition by the thermal decomposition of $Fe(acac)_3$ in presence of decanoic acid in dibenzylether. Recently, they further reported[18] that the decomposition products of dibenzylether would be crucial to synthesize cubic shaped NPs with control over the size and shape. Most of the reports agreed on a ligand directed growth for the synthesis of non-spherical shaped NPs[13,15,17,19]. Yet for each shape, various conditions are used, thus the mechanisms are hard to investigate.

Hence, despite rare investigations, the thermal decomposition mechanism still remains fully unravelled. Although several teams attack this problem, most of the studies rely on *ex-situ* analysis of fractions extracted from the synthesis media. *E.g.* Kwon et al.[20] studied the thermal decomposition of iron oleate in octadecene or eicosene with magnetic measurements, size exclusion chromatography and TEM. They have been able to identify the moment of nucleation in their system but most importantly they showed that intermediates species are formed before the nucleation step. Kwon et al. theorized these intermediates species as polyiron oxo molecules. Later in the same group, Kim[21] demonstrated using MALDI-TOF mass spectrometry that for iron oleate mixed with oleic acid and oleyl alcohol in diphenylether, those polyiron oxo molecules could be clusters of about 8 iron atoms coordinated on about 11 oleate molecules. More recently, Lassenberger and al[22] studied the *in-situ* NPs formation with Small Angle X-ray Scattering (SAXS). They have decomposed iron carbonyl $Fe(CO)_5$ with OA in octylether and were able to show that the mechanism was split in different parts. First, an iron oleate is forming from the reaction of the precursor with OA, then structures that are not NPs are observed before the burst of nucleation and growth step. These structures were ascribed to the polyiron oxo species reported by Kwon et al. but they suggest that it could be micellar structure of OA encapsulated precursor.

The issue in the investigation of the thermal decomposition mechanism is that many precursors of different nature can be used in association (or not) with one or several ligands. For iron oxide synthesis, Fe(acac)n (acac = acetylacetonate)[2,23,24], iron oleate[15,25–30] or carbonyls Fe(CO)x[31,32] are commonly used. Concerning the ligands, carboxylic acids are often used but amines, alcohols are also reported. The solvent is another parameter, as it can influence the synthesis, as for instance dibenzylether that has been shown to decompose during the synthesis[18] and Baaziz *et* al demonstrated that it has also an influence on the NPs size by interacting with the iron precursor and thus affecting its thermal stability[33]. Funnily enough, the structure of the iron precursor is often neglected. It is now well-know that iron oleate is modified by the washing step/solvents and also by ageing[33,34]. We demonstrated previously that the structure of iron stearate was strongly dependent on the reaction conditions and on the hydration degree (cf. Chapter III).

In that complex context, with the aim to get a better insight in the thermal decomposition mechanism, we deeply investigated the first steps of the thermal decomposition process by analyzing the reaction media just after the homogenization step at 120°C (necessary for dissolving all reactants) and by following the thermal decomposition by *in-situ* TEM in a liquid cell (the electron beam inducing a heating of the reaction media). The standard reaction mixture of 10 nm size NPs with the four different iron stearates (the hydrated and dehydrated iron stearates: $FeSt_2$; $FeSt_3$; $FeSt_{2,d}$; $FeSt_{3,d}$) as well as one reactant medium known to lead to anisotropic shape have been characterized by combining different fine characterization techniques such as conventional and liquid environment TEM, atomic force microscopy (AFM) in liquid conditions and small angle X-ray scattering (SAXS). We evidenced thus that the germination step occurs through a mixed vesicular/micellar process which would explain the nice separation between the germination and growth steps noticed for this synthesis method. Such a process would allow explaining all the difficulties in synthesizing doped ferrite with a homogeneous distribution of the doping element or NPs with anisotropic shapes.

IV.2 Experimental details

IV.2.1 NPs synthesis conditions

Isotropic conditions. 1.38 g of $FeSt_2$, 1.24 g of oleic acid and 20 mL of octylether were mixed together, and then heated to 120°C for 60 min in order to dissolve the reactants and remove the water residues. The temperature is abruptly decreased to freeze the system by pouring the reactant mixture in a vial in an ice bath. Sample is kept at +4 °C when waiting for analysis.

Anisotropic conditions. $FeSt_2$ (1.44 g, 2.3 mmol) was mixed with OA (0.18 g, 0.65 mmol) and NaOl (0.70 g, 2.30 mmol) in 15 mL of octadecene in a two neck RBF. The mixture is stirred and heated at 120 °C for 60 min without reflux condenser in order to dissolve the reactants and remove the water residues. The temperature is abruptly decreased to freeze the system by pouring the reactant mixture in a vial in an ice bath. Sample is kept at +4 °C when waiting for analysis.

IV.2.2 Other characterization techniques

In situ TEM. Liquid cell transmission electron microscope is a new method which allows to study liquid specimens. Inside the TEM a high vacuum should be generally present and because of this, only solid samples can be analysed in the traditional modes, as the liquid samples are incompatibility with a vacuum environment. In addition to the analysis in a liquid medium, the development of this new approach allows to realize *in-situ* electrochemical analysis, to directly visualize the mechanisms of nucleation, growth and coalescence of NPs as well as to obtain a better insight of the biological specimens in their natural environment[35].

The development of the liquid cell transmission electron microscopy (Figure IV.1) was possible due to the significant progresses in the fabrication of new windows that are electron transparent, thin enough to allow reasonable imaging and with a controlled submicrometer separation between the windows where the liquid should be confined. The liquid cell is made of a thin layer of silicon nitride (30-50 nm) which is deposited onto a silicon wafer. The silicon is etched from the back to form a window with dimensions around 100 µm to allow the beam to pass. The wafer is diced into chips that are placed face to face with a spacer material between like in a sandwich[36].

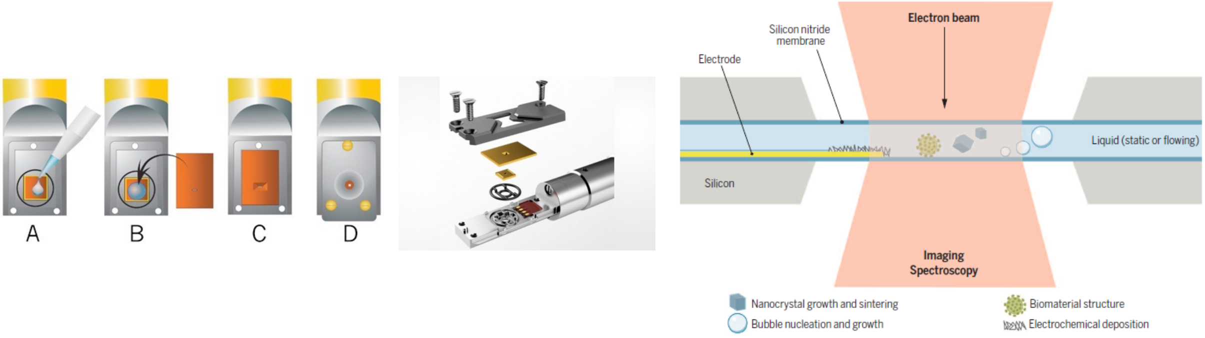

Figure IV.1 - a) Design of the holder and liquid cell transmitted electron microscope b) Scheme of a liquid cell transmission electron microscope.

The holder for the *in-situ* experiments is a particular one, made to keep the sample in security and to made electrical connections between external controllers or heater elements. Although the liquid cells are in continuous, it is in expansion. In this moment, still are two limitations: image resolution and unsuited electron beam effect. Image resolution is lost because of the electron scattering that occurs in the thickness of the windows and the liquid of the cell. The quantity of the liquid from the cell can be diminished, but in this case the experiments will not be any more a representation of a "real phenomena". (example: Brownian motion will differ in the ultrathin liquid layers). The electron beam causes radiolysis of the liquid, H_2 is produced and this changes the pH of the solution. The highly reactive hydrated electron can induce growth of metallic NPs by reducing metallic cations in aqueous salt solutions[35].

The liquid cell for the transmission electron microscope is made of two microchips placed together like in a sandwich. All the preparation needs to be done in a place with low dust. A carbon-coated tweezers is used to take the microchips from the storage box and then placed in a beaker with acetone for 2 minutes to remove the coated polymers from the surface of the microchips which protect the membrane. The microchips are transferred from the beaker with acetone and placed 2 minutes in the ethanol and another 2 minutes in the ultrapure ethanol to eliminate completely all the residues. The microchips are removed from the beaker with ethanol and dried using a thin flow of compressed air. All those manipulations are realized carefully to avoid the damage of the cell. The microchips are placed for 5 seconds at Plasma Cleaner to make the surface of the silicon nitride membrane hydrophilic. A light microscope is used to check that membrane doesn't indicate any rupture or fragility.

The TEM holder is cleaned with ethanol and placed on an aluminum foil. The microchip with the hole is placed carefully in the holder, 1 µl of NPs solution diluted is added on the microchip and then the second microchip is placed close to the cell. The liquid cell is checked under the light microscope and if this does not present any rupture can be inserted in TEM.

Atomic Force Microscopy. AFM images were performed under organic solvents (dioctylether, octadecene) using a Bioscope Resolve instrument (Bruker Nano, Palaiseau, France). Silicon wafer were cleaned 30 minutes with UV-Ozone Cleaner (Novascan) and then coated with polydopamine by immersion 15 min in a solution of 10 mM TRIS containing dopamine at 4g/L and at pH 8. Substrates were extensively rinsed with milli-Q water and then dried under nitrogen flow. 100 µL of NPs suspension were deposited 10 min onto the substrated and then rinsed with the appropriate solvent before imaging. Topographical images were performed by Peakforce TappingTM mode. Silicon nitride cantilevers of conical shape purchased from Bruker (PeakForce Tapping HIRS-FA, Bruker nano, Palaiseau, France) with spring constant of about 0.35 N/m were used for both imaging and mechanical measurements. All images were recorded with a resolution of 256 by 256 pixels and a scan rate of 1 Hz. Sections and Size distribution are obtained with the nanoscope analysis software.

IV.3 Results

IV.3.1 Characterizing the reaction mixture after the homogenization step

IV.3.1.1 First observations in *in-situ* TEM

The TEM studies in the conventional and *in-situ* liquid environment have been done in the framework of a collaboration with the 3D-TEM team of IPCMS led by Pr Ovidiu Ersen. Dris Ihiawakrim, Sorina Cretu and Natahaly Ortiz have performed the experiments.

A reaction mixture involving all the reactants for the synthesis of the standard 10 nm spheres (i.e. isotropic conditions) and for an anisotropic synthesis (in presence of a ratio NaOl/OA 80:20 (instead of only OA) in octadecene (instead of dioctylether)) were imaged first by TEM in liquid cell just after the homogenisation step at 120°C for 60 min. The in liquid cell TEM image of the isotropic condition is given in Figure IV.2.a and the anisotropic condition in Figure IV.2.b. Surprisingly, both images evidence the presence of spherical structures.

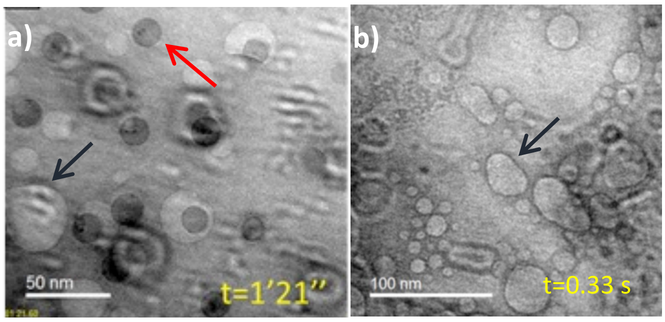

Figure IV.2 - In liquid cell TEM images of isotropic reaction mixture of FeSt$_{2,d}$ a) and anisotropic reaction mixture of FeSt$_2$ b) after the homogenisation step

In isotropic conditions, dehydrated iron stearate, FeSt$_{2,d}$, presented two populations of spherical structures. The first population presented a sharp dark contrast homogeneous within the structure with a mean size centred on 15 nm (red arrow). The second population is characterized by a lighter intensity inside the structure with a darker contrast at its surface (blue arrow). The size of this structure is in the range 30-50 nm and their characteristics are typical of bubbles. Note that the octylether solvent was imaged alone and no bubbles were observed in this case under the same conditions. This additional analysis confirms the hypothesis that such structures originate from the reaction mixture.

In anisotropic conditions, $FeSt_2$ in the presence of a ratio NaOl/OA 80:20 led to a less homogeneous medium. Only large and “lighter” structures with dark walls are clearly observed and they display a broader size distribution (50-100 nm) than previously.

This result being not expected, other characterisation techniques were used to confirm that these structures were not an artefact from the TEM and to gather some further information about them.

IV.3.1.2 Liquid Atomic Force Microscopy

Liquid AFM was performed on the reaction mixture in isotropic conditions of both hydrated and dehydrated iron stearates. Briefly, the mixture is deposited on a silicon wafer substrate functionalized with dopamine molecules (4g/L in 10 mM TRIS at pH 8.0). The substrate is then rinsed with octylether and after placed in the AFM fluid cell. The AFM images were performed in Peakforce Tapping^{TM} mode and the recorded results are given in Figure IV.3. Images revealed a homogeneous distribution of nanostructures over the whole surfaces and the presence of very few aggregates. These objects assemble to form “rings” as it is seen for hydrated $FeSt_2$ (IV.2 bottom). From the AFM images at least two sizes population can be measured. The size distributions collected for each sample after an image analysis are listed in Table IV.1.

Table IV.1 - Size distribution of the different structures in isotropic conditions

		Population 1		Population 2	
		Mean Length (nm)	**Mean Height (nm)**	**Mean Length (nm)**	**Mean Height (nm)**
$FeSt_2$	**Hydrated**	52.8 ± 5.9	3.3 ± 1.2	74.1 ± 6.7	4.6 ± 2.2
	Dehydrated	37.4 ± 6.1	4.5 ± 1.6	17.5 ± 3.6	2.8 ± 0.7
$FeSt_3$	**Hydrated**	56.6 ± 6.1	7.6 ± 6.4	88.8 ± 7.9	22.8 ± 7.9
	Dehydrated	37.6 ± 5.5	4.8 ± 1.7	19.9 ± 3.9	2.6 ± 0.7

Interestingly the size distributions are quite monomodal and the structure sizes are also comparable between both $FeSt_2$ and $FeSt_3$. The main difference is noticed between hydrated and dehydrated iron stearates. Hydrated $FeSt_x$ present a major population around 55 nm and a second one around 80 nm when the dehydrated precursors present two equivalent populations at around 37 and 20 nm. The observed sizes and populations are in agreement with in liquid cell TEM observations for dehydrated $FeSt_2$.

In anisotropic conditions, AFM images (Figure IV.4) also display two populations with the largest at 53.8 ± 7.3 nm and the smallest one at 25.5 ± 1.7 nm. The small population structures tend to form ring structures as observed for hydrated $FeSt_2$ in isotropic conditions.

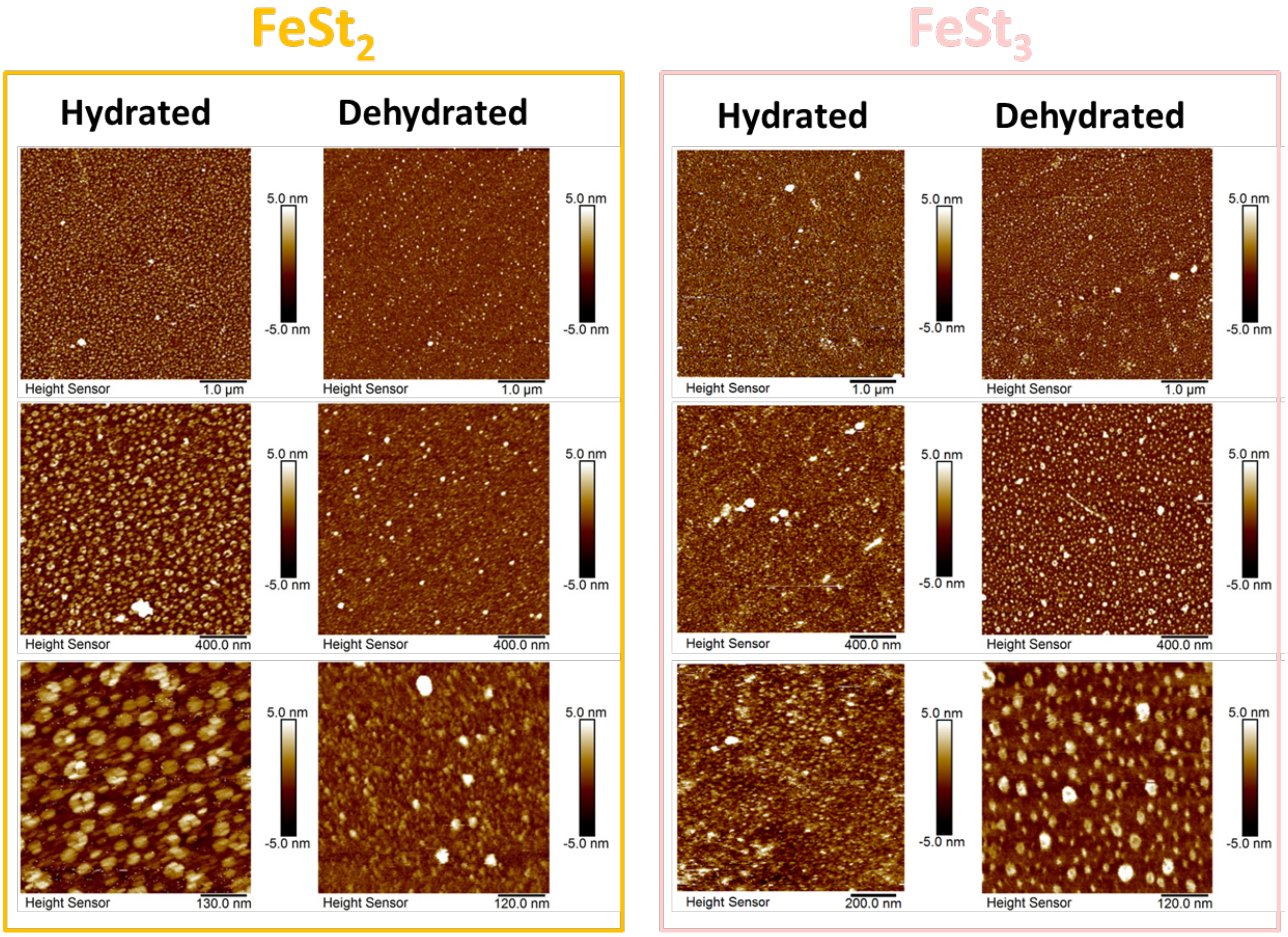

Figure IV.3 - Liquid AFM images of the reaction media of the different precursors. In each column, AFM images of the sample are zoomed from the top to the bottom.

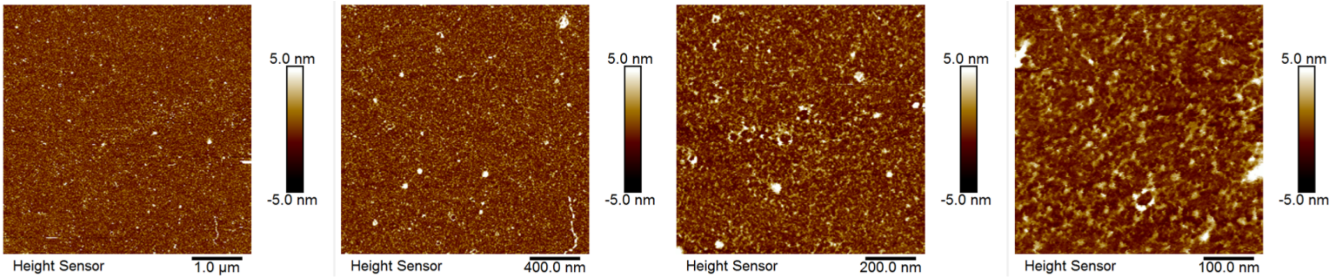

Figure IV.4 - Liquid AFM images in the anisotropic conditions zoomed from left to right

IV.3.1.3 SAXS measurements

To get better insights on the structure of these spherical nano-objects, SAXS measurements have been performed by Dr Benoit Heinrich at IPCMS on reaction mixtures in isotropic conditions for hydrated and dehydrated iron stearates at two temperatures, 20 and 60°C (Figures IV.5-6).

After the homogeneisation step at 120°C of isotropic reaction mixtures for all four iron stearates, the SAXS measurements at 20°C led to quite the same scattering intensities for all iron oxide stearates. All SAXS patterns are similar to those of hydrated iron stearates in the powdered state (cf. Chapter III). They are organized into a lamellar crystal phase "Lam0" (reflections (00l), periodicity d = 50.7 Å), with a lateral arrangement of the aliphatic chains in a two-dimensional hexagonal subarray of rotator type ($h_{ch,cr}$ =

4.12 Å; section of the chains: $S_{ch,cr}$ = 19.6 Å^2). One may notice that the peaks of stearic acid observed with powdered $FeSt_3$ are no more observed in solution.

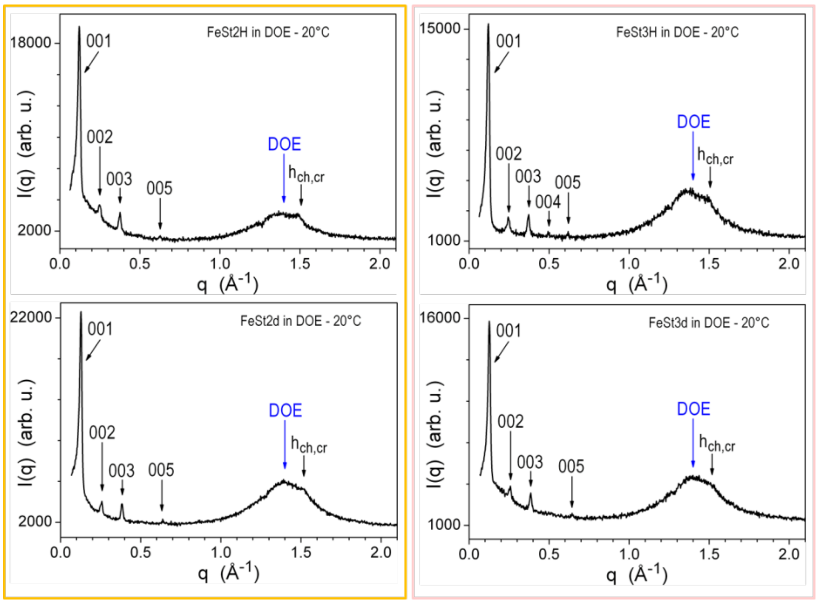

Figure IV.5 - Scattering intensities I(q) as a function of the magnitude of the scattering vector q of reaction mixtures with the four iron stearates in isotropic conditions at 20°C (DOE: dioctylether)

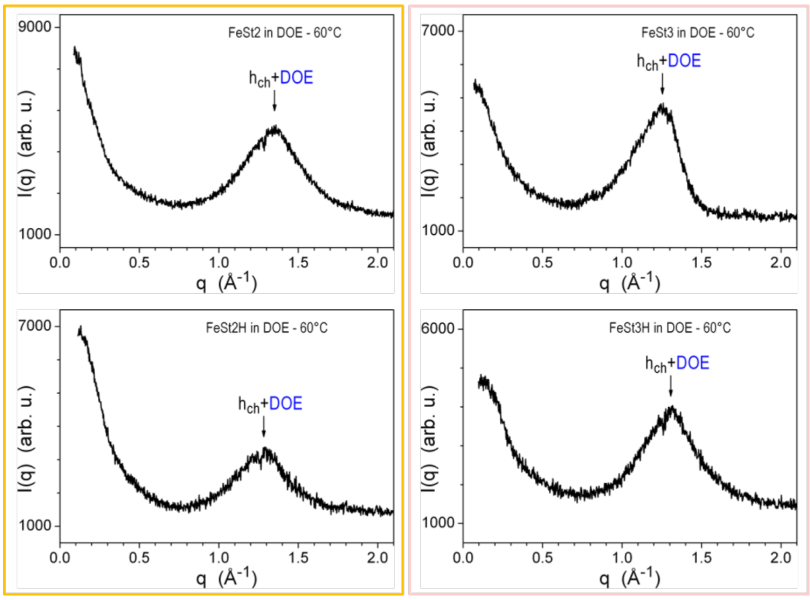

Figure IV.6 - Scattering intensities I(q) as a function of the magnitude of of the scattering vector q of reaction mixtures with the four iron stearates in isotropic conditions at 20°C (DOE: dioctylether)

Nevertheless, both powdered dehydrated iron stearates were observed to be amorphous at room temperature (Chapter III) and we observed that crystalline phases formed after the homogenisation step in the reaction mixture in dioctylether. SAXS measurements performed on powdered dehydrated iron stearates at different temperatures showed that they reorganized in fact in crystalline structures upon heating at 120°C (Figure IV.7).

Indeed $FeSt_{2,d}$ is amorphous at room temperature and reorganized in a lamellar structure upon heating at 70°C (i.e. at the middle of the melting domain, cf. Chapter III) (Figure IV.7b). Above the melting domain, at 120°C, $FeSt_{2,d}$ organized in mesophase Col_h (a = 31.0 Å ; S_{col} = 832 Å^2) (Figure IV.7c). After cooling down to room temperature, $FeSt_{2,d}$ crystallized in the Lam phase, with subpattern of aliphatic chain of rotator type (d = 49.9 Å, $h_{ch, cr}$ = 4.13 Å, $S_{ch, cr}$ = 19.7 Å^2) (Figure IV.7d). A small proportion of Col_h domains remained after return to ambient temperature, since the characteristic reflections of the mesophase are always detectable. Figure IV.7.e-f showed that in the melting domain of FeSt2,d, there is coexistence of the Col_h and Lam domains in different proportions.

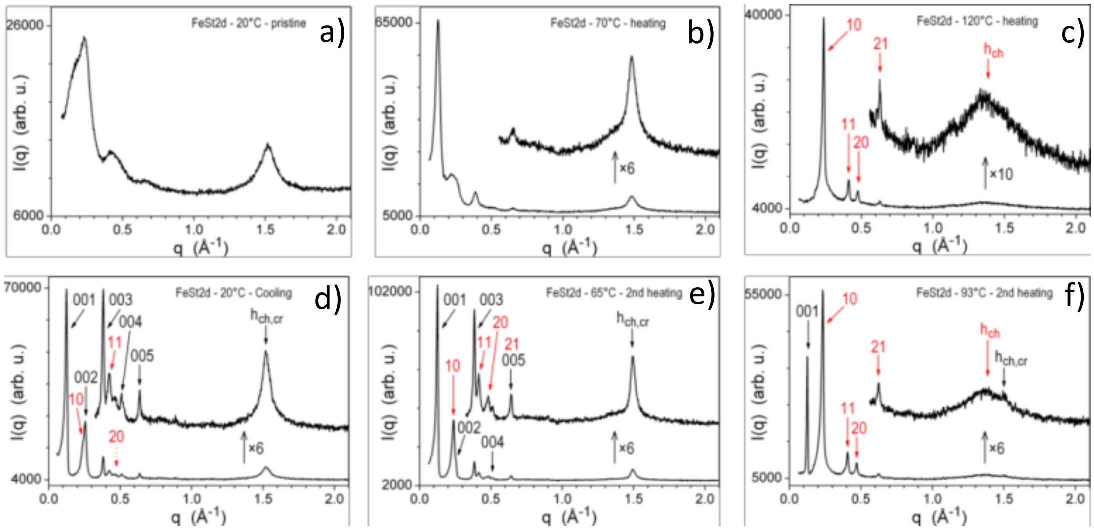

Figure IV.7 - Scattering intensities of powdered $FeSt_{2,d}$ sample before and after different heating/cooling treatments

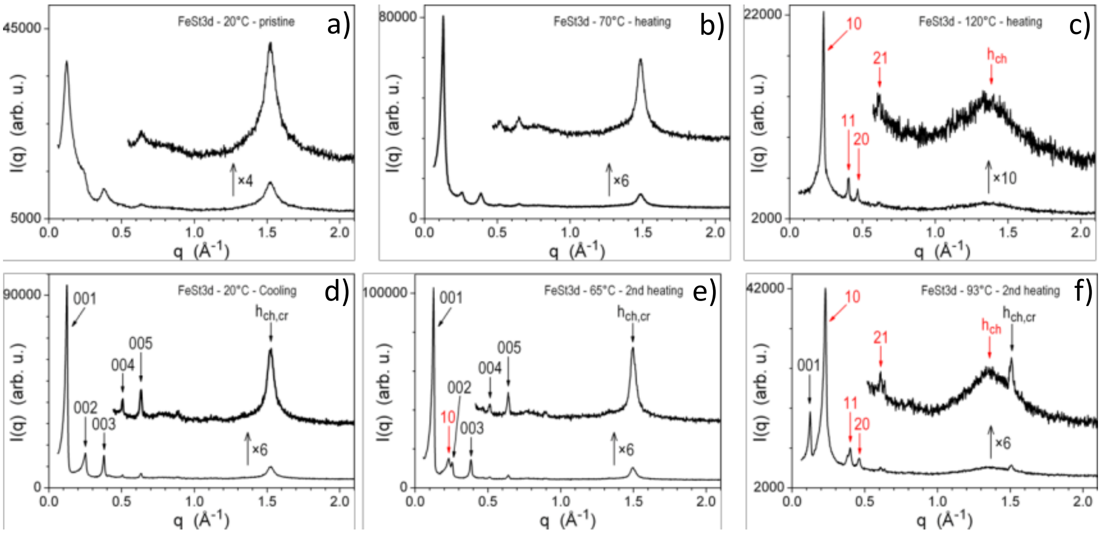

Figure IV.8 - Scattering intensities of powdered FeSt3,d sample before and after different heating/cooling treatments

Similarly, $FeSt_{3,d}$ amorphous at room temperature, reorganizes in lamellar structure at 70°C and is under a mesomorphous phase at 120°C: (*a* = 30.9 Å ; S_{col} = 828 Å^2) (Figure IV.8.a-c). After cooling down to room temperature from 120°C, $FeSt_{2,d}$ crystallized in the Lam phase, with a subpattern of aliphatic chains of rotator type (d = 50.0 Å, $h_{ch, cr}$ = 4.11 Å, $S_{ch, cr}$ = 19.5 Å^2) (Figure IV.8.d). As with $FeSt_{2,d}$, there is coexistence of the Col_h and Lam domains in different proportions in the melting domain.

When this reactant mixture is heated up to 60°C (Figure IV.6), only the intense diffuse band at high angles of the hexagonal columnar phase Col_h is observed coming from the lateral distances between melted chains (h ~ 4.5 Å).

All these results showed that after the homogenization step, all stearates and even the dehydrated ones, which were amorphous, displayed a tridimensional crystalline lamellar structure Lam: reflexions (00l) with a periodicity of about 50-51 Å.

IV.3.1.4 Ex-Situ TEM and HAADF imaging

Reaction mixtures of the four precursors in isotropic conditions have been deposited on TEM grids in order to get a sight of the structures previously observed. The TEM images are given in Figure IV.9.

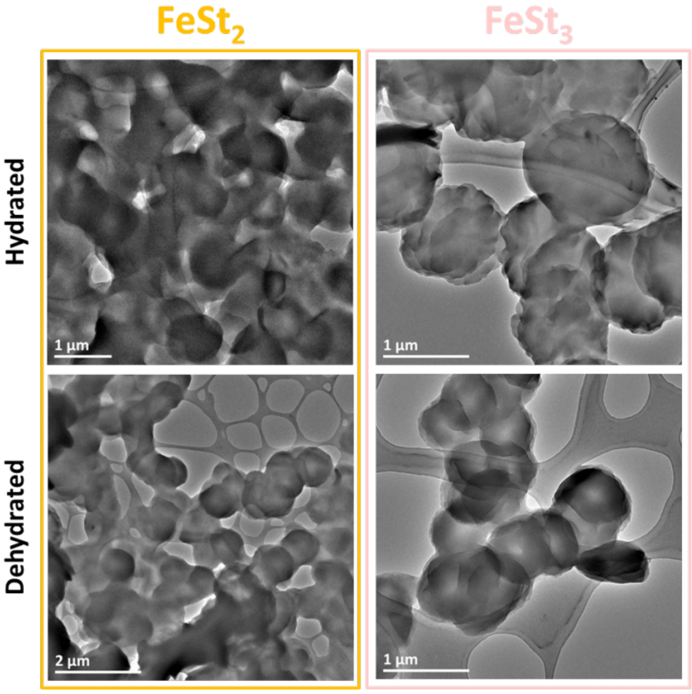

Figure IV.9 – TEM images of the reaction media of the four precursors in isotropic conditions

Polymer like capsules were detected with the TEM however they presented surprisingly, a much larger size (about 500-1000 nm) that what has been observed in *in-situ* TEM and liquid AFM. Yet, some smaller objects with a size in agreement with AFM and in situ TEM were found as seen in Figure IV.10.

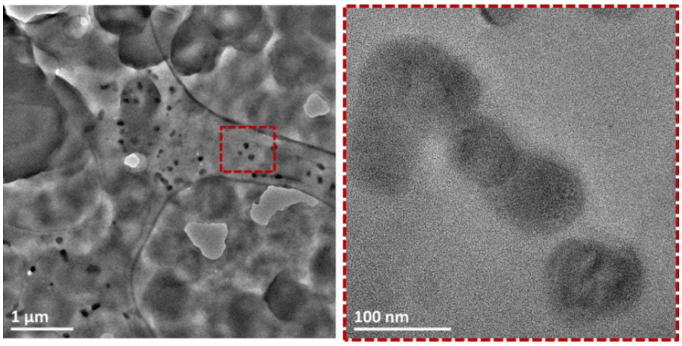

Figure IV.10 - Smaller objects detected for hydrated FeSt2 (left) and zoomed image (right)

It can be seen from the zoomed image (Figure IV.10.) that the smaller vesicles tend to stick and fuse to each other. Here we suggest that they are progressively coalescing which led us to think that the huge 1 µm capsules were due to the coalescence of smaller capsules when drying on the TEM grid. This is in agreement with the shape of structures in Figure IV.9 which seems not homogeneously spherical and displays some roughness with several bumps located at the surface. The vacuum inside the microscope may have led to the collapsing of this kind of structures. Thus, even if there was a coalescence of capsules during the drying on the TEM grid, we believe that these structures are the ones we observed in in-situ TEM but inflated due to the vacuum.

Annular Dark Field (ADF) element cartographies allowed co-localizing iron in the observed capsules for all the precursors studied thus confirming that iron is effectively and uniformly chelated to the surfactant architectures. The right image in Figure IV.11 shows that the iron level is not the same along some structures hinting at/suggesting a hollow core. The carbon coating of the TEM grid associated to the drying in the vacuum might have important influences in the reorganization and coalescence of the vesicles into larger capsules

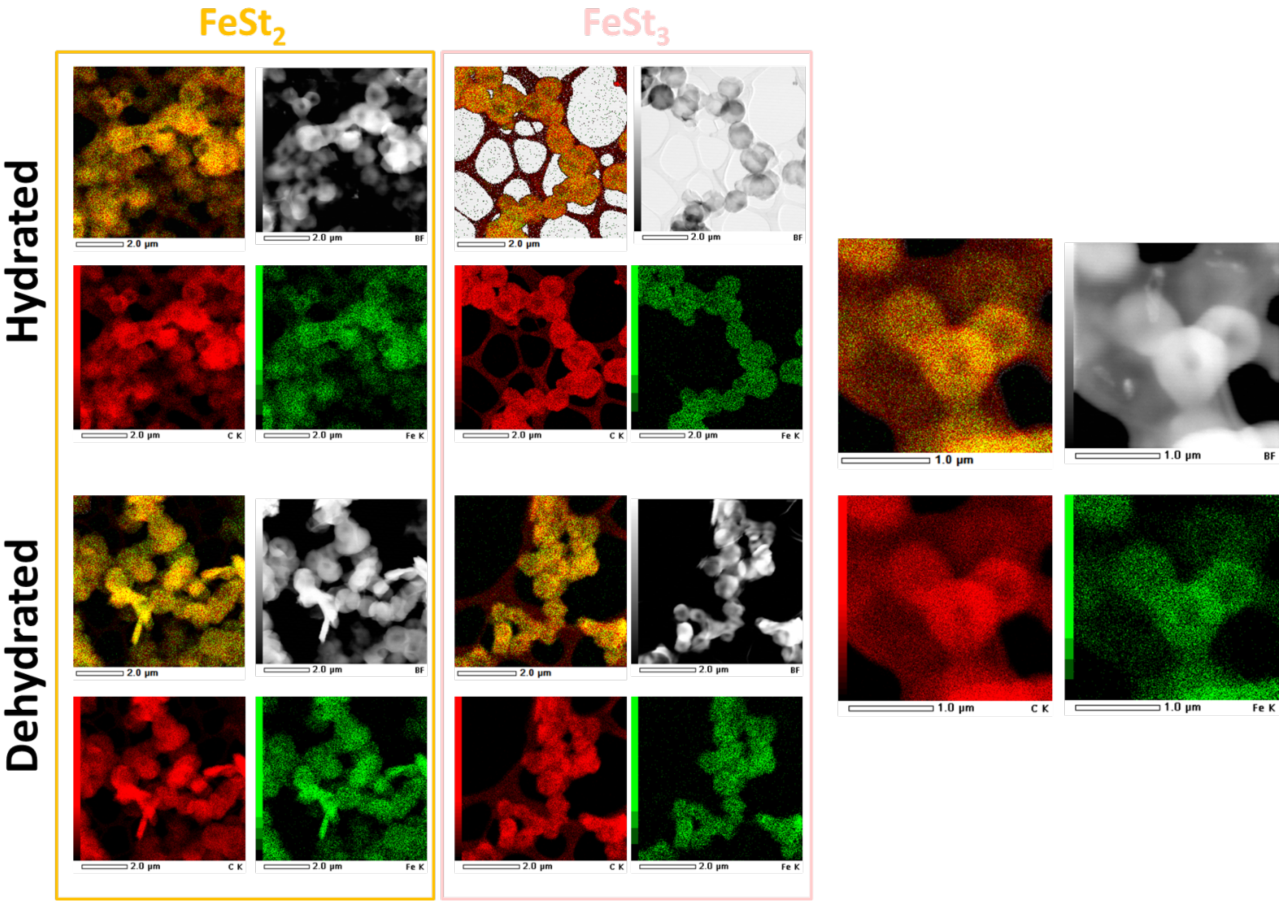

Figure IV.11 - ADF elemental mapping for all precursors structures (left) and zoomed image on FeSt$_2$ one structure (right) showing a fused image (FI) , a dark field (DF), carbon (Red), and iron (green) cartographies

IV.3.1.5 Discussion

From all TEM and AFM characterizations of the reaction mixtures after the homogenization step, we may conclude that spherical nano-objects are formed from iron stearates and oleic acid and/or sodium oleate in the organic solvent. SAXS measurements showed that the structure of these nano-objects is similar to that of the powdered stearates and a crystalline lamellar structure was identified.

Note that one of the most important characteristics of surfactants such as oleic acid and stearate/oleate is their ability to form molecular aggregates in solution by spontaneous self-assembly[37]. They may arrange into micelles, liquid crystals, vesicles and reverse micelles depending on the molecular architecture of surfactant and solvent, composition and temperature[38]. In that context, we assigned the observed spherical nano-objects to vesicles. Indeed, micelles are generally monolayers and only vesicles are multilayers. SAXS experiments suggested strongly/reported on a multilayer structure. The presence of some water can not be excluded but it should be inserted in these vesicules or form small micelles.

To the best of our knowledge, no study up to now reported on the formation of such multilayer vesicles involving ionic and non-ionic surfactants and a cationic counter-ion in organic solvent. Indeed, most micelles or vesicles studies dealt with water as solvent. The formation of aggregates takes place above a certain concentration called critical micellar concentration (CMC). Above the CMC, different concentration-dependent (lyotropic) phases can be observed in a typical binary water/surfactant solution as depicted in Figure IV.12.left. These concentration-dependent phases or lyotropic phases change with the concentration of the surfactant in the binary solution. It was also shown that surfactants form different phases depending on the temperature. In this case, the phases are formed at a fixed surfactant concentration while changing the temperature. This kind of phases are called thermotropic phases. The formation of micelles is a cooperative process that is spontaneous and reversible. Micelles are thermodynamically stable species that are in chemical equilibrium with free surfactants.

Some surfactants self-assemble into closed bilayers called vesicles (or liposomes when formed from phospholipids). Vesicles (Figure IV.12.right) are often spherical but can take other shapes and can be unilamellar or multilamellar. By contrast with micelles, vesicles may not be thermodynamically stable with temperature. Another important difference between vesicles and micelles is that vesicles have an inside than encloses some of the aqueous phase and an outside. At very low concentration, surfactants always start forming micelles that may turn into vesicles at higher concentrations. The formation of lamellar phases is a requirement for vesicle formation, since vesicles are built up by flexible bilayers.

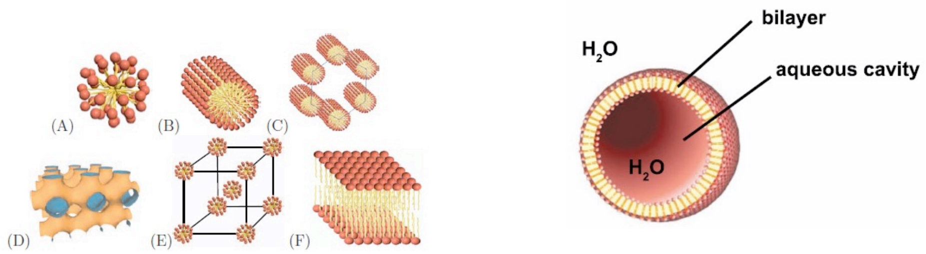

Figure 1.1: Micelle (A), cylindrical micelle (B), hexagonal phase H_α (C), cubic phase I (D), cubic phase II (E), bilayer (lamellar phase L_α) (F).

Figure 1.5: Schematic representation of a vesicle.

Figure IV.12 - The various structures of micelles (left) and a classical vesicle structure (right)

In our context, lamellar structures have been clearly identified by SAXS in powdered hydrated iron stearates and dehydrated iron stearates as well as in the reaction mixture after the homogeneisation step. Let us remind that it has been shown that amorphous dehydrated iron stearates recover quickly a lamellar structure as soon as they are heated. Thus, the observation of the presence of lamellar structure together with spherical hybrid nano-objects strongly suggested that multilayer vesicles have been formed. As we are in non-polar solvents, reverse vesicles are more likely to be formed. Indeed, vesicles formed from surfactants in non-polar solvents are generally named reverse/inverse vesicles. Nevertheless, reverse vesicles have been less observed as their formation was induced by the dispersion of lamellar liquid crystal in non-polar media.[39–41]

However, the formation of inverse micelles is not excluded as two size populations of nano-objects have been observed and micelles are generally smaller in size than vesicles. Reverse micelles are aggregates of surfactants formed in non-polar solvent, in which the polar head groups of the surfactants point inward and the hydrocarbon chains point toward to the non-polar medium[42]. One may notice that most reported reverse micelles involved small amount of water and the micellar size is controlled by the surfactant/water ratio. They have been widely used for the synthesis of NPs with micelles acting as a microreactor[43–45]. However, a hexagonal organisation is clearly observed in the reaction mixture which seems not in agreement with the presence of micelles.

Another form, which has been observed during the encapsulation of polyoxometalate complex by surfactants in water and organic solvent, is onion like agregates[46]. Onion like inner structures were observed in water when inverse vesicular aggregates were observed in organic phases. The structure reversal from vesicles up to onion like structure was induced by increasing the water content. Such onion like structures were also reported by Garg et al[47] during the elaboration of metal containing cationic liposomes. This kind of onion structures are composed of many bilayers. Such a structure would explain what is observed in ex-situ TEM, as we suspected that the more bilayer was present, the more solid was the structure. Thus, the structures observed in *ex-situ* TEM would be the *in-situ* homogeneously contrasted objects. The reverse vesicles that we suspected as the second population would then collapse in the vacuum as they should present less resistance because of their lower number of bilayers. Thus, they've collapsed and cannot be observed.

From our results, we assume that reverse vesicles as well as onion like inner structures, schematized in Figure IV.13, are present in the reaction mixture after the homogenisation step at 120°C in our experimental conditions.

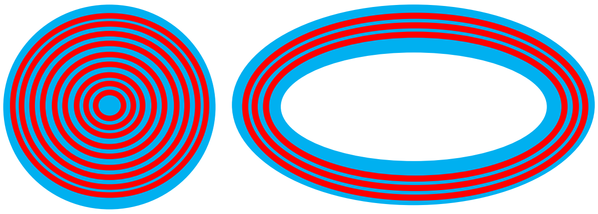

Figure IV.13 – Schematic representation of the onion structure (left) and reverse vesicle (right), the red lines represent the iron cations.

IV.3.2 Thermal decomposition mechanism by TEM in liquid cell

IV.3.2.1 In isotropic conditions

The isotropic reactant mixture involving dehydrated $FeSt_2$ after the homogeneisation step at 120°C has been systematically followed *in-situ* by liquid cell TEM after different exposure times to the electron beam (Figure IV.14).

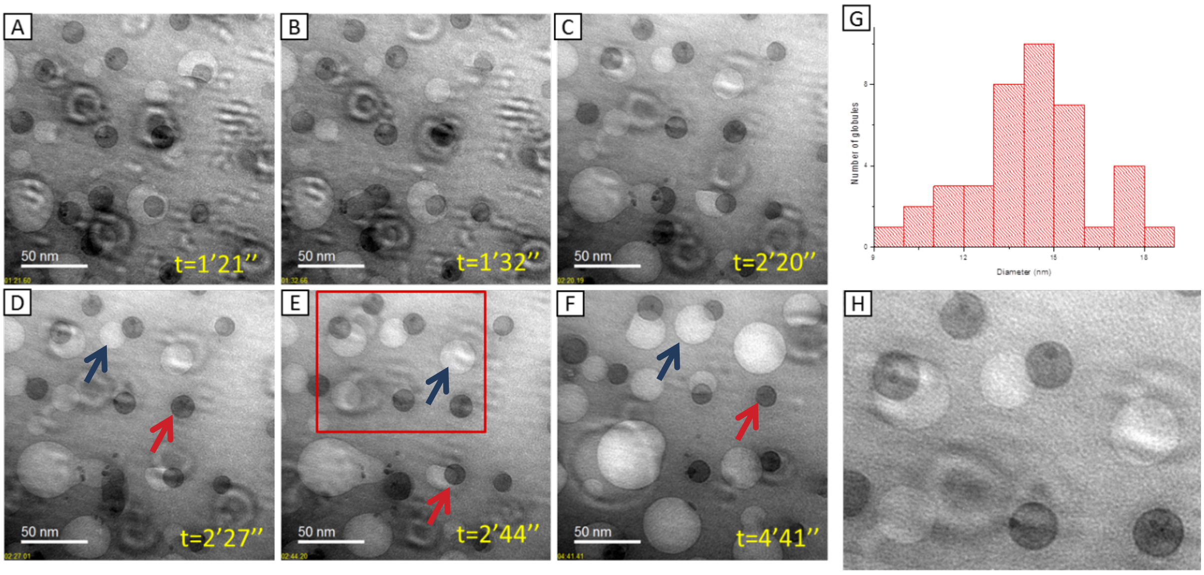

Figure IV.14 - TEM images of some representative areas from reaction medium at different times (A-F) and histogram of the size distribution of the contrasted structures (G) and the zoom of the area from (E) in (H)

Dehydrated $FeSt_2$ presented two populations of spherical structures before a short exposure time. One population presents a "light" intensity at the centre with a darker contrast on its outsides/peripheries and they may be considered to be inverse vesicles. Their size is in the range of 30-50 nm and increases through coalescence (blue arrow in Figure IV.14).

The size of the other population is centred around 15 nm. They present a dark grey contrast which seems to remain similar when increasing the exposure time (red arrow in Figure IV.14). This population could be attributed to onion like structure. By looking at higher magnification, the contrast is increasing in the small population with the exposure time and a darker phase is detected inside the structure. These sizes were measured in the range 2-3 nm. At the end of the experiment, the dark phases have been analysed by ex-situ HR-TEM (Figure IV.15) showing NPs with a size in the range 5-7 nm presenting interplanar distances in agreement with a spinel iron oxide phase.

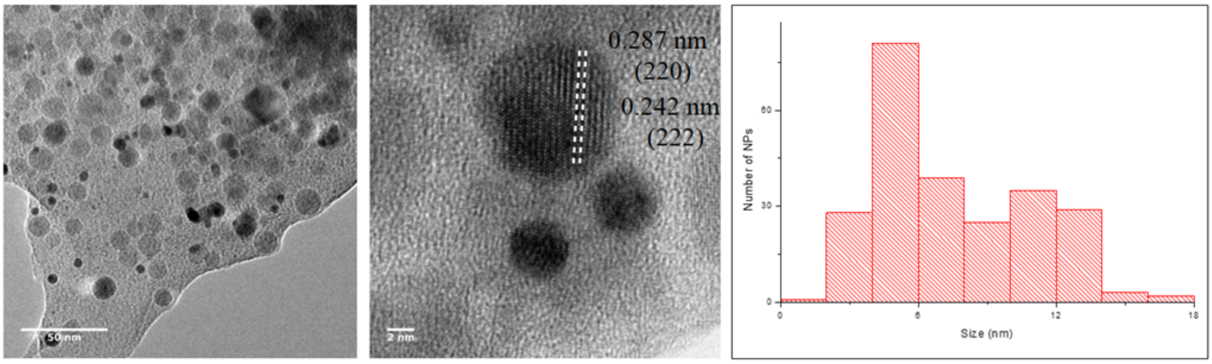

Figure IV.15 - Ex-situ HR-TEM images of the dark NPs

IV.3.2.2 In anisotropic conditions

The richness of the thermal decomposition method is to allow the synthesis of anisotropic shapes through the addition of specific ligand. For example cubes have been successfully synthesized in octadecene by replacing part of the oleic acid by sodium oleate[13,15]. Thus, we have been interested in investigating the evolution of such a reaction mixture under beam exposure.

A reaction mixture with hydrated $FeSt_2$ with a ratio NaOl/OA 80:20 in octadecene (more details in the experimental part) has been imaged in the same conditions as the isotropic medium. The resulting TEM images are given in Figure IV.16. A first, we may notice that the reaction mixture seems to be similar to vesicles having a light intensity at the center and black contours but they present a larger size here (50-100 nm). In Figure IV.16, the blue circles evidenced the formation of a dark phase at the periphery of the vesicles in their "walls" and then the vesicles disappeared and a dark grey phase is formed apparently without thick organic layers around. The red circles evidenced the growth of vesicles by coalescence with other vesicles under the electron beam.

A close look up to the walls of the vesicles (Figure IV.17) showed that the dark contrast intensified with time and electron beam exposure. Dark dots ended up appearing on the walls that might be the first nuclei of iron oxide.

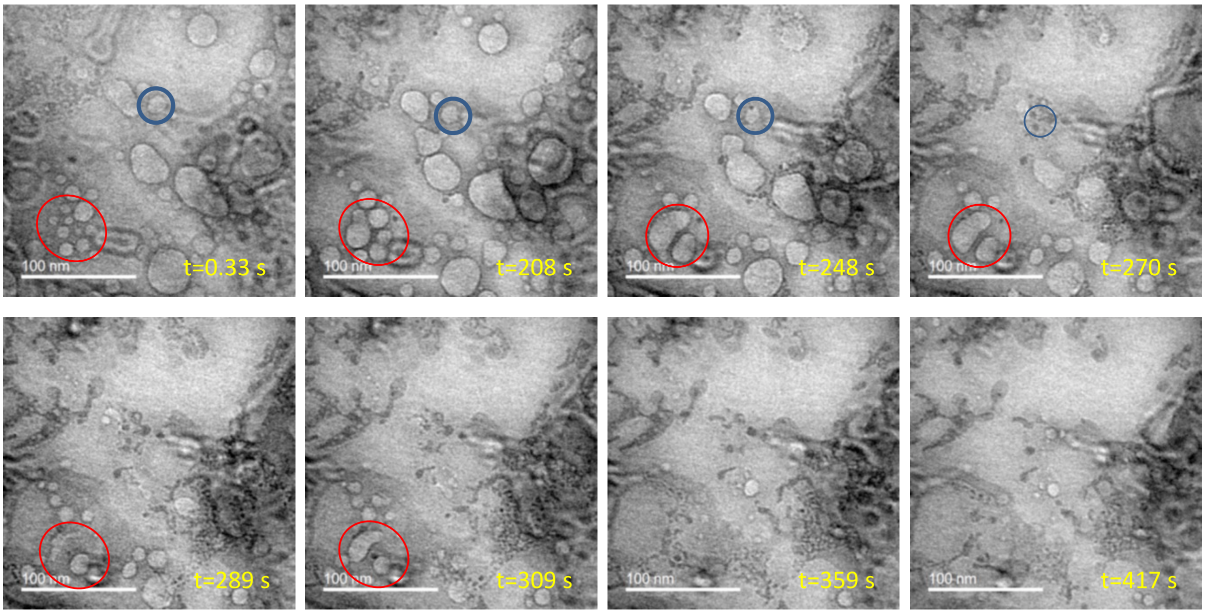

Figure IV.16 - In-situ TEM images of the anisotropic reaction mixture after different exposure times to the electron beam (Electron dose: $90e/A^2.s$)

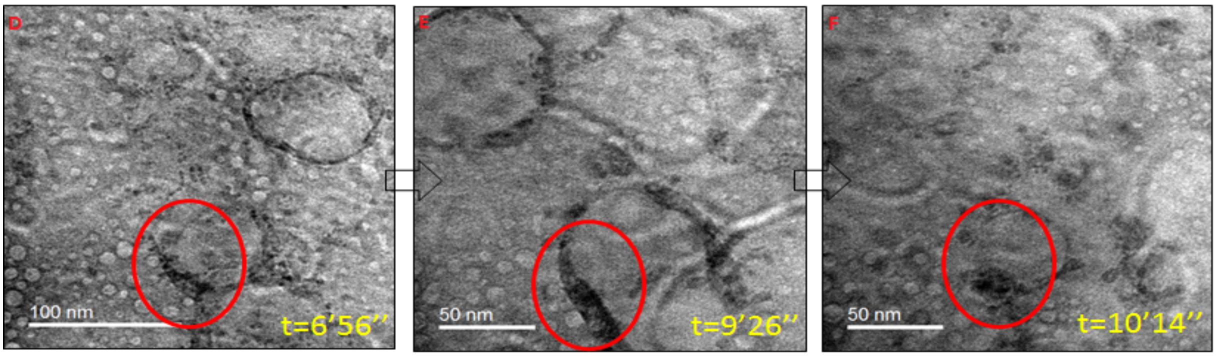

Figure IV.17 - TEM images close up to the walls of the structures (Electron dose: $90e/A^2.s$)

The same experiment with an electron dose of $575e/A^2.s$ with a longer beam exposure time gave a better insight (Figure IV.18). First, the vesicles coarsened as shown by the increasing dark contrast in their walls. In the first blue circle, we can see that dark phases formed again from the vesicle walls and the vesicles disappeared simultaneously leaving a uniform spherical object presenting a tiny, much contrasted dark spot that could be the nuclei. By then, the smallest structures coalesced or re-dissolved in the solvent. Then the same mechanism of coalescence seen with the isotropic conditions is observed on the largest structures. This mechanism of "local coalescence" is shown with more details in Figure IV.19.

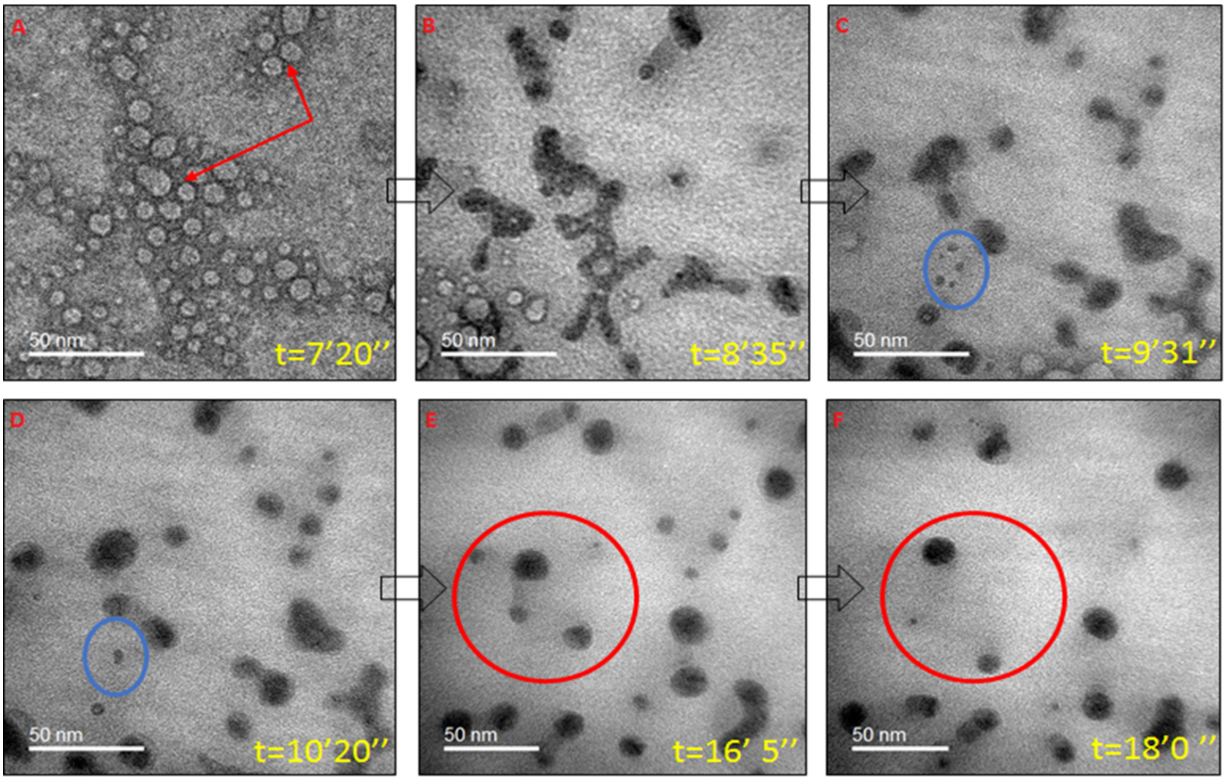

Figure IV.18 - Evolution of the system on a longer span of time (Electron dose: 575e/A²/s)

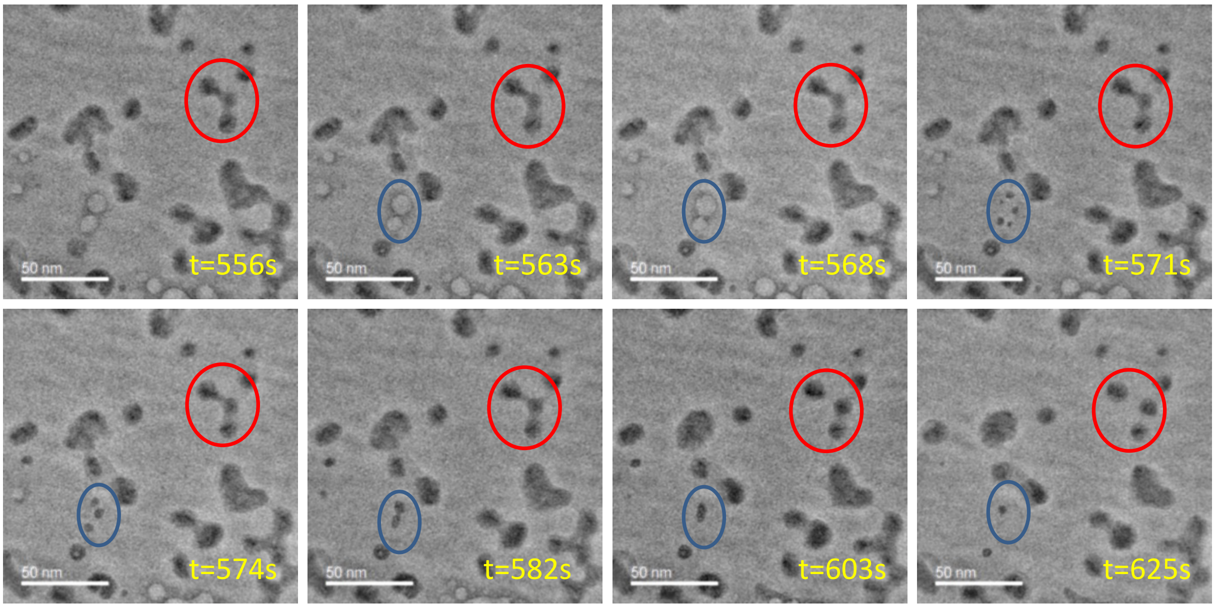

Figure IV.19 - In-situ TEM images of the anisotropic reaction mixture after different exposure times to the electron beam (Electron dose: 575e/A²/s)

The evolution of the structure when not coalescing is shown in Figures IV.20. These structures with less defined shapes contain some dark spots. They can be considered as onion like structures and by contrast with vesicles where iron atoms are located only in the vesicle wall, the atoms are in the whole structure and aggregation of atoms may occur inside these structures. From blue circles in Figure IV.18-

20, we can observe that dark spots formed, their density increased with exposure time and their sizes shrunk.

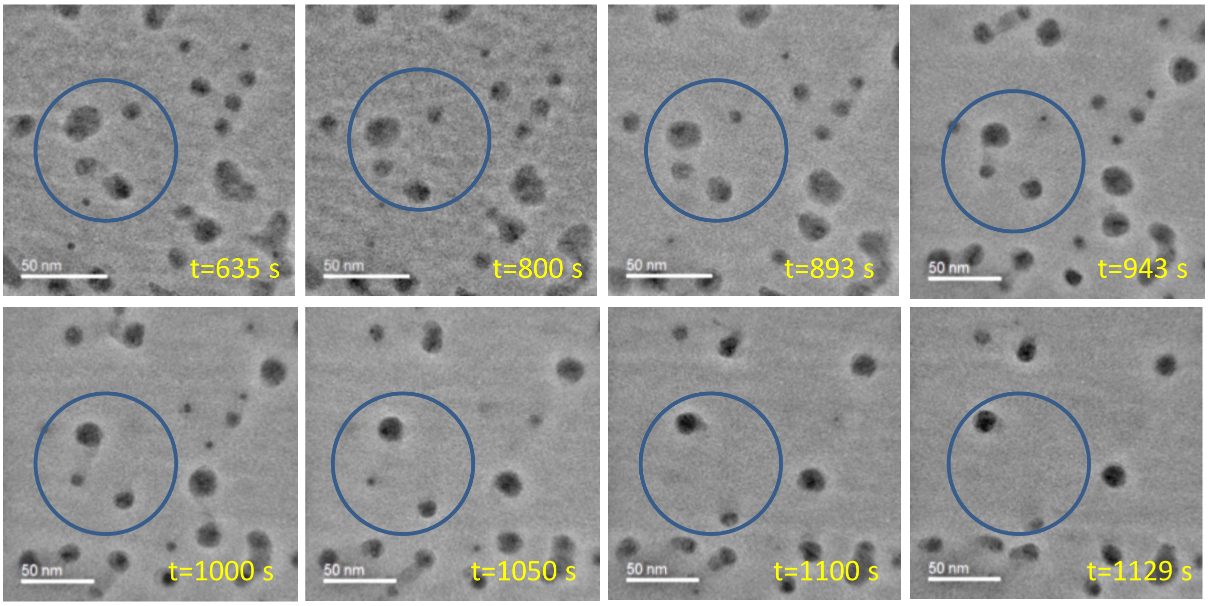

Figure IV.20 - In-situ TEM images of the anisotropic reaction mixture after different exposure times to the electron beam (Electron dose: 575e/A²/s)

IV.3.2.3 Discussion

From the different characterization techniques employed, we demonstrated that $FeSt_x$ can adopt different structures when put into a non-polar solvent in presence of ligands. Interestingly, some crystalline phase may also originate from these structures. Two size populations are observed in AFM but this technique did not provide more information to decide on whether two kinds of objects were presents or if the size distribution was due to coalescence. In-situ TEM gave a better insight by showing two kinds of objects. Reverse vesicles were ascribed to the objects presenting a light contrast centre and onion like inner structures were attributed to the smallest objects displaying a whole darker contrast due to iron being encapsulated in the whole structure. The fact that we have identified lamellar phases in our compounds in Chapter III and SAXs experiments on reaction mixtures are in agreement with the formation of such multi-layered structures.

It is at the moment difficult to conclude precisely on the type of self-assembled structure and the role of hydration degree of the precursor as the in-situ TEM experiments are ongoing on the three other precursors.

Yet, we've seen with ex-situ TEM that the same types of structures were observed for all FeSt. We made the hypothesis that these structures are actually inflated onion like structure due to the vacuum of the TEM chamber. If our hypothesis was correct, this would imply that onion like structures are present for all precursors. The question of either reverse vesicles are present for all remained open though. The question of hydration degree was still unclear but we believe that this will have an effect on the population distribution between the two kinds of objects that we identified. Nevertheless, we may suggest that the nano-objects that we observed here correspond to polyiron oxo molecules reported by Kwon *et al.*[20]

Concerning the NPs synthesis, this study is providing an unique insight on the phenomenon dictating the nucleation of NPs in the thermal decomposition process. Most of current explanations of the formation of nano crystals rely on the LaMer theory[48]. LaMer described in 1950, the nucleation growth processes as two distinct phenomena. First a precursor, source of metallic atoms, will decompose into monomers. The monomer concentration will build up with time and when a specific concentration referred as minimal nucleation concentration (C_{nu}^{min}) is reached, nucleation can occur. Depending on the rate of monomer formation, this concentration can be exceeded and the amount of monomers present when the nucleation occurs will dictate the number of nuclei formed. The nucleation leads to an abrupt decrease in the monomer concentration that will go below the C_{nu}^{min}. The monomers remaining (from the dissolution of too small nuclei or still forming from the continuous decomposition of the precursors) will then contribute to the growth of the nucleus into a NP. With the in-situ TEM, we observed that, in our experimental conditions, the nucleation process was driven by a vesicular process involving onion like and reverse vesicles structures. Due to the heating effect, the iron concentration is increasing in the onion or in the vesicle walls as seen with the contrast darkening. The nucleation took place inside the onion or vesicle walls. This is in agreement with the SAXS observations of Lassenberger[22] that observed a diffracting structure before the nucleation takes place. Hence we addressed the first observation of the nucleation phenomenon in the thermal decomposition process which was never reported up to now. Furthermore, the observation in anisotropic conditions unveiled a completely new description of the anisotropic shape synthesis. Figure IV.21 depicted how the nucleation occurred in the onion and reversed micelles.

In anisotropic conditions, solely large vesicles were a priori observed. This could be explained by the liquid crystal behaviour of NaOl[49]. But more importantly, NaOl can form various mesophases when combined with OA (Figure IV.22) depending on the temperature and the water content[50,51]. Thus, we expected to observe variation in the anisotropic synthesis (on which we've focus in Chapter VI) depending on the hydration degree of the precursor. As we observed for the condition tested that the nucleation took place in the wall of the vesicles, the role of these structures on the nucleation is expected to be capital for the synthesis of anisotropic nano objects.

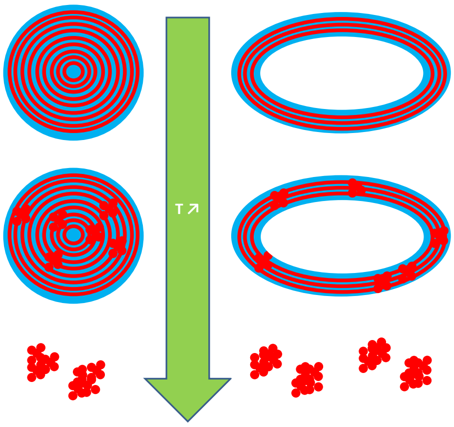

Figure IV.21 – Proposal of nucleation mechanism in both kinds of structures

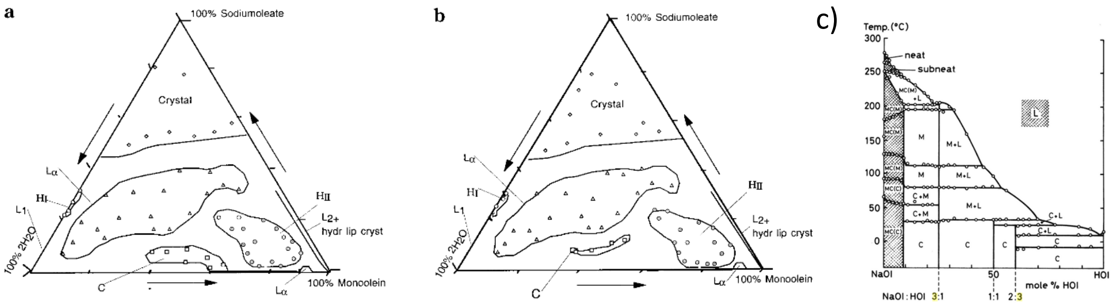

Figure IV.22 – Ternary phase diagram between NaOl/OA/H_2O at 25 °C a) and 37 °C b)[51]*, c) binary phase diagram between NaOl and OA* [50]*.*

Besides, this vesicular/onion based mechanism explains clearly why it has been so difficult to synthesize doped or mixed ferrite with a homogeneous distribution in the doping element. Indeed, the doping element has to be integrated homogeneously in both vesicle and/or onion like structures. Therefore, the precursor of the doping element would have to be "compatible" and to favour the formation of such structure together with iron cations.

Concerning the addition of sodium oleate to adsorb on specific faces of nucleates and thus favor the anisotropic growth of nucleates, we believe that the mechanism is much more complex with, in a first time, an effect of the NaOl on the vesicles formed. This would have an effect on the nucleation as it occurred in the wall of the vesicle that must present much more constraint than the nucleation in the onion. From the phase diagram, we've seen that NaOl can form various mesophases and they can be disturbed by water.

The observations of this chapter would support the formation of FeO. Indeed the nuclei would form inside a fatty acid structure which should prevent the diffusion of O_2 towards the nuclei.

IV.4 Conclusion

While this work was the first step to unveil the formation of NPs, it raised more questions than it answered. The stearates formed two kinds of structures when introduced in the organic solvent with the ligands. From the first part of the study using ex-situ techniques we believe that two kinds of structure are seen: onion like and reverse vesicles. The role of the structure and hydration degree on the distribution of population is still on going.

We've showed that the ligands play a role on the structures. This is major as we observed that the nucleation took place inside these structures. This study showed that a new parameter has to be taken into account with the presence of these onions and vesicles. But identifying and completing their characterization could open new and sharper ways to control size, shape and composition of the NPs in thermal decomposition.

REFERENCES

1. Hyeon, T., Lee, S. S., Park, J., Chung, Y. & Na, H. B. Synthesis of highly crystalline and monodisperse maghemite nanocrystallites without a size-selection process. *J. Am. Chem. Soc.* **123,** 12798–12801 (2001).
2. Sun, S. & Zeng, H. Size-Controlled Synthesis of Magnetite Nanoparticles. *Journal of the American Chemical Society* **124,** 8204–8205 (2002).
3. Deatsch, A. E. & Evans, B. A. Heating efficiency in magnetic nanoparticle hyperthermia. *Journal of Magnetism and Magnetic Materials* **354,** 163–172 (2014).
4. Kolosnjaj-Tabi, J. *et al.* Heat-Generating Iron Oxide Nanocubes: Subtle “Destructurators” of the Tumoral Microenvironment. *ACS Nano* **8,** 4268–4283 (2014).
5. Kumar, C. S. S. R. & Mohammad, F. Magnetic nanomaterials for hyperthermia-based therapy and controlled drug delivery. *Advanced Drug Delivery Reviews* **63,** 789–808 (2011).
6. Hergt, R., Dutz, S., Müller, R. & Zeisberger, M. Magnetic particle hyperthermia: nanoparticle magnetism and materials development for cancer therapy. *J. Phys.: Condens. Matter* **18,** S2919 (2006).
7. Laurent, S., Dutz, S., Häfeli, U. O. & Mahmoudi, M. Magnetic fluid hyperthermia: focus on superparamagnetic iron oxide nanoparticles. *Adv Colloid Interface Sci* **166,** 8–23 (2011).
8. Peddis, D. *et al.* Cationic distribution and spin canting in $CoFe_2O_4$ nanoparticles. *Journal of Physics: Condensed Matter* **23,** 426004 (2011).
9. Baaziz, W. *et al.* High Exchange Bias in Fe3−δO4@CoO Core Shell Nanoparticles Synthesized by a One-Pot Seed-Mediated Growth Method. *J. Phys. Chem. C* **117,** 11436–11443 (2013).
10. Liu, X. *et al.* Systematic Study of Exchange Coupling in Core–Shell Fe3−δO4@CoO Nanoparticles. *Chem. Mater.* **27,** 4073–4081 (2015).
11. Bodnarchuk, M. I. *et al.* Exchange-Coupled Bimagnetic Wüstite/Metal Ferrite Core/Shell Nanocrystals: Size, Shape, and Compositional Control. *Small* **5,** 2247–2252 (2009).
12. Baaziz, W. *et al.* Tuning of Synthesis Conditions by Thermal Decomposition toward Core–Shell CoxFe1–xO@CoyFe3–yO4 and CoFe2O4 Nanoparticles with Spherical and Cubic Shapes. *Chem. Mater.* **26,** 5063–5073 (2014).
13. Kovalenko, M. V. *et al.* Fatty Acid Salts as Stabilizers in Size- and Shape-Controlled Nanocrystal Synthesis: The Case of Inverse Spinel Iron Oxide. *J. Am. Chem. Soc.* **129,** 6352–6353 (2007).
14. Ru-Shi, L. *Controlled Nanofabrication: Advances and Applications.* (CRC Press, 2012).
15. Pichon, B. P. *et al.* Microstructural and Magnetic Investigations of Wüstite-Spinel Core-Shell Cubic-Shaped Nanoparticles. *Chem. Mater.* **23,** 2886–2900 (2011).
16. Wetterskog, E., Tai, C.-W., Grins, J., Bergström, L. & Salazar-Alvarez, G. Anomalous Magnetic Properties of Nanoparticles Arising from Defect Structures: Topotaxial Oxidation of Fe1–xO|Fe3–δO4 Core|Shell Nanocubes to Single-Phase Particles. *ACS Nano* **7,** 7132–7144 (2013).
17. Guardia, P. *et al.* Water-Soluble Iron Oxide Nanocubes with High Values of Specific Absorption Rate for Cancer Cell Hyperthermia Treatment. *ACS Nano* **6,** 3080–3091 (2012).
18. Guardia, P. *et al.* One pot synthesis of monodisperse water soluble iron oxide nanocrystals with high values of specific absorption rate. *J. Mater. Chem. B* (2014). doi:10.1039/C4TB00061G
19. Kim, D. *et al.* Synthesis of Uniform Ferrimagnetic Magnetite Nanocubes. *Journal of the American Chemical Society* **131,** 454–455 (2009).
20. Kwon, S. G. *et al.* Kinetics of monodisperse iron oxide nanocrystal formation by ‘heating-up’ process. *J. Am. Chem. Soc.* **129,** 12571–12584 (2007).
21. Kim, B. H. *et al.* Sizing by weighing: characterizing sizes of ultrasmall-sized iron oxide nanocrystals using MALDI-TOF mass spectrometry. *J. Am. Chem. Soc.* **135,** 2407–2410 (2013).
22. Lassenberger, A. *et al.* Monodisperse Iron Oxide Nanoparticles by Thermal Decomposition: Elucidating Particle Formation by Second-Resolved in Situ Small-Angle X-ray Scattering. *Chem. Mater.* **29,** 4511–4522 (2017).
23. Sun, S. *et al.* Monodisperse MFe2O4 (M = Fe, Co, Mn) nanoparticles. *J. Am. Chem. Soc.* **126,** 273–279 (2004).
24. Redl, F. X. *et al.* Magnetic, electronic, and structural characterization of nonstoichiometric iron oxides at the nanoscale. *J. Am. Chem. Soc.* **126,** 14583–14599 (2004).
25. Park, J. *et al.* Ultra-large-scale syntheses of monodisperse nanocrystals. *Nat Mater* **3,** 891–895 (2004).
26. Demortière, A. *et al.* Size-dependent properties of magnetic iron oxide nanocrystals. *Nanoscale* **3,** 225–232 (2011).
27. Wetterskog, E., Tai, C.-W., Grins, J., Bergström, L. & Salazar-Alvarez, G. Anomalous Magnetic Properties of Nanoparticles Arising from Defect Structures: Topotaxial Oxidation of $Fe_{1-x}O|Fe_{3-\delta}O_4$ Core|Shell Nanocubes to Single-Phase Particles. *ACS Nano* **7,** 7132–7144 (2013).
28. Lak, A. *et al.* Size dependent structural and magnetic properties of FeO–Fe3O4 nanoparticles. *Nanoscale* **5,** 12286 (2013).
29. Hai, H. T. *et al.* Size control and characterization of wustite (core)/spinel (shell) nanocubes obtained by decomposition of iron oleate complex. *Journal of Colloid and Interface Science* **346,** 37–42 (2010).
30. Sun, X., Frey Huls, N., Sigdel, A. & Sun, S. Tuning Exchange Bias in Core/Shell FeO/Fe_3O_4 Nanoparticles. *Nano Letters* **12,** 246–251 (2012).
31. Shipway, A. N., Katz, E. & Willner, I. Nanoparticle arrays on surfaces for electronic, optical, and sensor applications. *Chemphyschem* **1,** 18–52 (2000).
32. Herman, D. A. J. *et al.* How to choose a precursor for decomposition solution-phase synthesis: the case of iron

nanoparticles. *Nanoscale* **7,** 5951–5954 (2015).

33. Baaziz, W. *et al.* Magnetic Iron Oxide Nanoparticles: Reproducible Tuning of the Size and Nanosized-Dependent Composition, Defects, and Spin Canting. *J. Phys. Chem. C* **118,** 3795–3810 (2014).

34. Bronstein, L. M. *et al.* Influence of Iron Oleate Complex Structure on Iron Oxide Nanoparticle Formation. *Chem. Mater.* **19,** 3624–3632 (2007).

35. Ross, F. M. Opportunities and challenges in liquid cell electron microscopy. *Science* **350,** aaa9886-aaa9886 (2015).

36. TEM Liquid Microscopy Cell: Poseidon Select. *Protochips*

37. Brown, G. H. *Advances in Liquid Crystals*. (Academic Press, 2013).

38. Herrington, T. M. & Sahi, S. S. Phase behavior of some sucrose surfactants with water and n-decane. *J Amer Oil Chem Soc* **65,** 1677–1681 (1988).

39. Kunieda, H., Nakamura, K. & Evans, D. F. Formation of reversed vesicles. *J. Am. Chem. Soc.* **113,** 1051–1052 (1991).

40. Kunieda, H., Nakamura, K., Davis, H. T. & Evans, D. F. Formation of vesicles and microemulsions in a water/tetraethylene glycol dodecyl ether/dodecane system. *Langmuir* **7,** 1915–1919 (1991).

41. Kunieda, H., Nakamura, K., Infante, M. R. & Solans, C. Reversed vesicles from biocornpatible surfactants. *Adv. Mater.* **4,** 291–293 (1992).

42. Correa, N. M., Silber, J. J., Riter, R. E. & Levinger, N. E. Nonaqueous Polar Solvents in Reverse Micelle Systems. *Chem. Rev.* **112,** 4569–4602 (2012).

43. Pileni, M.-P. Water in oil colloïdal droplets used as microreactors. *Advances in Colloid and Interface Science* **46,** 139–163 (1993).

44. Lisiecki, I. & Pileni, M. P. Synthesis of copper metallic clusters using reverse micelles as microreactors. *J. Am. Chem. Soc.* **115,** 3887–3896 (1993).

45. Boutonnet, M., Kizling, J., Stenius, P. & Maire, G. The preparation of monodisperse colloidal metal particles from microemulsions. *Colloids and Surfaces* **5,** 209–225 (1982).

46. Yan, Y., Li, B., Li, W., Li, H. & Wu, L. Controllable vesicular structure and reversal of a surfactant-encapsulated polyoxometalate complex. *Soft Matter* **5,** 4047–4053 (2009).

47. Garg, P., Kaur, G., Chaudhary, G. R., Gawali, S. L. & Hassan, P. A. Fabrication of metalosomes (metal containing cationic liposomes) using single chain surfactants as a precursor via formation of inorganic organic hybrids. *Phys. Chem. Chem. Phys.* **19,** 25764–25773 (2017).

48. LaMer, V. K. & Dinegar, R. H. Theory, Production and Mechanism of Formation of Monodispersed Hydrosols. *J. Am. Chem. Soc.* **72,** 4847–4854 (1950).

49. Skoulios, A. & Luzzati, V. Structure of Anhydrous Sodium Soaps at High Temperatures. *Nature* **183,** 1310–1312 (1959).

50. Brouwer, H. W. & Spier, H. L. Acid-Soap Formation in Various Anhydrous Sodium Soaps. *SpringerLink* 131–144 (1972). doi:10.1007/978-3-0348-5775-8_11

51. Borné, J., Nylander, T. & Khan, A. Phase Behavior and Aggregate Formation for the Aqueous Monoolein System Mixed with Sodium Oleate and Oleic Acid. *Langmuir* **17,** 7742–7751 (2001).

Chapter V

Towards an optimization of the thermal decomposition process and extension to other metal stearates

V Towards an optimization of the thermal decomposition process and extension to other metal stearates

Introduction

This chapter aims at improving the thermal decomposition process to make it cheaper and easier to proceed and at demonstrating that the *in house* synthesis of the iron stearate precursors can be extended to other metal stearates. It is highly relevant since manganese and cobalt stearates are commonly used as precursors to synthesize Co and Mn ferrites.

The wide range of iron oxide nanoparticles (NPs) applications emulated researchers around the world to find new ways of synthesis. Today, two main synthesis methods are commonly used : the co-precipitation which consists in the coprecipitation of iron salts by a base in water and the thermal decomposition method which consists in the decomposition of an iron precursor in an organic solvent in presence of ligands. Both methods present advantages and drawbacks. The coprecipitation is simple, cheap and the scale up is possible/easy but the size and shape control remains difficult and NPs being uncoated tend to aggregate. The thermal decomposition method occurs in organic solvents. Although the purification step is time consuming (several washing steps), a scale up has been realized by Heyon et al.[1] and it provides NPs with a very narrow size distribution, high crystallinity and shape control. In fact, the synthesis method can be chosen according to the demands on applications. For example, in biomedical applications, to develop efficient MRI contrast agents and heating agents by magnetic hyperthermia, magnetic properties (e.g. high saturation magnetization, anisotropy) must be highly controlled in order to obtain the most efficient nano-objects[2]. That implies to tune the composition, size and the shape of NPs. Thus, the synthesis of NPs by thermal decomposition appears currently as a method of choice for such specific applications. Furthermore this method leads to non-aggregated NPs as they are *in situ* coated by ligands. Despite meeting the challenge of this area, the scale up is difficult. Few tracks are explored currently to overcome this issue for example, using microwave[3] or continuous flow[4] reactors.

But the synthesis is not the sole problem. In order to be used for biomedical applications, NPs need to be functionalized with biocompatible molecules. To ensure a good functionalization, the excess of ligands used for the control of the size and shape and by-products need to be removed. The most used purification method is to repeat several washings with solvents and centrifugation steps. The NPs covered with ligands are then suspended in a non-polar (or low polarity) solvent (e.g. hexane, chloroform, THF). For the purification step, a polar solvent (acetone, ethanol) is added with a large excess in the final reaction mixture. The role of the polar solvent is to solubilize the ligand molecules. As the NPs are not stable in polar solvents they will tend to precipitate. Centrifugation speeds up the process. The supernatant containing the solvent with ligand is discarded and the operation can be repeated. The removal of supernatant aims at displacing the equilibrium of desorption of ligand.

Considering the purification step, the thermal decomposition is thus not adapted for a large scale up as of today. The thing is that the current synthesis principles of thermal decomposition have not been questioned since its introduction[5–7]. Yet in the last two decades, the choice of precursors widened. What was true for Fe(acac) may not be true for iron alkanoates. This means that a proper reflexion and experiments needs to be done on such synthesis approaches. That's why, in this chapter, some optimizations have been done to improve the scale up of the synthesis of the precursors, the synthesis conditions and the purification process of the reaction mixtures containing NPs just after the synthesis.

Indeed we have developed in chapter III the synthesis of an *in house* precursor by a relatively green and cheap method. Thus some works needed to be performed on the scale up synthesis of this product.

Then we will question the thermal decomposition process. Are all the parameters or all reactants mandatory? Few reports mentioned the synthesis of iron oxide NPs without ligand[8,9] or solvent[10,11] or neither[12]. Thus, understanding what's central and mandatory could help to develop adapted methods that would be simpler and cheaper.

Finally, we have the problem of the purification method of NPs. The current centrifugation methods are time consuming and involve the manipulation of large amount of CMR (carcinogenic, mutagenic, or toxic for reproduction) solvents, exposing the experimenter and generating lot of wastes. This is also a black spot for the industrialisation of the thermal decomposition process.

We have also started to evaluate the cost of our current process on the synthesis of 10 nm iron oxide sphere that has been proven to lead to suitable dendronized MRI contrast agents.[13] To estimate the cost of a synthesis, the prices of the products were considered as much as the time required by a chemical technician to do a synthesis. We found that a batch of 10 nm sized NPs (containing about 150 mg of NPs before washing) costs 40 euros with over 40 % of the cost due to the solvent price. The ligand cost represents about 20 % of the cost. But then centrifuge washing is necessary and as it consume lot of solvent and time, the cost of the synthesis once washed and ready to be functionalized increased at a bit less than 130 euros. 70 % of this total price is thus due to the needed large volume of washing solvents and the long purification time.

Besides this synthesis process consideration, we wanted to show that our *in house* iron stearate synthesis may be applied for the synthesis of other metal stearates and that the so obtained metal stearates conducted to similar NPs as commercial products. Manganese and cobalt stearates have thus been synthesized and characterized. Their sole decomposition or their decomposition in presence of iron oxide NPs have been compared to previous results[14–17].

This chapter is thus divided in four parts: the first one on the optimization of the thermal decomposition process, the second and third ones on the thermal decomposition of *in house* manganese and cobalt stearates and the last one the synthesis of core-shell $Fe_{3-x}O_4$@MnO and $Fe_{3-x}O_4$@CoO NPs from the corresponding *in house* precursors using a seed mediated growth process.

V.1 Taking up the challenge of a cleaner and cheaper thermal decomposition production of IONPs

V.1.1 Experimental details

V.1.1.1 Precursor synthesis small batch

Iron stearate (II) and (III) were prepared by precipitation of sodium stearate and ferrous chloride or ferric chloride salts in an aqueous solution. Briefly, sodium stearate (2.45 g, 8 mmol) was transferred into a 2 necked to a round bottomed flask (RBF) and solubilized in distilled H_2O (80 ml). The solution was heated to reflux and stirred for 30 min until complete dissolution of the stearate. Separately, $FeCl_2.4H_2O$ (0.795g, 4 mmol) or $FeCl_3.6H_2O$ (0.72g, 2.7 mmol) was dissolved in distilled H_2O (40 ml) and added onto the sodium stearate solution under vigorous stirring. A light orange precipitate was formed immediately. The solution was kept under stirring at this temperature 15 min. Thereafter the solution was allowed to cool down to room temperature (RT). The obtained precipitate was washed once by centrifugation (hot dH2O, 14000 rpm, 10 min). The product was then filtrated with a büchner funnel and oven dried at 65 °C for 24 h.

V.1.1.2 Standard 10 nm NPs synthesis and washing conditions

1.38 g of FeSt2, 1.24 g of oleic acid and 20 mL of octylether were mixed together, and then heated to 120°C for 1 h to evaporate residual traces of water or ethanol. Subsequently, the temperature was increased up to 288°C (boiling point of octylether) for 2 h under air with a heating rate of 5°C/min. Finally, black products were washed several times by centrifugation by adding ethanol and chloroform. Final suspensions of NPs were stored in THF.

V.1.2. Results

V.1.2.1 Scaling up the precursor synthesis

The maximal theoretical masses that are obtained are 2.49 g and 2.49g for $FeSt_2$ and $FeSt_3$ respectively. To improve this maximal value, we've studied two parameters.

V.1.2.1.1 Influence of the volume of the reaction

Multiplying the reaction conditions is a first step towards a scaled-up synthesis. Here, a factor 4 was applied with the same protocol working at the same concentration. Figure V.1.1 presents the infra-red spectra of the iron II stearate synthesized following the original and scaled-up protocols. No differences in the band positions or intensities were noted.

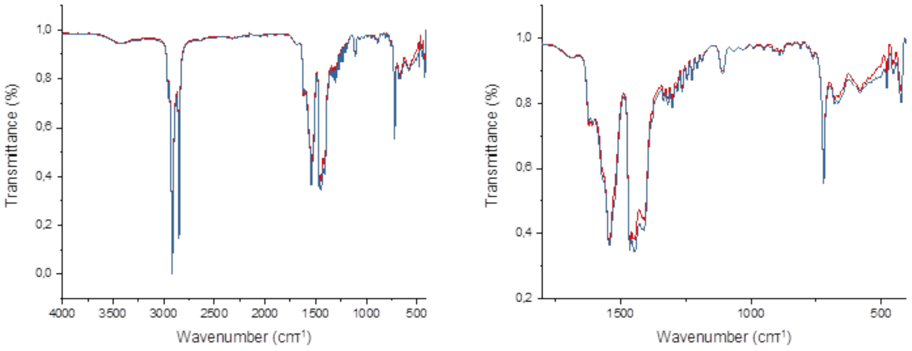

Figure V.1.1 - IR spectra of $FeSt_2$ synthesized with the standard protocol (red) and scaled-up (blue)

The major test for the scale-up of the precursor was the synthesis reproducibility of the "reference" 10 nm spherical NPs. The result of the thermal decomposition in those conditions was given in Figure V.1.2. In both cases, nanospheres were obtained with a mean diameter of 10.3 ± 0.8 nm and 10.2 ± 1 nm for standard $FeSt_2$ and up scaled $FeSt_2$ respectively. As the size and shape were the same, the scale up can be validated.

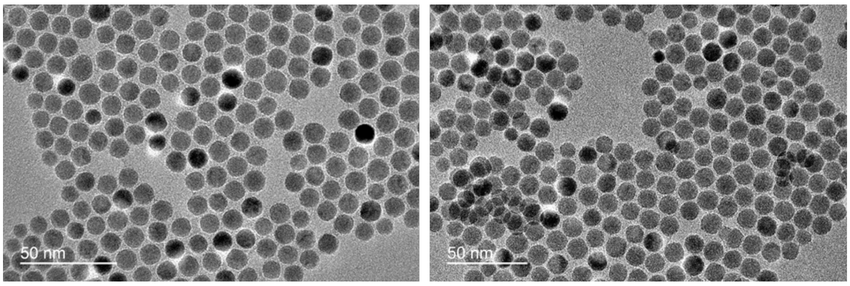

Figure V.1.2 - NPs obtained with standard $FeSt_2$ (left) and up-scaled $FeSt_2$

This first simple scale up of the reaction was successful. Yet one parameter has been detected as limiting for further scale up. The stirring of reaction medium has to be very strong when the chloride solution is added in order to have a good homogenisation. When the iron stearate precipitates, it tends to do it first around the magnet preventing a good agitation. Thus a larger scale up of the synthesis would require a mechanical agitation and some optimization. In average, this up scaled $FeSt_2$ synthesis allowed yielding about 92 ± 3 % of the synthesis. $FeSt_3$ synthesis yield was lower (70 ± 4 %) because of the tendency of this complex to remain on the magnetic stirrer. This up scaled protocol will be now used for the following synthesis optimisations. $FeSt_2$ will be considered since it requires lower amount of stearate than $FeSt_3$.

V.1.2.1.2 Influence of the concentration of reactants

As multiplying the synthesis reactants quantities will be limited at some point, the reactants concentration was investigated. Here, the limiting reactant was NaSt as hydrated $FeCl_x$ were highly soluble in water (685 g/L for $FeCl_2$ at 20 °C and 912 g/L for $FeCl_3$ at 25 °C). NaSt was poorly soluble in water at room temperature (about 150 mg/L). In the protocol, NaSt was solubilized at 30g/L at 100°C. To increase the concentration of NaSt in the synthesis, its solubility at 100 °C has been first estimated. Different amounts of NaSt were solubilized in water at 100 °C in order to identify an upper limit. Good solubilisation was possible up to 100 g/L of NaSt. Above that value, a yellow coloration appeared and by 160 g/L the solubilisation was not complete. The yellow coloration could be indicative of a sol-gel/emulsion process as a gel is obtained after cooling. To remain in the closest conditions of the protocol, the concentration of 100 g/L has been chosen which is already a 3.3 factor scale up. The IR spectrum of the complex synthesized in these conditions was very similar to the one of standard synthesis in Figure V.1.3.

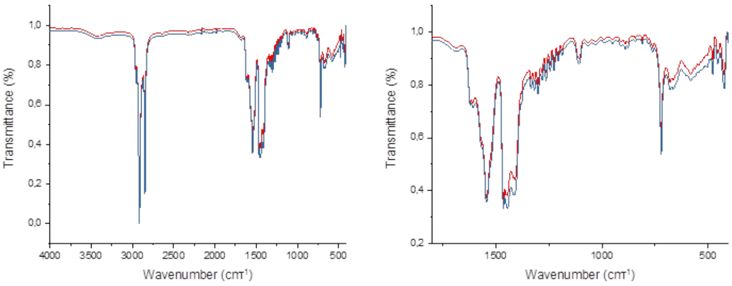

Figure V.1.3 - IR spectra of $FeSt_2$ synthesized with the standard protocol (red) and upscaled (blue)

The decomposition of this complex in the standard conditions led to spheres (Figure V.1.4) that presented a mean diameter of 8.4 ± 0.9 nm which are slightly smaller than the 10.3 ± 0.8 nm of the standard synthesis.

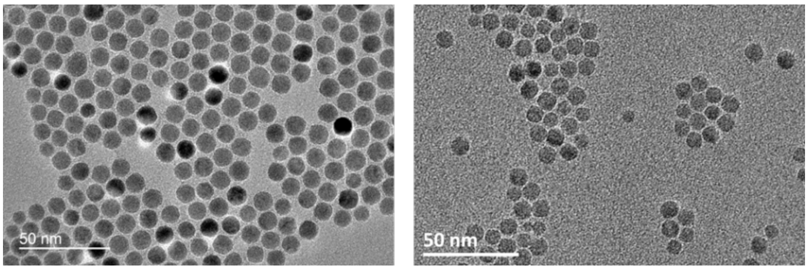

Figure V.1.4 - NPs obtained with standard FeSt2 (left) and upscaled FeSt$_2$

The smaller size could come from environmental difference. It has been noticed that the size of the NPs from the standard protocol varied along the year due to a variation of the humidity. This scale up study has been done during the summer where the humidity can be very high (60% instead of 30%). Thus a reproducibility of this experiment during winter could conclude on the sole role of humidity. The same stirring problem has been observed than for the previous experiment. We were then aware that this point needs to be looked upon for future developments.

V.1.2.1.3 Conclusion

We've managed to scale up the synthesis of our FeSt$_2$ complex by playing on two synthesis parameters. An increase in the reaction volume allowed a scale up by a factor 4 and the increase in the concentration of scale up by a factor 3.3. Yet it seems that the magnetic agitation was a problem during the scale up as the magnetic agitator freezes when FeSt$_2$ precipitated. Thus we didn't try to perform the synthesis with both parameters (volume and concentration) scaled up. A mechanical stirring would be required, but then a scale up by a factor 12 could be reached. This means that about 30 g of product could be synthesized at once; enough to synthesize 21 batches of 10 nm NPs.

V.1.2.2 Identifying the relevant parameters for the synthesis of 10 nm spheres

V.1.2.2.1 Ligands free synthesis

Despite the major role of ligands in the TD method, non-aggregated and more or less homogenous NPs were obtained by decomposing 3 mmol iron stearate in 15 ml of various alkene solvents without adding OA ligands (Figure V.1.5). The heating rates have been varied with a step at the boiling point of the solvent constant at 1h. The heating rate has also been varied as soon as first experiments have shown the formation of very small sized NPs with the standard heating rate of 5°C/min. Mean size values are summarized in Table V.1.1.

Table V.1.1 - Mean size of NPs after the ligand free TD synthesis

Solvent	**Hexadecene** **(B_p = 285 °C)**	**Octadecene** **(B_p = 315 °C)**		**Eicosene** **(B_p = 340 °C)**
Precursor	**FeSt2**	**FeSt2**	**FeSt3**	**FeSt2**
15 °C/min	4.4 ± 0.8 nm	4.6 ± 0.8 nm	11.9 ± 4.3 nm	5.6 ± 1.5 nm
5°C/min		5.3 ± 0.9 nm	7.5 ± 0.8 nm	5.9 ± 1.3 nm

Except for FeSt$_3$ at 15 °C/min, all syntheses presented spherical NPs. Whatever the heating rate and solvent with FeSt$_2$, the mean size was always around 5±1 nm. The mean size increased with the solvent boiling point and a decreasing heating rate as expected.[18] Yet, the size increase remained low. $FeSt_3$ led to larger NPs with two size populations. Reducing the heating rate allowed to obtain a monomodal size distribution centred around 7.5 nm. Indeed FeSt3 decomposing on a larger range of temperature (up to 380 °C) than $FeSt_2$, the monomer generation rate induced by the high heating rate made that the monomer limit concentration for nucleation is quickly reached at high temperature leading to a second nucleation step.

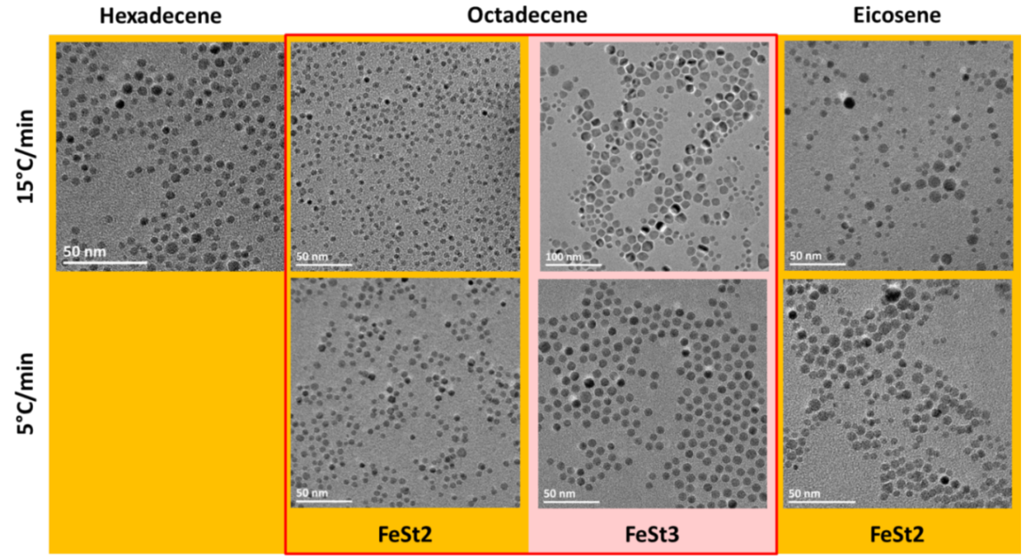

Figure V.1.5 - TEM images of NPs synthesized with the ligand free method in various solvents and at two different heating rates.

IR and XRD analyses were performed on the 4.5 nm NPs synthesized from $FeSt_2$ at 15 °C/min in OD and 7.5 nm NPs synthesized from $FeSt_3$ at 5 °C/min in OD. IR spectroscopy (Figure V.1.6) showed that the 4 nm NPs presented the typical IR spectrum of maghemite with the most intense band centred at 635 cm^{-1} close to the value of pure maghemite (640 cm^{-1}). Note: a band is observed around 720 cm^{-1} ascribed to remaining iron stearates due to an insufficient purification process. 7.5 nm NPs displayed also a spectrum charactheristic of a strongly oxidized magnetite with the two intense bands of the maghemite (at 633 cm^{-1}) and of magnetite (at 590 cm^{-1}). This oxidation degree according to the size has already been observed in a previous study[19] (Chapter I). More importantly, CH_2 bands are also visible at 2917 and 2850 cm^{-1} along with carboxylate bands in the region 1600-1400 cm^{-1} indicating the presence of organic chains at the surface of the NPs. This implied that even synthetized without adding OA ligands, NPs were covered with organic molecules coming certainly from the precursors.

Rietveld refinements of XRD patterns[20,21] (Figure V.1.7.a and b) confirmed that the 4.5 nm NPs have a maghemite (0.8346 nm, JCPDS file 39-1346) composition with a lattice parameter of 8.360 ± 0.002 Å. 7.5 nm NPs with a lattice parameter of 8.358 ± 0.001 Å was in agreement with a maghemite composition.

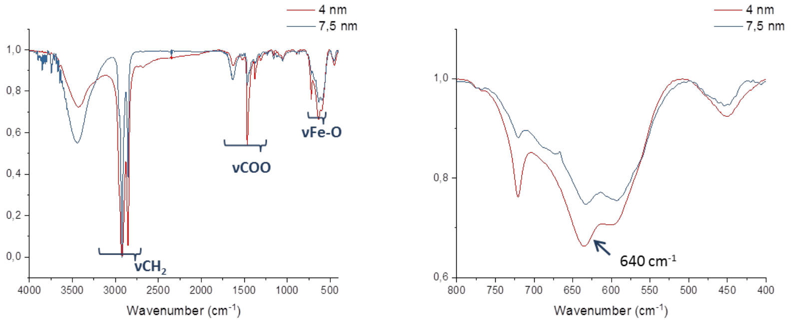

Figure V.1.6 - IR spectra of the 4.5 nm (red) and 7.5 nm (blue) NPs

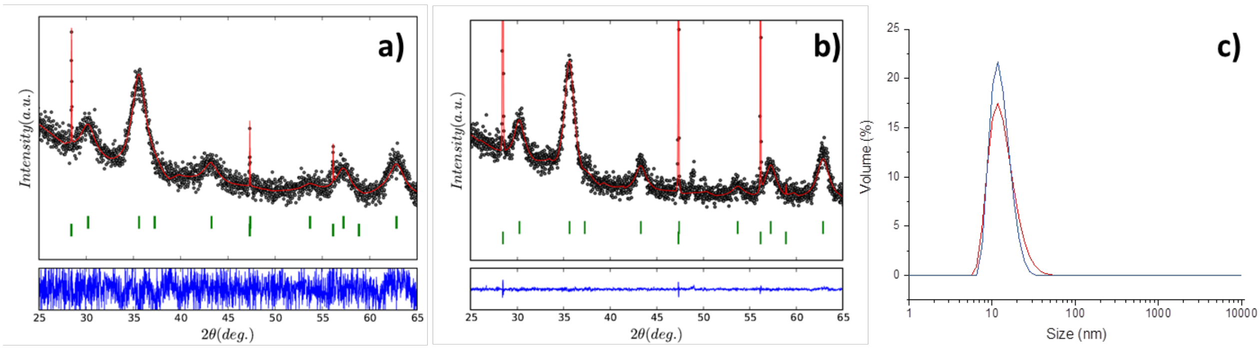

Figure V.1.7 – XRD refinement of the 4.5 a), 7.5 b) nm NPs and DLS measurements of the 4.5 nm (red) and 7.5 nm (blue) NPs c)

DLS measurements (Figure V.1.7.c) showed that NPs synthesized without ligands formed stable colloidal suspension with a monomodal size distribution centred at 11.7 nm. This is in agreement with the coverage of NPs by stearate molecules coming from precursors. To confirm that the stearate molecules are the one stabilizing the NPs, HRMAS measurements were performed. This method is used in solid state NMR spectroscopy and consists in performing NMR measurement by spinning the sample at the magic angle (about 54,74°) with respect to the magnetic field. This allows narrowing the signal usually broadened by the presence of iron. The NMR spectra then evidence the molecules grafted on the surface of the NPs. The Figure V.1.8 compared the HRMAS spectra of 7.5 nm NPs synthesized without ligand and 10 nm NPs synthesized with oleic acid from the standard protocol.

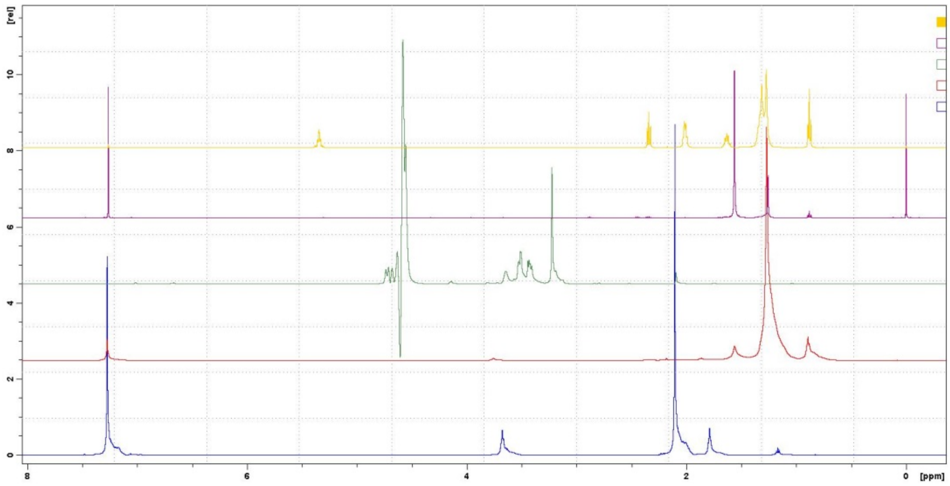

Figure V.1.8 - 1H HR-MAS spectra in $CDCl_3$ of standard 10 nm (blue), 7.5 nm (red), 4.5 nm (green), OA (purple) and NaSt (yellow)

It can be seen that the standard 10 nm NPs presented the representative peaks of OA corresponding to –CH_2- groups (shifted due to different chain organisation in solution and on the NPs) as expected. The peaks seen on the 7.5 nm NPs presented peaks that look like the one of OA and thus were attributed to the stearate chains. Interestingly, the 4.5 nm presented a profile quite different from the control molecules. One can hypothesize that some chain degradation occurred during the synthesis but more characterisations are required to conclude on that point.

It was not so surprising that NPs synthesised without added ligands were finally fully covered by organic molecules. Indeed, the stearate molecules that formed the precursor are also surfactants. With a simple calculation, we can see that when the precursor decomposed to form the NPs, it released in fact enough stearate chains to fully coat the NPs. If we consider 10 nm spheres of pure magnetite (for the simplicity of the calculation), we can determine the number of iron atoms necessary. Magnetite displays 24 Fe atoms per lattice. The elemental lattice presents a volume of 0.592 nm^3 and extrapolating to the volume of a 10 nm NPs (523.6 nm^3), we can estimate that there was about 885 lattices in one NPs. Thus gave us the number of iron atoms necessary to generate a 10 nm spheres: 21232. This mean that if we consider the ideal case where one $FeSt_2$ liberates two stearates chains, 42464 stearates chains will be released. Compared to the 79 nm^2 of the surface of a 10 nm NP, this means that there was up to 541 stearates available per nm^2. Thus even if some precursor didn't fully decompose or if some chains were degraded there are still enough chains to stabilize the NPs.

V.1.2.2.2 "Solvent free" synthesis

First of all, one has to be careful with the solvent free assertion. Indeed the ligand can act as a solvent. Solvent free synthesis is usually labelled as the synthesis without the alkene or dialkyl ether solvents commonly used. But the ligands can play the role of a solvent and so a solventless synthesis should actually be performed without ligand.

In order to highlight the role of the solvent during the synthesis, decomposition of $FeSt_2$ was performed with oleic acid as ligand and with or without solvent. In a second experiment, the ligand and solvent were removed and sole $FeSt_2$ was decomposed. The temperature program was kept similar for all experiments (standard 10 nm spherical synthesis). Figure V.1.9 displayed the TEM images and XRD of the standard 10 nm synthesis with solvent and ligand, "without solvent" but with ligand, and without solvent and ligands. Table V.1.2 listed the structural parameters of so synthesized NPs.

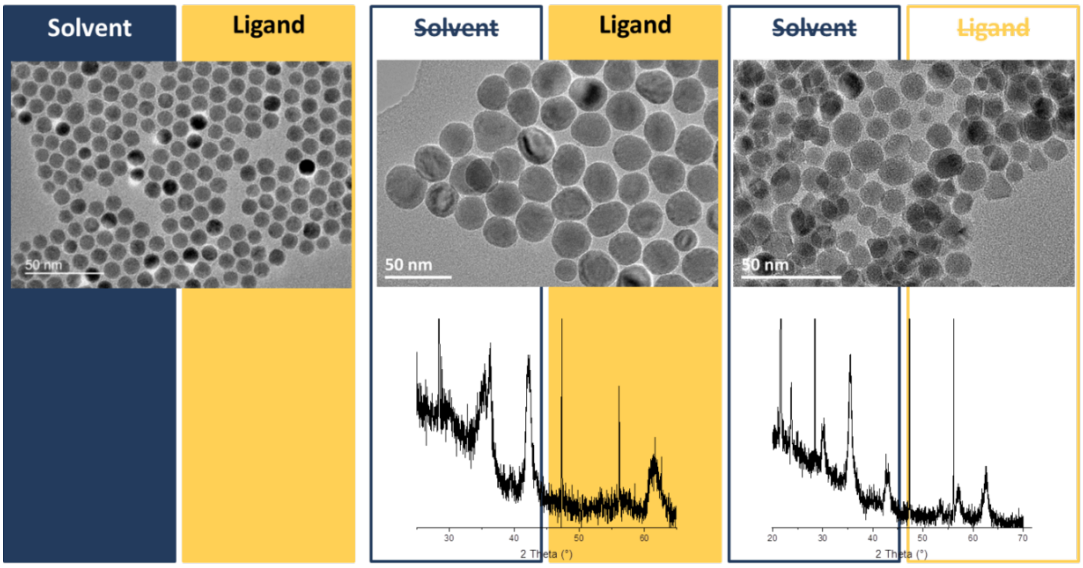

Figure V.1.9 - TEM images and XRD patterns of the NPs obtained in the different synthesis conditions

Table V.1.2 - Structural parameters of the NPs synthesized in the different conditions

	Size (nm)	Lattice parameter (Å)	Crystallite size (nm)	Phase
Solvent + ligand	10.3 ± 0.8	8.379 ± 0.001	10 ± 1	Fe_3O_4
Ligand	27.5 ± 3.8	4.262 ± 0.001	7 ± 1	$Fe_3O_4@FeO$
Ø	11.9 ± 2.3	8.386 ± 0.001	8 ± 1	Fe_3O_4

In the presence of solvent, 10.3 ± 0.8 nm sized and slightly oxidized magnetite spherical NPs were obtained as expected with the standard protocol. When the solvent is removed and sole OA is introduced, NPs with a mean size of 27.5 ± 3.8 nm, an ovoid shape and a $FeO@Fe_{3-x}O_4$ (oxidized wüstite) composition were obtained. When sole $FeSt_2$ is decomposed at 290 °C, slightly oxidized magnetite NPs with a mean size of 11.9 ± 2.3 nm and a quite spherical shape are obtained.

V.1.2.2.3 Discussion

All these experiments confirmed that the ligand (here OA) played a role on the size control during the synthesis. Yet, the size has also been controlled with the thermal parameters and especially the heating rate. This allowed us to synthesize 4.5 and 7.5 nm spherical NPs. This result is quite important as it could be used in a scale up of the synthesis.

Removing the ligand was a test to reduce the synthesis cost as it is quite expensive due to its high purity. Removing the ligand also means that the reaction media will be less viscous. This point could mater in large scale synthesis.

The second test was to remove the solvent that was calculated as among the main cost of the synthesis. The results are encouraging however additional works are still needed. Removing the solvent but keeping the ligand led to wüstite ovoid-like NPs. This results confirmed the previous studies reporting that oleate and oleic acid molecules provided a strong reducing environment favouring the formation of wüstite phase[22,23]. One great interest of this synthesis is that it demonstrated again the role of the solvent in the oxidation of nucleates/NPs: oleic acid/oleate chains at the surface of NPs should form a very compact and also hydrophobic shell and the solvent molecules should interact with the oleic or oleate chains at the surface of NPs, disturb their packing and thus favour the oxygen diffusion toward NPs surface. Therefore it showed that the solubility of ligands in the synthesis solvents could be an important parameter to ensure a good oxidation of NPs during the synthesis process.

Al least, when sole $FeSt_2$ was decomposed, NPs with heterogeneous size and prone to aggregation were obtained. Yet, their mean size and composition are quite close to our standard synthesis protocol. Working on the heating rate could help controlling the nucleation and growth processes. However, the main problem might come from the hydration of the precursor that disrupts its decomposition as seen in chapter III. Thus working with the dehydrated $FeSt_2$ should allow a better control on the final NPs. Synthetizing NPs by the simple pyrolysis of the precursor is a really interesting track for an industrial scale synthesis.

V.1.2.3 New purification process of IONPs

To remedy the long time-consuming purification step of the NPs, we have developed a protocol based on the controlled desorption of the ligands. The main problem was that we used room temperature solvents. The issue was that while the ligands freely adsorbed and desorbed (continuous exchange) from the nanocrystal surface at high temperature, they most likely remained on the surface at room temperature[24]. The proposed idea was to let NPs in contact with the washing solvent, acetone, under mild heating and agitation in order to favour the elimination of ligands excess without aggregating NPs. Typically, a standard 10 nm spherical NPs synthesis was poured in a washing cell right at the end of the NPs synthesis. Then 30 mL of chloroform (to well disperse the NPs) and 350 ml of acetone were added. The cell was heated up to 60 °C for 2h. Then, the NPs are precipitated by a magnet placed at the bottom of the cell and the supernatant is discarded. Fresh chloroform and acetone are again added in the same proportion as in the first step and the cell is heated for 2 more hours. At the end, the NPs are precipitated magnetically and the supernatant discarded. The NPs are dispersed in 10 mL of chloroform and stocked in vial. The experimental layout is shown in Figure V.1.10.

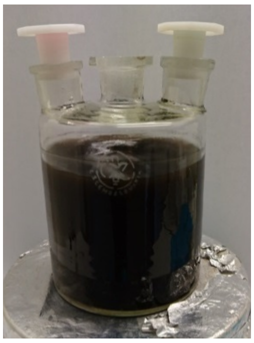

Figure V.1.10 - Experimental layout of the washing procedure

To evaluate the efficiency of our method, one batch of standard 10 nm was washed with centrifugation as reference (18 washing steps are required for cleaning NPs) and a second batch was washed with the established controlled ligand desorption method. The washing was monitored by infrared spectroscopy. It was previously shown that NPs presented a monolayer of ligand on their surface when the intensity of the band of vibration of CH_2 (2917 cm^{-1}) is quite equal to that of the Fe-O band (around 580 cm^{-1}). The IR spectra and the intensity ratio (I_{CH2}/I_{FeO}) evolution are represented in Figure V.1.11.

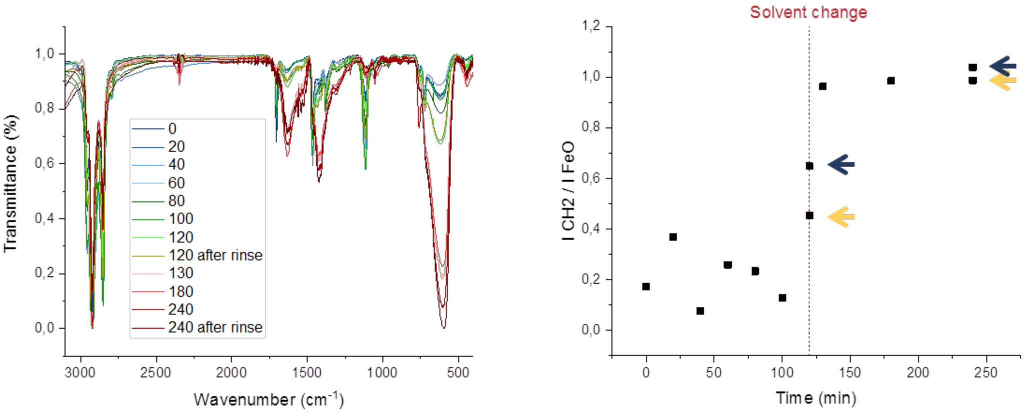

Figure V.1.11 - IR spectra evolution (left) and ratio evolution (right) the yellow arrow indicates a ratio before rinse and blue arrow after rinse

We observed quite no evolution during the first hour of the washing with no trend seen in ratio. A first evolution is noticed after 120 min of heating. IR spectrum was acquired at 120 min but also after the precipitation and solvent change (rinsing) The ratio after the rinsing step is larger due to the removal of precipitated organic by-products during the rinsing step and the shifted equilibrium towards desorption when new solvent is added. In the second step, the ratio already increased a lot after 10 extra min (130 min). It means that most of the ligands are desorbed quickly. Then the evolution is slow and the same evolution after the rinsing step is noted at 240 min.

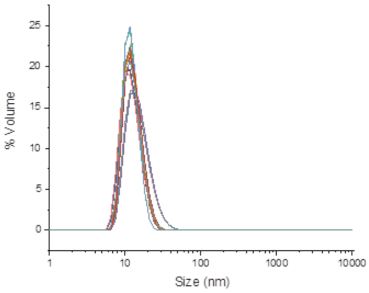

Figure V.1.12 - DLS (% volume) along the washing

The colloidal stability was also monitored during the purification process with DLS measurements (Figure V.1.12) without showing any sign of aggregation.

TEM images realised before and after washing (Figure V.1.13) showed no shape evolution. Mean diameter was measured at 9.3 ± 1.5 nm before washing and 9.7 ± 1.4 nm showing quite no size evolution.

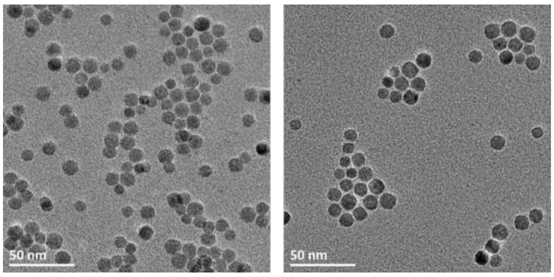

Figure V.1.13 - TEM images of the NPs before washing (left) and after (right)

V.1.2.4 Conclusion

The controlled ligand desorption has been demonstrated as an alternative to the purification process involving several manual washing and centrifugation steps. Some optimization work could be performed in order to reduce the second step that presented a strong evolution in the beginning but slowed afterwards. The yield after washing should also be determined in order to show if more or less NPs are lost with this method. Last but not least, the effect of this method should be tested on core-shell systems (e.g. Fe_3O_4@FeO) to see if it can be used for these systems or if the heat can induce the oxidation of the core phase.

V.1.3 General conclusion

This part demonstrated that the issue for the scaling up of the thermal decomposition process can be bypassed. First of all, we demonstrated that we could scale up the synthesis of our precursor and reached the limit of our lab equipment. Using a mechanic stirring should allow producing even bigger volume but would require new equipment.

We also managed to synthesize NPs without ligand or solvent. These parameters are not mandatory in the TD synthesis but their role is to direct the decomposition. Thus, their presence erased the inhomogeneities of the precursor leading to a homogeneous result. The work realized here with hydrated $FeSt_2$ could be also optimized using a dehydrated precursor.

Finally we have developed a simpler process for the washing of the NPs. Using this protocol, we calculated that the purification step was then representing only 30 % of the final price instead of 70 % with the previous time consuming and manual purification method.

Some works are required to finalize these ideas but we’ve showed strong trail for a large scale production of NPs.

V.2 Synthesis of MnO NPs from an *in house* manganese stearate

V.2.1 Introduction

The objective here is to check if our *in house* manganese stearate precursor would lead also to the same MnO NPs as with the commercial products or with published syntheses. The synthesis of MnO NPs through thermal decomposition (TD) is not so easy and the main difficulty is to tune the size and to control the composition as several phases exist such as MnO_2, Mn_2O_3 and Mn_3O_4. The interest in synthesizing MnO NPs is that they can be good candidate as T1 contrast agent for MRI if their size is very small[25]. Indeed, it was reported that Mn surface atoms were responsible for this T1 effect.

The synthesis of MnO nanocrystals relied for a long time on the hot injection technique which consist in injecting the precursor in the reaction mixture at high temperature by contrast with the heating up technique that we used here that involved the heating of the reaction mixture from room temperature up to high temperature. The first synthesis has been reported at the same time as the first iron oxide synthesis by Rockenberger et al[5] in 1999. Based on the hot injection of manganese cupferron in long chain amines heated around 250- 300 °C, 4 – 10 nm MnO NPs were synthesized. In the following years, several reports showed the synthesis of spherical MnO NPs based on various precursors: $Mn(acac)_2$[26], $Mn_2(CO)_{10}$[27] and $MnOl_2$[28]. Interestingly, the solvent used is always an amine (OAm, TOA) by contrast with the iron oxide NPs synthesis where alkenes were often used. Amines can be considered as solvent but also as a ligand, thus no ligand is introduced. An et al[29], reported the first heating up synthesis of MnO from manganese oleate ($MnOl_2$) in alkenes. Different shapes were obtained depending on the ligand used. With no ligand, 16 nm cubes or 30 nm truncated octahedrons were obtained by varying the boiling point of the solvent. When different long chain carboxylic acids were used, small spheres (<10 nm) were obtained. With an excess of carboxylic acid, rods were observed. The use of alcohols as ligand led to the synthesis of tetrahedrons.

Interestingly, several papers have reported the synthesis of more exotic shapes as multipods[30,31] or dumbbells[32]. These NPs seem to be made out of the assembly of spherical or diamond shaped NPs. In all the reports, the synthesis was carried out in tricotylamine (TOA) with oleic acid (OA) as ligand. Multipods synthesis was performed from the TD of $MnOl_2$[30] or $Mn(HCOO)_2.xH_2O$[31]. Dumbbells were synthesized from $Mn(HCOO)_2.xH_2O$[32]. The proposed mechanism is an oriented attachment mechanism due to dipole dipole interactions[30,32] or a two-step mechanism with an anisotropic growth due to the etching of the NPs[31].

Ould-Ely et al[31] were the only ones to investigate the synthesis parameters responsible for the formation of multipods. Water and excess of carboxylic acid were identified as main parameters that matter for the formation of such shapes. No deeper study was found on the MnO NPs formation and shape control. The problem is that metal precursors of same nature can react differently due to the metal chemistry as we noticed it with iron stearates (Chapter III). This led to a variation in the results of the TD often impacting the shape. Moreover, the nucleation and growth mechanisms that have been proposed for iron oxide may not be applied for other metal oxide as it relies on the precursor decomposition but also on the formed crystallographic phases. For example, manganese precursors were reported to lead to $Mn_{1-x}O$ wüstite phase. This wüstite phase with iron oxide $Fe_{1-x}O$ is not stable and tend to oxidize quickly.

Thus, as we have developed the iron stearate synthesis, it was interesting to expand it to that of Mn stearate and to investigate the so obtained MnO NPs. In this work, we have synthesised and characterized a manganese stearate precursor $MnSt_2$. The information gathered on its structure and stability have been linked to TD results. Thanks to the expertise developed on $FeSt_x$, we've been able to synthesize spherical MnO NPs of various diameters. Dumbbells and multipods synthesis were also reproduced with a different protocol than those already reported. A new mechanism of their formation different from those reported so far was proposed and would rely on the vesicular process identified during the IONPs synthesis (cf. Chapter IV). The protocol used in the following part (unless stated) is an adaptation from the O'Brien synthesis[26]. This adapted protocol has been used by a former PhD student, Aurelie Walter[16], and consisted in the synthesis of MnO NPs from $Mn(acac)_2$. The detailed protocol is given in the experimental part.

V.2.2 Experimental details

V.2.2.1 Precursor synthesis

Manganese (II) stearate was prepared by precipitation of sodium stearate and manganese chloride salts in an aqueous solution. Briefly, sodium stearate (9.8 g, 32 mmol) was transferred into a 2 necked to a round bottomed flask (RBF) and solubilized in distilled H_2O (dH_2O, 320 ml). The solution is heated to reflux and stirred for 30 min until complete dissolution of the stearate. Separately, $MnCl_2.4H_2O$ (3.16 g, 16 mmol) was dissolved in dH2O (160 ml) and added onto the sodium stearate solution under vigorous stirring. A white precipitate is formed immediately. The solution is kept under stirring at this temperature 15 min. Thereafter the solution is allowed to cool down to room temperature (RT). The obtained precipitate is washed once by centrifugation (hot dH2O, 14000 rpm, 10 min). The product is then filtrated with a büchner funnel and oven dried at 65 °C for 24 h.

V.2.2.2 NPs Synthesis

MnO NPs were synthesized with the following protocol adapted from the O'Brien's one[26]. Manganese stearate (1.86 g, 3 mmol) is mixed with OA (2.05 g, 7.2 mmol) in 20 ml of Octadecene in a two neck RBF. The mixture is stirred and heated at 120 °C for 30 min without reflux condenser in order to dissolve the reactants and remove the water residues. The cooler is then connected to the flask and the solution is heated to the boiling temperature (≈ 315 °C) with heating rate of 15 °C/min and heated to reflux for 1h under air. After solubilization the solution is pink and the color evolves quickly to orange. During the heating rate the solution becomes yellow and at the reflux, the solution becomes opaque and a green precipitate is observed and disappears. The solution evolves afterwards to a brown color. After cooling to RT, a brown suspension is obtained which is solubilized in 10 ml of chloroform. The NPs are then precipitated by the addition of an excess of acetone the first time and washed three times with chloroform and acetone at a ratio of 1:4 at 14000 rpm for 5 min by centrifugation. The NPs can finally be suspended in 50 ml of THF.

V.2.2.3 Other characterization techniques

EPR. X-band EPR spectra were recorded with a continuous-wave ESP-300-E spectrometer (Bruker Biospin GmbH, Germany). The resonator is a Bruker ER 4102ST standard rectangular cavity operating in the TE_{108} mode equipped with an ESR900 Oxford cryostat (ν~9.3 GHz in X-band). Temperature was measured with a Cernox sensor (accuracy: $\Delta T/T \sim 5\%$). The spectrometer was tuned so as the settings (modulation coils,incident microwave power) do not distort the EPR signal.

V.2.3 Results

V.2.3.1 Synthesis and characterization of Mn stearate

To synthesise $MnSt_2$ the protocol of $FeSt_2$ was strictly applied by replacing $FeCl_2.4H_2O$ with $MnCl_2.4H_2O$. The IR spectrum is given in Figure V.2.1.a with a zoomed area in the wavenumber range 1800-400 cm^{-1} in Figure V.2 1.b.

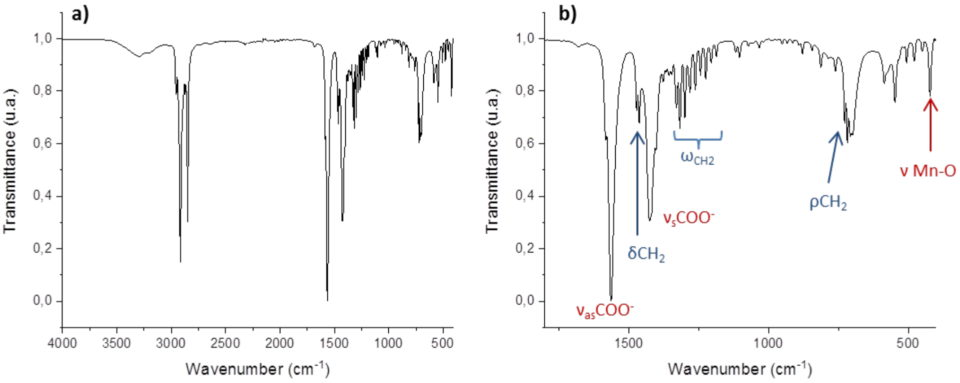

Figure V.2.1 – Infrared spectrum of a) MnSt and b) zoom in the wavenumber range 1800-400 cm^{-1}.

The bands were assigned by using the same approach as the one used for $FeSt_x$ in Chapter III. In the 3800-3000 cm^{-1} range, the broad vibration band between 3600 and 3200 cm^{-1} is assigned to the OH stretching vibrations of water molecules (physisorbed molecular water). The all trans conformation is confirmed for $MnSt_2$.

Two specific vibrational modes of the alkyl chain gave precious information about the organisation of the chains. The rocking of the chain ρCH_2 (720 cm^{-1}) and the scissoring δCH_2 (1465 cm^{-1}) of the methylene chains can split depending on how they crystallize. This splitting also referred as Davidov splitting, originated from the interaction of vibrational modes of two translationally non-equivalent molecules[33]. The value of the splitting $\Delta_{\nu D}$ is dependent of the intermolecular interactions and varies inversely to the cube of intermolecular spacing. Moreover, the intensity ratio of the two components of the doublet gave indication on their mutual orientation. With a triclinic packing leading to a strong and narrow band at 1470-1474 cm^{-1}, an orthorhombic one to a doublet at 1462 and 1474 cm^{-1}, a hexagonal packing will translate as a single band at 1468-1469 cm^{-1} [34,35]. This can be completed with the analysis of the in plane rocking of CH_2 (ρCH_2) at 720 cm^{-1}. If this band is splitted, an orthorhombic packing is confirmed; if not (singlet) it's either a triclinic or hexagonal packing[36]. Contrarily to $FeSt_x$, $MnSt_2$ present a splitting for both bands hinting toward an orthorhombic packing of the chains.

Table V.2.1 - Approximate assigments of the rocking and scissoring bands for HSt and $MnSt_2$

HSt	MnSt	Proposed assignment
1471	1472	δCH_2
1463	1462 s	
727	727 m	ρCH_2
720	717 m	

To determine the coordination of the stearate on Mn the carboxylate bands have been studied and the proposed assignments are given in Table V.2.2.

Table V.2.2 - Approximate assigment in the region 1800-1400 cm^{-1} for HSt, NaSt and MnSt

HSt	NaSt	MnSt$_2$	Proposed assignments
1700 vs		1681 vw	νC=O
	1558 vs	1582w, sh 1582w, sh	$\nu_{as}COO^-$
1470-1462 m	1467	1472 -1462 s	δCH_2
1429 s 1410	1441 s 1419 s	1423 s 1403 m, sh	ν_sCOO^-

Table V.2.3 - Δν calculated for HSt, NaSt and MnSt

	Monodentate	Bridging	Mixed	Chelating
HSt	271, 290			
NaSt		139	117	
MnSt		179 w, 140s		

IR spectra of Mn stearate displayed similar carboxyl bands as FeSt$_x$ with two ν_{as}COO bands and two ν_sCOO . The presence of a weak band at 1700 cm^{-1} suggested the presence of small amount of free stearic acid. Contrarily to FeSt$_x$, the weak band at 1620 cm^{-1} attributed to the bending mode of water molecules is not observed whereas the broad band between 3500-3000 cm^{-1} was clearly visible. Nevertheless, the foot of the band, where carboxyl bands are present, is quite large at this position and may include this small contribution.

The same methodology for band assignment then for FeSt$_x$ has been applied (cf. Chapter III). The IR spectra of stearic acid (HSt) and sodium stearate (NaSt) have been considered and compared to those of Mn stearate. The carboxyl asymmetric (ν_{as}COO) and symmetric (ν_sCOO) stretching vibrations have been indexed for HSt and NaSt and the position of the carboxylate bands are given in Table V.2.3. Based on the detailed analyses in Chapter III, the bands at 1582 and 1423 cm^{-1} of MnSt$_2$ would be attributed to a bridging conformation. The band at 1582 and 1403 cm^{-1} are in agreement with a second bridging coordination with a Δν of 180 cm^{-1}. As MnSt$_2$ presented noticeable bands of OH between 4000 and 3000 cm^{-1}, a bridging interaction involving water molecules, as we observed with FeSt (Chapter III), is thus probable. MnSt$_2$ would present then two bridging coordination with a minor one due to water molecule and a major one due to the bridging on two Mn atoms.

V.2.3.2 Thermal decomposition of Mn stearate

The TGA curve (Figure V.2.2) showed a similar behaviour with temperature than FeSt$_x$. Starting with a weight loss due to physisorbed water around 90°C, then a slight weight gain occurred at 195 °C that could be due to the oxidation of Mn (II) in Mn (III) as observed for hydrated iron stearates (Chapter III). The first noticeable weight loss happened at 207 °C at a lower temperature than that for FeSt$_x$ (around 250 °C). This first weight loss is often ascribed to the nucleation step in the TD process. MnSt$_2$ would decompose at lower temperature and would thus be less stable than FeSt$_x$. A third region is then identified at higher temperature with a succession of exothermic peaks in the DTA curves between 265 and 330°C. This region has been attributed in chapter III to the proper decomposition of the precursor with the loss of stearate chains leading to the generation of monomers necessary for the growth step. The multiple peaks would be an indication of a distribution of precursors presenting different thermal stabilities. The last strong exothermal peak at 392 °C would indicate the complete decomposition of the organic chain. The remaining mass is the oxide formed from Mn, most likely Mn$_2$O$_3$ (the most oxidized state) because of the high temperature. The total weight loss was determined to be of 86.9 %. Four regions are thus identified: (I) dehydration and Mn oxidation, (II) precursor decomposition/nucleation, (III) further decomposition/growth step, (IV) thermal degradation of organic chains.

Table V.2.4 – DTA and DTG peaks of $MnSt_2$

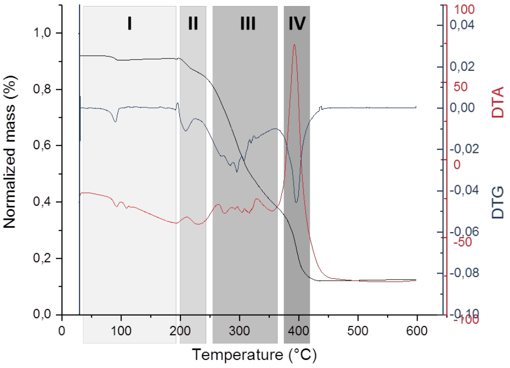

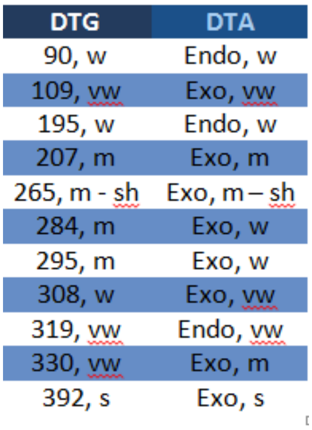

DTG	DTA
90, w	Endo, w
109, vw	Exo, vw
195, w	Endo, w
207, m	Exo, m
265, m - sh	Exo, m – sh
284, m	Exo, w
295, m	Exo, w
308, w	Exo, vw
319, vw	Endo, vw
330, vw	Exo, m
392, s	Exo, s

Figure V.2.2 - TGA, DTA and DTG curves of $MnSt_2$ under air (5°C/min)

$MnSt_2$ was decomposed using the adapted O'Brien protocol that has been reported to lead to spheres. The TEM images of the so synthesized NPs are given in Figure V.2.3.a.

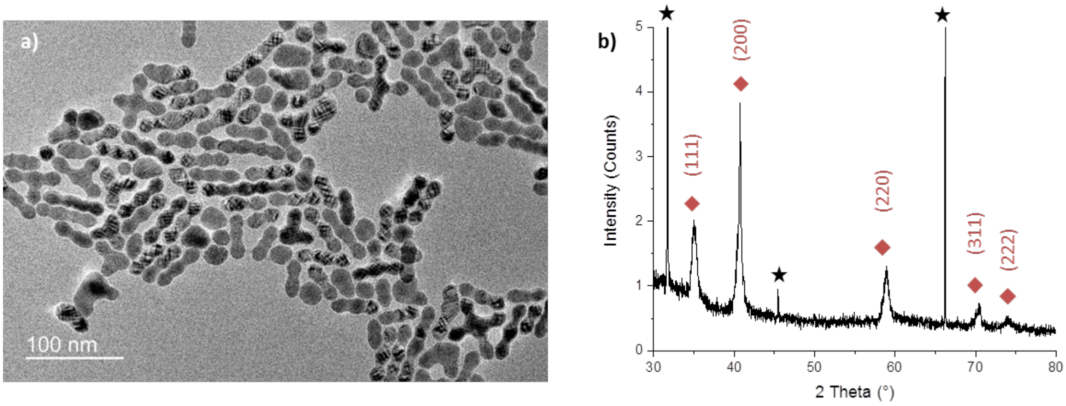

Figure V.2.3 - TEM image of the TD of MnSt a) and associated XRD, stars are for the Si reference b)

Interestingly, instead of forming nanospheres, elongated caterpillar-like NPs were obtained. The caterpillar looked like an assembly of spherical NPs that remind the dumbbell shape previously reported in literature. Yet the size of the spherical subparts is homogeneous along the NPs (13.9 ± 1.3 nm) contrarily to the dumbbell shape whose ends are larger. XRD (Figure V.2.3.b) pattern allowed identifying a rock salt cubic MnO crystallographic phase (JCPDS 04-005-4310). This result is quite unexpected as nothing in the synthesis protocol could explain the formation of such objects. Oriented attachment requires the presence of high surface energy crystallographic planes if not a lack of surfactants. However, nothing in the protocol should allow this process. Thus we can hypothesize that if the synthesis conditions are not responsible, the precursors itself shall be. To link a potential role of the precursor to the shape some work on the precursor synthesis is required.

V.2.3.3 Investigation of the caterpillar shape of manganese oxide NPs

V.2.3.3.1 The role of precursor structure

Even though $MnSt_2$ started to decompose earlier than $FeSt_x$, this shall not explain the caterpillar shape previously observed. What's most likely to happen is the presence of a disruptive element in the precursor itself. As the precursor synthesis is controlled, no impurity is expected from outer contamination. However we have seen in chapter III that $FeSt_x$ complexes did not present the expected stoichiometry in stearate chains and that water molecules interfered in the formation in stearates and in their structure. One possible “problem” would thus originate from the structure of the Mn stearate which would bear less stearate chains. Furthermore this hypothesis would be in agreement with the fact that an aggregation of NPs is generally observed when there is not enough surfactants in the reaction mixture. Nevertheless we have here a particular 1D aggregation.

Water would limit the coordination of stearate chains on Mn cations and the Mn stearate formation kinetics would be slower than that of FeSt. To highlight this point, the synthesis protocol of $MnSt_2$ has been varied. To favour the reaction between Mn and the stearate chains, the reaction time was extended to 1h15. To evaluate the role of a possible remaining reactant, the washing step during filtration, that is usually performed with water at room temperature (RT), has also been performed with warm water. As NaSt is poorly soluble in water at room temperature and soluble with increasing temperature, this washing step should help to better pin the responsibility on stearate chains. The four conditions are summarized in the Table in Figure V.2.4 along the name given to each precursor (note that the fill colour of each case will be the colour associated for each precursor in the following graphs). Figure V.2.4 presented the results of the thermal decomposition of the different precursors and Table in Figure V.2.4 summarized the size distribution of so synthesized NPs.

Reaction time	**15 min (short)**	**1h15 (long)**
Warm water filtration	Mn_{SW}	Mn_{LW}
	14.7 ± 1.5	11.9 ± 1.7
RT filtration	Mn_{SRT}	Mn_{LRT}
	13.9 ± 1.3	19.3 ± 3.3

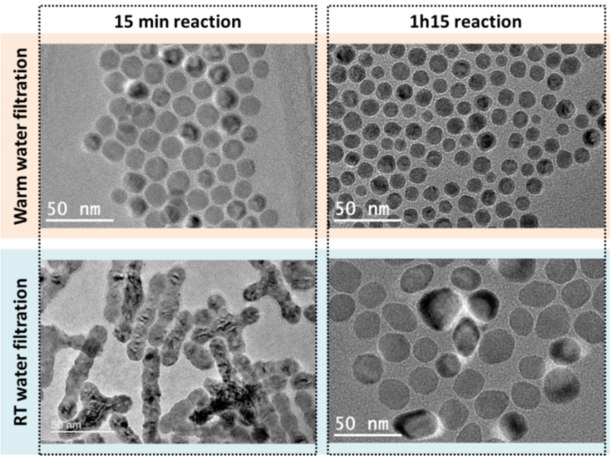

Figure V.2.4 – Table (left) and TEM images (right) of the NPs obtained after the TD of $MnSt_2$ synthesized in various conditions

The Mn precursors presented a high dependence on the filtration step. A filtration with warm water led to spherical 14.7 ± 1.5 nm NPs when RT water led to caterpillar like NPs made out of 13.9 ± 1.3 spheres for the 15 min reaction. At 1h15, 19.3 ± 3.3 nm ovoids are obtained for the RT water and 11.9 ± 1.7 nm spheres for warm water. The fact that non spherical shapes are obtained with the RT water filtration is in agreement with the role of unreacted NaSt in the shape control. Increasing the reaction time tended to agree with a better reaction of NaSt with Mn as the caterpillar shape is lost for the RT washing. The same rock salt cubic MnO crystallographic phase is identified by XRD for all NPs.

To clearly identify the reactant responsible for the caterpillar shape, the different $MnSt_2$ were thoroughly characterized. First, the IR spectra were expected to evidence major differences. Surprisingly, the four precursors presented quite the same spectrum as seen on Figure V.2.5. No effect on the coordination of carboxylate is denoted.

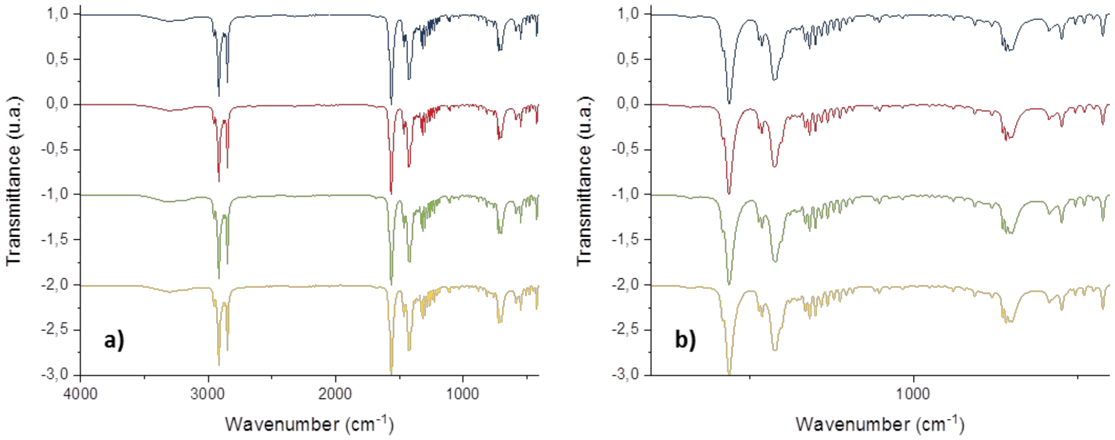

Figure V.2.5 - IR spectra of Mn_{SRT} (blue), Mn_{SW} (red), Mn_{LRT} (green) and Mn_{LW} (yellow) a) and zoomed in the region 1800-400 cm^{-1} b)

Secondly, X-band EPR spectra were acquired by Dr Nathalie Parizel. Two precursors giving different NPs results after their TD were analysed: Mn_{SRT} leading to caterpillars and Mn_{LW} leading to spheres. Figure V.2.7 presented the spectra acquired at 50 and 4 K. Both complexes present similar spectra.

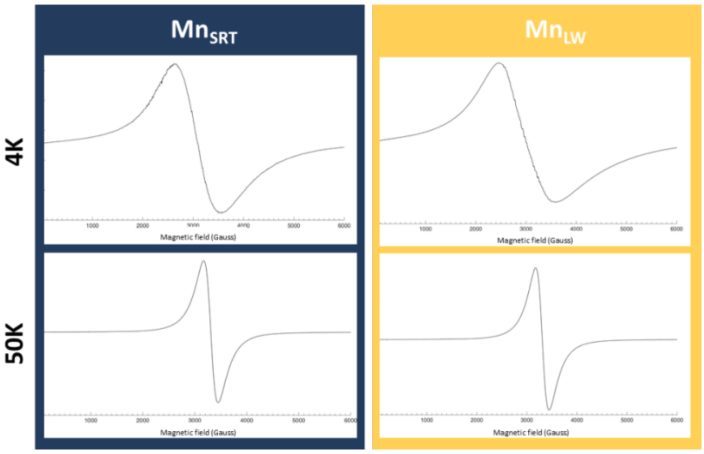

*Figure V.2.6 - EPR spectra of **Mn_{SRT}** and Mn_{LW}*

EPR spectra suggested thus that two Mn environments are present in both Mn stearates. It is in agreement with analyses of IR spectra from which two bridging coordinations of Mn were identified.

Powder XRD acquired on Mn_{SRT} and Mn_{LW} showed no differences (Figure V.2.7) with the same lamellar structure and interlamellar distance (50 Å , close to what was measured for $FeSt_x$).

These characterizations suggested that the structure of Mn stearates would not be responsible for the observed shape.

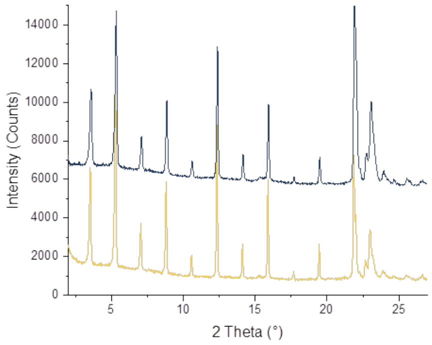

Figure V.2.7 - powder XRD of Mn_{SRT} (blue) and Mn_{LW} (yellow)

TGA was the first characterisation to evidence a difference. All the features identified in DTA and DTG curves are summarized in Table V.2.5. No major differences are observed up to 220 °C. This implies that the dehydration and oxidation mechanisms are quite the same for all complexes. The interesting variation occurred in the “nucleation” region and mostly in the “decomposition” region. The “nucleation” region is found to be different for **Mn_{LRT}**. The peak at 265 °C is reduced and another peak more intense is seen at 252 °C. For Mn_{LW}, this peak is not shifted but appeared more intense whereas its intensity was medium for the short synthesis. Thus the reaction time seems to have an effect on the beginning of the decomposition of MnSt.

Table V.2.5 - Features identified in DTA and DTG curves of the four precursors

Mn_{SRT}		**Mn_{SW}**		**Mn_{LRT}**		**Mn_{LW}**	
DTG	DTA	DTG	DTA	DTG	DTA	DTG	DTA
90, w	Endo, w	90, w	Endo, w	90, w	Endo, w	91, w	Endo, w
109, vw	Exo, vw	110, vw	Exo, vw	108, vw	Exo, vw	109, vw	Exo, vw
195,w	Endo,w	200 ,w -sh	Endo,w	195,w	Endo,w	186,w	Endo,w
207, m	Exo, m	214, w	Exo, w	202, m	Exo, w	201, m	Exo, w
				252, m	Exo, m		
265, m - sh	Exo, m - sh	266, m - sh	Exo, m - sh	269, w	Exo, m	265, s	Exo, w
284, m	Exo, w	289, m	Exo, m	281, m	Exo, w	275, s	Exo, w
295, m	Exo, w	297, m	Exo, w	292, m	Exo, w	292, s	Exo, w
308, w	Exo, vw	308, m	Exo, m	311, m	Exo, m	308, w	Exo, vw
319, vw	Endo, vw	323, m	Exo, m	324, w	Endo, vw	314, vw	Endo, vw
330, vw	Exo, m	330, m	Exo, m	335, w	Exo, m	329, m	Exo, m
						336, m	Exo, m
						363, w - sh	Exo, w - sh
		375, m	Exo, m	370, w – sh	Exo, w - sh	379, m	Exo, m
392, s	Exo, s	401, s	Exo, s	396, s	Exo, s	392, s	Exo, s
						412, s	Exo, s

The “decomposition” region was found to be changed with the synthesis conditions. The distribution of peaks in this region was associated with a distribution of precursors of different thermal stability for $FeSt_x$. In **Mn_{SRT}**, the decomposition is clearly marked from the degradation region (IV). **Mn_{SW}** present a peak at 375 °C that would indicate the formation of a highly stable intermediate that decomposed a bit before the organic chain decomposition. Same observation was made for **Mn_{LRT}** but for this precursor, the nucleation and decomposition region were not clearly separated with the appearance of a peak at 252 °C. Finally, Mn_{LW} present more peaks in the decomposition region that is not clearly separated from the final degradation. This would indicate the formation of lot of intermediates with various stabilities. The total weight loss was measured at 85 % for **Mn_{SW}**, 86 % for **Mn_{LRT}** and 94 % for Mn_{LW}. Thus the synthesis conditions have a strong influence on the precursor. With different intermediates formed the decomposition becomes more complex and might not be total during a NP synthesis.

SEM images were acquired on Mn_{SRT} and Mn_{LW} (Figure V.2.8). Both complexes presented the same flake morphology as observed for $FeST_x$. Yet a difference is denoted thanks to EDX analysis. Three areas of each precursor were analysed showing a variation in the ratio of intensities for C and Mn. Mn_{SRT} presented a ratio I_C/I_{Mn} of 45 ± 19 when Mn_{LW} presented a ratio of 15 ± 5. This indicates that more chains are present in Mn_{SRT} than for Mn_{LW}. In both case, no Na or Cl were detected hinting towards the role of the sole stearate chains in the caterpillar shape control.

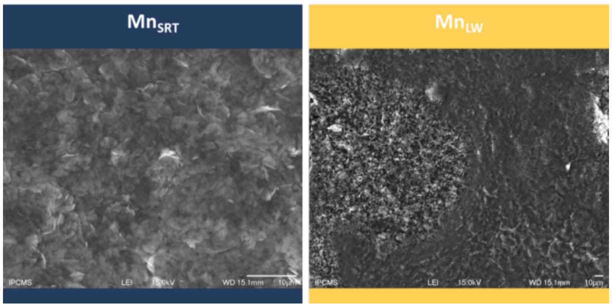

Figure V.2.8 - SEM images of ***Mn_{SRT}*** *and* ***Mn_{LW}*** *precursors*

V.2.3.3.2 Synthesis mechanism of caterpillar MnO NPs

The caterpillar shape observed for the decomposition of a specific MnSt is quite interesting. The caterpillar resembles to the dumbbells NPs. The dumbbells formation is explained by the oriented aggregation of MnO NPs. Yet an element of the caterpillar would hint at another formation mechanism: the Moiré patterns. The Moiré patterns (Figure V.2.9) are spatial interferences. They appear when two patterns (identical or not) are superposed but displaced or rotated. Then, dark and bright lines are observed.

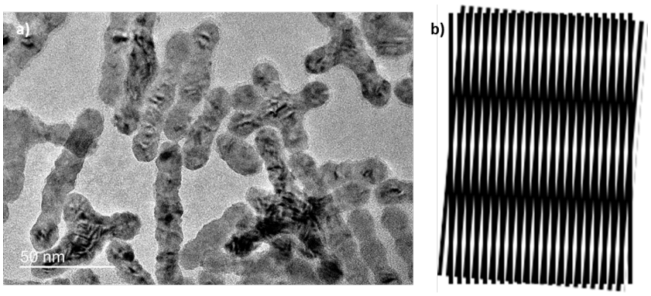

Figure V.2.9 - Caterpillar NPs presenting Moiré patterns a) and drawing of two rotated patterns creating a moiré pattern b)

The Moiré patterns observed on the caterpillar are mostly localized in the centre of the spherical part of the chain. Thus, this indicates that two MnO lattices are superimposed but not perfectly. The localisation of these patterns confirms that the caterpillars are made of a chain of spheres coated by a MnO layer. This hints at a two-step mechanism: the formation of MnO spheres and in a second time the deposit of MnO on the chain of spheres. Yet the question arised of why the spheres aligned and why MnO further deposited between aligned NPs.

Furthermore, we have seen in chapter IV that $FeSt_x$ are involved in reverse vesicles just after the homogeneisation steps of reaction mixture at 120°C (cf Chapter IV). Nucleates are observed to form in such vesicles which disappeared at high temperature due to the solvatation of surfactants. That was suggested that the growth step occured outside vesicles (as they have disappeared). Such a vesicular mechanism could also work for MnSt and could explain the caterpillar formation. It is further supported by the fact that was the precursor which was shown to contain the higher amount of stearate chains. The hypothesis of the formation of long 1D vesicles with **Mn_{SRT}** has thus been investigated.

The results of liquid AFM realized in the same conditions as in Chapter IV are presented in Figure IV.2.10. The first point was that vesicular structures were also detected for this precursor. Yet most of them were spherical with a size of about 15 nm. Nevertheless, larger objects were detected (red arrow). Thus, we supposed that the formation of elongated vesicles was concentration dependent. As the reactant media are diluted at 1/20^{e} for the AFM analysis, we assume that such dilution might have broken the elongated structures. Further investigations in more concentrated solutions will be performed in liquid AFM in future experiments.

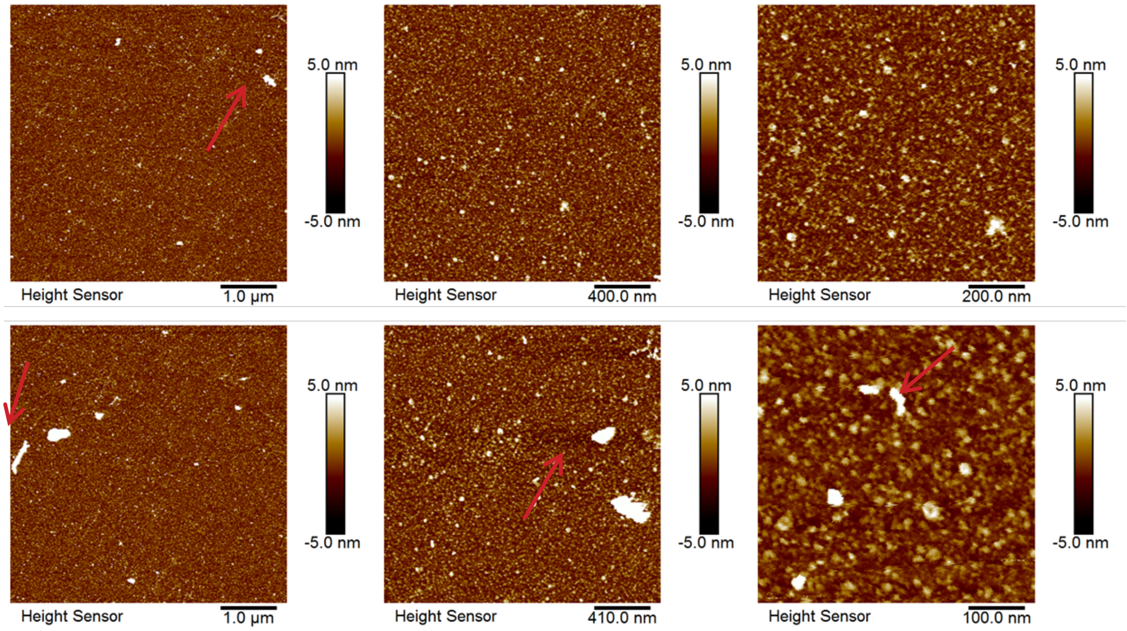

Figure IV.2.10 – Liquid AFM of the MnO caterpillar reactant media. AFM images are zoomed from the left to the right.

Thus, to confirm a vesicular process of formation of the caterpillar, additional experiments have been performed. Some reports concerning the dumbbells synthesis demonstrated also a role of water in the formation of such shapes[31]. To confirm if water would play a role in our system, **Mn$_{SRT}$** has been dehydrated following the protocol used for FeSt$_x$ (cf. chapter III). The dehydrated precursor has been decomposed with the adapted O'Brien protocol and the result of the TD is shown in Figure V.2.11.

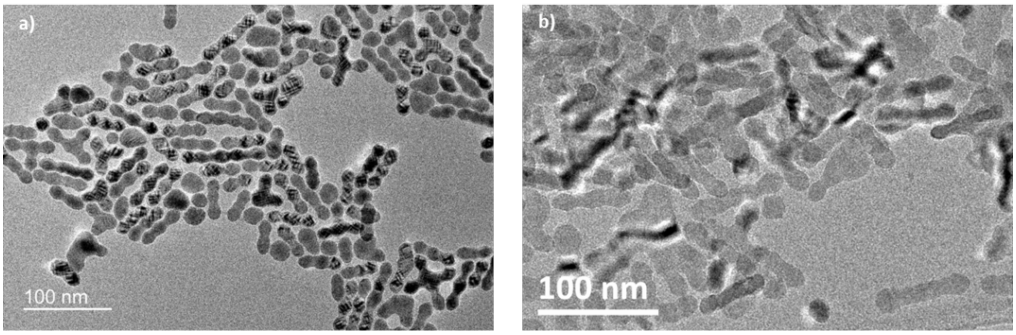

Figure V.2.11 - TEM images of NPs synthesized by TD of ***Mn$_{SRT}$*** *a) and* ***Mn$_{SRT,dehydrated}$*** *b)*

Caterpillars are always obtained demonstrating no role of water in our system. The same rock salt cubic MnO crystallographic phase is identified with XRD for all NPs. The NPs constituting the caterpillar have a mean diameter of 15.6 ± 3.5 nm. This value is in agreement with the one measured with the first caterpillar synthesis.

Another test/experiment to understand this specific shape formation was to reproduce the synthesis of caterpillar. The synthesis of **Mn$_{SRT}$** has been reproduced and the synthesis of the caterpillar NPs was found reproducible within **Mn$_{SRT}$** batches. Yet, their length varied from one batch of precursor to another. This is in agreement with the presence of a disruptive molecule in various amounts. To investigate the role of a disruptive element in the formation of caterpillars, **Mn$_{SRT}$** that led to short caterpillars was decomposed in replacing part of the oleic acid by hexadecylamine. The shape of surfactant structures relied on various parameters but it has been shown that a co-surfactant with a smaller head group tends to form larger structures[37,38]. The NPs shape was found to be tuned when part of the oleic acid was replaced with hexadecylamine (HDA) as shown in Figure V.2.12.

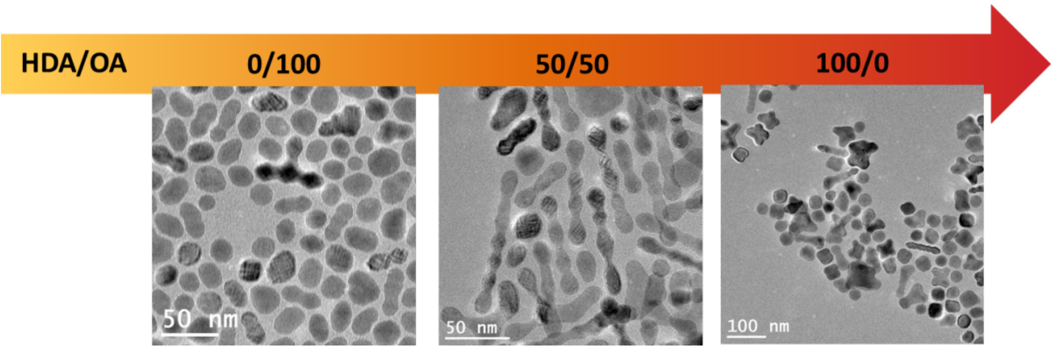

Figure V.2.12 - Shape evolution with the ratio OA/HDA

The shape evolved from small caterpillar to longer caterpillar for a ratio 50/50. Sole HDA led to octopods. This evolution has been observed several times and all the NPs presented the same rock salt cubic MnO crystallographic phase. Table V.2.6 summarized the measured mean size. In the case of caterpillar, the size of the NPs contained in the caterpillar are measured as well as the number of NPs per caterpillar.

Table V.2.6 - Size distribution of the TD with various HDA/OA ratios

Ratio OA/HDA	0/100	50/50	100/0
Size (nm)	18.2 ± 4.0	13.5 ± 2.5 (≈4)	50.5 ± 18

It seems that for caterpillar to be longer, the size of the NPs needs to be smaller. This is in agreement with the first caterpillar synthesis presented earlier (13.9 ± 1.3 nm). When sole HDA is introduced, octopods like shaped NPs are obtained. The thing is that amines can have a double role here as this surfactant family is known to destabilize the precursor[19]. Thus, the octopods could come from a too fast decomposition of the precursor that prevents the organized orientation seen for the former ratio. This study confirmed a vesicular process of caterpillar formation driven by molecules present during the synthesis. HDA can be used on a precursor prone to form this shape.

The next step has been to introduce surfactants to recreate the conditions of the caterpillars' synthesis from Mn_{LW}. We have seen from the different precursor analyses that the number of chains for a Mn atom seemed to be the major difference. Moreover, long chain carboxylic acids have been demonstrated to elongate the shape of surfactant structure[39]. HSt was tested as well as NaSt. As the surfactant is also present in **Mn_{SRT}**, the mass of Mn_{LW} was reduced of the amount of surfactant introduced. Control experiments were performed with the reduced amount of Mn_{LW} and without surfactants to evidence the role of the lower concentration. Figure V.2.13 showed the TEM images of the so obtained NPs and Table V.2.7 listed the size.

As during the synthesis of MnO NPs, a precipitation was observable, the precipitation time can be noted and are reported in Table V.2.7. The reduction of the concentration in Mn_{LW} led to bigger NPs. The NPs were longer to precipitate with the decrease of concentration. OA which is added as the NPs stabilization ligand seemed to stabilize the precursor delaying its decomposition towards higher temperature as it has been observed in chapter V.1. This is in favour of the growth of the NPs instead of the nucleation leading to bigger NPs.

The replacement of a part of Mn_{LW} by HSt led to spherical NPs whose size increased with the dilution as observed previously. HSt seems to play no significant role here. NaSt had an influence for the lowest amount introduced. The precipitation time was highly increased at 85 min. The NPs presented no defined shape with some being quite spherical when other are completely deformed. For the second amount of NaSt, MnO pods were obtained partly. Even though, this was not caterpillar, this morphology was related and relied probably on the same formation mechanism. The precipitation time is again highly increased around 260 min. As expected, higher amount of NaSt led to nothing as no precipitation was observed. The formation of NP was completely hindered. As sodium oleates were known to stabilize the precursor and delayed the nucleation step, this seems logical. Moreover, as there were fewer precursors, the chance to get enough monomer to nucleate is quite low explaining that no NPs are formed.

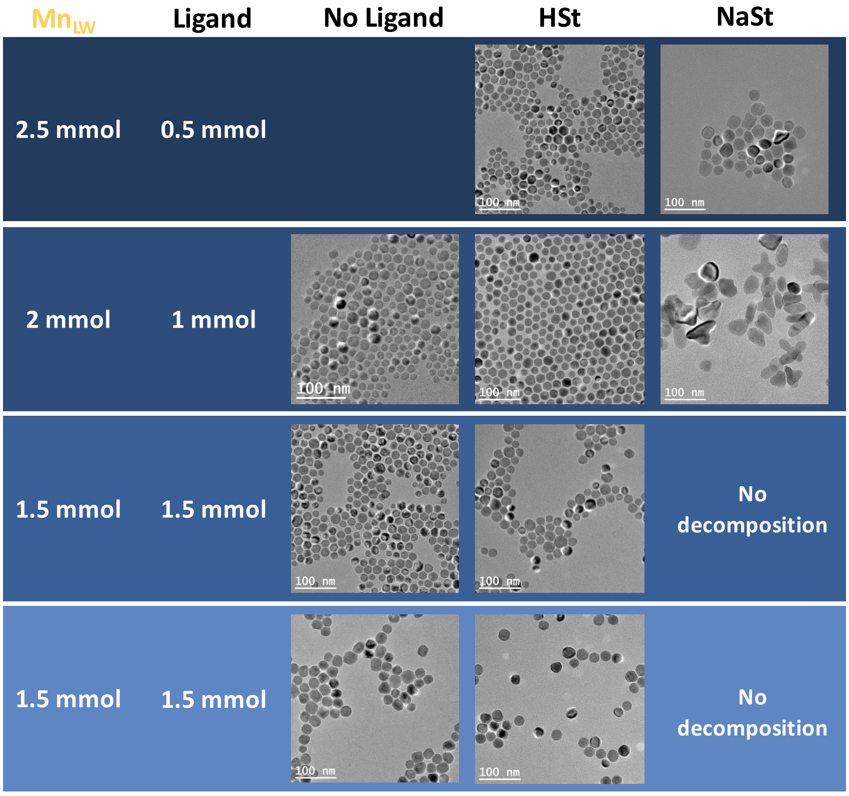

Figure V.2.13 - TEM images of the TD of Mn_{LW} with the different conditions

Table V.2.7 – Size distribution and precipitation time as a function of the various amounts of ligands

		No Ligands		HSt		NaSt	
MnSt	**Ligand**	**Size (nm)**	**Precipitation time (min)**	**Size (nm)**	**Precipitation time (min)**	**Size (nm)**	**Precipitation time (min)**
2.5 mmol	0.5 mmol			18.5 ± 3.2	47	19.6 ± 5.2	85
2 mmol	1 mmol	17.2 ± 2.8	48	19.4 ± 2.5	57	40.4 ± 1.4	256
1.5 mmol	1.5 mmol	20.1 ± 2.7	58	20.9 ± 4	69		
1 mmol	2 mmol	26.1 ± 3.5	109	26.7 ± 3.2	126		

Once again, all the NPs presented the same rock salt cubic MnO crystallographic phase. It was interesting that NaSt led to multi-particles and not HSt. From EDX analysis, we've seen that no counter ions (Na or Cl) were present. That let us thinking that the stearate chains were at play for the caterpillar formation. The thing is that NaSt is prone to dissociate when solubilized in organic solvent contrarily to

HSt. Thus, it seems that it is the charged stearate chain $CH_3(CH_2)_{17}COO^-$ that is required to control the vesicle morphology.

To get to the formation of caterpillar NPs, another strategy was needed. Instead of replacing part of the Mn_{LW} by NaSt, decomposition has been performed with a constant amount of Mn_{LW} (3 mmol) and various amounts of NaSt were added. The images of the resulting TD are given in Figure V.2.14 and the size and precipitation time in Table V.2.8.

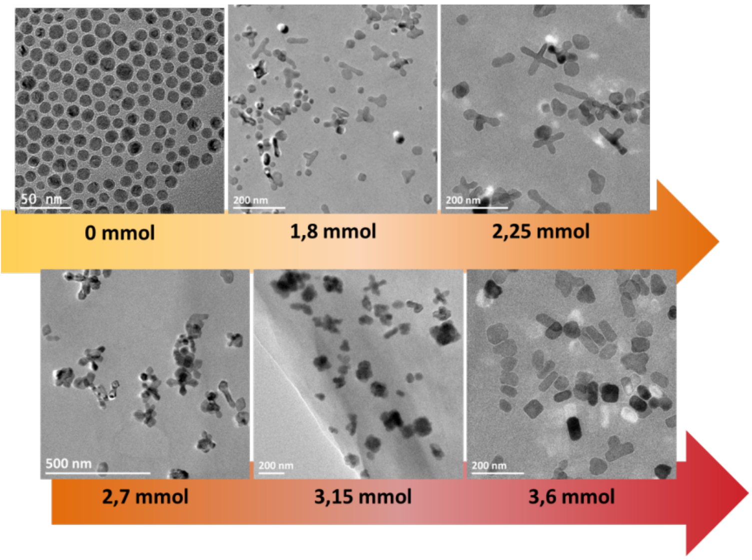

Figure V.2.14 - TEM images of the influence of NaSt amount on the shape of MnO NPs

TEM images confirmed the previous observation. By 1.8 mmol of NaSt, NPs with pod shapes are formed. These pods NPs are observed up to 3.15 mmol of NaSt. Interestingly, the pods size remained stable but the size of the NPs forming these pods increased. This would imply that between 1.8 and 3.15 mmol of NaSt, the vesicle shape and size remained constant. The only effect observed with the increasing amount of NaSt is the enhancement of the growth step leading to bigger NPs in the pods. This ended up by forming pods that looked alike flower as the NPs of each pods touched each other. When 3.6 mmol of NaSt is introduced, rods are observed. The precipitation time for this condition was found to be faster than for the 3.15 mmol of NaSt. As the opposite was expected, this hint at a different mechanism for this condition. The same rock salt cubic MnO crystallographic phase is observed for all NPs.

Table V.2.8 – Size distribution and precipitation time : influence of NaSt amount

Nast (mmol)	0	1.8	2.25	2.7	3.15	3.6
Size (nm)	11.9 ± 1.7	26.2 ± 5.9	30.6 ± 6.4	31.8 ± 7.9	51 ± 12	39.1 ± 5.5 (t)/ 79.6 ± 21 (l)
Precipitate time (min)	36	186	220	309	379	231

V.2.3.3.3 Controlling the size of MnO spheres

We have seen that MnSt composition can vary with the synthesis conditions. The vesicular process seems to be quite strong with this precursor. The shape was thus difficult to control but in the case of spherical NPs, the size control is also an issue. For iron oxide, the NPs size can be easily controlled by simply changing the boiling point of the solvent used for the TD[19]. However, with our precursor, size was not controllable using the common levers of the TD. To be able to tune the size, we were inspired from the protocol by Fortin et al[17] that synthesized 5 nm MnO NPs from $Mn(acac)_2$ without adding ligands. The ligand free synthesis was possible with $FeSt_x$ as seen in part V.1. The size was found to be tuned by the solvent boiling point and the size distribution by the heating rate. Moreover we also demonstrated that the NPs synthesized without added ligands were stable in solution thanks to their coating with stearate molecules from the precursor.

The Mn_{LW} precursor was thus decomposed using the adapted O'Brien protocol but without adding OA or any ligand. Different thermal decompositions were performed in various alkene solvents presenting increasing boiling points: hexadecene (b.p. 285°C), octadecene (b.p. 315°C) and eicosene (b.p. 340°C). The result of the TD is shown in Figure V.2.15. Mean sizes are given in Table V.2.9.

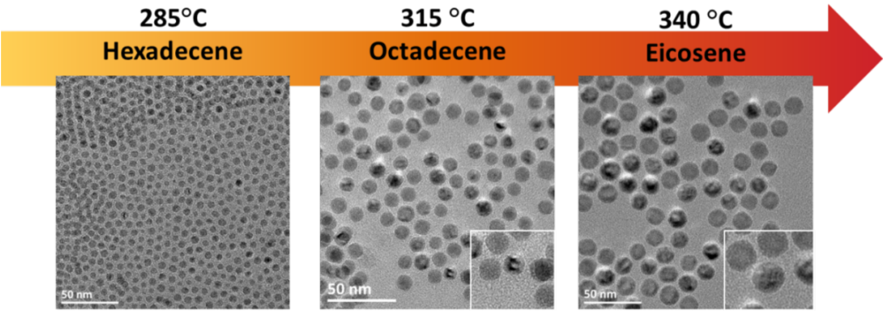

Figure V.2.15 - TEM images of the TD of Mn_{LW} in various alkenes solvents

Table V.2.9 - Size evolution with solvent boiling point

Solvent	Boiling Point	Size NPs (nm)
Hexedecene	285	5.9 ± 0.6 nm
Octadecene	315	11 ± 0.9 nm
Eicosene	340	16 ± 1 nm

The TD in the different solvents led to spherical NPs whose size increased with the solvent boiling point. Nevertheless, Moiré patterns were observed for the NPs synthesized in octadecene and eicosene. This would indicate that the growth of the NP occurred in the vesicle. This is opposed to what has been observed with $FeSt_x$ in Chapter V.1. For $FeSt_x$ only the nucleation happened in the vesicle that bursted with the temperature elevation. Thus, the results of the TD of MnSt tend to prove that the vesicles are more stable than in the case of $FeSt_x$. The fact that no Moiré pattern was observed for the NPs synthesised in hexadecene is explained by their size. At 6 nm the NPs are actually close to the nuclei stage. The growth didn't fully occur hence no deposition of a surface MnO layer. All the NPs were constituted of the MnO phase from XRD patterns.

V.2.4 Conclusion

In this part we demonstrated that the synthesis of FeSt is not simply transposable to Mn but had to be adapted. Nevertheless, it allowed us to identify and investigate the vesicular formation process of the MnO caterpillars. Due to an excess of stearate chains, spherical MnO NPs end up encapsulated in a layer of MnO. Despite the effort to reproduce their synthesis, few only got to synthesize multipods. Some more work should be done (e.g. introducing less NaSt, or combining it to HAD) to completely understand this mechanism. Indeed, the synthesis of the same object but with iron oxide could lead to interesting improved magnetic properties. The ligand free synthesis revealed here as successful as in chapter V.1.

V.3 CoO nanoparticles

V.3.1 Introduction

The objective here is to check if our *in house* cobalt stearate precursor leads also to the same CoO NPs as with the commercial products or with published syntheses. CoO NPs synthesis through thermal decomposition (TD) didn't follow the same frenzy in their synthesis as what has been seen for iron oxide NPs. Indeed, from published works, CoO NPs synthesis appeared more complex as various shapes have been reported to form[40–42]. This richness came partly from the crystallography of CoO that can crystallize into two lattices : cubic or hexagonal[43]. The first thermal decomposition synthesis has been reported by Seo *et al.* in 2005[43]. In decomposing $Co(aca)_3$ in oleylamine (OAm) at different ratios, they have been able to synthesize rods NPs of hexagonal CoO. A major contribution of this work was the demonstration of the link between the shape and the crystal structure. The rods adopted a hexagonal lattice when pyramids crystallized in the cubic rock salt structure. Seo *et al*. proposed that the shape control originated from the phase control that relied on the kinetic or thermodynamic control of the synthesis. Their results have been reproduced by An *et al.*[44] through the thermal decomposition of cobalt oleate ($CoOl_2$) in dioctylether (OE). The aspect ratio of the rods was simply tuned by varying the heating rate of the reaction. Interesting contributions were brought also by Zhang *et al.*[45,46] who have decomposed $CoOl_2$ in octadecene (OD) in presence of dodecanediol and oleic acid (OA). OA was added as a stabilizing agent retarding the precursor decomposition. On the opposite DDL was added to destabilize it. Zhang showed that the more OA was introduced the more complex was the shape with a flower like shape made of small CoO NPs. With an increasing amount of DDL the shape got simpler (polyhedrons). Despite presenting various shapes, only cubic CoO was detected in this work. Buck *et al*.[47] were the first to highlight the importance of the precursor purity on the shape obtention. Following the work of Bronstein *et al.*[48] on iron oleate, they identified the role of an impurity containing free hydroxide which would be responsible for the rod shape. This development allowed the synthesis of controlled rods from a purified precursor with the addition of ligands (NaOl or TMAOH) that mimicked the role of the hydroxide impurity. Other contributions showed that other shapes could be obtained: plates[49], multirods[49,50], or even multibranched rods[50].

In this part, an *in house* cobalt stearate will be synthesized and characterized. NPs will be synthesized in various conditions and NPs with different shapes were observed to form with CoSt whereas NPs with only spherical shape were obtained with FeSt. This result is quite surprising as cobalt and iron are very close atoms and simulation works on cobalt stearate with the team of Mauro Boero and Carlo Massobrio at IPCMS gave a first idea of the complexity of the decomposition of CoSt compared to FeSt.

V.3.2 Experimental details

V.3.2.1 Precursor synthesis

Cobalt stearate (II) was prepared by precipitation of sodium stearate and cobalt chloride salts in an aqueous solution. Briefly, sodium stearate (9.8 g, 32 mmol) was transferred into a 2 necked to a round bottomed flask (RBF) and solubilized in distilled H2O (dH_2O, 320 ml). The solution is heated to reflux and stirred for 30 min until complete dissolution of the stearate. Separately, $CoCl_2.6H_2O$ (3.80 g, 16 mmol) was dissolved in dH_2O (160 ml) and added onto the sodium stearate solution under vigorous stirring. A white precipitate is formed immediately. The solution is kept under stirring at this temperature for 15 min. Thereafter the solution is allowed to cool down to room temperature (RT). The obtained precipitate is washed once by centrifugation (hot dH2O, 14000 rpm, 10 min). The product is then filtrated with a büchner funnel and oven dried at 65 °C for 24 h.

V.3.2.2 CoO NPs synthesis

CoO NPs were synthesized with the following protocol adapted from the O'Brien's one[26]. Cobalt stearate (1.86 g, 3 mmol) is mixed with OA (2.05 g, 7.2 mmol) in 20 ml of Octadecene in a two neck RBF. The mixture is stirred and heated at 120 °C for 30 min without reflux condenser in order to dissolve the reactants and remove the water residues. The cooler is then connected to the flask and the solution is heated to the boiling temperature (≈ 315 °C) with heating rate of 15 °C/min and heated to reflux for 1h under air. After solubilization the purple solution turns blue. After cooling to RT, a brown suspension is obtained which is solubilized in 10 ml of chloroform. The NPs are then precipitated by the addition of an excess of acetone the first time and washed three times with chloroform and acetone at a ratio of 1:4 at 14000 rpm for 5 min by centrifugation. The NPs can finally be suspended in 50 ml of THF.

V.3.3 Results

V.3.3.1 Synthesis and characterization of cobalt stearate

As we observed a strong dependence of $MnSt_2$ with the synthesis conditions by contrast to FeSt, $CoSt_2$ synthesis was investigated by varying the same parameters as for $MnSt_2$. Table V.3.1 summarized the different conditions.

Table V.3.1 – Conditions tested for the synthesis of CoSt

Reaction time	**15 min (short)**	**1h15 (long)**
Warm water filtration	Co_{SW}	Co_{LW}
RT filtration	Co_{SRT}	

The IR spectra (Figure V.3.1) presented the exact same features for the $CoSt_2$ in all tested conditions. Nevertheless, Co_{LW} presented an IR peak at 1558 cm^{-1} with a higher intensity than that of the other two complexes together with the appearance of two peaks at 1555 and 1425 cm^{-1}.

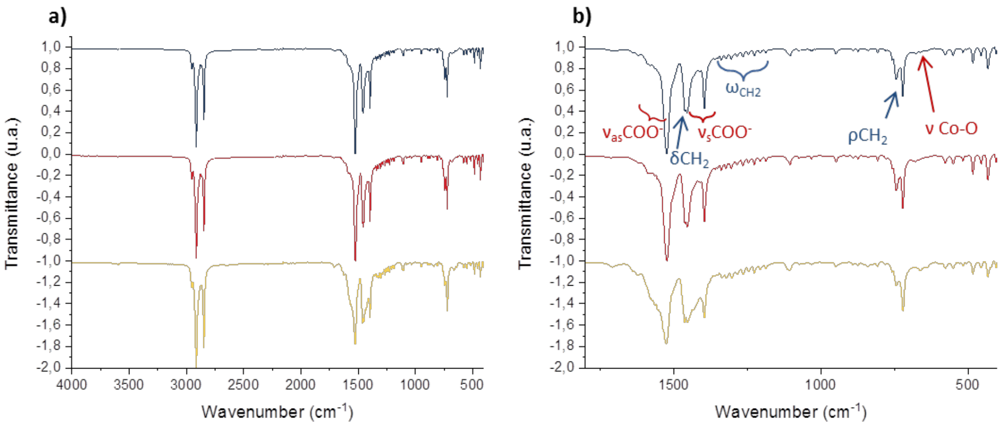

Figure V.3.1 - Infrared spectra of CoSt a) and zoomed in the region 1800-400 cm^{-1} b)

The bands were assigned by using the same approach as the one used for $FeSt_x$ in Chapter III. Two specific vibrational modes of the alkyl chain gave precious information about the organisation of the chains. No Davidov splitting was observed for any of the $CoSt_2$ on the rocking and scissoring bands of CH_2 indicating a hexagonal packing of the chains as seen for $FeSt_x$. The assignment of the carboxylate bands is given in Table V.3.2.

Table V.3.3 - Approximate assigment in the region 1800-1400 cm^{-1} for HSt, NaSt and CoSt

HSt	NaSt	CoSt	Co_{LW}	Proposed assignments
1700 vs		1708 w	1708 w	νC=O
	1558 vs	1577 m, sh	1577 m, sh	$\nu_{as}COO^-$
			1555 m, sh	
		1524 s	1524 s	
1470-1462 m	1467	1462 s		δCH_2
1429 s	1441 s	1455 s	1455 s	$\nu_{s}COO^-$
			1425 m, sh	
1410	1419 s	1397 s	1397 m, sh	

Table V.3.3 - Δν calculated for HSt, NaSt and CoSt

	Monodentate	Bridging	Mixed	Chelating
HSt	271, 290			
NaSt		139	117	
CoSt		181 w		69 s
Co_{LW}		181 m	130 m	69 s

IR spectra of Co stearates synthesized in 15 min displayed similar carboxyl bands as $FeSt_x$: two $\nu_{as}COO$ bands and two ν_sCOO displaying different intensities as a function of the nature of stearates (Table V.3.3). The presence of weak band at 1708 cm^{-1} suggests the presence of small amount of free stearic acid. As for $FeSt_x$, the weak band at 1620 cm^{-1} is observed even if no clear bands are observed in the region 3000 -3500 cm^{-1}. This indicated a poor hydration of the complexes. Co_{LW} presented three $\nu_{as}COO$ bands and three ν_sCOO displaying different intensities. An influence of the reaction time with the appearance of an additional intermediary coordination is noticed at 1555 cm^{-1} . The same remark is made on the band at 1620 cm^{-1} as previously.

Thus two kinds of CoSt are obtained presenting different coordinations. For **Co_{SW}** and **Co_{SRT}**, the bands at 1524 and 1455 cm^{-1} are attributed to the presence of a chelating coordination in agreement with the calculated Δν of 69 cm^{-1}. The weak $\nu_{as}COO$ band at 1582 cm^{-1} is attributed to a bridging configuration and associated with the ν_sCOO band at 1397 cm^{-1} with a Δν of 180 cm^{-1}.

Co_{LW} displayed the same coordination as the previous two stearates but a supplementary mixed coordination is also observed. This could be ascribed to an evolution of the precursor coordination from a chelate one to a bridging one. The higher intensity of the bridging band would be in agreement with that idea.

The formation of dimers have already been reported for CoSt[51]. This dimers formation has been ascribed to the splitting of bands below 900 cm^{-1} but not such splitting has been observed in our precursors.

EPR spectra were acquired by Dr Nathalie Parizel on Co_{LW}. Figure V.3.2 present an X-band EPR spectrum of powder sample of Co_{LW} recorded at 4 K.

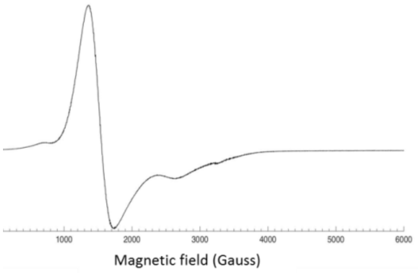

Figure V.3.2- EPR spectra of Co_{LW} at 4K

The spectrum at ν=9,316 GHz and 4 K is characteristic of an high spin Co ion with an axial symmetry S=3/2[52]. Spectra acquired between 4 and 70 K looked the same. No signal is detected above 70 K. No low spin S = 1/2 cobalt has been detected.

XRD pattern (Figure V.3.3) showed the presence of a same lamellar structure as already observed with Fe and Mn stearates. All CoSt presented the same diffractograms. The interlamellar distance was measured at 41.7 Å lower than Mn and Fe precursors. We've observed more peaks in the region 20-25 ° indicating various chain-chain interactions.

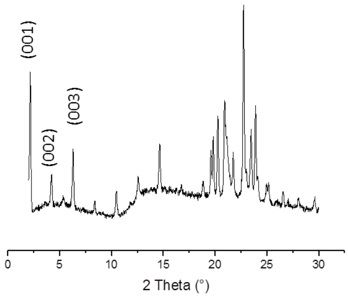

Figure V.3.3 - XRD pattern of CoSt

The TGA analysis was found to reveal a lot on precursor differences for MnSt. Figure V.3.4 showed the TGA, DTA and DTG curves of Co$_{SW}$. The same four regions are identified (I) dehydration/Co oxidation, (II) beginning of decomposition/nucleation, (III) decomposition/growth step, (IV) thermal degradation of organic chains. Figure V.3.4 presented all curves for all complexes and the different features are listed in Table V.3.4.

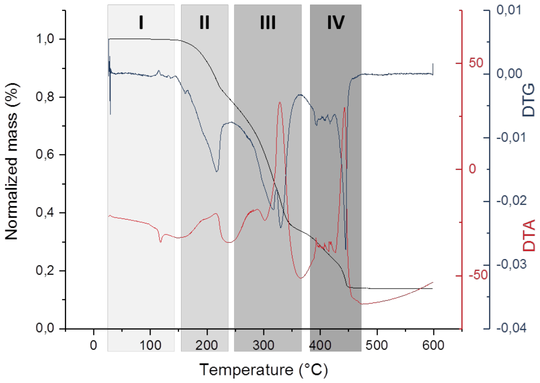

*Figure V.3.4- TGA, DTA and DTG of **Co$_{SW}$** under air (5°C/min)*

Contrarily to what has been observed with FeSt$_x$ and MnSt$_2$ no event below 90°C was detected. This agreed with a non-hydration of the precursor as noticed in the IR spectra. An event is detected at around 116 °C for the three complexes and was associated with an endothermal peak in the DTA curve. This event was similar to the events seen with FeSt$_x$ and MnSt$_2$ that was ascribed to the oxidation of the metal centre. Co (III) being a stable oxidation degree of the cobalt, this was possible.

The first weight loss was observed around 220 °C. This step that marked the beginning of the decomposition of the precursor was the same for all complexes. From that point, differences were recorded. The decomposition region varied from one complex to the other. The decomposition was well marked around 350 °C for **Co$_{SRT}$** but for **Co$_{SW}$** it can be seen up to the region IV. For Co$_{LW}$, there was no distinction between the decomposition (III) and the degradation region (IV). This most likely may be due to the mixed coordination observed in the IR spectra. The total weight loss was determined at 84 % for **Co$_{SRT}$**, 87 % for **Co$_{SW}$** and 92 % for Co$_{LW}$.

Thus, the effects of the synthesis conditions have been observed on the decomposition region of the precursors. All presented the same nucleation region but for **Co$_{SW}$** and **Co$_{LW}$** the precursor's distribution has changed with the formation of more stable intermediates.

Table V.3.4 - Features observed in the DTA and DTG curves of the three precursors

Co$_{SRT}$		Co$_{SW}$		Co$_{LW}$	
DTG	**DTA**	**DTG**	**DTA**	**DTG**	**DTA**
117, w	Endo, w	115, w	Endo, w	116, w	Endo, w
219, m	Exo, m	217, m	Exo, m	221, m	Exo, m
318, m	Exo, m	316, s - sh	Exo, s - sh	306, m	Exo, m
		330, s	Exo, s	330, m	Exo, m
346, m	Exo, m			350, w - sh	Exo, w - sh
356, w	Exo, w			374, w	Exo, w
		392, w	Exo, w	383, w	Exo, w
		407, w	Exo, w	404, w	Exo, w
423,w	Exo, w	418, w	Exo, w	431, w - sh	Exo, w - sh
448, s	Exo, s	444, s	Exo, s	445, s	Exo, s

V.3.3.2 Thermal decomposition of the different CoSt precursors

V.3.3.2.1 Influence of the precursor structure

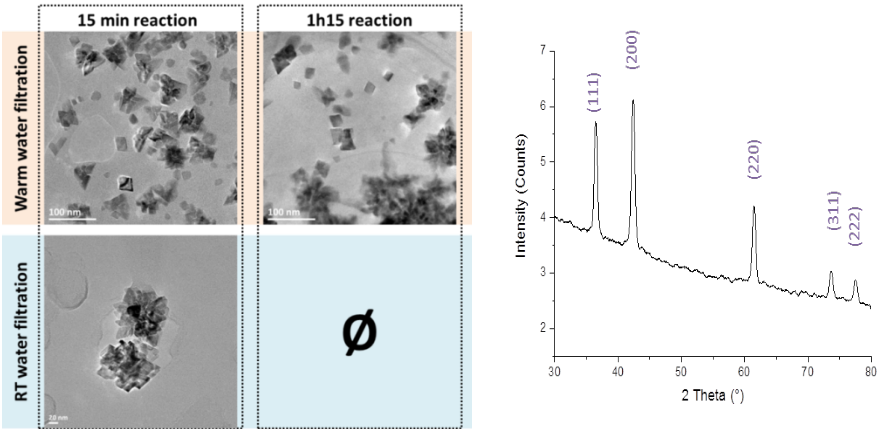

Figure V.3.5 - TEM images of the TD of the three precursors (left) and XRD pattern of CoO NPs, indexation for JCPDS 70-2856 (right)

The three precursors synthesized previously have been decomposed with the adapted O'Brien protocol. The TEM images are given in Figure V.3.5. After their TD, all three complexes led to the same nano-objects: diamond nanoplates aggregated into flowers of about 100 nm. This shape has been already reported by Zhang et al[46] in similar conditions. According to this study, the more OA was added, the more the NPs tended to this aggregated flower shape. Contrarily to what was observed with MnSt, this aggregated shape didn't seem to be linked to the precursor structure. Otherwise we might have observed a different result for **Co_{LW}** that presented notable differences from IR and TGA analyses. This confirmed the complexity of cobalt precursors decomposition observed in the literature. All the NPs displayed the cubic CoO rocksalt structure. A characteristic smoothed XRD is given in Figure V.3.5.

V.3.3.2.2 Influence of the TD synthesis conditions

We've seen in previous parts that many parameters may address the NPs shape. To demonstrate the richness of shapes that can be achieved with the *in house* CoSt, **Co_{SW}** has been treated with the dehydration procedure established in Chapter III. The "hydrated" and "dehydrated" precursors have then been decomposed considering the conditions of the adapted O'Brien protocol. The results of TD are given in Figure V.3.6.

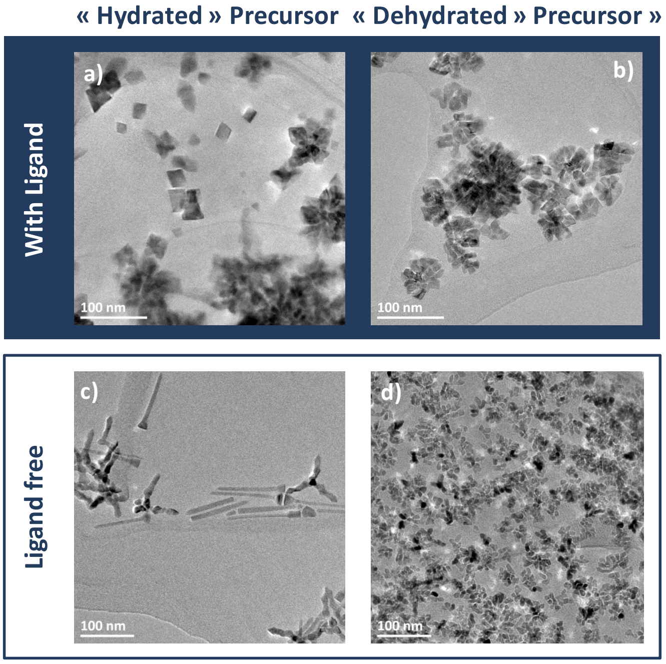

Figure V.3.6 - TEM images of NPs obtained by TD of "hydrated"(a,c) and "dehydrated"(b,d) **Co_{SW}** *with ligand (a,b) or without ligand (c,d).*

The results are quite different depending on the synthesis conditions. Yet most of the shapes reported in literature have been obtained. The 100 nm diamond flower aggregates when OA is involved in the synthesis were also observed by Zhang[45,46]. 100 nm length (10 nm thickness) Tea golf (or rods) with no ligands were reported by Buck[47]. The thermal treatment on the precursor led to a difficult to discern morphology but that remind MnO caterpillars.

V.3.3.3 Modeling of the decomposition of cobalt stearate

Modeling of the decomposition iron stearate in Chapter III has shown that stearate chains desorbed from iron cations, releasing iron atoms and thus the nucleation of iron oxide NPs may occur. It was also shown that the desorption seemed to be easier in dry conditions. The same simulations performed on cobalt stearate (Figure V.3.7-9) showed that this complex evolved rather differently, cobalt atoms reacted with oxygen and hydrogen of stearate chains and induced a decomposition of stearate chains. Byproducts are thus generated such as CO_2 and $O{=}C{=}C{=}CH_2$ and cobalt atoms interacted with oxygen and hydrogen. Cobalt atoms so generated are not free to react together perturbing thus the nucleation and growth step and preventing Co atoms from interacting and should aggregate according to given crystallographic directions.

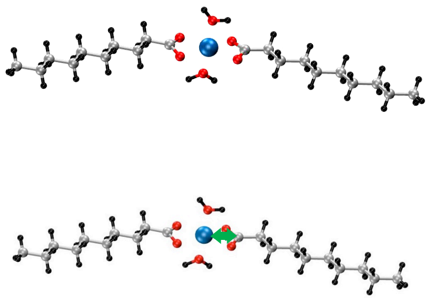

Figure V.3.7 - Co-based stearates at 300 K in wet conditions. The green arrow indicates the reaction coordinate used in Blue Moon ensemble simulations to desorb the stearate chain.

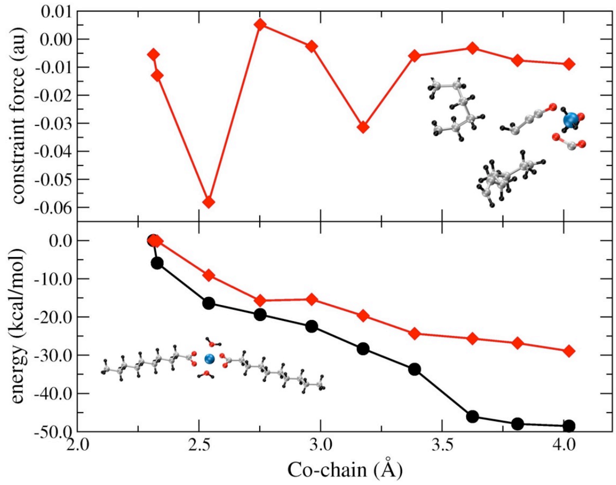

Figure V.3.8 - Co-based stearates at 300 K in wet conditions.

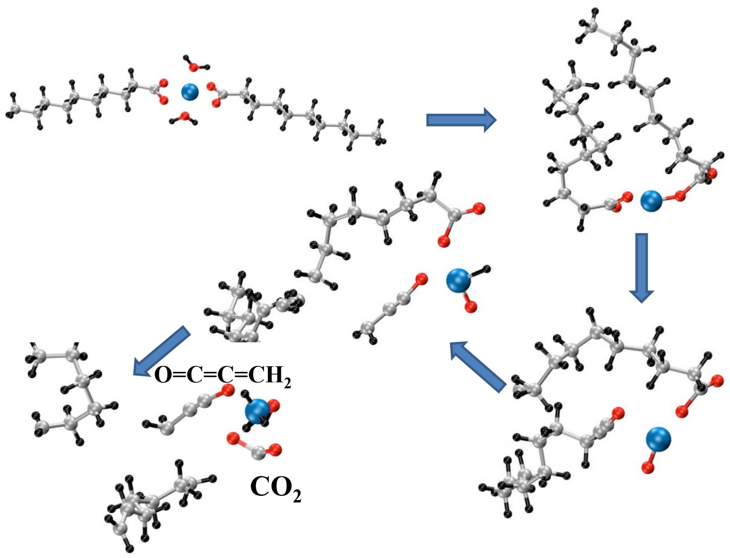

Figure V.3.9 - Co-based stearates at 300 K in wet conditions

V.3.3 Conclusion

In this part we demonstrated the lesser effect of the synthesis conditions of CoSt. Yet as seen with the modeling, the behaviour of the CoSt with temperature is quite complex. This explains the range of “exotic” nano objects that have been reported or that we have synthesized here. Nevertheless, a more detailed study would be interesting in order to better understand the mechanism of formation of these shapes.

V.4 Core-shell Synthesis

V.4.1 Introduction

Core-shell structures are interesting as they allow combining materials with different properties inside one nano-object. In particular core-shell nanoparticles constituted of two magnetic materials displaying different magnetic properties leads to interesting magnetic coupling enhancing the magnetic properties of individual materials. For example, core-shell NPs consisting of a core with a high magnetic anisotropy and of a shell with a small magnetic anisotropy have been shown to display a very important anti-tumor effect induced by magnetic hyperthermia attributed to the exchange coupling between both magnetic phases[53]. But at first, the coupling of an antiferromagnetic (AFM) phase with a ferro(i)magnetic (FiM) phase has been widely investigated as their interface induces an exchange bias (EB) coupling increasing the effective anisotropy by adding an EB anisotropy. Reported initially in Co@CoO nanoparticles[54], exchange bias coupling is a very complex phenomenon which depends on a wide panel of parameters[55]. Nevertheless, nanoparticles such as Co@CoO have been widely investigated as model systems because of the epitaxial growth relationship which warrants high crystallinity of the interface between F(i)M and AFM phases. Furthermore, new synthesis methods opened new perspectives toward the design of core−shell nanoparticles with new composition and fine control of their structure[56].

In that context, using commercial products, a systematic study focused in our lab on the exchange biased properties of core-shell $Fe_{3-x}O_4$@CoO NPs[15]. A CoO layer was grown on 10 nm iron oxide cores through a two-step thermal decomposition process (i.e. by a seeded growth method) (Figure V.4.1.a). The commercial cobalt stearate decomposes at higher temperature than the commercial iron stearate (Figure V.4.1.b) making very difficult the nucleation of CoO NPs in these experimental conditions and thus favouring its heterogeneous growth at the surface of presynthesized iron oxide NPs. The CoO shell thickness/structure has been modulated by varying the cobalt stearate (CoSt) concentration introduced in the reaction media after the synthesis of iron oxide NPs and defined as the ratio of molars amounts intoduced $R = CoSt_2/FeSt_2$. The magnetic properties were highly dependent on the CoO shell thickness and structure. When the shell was very thin (below 1 nm), a low exchange field (below 300 Oe) and a very large coercive field (up to 19 000 Oe) were concomitantly noticed. Such values were ascribed to the diffusion of Co species in the surface layer of iron oxide leading to a cobalt ferrite shell inducing a hard/soft coupling exchange. In contrast, large amounts of cobalt stearate favored the nucleation and growth of CoO nanocrystals on particular facets of the iron oxide seeds which resulted in a non-homogeneous CoO shell. Nanoparticles combining the highest interface quality and the thickest homogeneous CoO shell (R=1) displayed very unique exchange bias coupling (H_E = 5100 Oe) and coercive field (12 700 Oe)[15].

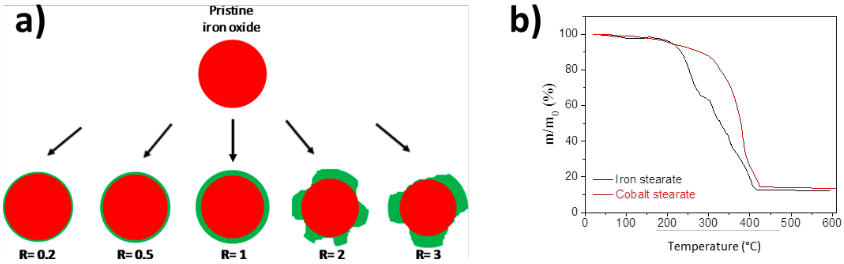

Figure V.4.1 - *a) Schematic illustration of core-shell structures of* $Fe_{3-\delta}O_4$*@CoO nanoparticles as a function of the* $CoSt_2/FeSt_2$ *molar ratio R.* $Fe_{3-\delta}O_4$ *in red and CoO in green*[15] *b) TGA curves of commercial iron and cobalt stearates*

In that context, we propose to investigate the synthesis of core-shell $Fe_{3-x}O_4$@CoO and $Fe_{3-x}O_4$@MnO NPs using an *in house* iron stearate. Previous chapters demonstrated the major matter of the control of the precursor through its synthesis. In this part, we are interested in reproducing the synthesis of $Fe_{3-x}O_4$@CoO NPs using *our* iron stearate. At first, only the FeSt will be *in house* synthesized and the CoSt will be commercial and in a second time, both precursors will be *in house*.

$Fe_{3-x}O_4$@MnO NPs will be also synthesized from *in house* precursors. The interest of such nano-object is that it will allow investigating exchange coupling with another AFM phase: MnO instead of CoO. In addition, Fe_3O_4 NPs are well-known T2 contrast agents for magnetic resonance imaging (MRI) and MnO NPs have been demonstrated promising as T_1 MRI CA[57]. Their combination in a core-shell could lead to a dual T_1/T_2 contrast agent as already reported by Cheon[58]. The synthesis of such core-shell NPs with controlled core and shell remains currently a challenge.

V.4.2 Experimental details

V.4.2.1 Precursor synthesis

Commercial cobalt stearate is provided by TCI with a purity of > 95%.

In house precursors (Manganese stearate (II), iron stearate (II) and cobalt stearate) were prepared by precipitation of sodium stearate and metal chloride salts in an aqueous solution. Briefly, sodium stearate (9.8 g, 32 mmol) was transferred into a 2 necked to a round bottomed flask (RBF) and solubilized in distilled H_2O (dH_2O, 320 ml). The solution is heated to reflux and stirred for 30 min until complete dissolution of the stearate. Separately, $MnCl_2.4H_2O$ (3.16 g, 16 mmol) was dissolved in dH_2O (160 ml) and added onto the sodium stearate solution under vigorous stirring. A white precipitate is formed immediately. The solution was kept under stirring at this temperature 15 min. Thereafter the solution is allowed to cool down to room temperature (RT). The obtained precipitate is washed once by centrifugation (hot dH_2O, 14000 rpm, 10 min). The product is then filtrated with a büchner funnel and oven dried at 65 °C for 24 h.

V.4.2.2 NPs synthesis conditions

Iron oxide NPs were synthesized at first. 1.38 g of $Fe(stearate)_2$, 1.24 g of oleic acid and 20 mL of octylether were mixed together, and then heated to 120°C for 1 h to evaporate residual traces of water or ethanol. Subsequently, the temperature was increased up to 288°C (boiling point of octylether) for 2 h under air with a heating rate of 5°C/min. The resultant black solution was then cooled down to 80°C, followed by extraction of 10 mL of solution from the flask for the characterization of iron oxide nanoparticles. In a second step, $CoSt_2$ (commercial or in house) was dissolved in 20 mL of octadecene and subsequently added to the remaining solution wich was kept at 80°C. The mass of $CoSt_2$ was calculated to correspond to molar ratios R = $CoSt_2/FeSt_2$. The reaction medium was heated again to reflux (which considering the octylether/octadecene mixture, is about 318 °C) for 1 h with a heating rate of 1°C/min. Finally, black products were washed four times by centrifugation by adding ethanol and chloroform. Final suspensions of nanoparticles were stored in THF.

Fe_3O_4@MnO NPs were synthesized following the same protocol by using first a ratio 0.5 and then a ratio 2.

V.4.2.3 Other Characterization techniques

SQUID. Magnetic measurements were recorded on samples by using a Superconducting Quantum Interference Device (SQUID) magnetometer (Quantum Design MPMS-XL 5). Temperature dependent zero-field cooled (ZFC) and field cooled (FC) magnetization curves were recorded as follows: the sample was introduced in the SQUID at room temperature and cooled down to 5 K with no applied field after applying a careful degaussing procedure. A magnetic field of 7.5 mT was applied, and the ZFC magnetization curve was recorded upon heating from 5 to 400 K. The sample was then cooled down to 5 K under the same applied field, and the FC magnetization curve was recorded upon heating from 5 to 400 K. Magnetization curves as a function of an applied magnetic field (M(H) curves) were measured at 5 and 400 K. The sample was also introduced in the SQUID at high temperature and cooled down to 5 K with no applied field (ZFC curve) after applying a subsequent degaussing procedure. The magnetization was then measured at constant temperature by sweeping the magnetic field from +7 T to −7 T, and then from −7 T to +7 T. To evidence exchange bias effect, FC M(H) curves have been further recorded after heating up at 400 K and cooling down to 5 K under a magnetic field of 7 T. The FC hysteresis loop was then measured by applying the same field sweep as for the ZFC curve. The coercive field (H_C) and the M_R/M_S ratio were measured from ZFC M(H) curves. The exchange bias field (H_E) was measured from FC M(H) curves.

XMCD. X-Ray Magnetic Circular Dichroism (XMCD) measurements were performed in SOLEIL synchrotron facility (DEIMOS beamline). XAS and XMCD spectra were recorded in total electron yield at the Fe and Co $L_{2,3}$ edges at 4K and under magnetic field at 6.5T.

V.4.3 Results

V.4.3.1 Synthesis of $Fe_{3-x}O_4$@CoO NPs

V.4.3.1.1 Synthesis and structural characterization of core-shell NPs

Core-shell NPs were synthesized from an *in house* hydrated iron stearate $FeSt_2$ and a commercial cobalt stearate according to the previously published seed mediated growth protocol[59]. We have used FeSt2 as the former studies used a commercial product sold as $FeSt_2$ that was hydrated. At first, a typical synthesis of 10 nm spherical $Fe_{3-x}O_4$ NPs is realised in dioctylether. Then half of the volume is removed and $CoSt_2$ is introduced along with octadecene solvent to increase the reaction media temperature for the coating step as the commercial cobalt stearate decomposes at higher temperature (Figure V.4.1b). Three $CoSt_2/FeSt_2$ ratios (R) were tested: 0.2, 0.4 and 2. TEM images realised after the synthesis of the core and after the CoO deposit are presented in Figure V.4.2. Measured mean sizes of NPs are listed in Table V.4.1.

TEM images show that the shape of NPs remains quite spherical after the CoO coating but some faceted surfaces are observed. A size increase is observed for all the R confirming the presence of a coating at the surface of NPs. However the mean size of iron oxide NPs after the first synthesis step varies a lot and we may now explain this size variation by variation in the hydration degree of *in house* $FeSt_2$ (Note : the protocol of the drying of hydrated $FeSt_x$ is now strict to avoid this reproductibility problems). The size increase appears quite high for R=0.2 by comparison with R=0.4 and R=2 but it is difficult to conclude due to the variation of the core size and also due to the fact that not all cobalt stearates decompose at the reaction temperature (i.e. in these experimental conditions). Indeed, metal stearate precursors display a distribution of precursors which decompose up to a very high temperature (chapter 3). Moreover, the study on hydrated $FeSt_2$ in Chapter III has shown that its decomposition was highly dependent of its structure affected by its hydration state. The *in house* hydrated FeSt2 has been demonstrated to not decompose completely during a classical 10 nm spherical NPs synthesis. When the temperature treatment is re applied after the standard synthesis process of 10 nm iron oxide NPs (i.e. the heating ramp up to 288°C has been done twice without further addition of Fe precursor), NPs with a mean size 9.6 ± 1.2 nm have been obtained after the first temperature treatment and their diameter has increased up to 11 ± 1.1 nm (shell thickness of 0.7 nm) after the second temperature treatment. This indicates clearly that there is some undecomposed Fe precursor remaining after the first step.

XRD patterns (Figure V.4.3) present no sign of a CoO phase whatever the R values but only peaks which can be indexed with a spinel phase. That is quite surprising as from R=0.5, CoO peaks were indexed in the XRD patterns of $Fe_{3-x}O_4$@CoO NPs in our former study[15]. From our former study[15] and the presence of a coating, one may suppose at this stage that a cobalt ferrite shell is formed.

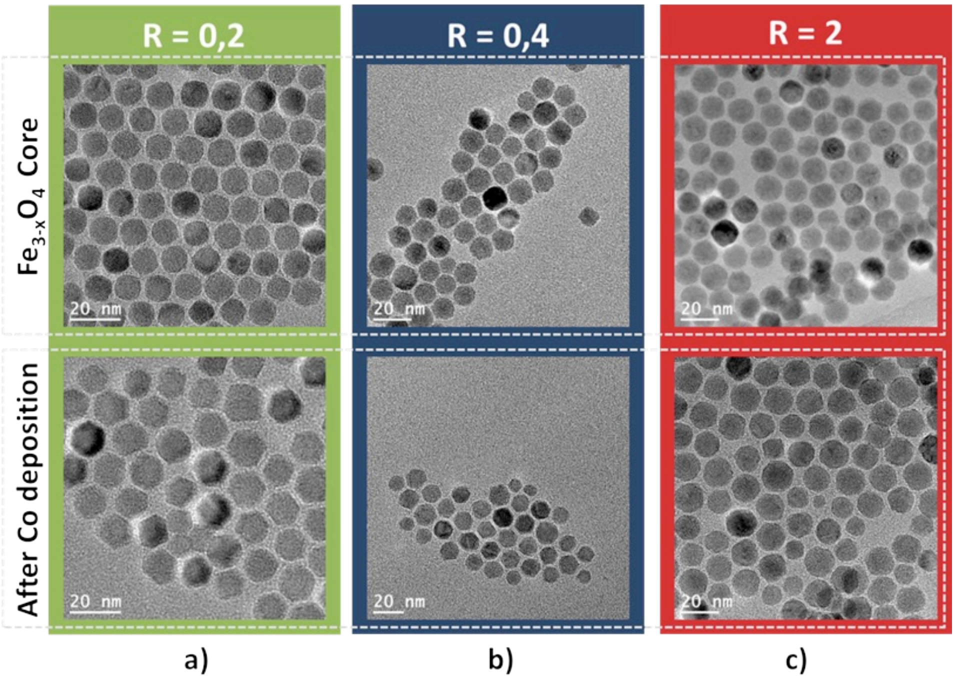

Figure V.4.2 - TEM images of the core-shell NPs for different R; 0.2 a), 0.4 b) and 2 c)

Table V.4.1 - Mean sizes (nm) of NPs obtained with the different R and CoO shell thickness (nm)

	R		
	0.2	**0.4**	**2**
Core	10.5 ± 0.8	11.2 ± 1.1	12.9 ± 1.2
After Co deposition	12.3 ± 1.4	12.1 ± 1.4	14.5 ± 1.3
Layer thickness	0.9	0.5	0.8

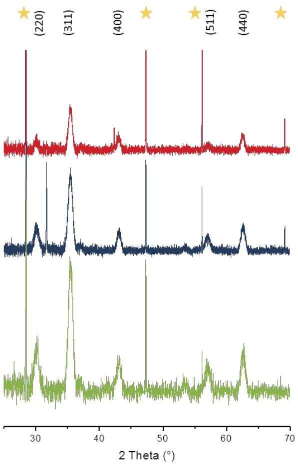

Figure V.4.3 - XRD patterns of NPs after the Co deposition for R=0.2 (green), 0.4 (blue) and 2 (red), yellow stars indicate Si used as a reference.

V.4.3.1.2 Magnetic characterization of core-shell NPs

Magnetic and XMCD studies have been performed by K. Sabouri and Dr B. Pichon from our team. Magnetic properties of the different NPs have been studied by SQUID magnetometry. Magnetization (M) curves recorded as a function of a magnetic field (H) (Figure V.4.4 Top) show that all NPs are superparamagnetic at 400 K. In contrast, hysteresis loops observed at 5 K after cooling under a zero field correspond to loops of blocked monodomain NPs (Figure V.4.4 bottom). The large hysteresis evidence huge coercive fields (H_C) (Table V.4.2). The exchange coupling that is usually observed at the F(i)M/AFM interface has been investigated by performing FC measurements at 5K. M(H) curves have been recorded at 5 K after cooling down under a magnetic field of 4 T (FC) (Figure V.4.4 bottom). Despite the high coercive fields, only a slight shift of the hysteresis curves is observed. The values of exchange field (H_E) characteristic of the strength of the exchange bias coupling are listed in Table V.4.2.

The low values of H_E for all three samples confirm XRD results that no or few CoO is present at the surface of the NPs. The low exchange field together with a high coercive field can be attributed as we have observed it earlier[15] to the presence of a cobalt ferrite $CoFe_2O_4$ shell at the surface of the NPs. The presence of a cobalt ferrite shell was also deduced for low R values in our former studies[15].

One may thus suppose that cobalt stearate and remaining iron stearate from the iron oxide core synthesis step have reacted together to form a cobalt ferrite shell at the surface of iron oxide NPs. The higher reaction temperature in that synthesis method (313 °C instead of 288°C) should have favour the decomposition of both precursors and the formation of cobalt ferrite.

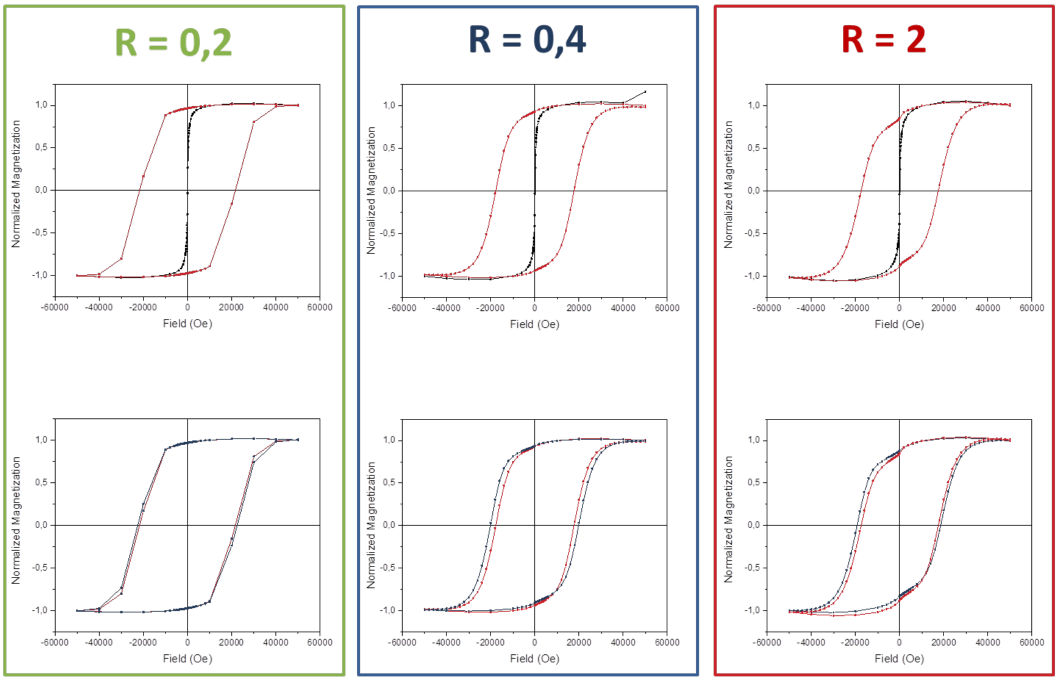

Figure V.4.4 – Magnetization curves of NPs as a function of R values. Top : ZFC curves at 400K (black) and 5 K (red). Bottom ZFC (red) and FC (blue) curves at 5K.

Table V.4.2 - H_c and H_E values determined from FC M(H) curves

	R		
	0.2	**0.4**	**2**
H_c (Oe)	21600	17700	19960
H_E (Oe)	-100	-100	-260

VI.2.3.1.3 XMCD studies

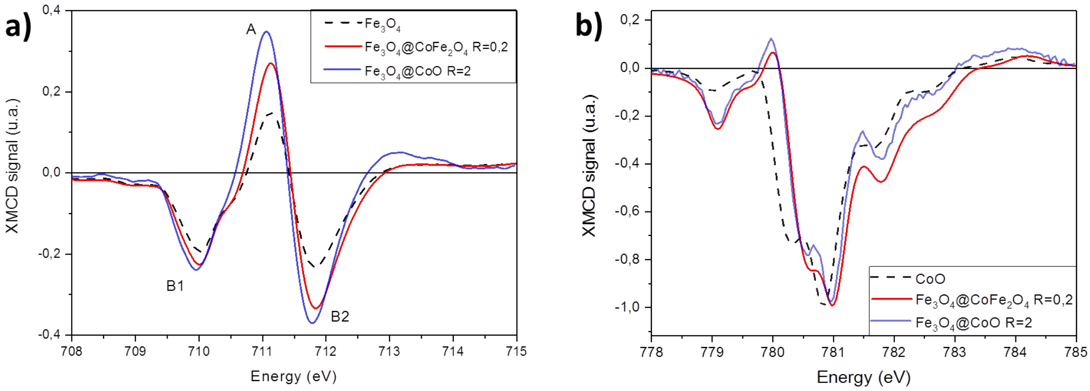

Figure V.4.5 - XMCD measurements of samples R= 0.2 and R=2 at a) the Fe edge and b) at the Co edge. Fe_3O_4 was recorded as references.

XMCD signals allow discriminating the oxidation state and site occupancy (O_h and T_d) of Fe and Co atoms in both core and shells. Measurements were performed on samples R = 0.2 and 2 in order to get a better insight on the electronic structure of nanoparticles (figure V.4.5). XMCD spectra recorded at Fe L_3 edge exhibit three peaks which agree with ferrite structure[60]. Two negative peaks at 715 and 717 eV correspond to Fe^{2+} and Fe^{3+} in O_h sites while the positive signal at 716 eV correspond to Fe^{3+} in T_d sites[61]. One can see that the presence of Co results in the decrease of surface area ratios B1/A and B2/A (Table V.4.3). It may be correlated to different environments of Fe species resulting from the diffusion of Co^{2+} in O_h sites, and so may attest the formation of an intermediate $Co_xFe_{3-x}O_4$ layer. Furthermore, XMCD spectra recorded at Co $L_{2,3}$ edge show typical signals of Co in O_h sites in agreement with CoO structure. The incorporation of Co^{2+} in O_h sites of the iron oxide surface is correlated to the decrease of the peak centred to 780 eV and to the increase of satellites peak centred to 779 eV and 781 eV which may correspond to O_h sites in $CoFe_2O_4$.

Table V.4.3 - Ratio between surface areas of Fe signals measured from XCMD spectra recorded for samples R = 0.2 and 2 and Fe_3O_4 nanoparticles.

Sample	B1/A	B2/A
Fe_3O_4@$CoFe_2O_4$ (R=0.2)	0,81	1,22
Fe_3O_4@CoO (R=2)	0,69	1,07
Fe_3O_4	1,31	1,57

V.4.3.1.4 Discussion

The structural and magnetic characterizations of NPs obtained by a seed mediated growth method, involving the synthesis at first of an iron oxide core and then the introduction of CoSt to induce the growth of a CoO shell in a second step, have shown that NPs consist in fact in core-shell NPs with a core of spinel iron oxide coated with a cobalt ferrite shell. Such thin shell leads to NPs with high coercive fields around 20 kOe. The observed low exchange field values may be attributed to spin canting as observed earlier in iron oxide NPs[19].

To better understand why the previous synthesis led to a layer of cobalt ferrite over a layer of CoO, the thermal behaviour of the commercial CoSt used has been investigated. The weight loss (TGA) and DTG curves are represented in Figure V.4.6. The TGA curve confirmed a higher stability of CoSt against temperature. The different "regions" of stability of the precursors identified on $FeSt_x$ in Chapter III and MnSt and CoSt in Chapter V.2 and V.3 have been identified in the DTG curves. The four "regions" are described as the following: (I) dehydration/oxidation, (II) beginning of decomposition/nucleation, (III) decomposition/growth, (IV) degradation of organic chains. It can be seen that all of those regions are shifted toward higher temperatures for CoSt. The "nucleation" region takes place between 300 and 350 °C which is above the temperature of nucleation with FeSt around 250°C (i.e. between 200-300°C) (cf. Chapter III). The "decomposition/growth" region is seen above 350 °C (up to 350°C for FeSt2, Chapter 3) and the organic chain degradation above 400 °C as for iron stearates.

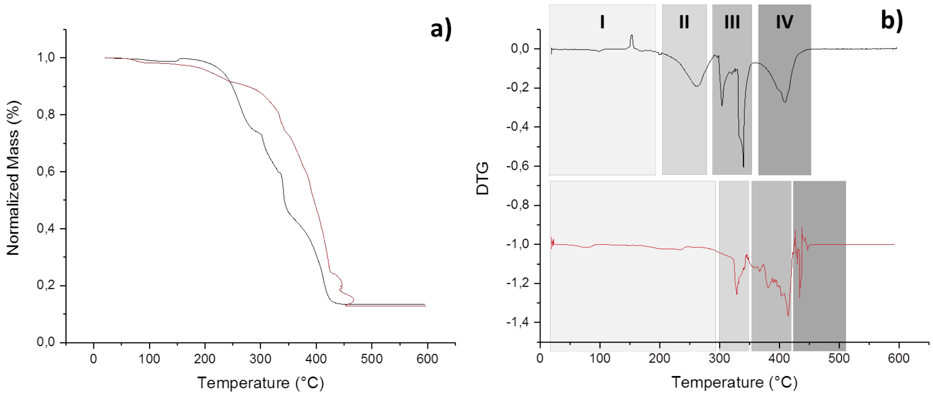

Figure V.4.6 - ATG a) and DTG curves b) of FeSt (black) and commercial CoSt (red) used in this study

The result obtained previously can be thus easily understood. When CoSt is introduced in the reaction media and when all the reactants mixture is heated up to 318°C, such high temperature allows decomposing more $FeSt_2$ but only a small part of the CoSt precursor decomposes to form monomers. Then, the Co monomer amount being too low and the amount of Fe monomer increasing, no proper CoO layer can be formed and only a cobalt ferrite layer formed.

V.4.3.2 Influence of the precursor structure and stability on the synthesis of $Fe_{3-x}O_4$@CoO

V.4.3.2.1 Characterization of in house CoSt

To go further in the role of the precursor stability, experiments were performed but only with the *in-house* precursors. The thermal stability of the *in-house* CoSt determined with TGA is compared to the one of the commercial precursor in Figure V.4.7.

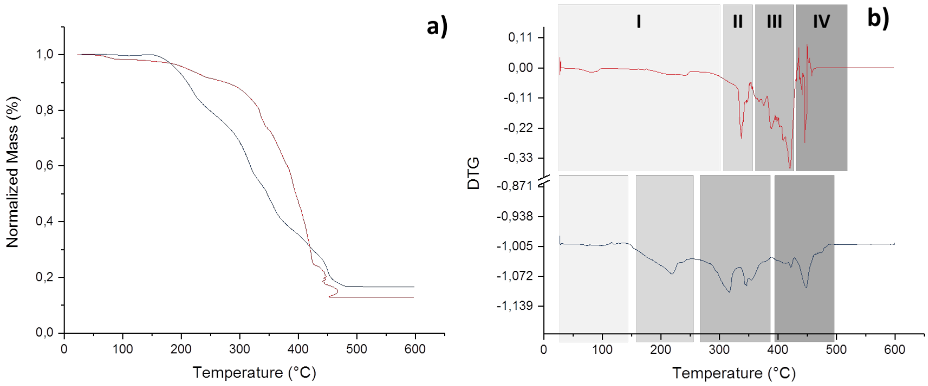

Figure V.4.7 - TGA a) and DTG b) curves of commercial CoSt (red) and in house CoSt (blue)

The *in-house* CoSt starts to decompose sooner with a “nucleation” step occurring around 250 °C and a decomposition/growth step between 300 and 400 °C. This CoSt precursor seems thus more adapted for the synthesis of a layer of CoO as its decomposition fits the temperature the boiling temperature (318 °C) of the octadecene/octylether mixture. However, one may not exclude the formation of an intermediate cobalt ferrite shell due to the presence of remaining iron stearate precursors.

V.4.3.2.2 Core-shell NPs synthesis

The core-shell synthesis protocol with both *in house* precursors has been realised with two ratios (R): 0.2 in order to see if a layer of CoO could be formed and 4 in order to be sure to observe the CoO layer. The shell formation has been followed as a function of the time after the boiling point of the solvent mixture has been reached, by collecting some fractions of the NP solution. at different times. TEM images are presented in Figure V.4.9. The measured mean sizes are listed in Table V.4.4 and the evolution of the shell thickness as a function of time in Figure V.4.8. Time 0h is for the beginning of the reflux step (end of the heating rate). The mean diameters for the cores are measured below the standard 10 nm. This is ascribed to a hydration of the precursor as seen in chapter III. Moreover, it has been observed that the hygroscopy variation along the year in the lab induced size variation for the 10 nm.

Table V.4.4 - Means sizes for both R in nm

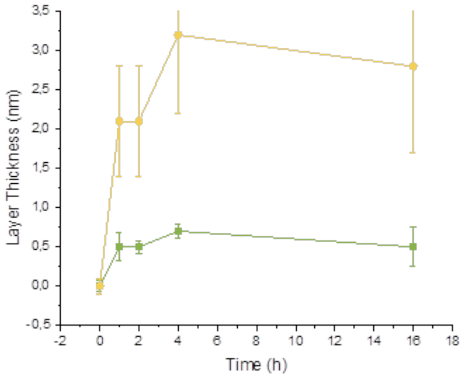

	R	
	0.2	4
Core	7.2 ± 0.9	8.5 ± 0.9
0	7.2 ± 1	8.5 ± 1
1	8.2 ± 1.1	12.6 ± 1.7
2	8.2 ± 1	12.6 ± 2.7
4	8.5 ± 1.1	14.9 ± 1.6
16	8.2 ± 0.9	14 ± 1.9

Figure V.4.8 - Evolution of the shell thickness as a function of time for R=0.2 (green) and 4 (yellow)

TEM images show that the spherical shape is preserved and only a small increase in size is observed for R = 0.2. With R=4, the shape of NPs strongly evolved during the reflux time and a larger increase in size is observed (the mean size has been measured along the longest dimension of the NPs). The mean sizes measured at the time 0h ensured that no growth occurred, for both R, during the heating rate step up to the reflux temperature. The shell thickness increases only from the reflux temperature. Its evolution/variation occurs in several steps.

For R=0.2, a 0.5 nm layer grew during the first hour of the synthesis. This layer doesn’t evolve during the second hour of reaction but increases slightly to 0.7 nm at 4h. This might be due to the precursor distribution that we theorized in Chapter III. In this phase, the regrowth is due to the most stable precursors that required more energy to decompose. At 16 h the layer thickness have decreased back to 0.5 nm. This might be explained by the Ostwald ripening mechanism.

For R = 4, a larger increase of the shell thickness is observed but it follows the same trend than previously with R=0.2. Such inhomogeneous shape for high R has already been observed in the former study[15] and has been explained by a heterogeneous nucleation of CoO at the surface of the iron oxide core. The NPs shapes homogenised with the reflux time thanks to Ostwald ripening.

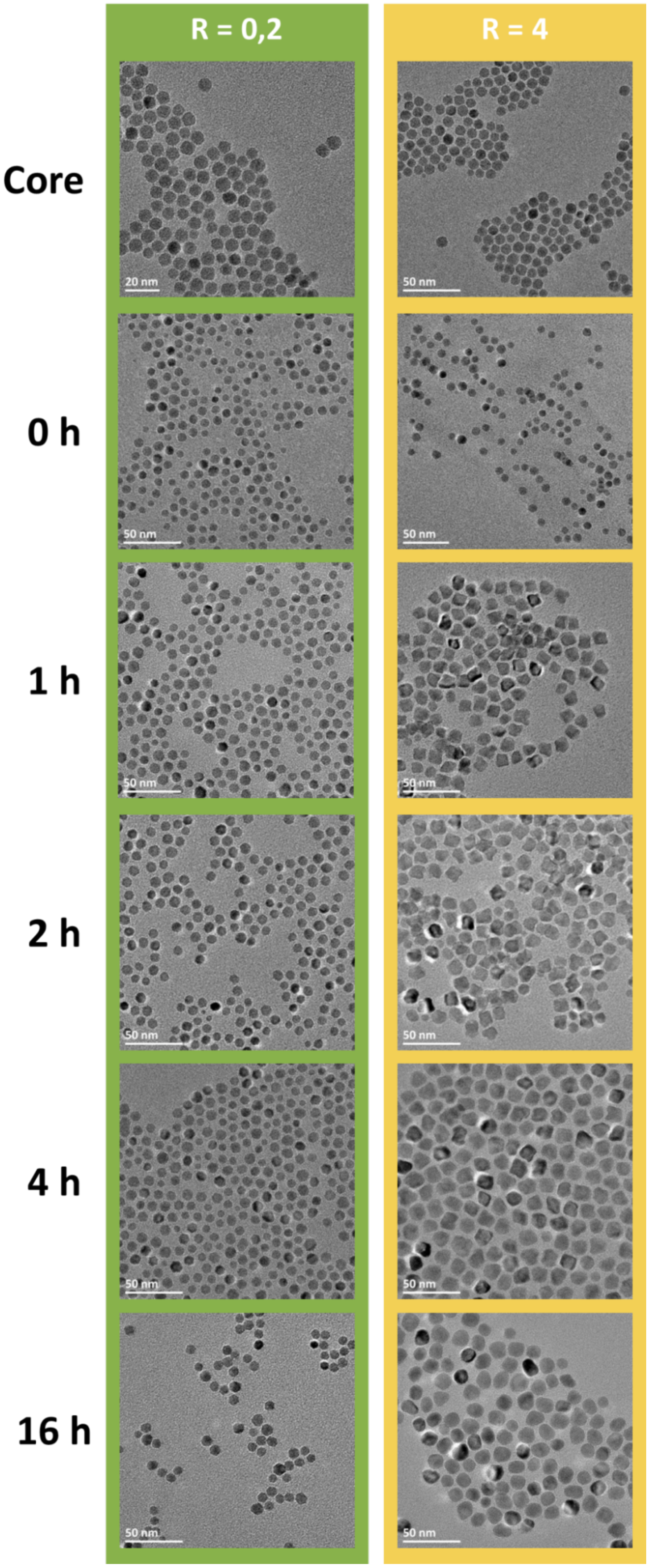

Figure V.4.9 - TEM images of the NPs as a function of R and reflux time

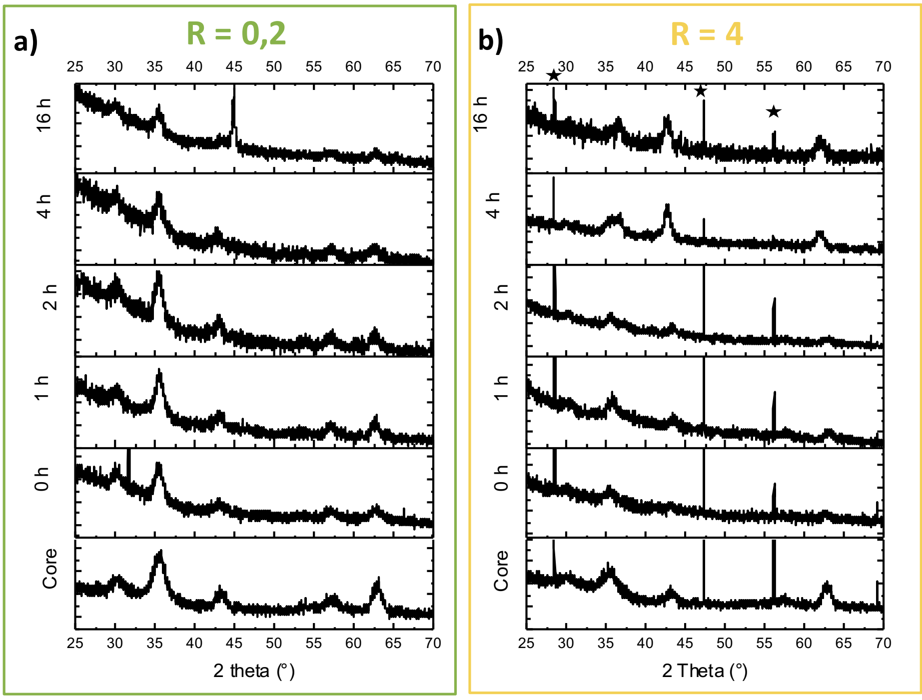

Figure V.4.10 - XRD patterns of NPs collected as fucntion of the reaction time. Stars shows lines corresponding to silicon which was used as a reference.

XRD pattern (Figure V.4.10) exhibits no peaks of CoO in the case of R=0.2 and does for R=4. This was expected in regard of the larger shell thickness increase with R = 4.

V.4.3.2.3 Discussion

The thermal stability of an *in house* CoSt allows providing more Co monomers for the growth step of a CoO shell at the surface of the iron oxide core by comparison with the commercial CoSt. The growth step of the CoO shell has been investigated by using two ratios R. The low R ratio (R=0.2) leads to the formation of a cobalt ferrite shell whereas the ratio R=4 leads to the formation of a CoO shell but the presence of an intermediate cobalt ferrite shell is not to exclude.

The NPs obtained with R = 4 present a non-regular shape. This may be easily explained thanks to the Lamer theory[62]. It states that to nucleate into a NPs, the monomer concentration formed by decomposition of the precursor needs to reach a minimal nucleation concentration (C_{min}^{nu}). Thus when CoSt decomposes and forms monomers, their concentration needs to remain under the C_{min}^{nu}. Otherwise the monomers will tend to form new nuclei on the NPs instead of growing heterogeneously on the already present iron oxide surface (Figure V.4.11). Nevertheless a heterogeneous nucleation may also occur/be favoured at the surface of iron oxide if the monomer concentration is close to C_{min}^{nu}. This is what seems to be at work here. But if we take a closer look at the inhomogeneous NPs formed at 1h, we see that they all tend to be somehow octahedral (Figure V.4.12.a). One explanation could come from the structure of the spherical iron oxide NPs. Spheres come from the compromise among different crystallographic planes. Usually, for an fcc structure, the plane {100} and {111} are considered. The planes {111} present the lowest surface energy[63] and thus should enclose the whole NPs leading to octahedra. The cubic shape enclosed by {100} planes is then not favoured. But as for a given volume, a cube presents a lower surface than an octahedron, the stable shape would be a compromise between the two planes family. The spheres are thus a truncated octahedron presenting both planes family. This point is major in our system. As the planes family presents different energy, it seems possible that the CoO nuclei form on the higher energy surface (Figure V.4.12.b). In the case of iron oxide, the {100} plane family.

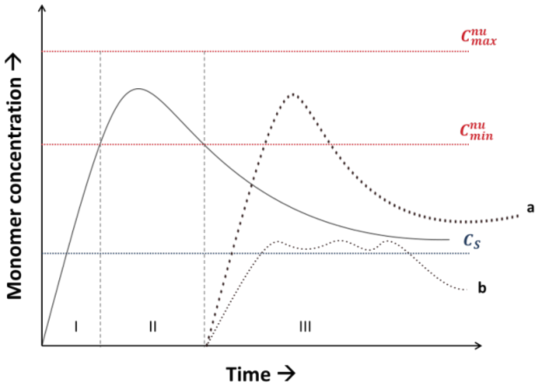

Figure V.4.11 - LaMer theory representation, Monomer evolution for FeSt (full line), CoSt that nucleate (doted line a) and CoSt that form a shell (doted line b)

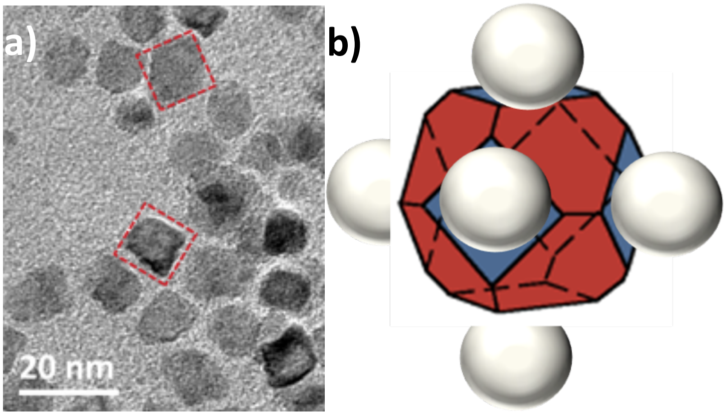

Figure V.4.12 - The octahedral position of the CoO NPs on the surface of iron oxide a) and schematic representation of the theory, the planes {111} are represented red and the {100} blue, white spheres symbolize CoO nuclei b)

V.4.3.3 Synthesis of $Fe_{3-x}O_4$@MnO NPs

By taking into account the previous study, we have established a protocol for the synthesis of $Fe_{3-x}O_4$@MnO NPs. The protocol will take place in three steps instead of two steps. The first step will consist in the synthesis of 10 nm spherical iron oxide NPs through our standard protocol. The second step will be a deposition of a thin layer of “Mn” (R=0.5) in order to promote the diffusion and create a “grip” shell for the deposition of a MnO shell in the third step. The result of this protocol is given in Figure V.4.13.

The mean NPs size evolves from 11.6 ± 1.1 nm to 14.9 ± 1.9 nm. Thus a shell of 1.5 nm has been deposited. Interestingly, some Moiré patterns can be observed in core-shell NPs in agreement with a core-shell structure. The shape is not perfectly spherical after deposit. This may be due to the R =2 that may lead to limited heterogeneous nucleation. XRD (Figure V.4.14) pattern confirmed that MnO peaks are present along with the ones of the spinel iron oxide that might be doped through the diffusion of Mn. More precise characterisations would be required to conclude.

We have therefore succeeded in synthesizing core-shell $Fe_{3-x}O_4$@MnO NPs. Despite a probable layer of $MnFe_2O_4$ at the interface, a thick layer of MnO has been deposited.

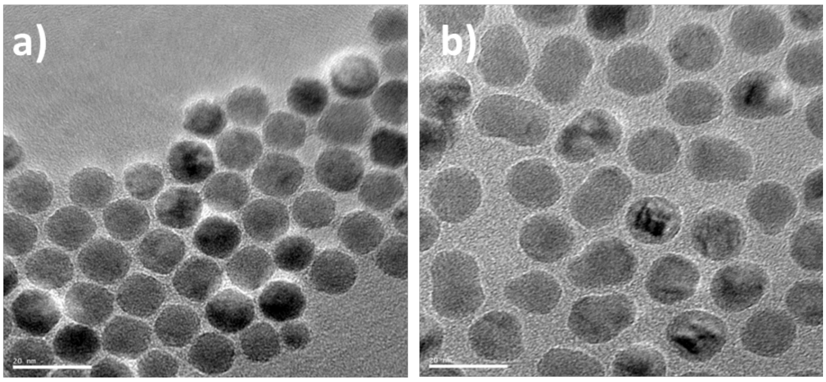

Figure V.4.13 – TEM images of the iron oxide core a) and of the core-shell structure after the second step.

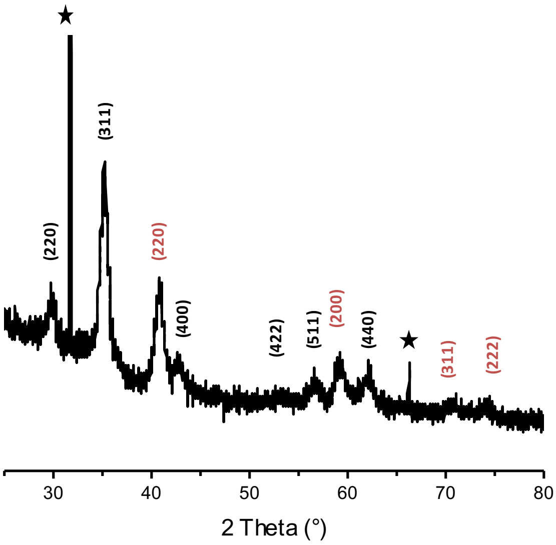

Figure V.4.14 – XRD pattern after the third deposition process : black indexation for spinel phase, pink for cubic MnO and stars for Si reference

V.4.4 Conclusion on core-shell NPs

In this part we demonstrated the role of the stability of the precursor for the synthesis of core shell structures. Synthesis with hydrated $FeSt_2$ that present a regrowth during the second heating up of the system favours the formation of mixed ferrite layer on pre-synthesized NPs. This phenomenon is also helped by the late decomposition of the commercial CoSt. Nevertheless, the formation of a mixed ferrite can be interesting due to the new magnetic properties brought by the magnetic coupling between both phases.

Thus, depending on the wanted structure, the precursor must be carefully chosen. For the formation of a mixed ferrite layer, a precursor that presents the regrowth when reheated (i.e. decompose up to high temperature) is preferable. Otherwise, If the aim is to form a different phase (as CoO), the regrowth phenomenon is deleterious and the second precursor should be chosen as presenting a decomposition temperature right in the range of the applied thermal program.

This work confirmed that the NPs design comes through a phase of precursor design or at least a selection.

V.5 General conclusion

In this chapter we've seen that we could scale up the synthesis of our precursor. Then we've demonstrated that there were paths to explore as the pyrolysis of the precursor for a greener and large scale synthesis of the NPs. One interesting result was that when sole oleic acid is introduced, wüstite was obtained. This would be in agreement with the formation of a FeO nuclei (as seen in chapter III). An alternative to the centrifugation has also been developed.

The precursor synthesis was found transposable to Mn and Co. We've show that we could obtain many of the shapes reported in literature for those oxides. Thus our approach with FeSt could be applied for those precursor and could maybe help unravel the mechanisms that rule the anisotropic shapes observed for MnO and CoO.

We've also observed the formation of vesicular structure when MnSt was put in solution as seen for FeSt. The resulting spheres or caterpillar led us to think that a control from the vesicle/onion could be opening new ways for the synthesis non spherical NPs.

Finally, we've seen with the core shell study that the design of NPs has to come through the selection of the right precursor. Thus engineering the precursor to get a precise control over its decomposition could be a powerful way to ease the synthesis of such complex systems.

REFERENCES

1. Park, J. *et al.* Ultra-large-scale syntheses of monodisperse nanocrystals. *Nat Mater* **3,** 891–895 (2004).
2. Blanco-Andujar, C. *et al.* Design of iron oxide-based nanoparticles for MRI and magnetic hyperthermia. *Nanomedicine (Lond)* **11,** 1889–1910 (2016).
3. Pellico, J., Ruiz-Cabello, J. & Herranz, F. Microwave-driven Synthesis of Iron Oxide Nanoparticles for Fast Detection of Atherosclerosis. *J Vis Exp* (2016). doi:10.3791/53472
4. Jiao, M., Zeng, J., Jing, L., Liu, C. & Gao, M. Flow Synthesis of Biocompatible Fe3O4 Nanoparticles: Insight into the Effects of Residence Time, Fluid Velocity, and Tube Reactor Dimension on Particle Size Distribution. *Chem. Mater.* **27,** 1299–1305 (2015).
5. Rockenberger, J., Scher, E. C. & Alivisatos, A. P. A New Nonhydrolytic Single-Precursor Approach to Surfactant-Capped Nanocrystals of Transition Metal Oxides. *Journal of the American Chemical Society* **121,** (1999).
6. Hyeon, T., Lee, S. S., Park, J., Chung, Y. & Na, H. B. Synthesis of highly crystalline and monodisperse maghemite nanocrystallites without a size-selection process. *J. Am. Chem. Soc.* **123,** 12798–12801 (2001).
7. Sun, S. & Zeng, H. Size-Controlled Synthesis of Magnetite Nanoparticles. *Journal of the American Chemical Society* **124,** 8204–8205 (2002).
8. Ahniyaz, A. *et al.* Preparation of iron oxide nanocrystals by surfactant-free or oleic acid-assisted thermal decomposition of a Fe(III) alkoxide. *Journal of Magnetism and Magnetic Materials* **320,** 781–787 (2008).
9. Pinna, N. & Niederberger, M. Surfactant-Free Nonaqueous Synthesis of Metal Oxide Nanostructures. *Angewandte Chemie International Edition* **47,** 5292–5304 (2008).
10. Jang, B. *et al.* Solventless synthesis of an iron-oxide/graphene nanocomposite and its application as an anode in high-rate Li-ion batteries. *J. Mater. Chem. A* **1,** 15442–15446 (2013).
11. Maity, D., Choo, S.-G., Yi, J., Ding, J. & Xue, J. M. Synthesis of magnetite nanoparticles via a solvent-free thermal decomposition route. *Journal of Magnetism and Magnetic Materials* **321,** 1256–1259 (2009).
12. Dou, Q. & Ng, K. M. Synthesis of various metal stearates and the corresponding monodisperse metal oxide nanoparticles. *Powder Technology* **301,** 949–958 (2016).
13. Walter, A. *et al.* Validation of a dendron concept to tune colloidal stability, MRI relaxivity and bioelimination of functional nanoparticles. *J. Mater. Chem. B* **3,** 1484–1494 (2015).
14. Baaziz, W. *et al.* Tuning of Synthesis Conditions by Thermal Decomposition toward Core–Shell CoxFe1–xO@CoyFe3–yO4 and CoFe2O4 Nanoparticles with Spherical and Cubic Shapes. *Chem. Mater.* **26,** 5063–5073 (2014).
15. Liu, X. *et al.* Systematic Study of Exchange Coupling in Core–Shell Fe3−δO4@CoO Nanoparticles. *Chem. Mater.* **27,** 4073–4081 (2015).
16. Walter, A. *Élaboration de nano-objets magnétiques dendronisés à vocation théranostic*. (Strasbourg, 2014).
17. Chevallier, P. *et al.* Tailored biological retention and efficient clearance of pegylated ultra-small MnO nanoparticles as positive MRI contrast agents for molecular imaging. *Journal of Materials Chemistry B* **2,** 1779 (2014).
18. Baaziz, W. *et al.* Magnetic Iron Oxide Nanoparticles: Reproducible Tuning of the Size and Nanosized-Dependent Composition, Defects, and Spin Canting. *The Journal of Physical Chemistry C* **118,** 3795–3810 (2014).
19. Baaziz, W. *et al.* Magnetic Iron Oxide Nanoparticles: Reproducible Tuning of the Size and Nanosized-Dependent Composition, Defects, and Spin Canting. *J. Phys. Chem. C* **118,** 3795–3810 (2014).
20. Rodríguez-Carvajal, J. Recent advances in magnetic structure determination by neutron powder diffraction. *Physica B: Condensed Matter* **192,** 55–69 (1993).
21. Thompson, P., Cox, D. E. & Hastings, J. B. Rietveld refinement of Debye–Scherrer synchrotron X-ray data from Al2O3. *J Appl Cryst, J Appl Crystallogr* **20,** 79–83 (1987).
22. Baaziz, W. *et al.* Tuning of Synthesis Conditions by Thermal Decomposition toward Core–Shell $Co_x Fe_{1-x} O@Co_y Fe_{3-y} O_4$ and $CoFe_2 O_4$ Nanoparticles with Spherical and Cubic Shapes. *Chemistry of Materials* **26,** 5063–5073 (2014).
23. Pichon, B. P. *et al.* Microstructural and Magnetic Investigations of Wüstite-Spinel Core-Shell Cubic-Shaped Nanoparticles. *Chem. Mater.* **23,** 2886–2900 (2011).
24. Yin, Y. & Alivisatos, A. P. Colloidal nanocrystal synthesis and the organic–inorganic interface. *Nature* **437,** 664–670 (2005).
25. Na, H. B., Song, I. C. & Hyeon, T. Inorganic Nanoparticles for MRI Contrast Agents. *Advanced Materials* **21,** 2133–2148 (2009).
26. Yin, M. & O'Brien, S. Synthesis of Monodisperse Nanocrystals of Manganese Oxides. *J. Am. Chem. Soc.* **125,** 10180–10181 (2003).
27. Park, J. *et al.* Synthesis, Characterization, and Magnetic Properties of Uniform-sized MnO Nanospheres and Nanorods. *The Journal of Physical Chemistry B* **108,** 13594–13598 (2004).
28. Li, Q., Wang, J., He, Y., Liu, W. & Qiu, X. Growth of Nearly Monodisperse MnO Nanocrystals in a Two-Size Distribution System. *Crystal Growth & Design* **9,** 3100–3103 (2009).
29. An, K. *et al.* Synthesis of Uniformly Sized Manganese Oxide Nanocrystals with Various Sizes and Shapes and Characterization of Their T1 Magnetic Resonance Relaxivity. *Eur. J. Inorg. Chem.* **2012,** 2148–2155 (2012).
30. Zitoun, D., Pinna, N., Frolet, N. & Belin, C. Single Crystal Manganese Oxide Multipods by Oriented Attachment. *Journal of the American Chemical Society* **127,** 15034–15035 (2005).
31. Ould-Ely, T. *et al.* Manganese(II) Oxide Nanohexapods: Insight into Controlling the Form of Nanocrystals. *Chemistry of Materials* **18,** 1821–1829 (2006).

32. Zhong, X., Xie, R., Sun, L., Lieberwirth, I. & Knoll, W. Synthesis of Dumbbell-Shaped Manganese Oxide Nanocrystals. *J. Phys. Chem. B* **110,** 2–4 (2006).

33. Davydov, A. S. *Theory of molecular excitons*. (Plenum Press, 1971).

34. Weers, J. G. & Scheuing, D. R. Micellar Sphere to Rod Transitions. in *Fourier Transform Infrared Spectroscopy in Colloid and Interface Science* **447,** 87–122 (American Chemical Society, 1990).

35. Ren, Y., Iimura, K., Ogawa, A. & Kato, T. Surface Micelles of CF3(CF2)7(CH2)10COOH on Aqueous La3+ Subphase Investigated by Atomic Force Microscopy and Infrared Spectroscopy. *J. Phys. Chem. B* **105,** 4305–4312 (2001).

36. Snyder, R. G., Strauss, H. L. & Elliger, C. A. Carbon-hydrogen stretching modes and the structure of n-alkyl chains. 1. Long, disordered chains. *J. Phys. Chem.* **86,** 5145–5150 (1982).

37. Kabir-ud-Din, Kumar, S., Aswal, V. K. & Goyal, P. S. Effect of the addition of n-alkylamines on the growth of sodium decyl sulfate micelles. *J. Chem. Soc., Faraday Trans.* **92,** 2413–2415 (1996).

38. Kumar, S., David, S. L., Aswal, V. K., Goyal, P. S. & Kabir-ud-Din. Growth of Sodium Dodecyl Sulfate Micelles in Aqueous Ammonium Salts. *Langmuir* **13,** 6461–6464 (1997).

39. Patriati, A., Putra, E. & Seong, B. Effect of A Long Chain Carboxylate Acid on Sodium Dodecyl Sulfate Micelle Structure: A SANS Study. *AIP Conference Proceedings* **1202,** (2010).

40. Mrad, K. *et al.* Control of the crystal habit and magnetic properties of Co nanoparticles through the stirring rate. *CrystEngComm* **19,** 3476–3484 (2017).

41. Atmane, K. A. *et al.* Control of the anisotropic shape of cobalt nanorods in the liquid phase: from experiment to theory… and back. *Nanoscale* **6,** 2682–2692 (2014).

42. Soumare, Y. *et al.* Kinetically Controlled Synthesis of Hexagonally Close-Packed Cobalt Nanorods with High Magnetic Coercivity. *Adv. Funct. Mater.* **19,** 1971–1977 (2009).

43. Seo, W. S. *et al.* Phase- and Size-Controlled Synthesis of Hexagonal and Cubic CoO Nanocrystals. *J. Am. Chem. Soc.* **127,** 6188–6189 (2005).

44. An, K. *et al.* Synthesis, Characterization, and Self-Assembly of Pencil-Shaped CoO Nanorods. *J. Am. Chem. Soc.* **128,** 9753–9760 (2006).

45. Zhang, Y., Zhong, X., Zhu, J. & Song, X. Alcoholysis route to monodisperse CoO nanotetrapods with tunable size. *Nanotechnology* **18,** 195605 (2007).

46. Zhang, Y., Zhu, J., Song, X. & Zhong, X. Controlling the Synthesis of CoO Nanocrystals with Various Morphologies. *J. Phys. Chem. C* **112,** 5322–5327 (2008).

47. Buck, M. R., Biacchi, A. J. & Schaak, R. E. Insights into the Thermal Decomposition of Co(II) Oleate for the Shape-Controlled Synthesis of Wurtzite-Type CoO Nanocrystals. *Chemistry of Materials* **26,** 1492–1499 (2014).

48. Bronstein, L. M. *et al.* Influence of Iron Oleate Complex Structure on Iron Oxide Nanoparticle Formation. *Chem. Mater.* **19,** 3624–3632 (2007).

49. Lu, A. *et al.* Shape-related optical and catalytic properties of wurtzite-type CoO nanoplates and nanorods. *Nanotechnology* **25,** 035707 (2014).

50. Qi, Q., Chen, Y., Wang, L., Zeng, D. & Peng, D.-L. Phase-controlled synthesis and magnetic properties of cubic and hexagonal CoO nanocrystals. *Nanotechnology* **27,** 455602 (2016).

51. Alokmay, D. Headgroup Conformation and Film Structure. in *Structural and Morphological Evolution in Metal-Organic Films and Multilayers* 113–138 (CRC Press, 2015).

52. Fliedel, C. *et al.* Zwitterionic Cobalt Complexes with Bis(diphenylphosphino)(N-thioether)amine Assembling Ligands: Structural, EPR, Magnetic, and Computational Studies. *Inorg. Chem.* **55,** 4183–4198 (2016).

53. Lee, J.-H. *et al.* Exchange-coupled magnetic nanoparticles for efficient heat induction. *Nat Nano* **6,** 418–422 (2011).

54. Meiklejohn, W. H. & Bean, C. P. New Magnetic Anisotropy. *Phys. Rev.* **102,** 1413–1414 (1956).

55. Nogués, J. *et al.* Exchange bias in nanostructures. *Physics Reports* **422,** 65–117 (2005).

56. López-Ortega, A., Estrader, M., Salazar-Alvarez, G., Roca, A. G. & Nogués, J. Applications of exchange coupled bi-magnetic hard/soft and soft/hard magnetic core/shell nanoparticles. *Physics Reports* **553,** 1–32 (2015).

57. Gao, Z. *et al.* Small is Smarter: Nano MRI Contrast Agents - Advantages and Recent Achievements. *Small* **12,** 556–576 (2016).

58. Shin, T.-H. *et al.* T1 and T2 Dual-Mode MRI Contrast Agent for Enhancing Accuracy by Engineered Nanomaterials. *ACS Nano* **8,** 3393–3401 (2014).

59. Baaziz, W. *et al.* High Exchange Bias in Fe3−δO4@CoO Core Shell Nanoparticles Synthesized by a One-Pot Seed-Mediated Growth Method. *J. Phys. Chem. C* **117,** 11436–11443 (2013).

60. Signorini, L. *et al.* Local magnetism in granular iron/iron oxide nanostructures by phase- and site-selective x-ray magnetic circular dichroism. *Phys. Rev. B* **74,** 014426 (2006).

61. Ho, C.-H. *et al.* Shape-Controlled Growth and Shape-Dependent Cation Site Occupancy of Monodisperse Fe3O4 Nanoparticles. *Chem. Mater.* **23,** 1753–1760 (2011).

62. LaMer, V. K. & Dinegar, R. H. Theory, Production and Mechanism of Formation of Monodispersed Hydrosols. *J. Am. Chem. Soc.* **72,** 4847–4854 (1950).

63. Xia, Y., Xiong, Y., Lim, B. & Skrabalak, S. E. Shape-controlled synthesis of metal nanocrystals: simple chemistry meets complex physics? *Angew. Chem. Int. Ed. Engl.* **48,** 60–103 (2009).

Chapter VI

Unravelling the thermal decomposition parameters for the synthesis of anisotropic iron oxide nanoparticles

VI Unravelling the thermal decomposition parameters for the synthesis of anisotropic iron oxide nanoparticles

VI.1 Introduction

The design of iron oxide nanoparticles (IONPs) is currently a hot topic of research given the wide range of applications (biomedical, energy …) where they can be are envisioned. The interest of IONPs comes from their specific magnetic properties at the nanoscale along with their high surface to volume ratio. A lot of papers reported on the synthesis of NPs with a spherical shape but, now, thanks to the progress in chemical synthesis methods, the shape can also be modulated allowing enhancing the IONPs properties. Indeed, modifying the shape of the NPs will have different impacts. Specific shapes are determined by different crystallographic planes which present different surface energies. The NPs having specific surface energy are particularly important for catalytic applications where looking for high energy surfaces is needed. However, interest for anisotropic shapes does not rely only on the surface energy. Modifying the morphology will also have an impact on the magnetic properties by adding shape anisotropy to the NPs effective anisotropy. Bergstrom *et* al have thus demonstrated that nanocubes displayed a shape anisotropy[1]. Besides, nanocubes of 19 nm have been shown to be very good heating agents for therapy by magnetic hyperthermia[2]. Furthermore, NPs with faceted shapes exhibited very high contrast enhancement properties promising for imaging by MRI[3–5].

However, the control of the NPs shape is not an easy task. New synthesis processes allowed to better address the NPs shapes. In the beginning of the 2000's, one very well-established method is thermal decomposition (TD) which involved the thermal decomposition of an iron precursor in presence of ligands in an organic solvent. Thus, iron precursors such as acetylacetonates[1,6,7], acetates[1] or oleates[6,8–10] have been decomposed in organic solutions containing surfactants. The strength of this method comes from the possibility to easily separate the NPs nucleation and growth steps. It follows the theory of nucleation-growth proposed by Lamer[11]. In the case of the heating-up method which is used here, with the temperature increase of the reactants mixture, the iron precursor decomposed forming monomers with a specific rate of formation depending on the nature of ligands and solvents[12]. These monomers have been hypothesized by Kwon[13] as polyiron oxo cluster species. When the monomer concentration reached a critical value above the minimal nucleation concentration, the nucleation step occurred. Then the remaining monomers and the ones that continued forming during the process contributed to the growth of the NPs. The ligands, which are mainly carboxylic acid or amine based ligands, *in situ* coated the NPs during the synthesis process and allowed controlling the growth step and prevent NPs from aggregation. They have also been shown to contribute to the stabilisation or destabilisation of the iron precursor[12,14]. The nature of solvents has also been evidenced to affect the thermal decomposition of precursors by impacting their thermal stability[12]. The separation of nucleation and growth steps provided by the thermal decomposition method is the key parameter as it allows influencing the nucleation and/or the growth steps.

Anisotropic shaped IONPs started to be reported in the mid 2000's with the synthesis of nanocubes. Kovalenko et al[15] reported at first the synthesis of nanocubes by decomposing an iron oleate precursor using an oleate salt as ligand. The role of the ligands, which was at first to stabilize colloidally the NPs in solution, was then to direct the growth of the nanocrystal towards anisotropic shapes. The theory of the shape control through ligand adsorption is quite simple. The crystallographic planes of fcc materials such as magnetite do not present the same surface energy γ. Typically, the ranking established from the lowest energy planes is $\gamma_{\{111\}} < \gamma_{\{100\}} < \gamma_{\{110\}} < \gamma_{\{hkl\}}$ (with h,k,l>1)[16,17]. When a nucleus is formed, it should be then enclosed by the {111} planes that present the lowest surface energy. Thus, a cube which is enclosed by {100} planes wouldn't be favoured. However, as for a given volume, the surface of a cube is lower than the one of an octahedron, the stable nucleus is thus a compromise between both family planes to reduce the surface energy: the cuboctahedron. But depending on the conditions, twin defects can occur in the nucleus. The presence of defect in the nucleus will have a major effect on the final shape of the nanocrystal. For example, a mirror (111) plane can lead to flat nanoparticles[18]. The nucleus shape and structure appear thus major points for the NP shape control. The role of the ligands in the shape control has been ascribed to the tuning of growth rate of certain planes[1,7]. E.g. the adsorption of a ligand on {111} planes of the cuboctahedron nucleus will reduce their growth rate. The {100} planes will grow faster leading to their disappearance. The final shape will be then an octahedron. Rath and al[19] showed through simulation that the {111} plane family of magnetite has a most active surface for adsorption than the {311} and {110}. When a chelating ligand such as oleate is present, it would then adsorbate on the {111} planes of the nuclei reducing its growth rate. More recently, nanocubes have been synthesized by thermal decomposition in dibenzylether (DBE) as solvent in presence of non-chelating ligands such as oleic acid.[20,21] Guardia et al[21] demonstrated that the shape control was induced by the product of decomposition of DBE at high temperature. While most of the reports emphasize the role of the ligands, Kim[22] underlined the role of a kinetically controlled growth under high monomer concentration.

Currently, most published results on the synthesis of nanocubes are based on the Kovalenko's method using different combination of ligands (NaOl/OA[23–27] – OA/OAm[28] – OA/ 4-Bisphenyl carboxilic acid[20,29]) and iron precursors. Zhou et al[4] succeeded in the synthesis of various anisotropic IONPs from iron oleate with a combination of NaOl and OA. By varying the ratio FeOl/NaOl, cubes and plates among other shapes were obtained. Nevertheless, there are many protocols for the synthesis of anisotropic shapes and every protocol differed from the other involving different heating rates, different ligands, and different concentration as shown in Table VI.1.

Unfortunately, no defined trend came out from the literature. There are as many protocols of nanocubes synthesis as there are publications and a huge variety of precursors, ligands combinations and solvents are used. Thus, no general rule came out. Yet, what is often commented in the published works is that the ligands used in the synthesis and the heating rates appeared to be the main parameters for the shape control. However, the synthesis mechanism of anisotropic shape is not yet clearly understood.

Iron oxide nanocubes were previously synthesized in our lab by thermal decomposition of an iron oleate precursor in presence of sodium oleate and oleic acid (ratio 3.6:1) in octadecene by adapting the Kovalenko's method[30]. Nevertheless, the shape quality of nanocubes was highly dependent on the iron oleate batch and several iron oleate batches were often synthesized without succeeding in obtaining homogeneous nanocubes. In addition, iron oleate batches suffered from ageing and "old" iron oleate batches (one or two weeks) did not lead to reproducible nanocubes. We tried to synthesize nanocubes by using a commercial iron stearate but without success. By observing experimentally an influence of the drying time on $MgSO_4$ of iron oleate and that the iron oleate was in an oily state by comparison with the iron stearate which is under the form of a powder, we supposed that the hydration state of the precursor and thus its structure could have an influence. However very few papers dealt with the influence of the iron precursor structure on the formation of anisotropic shape by the thermal decomposition method. There was the pioneer work of Bronstein et al[10,31] which have pointed at the role of the precursor structure which would be affected by washing solvents. Buck et al reported on the role of the precursor with the study of cobalt oleate ($CoOl_2$)[32].

Table VI.1 – Reported nanocubes syntheses from litterature

Ref.	Precursor	Solvent	Ligand	Reflux T and duration	Heating rate	Observations
20	$Fe(acac)_3$	DBE	OA	290 °C / 30'	20 °C/min	Size and shape control with time and quantity of DBE
	$Fe(acac)_3$	DBE	OA / 4-Bisphenyl carboxilic acid	290 °C / 30'	20 °C/min	Smaller cubes
4	$Fe(Ol)_3$	OD or TOA	OA	340°C / 4h	10-15 °C/min	Size controled with T
29	$Fe(acac)_3$	DBE	OA / 4-Bisphenyl carboxilic acid	290 °C / 30'	ND	
23,24	$Fe(Ol)_3$	Squalane	NaOl / OA	315 °C / 2h	20 °C/min	Coreshell
28	$Fe(acac)_3$	DBE	OA / HDD /OAm	290 °C / 1h	15 °C/min	If heating rate increase along shorter reflux bigger NPs on the opposite smaller NPs
25	$Fe(Ol)_3$	eicosane	NaOl / OA	350 °C / 30'	3,3 °C/min	Coreshell
33	$Fe(Ol)_3$ in situ	OD	NaOl	315 °C/ 2h	ND	Shape control through amount of NaOl
34	$Fe(Ol)_?$	OD	OA	320 °C / 30 '	5,5 °C/min	
7	$Fe(Ol)_3$	OD	NaOl / OA or DBAOL	315 °C / 30'	3,3 °/min	
26	$Fe(Ol)_3$	OD	NaOl /OA	315 °C / 30 '	4 °C/min	Ratio Fe(Ol)/NaOl control the size
27	$Fe(St)_2$	OA	NaOl /OA	380 °C / 2h	5 °C/min	
35	$Fe(acac)_3$	Squalane	Decanoic acid / DBE	310 °C / 1h	7 °C /min	Size controled with ratio squalane/DBE

In chapter III, we managed to control the synthesis of iron stearate precursors. The structure (depending on the type of Fe(+II) or Fe(+III) based reactants) and hydration degree have been tuned. Four types of stearates were thus obtained: iron II stearate synthesized from hydrated iron chloride II ($FeSt_2$), iron III stearate synthesized from hydrated iron III chlorides and these both iron stearates after a dehydration step at 140°C for 48h and named respectively $FeSt_{2,d}$ and $FeSt_{3,d}$. The so obtained structure of stearates was shown to have a great effect on the stability of the precursor against temperature and thus on the germination and growth steps. These parameters were shown to have quite no influence on the synthesis of spherical NPs but one on that of nanocubes. Dehydrated iron stearates were found necessary to form nanocubes. That was explained by different thermal stability of stearates and kinetic considerations of the monomer generation in chapter III. However in chapter IV, we showed that the germination occurred in vesicles followed by a growth step outside vesicles.

Considering that the synthesis of anisotropic shaped NPs is very important due to their enhanced properties for several applications, the understanding of their synthesis mechanisms is of paramount interest however, this remains challenging. In that context, and based on our previous investigations (Chapters III & IV), we propose to investigate the effect of the precursor structure which has been poorly studied up to now. That's why in this work, four precursors, hydrated and dehydrated $FeSt_2$ and $FeSt_3$, have been decomposed in anisotropic conditions from an adapted Kovalenko's method[30]. Some important reported parameters were thus investigated to better understand the mechanism addressing the shape of NPs: the influence of the structure (and hydration degree) of iron stearate, the ratio sodium oleate/oleic acid (NaOl/OA) and the heating rate. This last parameter was in particular studied by performing in situ liquid TEM studies.

VI.2 Experimental details

VI.2.1 Synthesis methods

Synthesis of iron stearate precursors

Iron stearate (II) and (III) were prepared by precipitation of sodium stearate and ferrous chloride or ferric chloride salts in an aqueous solution. Briefly, sodium stearate (9.8 g, 32 mmol) was transferred into a 2 necked to a round bottomed flask (RBF) and solubilized in distilled H2O (dH2O, 80 ml). The solution is heated to reflux and stirred for 30 min until complete dissolution of the stearate. Separately, $FeCl_2.4H_2O$ (3.16 g, 16 mmol) or $FeCl_3.6H_2O$ (2,88 g, 16 mmol) was dissolved in dH2O (40 ml) and added onto the sodium stearate solution under vigorous stirring. A light orange precipitate is formed immediately. The solution is kept under stirring at this temperature 15 min. Thereafter the solution is allowed to cool down to room temperature (RT). The obtained precipitate is washed once by centrifugation (hot dH2O, 14000 rpm, 10 min). The product is then filtrated with a büchner funnel and oven dried at 65 °C for 24 h.

NPs synthesis

2,32 mmol of iron stearate is mixed with 3 mmol of ligands (OA and NaOl at different ratios) in 15 mL OD. The mixture is stirred and heated at 120 °C for 60 min without reflux condenser in order to dissolve the reactants and remove the water residues. The cooler is then connected to the flask and the solution is heated up to 200 °C for 10 min with a heating rate of 5 °C/min. The solution is then heated up to 315 °C with a heating rate of 1 °C/min and refluxed for 60 min under air. After cooling to RT, a black and viscous suspension is obtained which is solubilized in 10 ml of chloroform. The NPs are then precipitated by the addition of an excess of acetone the first time and washed three times with chloroform and acetone at a ratio of 1:4 at 14000 rpm for 5 min by centrifugation. The NPs can finally be suspended in 50 ml of THF.

VI.2.2 Other characterization techniques

In situ Transmission Electron Microscopy

(see §IV.2.3)

VI.3 Results

VI.3.1 Influence of the structure of precursors and of sodium oleate ligand

VI.3.1.1 Influence on the shape and size

$FeSt_2$ and $FeSt_3$ have been synthesized by a co-precipitation method using $FeCl_2.4H_2O$ and $FeCl_3.6H_2O$ respectively and these stearates have been heat-treated at 140°C for 48h to remove main crystallized water molecules leading to partially dehydrated stearates ($FeSt_{3,d}$ and $FeSt_{2,d}$). All stearates are mainly composed of Fe^{3+} but their structures differed due to different amounts of stearate ligand and different Fe III-carboxylate coordination. It was seen before that the thermal stability of the different iron stearates was highly dependent on their structure as well as on the hydration degree.

These different stearates have been decomposed according to a previously published protocol[30] adapted from the Kovalenko method[7] which has led to the synthesis of nanocubes using a pre-synthesized iron oleate precursor. The synthesis involved a quick heating (5 °C/min) to a step at 200 °C for 10 min which is applied to favour the nucleation of NPs (more homogeneous mean size are obtained[36]) and then the reactant mixture is heated up to 315 °C with a heating rate of 1 °C/min and refluxed for 60 min under air.

The role of the iron stearate structure was further investigated by decomposing hydrated and dehydrated $FeSt_2$ and $FeSt_3$ in presence of different ratios of NaOl and OA (keeping the same molar amount of ligands, only the ratio is varied) in order to correlate the shape to these parameters. Same batch was used for the 5 ratios on each precursor. Figure VI.1 showed TEM images of NPs obtained by tuning the type of iron stearates and the amount of NaOl. The main results are summarized in Table VI.2.

Table VI.2 - Size and shape summary as a function of the nature and amount of reactants (M Majority, m minatory, r rare)

Precursor		NaOl/OA				
		0/100	20/80	50/50	80/20	100/0
FeSt2	Size (nm)	9.4 ± 1.9	11.7 ± 2.5	13.5 ± 2.5	17.5 ± 4.4 (L) 6.3 ± 1.3 (t)	7.2 ± 2.4
	Shape	Spheres	Quasi octahedron	Deformed Cubes	Plates	Faceted
FeSt2,d	Size (nm)	10.0 ± 1.5	10.9 ± 1.4	10 ± 0.6	13.5 ± 5.2 (L) 6.5 ± 1.7 (t)	9 ± 2.7
	Shape	Spheres	Quasi spherical	Cubes	Plates	Various faceted plates
FeSt3	Size (nm)	10.8 ± 1.7	12.4 ± 1.7	8.3 ± 2.2	11.3 ± 4.3	11.7 ± 1.5
	Shape	Spheres	Quasi spherical	Faceted	Faceted	Cubes
FeSt3,d	Size (nm)	9.2 ± 1.5	9.8 ± 1.4	15.3 ± 1.8	20 ± 1.9/14 ± 1.4	13.9 ± 2.2
	Shape	Spheres	Quasi spherical (M) / Octahedrons (r)	Cubes	Cubes (M)/Plates (m)	Elongated cubes

*For plates : L for length and t for thickness.

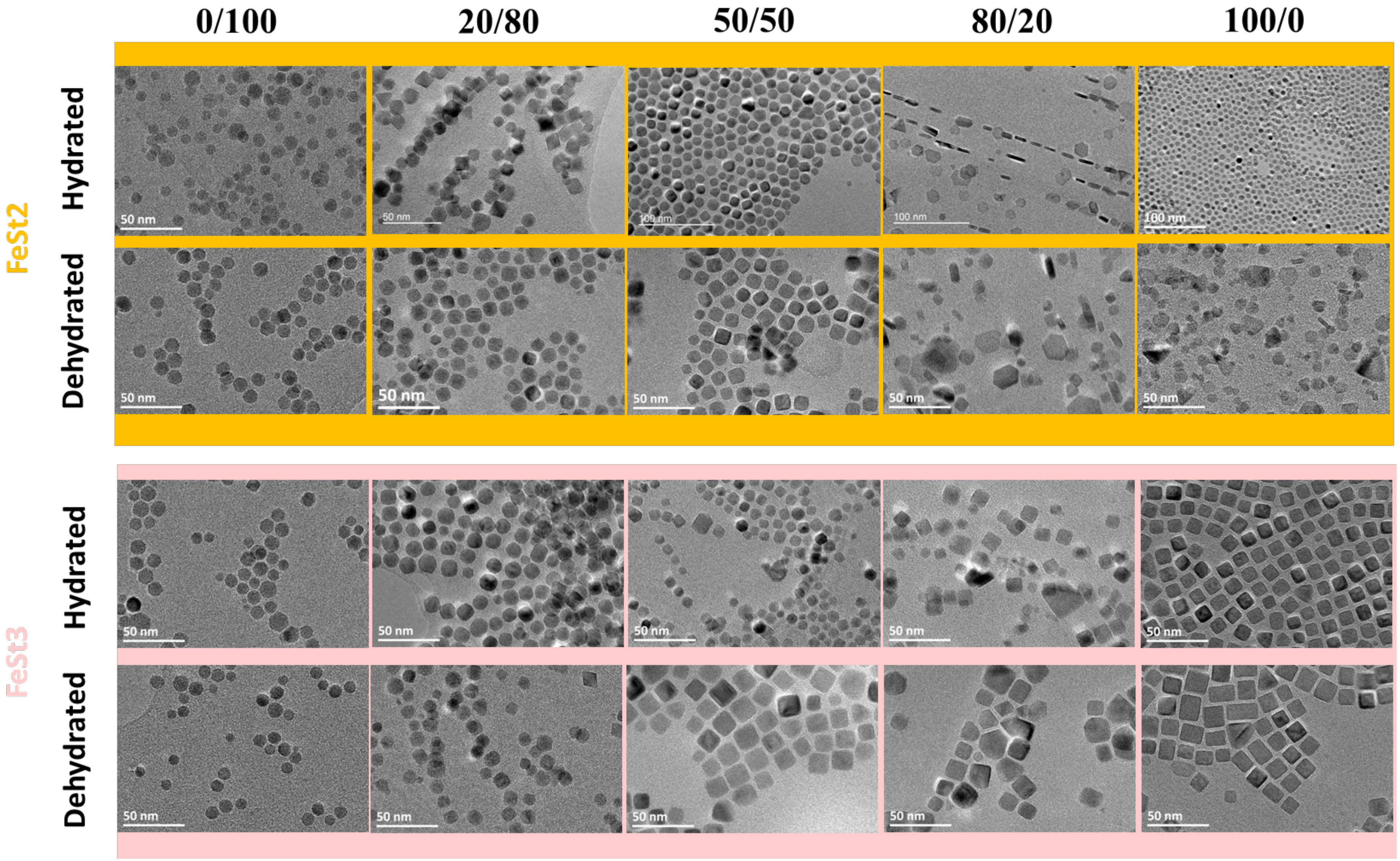

Figure VI.1 - Influence of the ratio NaOl/OA on the shape of the NPs depending on the precursor structure and hydration degree

From Figure VI.1 and Table VI.2, we can conclude that the introduction of NaOl had clearly an effect on the shape of NPs,. However depending on the type of stearates, $FeSt_2$ and $FeSt_3$, and on their hydration degree, the shape evolution and nature are different:

- Some shapes are preferentially obtained from a given precursor structure. Here, both $FeSt_2$ and $FeSt_{2,d}$ allowed to easily obtain plates when it was not possible with $FeSt_3$. $FeSt_3$ led preferentially and quite easily to cubes.
- The hydration degree appeared to play a major role too: the more hydrated the iron stearate is, the highest the amount of introduced NaOl has to be to obtain well-defined shapes. With dehydrated iron stearates, defined shapes were obtained as soon as NaOl wass introduced: at the ratio 20/80, $FeSt_2$ and $FeSt_3$ led to spherical NPs when some octahedrons were already observed with dehydrated ones. At the ratio 50/50, faceted NPs or deformed nanocubes were obtained with $FeSt_3$ and $FeSt_2$ respectively when nanocubes were obtained with dehydrated stearates. At 80/20, $FeSt_3$ (mean formula from Chapter III: $FeSt_{2.1}@15H_2O$) which is more hydrated than $FeSt_2$ (mean formula from Chapter III: $FeSt_{1.5}@6H_2O$) led to faceted NPs when nanoplates were obtained with $FeSt_2$. Dehydrated $FeSt_{2,d}$ (mean formula from Chapter III: $FeSt_{1.5}@2H_2O$) led further to nanoplates when nanocubes and some nanoplates were obtained with $FeSt_{3,d}$ (mean formula from Chapter III: $FeSt_{2.1}@5H_2O$). At 100/0, extremely faceted ultra-small NPs were obtained with both hydrated and dehydrated $FeSt_2$ when nanocubes were synthesized with both hydrated and dehydrated $FeSt_{2.}$

The effect of these parameters on the size of NPs is difficult to evaluate as their shape varies but it would appear that the size is affected by the hydration degree of iron stearates. Indeed the size of NPs is quite always smaller with hydrated iron stearates than with dehydrated ones (Table VI.2). This result is in agreement with the observed effect of water on the size of spherical NPs in an earlier study[12]. We found the synthesis of spherical NPs was very sensitive to hygroscopic conditions. Water traces led to smaller NPs.

As the shape is dictated by the introduction of NaOl in the synthesis and as the more hydated the precursor is, the less defined is the shape, one hypothesis would be that NaOl interacted with water and thus it cannot adsorb on specific faces of nucleus to trigger the growth of given shape.

This confirmed that the hydration degree is a parameter that required to be carefully monitored for the synthesis of homogenous and shape defined NPs. This could explain why similar cubes are obtained for 0/100 with the hydrated $FeSt_3$ but at 50/50 for the dehydrated complex.

The nanocubes and nanoplates are very interesting to investigate for their properties and these NPs have been then more carefully structurally characterized.

For all stearates, the increase in the amount of sodium oleate induced the formation of faceted NPs but the final shapes were very different depending on the amount of sodium oleate and the structure of stearates were influenced by their hydration rate.

Therefore sodium oleate is involved clearly in the formation of anisotropic NPs but the structure of precursors appeared to disturb its role.

VI.3.1.2 Characterisation of the anisotropic NPs

High resolution TEM (HR-TEM) and 3D TEM tomography have already been performed earlier on nanocubes to confirm their shape[37]. They were performed here on the nanoplates as this shape has rarely been reported.

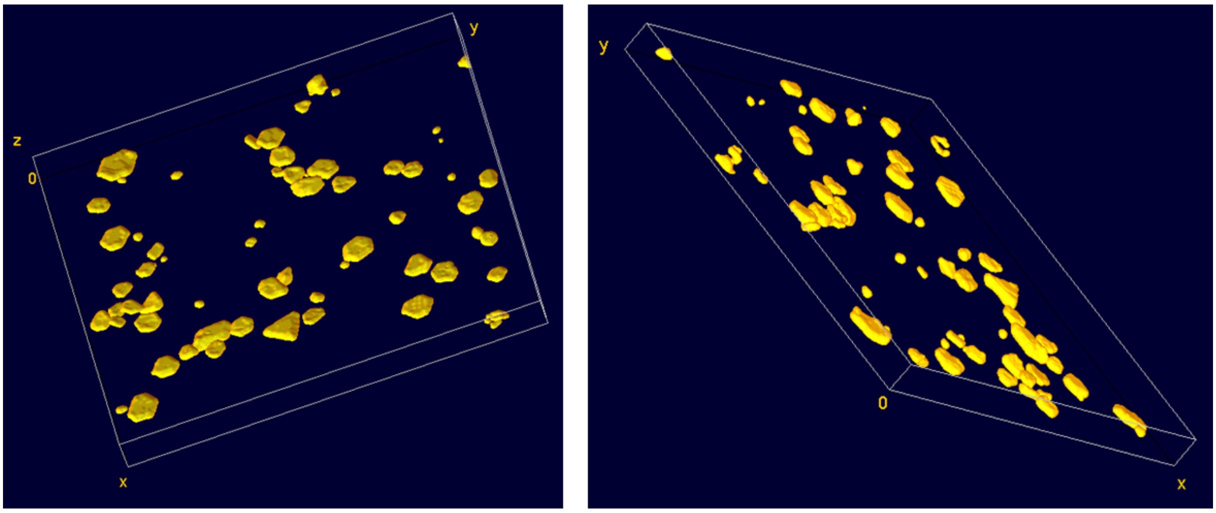

Figure VI-2 – 3D TEM reconstruction of the nanoplates

The 3D TEM tomography images in Figure VI.2 confirmed the flat shape of nanoplates and showed that the fully formed nanoplates are not perfectly flat but concave. The smaller NPs are rather convex confirming the spherical profile to reduce the surface energy. The plates analysed here were the 17.5 ± 4.4 nm length and 6.3 ±1.3 nm thickness plates from hydrated $FeSt_2$. HR-TEM (Figure VI.3) showed that the long face of the plate is made out of {111} planes when the sides are made out of {220} planes.

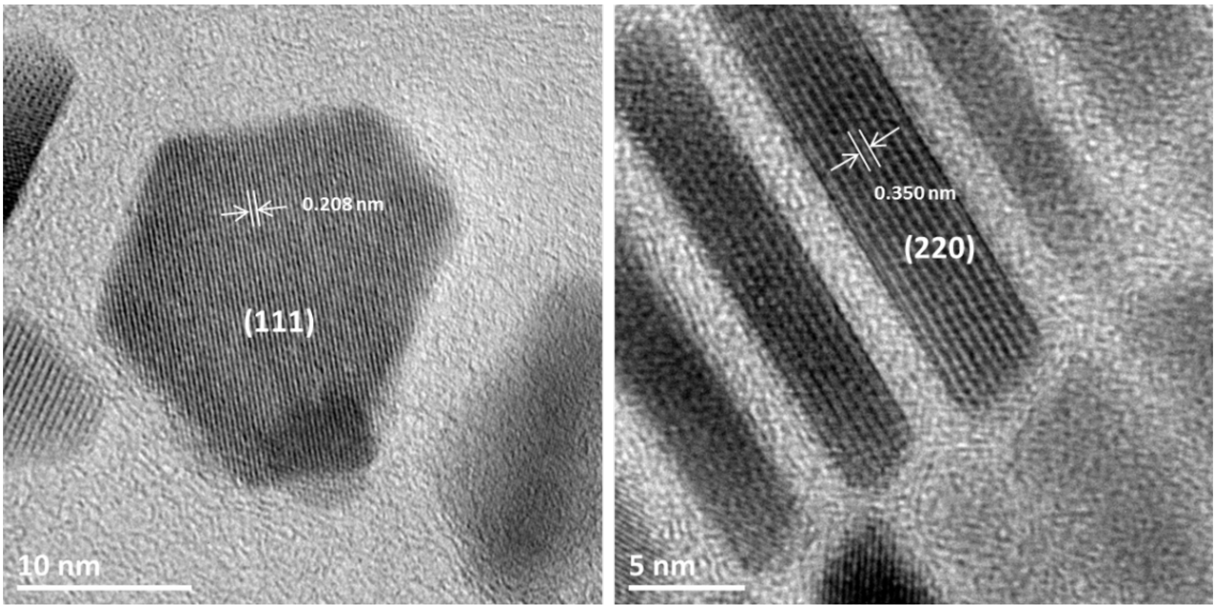

Figure VI-3 - HR-TEM images of the long face of a platelets (left) and of the side (right)

Figure VI.4 displayed XRD patterns of the nanocubes with a mean size of 15.3 nm (and nanoplates with a mean size of 17.5 ± 4.4 nm length (6.3 ±1.3 nm thickness) obtained from the following synthesis conditions: $FeSt_{3,d}$ and a ratio 50/50 for nanocubes and $FeSt_2$ and ratio 80/20 for nanoplates. Nanoplates presented a XRD pattern consistent with the formation of a spinel phase either magnetite or maghemite. XRD pattern of the nanocubes showed the presence of two phases: a spinel phase and wüstite FeO. It has already been observed that the Kovalenko's method led to such a core-shell structure with a core of wüstite and a magnetite shell[30,38]. It is reported that the strong reducing conditions induced by the synthesis conditions (high temperature alkene, NaOl …) were responsible for the formation of FeO nanocubes which oxidized when exposed to air.

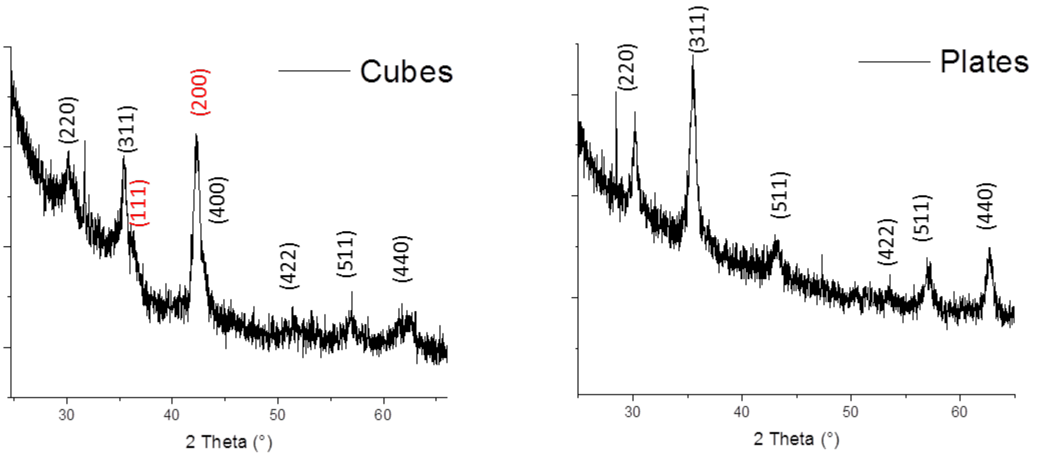

Figure VI.4 - XRD pattern of the cubes (left) and plates (right)

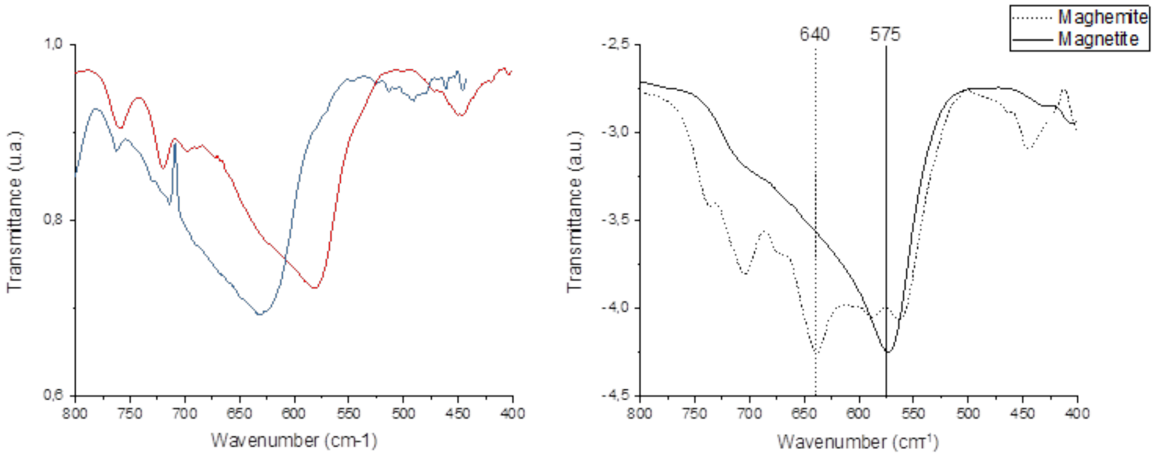

Figure VI-5 - IR spectra in the region 800 - 400 cm^{-1} for nanocubes (blue) and nanoplates (red) [left] and IR spectra of magnetite and maghemite [right]

The IR spectra in the Fe-O region 800-400 cm^{-1} in Figure VI.5 are in agreement with XRD conclusion. Indeed IR spectroscopy allowed discriminating both magnetite and maghemite phases as they displayed different IR bands (cf. Chapter II). We demonstrated that the oxidation degree of magnetite may be determined from the position of the maximum of the broad Fe-O band[36] (which is compared to that of magnetite and maghemite. The maximum of the Fe-O band at 590 cm^{-1} and the presence of a shoulder in the higher wavenumbers confirmed the formation of a slightly oxidized magnetite phase for nanoplates. Nevertheless the presence of FeO is not easy to check by IR spectroscopy and for nanocubes, the Fe-O band with a maximum at 630 cm^{-1} was closer to the characteristic band of maghemite against what was expected. As the core shell cubes have been demonstrated to be made out of FeO and Fe_3O_4[30] we would have expected to observed a band closer to one of magnetite as FeO was composed of Fe^{2+}. Thus we believed that the spinel shell seen with XRD could be actually constrainted maghemite but only more precise characterisation would let conclude.

VI.3.2 Influence of the heating rate on the shape definition

As it was suggested the kinetic conditions favoured the cubic shape[20] and one parameter that is probably key in the synthesis is the heating rate. Indeed, lot of reports[20,23,24,39] showed that high heating rates were rather used for nanocube synthesis. Thus in our experiments, the heating rate was varied (from 1 to 5 °C/min) by using hydrated $FeSt_2$ for two NaOl/OA ratios : 50/50 and 80/20. which led with 1°C/min respectively deformed nanocubes and nanoplates (cf. §VI.3.1.1). The hydrated precursor $FeSt_2$ has been chosen as it led to poorly defined cubes and also would be the *in house* iron stearate with the lowest manufacturing price.

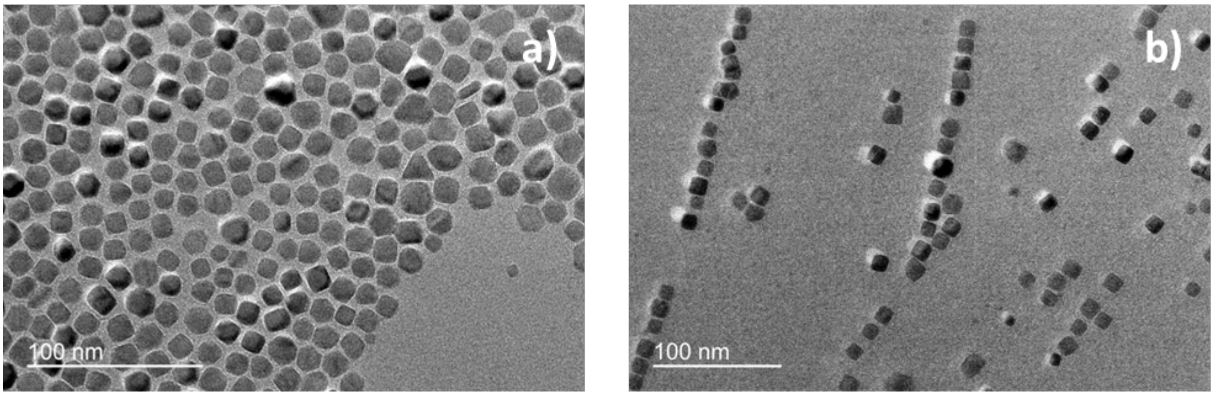

Figure VI.6 – Hydrated $FeSt_2$, ratio 50/50 a) 1°C/min and b) 5°C/min

Figure VI.6 compared the TEM images of NPs synthesized with FeSt2 and a ratio 50/50 with heating rates at 1 and 5°C /min. A higher heating rate is observed to favour the formation of more defined cubes (Figure VI.6) and lead to a decrease in the NPs mean size from 13.5 ± 2.5 nm to 11.8 ± 1.8 nm.

With a 80/20 ratio and whatever the heating rate (from 1 to 10°C /min) (Figure VI.7), nanoplates are obtained. The mean sizes are for 1°C/min: l=16.7± 5.2 nm and t=8.6 ±1.7 nm and for 5°C/min: l=16.6 ± 4.9 nm and t=6.1 ± 1 nm: the thickness decreased with the increase in the heating rate. An increase in the heating rate up to 10 °C/min promoted partly the formation of cubic NPs (Figure VI.7). At 10 °C/min, the length decreased (15.8 ± 4.5 nm) and the thickness is in between the two former values (7.1 ± 1.4 nm).

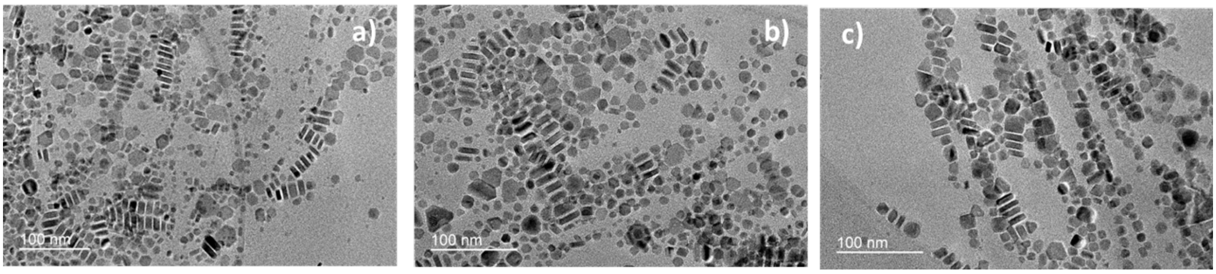

Figure VI-7 - Ratio 80/20 a) 1°C/min, b) 5°C/min and c) 10 °C/min

The formation of nanocubes is therefore more dependent on the heating rate and high heating rates are required to favour the cubic shape in our conditions.

As the nanoplates shape did not present the same dependence on the heating rate as the cubic one, one may suppose that the main step to control the nanoplates shape is not the growth step (case of nanocubes) but rather the nucleation one.

We have thus investigated the effect of the "nucleation step", that we have introduced in our experimental conditions, on the nanoplates formation and we have varied the "nucleation step" temperature. When this step was removed or was below 200 °C, nanoplates were observed to form (Figure VI.8). Above 200°C, the plate's occurrence decreased. Moreover, when the duration of the step was increased from 10 to 30 at 210°C, no plates were observed at all (Figure VI.8).

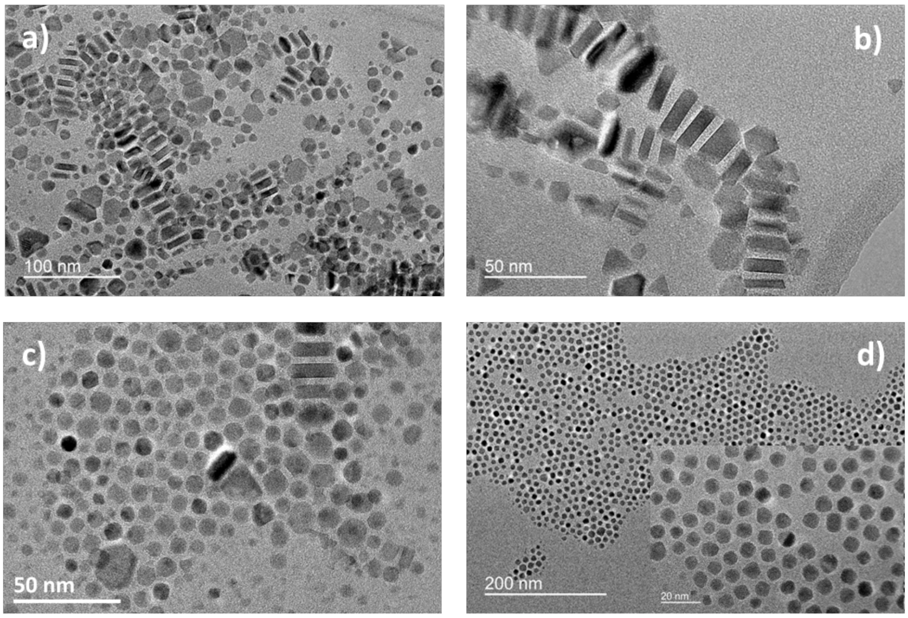

Figure VI.8 - Influence of the germination step with the ratio 80/20 a) no germination step, germination step at b) 190 °C for 10 min, c) 210 °C for 10 min and d) 210°C for 30 min

Curiously, the presence or absence of a nucleation step at 190 °C didn't have any impact on the nanoplates size, 16.6 ± 4.6 nm (t: 6.1 ± 1 nm) and 16.7 ± 5.7 nm (t: 6.3 ± 1.4 nm) without or with a nucleation step respectively. The step at 210 °C gave mostly spherically shaped NPs with a mean diameter of 6.6 ± 1.9 nm and few nanoplates slightly longer than previously 19.8 ± 2.3 nm. The increase of this step duration led to 8.1 ± 0.9 nm faceted NPs. That confirmed a major dependence of the plate shape towards the temperature around the "imposed" nucleation step.

Moreover, as shown in chapter IV, the NPl nucleated in the wall of the reversed vesicles. We suggested that these structures might not be stable above 200°C or evolved towards another structure.

IV.3.3 Influence of the heating power: *in situ* TEM

To better understand the role of the energy brought to the system, in situ TEM has been performed on a reaction mixture (ratio 80/20, $FeSt_2$) leading normally to nanoplates after the homogenization step at 120°C for 60 min. We've seen in chapter IV, that in these conditions, vesicles were formed and the nucleation occurred in the walls of the vesicles.

We were able to observe the beginning of nucleation step but we have not investigated the nanoplate growth. To continue the experiment, the reaction mixture was imaged *in situ* in STEM mode. Contrary to the TEM mode, STEM allowed to tune the energy brought to the system by the electron beam. Thus, two energies (electron dose) were applied, a low dose (2.3 $e.A^{-2}.s^{-1}$) and a higher dose (9 $e.A^{-2}.s^{-1}$). Figure VI.9 shows the result of both electron dose applications.

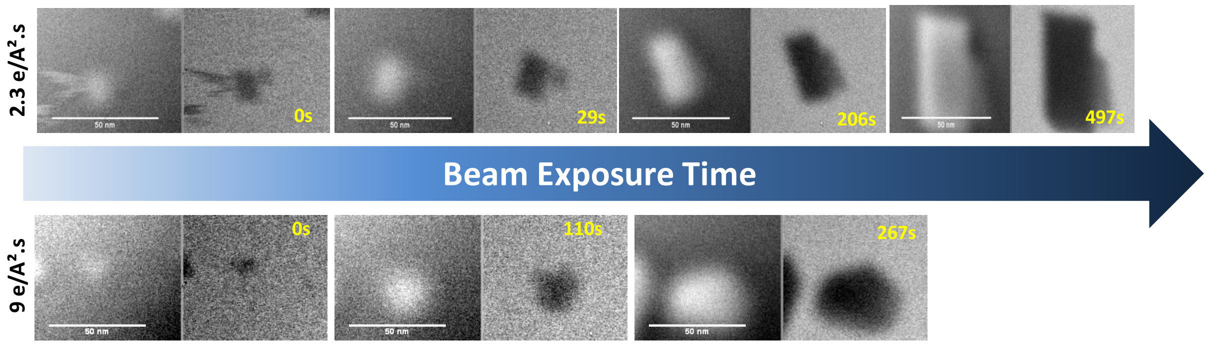

Figure VI-9 - TEM images on the in situ observation of the NP growth as a function of electron doses

When the electron dose is low, the NP nucleated and grew with an anisotropic shape since the beginning. The shape looked quite alike a rectangle and evolved towards a plate like NP. On the opposite, with the high electron dose, the NPs looked more isotropic in shape since the beginning. Then, it evolved towards a final spherical shape.

Interestingly, this evolution with the electron dose could be correlated to the effect of the temperature of the isothermal treatment around the nucleation step. An isothermal step at low temperature favoured the nanoplate shape when one at higher temperature inhibited the synthesis of the plate shape. A low electron dose or low nucleation temperature appeared necessary to make the nucleus adapted for a shaped growth.

VI.4 Discussion

The influence of the precursor structure on the shape of the NP has been scarcely investigated in the literature. We have thus studied the thermal decomposition of hydrated and dehydrated FeSt2 and FeSt3 as a function of the amount of NaOl introduced in the reaction mixture.

We have mainly confirmed that 1) NaOl was of key importance effectively to determine the NPs shape, that 2) hydrated stearates needed more NaOl to form shaped NPs and that 3) $FeSt_2$ favoured the formation of nanoplates when $FeSt_3$ favoured that of nanocubes. Dehydrated iron stearates and $FeSt_2$ which is less hydrated than $FeSt_3$ or $FeSt_{3,d}$ conducted more easily/at lower NaOl amount to shaped NPs.

To remind : at ratio NaOl/OA 80/20, $FeSt_3$ (mean formula from Chapter III: $FeSt_{2.1}@15H_2O$) which is more hydrated than $FeSt_2$ (mean formula from Chapter III: $FeSt_{1.5}@6H_2O$) led to faceted NPs when nanoplates are obtained with $FeSt_2$. Dehydrated $FeSt_{2,d}$ (mean formula from Chapter III: $FeSt_{1.5}@2H_2O$) led further to nanoplates when nanocubes and some nanoplates are obtained with $FeSt_{3,d}$ (mean formula from Chapter III: $FeSt_{2.1}@5H_2O$).

By knowing that NaOl is added to adsorb on specific faces of germs to induce a growth along specific faces, we may conclude that water should interact with NaOl and thus inhibited the "shaping" role of NaOl. In fact, we have shown in chapter IV that at the beginning of the thermal decomposition synthesis, inverse vesicles are formed from iron stearates and oleic acid and that the germination occurred from these inverse vesicles. NaOl played also a role and is involved in the vesicular structures formation. However it is also well-known that NaOl formed easily water micelles at low concentration as it has a low critical micellar concentration (CMC) in water[40]. Therefore, we may assume that NaOl, instead of adsorbing at the surface of nucleus to trigger the shape, formed water micelles. Thus, not enough NaOl would be available to absorb on nucleus and the shape directed growth could not occurred. To be more precise, the NaOl trapped in these micellar structures won't be able to participate to the formation of the vesicle at the beginning of the synthesis. As the synthesis reflux took place at high temperature (around 300°C), one may think that this structure will break apart at some point. The NaOl released too late in the reaction media and should participate to an erratic anisotropic growth as seen for 20/80 and 50/50 and hydrated $FeSt_3$. It would explain thus why a high NPs faceting is observed with dehydrated iron stearates when the hydrated ones needed larger amount of NaOl to conduct to faceted/shaped NPs.

All these results are in agreement with the observation that better defined nanocubes are obtained with a lower amount of NaOl for dehydrated $FeSt_3$ than for the hydrated complex. It confirmed unambiguoulsy that the hydration state of precursor is an important parameter to control for obtaining a nanocube morphology. It was again confirmed by the fact that nanocubes were easier to obtain with iron oleate which is under the form of an oily hydrophobic compound. The oily iron oleate is more easily obtained directly with a lower hydratation degree than the iron stearate (which is always obtained under the form of powder). However, it should hydrate with time and it may explain the poor reproducibility of the nanocube synthesis when aged iron oleates were further used.

We have also demonstrated that a high heating rate during the grain growth step is required to obtain a well-defined cubic shape. To explain the effect of the heating rate, the core-shell $FeO@Fe_{3-x}O_4$ structure of the cubes could be indicative of something quite important. Indeed, the formed nucleus is actually composed of FeO as explained in Chapter III. During the growth step, there is a competition between the growth of FeO and its oxidation as the synthesis proceeded in air and that some water are present. The cubic FeO structure should rather favor a cubic growth and therefore an oxidation may affect this cubic growth. Thus if the growth kinetics is larger than the oxidation kinetics, a FeO cubic NP is first grown which oxidized afterwards. On the opposite, if the growth kinetics is smaller than the oxidation kinetics, the NPs will be fully oxidized in spinel phase at the end. That would explain why high heating rates are necessary to form defined nanocubes. We have also shown that high heating rates were required to favour the cubic shape whereas it was not the case for the nanoplate formation. However, plates whose thickness is very small should be easily oxidized when exposed to air despite the growth kinetics. In fact the FeO nucleus would not be the limiting step for nanoplate synthesis.

On the other hand, the control of the monomer formation at the nucleation step was found very important for the nanoplate synthesis. Therefore the nucleation step appeared very important to direct the nanoplate formation. The mechanism of iron oxide plates formation has been ascribed in the literature to a 2D growth due to the presence of a (111) mirror plane in the nuclei.[4,41] Yet no (111) mirror planes was observed in our plates. However another mechanism has been introduced by Park et al[42] with the synthesis of MnO nanoplates. Park suggested that the plate shape originated in the lamellar structure of its surfactant (2,3-dihydroxynaphtalene) that guided the nucleation and growth towards a 2D shape. As we've seen in chapter III that our precursor tended to form lamellar phase and in chapter IV that in the plates conditions the nucleation took place in the walls of the vesicles, the proposed Park's mechanism or very similar one might occur in our case.

Indeed we shown that the germination step occurred inside vesicles but that they disappeared during the growth step due to the germination and also certainly due to the solubilisation of ligands in solvent at high temperature. Therefore, the fact that low electron dose and a low temperature isothermal step (before the germination step) were shown very important to obtain nanoplates supported this mechanism. Such low temperature/energy conditions would favour more the controlled germination of nanoplate nucleus inside the wall of inverse vesicles (i.e. through templating by the vesicule walls) whereas high electron dose or an isothermal step at higher temperature would accelerate the destruction of vesicles and a less controlled germination.

Then once the flat nuclei are formed, the growth took place when the vesicles exploded. The convex shape of the fully formed plates is coherent with the mechanism described above. The nuclei grew into 2D dimensions thanks to the oleate stabilisation but at some point, ther wass not enough oleate to stabilize the surface. The growth was then possible in the perpendicular direction leading to the concave shape. Yet, a proper in situ growth study would be necessary to confirm this mechanism and this behavioris observed solely for $FeSt_2$.

As reported for metals NPs, shaping the nuclei is a way to obtain anisotropic shapes as depicted in Figure VI.10.

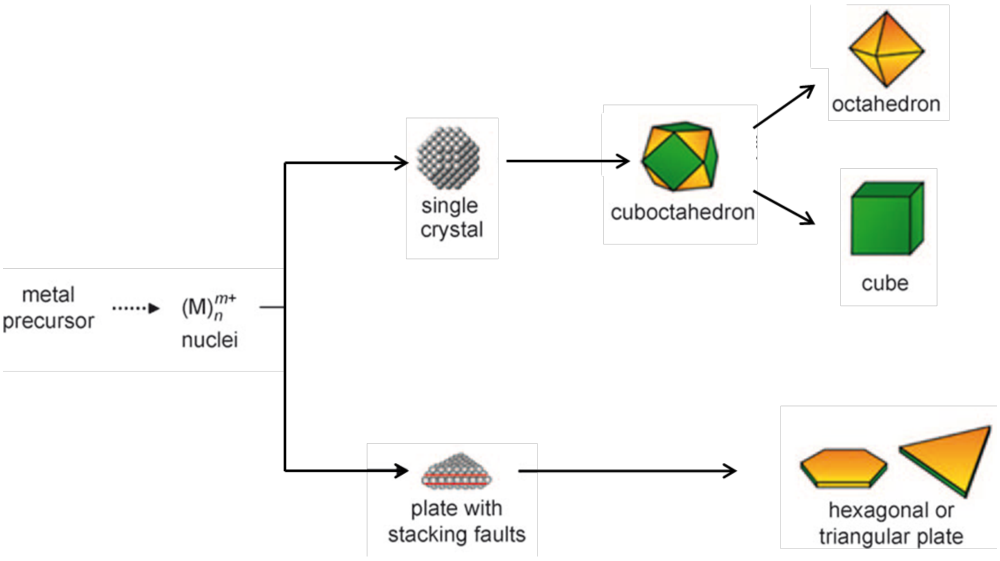

Figure VI-10 – Variation of the shape through the control of the nuclei shape. Modified from[18]

VI.5 Conclusion

This study agrees with the reported effect of NaOl as shape director. Yet we've demonstrated that the role of NaOl can vary depending on the precursor structure and hydration. First water seemed to hinder the effect of NaOl. Thus dehydrated precursors allowed a better control over the shape.

Secondly, the NaOl effect can be tuned to obtain various shapes depending on the structure by mixing it with OA. But the shapes synthesized were bound to the structure of the precursor. The plate shape formation seemed to be bound to the vesicular structures formed by $FeSt_2$ in presence of a certain amount of NaOl. $FeSt_3$ led most preferentially to cubes. We believe that this is due to the various amounts of monomers that each structure can release.

As a conclusion we showed that the nature of the precursor is actually a parameter to consider for the synthesis of anisotropic shapes.

REFERENCES

1. Wetterskog, E. *et al.* Precise control over shape and size of iron oxide nanocrystals suitable for assembly into ordered particle arrays. *Sci Technol Adv Mater* **15,** (2014).
2. Guardia, P. *et al.* Water-Soluble Iron Oxide Nanocubes with High Values of Specific Absorption Rate for Cancer Cell Hyperthermia Treatment. *ACS Nano* **6,** 3080–3091 (2012).
3. Lee, N. *et al.* Water-Dispersible Ferrimagnetic Iron Oxide Nanocubes with Extremely High r_2 Relaxivity for Highly Sensitive in Vivo MRI of Tumors. *Nano Letters* **12,** 3127–3131 (2012).
4. Zhou, Z. *et al.* Anisotropic Shaped Iron Oxide Nanostructures: Controlled Synthesis and Proton Relaxation Shortening Effects. *Chemistry of Materials* **27,** 3505–3515 (2015).
5. Zhao, Z. *et al.* Octapod iron oxide nanoparticles as high-performance T2 contrast agents for magnetic resonance imaging. *Nat Commun* **4,** 2266 (2013).
6. Park, J. *et al.* Ultra-large-scale syntheses of monodisperse nanocrystals. *Nat Mater* **3,** 891–895 (2004).
7. Kovalenko, M. V. *et al.* Fatty Acid Salts as Stabilizers in Size- and Shape-Controlled Nanocrystal Synthesis: The Case of Inverse Spinel Iron Oxide. *J. Am. Chem. Soc.* **129,** 6352–6353 (2007).
8. Sun, S. & Zeng, H. Size-Controlled Synthesis of Magnetite Nanoparticles. *Journal of the American Chemical Society* **124,** 8204–8205 (2002).
9. Hyeon, T., Lee, S. S., Park, J., Chung, Y. & Na, H. B. Synthesis of Highly Crystalline and Monodisperse Maghemite Nanocrystallites without a Size-Selection Process. *Journal of the American Chemical Society* **123,** 12798–12801 (2001).
10. Bronstein, L. M. *et al.* Influence of Iron Oleate Complex Structure on Iron Oxide Nanoparticle Formation. *Chem. Mater.* **19,** 3624–3632 (2007).
11. LaMer, V. K. & Dinegar, R. H. Theory, Production and Mechanism of Formation of Monodispersed Hydrosols. *J. Am. Chem. Soc.* **72,** 4847–4854 (1950).
12. Baaziz, W. *et al.* Magnetic Iron Oxide Nanoparticles: Reproducible Tuning of the Size and Nanosized-Dependent Composition, Defects, and Spin Canting. *J. Phys. Chem. C* **118,** 3795–3810 (2014).
13. Kwon, S. G. & Hyeon, T. Colloidal Chemical Synthesis and Formation Kinetics of Uniformly Sized Nanocrystals of Metals, Oxides, and Chalcogenides. *Accounts of Chemical Research* **41,** 1696–1709 (2008).
14. Kwon, S. G. *et al.* Kinetics of monodisperse iron oxide nanocrystal formation by 'heating-up' process. *J. Am. Chem. Soc.* **129,** 12571–12584 (2007).
15. Kovalenko, M. V. *et al.* Fatty acid salts as stabilizers in size- and shape-controlled nanocrystal synthesis: the case of inverse spinel iron oxide. *J. Am. Chem. Soc.* **129,** 6352–6353 (2007).
16. Wang, Z. L. Transmission Electron Microscopy of Shape-Controlled Nanocrystals and Their Assemblies. *J. Phys. Chem. B* **104,** 1153–1175 (2000).
17. Yang, C., Wu, J. & Hou, Y. Fe3O4 nanostructures: synthesis, growth mechanism, properties and applications. *Chemical Communications* **47,** 5130 (2011).
18. Xia, Y., Xiong, Y., Lim, B. & Skrabalak, S. E. Shape-controlled synthesis of metal nanocrystals: simple chemistry meets complex physics? *Angew. Chem. Int. Ed. Engl.* **48,** 60–103 (2009).
19. Rath, S. S., Sinha, N., Sahoo, H., Das, B. & Mishra, B. K. Molecular modeling studies of oleate adsorption on iron oxides. *Applied Surface Science* doi:10.1016/j.apsusc.2014.01.014
20. Kim, D. *et al.* Synthesis of Uniform Ferrimagnetic Magnetite Nanocubes. *Journal of the American Chemical Society* **131,** 454–455 (2009).
21. Guardia, P. *et al.* One pot synthesis of monodisperse water soluble iron oxide nanocrystals with high values of the specific absorption rate. *Journal of Materials Chemistry B* **2,** 4426 (2014).
22. Kim, D. *et al.* Synthesis of Uniform Ferrimagnetic Magnetite Nanocubes. *Journal of the American Chemical Society* **131,** 454–455 (2009).
23. Shavel, A. & Liz-Marzán, L. M. Shape control of iron oxide nanoparticles. *Phys. Chem. Chem. Phys.* **11,** 3762–3766 (2009).
24. Shavel, A., Rodríguez-González, B., Spasova, M., Farle, M. & Liz-Marzán, L. M. Synthesis and Characterization of Iron/Iron Oxide Core/Shell Nanocubes. *Adv. Funct. Mater.* **17,** 3870–3876 (2007).
25. Wetterskog, E., Tai, C.-W., Grins, J., Bergström, L. & Salazar-Alvarez, G. Anomalous Magnetic Properties of Nanoparticles Arising from Defect Structures: Topotaxial Oxidation of $Fe_{1-x}O|Fe_{3-\delta}O_4$ Core|Shell Nanocubes to Single-Phase Particles. *ACS Nano* **7,** 7132–7144 (2013).
26. Hai, H. T. *et al.* Size control and characterization of wustite (core)/spinel (shell) nanocubes obtained by decomposition of iron oleate complex. *Journal of Colloid and Interface Science* **346,** 37–42 (2010).
27. Kim, D. *et al.* Synthesis of Hollow Iron Nanoframes. *Journal of the American Chemical Society* **129,** 5812–5813 (2007).
28. Yang, H., Ogawa, T., Hasegawa, D. & Takahashi, M. Synthesis and magnetic properties of monodisperse magnetite nanocubes. *Journal of Applied Physics* **103,** 07D526 (2008).
29. Cervadoro, A. *et al.* Synthesis of Multifunctional Magnetic NanoFlakes for Magnetic Resonance Imaging, Hyperthermia, and Targeting. *ACS Applied Materials & Interfaces* **6,** 12939–12946 (2014).
30. Pichon, B. P. *et al.* Microstructural and Magnetic Investigations of Wüstite-Spinel Core-Shell Cubic-Shaped Nanoparticles. *Chem. Mater.* **23,** 2886–2900 (2011).
31. Bronstein, L. M. *et al.* Nanoparticles by Decomposition of Long Chain Iron Carboxylates: From Spheres to Stars and

Cubes. *Langmuir* **27,** 3044–3050 (2011).
32. Buck, M. R., Biacchi, A. J. & Schaak, R. E. Insights into the Thermal Decomposition of Co(II) Oleate for the Shape-Controlled Synthesis of Wurtzite-Type CoO Nanocrystals. *Chemistry of Materials* **26,** 1492–1499 (2014).
33. Xu, Z., Shen, C., Tian, Y., Shi, X. & Gao, H.-J. Organic phase synthesis of monodisperse iron oxide nanocrystals using iron chloride as precursor. *Nanoscale* **2,** 1027–1032 (2010).
34. Yin, Y. & Alivisatos, A. P. Colloidal nanocrystal synthesis and the organic–inorganic interface. *Nature* **437,** 664–670 (2005).
35. Guardia, P. *et al.* One pot synthesis of monodisperse water soluble iron oxide nanocrystals with high values of specific absorption rate. *J. Mater. Chem. B* (2014). doi:10.1039/C4TB00061G
36. Baaziz, W. *et al.* Magnetic Iron Oxide Nanoparticles: Reproducible Tuning of the Size and Nanosized-Dependent Composition, Defects, and Spin Canting. *The Journal of Physical Chemistry C* **118,** 3795–3810 (2014).
37. Pichon, B. P. *et al.* Microstructural and Magnetic Investigations of Wüstite-Spinel Core-Shell Cubic-Shaped Nanoparticles. *Chemistry of Materials* **23,** 2886–2900 (2011).
38. Wetterskog, E., Tai, C.-W., Grins, J., Bergström, L. & Salazar-Alvarez, G. Anomalous Magnetic Properties of Nanoparticles Arising from Defect Structures: Topotaxial Oxidation of $Fe_{1-x}O|Fe_{3-\delta}O_4$ Core|Shell Nanocubes to Single-Phase Particles. *ACS Nano* **7,** 7132–7144 (2013).
39. Zhou, Z. *et al.* Anisotropic Shaped Iron Oxide Nanostructures: Controlled Synthesis and Proton Relaxation Shortening Effects. *Chem. Mater.* **27,** 3505–3515 (2015).
40. Mahieu, N., Canet, D., Cases, J. M. & Boubel, J. C. Micellization of sodium oleate in water-d2 as probed by proton longitudinal magnetic relaxation and self-diffusion measurements. *J. Phys. Chem.* **95,** 1844–1846 (1991).
41. Zhou, Z. *et al.* Interplay between Longitudinal and Transverse Contrasts in Fe3O4 Nanoplates with (111) Exposed Surfaces. *ACS Nano* **8,** 7976–7985 (2014).
42. Park, M. *et al.* Large-Scale Synthesis of Ultrathin Manganese Oxide Nanoplates and Their Applications to T1 MRI Contrast Agents. *Chemistry of Materials* **23,** 3318–3324 (2011).

Chapter VII

Engineering and characterization of smart anisotropic magnetic nano-objects suitable as contrast agent for MRI and as heating agent for magnetic hyperthermia

Note : The structural and magnetic properties study having started before the synthesis of well defined cubes with dehydrated FeSt$_3$, other nanocubes have been studied.

VII Engineering and characterization of smart anisotropic magnetic nano-objects suitable as contrast agent for MRI and as heating agent for magnetic hyperthermia

VII.1 Introduction

Inorganic nanoparticles (NPs) are expected to take the challenge to revolutionize the biomedical field. In the field of the synthesis and functionalization of iron oxide NPs for biomedical applications, most researchers aim at developing multifunctional theranostic NPs. These can both identify disease states and deliver therapy, thus allowing monitoring the effect of the therapy by imaging[1–6]. The current challenge for iron oxide based NPs is thus to improve their design to allow combining in one nano-object both magnetic hyperthermia (MH) and MRI properties with the best efficiency in order to reduce the dose injected to the patient. Iron oxide NPs have already been commercially used as T$_2$ contrast agent for MRI[7]. The use of MH as a stand-alone or an adjacent therapy for cancer is closer to be a reality in every hospital thanks to the positive results achieved by the clinical trials carried out by *Magforce*^{TM}(Germany)[7–10]. Nonetheless, there is currently a need to improve the available nanomaterials for MH. Different parameters may be varied to increase the effective heat loss of a ferrofluid such as size, shape anisotropy or composition, among others. The objective here is to synthesize iron oxide nanoparticles displaying both optimal MRI and MH properties.

For MRI, the higher their magnetisation saturation (Ms) value, the better contrast would be created. Yet this value is not only dependent of the NP structure but also of its aggregation state and the ability of water to diffuse through the organic coating close to the magnetic core[7,11].

In magnetic hyperthermia, the application of an alternative magnetic field of precise amplitude and frequency will make the NP releasing heat that can lead to the death of cancerous biological tissue. This means that magnetic energy is lost as heat. For frequencies and magnetic field amplitudes used in hyperthermia, prior studies compatible with clinical use ($Hf<5 \times 10^9$ Am^{-1}s^{-1}), suggested an optimal diameter of 14 nm for standard spherical NPs but, given the variation in the anisotropy of the different synthesized magnetite (Fe$_3$O$_4$) NPs, the experimental optimal diameter appeared to fall in a broad range between 12 and 20 nm[12–14]. Indeed the magnetic properties of iron oxide NPs strongly depend on the synthesis method,[15–17] and SAR values depend strongly on the measurement parameters (field frequency and amplitude, viscosity, NPs concentration) which strongly vary from one paper to another.

Changes on size are limited as the superparamagnetic behaviour will disappear below a specific size leading to suspensions with a colloidal stability affected by magnetic interactions. To circumcise this problem, other levers are available. The magnetocristalline energy of the NP can be increased by varying the anisotropy energy. This can be done by changing its shape or its composition. Among the highest SAR values reported on NPs with different shapes, one may cite Guardia et al[18] who showed that cubic IONPs with a mean size of 19 nm presented tremendous heating power as well as Lartigue et al[19] who developed nanoflowers consisting of aggregates of nanocrystals sharing common crystallographic planes. Alternatively, doping with Mn or Co[12,13,20] was also found to increase heating power. Recently, Pellegrino *et al.* boosted the heating power of the cubic NPs by doping with cobalt[21].

The previous part demonstrated that the shape control of anisotropic NPs is a fragile equilibrium where the thermal energy (heating rate, growth temperature), precursor nature, hydration and the right combination of ligands play a major but complex role. From the knowledge acquired, different shapes synthesis can now be optimized in order to bring into light the anisotropy effect on the magnetic properties and to evaluate thus their properties as contrast agents for MRI and as heating agents by magnetic hyperthermia.

For biomedical applications, another key point is the design of the organic coating[22] which is also challenging. Indeed, the molecules anchored to the surface of NPs may add different functions, such as dyes for optical imaging, targeting ligands to reach target tissue or cells, or therapeutic agents (drug delivery). There must be also functions preventing NPs from agglomeration in a physiological environment and favoring their biodistribution and bioelimination (preventing opsonisation of NPs and increasing their ability to evade the RES). Besides polymers which have been widely studied up to now, another class of molecule is emerging *i.e* small dendrons[23–26]. Bifunctional dendrons are promising as the diversity of functionalization brought by the arborescent structure simultaneously responded to the need for biocompatibility, low toxicity, large *in vivo* stability and specificity. The grafting of dendrons on the surface of 10 nm iron oxide NPs using phosphonate group as coupling agent has led to a new generation of MRI CAs. These nano-objects display relaxivity values higher than those of commercial CAs combined to a very favorable biodistribution in mice without a significant uptake in healthy tissues and in particular liver (good bioelimination)[17,27–29]. The use of such dendrons appeared as a good way to ensure, after the grafting step, a mean hydrodynamic particle size below 100 nm together with a narrow size distribution in suspension, both being prerequisites for a good biodistribution, *i.e* avoiding reticulo-endothelial system (RES) uptake.

In this work, the synthesis of various shapes of NPs was optimized in order to obtain NPs with added shape anisotropy and they were thereafter structurally characterized. These NPs have been then coated with dendron molecules and their colloidal stability has been established. Their magnetic properties have been investigated in depth to evaluate their suitability as contrast agent for MRI and heating agent by magnetic hyperthermia.

VII.2 Experimental conditions

VII.2.1 NPs synthesis conditions

Synthesis of Iron Stearate Precursor.

Iron stearate (II) and (III) were prepared by precipitation of sodium stearate and ferrous chloride or ferric chloride salts in an aqueous solution. Briefly, sodium stearate (9.8 g, 32 mmol) was transferred into a 2-necked round bottomed flask (RBF) and solubilized in distilled H_2O (dH_2O, 80 ml). The solution was heated to reflux and stirred for 30 min until complete dissolution of the stearate. Separately, $FeCl_2.4H_2O$ (3.16 g, 16 mmol) or $FeCl_3.6H_2O$ (2,88 g, 16 mmol) was dissolved in dH_2O (40 ml) and added onto the sodium stearate solution under vigorous stirring. A light orange precipitate was formed immediately. The solution was kept under stirring at this temperature 15 min. Thereafter, the solution was allowed to cool down to room temperature (RT). The obtained precipitate was washed once by centrifugation (hot dH_2O, 14000 rpm, 10 min). The product was then filtrated with a büchner funnel and oven dried at 65 °C for 24 h.

Commercial stearate

A commercial product from TCI was at first used for some of the synthesis experiments.

Synthesis of spheres

Iron oxide nanospheres (NS) were synthesised by thermal decomposition of an iron stearate precursor (commercial or home-made) in the presence of oleic acid (OA) in an organic solvent. For the synthesis of NPs with a mean size around 20 nm: iron (III) stearate (1.85 g, 2 mmol) was mixed with OA (1.89 g, 6.7 mmol) in squalene (15.8 g, 19.5 ml) and DBE (0.53 g, 0.5 ml) in a two neck RBF. The mixture was heated under stirring to 120 °C and kept at this temperature for 60 min without reflux condenser in order to dissolve the reactants and remove water residues. The condenser was then connected to the flask and the solution heated to 330 °C (5 °C/min) and kept under reflux for 60 min under air. After cooling to RT, a black and viscous suspension was obtained which was solubilized in chloroform (10 ml). The NPs were precipitated by addition of an excess of acetone and washed three times with chloroform and acetone at a ratio of 1:4 at 14000 rpm for 5 min by centrifugation. The NPs were resuspended in THF (50 ml) and stored until further use.

Synthesis of cubes

Iron oxide nanocubes (NC) were synthesised from iron stearate (III). Iron (III) stearate (2.72 g, 3 mmol) was mixed with OA (0.45 g, 1.5 mmol) and NaOl (0.45 g, 1.6 mmol) in eicosene (15 ml) in a two neck-RBF. The mixture was heated to 120 °C under stirring and kept at this temperature for 30 min without reflux condenser in order to dissolve the reactants and remove the water residues. The condenser was then connected to the flask and the solution heated to boiling temperature (≈343 °C, 15 °C/min). The solution was kept at reflux for 90 min under air. After cooling to RT, a black gel was obtained. The NPs were washed as previously described.

Synthesis of plates

Iron oxide nanoplates (NPl) were synthesised from iron stearate (II). Iron (II) stearate (1.44 g, 2.3 mmol) was mixed with OA (0.18 g, 0.65 mmol) and NaOl (0.70 g, 2.30 mmol) in octadecene (15 ml) in a two neck-RBF. The mixture was heated to 120 °C and kept at this temperature for 60 min without reflux condenser in order to dissolve the reactants and remove the water residues. The condenser was then connected to the flask and the solution was heated to 200 °C (5 °C/min) and kept at this temperature for 10 min. The temperature was then increased to 300 °C (1 °C/min) and heated to reflux for 120 min under air. After cooling to RT, a black gel was obtained. The NPs were washed as previously described.

Synthesis of octopods

Iron oxide Nano-octopods (NO) were synthesized from commercial iron stearate (III). Iron (III) stearate (0.735 g, 0.9 mmol) was mixed with OA (1.02 g, 3.6 mmol) in DBE (20 mL) in a two neck-RBF. The mixture heated at 120 °C under stirring and kept at this temperature for 60 min without reflux condenser in order to dissolve the reactants and remove the water residues. The condenser was then connected to the flask and the solution heated to 250 °C (5 °C/min) and kept at this temperature for 60 min. The solution was then brought to 320 °C (10 °C/min) and kept at reflux temperature for 60 min under air. After cooling to RT, a black solution was obtained. The NPs were washed as previously described.

VII.2.2 Dendronization of nanoparticles by a direct grafting process

We have already reported the synthesis of the dendron molecule[30–32]. The scheme of the dendron D2-2P is presented in the Figure VII.6.

The dendronization consists in a direct grafting process, typically a suspension of 1mL of NP@OA in THF (5 mg/mL) was put in contact with 7 mg of dendron molecule in 4 mL of THF. The mixture was magnetically stirred during 24h. The NP@dendron were then precipitated by addition of hexane and centrifugation (8000rpm/min, 3 min). The supernatant was eliminated and the NPs were easily dispersed in 10mL DI water.

The standard protocol was adapted depending on the shape. For all shapes, the concentration of NPs was decreased by increasing the volume of the NPs solution at 20 ml instead of 1 ml. Then the time was adapted. 20 nm spheres were put in contact for 48 h. The three other shapes were grafted with a two-step process. After 48 h for the plates and the octopods and 96 h for the cubes, the solutions were purified by ultrafiltration to remove the free oleic acid. After 3 steps of purification, the NPs were put in contact with 7 mg of dendron for the same time as the first step.

The grafted NPs were then separated from the ungrafted dendron molecules by ultrafiltration. After at least 4 purification steps, the pH of the NPs suspensions was adjusted to 7.4 and the suspensions were ready for characterizations.

VII.2.3 Other characterisation techniques

Detailed insight on the crystallographic structure and morphology of these nano-objects was obtained using a TEM/STEM JEOL 2100F microscope with a probe corrector operating also at 200 KV. The EELS analyses were performed by Michael Chatzidakis and Andreas Korinek in the framework of a collaboration with the CCEM (Canadian Center for Electron Microscopy) led by Prof. Gianluigi Botton, by using in this case a monochromated TITAN 80-300 microscope. To separate the Fe signal in its different contribution due to different valence states, a principal component analysis and then and independent component analysis were used.

^{57}Fe Mössbauer spectra were performed at 300 K using a conventional constant acceleration transmission spectrometer with a ^{57}Co(Rh) source. The spectra were fitted by means of the MOSFIT program[33] and an α-Fe foil was used as calibration sample. The values of isomer shift are quoted to that of α-Fe at 300K.

The dendron grafting rate was determined by elemental analysis which has been performed by ICP-MS (Induced Coupled Plasma Mas Spectrometry).

The efficiency of ligand exchange was accessed by performing High resolution magic–angle spinning NMR (HR–MAS NMR). HRMAS experiments were carried out on a Bruker FT–NMR Avance 500 equipped with an 11.75T superconducting ultrashield magnet. All the experiments were performed at spinning rate of 5kHz with a 50µL zirconium rotor.

Magnetic Measurements- Experimental setting

DC magnetic measurements were carried out on all synthesised magnetic NPs using a Magnetic Property Measurement System Model 3 (MPMS3) from Quantum Design (QD). Before measurement the MPMS3 was calibrated using the *Pd* standard reference sample provided from QD. The calibration was carried out at 298 K following the standard QD procedure for the VSM moment calibration. The VSM calibration factor was adjusted in a way that the difference between calibration measurement and the theoretical value was less than 0.1 %. The MPMS3 measurements were carried out using the QD powder caps and a brass holder. Prior measurements, a blank measurement of the empty brass holder was carried out, but it revealed negligible contribution to the magnetic moment of the sample.

Mass determination: Dry residues of NP suspensions were measured instead of liquid state samples. The iron mass per sample was determined by weighing the NP suspensions before drying and considering the previously known iron concentration. The NP suspensions dried in air at 300 K for about 24 h. The masses were determined with a precision balance from Ohaus (precision 0.01 mg at 0.1 mg, repetition 0.02mg at 0.1 mg) with internal calibration and compensation for air flow and vibrations). The balance is mounted onto an anti-vibration table.

The empty capsule mass was determined 8 to 11 times, the NP suspension mass was determined at least 11 times. On average, the mass of the NP suspension was about 26.29 ± 0.18 mg. Next, the NP volume was calculated using the water density at 25°C. The previously determined Fe concentrations of the suspensions permitted then to calculate the mass of Fe in the dry residue. A direct mass determination of the dry residue was not possible. The measured magnetic moments were then normalised by the mass of Fe in the dry residue.

Magnetic Hysteresis. Four quadrant hysteresis loops were acquired in vibrating measurement mode (VSM) between ± 3 T, using a vibration peak amplitude of 6 mm and an averaging time of 2 s. The field was stabilised at each step before measurement; the field driving rate between steps was set to 10 mT/s. Loops were acquired at various temperatures between 1.8 and 300 K. For some low temperature loops the sample was cooled in a field of +3 T. Each loop consists of about 190 points per branch, which are logarithmically distributed over the ± 3 T range.

ZFC/FC experiments. Next, zero-field cooled (ZFC) and field cooled (FC) experiments were performed. Due to the always present residual field of the superconducting magnet, two procedures were tested prior the experiments to limit this effect. A) The field was set to zero in oscillating mode after centring the sample in a 1 T field and B) repeating step A) and subsequent application of a small field opposite to the residual field of the magnet. No difference was observed and therefore procedure A was applied prior ZFC experiments.

The measurements were carried out under the same conditions as the hysteresis loops, i.e. VSM mode, 6 mm peak amplitude and 2 s averaging time. A rate of 5 K/min was chosen for all cooling and warming curves. The magnetic moment was measured continuously during warming and cooling (scanning mode). Data acquisition started after ZFC and 20 min waiting time at 3 K. ZFC/FC measurements were generally acquired in 3 different fields: 5, 10 and 20 mT. Only the curves of sample NC were acquired in different 18 fields from 0.2 to 500 mT.

Henkel plot measurements. Henkel plot measurements (original method: Henkel, O., Phys. Stat. Solidi 7 (3), pp. 919-929, 1964) require the measurement of magnetic remanence, i.e. a measurement when the applied magnetic field equals zero. Even if the field is set to zero, there are persisting currently in the superconducting magnet producing a small residual field. This field can be reduced by applying a small opposite field. In order to determine this residual field after each magnetisation step, a test procedure was carried out with the paramagnetic Pd reference standard sample in following way for each field step:

(1) Apply field
(2) Measure magnetic moment (3 single measurements)
(3) Set field to zero
(4) Measure magnetic moment (3 single measurements)

The determination of the residual field required the Pd susceptibility, which was obtained by fitting a slope through all steps (2). In this manner residual field was obtained for each step. On average, the residual field of the instrument used amounts to about 1.520 ± 0.167 mT. These measurements were carried out at 5 K.

Next, the above procedure was repeated, but instead of setting the field to zero in step (3) above, opposite residual field values were now set for each step. For checking the efficiency of the procedure, the field offset was recalculated, being now 0.099 ± 0.010 mT on average.

Henkel plot measurements were carried out at 1.8 and 50 K. Albeit the residual field should not depend on the temperature of the sample chamber, the procedure was repeated at both temperatures. On average, they are 1.440 ± 0.184 mT and 1.333 ± 0.175 mT at 1.8 and 50 K, respectively. There is no statistically significant difference between both values at 1.8, 5 and 50 K. The residual fields obtained at 50 K were used for sample measurements.

Magnetic Measurements – data processing

Hysteresis. The measured data was corrected for the residual field of the superconducting magnet. In short, a correction function C(H) was calculated from hysteresis measurements of the Pd standard reference sample. C(H) was then subtracted from the hysteresis measurements of the samples. Also, the high-field slope, caused by dia- or paramagnetic contributions, was determined following the approach of saturation method (Fabian, K., Physics of the Earth and Planetary Interiors 154, 2006). This consists in fitting the high-field data between 1 and 3 T resp. -1 and -3 T with the function $a - b H^p + c H$, with $p = 1$ in the present case. The procedure was applied to all four hysteresis quadrants. Only quadrants with $R^2 > 0.9$ (regarding the fit of the data) were taken to calculate the average high-field susceptibility. Finally, a mean high-field correction was subtracted from the hysteresis data. Saturation magnetisation σ_s saturation remanence σ_{rs} and coercive fields at $\sigma = 0$, were obtained from the interpolated, corrected hysteresis data by root finding.

ZFC/FC experiments. ZFC and FC curves consists of about 1800 data point and were filtered with a simple moving average filter with a length of 21 points. The filtered ZFC and FC curves were interpolated linearly to obtain an analytical expression. The derivative of the difference –[FC(T)-ZFC(T)] was calculated and then then digitised. This resulted in a dataset consisting of about 2600 points, which was filtered also with a simple moving average filter of length 21. For data interpretation, the –[FC(T)-ZFC(T)] vs. T curve was used for interpretation.

VII.3 Results

VII.3.1 Synthesis conditions and structural characterizations of the different forms

The synthesis of spherical, cubic, octopod and plate –shaped NPs was performed by thermal decomposition of an iron stearate precursor by controlling the heating rate, the solvent and the amount and nature of the surfactants.

VII.3.1.1 20 nm spheres synthesis

In order to highlight the effect of shape anisotropy on the magnetic properties, the synthesis of an isotropic NP (i.e. spheres) is interesting for comparison. NPs with a 20 nm mean diameter were targeted as they have been shown to display very good heating properties[14]. It has been shown earlier that the size of nanospheres is mainly controlled by the growth step[34]. The germination occurred around 240°C where a large amount of monomer is formed, as previously reported[35–37] and as also demonstrated in chapter III. The monomer formation was reported[35,37] to be reaction time- and/or temperature-dependent which is due to changes in its stability as a function of the type of solvent and the used ligands. Moreover, as seen in chapter III, a distribution of precursors existed in the “starting” precursor with different decomposition temperature up to 380°C depending on the nature of stearate used (FeII or FeIII) and of its hydration degree. Therefore, the higher the boiling point of the solvent the larger is the NPs size (as the amount of monomer available for the growth step increases with temperature). [34]

Firstly, the reflux/boiling point of the mixture can be increased by increasing the length of the chain of the alkene solvents which were reported to be more “inert”. Increasing the boiling point allowed to increase the NP size[34,36]. Spinel iron oxide NPs with a mean size of 20 nm have been thus previously synthesized in our lab using docosene[34]. However, the alkyl chain of C_{20} means that the solvent is solid at room temperature which complicates the washing of the NPs. In addition, sometimes, the syntheses led to core-shell NPs with a core of wüstite FeO without an obvious explanation[38].

In this work, squalane was chosen as it presents a boiling temperature of 470°C at atmospheric pressure while staying liquid. Nevertheless, a temperature above 400 °C has been previously shown to induce the decomposition of the ligand (Chapter III) and additionally, under these synthesis conditions, an uncontrolled growth with various size and shape NPs was observed experimentally. When the reaction temperature is kept around 340 °C (below the boiling point), spherical NPs with a mean size around 20 nm are obtained. However, we observed again that the synthesis was not reproducible in composition and sometimes led to core-shell NPs with a wüstite core. Based on the publication of Pellegrino et al[18] where they introduced dibenzyl ether (DBE) with squalane and obtained thus fully oxidized NPs, the synthesis has been conducted in presence of a small amount of DBE. The presence of the oxidizing solvent not only led to a reproducible synthesis of 20 nm NPs but also yielded iron oxide with spinel composition. By playing on the growth temperature, NPs with a mean size of 18 nm (NS18) and 22 nm (NS22) have been synthesized (Figure VII.1).

However, DBE has been shown to decompose during the thermal decomposition process and residual products may form. We have tried to understand why depending on the experimental conditions in squalane, the composition was varied. By checking all parameters and especially, by comparing the experimental heating ramp with the theoretical one, we noticed that the "final" temperature was not always exactly at the programmed theoretical temperature. By correlating the final temperature with the composition of NPs, we have shown by XRD analysis by using *in house* $FeSt_3$ precursor that if the temperature is below 335°C, the composition is wüstite FeO but if it is maintained between 335°C and 345°C, only magnetite would be formed. Above 350°C, heterogeneous shaped NPs were formed.

We have shown in Chapter III that Fe^{3+} cations are reduced during the germination step leading to the formation of FeO nucleates. The possible explanations would be that the organic coating may hamper the oxygen diffusion and/or there is a competition as function of temperature (and certainly heating rate) between the grain growth and oxidation kinetics. If the growth is faster than the oxidation, the growth of a FeO phase will be favoured (this could also perhaps explain the observed faceting of these NPs). Nevertheless, the boiling point of stearic acid ou oleic acid is around 360°C and therefore the thermal energy may induce a "destabilization" in the ligand shell at the NPs surface and thus increase the oxidation kinetics. From these considerations, one may suppose that the oxidation kinetics is favoured at higher temperature. We suspect that if the temperature is close to the boiling point of the ligands, the organic shell will be less compact and favour the diffusion of oxygen towards the NPs. This would also explain why the size and shape control was not possible above 345 °C. The closer the temperature gets to the boiling point of the ligand, the more they will be disturbed by thermal agitation. Thus they won't be able to play their role in the control of the growth.

Concerning the effect of DBE on the composition, DBE may help the destabilisation of the ligand shell. This theory is supported by works conducted in the laboratory of C. Petit at University Pierre et Marie Curie in Paris on cobalt NPs[39]. They've showed that cobalt NPs could be protected from oxidation if they present a dense coverage of dodecanoic acid on their surface. However this coating prevented NPs from growth and they have shown recently that if there is an affinity between ligands and the used solvent, a grain growth may occur due to interaction between both ligands and solvent enabling the monomer diffusion[40,41]. Non-polar solvent (alkenes, alcanes …) should less interact with the hydrophobic ligands contrary to DBE. DBE would disfavour the formation of a dense ligand shell on the surface or destabilize this shell. Of course the reaction media should also help to provide oxygen and to be not too reducing.

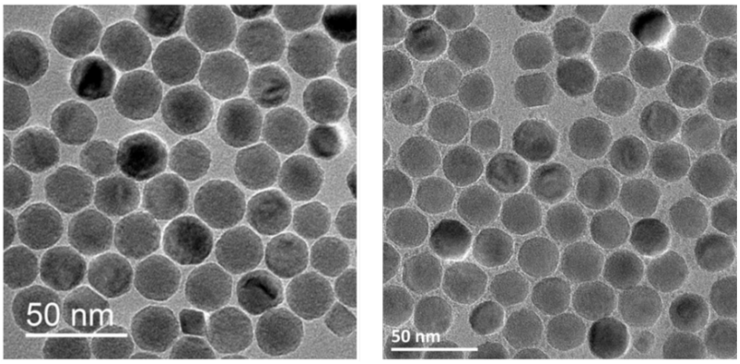

Figure VII.1 - TEM images of NS18 a) and NS22 b) NPs.

The XRD pattern of the NS22 in Figure VII.2.a is characteristic of both NS18 and NS22 samples and presented the X-ray peaks of a spinel structure. Rietveld refinements led to a lattice parameter of 8.391 ± 1 Å suggesting a composition close to that of the stoichiometric magnetite Fe_3O_4 phase (0.8396 nm, JCPDS file 19-629). A crystallite size of 13 ± 1 nm was also determined from XRD refinement which is lower than the 22 nm measured with TEM. This result would confirm that such spinel nanospheres resulted from the oxidation of FeO. Indeed, from our previous studies on core-shell $FeO@Fe_{3-x}0_4$ nanocubes[38,42] and the work of Bergstrom et al[43], the post-oxidation of FeO induced the formation of lattice dislocations and/or antiphase boundaries in NPs. That would explain the smaller structural coherence length compared to the TEM size.

The consideration of the Fe-O bands in the IR spectra showed a main broad band centered at 610 cm^{-1} with a shoulder at higher wavenumbers (Figure VII.2.b and d) which indicate that the magnetite phase is in fact slightly oxidized[34,44]. The defects induced by the oxidation are certainly responsible of the lattice parameter value very close to that of stoichiometric magnetite. That demonstrated again that a combination of different characterization techniques is necessary to really determine the composition of the spinel phases.

In earlier characterization studies on spinel iron oxide NPs with a mean size of 20 nm, the same XRD and IR results were obtained and a composition closed to $Fe_{2.85}O_4$ was deduced from Mössbauer spectra[34]. Mössbauer spectroscopy is currently the most adapted method to ascertain the composition of the spinel phase.

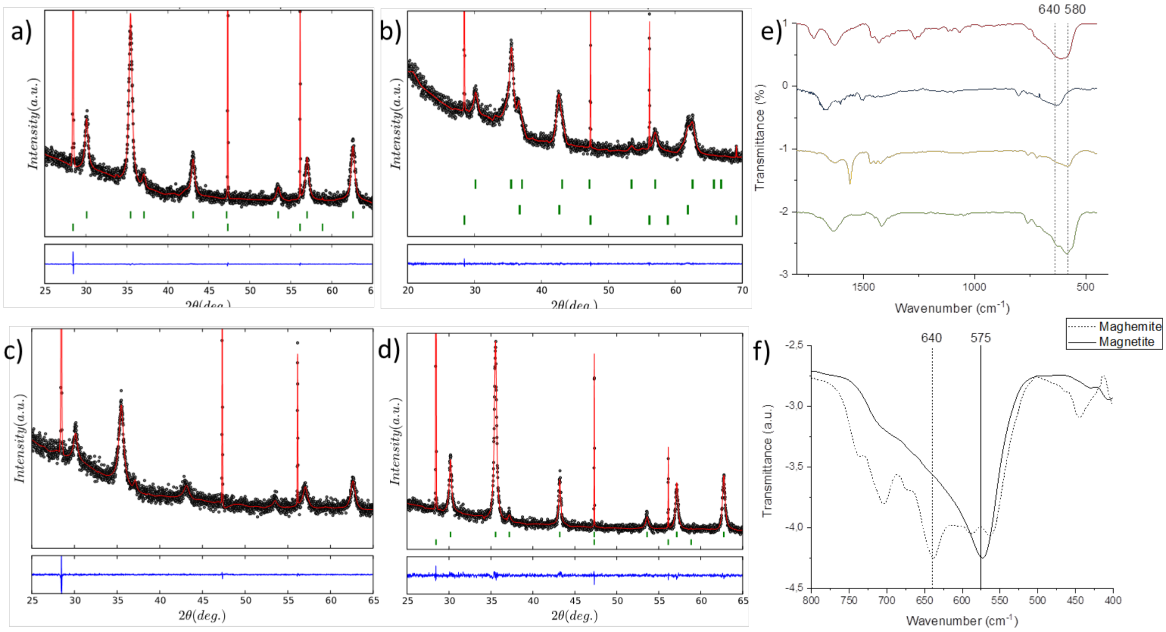

Figure VII.2 - XRD refinement of NS22 a), NC15 b), NPl c), NO28 d), IR spectra of NS22 (red), NC (blue), NPl (yellow) and NO28 (green) e) and typical IR spectra of slightly oxidized magnetite and maghemite f).

VII.3.1.2 Optimisation of the cubic shape NPs

It has been shown that the cubic morphology boosted the magnetic properties of IONP[18,43,45,46]. As shown in Chapter III, in order to obtain well-defined cubes, the iron stearate precursor has to be dehydrated to be sure to have sufficient oleate molecules available for the oriented growth. The synthesis conditions would favour the formation of FeO nucleates (Chapters III & IV). Oleate chains introduced as NaOl in the reaction mixture of nanocubes would contribute to prevent nuclei from oxidation. Furthermore, a low growth kinetic due to a low monomer formation kinetic should favour the oxidation of NPs when the high growth rate would hamper their oxidation. The heating rate is faster with nanocubes than with nanospheres. Therefore the growth kinetic during nanocubes synthesis has to be faster than that of the oxidation which should hinder the oxidation of NPs. The nucleation step has thus been suppressed and a high heating ramp of 15 °C/min was chosen to ensure the growth step to happen in the kinetic regime, i.e. fast enough to favour the cubic morphology which is not favoured in the thermodynamic controlled conditions.

As the nanocubes formerly obtained in chapter VI had a mean size of 15.3 nm and presented often rounded corners, the ratio Precursor/Ligands was increased from 0.75 to 1 just by adjusting the amount of FeSt$_3$. The hypothesis being that the round corners originated from a lack of the surfactants (oleate) involved in the cubic growth control. Introducing more NaOl would provide more ligands to control the growth of flat faces. To reach the 20 nm size target, the nature of solvent (i.e. the reflux temperature) and the reflux time were varied. Eicosene was used as solvent instead of octadecene to increase the boiling temperature to 340 °C and the reflux time was increased to 90 min instead of 60 min, which yielded thus optimal conditions. TEM images in Figure VII.3 showed the "shape" improvement by comparing the shape of nanocubes obtained by the first protocol (a) and those obtained with the optimized protocol with hydrated (b) and dehydrated FeSt$_3$ (c). The modifications of the synthesis protocol allowed improving the definition of the nanocube shape with both hydrated and dehydrated precursors.

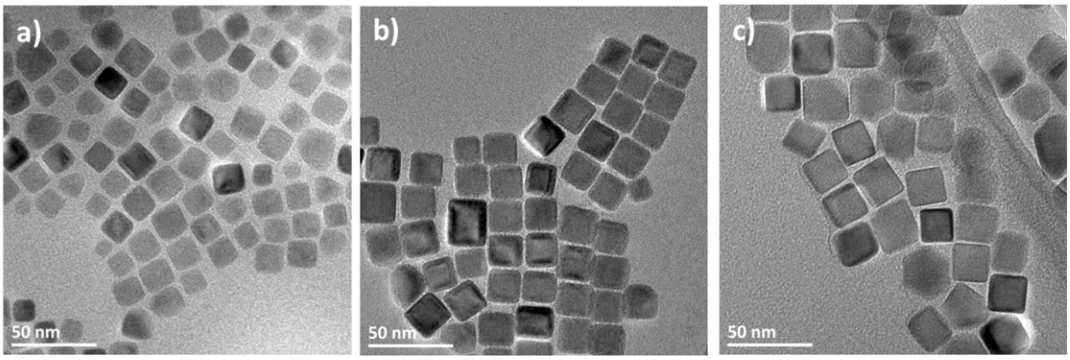

Figure VII.3 - TEM images of nanocubes obtained with the previous protocol (chapter VI)and $FeSt_{3,d}$ *a) and with the optimized conditions and* $FeSt_3$ *b) and with the optimized conditions and* $FeSt_{3,d}$

The mean size of the nanocubes increased from 15.3 ± 1.8 nm (previous protocol) to 21.4 ± 3.3 nm when using the optimized conditions and the dehydrated $FeSt_3$; but was virtually unaffected by the use of the hydrated $FeSt_3$, with a mean size of 14.5 ± 1.6 nm (NC15), as seen by TEM. This result would be in agreement with the hypothesis that we developed in chapter VI: water was suspected to hinder the role of NaOl due to the formation of micelles. However, with the new protocol, a higher heating ramp is applied meaning that those micelles are likely to be destabilized before the nucleation step; consequently, NaOl is released in time to direct the growth towards cubes. A size variation is observed between the hydrated and dehydrated precursor as seen in chapter VI in agreement with the report of size decrease of the NPs in presence of water[34,47].

The XRD pattern of NC15 (Figure VII.2.b) indicated that nanocubes are made of a core of wüstite FeO with a shell of spinel, as previously observed[38,42]. Considering the previous observations with nanospheres, such composition may be related to the competition between the growth rate and the oxidation kinetic of the FeO nuclei within this temperature range. Lattice parameters calculated for NC15 from Rietveld refinement gave a parameter of 8.392 ± 1 Å for the shell close to that of stoichiometric magnetite (0.8396 nm, JCPDS file 19-629) and of 4.237 ± 1 Å for the wüstite core. From an earlier study on nanocubes synthesized using iron oleate as precursor[42] (which was confirmed by the study on the decomposition of iron stearates (chapters III&VI)), we know that, under the used experimental conditions, FeO is formed at first and is then oxidized with time. The shell displayed generally a lattice parameter close or slightly larger to that of stoichiometric magnetite which is ascribed to an epitaxial matching between both phases and the lattice parameter of the wüstite phase strongly depended on its oxidation state. According to the formula Fe_xO, the iron content x can be easily calculated from the cell parameter using the relationship $a_{FexO} = 0.3856 + 0.0478x$[48]. The result gives x value of 0.8 which suggested that the wüstite core has been formed in strong reducing conditions and even that the current synthesis conditions are stronger than that observed in our previous study (max 0.83)[42]. The wüstite phase was shown to be metastable and to transform into wüstite with higher iron content and spinel phases through an oxidation mechanism with ageing time in former nanocubes[42]. The oxidation mechanism and the epitaxial growth resulted in the diffusion of cations and vacancies that generated high strains at the AFM/FIM interface and in the FIM shell.

IR spectra (Figure VII.4.b) showed that the washing of nanocubes was not perfect as some traces of iron stearates are always observed but the Fe-O bands are characteristic of a slightly oxidized magnetite (presence of FeII and FeIII cations). The broad band maximum is between those of the stoichiometric magnetite and maghemite phases[34].

We have tested different synthesis conditions in order to obtain nanocubes with a homogeneous composition in the spinel phase (i.e. without a wüstite core): bubbling of air, other solvents than alkene;

among others. Unfortunately, a loss of the cubic shape was generally observed. Indeed, the synthesis conditions of the cubic shaped NPs are constrained and reducing and these strict conditions affected the oxidation kinetic. It has been often reported[42,49] that the combination of NaOl and OA led to core shell cubes suggesting a strong influence of the amount of oleate chains. The environment generated by the carboxylate and/or alkenes at high temperature is certainly reducing. The nucleates have a composition close to $Fe_{1-x}O$ and the growth rate of nucleates is superior to the oxidation rate. The nice cubic shape could be attributed to this growth under the FeO structure. Our hypothesis is that well resolved nanocubes are obtained in our used experimental conditions only if the nucleation and growth steps occurred on NPs with a FeO composition. Then, FeO is oxidized when exposed to air leading to core-shell NPs with a magnetite shell. That would be in agreement with our previous observations during the synthesis of nanocubes using the iron oleate precursor[42].

Nevertheless, other published methods have reported nanocubes with a spinel composition. To obtain nanocubes with a homogeneous spinel composition, we decided to test some published methods reported to lead to homogeneous nanocubes[18,43,47,48]. The objective was to compare their properties with those of other morphologies which have all a spinel composition. Among the tested method, the Pellegrino's method using a mixture of squalene and dibenzylether (DBE) as a solvent has led to interesting results. Pellegrino et al reported that the products of decomposition of the DBE were responsible for the control of the shape of the material to a full spinel phase[45]. The adapted Pellegrino protocol (see experimental part for details) using a commercial iron (III) stearate and only DBE led to a cubic shape with elongated corners named octopods (Figure VII.5). These experiments have been then reproduced with *in-house* synthesized iron (III) stearates and the same results were obtained.

Such variation in experimental conditions to obtain nanocubes conducted often to heterogeneous shapes and size without succeeding in obtaining well-defined nanocubes but we considered that this octopod shape would be interesting to investigate. Moreover, the fact that the octopods were oxidized was indications that the reaction media is oxidizing and/or the affinity of the ligands towards DBE should be higher than with the alkene. DBE wouldn't favour the formation of a dense ligand shell on the surface of the NPs letting oxygen diffuse towards the NP leading to oxidized NPs.

Such a shape would originate from a difference in the kinetics of the reaction. It has been explained that when the cubic NP is formed, if the amount of monomers that precipitated on the surface is large, it will preferentially remain on the corner that presented the higher surface energy instead of diffusing on the whole surface of the NPs. As the heating rate up to the growth step is rather fast (10°C/min), this could be what is at work here. In Pellegrino's protocol, the ratio DBE:Squalene was demonstrated to drive size control. The more DBE was introduced, the smaller the NPs.

In our system, the size has been tuned by adapting the ratio FeSt:OA and mean sizes of 17.2 ± 2.2 nm (NO18) for a ratio of 1:3 and of 27.8 ± 4.2 nm (NO28) for a ratio of 1:4.5 were thus synthesized. These objects are quite interesting as the presence of the elongated corner should increase the shape anisotropy of NPs. They presented a homogeneous spinel composition. The XRD refinement (figure VII.6.d) gave a lattice parameter of 8.364 Å for NO18 and 8.370 Å for NO28. These lattice parameters values in-between those of magnetite and maghemite (0.8346 nm, JCPDS file 39-1346) indicated an oxidation of both NO. The indexation of the broad Fe-O band (Figure VII.2.e) at 580 cm^{-1} (magnetite) along with the band at 630 cm^{-1} (maghemite) is in agreement with an oxidized magnetite composition.

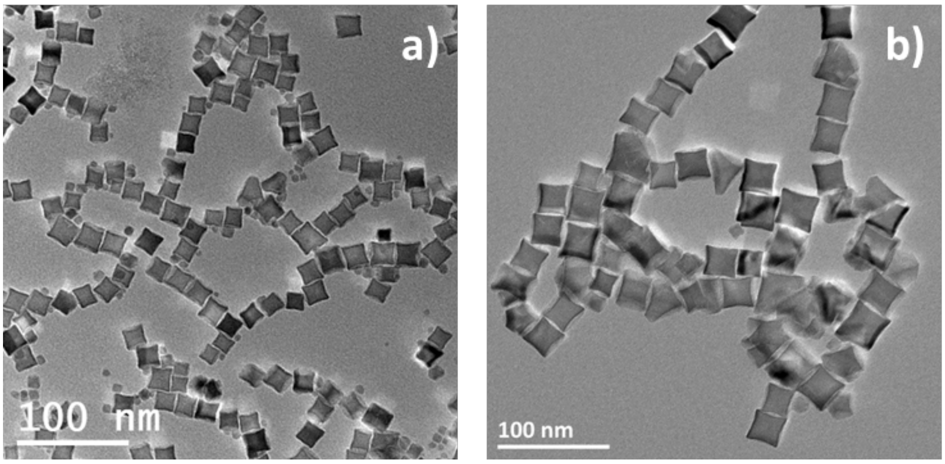

Figure VII.4 - TEM images of NO18 a) and NO28 b)

Due to the anisotropic shape, the crystallite size has been determined from Rietveld refinement as a function of the (hkl) planes (Table VII.1). The crystallites size depended on the size with the largest directions being (400) and (511) for NO28 and (220) and (440) for NO18. The longest directions for NO18 are thus the one belonging to the (110) family implying that the diagonal of the face is longer than the diagonal of the assimilated cube. For NO28, the longest direction is the (400) one followed by the (511) one which indicates a different exposition of crystallographic planes in the corner.

Table VII.1 – TEM size and lattice parameter and crystallites size determined from XRD refinement

Sample	TEM (nm)	Lattice parameter (Å)	Crystallite size (nm)										
			220	311	222	400	331	422	511	333	440	531	442
NO18	17.2 ± 2.2	8.364	15	13	11	11	11	12	13	11	15	12	11
NO28	27.8 ± 4.2	8.370	19	20	13	25	18	17	23	12	19	21	16

VII.3.1.3 Nanoplates

The nanoplates synthesized during the shape control study in chapter VI presented a low thickness (<10 nm). Despite their high anisotropy ratio (defined as the ratio length/thickness) around 3 and considering that the surface over volume ratio is high, a larger surface contribution is expected for this shape. To try to increase the thickness, the growth time has been doubled from 60 to 120 min. Figure VII.7 showed the TEM images at 60 a) and 120 min b).

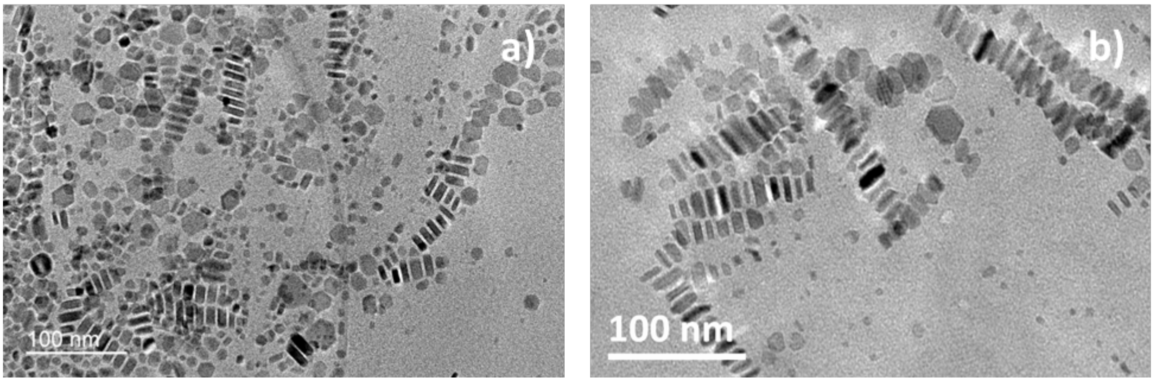

Figure VII.5 - Plates with 60 min growth step a) and 120 min b)

Unfortunately, the size increase did not follow the expected tendency. The length increased from 16.7 ± 5.2 nm to 20.3 ± 5.5 nm but the thickness decreased from 8.6 ± 1.7 nm to 6.6 ± 1.5 nm. This would agree with the hypothesis that the thickness of the plate is addressed by the size of the nucleus. Once the growth started, it can only occur in the 2D plane as it is triggered by the high amount of oleate ligands. The decrease of the thickness with time can be seen as a maturation process such as Ostwald ripening. There can be some re-dissolution of iron atoms into solution that will contribute to the anisotropic growth.

The XRD pattern (Figure VII.2.c) presented the peaks characteristic of a spinel phase with a lattice parameter of 8.384 ± 1 Å, determined through Rietveld refinement. The nanoplates are thus slightly oxidized in agreement with the IR spectrum (Figure VII.2.e) where a broad band with a maximum at 580 cm^{-1} (close to the magnetite one) is observed. The crystallite size according to specific crystallographic directions was also determined by Rietveld refinement (Table VII.2). The crystallite size of 17 nm in the direction <111> is in agreement with its 2D growth formation mechanism and TEM study. As most of the plates tended to lay flat during the XRD acquisition. It is hard to clearly see the planes within the thickness. Yet the value of 8 nm close to the one measured for the thickness would imply that the planes (400), (511) enclose the sides of the plates.

Table VII.2 - TEM size, lattice parameter and crystallite size determined from XRD refinement

Sample	TEM (nm)	Lattice parameter (Å)	Crystallite size (nm)										
			220	311	222	400	331	422	511	333	440	531	442
NPl17	16.7 ± 5.2	8.384	11	9	17	8	11	10	8	17	11	9	12

VII.3.1.4 Summary of the characterization of the different shaped NPs

All the shapes synthesized presented a spinel structure more or less close to magnetite except for the nanocubes (core-shell FeO@$Fe_{3-x}O_4$). The obtained crystallite size was lower than the size determined from the TEM images for nanospheres due to a spinel composition resulting from an oxidation of the FeO phase, which would be the composition of the first nucleates. For octopodes (NO) and nanoplates (NPl), the crystallite size is strongly dependant on the crystallographic directions. For NPl, a crystallite size of 17 nm has been found along the <222> direction confirming that this morphology is composed of a single crystallographic domain. For NO, the direction presenting the biggest crystallite size is dependent on the size with a crystallite size of 15 nm along <220> and <440> for NO18 and a crystallite size of 25 nm along <400> and 23 nm <511> for NO28. The fact that the crystallite size relied on the crystallographic direction is in favour of a proper anisotropy of the NP. This point should be confirmed through the magnetic characterization.

VII.3.2 Functionalisation of NPs by dendron molecules

The dendronization has been performed on spherical NPs (named NS22) with mean size of 22.2 nm (± 8%), nanocubes (named NC) of 19.9 nm (± 8%), octopod shaped NPs (named NO28) with a mean size of 27.8 nm (± 15%) and finally plate shaped NPs (named NPl) with a length of 20 nm (± 35%) and a 5,7 nm (± 28%) thickness. Main structural parameters are listed in Table VII.3.*

Table VII.3 – Main structural parameters of the different shaped NPs deduced from characterization techniques

NPs	Mean TEM size (nm)	Crystallites size (nm)	Lattice parameter (Å)		Composition
			Spinel phase	Wüstite phase	
NS22	22.2 ± 1.8	13	8.391	X	$Fe_{3-x}O_4$
NC	15.9 ± 1.8	8	8.392	4.237	$Fe_{3-x}O_4$@FeO
NO28	27.8 ± 4.2	25 <400> /23 <511>	8.370	X	$Fe_{3-x}O_4$
NPl	16.7 ± 5.2	17 <222>	8.384	X	$Fe_{3-x}O_4$

VII.3.2.1 Dendronization by direct ligand exchange

At the end of the thermal decomposition synthesis, the NPs are coated with the hydrophobic ligands used during the synthesis (oleic acid, oleate). They ensured their colloidal stability in organic solvent. But to be used in aqueous and physiological media, the organic ligand needed to be replaced with a biocompatible molecule. A branched and hydrophilic oligoethyleneglycol derivatized molecule (called Dendron) is used to replace the ligand through a direct grafting process[17]. The dendron molecule presented two phosphonic acid groups at its focal point to provide a strong anchorage on the surface of the NPs and three biocompatible tetraethyleneglycol chains amongst which one bears a terminal carboxylic acid function. Previous reports[52–54] demonstrated the advantages of using this molecule on 10 nm NPs, providing them very good colloidal stability in physiological media, bio-distribution and bio-elimination and *in vitro* and *in vivo* MRI properties by comparison with commercial products. The molecule is named D2-2P (Figure VII.6).

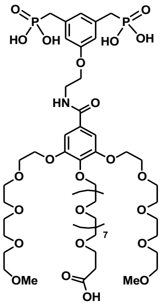

Figure VII.6 - Scheme of the D2-2P dendron molecule

The dendronization of spherical NPs is quite easy and allows the replacement of nearly all oleic acid molecules on the surface of 10 nm NPs thanks to the biphosphonic tweezer[52]. However, the dendronisation of anisotropic shaped NPs is more difficult as previously reported during dendronization of nanocubes[38]. Longer dendronization times are necessary by comparison with standard 10 nm NPs and often a two-step dendronization process is performed. We have previously seen that a difference in the shape of the NPs is also translated into a difference in the crystallographic planes exposed on the surface. Each facet presents a different structure and thus different exposed/surface iron cations[56]. As a result, some plane families may be easier to functionalize as they present a surface compatible with the geometry of the anchoring tweezer and/or a higher surface density in iron cations. Also, the anisotropic growth is induced by the presence of a large amount of chelating ligands. Those ligands tend to remain strongly attached to the surface of the NP at the end of the purification steps. The packing of stearate/oleate chains on the flat/planar surfaces of anisotropic NPs would be stronger. This led to longer washing steps and despite lots of purification repetition, lots of ligands can remain on the surface. The dendronization required thus longer time of ligand exchange and sometimes two dendronization steps to displace the oleic acid/dendron equilibrium. This is in agreement with the washing process which is longer for plates and cubes compared to spheres and octopods. As the ligand is strongly attached to the surface, the time of exchange with the dendron molecule is increased from 48h for the spheres, plates and octopods to 96h for cubes. Also, the cubes are the hardest shape to stabilize and required 15 mg of dendron whereas 10 mg were sufficient for the other shapes. Cubes were found to be the morphology the most difficult to graft and we will see that it would affect their colloidal stability.

The ligand exchange is first assessed by FTIR spectroscopy[53,54,57]. The IR spectra of the NP after grafting (NP@D2-2P) are compared to the one after synthesis (NP@OA) and the one of the D2-2P molecules (figure VII.7). The IR spectrum of the D2-2P molecule presented various P-O bands with a P=O band appearing at 1200 cm^{-1} and P-OH bands at 1027 and 995 cm^{-1} [17,28,29,56]. An intense C-O-C band is detected at 1110 cm^{-1} and the C=O band appears at 1700 cm^{-1}. After the grafting step, the carboxylate bands observed on the NP@OA at around 1500 and 1400 cm^{-1} are replaced with the C=O band of the D2-2P at 1700 cm^{-1} and N-CO at 1640 cm^{-1}. The alkyl chain bands at 2900 and 2800 cm^{-1} have almost completely disappeared. The C-O-C and the P=O bands are not observed such as P-OH bands due to the formation of the P-O-Fe (992 cm^{-1}) bonds[28]. The disappearance of the three bands indicated a strong coordination of the dendron at the NPs surface. The weak band at 716 cm^{-1} from the precursor still observed before dendronisation is not seen after.

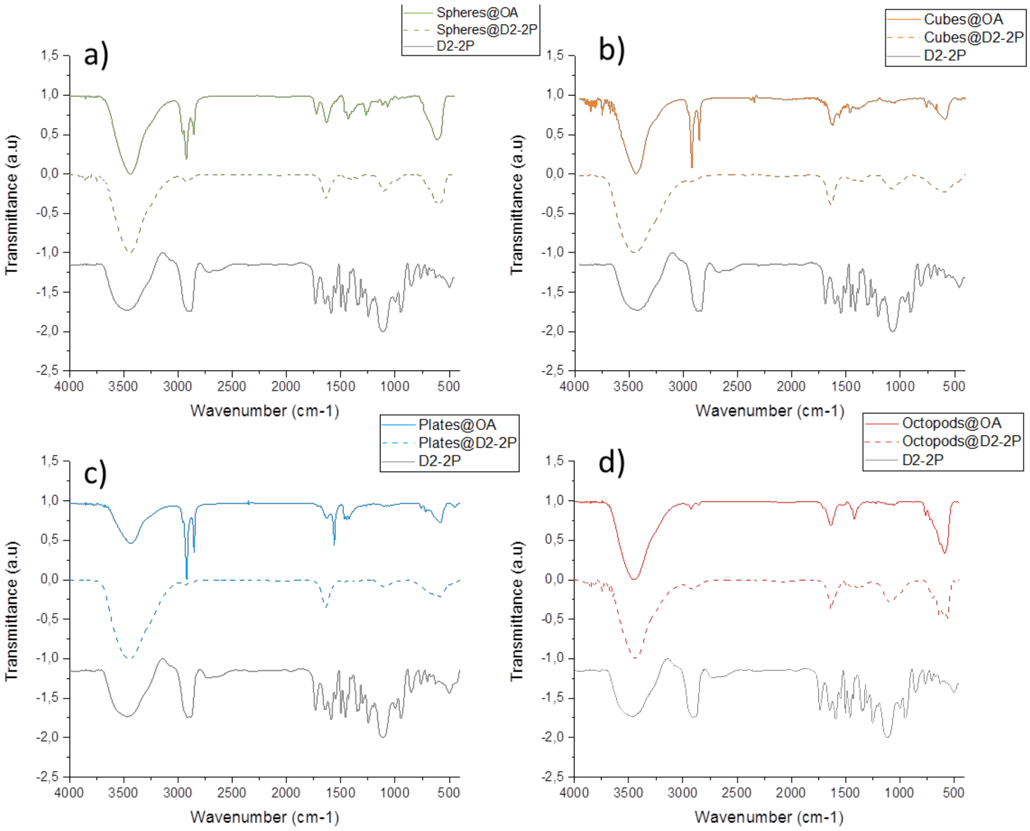

Figure VII.7 - FTIR spectra of the NPs before (NP@OA, plain) and after (NP@D2-2P, dashed) grafting and of the dendron (gray) for NS a), NC b), NPl c) and NO d)

FTIR is a good method to evidence to replacement of the carboxylic acid ligand by dendron but it is only qualitative and not quantitative. To complete this measurement, quantitative measurements were performed with HR-MAS. This method is used in solid state NMR spectroscopy and consisted in performing NMR measurement by spinning the sample at the magic angle (about 54,74°) with respect to the magnetic field. This allowed narrowing the signal usually broadened by the presence of iron. The

NMR spectra then evidenced the molecules grafted on the surface of the NPs. The four dendronized shapes were measured and the associated spectra are given in Figure VII.8-9.

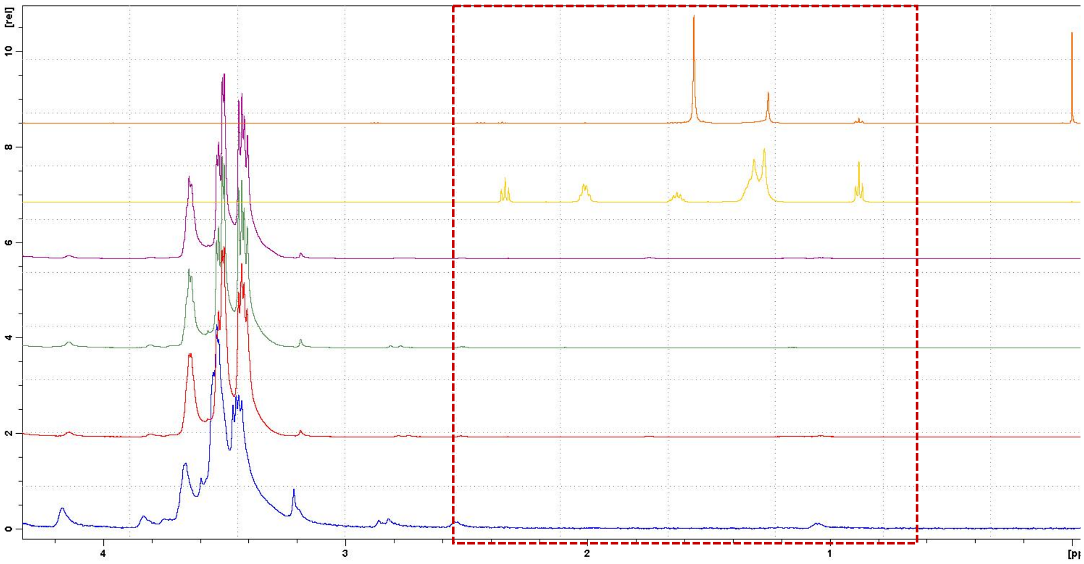

Figure VII.8 - 1H HR-MAS spectra of NS22 (red), NC (green), Plates (purple), compared to 1H NMR spectra of the dendron molecule in D2O (blue), NaSt in CDCl3 (yellow) and OA in CDCl3 (orange)

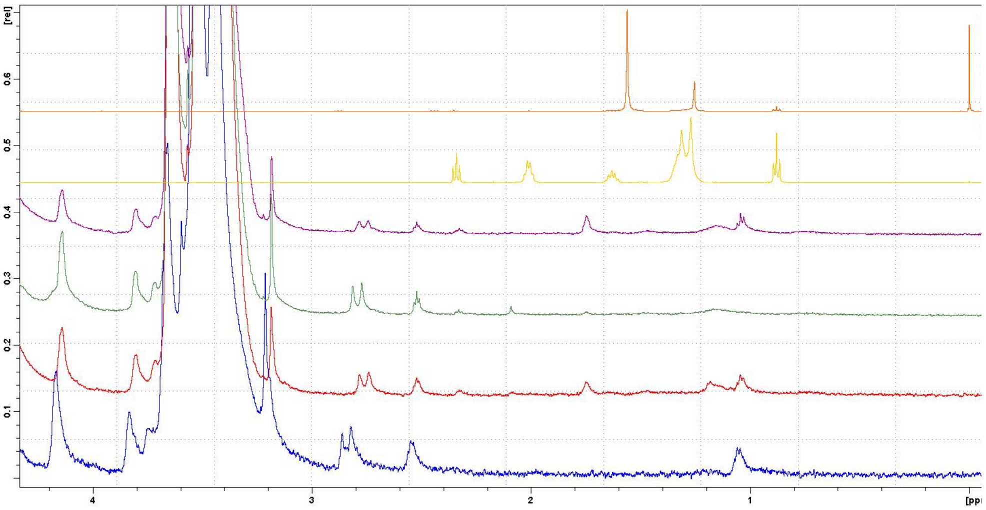

Figure VII.9 - Enlargement of figure VII.11

The spectra confirmed the presence of the dendron molecule on the surface of all shapes. Very weak peaks not ascribed to the dendron molecule are observed in the range 0.9 -2.5 ppm. These peaks could be attributed to free stearate that presents its typical peaks in the same region. The peaks are shifted on the NPs but this is explained by the solvent nature,[58] as stearate chains are probably not fully extended in D_2O which is much more polar than $CDCl_3$. The weak intensity of the stearate signal indicated that only traces would be present on the surface of the NPs.

VII.3.2.2 Colloidal stability

After the grafting step, the colloidal stability in water has been evaluated by Dynamic Light Scattering (DLS) (Figure VII.10). Dendronized NS presented no sign of aggregation with a monomodal hydrodynamic size distribution centred at about 28 nm, larger than the TEM size of NPs of about 22 nm which may be attributed to the dendron coating and solvatation layer.

For the other shaped NPs, this measurement is an indication of a possible aggregation but can not be considered as a precise measurement of the hydrodynamic diameter. The optical model used to calculate the size distribution considered spherical NPs. Anisotropic NC, NO and NPl may be present in front of the laser under different orientations that can be longer than the edge length or the diameter. Therefore, the values of hydrodynamic diameter are just given for comparison and can not be considered as relevant. All the mean hydrodynamic sizes (in volume %) are listed in table VII.5. Dendronized NO presented a monomodal distribution in water centred at 32 nm. With dendronized NPl, a bimodal size distribution is noticed but may be ascribed to the anisotropic shape of NPl which exhibit a L/t of 4. Dendronized nanocubes displayed in water a multimodal size distribution with a main DLS peak around 38 nm exhibiting a small shoulder at 150 nm and another peak at 5000 nm. The dendronization of nanocubes has already been evidenced as a delicate step and it explained the observed aggregation. For *in vivo* experiments, all the suspensions were filtrated to remove large aggregates.

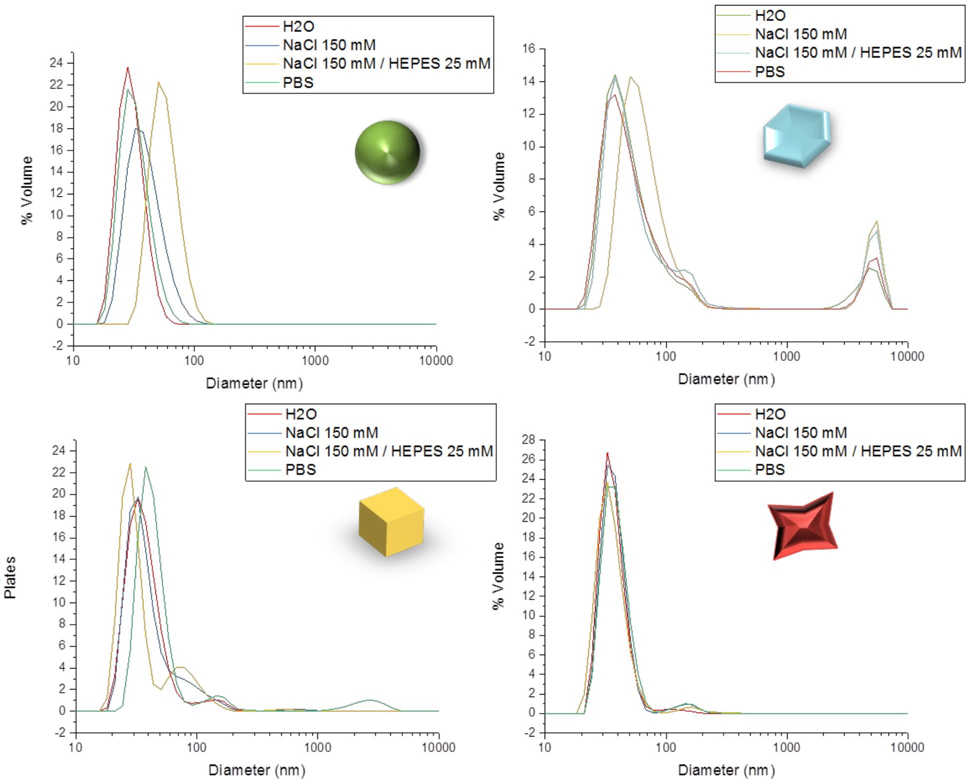

Figure VII.10 - DLS measurements of the different shapes in water

Table VII.3 - Main hydrodynamic diameters of the NPs in water

Shape	NS	NC	NO	NPl
Mean hydrodynamic diameter (nm)	28	38 / 5500	32 / X	32 / 150

VII.3.3 Complementary structural characterizations

VII.3.3.1 Mössbauer spectroscopy

^{57}Fe Mössbauer spectrometry is very useful for determining the oxidation state of Fe species. Mössbauer spectromscopy has been performed by Dr JM Greneche from Le Mans University. Mössbauer spectra have been performed on all dendronized NPs (except nanocubes consisting in core-shell FeO@Fe3O4) but some experiments have been also performed on oleic acid coated NPs for comparison. Mössbauer spectra under an applied field have allowed to better evaluate the oxidation state of iron and the presence of spin canting. It is important to emphasize that the following Mössbauer spectra were recorded on samples containing very small quantities (2-5 mg) of powders after focusing with a lead mask to get an efficient surface containing about 5mg Fe/cm^2.

The Mössbauer spectra of all dendronized NPs at 300 K and 77 K look *a priori* quite similar as all of them exhibit magnetic sextets in addition to a small quadrupolar feature at the center. At 300 K, the lines exhibit some asymmetrical broadening resulting from intrinsic electronic properties. Indeed, both the large size of NPS and the presence of dendrons prevent *a priori* the observation of superparamagnetic relaxation phenomena at 300K (and at 77K) by means of Mössbauer spectrometry. Thus, the magnetic component has to be described by means of several magnetic sextets with different isomer shift values. They are ranged from 0.3 up to 0.45 mm/s, attributed to Fe ions with different oxidation states between Fe^{3+} and about Fe$^{2.7+}$. In addition, the central part is better described by adding a quadrupolar component assigned to Fe^{3+} species. At this stage, this small component could be attributed to the presence of Fe species connected to dendrons, originating some local Fe environments close to those of iron phosphate compounds. At 77K, the spectra are composed of lines which are narrower than those observed at 300K. The fitting procedure consists in using two components in the case of nanoplates and several magnetic sextets to better describe the internal wings of the lines in the case of octopods and spherical NPs, in addition to a quadrupolar component. The mean values of hyperfine parameters are listed in Table VII.4 for the present types of NPs after dendronization.

Table VII.4 - Mean values of hyperfine parameters refined from Mössbauer spectra recorded on NPs with different samples (IS : isomer shift, B_{HF}: Hyperfine field, stoechiometry "3-x" in $Fe_{3-x}O_4$, <e> thickness of the maghemite shell)

	<IS> mm/s ± 0.01	<B$_{hf}$> T ± 0.5	γ-Fe$_2$O$_3$ (%) ±3	Fe$_3$O$_4$ (%) ±3	<Stoichiometry> ± 0.02	<e> $_{\gamma\text{-Fe2O3}}$ nm ± 0.5
NS22	0.524	50.5	60	40	2.80	3.7
NO18	0.483	51.4	79	21	2.74	
NPl17	0.451	52.0	94	6	2.68	

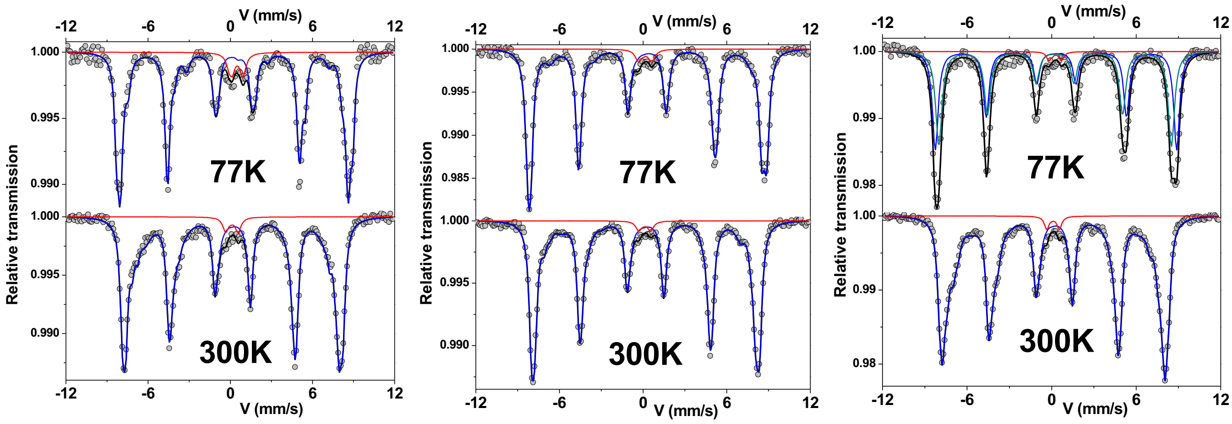

Figure VII.11 Mössbauer spectra at 300 and 77K of nanospheres (NS22) (left), octopods (NO18) (middle) and nanoplates (NPl 17) (right)

It is important to emphasize that the mean value of isomer shift which is independent on the fitting model acts as a relevant parameter. Indeed it provides the mean stoichiometry (given in Table VII.4) of the Fe oxide intermediate between magnetite and maghemite, the later resulting from an oxidation of the first one. In addition, it allows the respective absorption areas on the basis of a "naïve" model composed of such stoichiometric phases to be estimated. Assuming a core-shell model, it is thus possible to estimate the thickness <e> of the maghemite outer layer (as listed in Table VII.4). One does also mention a significant difference between 77K spectra at about -4 mm/s: only that of spheres exhibits some shoulder, that can be assigned to the presence of blocked Fe^{2+} states, contrarily to others. This feature suggests that the core of the spheres consists of magnetite recovered by maghemite while the other octopod- and plate-shaped ones probably result from a rather continuous distribution of oxidation states ranging from ferric to intermediate ferric-ferrous-state.

Mössbauer spectra have been recorded under an applied field of 8T at 12K on the three samples; because the instrumental calibration is not yet completely achieved, one can only report here the qualitative results. The magnetic sextets are well split into two magnetic sextets attributed to tetrahedral and octahedral Fe sites, according to the ferrimagnetic structure. Their proportions can be clearly estimated and are rather close to 1:2, respectively. The isomer shift values are also well consistent with those observed at 77K and 300K but one can give evidence for the presence of Fe species with valency states intermediate 2 and 3, in perfect agreement with results as abovementionned. An other feature results from the intensity of intermediate lines which remain small for the three samples: this does provide an estimation of the thickness of the canted magnetic layer.

VII.3.3.2 TEM-EELS analysis

Nanospheres. In the particular case of the nanospheres, the EELS analysis performed on several NPs showed that the Fe valence is almost the same in the core of NPs and at their surface. Two typical spectra obtained by separating the EELS signals corresponding preferentially to the two core and surface regions are shown in Figure VII.12. While the energy position of the peak did not change, they appeared to be a slight broadening of the Fe L23 edge. This effect could be due to the presence of Fe within the ligand molecules.

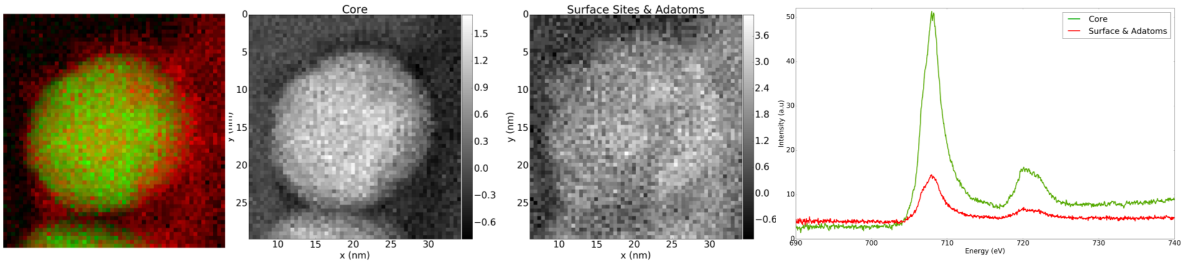

Figure VII.12 - EELS analysis of the spherical NPs. EELS signals corresponding to the core and the surface of NPs extracted using principal component analysis (PCA) or independent component analysis (ICA). The last contribution contained probably the signal from the ligand molecules around the NPs.

Octopodes (NO). The EELS analysis performed on some typical NO showed that the core contained a larger relative amount of Fe^{3+} atoms comparing to that of Fe^{2+}, while the surface has more a Fe^{2+} component (Figure VII.13). That allowed us to unambiguously conclude that for all the analysed NPs the surface layer has a lower valence than the core one. The inhomogeneous distribution of the Fe^{2+} and Fe^{3+} components through the particle could be the result of the presence of a very localized FeO phase or possibly a mixed oxide with reduced valence (such as Fe_3O_4). It should be mentioned here that, as the spectra acquired at this edge are relatively noisy, it is difficult to properly determine an eventual change in the spectral shape through the particle.

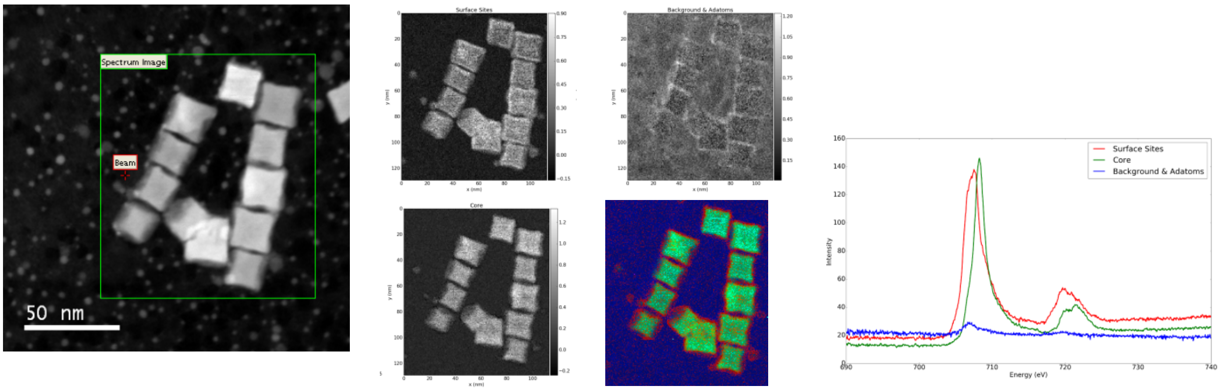

Figure VII.13 - EELS analysis of several NO NPs: HHADF image of the chosen NPs, the decomposition of the EELS signals in its different contributions (the corresponding surface layer, core and the background&adatoms), the superposed image of these contributions and the associated EELS spectra.

Nanoplates (NPl). The same type of analysis of the EELS spectra acquired on these 2D nano-objects (Figure VII.14) provided similar results: the surface of NPls has also a reduced valence of Fe as compared to the Fe valence in the core. However, the difference in the corresponding EELS spectra characterizing the core and surface difference is less important than in the case of the octopods. In addition, the Fe on the core did not exhibit the same shoulder as in the case of the octopods.

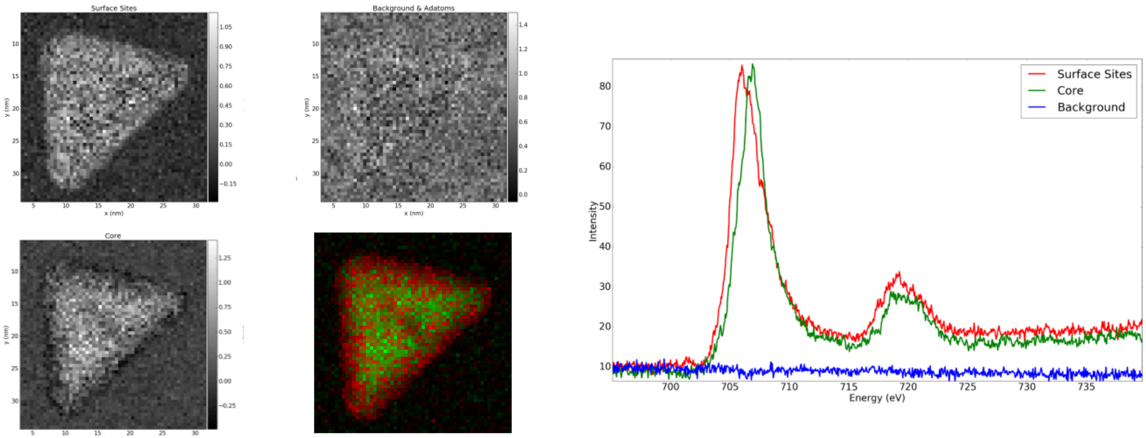

Figure VII.14 - The EELS analysis of one of the triangular platelet showing the contributions to the EELS spectra of the surface layer, the core and the background and adatoms, as well as the superposed image of these contributions and the average EELS spectra.

TEM-EELS analysis showed that the surface of octopods and nanoplates would contain some lower valence iron cations and that may related to Mössbauer results which reported that the core of the spheres consists of magnetite recovered by maghemite while the other octopod- and plate-shaped ones probably result from a rather continuous distribution of oxidation states ranging from ferric to intermediate ferric-ferrous-state.

Therefore both TEM-EELS analysis and Mössbauer spectroscopy support that the surface of octopods and nanoplates is quite different from that of isotropic NPs.

VII.3.4 Magnetic characterisation

VII.3.4.1 Magnetic measurements

Magnetic measurements have been performed by Dr Daniel Ortega and Cristina Blanco-Andujar at IMDEA, Madrid and Dr. Simo Spassov at Centre de Physique du Globe de l'Institut Royal Météorologique de Belgique in the framework of RADIOMAG COST. Different magnetic measurements have been performed on the different samples: FC (field cool) and ZFC (zero field cool) magnetization curves as a function of an applied field as well as ZFC/FC curves as function of temperature. The temperature dependence of the magnetization measured through this technique allows to track the blocking/unblocking processes of NPs, along with other aspects related to NP dynamics, such as inter-particle interactions, phase transitions, as well as finite-size and surface effects.

N.B.: all ZFC/FC plots shown here in this chapter refer to a 5 *mT* field

VII.3.4.1.1 Nanospheres NS18

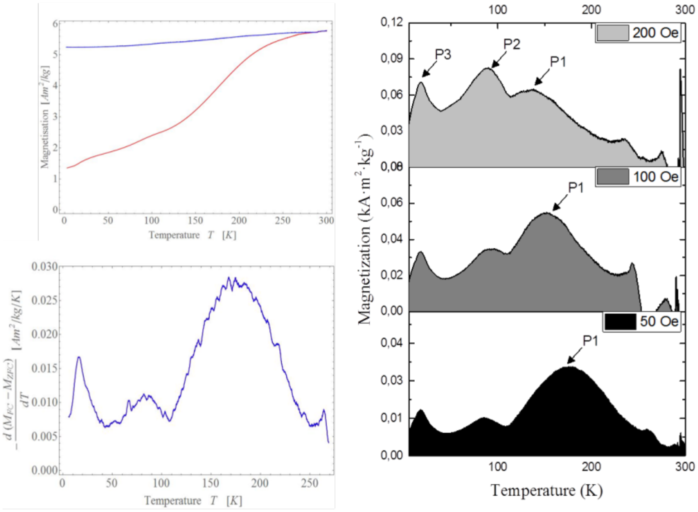

Figure VII.15 - 5 mT - ZFC warming (curve red), FC cooling (curve blue) & difference between both (left down) and comparison of the corresponding temperature derivatives of 50, 100 and 200 Oe ZFC curves (right) for NS18

The ZFC/FC curves are charateristic of superparamagnetic NPs with a blocking temperature often assumed as the maximum of the ZFC curve. Indeed the broad intense peak at 178 K (P1) (Figure VII.15 right) shows a marked field dependence; this means that it represents the blocking process of most of NPs within the sample. It shifts towards lower temperatures as the field increases because the probing field decreases the anisotropy barrier the NPs have to overcome during their unblocking process. Consequently, the population of unblocked NPs at the lower end of the temperature range increases for higher applied fields. The peak at around 85 K (P2) does not show a field dependence, although it becomes more intense for higher applied fields. It corresponds to the Verwey transition of magnetite, and it is confirmed by the small bump in the FC branch at the same temperature. Although this transition is expected to occur at higher temperatures in the bulk phase, it has been reported that it shifts towards lower temperatures for smaller particle sizes[59], similarly to the experimental observations for the Morin transition in hematite nanoparticles[60], but which even disappears for sufficiently small NPs[61]. The progressive intensity increase of P2 is merely incidental, and stems from the shift of P1 at increasing fields. The Verwey transition is usually seen as an abrupt jump in both ZFC and FC magnetization, and the fact that here we only see a modest peak may be due to a lower content of magnetite in the NPs as confirmed by the above structural characterizations (they are oxidized to maghemite to a sizeable extent). The peak at 20 K (P3) does not depend on the applied field, and given the low temperature at which it appears, it is ascribed to the spin-glass-like behaviour of the superficial spins. The field is not able to contribute to their blocking process, and only very low temperatures can freeze them and block their magnetic moments. That is in agreement with our previsous results on dendronized 10 nm sized NPs where a spin canted layer was evidenced with a thichness of about 0.7-0.8 nm determined from Mössbauer esperiments under an apllied field[62].

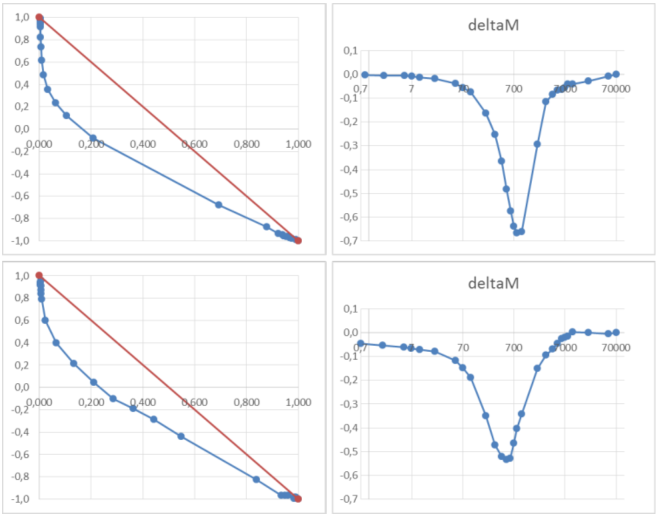

Figure VII.16 - Henkel plot (left) & ΔM(H) (right) at 1.8 K (top) and 50 K (bottom) for NS18

Henkel plots (Figure VII.16 left) have been acquired to estimate the degree of interparticle interactions as well as their nature[63,64]. These experiments have been carried out at two temperatures for comparison, namely 50 and 1.8 K. In any case, the acquisition temperature should be well below the blocking temperature of the system, otherwise the contribution from the unblocking processes of the NPs may introduce artefacts, inducing to erroneous interpretations. Since 1.8 K is even below the unblocking of surface spins, we take plots acquired at this temperature as the most reliable ones.

In short, the distance from the experimental points (blue dots) of the Henkel curve to the Wohlfarth line (y = -x line in orange) and the sign of this difference give an idea of the nature and intensity of the interactions taking place. The Wohlfarth line is the ideal limit for non-interacting particles, and Henkel curves below that line represent demagnetising interactions, whereas Henkel curves above that line represent magnetising interactions. ΔM graphs (Figure VII.16.right) further help in the interpretation of interacting phenomena, even improving the information extracted from the latter as they explicitly show the dependence of the measurements with the field. A sample where ΔM = 0 is regarded as a non-interacting one. As observed for similar systems[64], in the case of this sample (and the rest of the samples) all the measured interactions at both 50 and 1.8 K are only of *dipole-dipole* nature (the samples are said to be exchange decoupled, as no exchange interactions are observed). These interactions are negative (ΔM < 0), and may be thought as detrimental to both the magnetization of the sample and its heating capabilities. This sample has the second highest absolute value of the ΔM peak, but on the contrary has the second lowest magnetisation value of the set. In principle, the value of the ΔM peak is linked to its high magnetic moment compared to the other samples (see magnetisation values σ_S in the Table VII.5), hence making interactions more intense. This can be verified from the expression for the dipole interaction energy E_d:

$$E_d \approx \frac{\mu_0}{4\pi}\frac{\mu^2}{d^3}$$

where μ is the magnetic moment, μ_0 is the permeability of the vacuum and *d* is the distance between nanoparticles. Consequently, the origin of this relatively high ΔM peak in sample NS18 should be due to something different to the magnitude of the magnetic moment. Going back again to the E_d expression, another explanation could be based on the interparticle distance *d*, which in this case may have been shortened due to a higher packing fraction of the NPs as a consequence of the dragging forces acting during solvent evaporation (in sample preparation for SQUID). A close inspection of the others parameters do not lead to point out additional factors explaining the high ΔM in sample NS18.

Additional data may be extracted from Henkel plots, such as the interaction field (H_{int}), which is calculated from the expression:

$$H_{int} = \frac{1}{2}|H_r' - H_d'|$$

Where H_r' and H_d' are obtained by fitting a lognormal function to the field derivative of the isothermal remanence magnetisation (x axis of the Henkel plot) and the direct current demagnetisation (y axis), respectively. The values of this parameter for all the samples are listed in the Table VII.5.

Table VII.5 – Summary of the magnetic parameters (σ_S saturation magnetisation; exchange field=| μ_0H_r'- μ_0H_d'|/2; Hc = coercive field)

Sample	| μ_0H_r'- μ_0H_d'|/2*	ΔM@field*	σ_S 300K (Am^2/kg_{Fe})**	σ_S 5K (Am^2/kg_{Fe})**	H_C^* (300K)	H_C^* (5K)	Size (nm)	Morphology	Phases
NC15	69.2	-0.58@150	139.03	151.28	1.10	89.76	14.5 ± 1.6	Cubes	$FeO@Fe_3O_4$
NS18	27.6	-0.67@80	89.28	95.81	0.09	40.67	17.9 ± 1,4	Spheres	Fe_3O_4
NO18	15.6	-0.55@70	149.12	170.80	0.70	26.89	17.2 ± 2.2	Octopods	Fe_3O_4
NO28	18.7	-0.60@70	115.62	129.63	3.73	31.01	27.8± 4.2	Octopods	Fe_3O_4
NS22	14.5	-0.82@50	114.24	123.00	0.68	27.20	22 ± 1.8	Spheres	Fe_3O_4
NPl	17.1	-0.22@200	43.45	48.23	0.13	59.56	16,1 ± 0.5	Platelets	Fe_3O_4

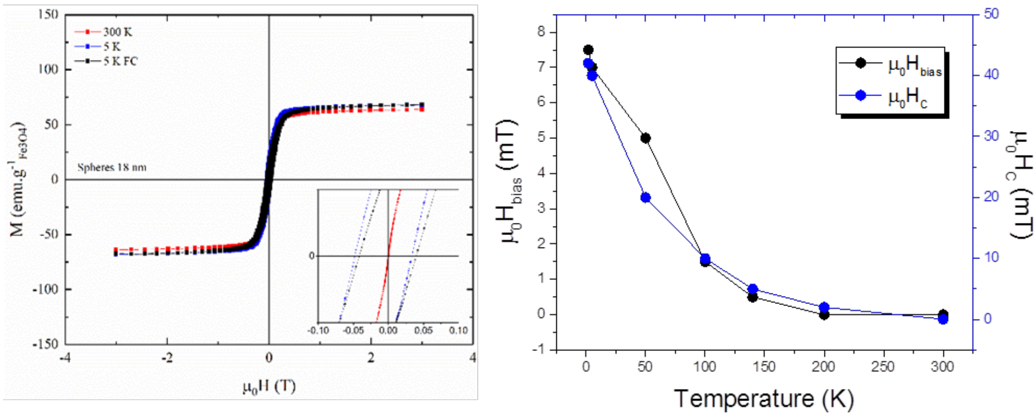

Figure VII.17 – Hysteresis curves measured at 300 and 5 K and Hysteresis loop FC at 3T and measured at 5 K.(red loop uncorrected of paramagnetic contributions, blue corrected) Insert: zoom of the figure (left) and temperature dependence of the coercivity (H_C) and exchange bias (H_{bias}) effect (right) for NS18

Magnetization (M(H)) curve at room temperature is characteristic of a superparamagnetic behavior (Figure VII.17 left) when a ferrimagnetic behavior is noticed at 5K as expected for NPs below their blocking temeprature. To evaluate possible exchange interactions between the core of NPs and a canted layer at the surface or between the magnetite core and the oxidized shell[34], FC (M(H)) curves have been further recorded and an exchange field H_{bias} characteristic of such exchange has been determined.

Both the H_c and H_{bias} effect in this sample follow a typical exponential decay with temperature (Figure VII.17 right), with values that are on a pair of those reported for other NPs systems[64,65]. Quite possibly, smaller NPs with a large fraction of surface spins and a higher applied field would have resulted in a more intense H_{bias}. In any case, we can say that there is something producing an exchange bias effect, be it a non-compensated interphase or canted surface spins. Other features observed in the measured exchange bias of almost all these samples are:

- The shift of the hysteresis loop takes place in the opposite direction of the cooling field, i.e. towards negative field values.
- The exchange bias is observed, obviously, below the Tc of the constituent phase/s and also below the freezing temperature of the surface spins, where the latter get blocked in random directions thus “breaking” the original ferrimagnetic order due to the decrease of the coordination number of surface atoms (the exchange angle is modified). As a result, a disordered/ordered ferrimagnetic interphase is formed and hence the exchange bias may show up.

VII.3.4.1.2 Octopods NO18 and NO28

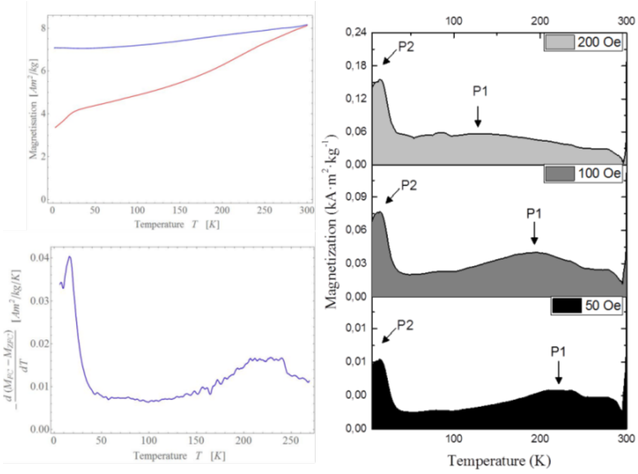

Figure VII.18 - 5 mT - ZFC warming curve – red, FC cooling curve blue & difference between both (left) and Comparison of the corresponding temperature derivatives of 50, 100 and 200 Oe ZFC curves for NO18

NO18. For octopods NO18, the interpretation of the derivative ZFC curves (Figure VII.18 right) is very similar to that given for sample NS18, with the only exception of the Verwey transition, which is not observed here. This is agreement with XRD, IR and Mössbauer spectroscopies results which have shown that octopods were strongly oxidized. Thus, P1 represents the unblocking process of the NPs inner moments and P2 represents those at the surface.

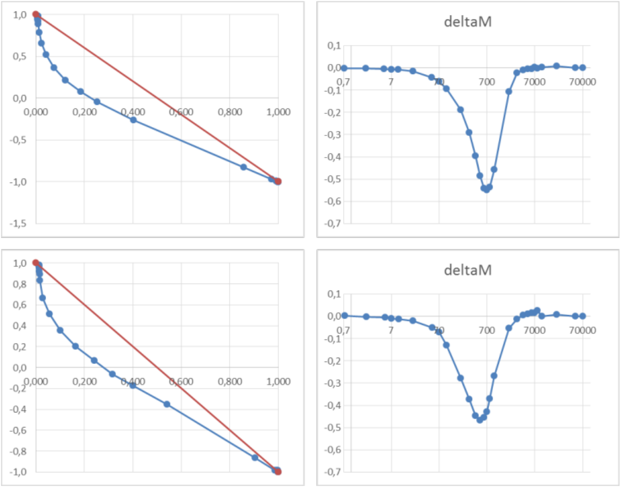

Figure VII.19 - Henkel plot (left) & ΔM(H) (right) at 1.8 K (top) and 50 K (bottom)for NO18

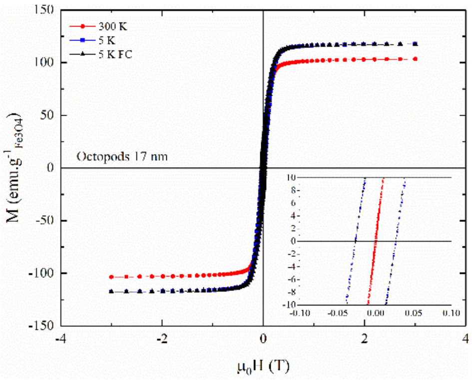

Figure VII.20 – Hysteresis curves measured at 300 and 5 K and Hysteresis loop FC at 3T and measured at 5 K.(red loop uncorrected of paramagnetic contributions, blue corrected) Insert: zoom of the figure, for NO18.

NO28

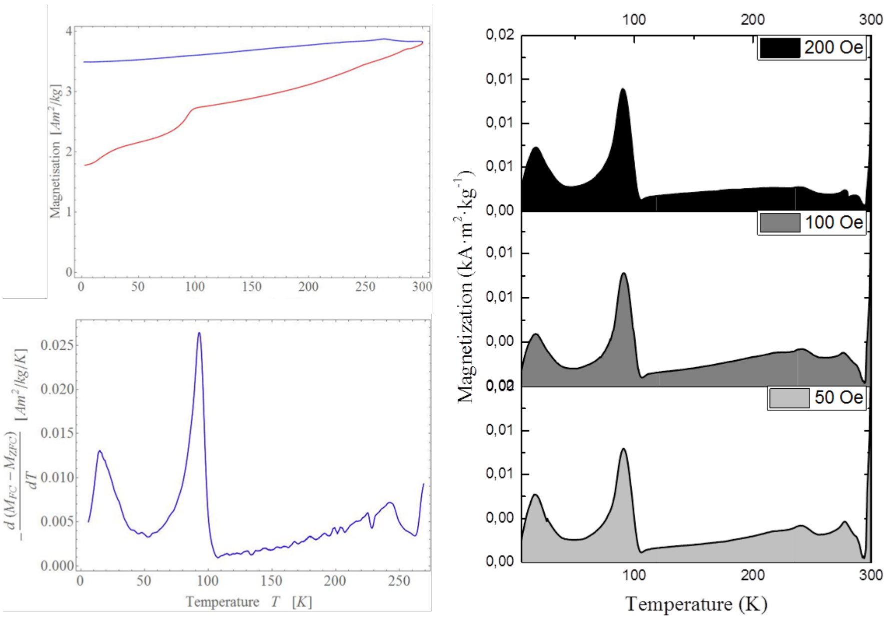

Figure VII.21 - 5 mT - ZFC warming curve – red, FC cooling curve blue & difference between both (left) and Comparison of the corresponding temperature derivatives of 50, 100 and 200 Oe ZFC curves for NO28

The interpretation of the derivative ZFC curves (Figure VII.21) for NO28 is very similar to that given for sample NS18. Both the position and the intensity relation of the peaks corresponding to the Verwey transition (around 85 K) and the glassy surface spins remain unaltered for changing applied fields. On this occasion, the magnetization jump due to the Verwey transition happens abruptly, in the form of a sudden jump, as expected. That could be explained by the fact that for NO28, 20% of magnetite would be present from Mössbauer results assuming a core-shell composition with a magnetite core and a maghemite shell. The unblocking process of the inner spins of the NPs takes place monotonically throughout a temperature range that goes from 100 to 240 K.

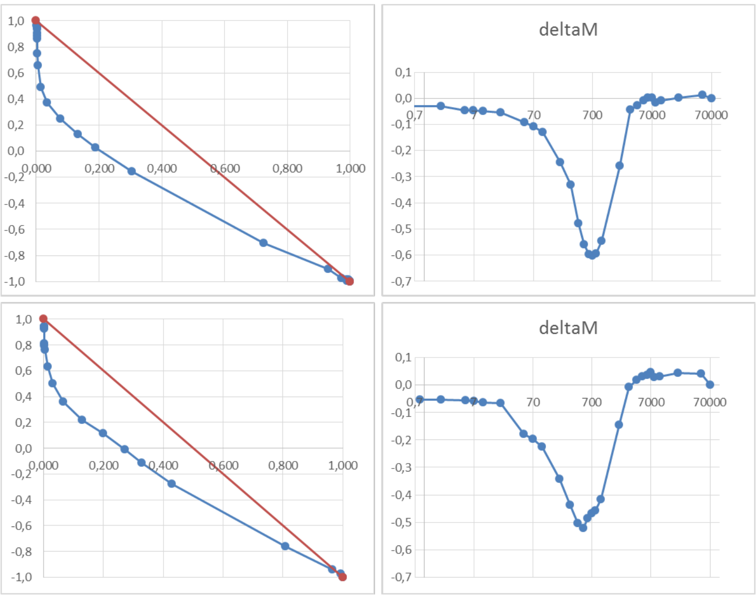

Figure VII.22 - Henkel plot (left) & ΔM(H) (right) at 1.8 K (top) and 50 K (bottom)for NO28

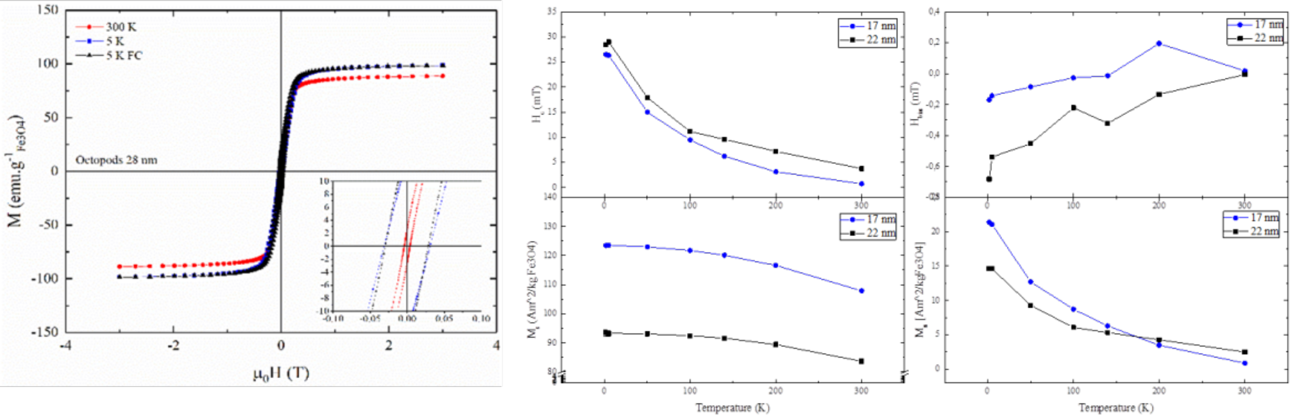

Figure VII.23 – Hysteresis curves measured at 300 and 5 K and Hysteresis loop FC at 3T and measured at 5 K.(red loop uncorrected of paramagnetic contributions, blue corrected) Insert: zoom of the figure, for NO28 (left) and *comparison of the main hysteresis parameters of samples NO28 (black curves) and NO18 (blue curves) (right).*

ZFC and FC magnetization curves and results of NO18 and NO28 are presented in Figure VII.20 and 23 respectively as well as Henkel plot and ΔM(H) curves in Figure VII.19 and 22 respectively. In Figure VII.23, are further compared the main hysteresis parameters of both octopod shaped NPs. The trend observed for most of the hysteresis parameters are within the expected. The temperature decrease of the saturation magnetisation (Figure VII.23) follows a Bloch-like law that will end up vanishing down to zero several hundred kelvins ahead once the Curie temperature is reached. The coercivity shows an exponential decrease with temperature; this is probably due to the higher anisotropy energy associated with the core spins in the NPs, which tend to “drag” those located at the surface—with lower anisotropy energy—during their magnetisation reversal process. As expected, the temperature dependence of the remanence is similar to that of the coercivity.

The not-so-expected trend is that shown by the exchange bias (H_{bias}) effect in each sample. When plotting the absolute value of this parameter, an exponential-like decay with temperature similar to that of coercivity is observed (not shown), whereas considering its sign leads to a completely different scenario. More precisely: in sample NO18, the H_{bias} is changing sign from negative to positive when going from 1.8K FC to 200 K FC; in sample NO28, H_{bias} is always negative going up to 0 from 1.8K to 200 K, although at 100 K, H_{bias} drops suddenly. Given the small intensity of H_{bias} for these samples, much less than those reported for many other nano-systems (e.g. core/shell $Fe_3O_4/\gamma\text{-}Fe_2O_3$ NP H_{bias} = 14 mT[66]), no apparent interpretation can be offered. Perhaps repeating at least one of the samples in liquid form in a dedicated sealed container would throw a bit more light on the effect. Nevertheless, this pointed out again an unusual behavior of octopod shaped NPs.

VII.3.4.1.3 Nanospheres NS22

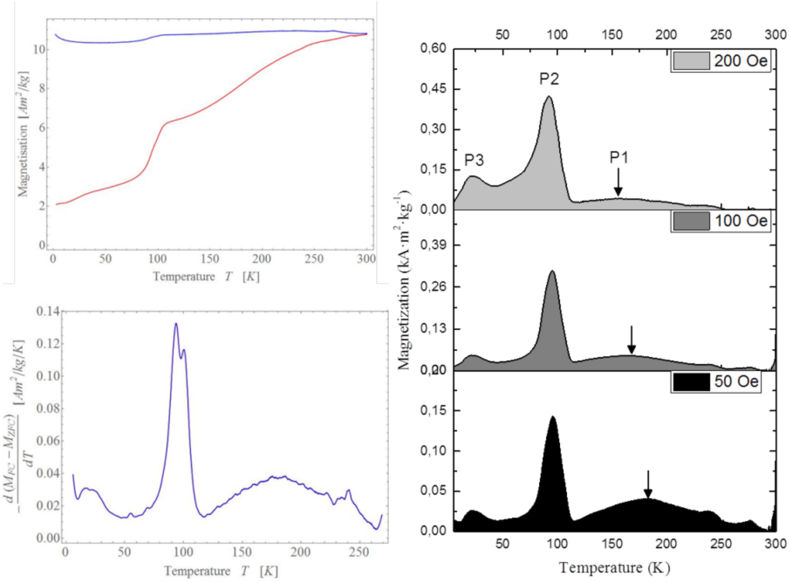

Figure VII.24 - 5 mT - ZFC warming curve – red, FC cooling curve blue & difference between both (left) and Comparison of the corresponding temperature derivatives of 50, 100 and 200 Oe ZFC curves for NS22

The ZFC/FC curves of NS22 are presented in Figure III.24. The interpretation of the ZFC derivative curves is very similar to that of sample NO28. The assignment of the peaks and the trends observed are the same.

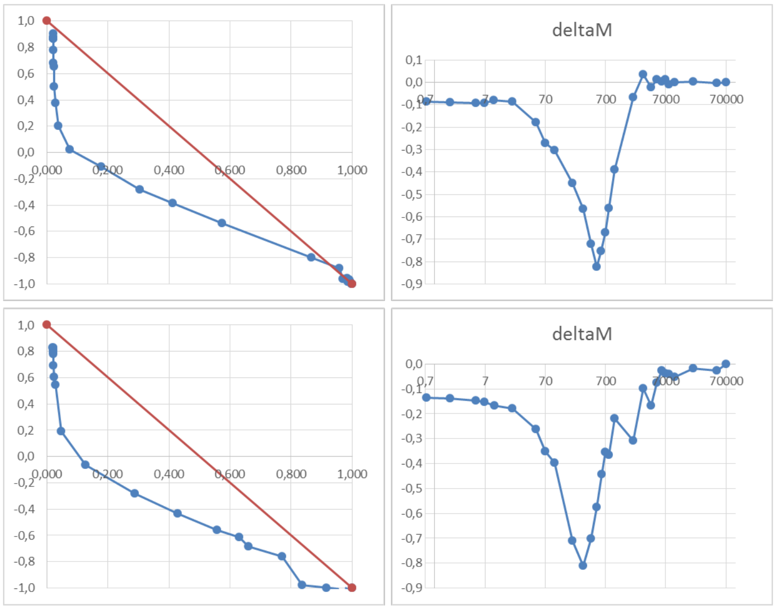

Figure VII.25 - Henkel plot (left) & $\Delta M(H)$ (right) at 1.8 K (top) and 50 K (bottom) for NS22

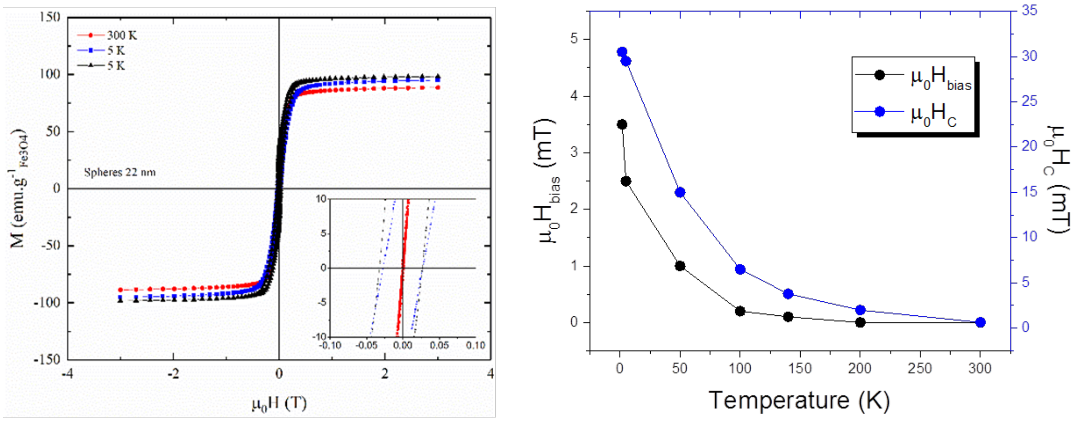

Figure VII.26 – Hysteresis curves measured at 300 and 5 K and Hysteresis loop FC at 3T and measured at 5 K.(red loop uncorrected of paramagnetic contributions, blue corrected) Insert: zoom of the figure (left) and temperature dependence of the coercivity (H_C) and exchange bias (H_{bias}) effect (right) for NS22

The magnetization curves are given in Figure VII.26 as well as the FC magnetization curve at 3T. In the inset of the FC hysteresis loop at 5 K it can be observed the so-called “wasp-waisted” behaviour (Figure VII.26 left,insert). This effect has been traditionally associated with the coexistence of multiple phases (which is a possibility here as we have shown from XRD measurement that the coherence length was smaller than the TEM size and explained by the presence of defects) although it has been also proposed that it may well be due to the apparition of two switching fields in a single phase sample[67]. Such duality would stem from the combination of interparticle interactions (for example due to a concentration increase) with easy-plane anisotropy, which correspond to a negative first anisotropy constant, as opposed to the uniaxial anisotropy (positive first anisotropy constant) typically considered in systems of single-domain and superparamagnetic NPs. The subtle wasp-waisted hysteresis effect on the sample is also compatible with the existence of a residual multi-domain fraction.

VII.3.4.1.4 Nanocubes NC15

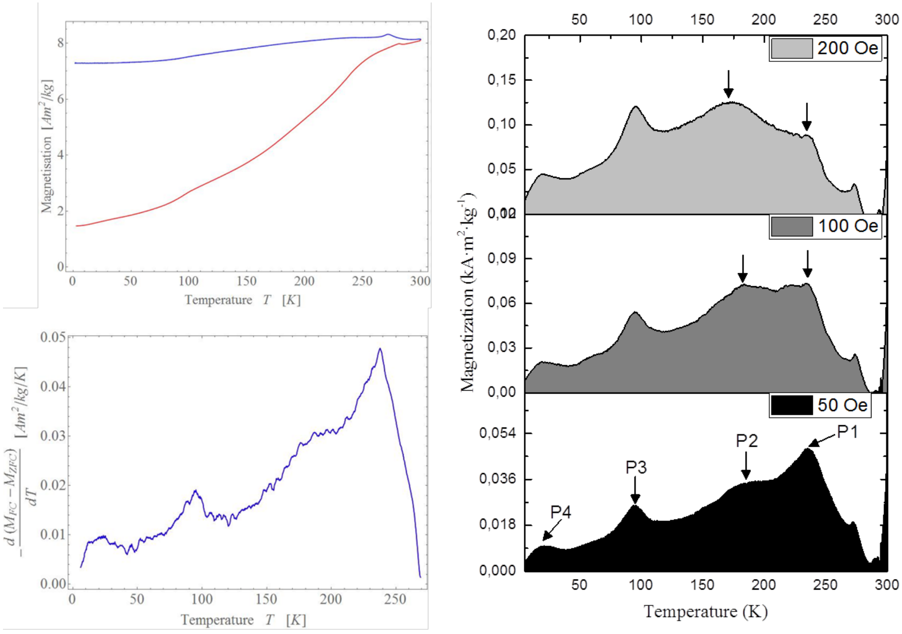

Figure VII.27 - 5 mT - ZFC warming curve – red, FC cooling curve blue & difference between both (left) and Comparison of the corresponding temperature derivatives of 50, 100 and 200 Oe ZFC curves for NC15

The nanocubes NC15 are constituted of a core of wüstite FeO with an oxidized shell at the surface. The lattice parameter of the shell is close to that of magnetite abut it is known that epitaxial strain and oxidation defect may affect the lattice parameter. With little exceptions, the derivative ZFC curves (Figure VII.27) for this sample resemble those for sample NS18. The intensity of P2 increases at the expense of that of P1, and the latter occurs at the same temperature regardless of the applied field. This peak P2 is attributed to the Neel temperature of FeO. The intensity of P3, assigned to the Verwey transition (this time occurring at 95 K) is lower than that of other samples, in agreement with the lower presence of magnetite phase in the NPs.

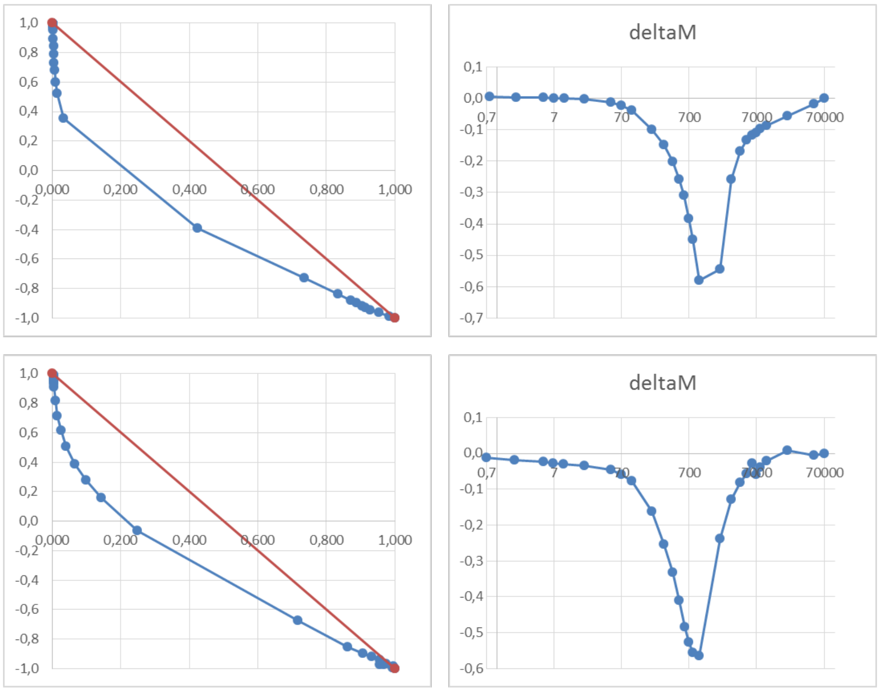

Figure VII.28 - Henkel plot (left) & ΔM(H) (right) at 1.8 K (top) and 50 K (bottom)for NC15

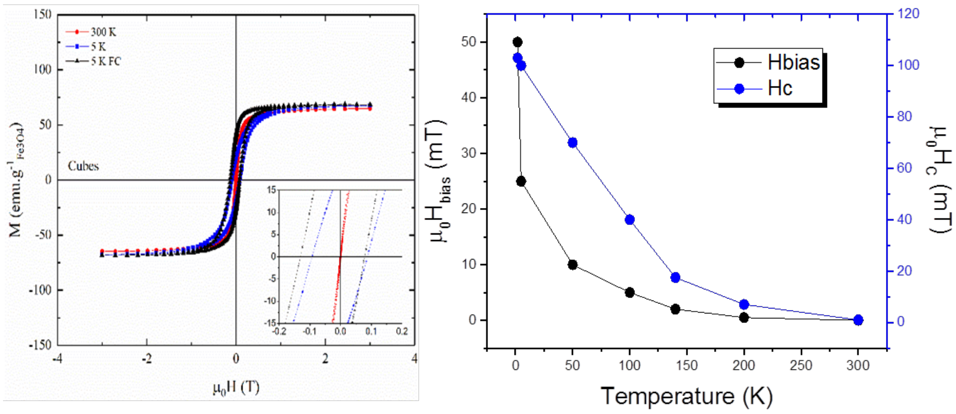

Figure VII.29 – Hysteresis curves measured at 300 and 5 K and Hysteresis loop FC at 3T and measured at 5 K.(red loop uncorrected of paramagnetic contributions, blue corrected) Insert: zoom of the figure (left) and temperature dependence of the coercivity (H_C) and exchange bias (H_{bias}) effect (right) for NC15

As expected due to its core-shell structure with an antiferromagnetic core and a ferrimagnetic shell, this is the sample exhibiting the most noticeable exchange bias effect throughout the entire sample series. The loop shift towards negative field values can be readily seen in the right hysteresis loop above. The temperature dependence of this effect follows the expected exponential decay shown in the graph below. The intensity of the H_{bias} is of course above than that expected for just the contribution of surface spins. Indeed H_{bias} is quite high now because the presence of the exchange bias interaction between the antiferromagnetic FeO core and the ferrimagnetic $Fe_{3-x}O_4$ shell. We had already observed earlier this effect in such core-shell nanocubes[42].

VII.3.4.1.5 Nanoplates NPl17

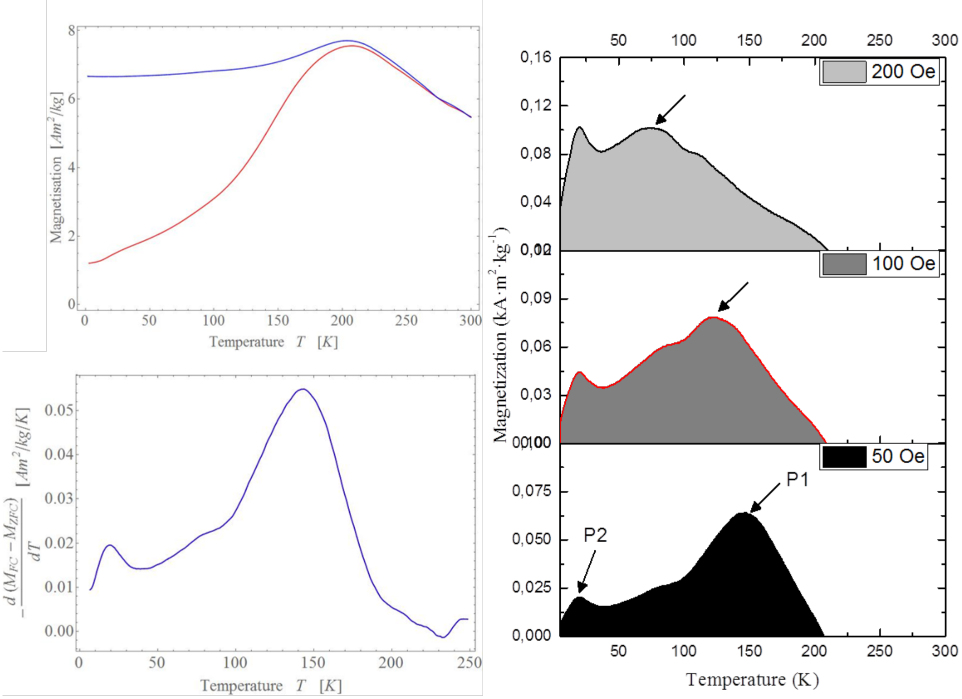

Figure VII.30 - 5 mT - ZFC warming curve – red, FC cooling curve blue & difference between both (left) and Comparison of the corresponding temperature derivatives of 50, 100 and 200 Oe ZFC curves for NPl17

The ZFC/FC curves in Figure VII.30 show that the Verwey transition is barely seen in this sample as expected. Indeed these NPl have been shown to be strongly oxidized from the structural characterizations. The assignment for peaks P1 and P2 is the same as for the previous samples.

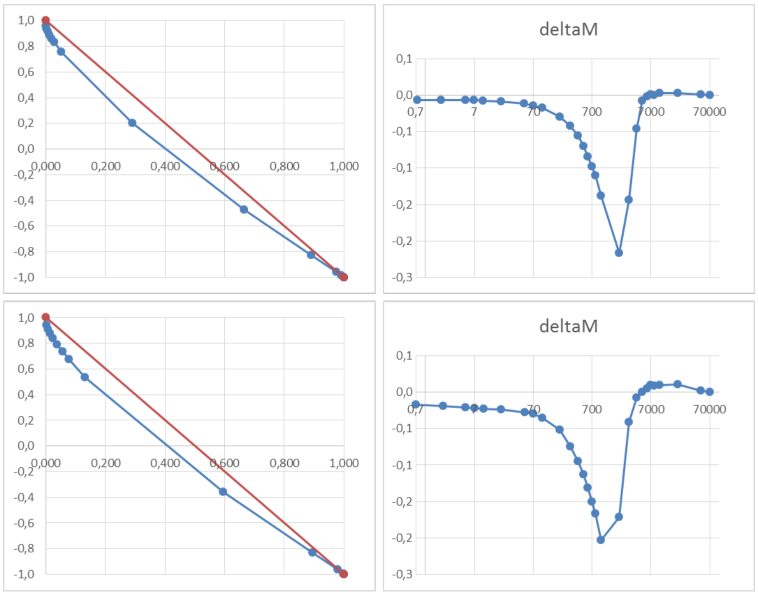

Figure VII.31 - Henkel plot (left) & ΔM(H) (right) at 1.8 K (top) and 50 K (bottom)for NPl17

Compared to the other samples of the set, the platelets show the lowest degree of interparticle interactions. The 50 K Henkel plot (Figure VII.31) shows a positive contribution of its right branch, but instead of a pure interaction effect, this could be rather considered as a relaxational effect (blocking/unblocking). This can be explained because there is another unblocking process (maximum P3 in the ZFC derivative graph).

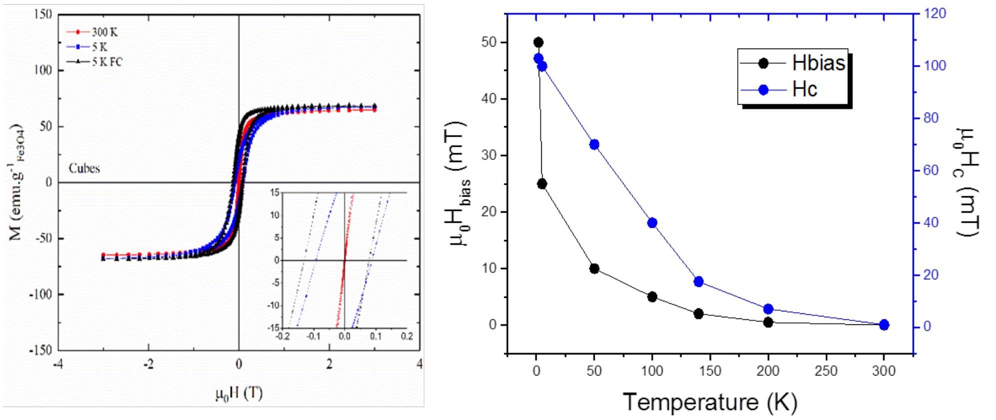

Figure VII.32 – Hysteresis curves measured at 300 and 5 K and Hysteresis loop FC at 3T and measured at 5 K.(red loop uncorrected of paramagnetic contributions, blue corrected) Insert: zoom of the figure (left) and temperature dependence of the coercivity (H_C) and exchange bias (H_{bias}) effect (right) for NPl17

The coercivity values are very low, as it is expected for superparamagnetic samples, and show an exponential-like temperature dependence. The H_{bias} values are so small that no reliable interpretation could be done; H_{bias} is practically zero in. That suggested that quite no spin canting is present in NPls which would be in agreement with the presence of more flat surfaces in these NPs.

VII.3.4.2 Evaluation of inter and intra-particle interactions

To estimate the degree and nature of inter-particle interactions in such shaped NPs, Henkel plots were acquired (cf. Figures above for all NPs and Figure VII.31). Indeed one must then point out that the magnetic NPs heat release does not only depend on their shape, composition or size, but also on the magnetic interaction between individual NPs. The latter is an important issue intimately related to the efficiency of MH agents that has not been properly addressed in the past years[68–70]. Experimental studies reported either a decrease or an increase of SAR with interactions[71–75]. In fact, depending on the NPs anisotropy, dipolar interactions may act differently on the clustering/spatial arrangement of NPs under an applied magnetic field leading either to their aggregation or to their alignment in chains. For NPs with mean size near the superparamagnetic/blocked single domain size threshold, magnetic interactions are strong and NPs tend to aggregate or align in chains during magnetic field application. Very recent evaluations of these interaction effects[68,69] and studies on magnetosomes synthesized by bacteria[71] pointed out that chains of magnetic NPs are ideal for obtaining high heating properties.

Furthermore, the cubic shape of NPs would favor the NPs geometrical arrangement compared to the spherical shape. Indeed chains of nanocubes can form due to the existence of strongly anisotropic dipolar forces mediating nanoparticle attachment. Serantes et al reported the positive effect of oriented attachment of 44 nm NPs on hyperthermia properties[72]. In our preliminary studies[38], the formation of chains with core-shell nanocubes at low concentration was observed by TEM without applying any magnetic field.

The value of ΔM can then inform on these interactions. If it equals to 0, the NPs are not interacting. Negative values indicate dipole-dipole interaction (they are considered as exchange decoupled as no exchange interaction is observed). From Henkel plots, the interaction field can also be calculated.

The distance from the experimental points (blue dots) of the Henkel curve to the Wohlfarth line (y = -x line in orange) and the sign of this difference give an idea of the nature and intensity of the interactions taking place. The Wohlfarth line is the ideal limit for non-interacting particles, and Henkel curves below that line represent demagnetising interactions, whereas Henkel curves above that line represent magnetising interactions. ΔM graphs further help in the interpretation of interacting phenomena, even improving the information extracted from the latter as they explicitly show the dependence of the measurements with the field. A sample where ΔM = 0 is regarded as a non-interacting one. As observed for similar systems[64], in all the samples, all the measured interactions at both 50 and 1.8 K are only of *dipole-dipole* nature (the samples are said to be exchange decoupled, as no exchange interactions are observed). These interactions are negative (ΔM < 0), and may be thought as detrimental to both the magnetization of the samples and their heating capabilities. NS18 has the second highest absolute value of the ΔM peak, but on the contrary has the second lowest magnetisation value of the set. In principle, the value of the ΔM peak is linked to its high magnetic moment compared to the other samples (see magnetisation values σ_S in the table), hence making interactions more intense. This can be verified from the expression for the dipole interaction energy E_d:

$$E_d \approx \frac{\mu_0}{4\pi}\frac{\mu^2}{d^3}$$

where μ is the magnetic moment, μ_0 is the permeability of the vacuum and d is the distance between nanoparticles.

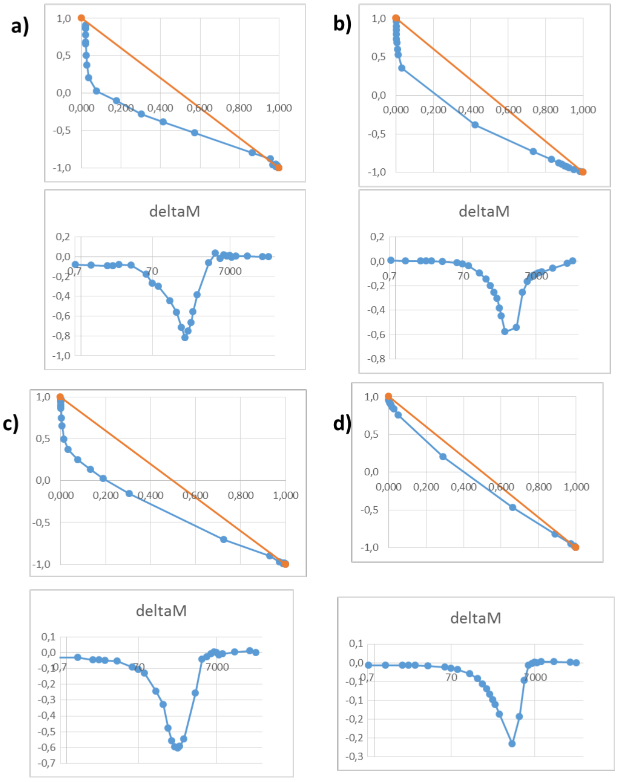

Figure VII.31 - Henkel plot & ΔM(H) at 1.8 K for samples a) NS22, b) NC, c) NO28, and d) NPI

From Henkel plots, the interaction field (H_{int}), can be calculated from the expression:

$$H_{int} = \frac{1}{2}|H'_r - H'_d|$$

Where H_r' and H_d' are obtained by fitting a lognormal function to the field derivative of the isothermal remanence magnetisation (x axis of the Henkel plot) and the direct current demagnetisation (y axis), respectively. The values of this parameter for all the samples are listed in the Table VII.6.

Table VII.6 – H_{int} values calculated for all shapes

	H_{int}	Morphology	Composition	Mössbauer spectroscopy
NC	69.2	Cubes	$FeO@Fe_{3-x}O_4$	
NS18	27.6	Spheres	$Fe_{3-x}O_4$	
NO28	18.7	Octopods	$Fe_{3-x}O_4$	$Fe_{2.74}O_4$
NPl	17.1	Platelets	$Fe_{3-x}O_4$	$Fe_{2.68}O_4$
NO18	15.6	Octopods	$Fe_{3-x}O_4$	
NS22	14.5	Spheres	$Fe_{3-x}O_4$	$Fe_{2.8}O_4$

Compared to the other samples of the set, NPl sample shows the lowest degree of inter-particle interactions. The 50 K Henkel plot shows a positive contribution of its right branch, but instead of a pure interaction effect this could be rather considered a relaxational effect (blocking/unblocking). This can be explained because there is another unblocking process (maximum P3 in the ZFC derivative graph).

Regarding the specific role of particle morphology on some of the static magnetic properties, we can conclude the following. Octopod samples show high σ_S values and the highest σ_S ratios, that is, the highest rate of change on σ_S from ambient to low temperature. On the opposite side, we have the two spherical samples, showing the lowest σ_S ratios. The simplest, and probably more plausible explanation, is that, at a given temperature, spheres tend to reach saturation more easily due to their zero-shape anisotropy. Nonetheless, it has to be noted that this ratio is around 1 for all the samples, so the difference is not so big across the whole set.

Spherical sample show the deepest ΔM peak at relatively low applied field values.

Octopod samples show the lowest H_C increase from 300 K to 5 K.

Cubes have far more the highest interaction field of the set, although the spherical samples have the deepest ΔM peak.

III.3.4.3 Conclusion on magnetic measurements

Static magnetic measurements do help in understanding the magnetic behavior of the samples and their performance in possible applications. The most immediate conclusion one can extract from this characterization set is that none of the samples is superparamagnetic, since all present both non-zero coercivity and remanence. In principle, the average particle size plays a prominent role, but there exist other sizeable contributions, such as surface effects. Other feature to note is that all the samples show an exchange bias effect to a different extent. Some common features observed in the measured exchange bias of almost all these samples are:

- The shift of the hysteresis loop takes place in the opposite direction of the cooling field, i.e. towards negative field values.
- The exchange bias is observed, obviously, below the Tc of the constituent phase/s and also below the freezing temperature of the surface spins, where the latter get blocked in random directions thus “breaking” to some extent the original ferrimagnetic order due to the decrease of the coordination number of surface atoms (the exchange angle is modified). As a result, a disordered/ordered ferrimagnetic interphase is formed and hence the exchange bias may show up.

Concerning the saturation magnetization of the samples which is very important for evaluating their MRI and magnetic hypertheria potentials, the saturation magnetisation values have been calculated in Am^2/kg_{Fe} and Am^2/kg_{Fe3O4} for each samples but the composition inside NPs is not homogeneous for all samples (Table VII.7). For example, nanocubes consist in core-shell FeO@$Fe_{3-x}O_4$ NPs and other samples are more less oxidized with a composition intermediate between those of magnetite and maghemite and certainly some oxidation gradients. Therefore the value for nanocubes can not be considered here even if we can notice that it is really too high and unrealistic.

We have introduced also some saturation magnetization values from magnetic measurements realized at IPCMS (Table VII.7). The experiments have been conducted by introducing a known volume of suspension which should reduce the errors on mass calculation.

The saturation magnetization values at Madrid and Strasbourg are in the same range for nanospheres and nanoplates. The higher value for NS22 by comparison with NS18 is directly correlated to its increased size and the values measured are in agreement with those reported with NPs with similar sizes after their TD synthesis[34]. There is a very good agreement with values for nanoplates.

The main problem arises from saturation magnetisation values of octopods which are both too high from measurements in Madrid. These NPs have been shown to be oxidized and so this is very surprising to obtain values close or higher than the magnetite one. One may suppose some errors in the determined iron mass but one may notice that the magnetic behavior of NO18 is not standard. However these samples exhibit the higher saturation magnetization values.

From the saturation magnetisation measurements, we may establish the following ranking with increasing σs values: NO18 ≥ NO28 ≥ NS22 ≥ NS18 ≥ NPls.

Table VII.7 – Saturation magnetization and characteristics of different shaped NPs

Sample	σ_S 300K (Am^2/kg_{Fe})	σ_S 300K (Am^2/kg_{Fe3O4})	σ_S 5K (Am^2/kg_{Fe})	σ_S 5K (Am^2/kg_{Fe3O4})	σ_s 300K IPCMS	Size (nm)	Morphology	Phases
NC15	*139.03*	~~*100.6*~~	*151.28*	~~*109*~~		14.5 ± 1.6	Cubes	FeO@Fe_3O_4
NS18	89.28	64.6	95.81	69	58	17.9 ± 1,4	Spheres	Fe_3O_4
NO18	149.12	107.9	170.80	124	69	17.2 ± 2.2	Octopods	Fe_3O_4
NO28	115.62	83.7	129.63	94		27.8± 4.2	Octopods	Fe_3O_4
NS22	114.24	82.7	123.00	89		22 ± 1.8	Spheres	Fe_3O_4
NPl	43.45	31.4	48.23	35	33	16,1 ± 0.5	Platelets	Fe_3O_4

In terms of inter-particle interactions, there is no apparent correlation between morphology and interaction field. That said, it is clear than cubes present a far higher interaction field than any other morphology as we have already noticed it in earlier studies[38]. Saturation magnetization seems difficult to directly correlate with the morphology of NPs but should correlate with structural characterizations. It is therefore hypothesized that the density of defects may play a role on this, taking into account that the saturation magnetization is an intrinsic magnetic property of the samples and that it is dominated by the crystalline structure of NPs. Nevertheless, of particular note is the difference between the samples with the lowest σ_S values, NS18 and NPl. As previously discussed, the higher degree of spin frustration in platelets due to their higher surface to volume ratio may be behind this effect: their surface are flat and their thickness is very small.

Within the 300 – 5 K temperature range, there are two main relaxation processes taking place. One is field dependent, and it is ascribed to the unblocking processes of the NP magnetization. The temperature range over which this occurs differs depending on the statistical size distribution associated to each sample. The second process is independent of the applied field, and it is due to the impossibility to align (with the typical fields employed in ZFC/FC experiments) frustrated surface spins. In addition, in some samples, a steep change in magnetization is observed under 100 K. Considering the composition of the samples, it has been interpreted as the Verwey transition of magnetite, and the shift towards lower temperatures is a consequence of finite-size effects in nanoparticles.

Finally, a qualitative and quantitative analysis of interactions effects reveals that most of the samples show a similar value of interaction field except cubes. A combined effect of the magnetization value (the interaction energy is proportional to the average magnetic moment) and the high packing factor of the particles with this morphology is thought to be responsible of the experimental observations.

VII.4 CONCLUSION

The synthesis conditions of nanoparticles with different shapes have been optimized and thus different batches have been produced: two batches of nanospheres with mean diameters around 18 (NS18) and 22 (NS22) nm ; two nanoplate batches: the first one with a length of ~17 nm and a thickness of 8.6 nm (NPl17), the second one with a length of 20 nm and a thickness of 6.6 nm; nanocubes with a mean size of 14.5 nm (NC15) and two batches of octopode shaped NPs with mean sizes (length of diagonal) of 18 (NO18) and 28 (NO28) nm.

The structural characterizations have been mainly centred on NS22, NC15, NO28 and NPl17 samples. The combination of different techniques (XRD and IR and Mössbauer spectroscopies) has shown that:

- Nanospheres are not monocristalline but contain some defects due to their formation by oxidation of a FeO phase. They consist in an oxidized magnetite as given in the Table below.
- Nanocubes are core-shell structures with a core of the antiferromagnetic FeO shelled by a ferrimagnetic $Fe_{3-x}O_4$. We do not succeed in obtaining nanocubes with a homogeneous composition despite varying different conditions. In fact the reaction mixture and the strict synthesis conditions make that the medium is reducing and that the growth kinetics on FeO nuclei is faster than the oxidation one.
- Nanoplates are monocristalline but very thin which make that they are strongly oxidized.
- Octpodes are complex structures due to their elongated corners, they are also constituted of oxidized magnetite.

From all investigated shaped NPs, NPls and in particular octopodes present peculiar phenomena: EELS – TEM suggested the presence of iron cations with reduced oxidation degree at their surface which may be related to Mössbauer experiments which reported a rather continuous distribution of oxidation states. Magnetic measurements were also not simple with octopods and in particular, the measurement of their saturation magnetisation.

From the saturation magnetisation measurements, we may establish the following ranking with increasing σs values: NO18 $\geq$ NO28 $\geq$ NS22 $\geq$ NS18 $\geq$ NPls. Therefore the NPs with highest σs values are supposed to present an highest potential for MRI and magnetic hyperthermia. One may expect also that the anisotropic shape which is more evident for octopodes and nanoplates will have also an influence.

As dipole-dipole interactions are also very important for magnetic hyperthermia, to estimate the degree and nature of inter-particle interactions in such shaped NPs, Henkel plots were acquired and a interaction field has been determined (Table below). There is no apparent correlation between morphology and interaction field. Core-shell nanocubes which display an added anisotropy due to exchange bias interactions present a far higher interaction field than any other morphology. That would be in agreement with our earlier published results where such nanocubes were shown to align spontaneously. We observe also such spontaneous alignement with octopods (cf. Figure VII.5) and thus the observed interaction field appear quite low. Nevertheless it has been very recently reported that ΔM plots may be misleading when the nanoparticles do not have a homogeneous internal magnetic configuration and in particular when NPs display spin disorder[76]. The investigation need to be continued in order to confirm or infirm the Henkel plots result. The determination of the main relaxation mechanism, Neel or Brown, needs to be determined as a function of the shape.

NPs	**Mean TEM size (nm)**	**Crystallite size (nm)**	**Lattice parameter (Å)**		**Composition**	H_{int}
			Spinel phase	Wüstite phase	Mössbauer	
NS22	22.2 ± 1.8	13	8.391	X	$Fe_{2.8}O_4$	14.5
NC	15.9 ± 1.8	8	8.392	4.237	$Fe_{3-x}O_4$@FeO	69.2
NO28	27.8 ± 4.2	25 <400> /23 <511>	8.370	X	$Fe_{2.74}O_4$	18.7
NPl	16.7 ± 5.2	17 <222>	8.384	X	$Fe_{2.68}O_4$	17.1

REFERENCES

1. Liong, M. *et al.* Multifunctional Inorganic Nanoparticles for Imaging, Targeting, and Drug Delivery. *ACS Nano* **2,** 889–896 (2008).
2. Kim, J., Piao, Y. & Hyeon, T. Multifunctional nanostructured materials for multimodal imaging, and simultaneous imaging and therapy. *Chemical Society Reviews* **38,** 372–390 (2009).
3. De, M., Ghosh, P. S. & Rotello, V. M. Applications of Nanoparticles in Biology. *Advanced Materials* **20,** 4225–4241 (2008).
4. Mornet, S., Vasseur, S., Grasset, F. & Duguet, E. Magnetic nanoparticle design for medical diagnosis and therapy. *Journal of Materials Chemistry* **14,** 2161–2175 (2004).
5. Yoo, D., Lee, J.-H., Shin, T.-H. & Cheon, J. Theranostic Magnetic Nanoparticles. *Acc. Chem. Res.* **44,** 863–874 (2011).
6. Fang, C. & Zhang, M. Multifunctional Magnetic Nanoparticles for Medical Imaging Applications. *Journal of materials chemistry* **19,** 6258–6266 (2009).
7. Laurent, S. *et al.* Magnetic Iron Oxide Nanoparticles: Synthesis, Stabilization, Vectorization, Physicochemical Characterizations, and Biological Applications. *Chemical Reviews* **108,** 2064–2110 (2008).
8. Maier-Hauff, K. *et al.* Intracranial thermotherapy using magnetic nanoparticles combined with external beam radiotherapy: results of a feasibility study on patients with glioblastoma multiforme. *J. Neurooncol.* **81,** 53–60 (2007).
9. Maier-Hauff, K. *et al.* Efficacy and safety of intratumoral thermotherapy using magnetic iron-oxide nanoparticles combined with external beam radiotherapy on patients with recurrent glioblastoma multiforme. *J Neurooncol* **103,** 317–324 (2011).
10. http://www.magforce.de/en/home.html.
11. Blanco-Andujar, C. *et al.* Design of iron oxide-based nanoparticles for MRI and magnetic hyperthermia. *Nanomedicine (Lond)* **11,** 1889–1910 (2016).
12. Deatsch, A. E. & Evans, B. A. Heating efficiency in magnetic nanoparticle hyperthermia. *Journal of Magnetism and Magnetic Materials* **354,** 163–172 (2014).
13. Kolosnjaj-Tabi, J. *et al.* Heat-Generating Iron Oxide Nanocubes: Subtle 'Destructurators' of the Tumoral Microenvironment. *ACS Nano* **8,** 4268–4283 (2014).
14. Gazeau, F., Lévy, M. & Wilhelm, C. Optimizing magnetic nanoparticle design for nanothermotherapy. *Nanomedicine (Lond)* **3,** 831–844 (2008).
15. Daou, T. J. *et al.* Hydrothermal Synthesis of Monodisperse Magnetite Nanoparticles. *Chemistry of Materials* **18,** 4399–4404 (2006).
16. Santoyo Salazar, J. *et al.* Magnetic Iron Oxide Nanoparticles in 10−40 nm Range: Composition in Terms of Magnetite/Maghemite Ratio and Effect on the Magnetic Properties. *Chem. Mater.* **23,** 1379–1386 (2011).
17. Basly, B. *et al.* Effect of the nanoparticle synthesis method on dendronized iron oxides as MRI contrast agents. *Dalton Trans.* **42,** 2146–2157 (2013).
18. Guardia, P. *et al.* Water-Soluble Iron Oxide Nanocubes with High Values of Specific Absorption Rate for Cancer Cell Hyperthermia Treatment. *ACS Nano* **6,** 3080–3091 (2012).
19. Lartigue, L. *et al.* Cooperative Organization in Iron Oxide Multi-Core Nanoparticles Potentiates Their Efficiency as Heating Mediators and MRI Contrast Agents. *ACS Nano* 121129155806007 (2012). doi:10.1021/nn304477s
20. Kumar, C. S. S. R. & Mohammad, F. Magnetic nanomaterials for hyperthermia-based therapy and controlled drug delivery. *Adv. Drug Deliv. Rev.* **63,** 789–808 (2011).
21. Cabrera, D. *et al.* Unraveling viscosity effects on the hysteresis losses of magnetic nanocubes. *Nanoscale* **9,** 5094–5101 (2017).
22. Thanh, N. T. *Magnetic Nanoparticles: From Fabrication to Clinical Applications*. (CRC Press, 2012).
23. Rolland, O., Turrin, C.-O., Caminade, A.-M. & Majoral, J.-P. Dendrimers and nanomedicine: multivalency in action. *New J. Chem.* **33,** 1809–1824 (2009).
24. Cloninger, M. J. Biological applications of dendrimers. *Current Opinion in Chemical Biology* **6,** 742–748 (2002).
25. Stiriba, S.-E., Frey, H. & Haag, R. Dendritic polymers in biomedical applications: from potential to clinical use in diagnostics and therapy. *Angew. Chem. Int. Ed. Engl.* **41,** 1329–1334 (2002).
26. Duncan, R. & Izzo, L. Dendrimer biocompatibility and toxicity. *Adv. Drug Deliv. Rev.* **57,** 2215–2237 (2005).
27. Ghobril, C. *et al.* A bisphosphonate tweezers and clickable PEGylated PAMAM dendrons for the preparation of functional iron oxide nanoparticles displaying renal and hepatobiliary elimination. *Chem. Commun. (Camb.)* **49,** 9158–9160 (2013).
28. Basly, B. *et al.* Dendronized iron oxide nanoparticles as contrast agents for MRI. *Chem. Commun.* **46,** 985–987 (2010).
29. Lamanna, G. *et al.* Dendronized iron oxide nanoparticles for multimodal imaging. *Biomaterials* **32,** 8562–8573 (2011).
30. Chevallier, P. *et al.* Tailored biological retention and efficient clearance of pegylated ultra-small MnO nanoparticles as positive MRI contrast agents for molecular imaging. *Journal of Materials Chemistry B* **2,** 1779 (2014).
31. Walter, A. *et al.* Mastering the Shape and Composition of Dendronized Iron Oxide Nanoparticles To Tailor Magnetic Resonance Imaging and Hyperthermia. *Chem. Mater.* **26,** 5252–5264 (2014).
32. Walter, A. *et al.* Effect of the Functionalization Process on the Colloidal, Magnetic Resonance Imaging, and Bioelimination Properties of Mono- or Bisphosphonate-Anchored Dendronized Iron Oxide Nanoparticles. *ChemPlusChem* **82,** 647–659 (2017).
33. Teillet, J. & Varret, F. Unpublished MOSFIT program.

34. Baaziz, W. *et al.* Magnetic Iron Oxide Nanoparticles: Reproducible Tuning of the Size and Nanosized-Dependent Composition, Defects, and Spin Canting. *J. Phys. Chem. C* **118,** 3795–3810 (2014).

35. Kwon, S. G. *et al.* Kinetics of monodisperse iron oxide nanocrystal formation by 'heating-up' process. *J. Am. Chem. Soc.* **129,** 12571–12584 (2007).

36. Bronstein, L. M. *et al.* Influence of Iron Oleate Complex Structure on Iron Oxide Nanoparticle Formation. *Chem. Mater.* **19,** 3624–3632 (2007).

37. Hyeon, T., Lee, S. S., Park, J., Chung, Y. & Na, H. B. Synthesis of highly crystalline and monodisperse maghemite nanocrystallites without a size-selection process. *J. Am. Chem. Soc.* **123,** 12798–12801 (2001).

38. Walter, A. *et al.* Mastering the Shape and Composition of Dendronized Iron Oxide Nanoparticles To Tailor Magnetic Resonance Imaging and Hyperthermia. *Chem. Mater.* **26,** 5252–5264 (2014).

39. Lisiecki, I. & Pileni, M. P. Synthesis of Well-Defined and Low Size Distribution Cobalt Nanocrystals: The Limited Influence of Reverse Micelles. *Langmuir* **19,** 9486–9489 (2003).

40. Costanzo, S. PhD Thesis. (Université Pierre et Marie Curie, 2017).

41. Costanzo, S., Simon, G., Richardi, J., Colomban, P. & Lisiecki, I. Solvent Effects on Cobalt Nanocrystal Synthesis—A Facile Strategy To Control the Size of Co Nanocrystals. *J. Phys. Chem. C* **120,** 22054–22061 (2016).

42. Pichon, B. P. *et al.* Microstructural and Magnetic Investigations of Wüstite-Spinel Core-Shell Cubic-Shaped Nanoparticles. *Chem. Mater.* **23,** 2886–2900 (2011).

43. Wetterskog, E., Tai, C.-W., Grins, J., Bergström, L. & Salazar-Alvarez, G. Anomalous Magnetic Properties of Nanoparticles Arising from Defect Structures: Topotaxial Oxidation of $Fe_{1-x}O|Fe_{3-\delta}O_4$ Core|Shell Nanocubes to Single-Phase Particles. *ACS Nano* **7,** 7132–7144 (2013).

44. Daou, T. J. *et al.* Coupling Agent Effect on Magnetic Properties of Functionalized Magnetite-Based Nanoparticles. *Chemistry of Materials* **20,** 5869–5875 (2008).

45. Guardia, P. *et al.* One pot synthesis of monodisperse water soluble iron oxide nanocrystals with high values of specific absorption rate. *J. Mater. Chem. B* (2014). doi:10.1039/C4TB00061G

46. Wetterskog, E. *et al.* Precise control over shape and size of iron oxide nanocrystals suitable for assembly into ordered particle arrays. *Sci Technol Adv Mater* **15,** (2014).

47. Macdonald, J. E., Brooks, C. J. & Veinot, J. G. C. The influence of trace water concentration on iron oxide nanoparticle size. *Chem. Commun.* **0,** 3777–3779 (2008).

48. McCammon, C. A. & Liu, L. The effects of pressure and temperature on nonstoichiometric wüstite, FexO: The iron-rich phase boundary. *Phys Chem Minerals* **10,** 106–113 (1984).

49. Hai, H. T. *et al.* Size control and characterization of wustite (core)/spinel (shell) nanocubes obtained by decomposition of iron oleate complex. *Journal of Colloid and Interface Science* **346,** 37–42 (2010).

50. Yang, H., Ogawa, T., Hasegawa, D. & Takahashi, M. Synthesis and magnetic properties of monodisperse magnetite nanocubes. *Journal of Applied Physics* **103,** 07D526 (2008).

51. Kim, D. *et al.* Synthesis of Uniform Ferrimagnetic Magnetite Nanocubes. *Journal of the American Chemical Society* **131,** 454–455 (2009).

52. Walter, A. *et al.* Validation of a dendron concept to tune colloidal stability, MRI relaxivity and bioelimination of functional nanoparticles. *J. Mater. Chem. B* **3,** 1484–1494 (2015).

53. Walter, A. *et al.* Effect of the Functionalization Process on the Colloidal, Magnetic Resonance Imaging, and Bioelimination Properties of Mono- or Bisphosphonate-Anchored Dendronized Iron Oxide Nanoparticles. *ChemPlusChem* **82,** 647–659 (2017).

54. Walter, A. *et al.* Modulation of Relaxivity, Suspension Stability, and Biodistribution of Dendronized Iron Oxide Nanoparticles as a Function of the Organic Shell Design. *Part. Part. Syst. Charact.* **32,** 552–560 (2015).

55. Bordeianu, C. *et al.* How a grafting anchor tailors the cellular uptake and in vivo fate of dendronized iron oxide nanoparticles. *J. Mater. Chem. B* **5,** 5152–5164 (2017).

56. Daou, T. J. *et al.* Phosphate Adsorption Properties of Magnetite-Based Nanoparticles. *Chem. Mater.* **19,** 4494–4505 (2007).

57. Basly, B. *et al.* Effect of the nanoparticle synthesis method on dendronized iron oxides as MRI contrast agents. *Dalton Trans.* **42,** 2146–2157 (2013).

58. Polito, L. *et al.* Resolving the Structure of Ligands Bound to the Surface of Superparamagnetic Iron Oxide Nanoparticles by High-Resolution Magic-Angle Spinning NMR Spectroscopy. *Journal of the American Chemical Society* **130,** 12712–12724 (2008).

59. Mitra, A., Mohapatra, J., Meena, S. S., Tomy, C. V. & Aslam, M. Verwey Transition in Ultrasmall-Sized Octahedral Fe3O4 Nanoparticles. *J. Phys. Chem. C* **118,** 19356–19362 (2014).

60. Özdemir, Ö., Dunlop, D. J. & Berquó, T. S. Morin transition in hematite: Size dependence and thermal hysteresis. *Geochem. Geophys. Geosyst.* **9,** Q10Z01 (2008).

61. Bødker, F. & Mørup, S. Size dependence of the properties of hematite nanoparticles. *Europhys. Lett.* **52,** 217–223

62. Basly, B. *Conception et caractérisation de nano-objets magnétiques pour l'imagerie par résonance magnétique (IRM).* (Strasbourg, 2010).

63. Ortega, D., Kuznetsov, M. V., Morozov, Y. G., Belousova, O. V. & Parkin, I. P. Thermal relaxation and collective dynamics of interacting aerosol-generated hexagonal NiFe2O4 nanoparticles. *Phys. Chem. Chem. Phys.* **15,** 20830–20838 (2013).

64. Blanco-Andujar, C., Ortega, D., Southern, P., A. Pankhurst, Q. & K. Thanh, N. T. High performance multi-core iron oxide

nanoparticles for magnetic hyperthermia: microwave synthesis, and the role of core-to-core interactions. *Nanoscale* **7,** 1768–1775 (2015).

65. Kaur, M., McCloy, J. S., Jiang, W., Yao, Q. & Qiang, Y. Size Dependence of Inter- and Intracluster Interactions in Core–Shell Iron–Iron Oxide Nanoclusters. *J. Phys. Chem. C* **116,** 12875–12885 (2012).

66. Hwang, Y. *et al.* Exchange bias behavior of monodisperse Fe3O4/γ-Fe2O3 core/shell nanoparticles. *Current Applied Physics* **12,** 808–811 (2012).

67. Alves, T. M. de L. *et al.* Wasp-waisted behavior in magnetic hysteresis curves of CoFe2O4 nanopowder at a low temperature: experimental evidence and theoretical approach. *RSC Adv.* **7,** 22187–22196 (2017).

68. Martinez-Boubeta, C. *et al.* Learning from Nature to Improve the Heat Generation of Iron-Oxide Nanoparticles for Magnetic Hyperthermia Applications. *Sci. Rep.* **3,** (2013).

69. Mehdaoui, B. *et al.* Increase of magnetic hyperthermia efficiency due to dipolar interactions in low anisotropy magnetic nanoparticles : theoretical and experimental results. *Physical Review B* **87,** (2013).

70. Burrows, F. *et al.* Energy losses in interacting fine-particle magnetic composites. *J. Phys. D: Appl. Phys.* **43,** 474010 (2010).

71. Alphandéry, E., Faure, S., Seksek, O., Guyot, F. & Chebbi, I. Chains of Magnetosomes Extracted from AMB-1 Magnetotactic Bacteria for Application in Alternative Magnetic Field Cancer Therapy. *ACS Nano* **5,** 6279–6296 (2011).

72. Serantes, D. *et al.* Multiplying Magnetic Hyperthermia Response by Nanoparticle Assembling. *J. Phys. Chem. C* **118,** 5927–5934 (2014).

73. de la Presa, P. *et al.* Study of Heating Efficiency as a Function of Concentration, Size, and Applied Field in γ-Fe2O3 Nanoparticles. *J. Phys. Chem. C* **116,** 25602–25610 (2012).

74. Dennis, C. L. *et al.* Nearly complete regression of tumors via collective behavior of magnetic nanoparticles in hyperthermia. *Nanotechnology* **20,** 395103 (2009).

75. Dennis, C. L. *et al.* The influence of collective behavior on the magnetic and heating properties of iron oxide nanoparticles. *Journal of Applied Physics* **103,** 07A319 (2008).

76. De Toro, J. A. *et al.* Remanence Plots as a Probe of Spin Disorder in Magnetic Nanoparticles. *Chem. Mater.* **29,** 8258–8268 (2017).

Chapter VIII

Imaging capabilities of dendronized NPs with various anisotropic shapes as T_2 contrast agents

VIII Imaging capabilities of dendronized NPs with various anisotropic shapes as T2 contrast agents

VIII.1 Introduction

In previous chapters (VI & VII), we have synthesized iron oxide based NPs displaying different shapes and exhibiting different structural and magnetic properties. These NPs have been coated by dendron molecules and the resulting dendronized NPs were shown to display a good colloidal stability in water, except nanocubes which tend to aggregate (cf. Chapter VII). We are now interested in evaluating their cytotoxicity, their properties as T2 contrast agents and their in *vivo* biodistribution.

Indeed ultra-small iron oxide NPs have already been commercially used as T_2 contrast agent for MRI[1,2] and are of particular interest as biodegradable and non-toxic nano-objects compared to other contrast agents families (CAs). The saturation magnetization of NPs, their aggregation state and the ability of the coating to diffuse water molecules are important parameters to provide a good MRI contrast.[1–3] The size and composition of the NPs are important parameters that control the relaxivity values. The size effect on relaxivity has been studied by many groups[4–6] as commonly the higher is the NP size, the larger is the saturation magnetisation.[7] The NPs composition has also been tuned to obtain NPs with high Ms value.[8.]Yoon[9] established a diagram which gives the transverse relaxivity of different NPs according to their size, composition and saturation magnetization. Lee et al.[5] synthesized different ferrites MFe_2O_4 (with M = Fe, Co, Ni, Mn) and measured high relaxivities for manganese ferrite NPs due to their important magnetic moment. The highest M_s values were obtained with metal NPs covered with a natural oxide layer[10–12] or a ferrite layer[9]. Other parameters such as the shape[4,6,13.]or the aggregation state[14–18] can also greatly influence relaxivity values. Iron oxide NPs with cubic shape showed significant transverse relaxivity values.[19–21] Faceted NPs generally display higher relaxivity than the spherical NPs of similar size. The shape should affect the demagnetizing field, thus the anisotropy energy and consequently the relaxivity.

MRI properties of iron oxide NPs are not only influenced by the intrinsic magnetic properties of the magnetic core but also by the water molecules diffusion in the magnetic field gradient around the magnetic NPs. The nature of the NPs functionalization can thus affect the water molecules movement. Indeed, by its nature, the coating can exclude water molecules of the magnetic core or slow down their approach or on the contrary increase their residence time close to the magnetic core. Previous studies of our group demonstrated the pertinence of the use of a dendron molecule as coating agent to favour good water diffusion around the core as much as excellent colloidal stability and bio-distribution on 10 nm iron oxide spheres [22,23]

In that context, the objectives of this chapter are to assess the cytotoxicity, MRI properties and *in vivo* biodistribution of dendronized NPs displaying different shapes.

VIII.2 Experimental conditions

VIII.2.1 Granulometric measurements

The stability of the functionalized NPs suspensions was assessed using a nano-size MALVERN zetasizer. Particle size distributions in water, in 150 mM NaCl but also in 25 mM HEPES/150mM NaCl and PBS water solutions were assessed at pH 7.4.

VIII.2.2 Biological characterizations

Cell culture : Human hepatocarcinoma Huh7 cells were propagated in Dulbecco's modified Eagle's medium supplemented with 10% of decomplemented foetal bovine serum (FBS), 0,5% penicilin and 0,5 % non-essential amino acids.

MTT assay: The number of viable cells after dendronized NPs exposure was evaluated by the MTT (3-[4,5-methylthiazol-2-yl]- 2,5-diphenyl-tetrazolium bromide) assay. In brief, Huh7 cells (1.10^4 cells per well) were seeded in a 96-well plate and kept overnight for attachment. The next day, the medium was replaced with fresh medium with various concentrations of dendronized NPs diluted in complete culture medium and cells were allowed to grow for 24 h. After completion of incubation, the medium was discarded and well thoroughly washed with 200 µL of PBS in order to eliminate all remaining extracellular nanoparticles. 200 µL of cell culture medium + MTT ($0.5\ mg.mL^{-1}$) is added to each well and cells are incubated for further 3h30 at 37°C and 5% CO2. After completing the incubation, Medium is carefully discarded and 100 µl of DMSO was added to each well and incubated 15 min at room temperature under orbital shaking. Color developed after the reaction was measured at 550 nm using Xenius microplate reader (SAFAS, Monaco). Cell viability percentage was calculated as the ratio of mean absorbency of triplicate readings of sample wells (A_{sample}) compared to the mean absorbance of control wells ($A_{control}$). At each experiment DMSO was used as a negative control, A_{DMSO}, as shown in the following equation.

$$Cell\ viability\ = \frac{A_{sample} - A_{DMSO}}{A_{control} - A_{DMSO}} \times 100\%$$

VIII.2.3 MRI experiments

Relaxivity measurements. $\mathbf{T_1}$ and $\mathbf{T_2}$ relaxation time measurements of dendronized IONPs were performed on a Brucker Minispec 60 (Karlsruhe, Germany) working at a Larmor frequency of 60 MHz (1.41 T) at 37°C. The longitudinal ($\mathbf{r_1}$) and transverse ($\mathbf{r_2}$) relaxivity values were obtained according to the general equation of relaxivity $\mathbf{R = R_0 + r^*[CA]}$, where [CA] is the concentration of the contrast agent (CA) (i.e.) the concentration of Fe in IONPs, **R** is the relaxation rate (1/T) in the presence of the CA, $\mathbf{R_0}$ is the relaxation rate of the aqueous medium in the absence of the CA and **r** is the relaxivity value of the CA.

Nuclear Magnetic Resonance Dispersion (NMRD) profiles. Proton NMRD profiles were recorded using a Stelar Fast Field Cycling relaxometer (Mede, Italy). The system operates over a range of magnetic field extending from 0.25 mT to 0.94 T (0.01-40 MHz) at 37°C. T_1 and T_2 measurements were performed on a Bruker Minispec mq60 (Karlsrushe, Germany) working at a Larmor frequency of 60 MHz (1.41T) at 37°C.

Ghost images. Ghost images were acquired on a clinical MRI (GE Signa HDxt 3T) with a field of 3T. T_2 images were acquired with a spin echo sequence (TR=400 ms , TE=10 ms) and the T_2 images were acquired with a fast spin echo sequence (TR=2 ms, TE=52 ms).

VIII.2.4 *In vivo* experiments

Mice were anesthetized by inhalation of isoflurane vaporized in oxygen. The experiments were performed on a 400 MHz (9.4T) Bruker Biospec imaging system according the procedure accepted by the ethical committee of the center for microscopy and molecular imaging (project CMMI-2011-07). The contrast agent was injected intravenously at a dose of 45 µmol [Fe]/kg body weight to female CD-1 mice (5-10 weeks old, from Charles River Laboratories (France)). The signal intensity (SI) was measured in the regions of interest (ROIs) drawn on the liver and the bladder, and in an external reference tube. The SI enhancement (ΔSI%) was calculated according to the following equation, where SI_{post} =post- contrast and SI_{pre} = pre-contrast SI.

$$\Delta SI\% = \left| \frac{{}^{SI_{post}}\!/_{ref} - {}^{SI_{pre}}\!/_{ref}}{{}^{SI_{pre}}\!/_{ref}} \right| x100$$

VIII.3 Results

VIII.3.1 Effect of the shape of iron oxide NPs on the T_2 relaxivity

VIII.3.2.1 Structural and magnetic characterizations of NPs (summary)

Previously, the control of the precursor structure and of its interaction with different ligands has shown to be a powerful method to synthesize NPs with various shapes. Transmission electron microscopy (TEM) images of the spheres, cubes, octopods and plates are shown in Figure VIII.1. A mean size of 22.2 nm (± 8%) was measured for the spherical NPs (named NS22), 14.5 nm (± 11%) for the nanocubes (named NC), 27.8 nm (± 15%) for the octopod shaped NPs (named NO28) and finally a length and thickness of respectively 20 (± 35%) and 5,7 (± 28%) nm were obtained for the plate shaped NPs (named NPl).

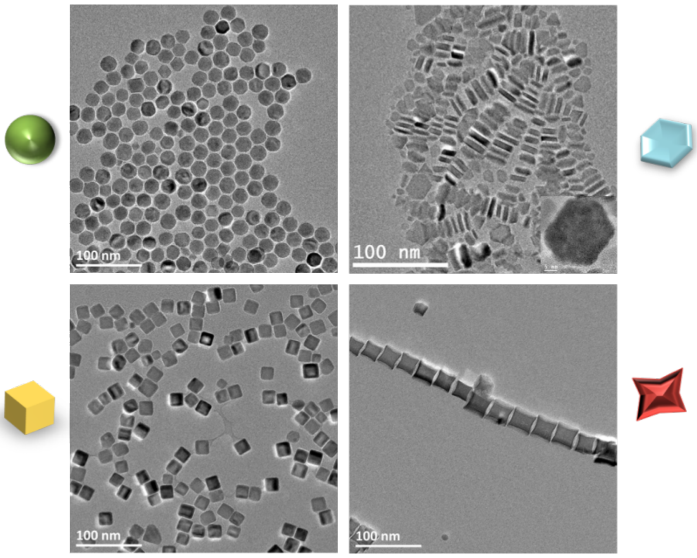

Figure VIII.1 - TEM images of a) NS22, b) NPl, c) cubes and d) NO28

The composition of NPs was determined by combining XRD analysis and IR and Mössbauer spectroscopies. Indeed magnetite Fe_3O_4 can be easily oxidized into maghemite Fe_2O_3 at the nanoscale and they display similar XRD or SAED diffractograms. Different characterization techniques have to be combined to better ascertain the composition.[7] By XRD, the lattice parameter of synthesized NPs determined from XRD pattern is compared to those of stoichiometric magnetite Fe_3O_4 (0.8396 nm, JCPDS file 19-629) and maghemite γ-Fe_2O_3 (0.8346 nm, JCPDS file 39-1346) phases. IR spectroscopy is also well adapted as the magnetite displays a single broad band located at 580-590 cm^{-1} and a shoulder at about 700 cm^{-1} attributed to surface oxidation, while the maghemite phase displays several bands between 800-400 cm^{-1} whose number and resolutions depend on the structural order of vacancies in maghemite.[24,25] The most adapted characterization technique to ascertain the composition of spinel iron oxide is Mössbauer spectroscopy[7,26]. The NPs have already been characterized by these characterization techniques in Chapter VII and we remind here the main results. Table VIII.1 gives the lattice parameters calculated for all the NPs.

Table VIII.1 – Main structural parameters of the different shaped NPs deduced from characterization techniques

NPs	Mean TEM size (nm)	Crystallites size (nm)	Lattice parameter (Å)		Composition
			Spinel phase	Wüstite phase	
NS22	22.2 ± 1.8	13	8.391	X	$Fe_{3-x}O_4$
NC	14.5 ± 1.6	8	8.392	4.237	$FeO@Fe_{3-x}O_4$
NO28	27.8 ± 4.2	25 <400> /23 <511>	8.370	X	$Fe_{3-x}O_4$
NPl	16.7 ± 5.2	17 <222>	8.384	X	$Fe_{3-x}O_4$

All the NPs synthesized present a spinel structure more or less close to magnetite except the nanocubes which consist in a core of wüstite FeO and a shell of magnetite. The crystallite size has been found to be lower than the size determined in TEM images for nanospheres due to a spinel composition resulting from an oxidation of the FeO phase which is the composition of the first nucleates. For octopods (NO) and nanoplates (NPl), the crystallite size is strongly dependant on the crystallographic directions. For NPl, a crystallite size of 20 nm has been found along the <222> direction confirming that this morphology is composed of a single crystallographic domain. For octopods NO28, the direction presenting the biggest crystallite size is dependent on the size with a crystallite size of 25 nm along <400> and 23 nm <511>. The fact that the crystallite size relies on the crystallographic direction is in favour of a proper anisotropy of the NP.

The saturation magnetisation σ_s of the NPs is one of the major parameter for their used as MRI contrast agent and the ranking in σ_s is the following NO28 $\geq$ NS22 $\geq$ NPs17. The σ_s for nanocubes is difficult to calculate because they are core-shell with an antiferromagnetic core.

VIII.3.2.2 Colloidal stability

After the grafting step, the colloidal stability has been evaluated by Dynamic Light Scattering (DLS). Colloidal stability was not only checked in water but also in several physiological relevant media such as NaCl, NaCl/HEPES and PBS (Figure VIII.2). Dendronized NS present no sign of aggregation whatever the media with a monomodal hydrodynamic size distribution varying with the media. The mean hydrodynamic size in water of dendronized NS is about 28 nm, larger than the TEM size of NPs of about 22 nm but considering the dendron coating (thickness of 1.5-2 nm) and the solvatation layer, no aggregation is noticed after the dendronisation step.

For the other shaped NPs, this measurement is an indication of a possible aggregation but cannot be considered as a precise measurement of the hydrodynamic diameter. The optical model used to calculate the size distribution considers spherical NPs. Anisotropic NC, NO and NPl may be present in front of the laser under different orientations that can be longer than the edge length or the diameter. Therefore, the values of hydrodynamic diameter are just given for comparison and cannot be considered as relevant. All the mean hydrodynamic sizes are listed in Table VIII.2. Dendronized NO present a monomodal distribution in water centred at 32 nm. In physiological media, a very small agregation is evidenced by the appearance of a low second population above 100 nm. Nevertheless the size distribution may be considered as mainly monomodal.

With dendronized NPl, a bimodal size distribution is noticed but may be ascribed to the anisotropic shape of NPl which exhibit an aspect ratio = L/t of 4. The main DLS peak may be observed constant in physiological media and thus the dendronized NPls exhibit a quite good colloidal stability in physiological media.

Dendronized nanocubes display in water a multimodal size distribution with a main DLS peak around 38 nm exhibiting a small shoulder at 150 nm and another peak at 5000 cm^{-1}. The dendronization of nanocubes has already been evidenced as a delicate step and it explains the observed aggregation. Nevertheless one may notice that the colloidal stability in physiological media is quite similar to that in water.

For in vivo experiments, all the suspensions were filtrated to remove large aggregates.

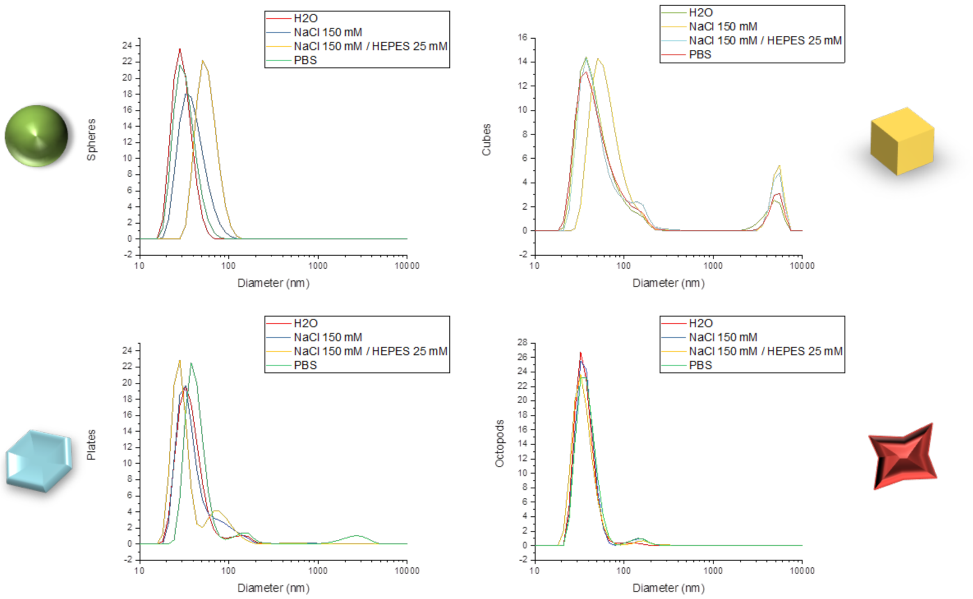

Figure VIII.2- DLS measurements of the different shapes in water (red), NaCl 150 mM (blue), NaCl 150 mM/HEPES 25 mM (yellow) and PBS (green).

Table VIII.2 – Main hydrodynamic diameters of the NPs in various media.

	Mean hydrodynamic diameter (nm)			
Shape	H_2O	NaCl 150 mM	NaCl 150 mM / HEPES 25 mM	PBS
NS	28	35	51	28
NC	38	50	38	38
	5500	5000	5000	5000
NO	32	35	32	34
	X	150	160	150
NPl	32	32	28	38
	150	X	74	150

VIII.3.2.3 Relaxivity/contrast enhancement properties for MRI

VIII.3.2.3.1 Relaxivity measurements

Relaxivity measurements were performed in the Laboratory of Pr. Sophie Laurent in Mons for all dendronized shapes at 0.41 T (20 MHz), 1.47 T (60 MHz) and 7.04 T (300 MHz). The longitudinal r_1 and transverse r_2 relaxivities are given in Table VIII.3.

A good T_2 contrast agent shall display high r_2 and r_2/r_1 values[3]. Compared to a commercial product and 10 nm spheres from a previous study, all the shapes presented very high transversal relaxivities (with a r_2 at least 2.8 times higher at 0.41T) which were not only due to their larger mean hydrodynamic sizes.

For all samples, there was an evolution in r_2 values with increasing field in agreement with the observation of Gillis that demonstrated that r_2 evolution with the field should increase linearly until a plateau when the saturation magnetization is reached.[27] The r_2 and r_2/r_1 values showed that the NPs with different shapes are already efficient at the lowest field (0.41 T). The r_2 values were ranked in the following NO, NS and NPl in agreement with the ranking of their saturation magnetization.

NS22 and NO28, which display similar σs, present quite the same r_2 and the r_1 value of octopods is slightly lower making their ratio slightly higher (except for 1.4 T). The similarity in the r_2 values was explained with their close saturation magnetization and the difference in the r_1 value was explained by the difference in the structural composition. Indeed octopods displayed an original shape and presented different crystallographic planes on their surface. The lower r2 and r2/r1 values of NPl by comparison with other NPs may be related to their lower saturation magnetization. Nevertheless, these values are quite similar to those of the commercial product (RESOVIST).

At 37 °C			Relaxivity at 0.41 T			Relaxivity at 1.47 T			Relaxivity at 7.04 T		
	TEM (nm)	DLS (nm)	r_1 (s^{-1} mM$^{-1)}$	r_2 (s^{-1} mM$^{-1)}$	r_2 /r_1	r_1 (s^{-1} mM$^{-1)}$	r_2 (s^{-1} mM$^{-1)}$	r_2/r_1	r_1 (s^{-1} mM$^{-1)}$	r_2 (s^{-1} mM$^{-1)}$	r_2/r_1
Resovist	3-5	62	25.4	151	5.9	9.7	189	19.5	ND	ND	ND
NS10*	10	18	31	76	2.5	13	78	6	ND	ND	ND
NS22	22	28	42	298	7	10	303	32	0.6	300	515
NC	15	38	41	356	9	11	332	30	0.8	309	487
NPl	20	32	43	212	5	13	198	15	1.1	186	169
NO28	28	32	42.5	306	7.2	8	274	34	0.5	295	590
Cubes16*	16	74	13	113	8.6	5	116	23	4.1	226	55
Cubes16ox	16	42	24	201	8.4	8	221	27	7.1	509	71.8

Table VIII.3 - *Relaxivity values of all T_2 dendronized NPs at 0.41, 1.47 and 7.04* T (*Values from Walter and al[28])

The values for NC were very high contrarily to the one measured in a previous study[28]. This may be explained by a higher saturation magnetization. This was probably due to the oxidation of the sample with time. This hypothesis is confirmed by relaxivities measurement realized in Strasbourg on the same sample (before sending it to Mons) that presented a much lower r_2 value (Table VIII.4).

Table VIII.4 – Relaxivity measurements realized in Strasbourg at 1.47T

At 37 °C			Relaxivity at 1.47 T		
	TEM (nm)	DLS (nm)	r_1 (s^{-1} mM$^{-1)}$	r_2 (s^{-1} mM$^{-1)}$	r_2/r_1
NS18	17.9	35	12.2	189.2	15.5
NC	14.5	90	5	138	27.6
NPl	20	25	15	265	17.7
NO18	17.2	51	16.9	405.5	24

The nanoplates values measured in Strasbourg are in agreement with the one of Mons. NS18 and NO18 were also measured in Strasbourg. NS18 presented a lower r_2 value in agreement with a lower saturation magnetization by comparison with NS22 (and the observation of Smolensky[4]).

NO18 presented a larger value than NO28. We believed that it is due to a tip (elongated corner) effect more important for NO18 than for NO28. Indeed the tip/corner represents a higher part of the volume for NO18 and may introduce a higher local magnetic heterogeneity favourable for enhancing the relaxivity[29].

It is now admitted that relaxivity values can be optimised by varying NP shape[4–6]. Saturation magnetisation is directly influenced by the effective particle anisotropy, which will vary by the addition of shape anisotropy. This was observed by Joshi *et al*[6] and Smolenski *et al.*[4] when they compared spherical and faceted NPs, leading in both cases to higher values of relaxivity for faceted NPs. Similarly, cubic iron oxide NPs (r_2 = 761 $mM^{-1}.s^{-1}$ at 3 T)[20], as well as octopod IONPs (edge length of 30 nm) (r_2 = 679.3 ± 30 $mM^{-1}.s^{-1}$ at 7 T) exhibited significant transverse relaxivity values (Table VIII.5)[30]. At the same time, shape and composition can be simultaneously tuned to achieve an enhanced effect on relaxivity. This was recently reported with single core and core-shell cobalt ferrite nanocubes -exhibiting spring magnet behaviour- with maximum relaxivity found with concave-like nanocubes- (r_2 = 958 $mM^{-1}.s^{-1}$ at 1.5 T)[31]. Table VIII.5 listed several relaxivity values for various shapes with their organic coating reported in literature. NO28 presented a close value to the one reported for homogenous octopods[30]. NPl are in agreement with the report of Zhou[32]. This confirmed that an increase of the thickness would help to boost the properties of the NPl. NC even oxidized (Mons experiments) remain below the reported values.

Table VIII.5 - Values of r_2 for different iron oxide shapes from literature

Type	*Magnetic core*	*Coating*	*D_{TEM} (nm)*	*D_H (nm)*	*M_S (emu.g^{-1})*	*r_2 (mM^{-1} s^{-1})*	*B (T)*	*Ref.*
NPs clusters/aggregates	*Fe_3O_4*	*PVP*	*7.6-65.3*	*30-120*	*ND*	*174-249*	*7*	33
	Fe_3O_4	*pH-sensitive hydrogel*	*45-79*	*53-94*	*62*	*245-416*	*3*	16
	Fe_3O_4	*PEI-PCL-PEG polymer*	*9.1*	*51-141*	*ND*	*256-289*	*1.41*	14
	Fe_3O_4	*DMSA*	*3.8-14.2*	*50-70*	*32-82*	*84-204*	*1.5*	17
	Fe_3O_4	*Citrate*	*19.7-28.8*	*11-15.6*	*65.4-81.8*	*365*	*9.25*	18
Nanocubes	*Iron oxide*	*PEG phospholipid*	*57.8*		*132.1*	*324*	*1.5*	21
	Iron oxide	*PEG phospholipid*	*22*	*43*	*130*	*761*	*3*	20
	$Co_{0.5}Fe_{1.5}O_4$	*PMAO*	*20*		*~60*	*958*	*1.5*	31
Octopods	*Iron oxide*	*HAD-G2*	*30*	*58*	*71*	*679*	*7*	30
	Iron oxide coreshell	*DMSA*	*30*	*ND*	*42.9*	*224.37*	*0.5*	34
Nanoplates	*Iron oxide*	*DMSA*	*20*	*ND*	*44.9*	*<100*	*0.5*	34
	Iron oxide	*DMSA*	*8.8-2.8 (thickness)*	*ND*	*74.1-34.5*	*311.88-78.63*	*0.5*	32

VIII.3.2.3.2 Nuclear magnetic resonance dispersion profiles

The nuclear magnetic resonance dispersion (NMRD) profiles have been recorded for all the shapes. This technique gives the relaxivity evolution with respect to the external magnetic field. The profiles are represented in Figure VIII.3. NC and NPl present the typical profiles expected for superparamagnetic NPs. The relaxivities of NPl are low compared to those of NC despite the possible influence of the non-magnetic $Fe_{1-x}O$ core for NC. The value of the r_1 maxima is lower for NPl than for NC.

NS22 and NO28 present a different behaviour. The bump observed around 1-3 MHz for NC and NPl disappeared. The position of this bump is dependent on the size of the NPs. The profile of the NS can be explained thanks to their size (22 nm) and some aggregation under the applied magnetic field. The NO profile presents increasing and high relaxivities at low field. This is not explained by the NMRD theory. Indeed, this theory was developed for symetrical systems. Moreover at low field, anisotropy energy controls the behaviour. As NO are highly anisotropic, this may explain the high relaxivities values. Unfortunately, no theoretical model was developed for such kind of structures at this day. Main hypothesis could be that octopods align during the measurements increasing thus their anisotropy but another hypothesis could be that their peculiar shape with elongated corners induces local magnetic field heterogeneities which affect positively relaxivity values. The NMRD of smaller octopods (17 nm ± 12%) (Figure VIII.3 right) is in agreement with this theory.

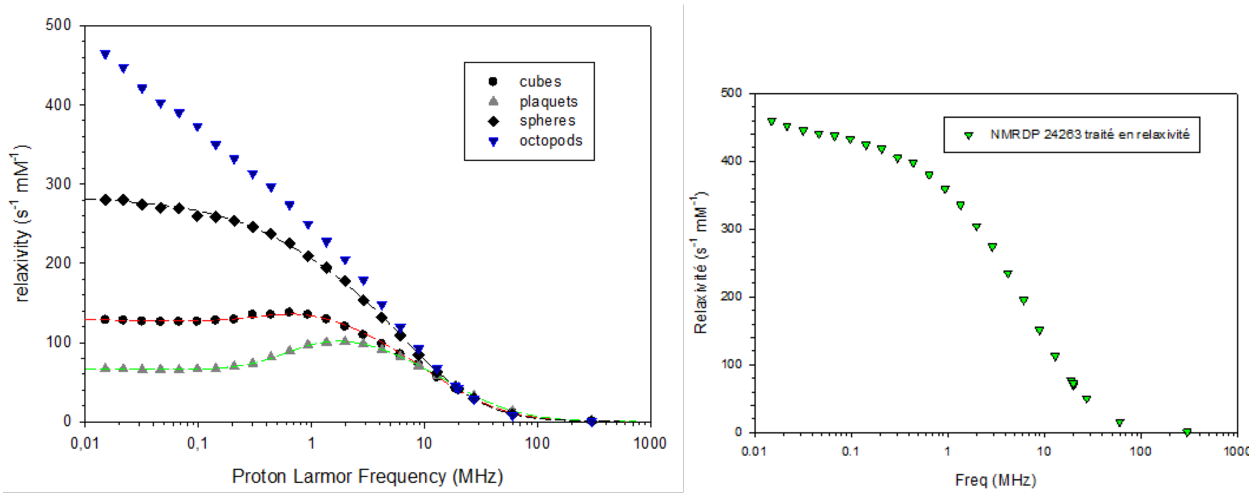

Figure VIII.3 - NMRD profiles of the different shaped NPs (left) and NO17 (right)

The fitting of NMRD curve can only be done on spherical NPs, NS22, as the usual model is assuming a spherical shape of the particles. The fitting gives a D_{NMRD} (nm) = 23.4 nm very close to the TEM diameter meaning that water molecules diffuse quite close to the magnetic core and the M_S^{NMRD} is about 48 emu/g Fe_3O_4 ($A.m^2.Kg^{-1}$).

VIII.3.2.3.3 Ghost images

Ghost images of the different suspension of NPs were acquired on a MRI apparatus with a field of 3T at room temperature. These acquisitions allow a visual assessment of the contrast enhancement and the determination of the Enhancement Contrast Ratio (EHC). The EHC permits to better determine the extinction of the signal in order to compare the different shapes. EHC is defined as follows:

$$EHC_{sample} = \frac{S_{sample} - S_{water}}{S_{water}} x100$$

With S_{sample} and S_{water} the intensity of the sample and water respectively. T_1 and T_2 weighted ghost images and EHC evolution are given in Figures VIII.4&5.

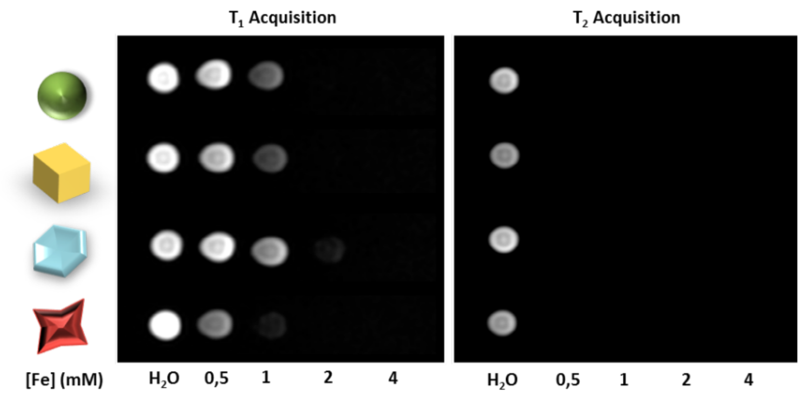

Figure VIII.4 - Ghost images at 3T, T_1 acquisition (left) and T_2 acquisition (right)

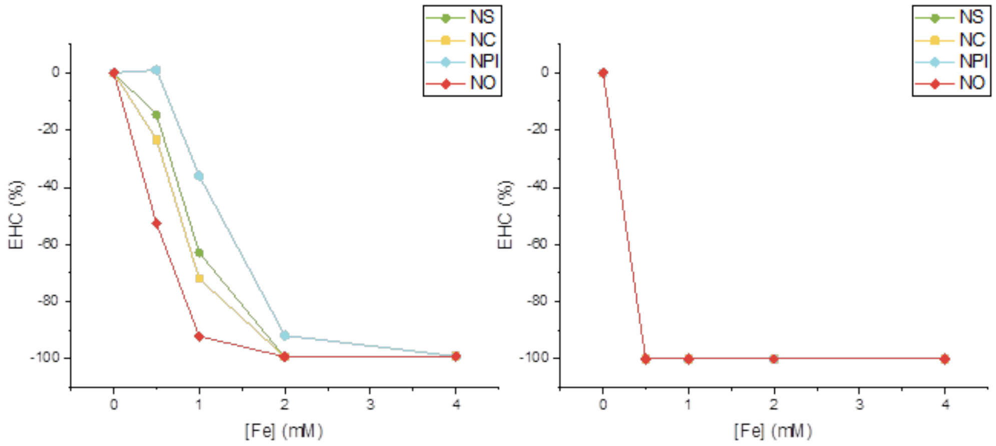

FigureVIII.5 - EHC evolution with the concentration in iron for the T_1 (left) and T_2 (right) acquisition

Ghost images performed at 3T confirmed a strong T2 behaviour for all shapes as seen with the previous relaxivities measurements. T_2 weighted ghost images showed a massive hypo-contrast already at low concentration. T_{2w} EHC indicates that, for all shapes, the extinction was complete (-100 %) with the smaller concentration used of 0.5 mM in iron. T_{1w} acquisitions presented a difference of behaviour between the shapes. An evolution was observed with the concentration and was shape dependent. At low concentration (0.5 mM), NO presented the highest hyposignal (-52.7 %). NC (-23.3 %) and NS (-14.6 %) were intermediate. But NPl presented a weak hypersignal (+0.95). This was explained by the large (111) surface exposed by NPl. Indeed, these surfaces were Fe rich thus promoting a T_1 relaxation. But in T_{1w} acquisitions the transversal relaxivity cannot be completely neglected for IONPs. There's a competition between both relaxations and when the concentration increases the tranversal relaxation takes over and the extinction is observed. Afterwards, with an increasing iron concentration, the T_{1w} EHC dropped for all morphologies while keeping the same trend. By 2 mM, all shapes except NPl (-91.8%) were extinct. The extinction for all shapes is complete at 4 mM.

VIII.3.2.4 Biological studies

VIII.3.2.4.1 Cytotoxicity test

The cytotoxicity of the NPs was assessed by MTT assay on Huh7, an hepatocarcinoma cell line. Huh7 Cells at 70 % confluence were incubated with NPs diluted in complete cell culture media for 24 h at 37 °C. After this incubation time, the cell viability is determined (Figure VIII.6). The four shapes do not present any sign of cytotoxicity up to 440 mg/L. At 880 mg/L a difference can be seen between the shapes. An acute cell toxicity with a drop of cell viability below 30 % is observed for all shapes except NO for whom a survival rate of 50 % is measured. Yet the cytotoxicity test was performed using dilute solution of NPs at the beginning. This implied that for 880 mg/L, the complete cell culture media contained NPs but also a large amount of water. Thus, this experiment should be reproduced to confirm the cytoxicity between 440 and 880 mg/L or higher.

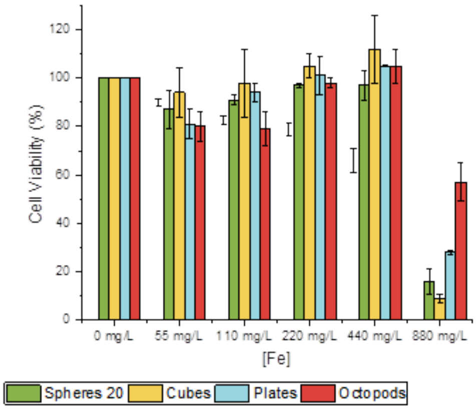

Figure VIII.6 - Cell viability of Huh-7 cell monolayer in regard of the different shapes, spheres (green), cubes (yellow), plates (blue) and octopods (red)

VIII.3.2.5 Preliminary In vivo bio-distribution by MRI

The bio-distribution of the different shapes was followed with MRI and was performed by Sebatien Boutry in the Center for Microscopy and Molecular Imaging in Gosselies (Belgium).

Mice were imaged before and after intravenous injection at different times after the injection (15 min, 45 min, 1h30, 2h20, 3h) and after 24 h. Three mices per shape were imaged. They were then sacrificed and their organs harvested for iron titration. Three mices were also injected and sacrificed 4 h after the injection (but not imaged) to get an insight of iron distribution close to the injection. In vivo MR images of mice with slightly T_2 weighted coronal spin echo sequence for liver (TR = 2000 ms, TE = 17 ms) and T_2 weighted axial spin echo sequence for urinary bladder (TR = 7726 ms, TE = 52 ms) are given in Figure VIII.10 and VIII.11 respectively. The ΔSI evolutions measured in the liver and the bladder were given in Figure VIII.7 and the evolutions in the renal pelvis and the bladder were given in Figure VIII.8. We observed a strong signal decrease in the liver already 15 min after the injection for all shapes, which was confirmed with the ΔSI measurement. The signal in the liver slightly varied afterwards but remained strongly attenuated. This indicated a capture of the NPs by the liver. On the opposite, the evolution of the ΔSI in the bladder suggested elimination through urinary pathway during the first 3h for all shapes except NPl. This was in agreement by the comparison of the evolution of the ΔSI between the renal pelvis and the bladder (Figure VIII.8)**.** Yet the error was quite important in the renal pelvis.

ICP-MS titration on harvested organs allowed measuring the amount of iron in various organs (liver, kidneys, lungs and bone marrow). The spleen was also measured but too large variation including in the control did not allow concluding on this organ. Figure VIII.9 represented the mean amount of iron titrated for each shape in each organ at 4 and 24h. The titration showed that no NPs seem to have ended up in the kidneys, bone marrow and lungs. The values measured in the liver at 4h show no capture except maybe for the octopods. At 24 h, all shapes seemed to have been captured in some extent by the liver except the NPl. Yet the injected value of 45 µmol/kg body weight corresponds to 2.5 mg/kg body weight of iron. To give an order of idea, the mean mass of a mice is between 25 and 30 g. The difference of iron measured in the liver of injected mice with control mice is thus higher compared to what has been injected in the whole body. Combined to the fact that we see elimination through urines led us to think that there might have been little liver capture but as the T_2 effect is strong with all the shapes the little amount induced a strong contrast constant with time. Few samples of urine were collected and confirmed a strong urinary elimination yet the number of samples being too low no statistic could be done.

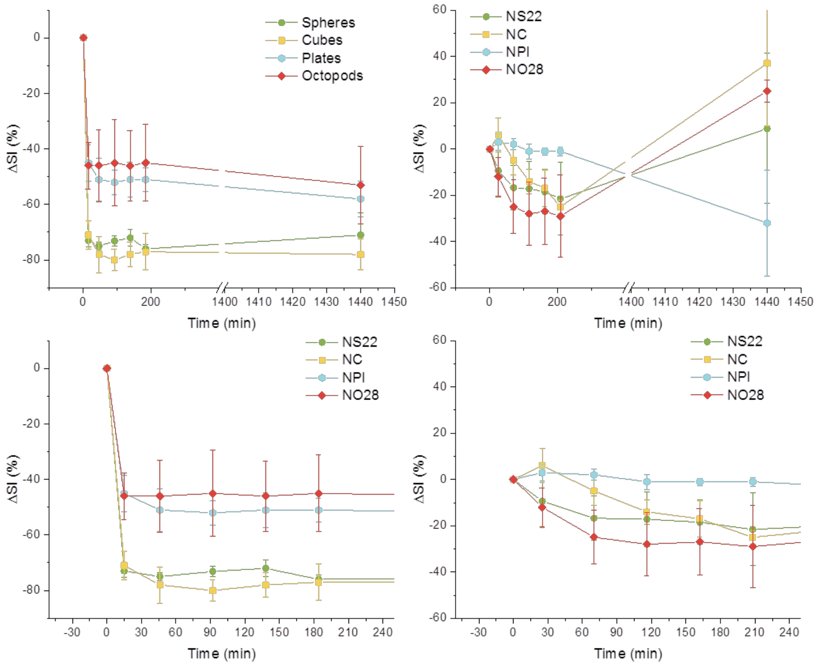

Figure VIII.7 – ΔSI variation in the liver (left) and the bladder (right), bottom line is a zoom in the beginning

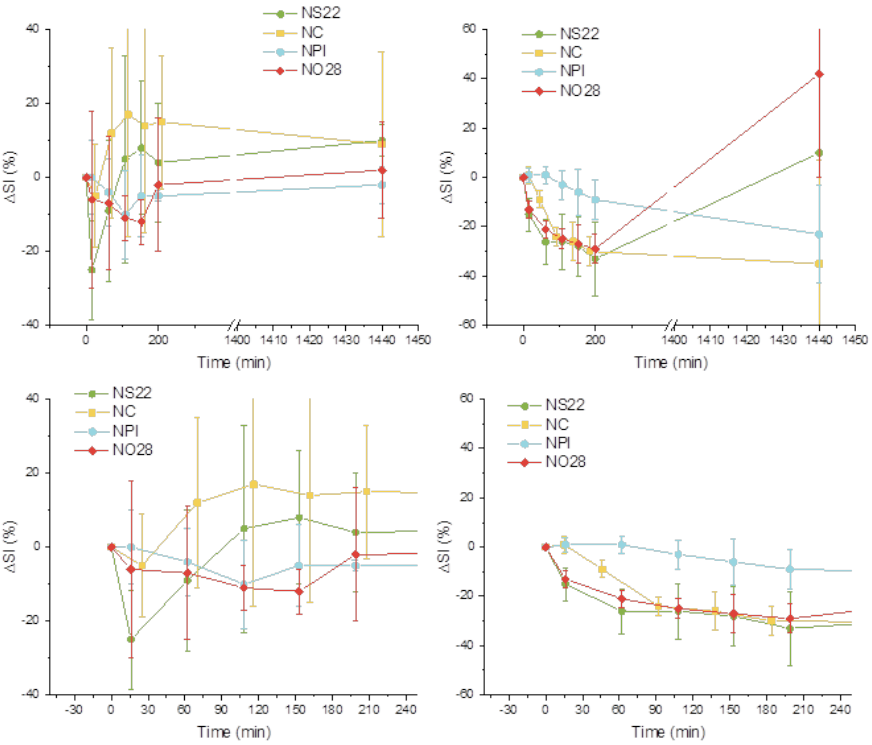

Figure VIII.8 - ΔSI variation in the renal pelvis (left) and the bladder (right), bottom line is a zoom in the beginning

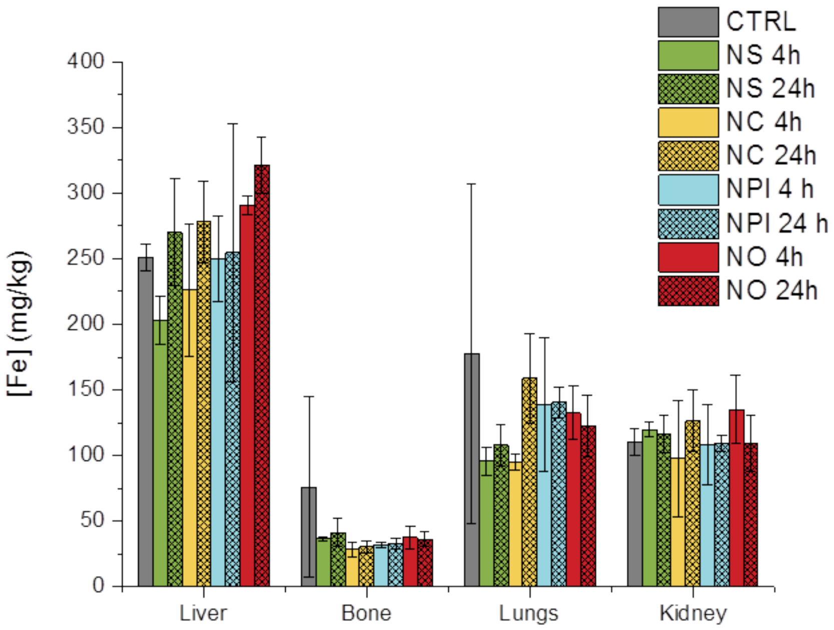

Figure VIII.9 - ICP-MS iron titration in various organs

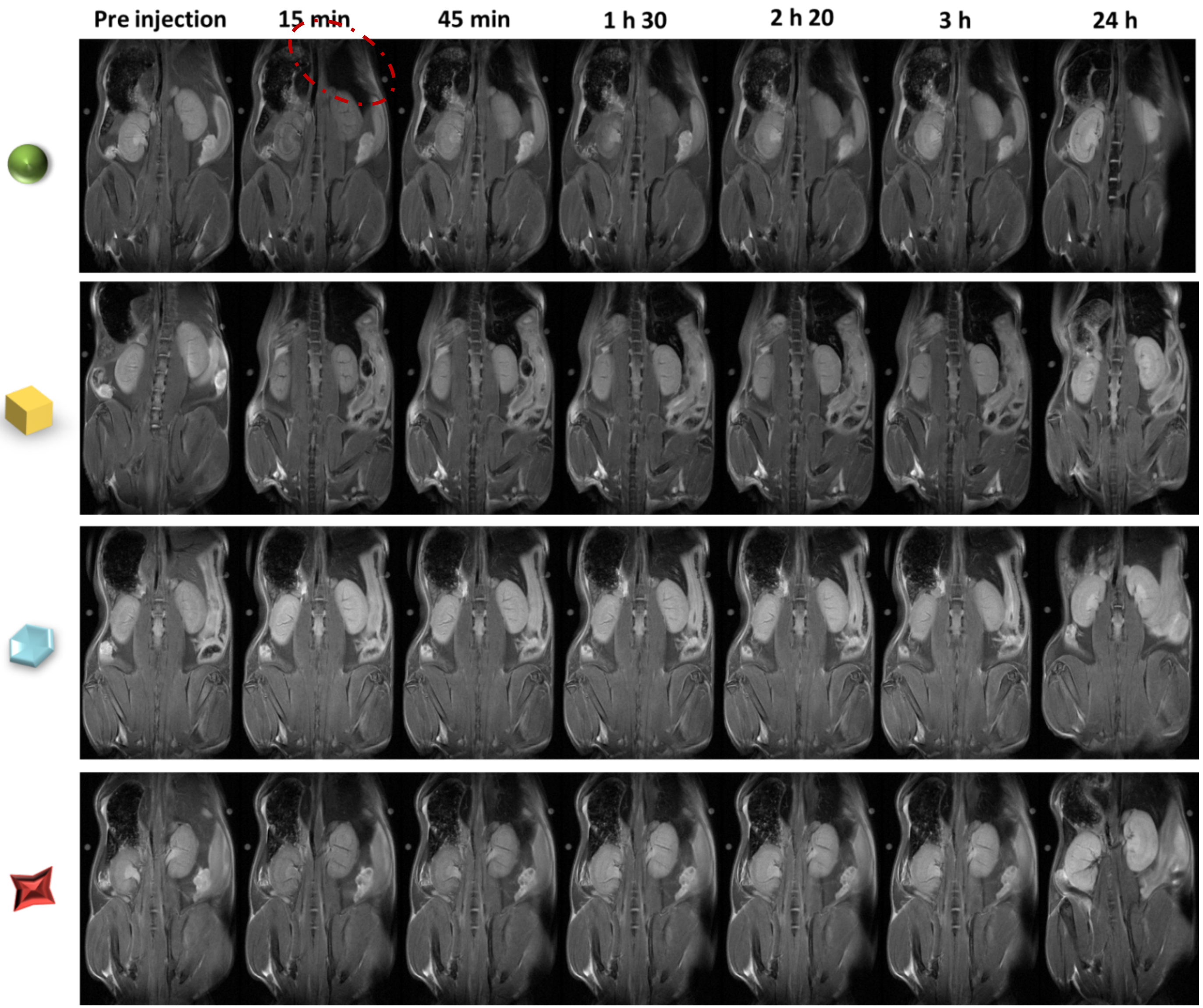

Figure VIII.10 - T_2 weighted with a spin echo sequence (TR= 2000 ms, TE = 17 ms), red circle for liver

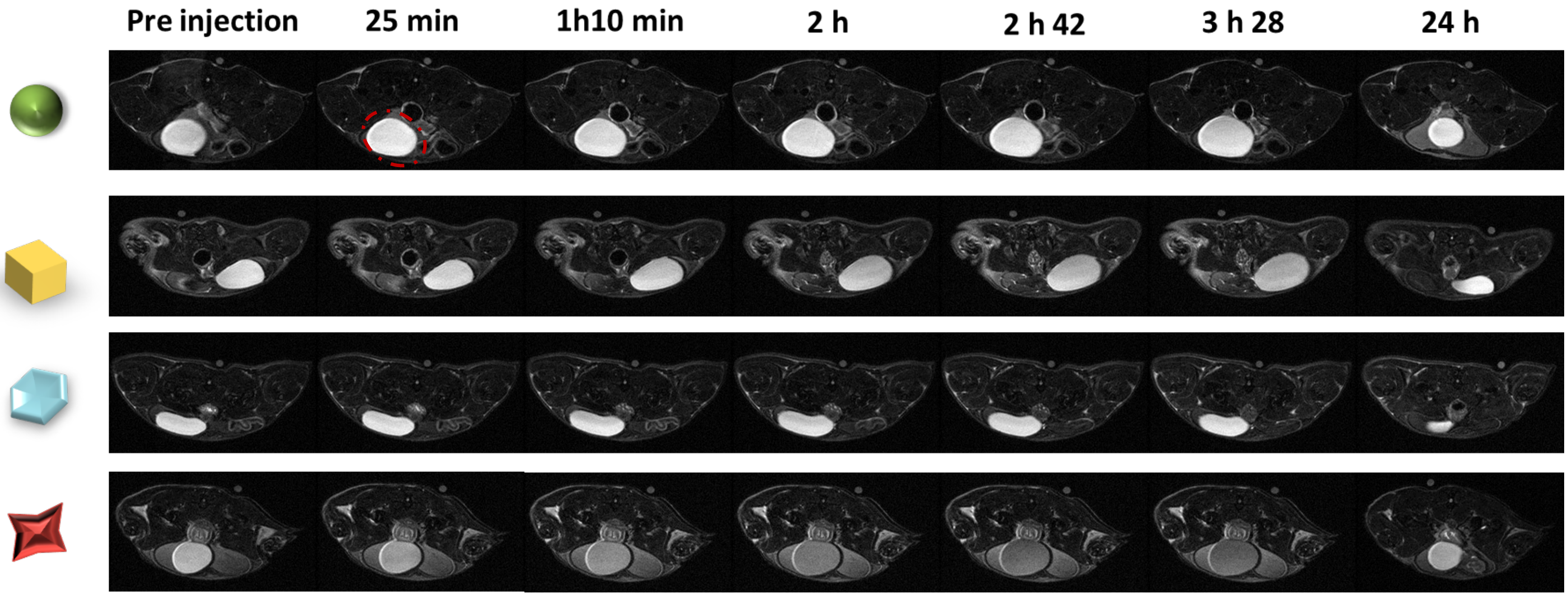

Figure VIII.11 - T_2 weighted with an axial sequence (TR = 7726 ms, TE =52 ms), the red circle the bladder

VIII.3 Conclusion

In this work, we demonstrated that the four dendronized shaped NPs present a good colloidal stability in physiological media although a slight and limited aggregation of nanocubes was observed. They display all good T_2 MRI contrast agent properties however it was clearly shown that the shape had an influence on the measured T_2 relaxivity values.

The octopod morphology presented high relaxivity values as reported in literature yet the size is major as NO18 present higher properties than NO28. We believe that it may be due to the shape with tip/elongated corner which may induce local magnetic field heterogeneity or favour alignment of octopods in chain increasing their anisotropy. Yet NO28 presented very good T_2 CA properties.

Plates did present an interesting behaviour with a slight T_1 effect detected on ghost images at low concentration due to the large iron rich surfaces it present. Though this effect disappears when the concentration increases and T_2 effect becomes majority.

An *in vivo* biodistribution was performed by MRI showing the suitability of dendronized shaped NPs as *in vivo* contrast agent for MRI. Urinary and hepato-biliary elimination pathways were observed though some NPs accumulated in the liver. Nevertheless, we are not sure if the size or the shape is responsible and Further investigations are required to confirm these experiments and to determine if the NPs size and/or the shape may be optimized to limite the liver captation.

REFERENCES

1. Laurent, S. *et al.* Magnetic Iron Oxide Nanoparticles: Synthesis, Stabilization, Vectorization, Physicochemical Characterizations, and Biological Applications. *Chemical Reviews* **108,** 2064–2110 (2008).
2. Na, H. B., Song, I. C. & Hyeon, T. Inorganic Nanoparticles for MRI Contrast Agents. *Advanced Materials* **21,** 2133–2148 (2009).
3. Blanco-Andujar, C. *et al.* Design of iron oxide-based nanoparticles for MRI and magnetic hyperthermia. *Nanomedicine (Lond)* **11,** 1889–1910 (2016).
4. Smolensky, E. D. *et al.* Scaling laws at the nanosize: the effect of particle size and shape on the magnetism and relaxivity of iron oxide nanoparticle contrast agents. *Journal of Materials Chemistry B* **1,** 2818 (2013).
5. Lee, J.-H. *et al.* Artificially engineered magnetic nanoparticles for ultra-sensitive molecular imaging. *Nat Med* **13,** 95–99 (2007).
6. Joshi, H. M. *et al.* Effects of shape and size of cobalt ferrite nanostructures on their MRI contrast and thermal activation. *J Phys Chem C Nanomater Interfaces* **113,** 17761–17767 (2009).
7. Baaziz, W. *et al.* Magnetic Iron Oxide Nanoparticles: Reproducible Tuning of the Size and Nanosized-Dependent Composition, Defects, and Spin Canting. *J. Phys. Chem. C* **118,** 3795–3810 (2014).
8. Wang, W. *et al.* Size and Compositional Effects on Contrast Efficiency of Functionalized Superparamagnetic Nanoparticles at Ultralow and Ultrahigh Magnetic Fields. *J. Phys. Chem. C* **116,** 17880–17884 (2012).
9. Yoon, T.-J., Lee, H., Shao, H. & Weissleder, R. Highly magnetic core-shell nanoparticles with unique magnetization mechanism. *Angew Chem Int Ed Engl* **50,** 4663–4666 (2011).
10. Cheong, S. *et al.* Simple Synthesis and Functionalization of Iron Nanoparticles for Magnetic Resonance Imaging. *Angew. Chem. Int. Ed.* **50,** 4206–4209 (2011).
11. Lacroix, L.-M. *et al.* Stable single-crystalline body centered cubic Fe nanoparticles. *Nano Lett.* **11,** 1641–1645 (2011).
12. Khurshid, H. *et al.* Core/shell structured iron/iron-oxide nanoparticles as excellent MRI contrast enhancement agents. *Journal of Magnetism and Magnetic Materials* **331,** 17–20 (2013).
13. de Montferrand, C. *et al.* Iron oxide nanoparticles with sizes, shapes and compositions resulting in different magnetization signatures as potential labels for multiparametric detection. *Acta Biomaterialia* **9,** 6150–6157 (2013).
14. Pöselt, E. *et al.* Relaxivity optimization of a PEGylated iron-oxide-based negative magnetic resonance contrast agent for T_2-weighted spin-echo imaging. *ACS Nano* **6,** 1619–1624 (2012).
15. Saha, I. *et al.* pH-Sensitive MR Responses Induced by Dendron-Functionalized SPIONs. *J Phys Chem C Nanomater Interfaces* **117,** 1893–1903 (2013).
16. Paquet, C. *et al.* Clusters of Superparamagnetic Iron Oxide Nanoparticles Encapsulated in a Hydrogel: A Particle Architecture Generating a Synergistic Enhancement of the T2 Relaxation. *ACS Nano* **5,** 3104–3112 (2011).
17. Roca, A. G. *et al.* Effect of Nanoparticle and Aggregate Size on the Relaxometric Properties of MR Contrast Agents Based on High Quality Magnetite Nanoparticles. *The Journal of Physical Chemistry B* **113,** 7033–7039 (2009).
18. Lartigue, L. *et al.* Cooperative Organization in Iron Oxide Multi-Core Nanoparticles Potentiates Their Efficiency as Heating Mediators and MRI Contrast Agents. *ACS Nano* 121129155806007 (2012). doi:10.1021/nn304477s
19. Guardia, P. *et al.* Water-Soluble Iron Oxide Nanocubes with High Values of Specific Absorption Rate for Cancer Cell Hyperthermia Treatment. *ACS Nano* **6,** 3080–3091 (2012).
20. Lee, N. *et al.* Water-Dispersible Ferrimagnetic Iron Oxide Nanocubes with Extremely High r_2 Relaxivity for Highly Sensitive in Vivo MRI of Tumors. *Nano Letters* **12,** 3127–3131 (2012).
21. Lee, N. *et al.* Magnetosome-like ferrimagnetic iron oxide nanocubes for highly sensitive MRI of single cells and transplanted pancreatic islets. *Proc. Natl. Acad. Sci. U.S.A.* **108,** 2662–2667 (2011).
22. Walter, A. *et al.* Validation of a dendron concept to tune colloidal stability, MRI relaxivity and bioelimination of functional nanoparticles. *J. Mater. Chem. B* **3,** 1484–1494 (2015).
23. Walter, A. *et al.* Effect of the Functionalization Process on the Colloidal, Magnetic Resonance

Imaging, and Bioelimination Properties of Mono- or Bisphosphonate-Anchored Dendronized Iron Oxide Nanoparticles. *ChemPlusChem* **82,** 647–659 (2017).

24. Tartaj, P., Morales, M. del P., Veintemillas-Verdaguer, S., González-Carreño, T. & Serna, C. J. The preparation of magnetic nanoparticles for applications in biomedicine. *J. Phys. D: Appl. Phys.* **36,** R182 (2003).

25. Daou, T. J. *et al.* Coupling Agent Effect on Magnetic Properties of Functionalized Magnetite-Based Nanoparticles. *Chem. Mater.* **20,** 5869–5875 (2008).

26. Santoyo Salazar, J. *et al.* Magnetic Iron Oxide Nanoparticles in 10−40 nm Range: Composition in Terms of Magnetite/Maghemite Ratio and Effect on the Magnetic Properties. *Chem. Mater.* **23,** 1379–1386 (2011).

27. Gossuin, Y., Gillis, P., Hocq, A., Vuong, Q. L. & Roch, A. Magnetic resonance relaxation properties of superparamagnetic particles. *Wiley Interdiscip Rev Nanomed Nanobiotechnol* **1,** 299–310 (2009).

28. Walter, A. *et al.* Mastering the Shape and Composition of Dendronized Iron Oxide Nanoparticles To Tailor Magnetic Resonance Imaging and Hyperthermia. *Chem. Mater.* **26,** 5252–5264 (2014).

29. Zhou, Z. *et al.* Artificial local magnetic field inhomogeneity enhances T_2 relaxivity. *Nature Communications* **8,** ncomms15468 (2017).

30. Zhao, Z. *et al.* Octapod iron oxide nanoparticles as high-performance T2 contrast agents for magnetic resonance imaging. *Nat Commun* **4,** 2266 (2013).

31. Sathya, A. *et al.* CoxFe3–xO4 Nanocubes for Theranostic Applications: Effect of Cobalt Content and Particle Size. *Chem. Mater.* **28,** 1769–1780 (2016).

32. Zhou, Z. *et al.* Interplay between Longitudinal and Transverse Contrasts in Fe3O4 Nanoplates with (111) Exposed Surfaces. *ACS Nano* **8,** 7976–7985 (2014).

33. Huang, J. *et al.* Effects of Nanoparticle Size on Cellular Uptake and Liver MRI with Polyvinylpyrrolidone-Coated Iron Oxide Nanoparticles. *ACS Nano* **4,** 7151–7160 (2010).

34. Zhou, Z. *et al.* Anisotropic Shaped Iron Oxide Nanostructures: Controlled Synthesis and Proton Relaxation Shortening Effects. *Chemistry of Materials* **27,** 3505–3515 (2015).

Chapter IX

Magnetic hyperthermia properties of dendronized nanoparticles with various shapes

IX Magnetic hyperthermia properties of dendronized nanoparticles with various shapes

IX.1 Introduction

Cancer is a major cause of death in the world– 7,6 million deaths worlwide in 2008, (13% mortality in the world) according to WHO. Surgery, chemotherapy, and radiotherapy are the most common conventional therapies currently applied. Although much progress has been made in cancer treatment this last decade, new approaches are necessary at the same time for improving existing therapies or developing new techniques of treatment in order to minimise deleterious side effects and to increase the patient survival rates. Therefore, there is currently a medical need to develop novel efficient nano-objects for cancer treatment. Image-guided therapy will be also crucial for the development of these compounds. Therefore the future of nanomedicine lays in the development of multifunctional nanoplatforms which combine both therapeutic components and multimodality imaging and which also act locally in tumors to avoid side-effects[1–8].

In that challenging context, iron oxide NPs are very promising because IONPs have already been shown to be applicable to diagnosis with MRI imaging and they are now widely developed for therapy with magnetic hyperthermia (MH). When exposed to alternating magnetic fields of appropriate intensity and frequency, these NPs release heat locally (where they are concentrated), which reduces the viability of cancer cells. The MH potential is demonstrated with the favorable recent results of the “nanothermotherapy” study in clinical phase II led by a German company *MagForce Nanotechnology* **(**hospital Charité in Berlin)[9–11] and with its use to enhance the sensitivity of tumor cells towards chemio or radio-therapy, to trigger a thermally-induced release of drugs or to act on cell membranes[9–13]. However, one of MH limitations is the low power heating of usual magnetic NPs, requiring a local injection of large quantities of NPs. Given the clinical importance of these results, there is thus currently a crucial need to design optimized NPs for efficient MH[14,15].

However optimization is not yet well-understood and experimental results from NPs systems vary widely. Indeed in MH, very specific physical properties are required for an optimal conversion of the supplied magnetic energy into heat. Three independent mechanisms result in thermal energy upon stimulation: Néel relaxation (internal friction with respect to the crystal lattice of NPs), Brown relaxation (internal friction of the NPs in the surrounding medium) and hysteresis loss (shift of domain walls)[16,17]. The relative contribution of each is strongly dependent on size, shape, crystalline anisotropy and degree of aggregation or agglomeration of NPs. Hysteresis loss deals with large multi domain particles. Single domain magnetic superparamagnetic NPs, which display smaller size than that of multi-domain particles absorb much more power at biologically tolerated magnetic fields and frequencies and form more easily stable suspensions. For these small sized NPs, the Néel and Brown relaxations are the main heating mechanisms. Néel and Brown relaxation times are mainly governed by the magneto crystalline anisotropy, a property of the material, which gives a preferred orientation in the magnetic moment, the volume of NPs and the viscosity of the media. Brownian relaxation will tend to dominate at larger particle volume and lower viscosities while the Néel relaxation will at smaller volumes of NPs and in viscous solutions. However the occurrence of these relaxation phenomena depends also strongly on the NPs anisotropy[14,15] and there is currently a key challenge to overcome in the design of NPs with magnetic properties specifically tailored for hyperthermia related applications[14,17–19].

However the heating efficiency of an ensemble of magnetic NPs depends not only on the structural and magnetic properties of NPs but also on the magnitude and frequency of the applied magnetic field. Indeed the heating performance is usually assessed by determining the specific absorption rate (SAR) which is the power dissipated by magnetic NPs per unit of mass[20] : SAR = C/m * dT/dt with C, the water specific heat per unit of volume, m the iron concentration in suspension (Fe g/L) and dT/dt the increase in measured temperature. SAR (in W/g) values depend on the structure and composition of the NPs but also on the frequency (f) and the amplitude of the magnetic field (H) applied during the measurements[5,7]. For an efficient heat treatment with minimal invasiveness for the patient, the search for new magnetic nanomaterials which show the highest SAR values at the lowest NPs dose administered and at the lowest frequency and/or magnetic field amplitude applied is of paramount relevance[14,15,21,22].

Besides, it has not been systematically investigated if, and under which conditions, the MH effect is efficient in living cells. It is clear that the understanding of MH at the cell level is far from complete[23].

In Chapter VII, we have coated iron oxide NPs displaying different shapes (spherical, cubic, plate and octopode shaped NPs) with dendron molecules and investigated their magnetic properties to evaluate their potential/suitability as heating agent with magnetic hyperthermia. Both, nanospheres with a mean size of 22 nm and octopods with a mean size of 18 nm were shown promising for magnetic hyperthermia by fine magnetic characterization. They demonstrated very good contrast agent properties for MRI in Chapter VIII.

In that context, the effect of the NPs shape on the heating power is discussed and the evolution in regard of NPs concentration has been studied. In a second time, *in vitro* tests were performed to measure the internalisation degree depending on the shape. Magnetic hyperthermia was then performed on cells internalized with NPs. Finally preliminary magnetic hyperthermia tests were performed on mices presenting tumors.

IX.2 Experimental conditions

IX.2.1 Magnetic hyperthermia

Magnetic hyperthermia in solution was measured on a DM1 apparatus from Nanoscale Biomagnetics^{TM}. NPs suspensions in water are left for 5 min in the apparatus for temperature adjustments. The MH was then applied for 5 min.

IX.2.2 Cell studies

Cell **:** Human hepatocarcinoma Huh7 cells were propagated in Dulbecco's modified Eagle's medium supplemented with 10% of decomplemented foetal bovine serum, 0,5% penicilin and 0,5 % non-essential amino acids.

Flow cytometry**:** Huh7 (2. 105 cells per well) were seeded in a 24-well plate (Greiner, Dominique Dutscher, ref 165305) and kept overnight for attachment. Cell were then incubated, with 1 mL per well of NP diluted in complete medium, for 24 at 37°C in 5% CO2. Cells were then thoroughly rinsed with 1 mL of cold PBS. Cells were then incubated with 300 µL of tryspin/EDTA solution (GIBCO, Ref R001100, Thermofisher) for 5 minutes. Cells were then resuspended by addition of 500 µL of PBS and harvested by centrifugation at 1000 rpm for 5 min. Cell were resuspended in 1 mL PB + 2% paraformaldehyde (PFA) and kept at 4°C protected from light until analysis. Cell fluorescence was analyzed by flow cytometry using a FACS flow cytometer with Novios software. Cells were analyzed in FL1 canal (Exc 488 nm Em 505 nm). Fluorescence threshold was determined using none treated cells. 10 000 cells were analyzed by sample.

Fluorescence microscopy: Huh-7 cells were seeded in 9.3 mm petri dish at a concentration of 1.10^5 cell per well. Then the cells were incubated with complete medium and kept overnight for attachment at 37 °C in 5% CO_2. Cell were then incubated, with 2 mL per well of NP diluted in complete medium, for 24 at

37°C in 5% CO2. Cells were then thoroughly rinsed with 2 mL of cold PBS and 2 ml of completed medium with 25 mM HEPES was added . The dished were treated with magnetic hyperthermia at 401 KHz and 13 $k.A.m^{-2}$ for 50 min on a nanoscale biomagnetic DM3 magnetic hyperthermia apparatus. The cells were then dyed for cell death detection with the Apoptic/necrotic/healthy cells detection kit (PromoKine). Fluorescence images were captured using Nikon Elipse TE200 with 63× PL APO (1.4 NA) objectif equipped with Nikon Digital Camera (DS-Q11MC with NIS-Elements softwares), and processed with ImageJ (http://rsb.info.nih.gov/ij/).

IX.2.3 *In vivo* magnetic hyperthermia study

Female 6-week C57BL/6 mice were commercially obtained (Charles River) and after a week of acclimation 2,5 10^5 EL6 cells in 100 μL cell culture medium were injected subcutaneous in the right flank with a 25G needle. After 7 days tumors were small but big enough to inject MNPs intratumorally. 70 uL of a sterile (passed through a 0,2 μm filter) 2,6 ± 0,2 mgFe/mL (in PBS) MNPs solution were injected intratumorally per mice (about 182 μgFe/tumor) with a 30G needle. MNPs injection was performed in one point of the tumor. The same day of MNPs injection and the following two days mice were exposed to alternating magnetic fields (AMF). The device is from NanoScale Biomagetics company (DM3 model). Each exposure time was 30 min at 105 kHz and 225 Gauss. Mice were anesthetized with isofluorane and were maintained during the AMF exposure into a hot water bath system that prevent the mice to suffer hypothermia. Rectal temperature was registered during the AMF exposure to control general state of the animals.

Tumor dimensions (length, with and height) and mice weight were daily measured with a caliper.

After the last AMF exposure, mices were maintained 3 days or until tumors started to ulcerate.

Mice were euthanasiated by CO_2 inhalation and blood was directly extracted from the heart and tumor was removed and fixed in 4% PFA and processed to perform Hematoxylin/Eosin staining and Blue Perls staining. Figure IX.1 depicts the experiment.

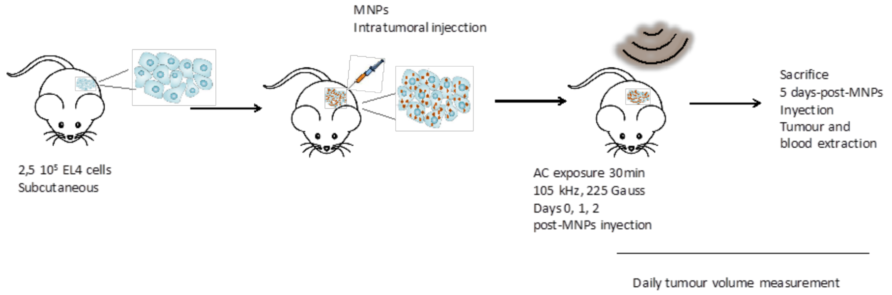

Figure IX.1- Experimental set up for In vivo magnetic hyperthermia

IX.3 Results

IX.3.1 Structural and magnetic characterizations of as-synthesized NPs (summary)

Dendronized spherical NPs (named NS22) with a mean size of 22.2 nm (± 8%), nanocubes (named NC), with a mean size of 14.5 nm (± 11%), octopod shaped NPs (named NO28) with a mean size of 27.8 nm (± 15%) and finally the plate shaped NPs (named NPl) with a length of 20 nm (± 35%) and a 5,7 nm (± 28%) thickness were fully characterized (structural and colloidal features) in previous chapters (VII & VIII).

IX.3.2 Relaxivity (summary)

IX.3.4.1 Relaxivity measurements

Relaxivity measurements were performed for all dendronized shaped NPs at 0.41 T (20 MHz), 1.47 T (60 MHz) and 7.04 T (300 MHz). The transverse r_2 relaxivity of dendronized NPs was compared in regard of the size and shape in Figure IX.2 to that of the commercial product (Resovist) and to the standard 10 nm dendronized NPs (Spheres 10).

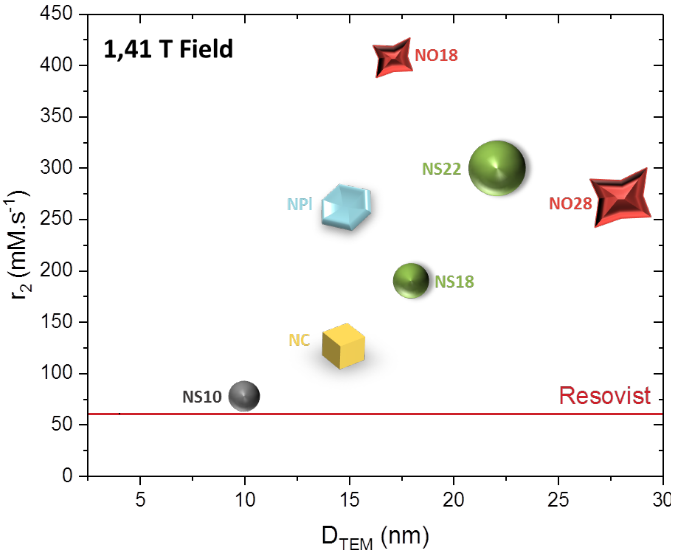

Figure IX.2 - Transverse relaxivity r_2 as a function of the shape and size of dendronized NPs

Figure IX.2 demonstrated that all dendronized NPs displayed high r_2 values larger than the commercial one and suitable for being used as contrast agent for MRI. NO18, NO28 and NPl are the NPs which presented the highest r_2. Their contrast enhancement was also ascertained by analysing their NMRD profiles (cf. Chapter VIII) but a particular behaviour has been noticed for octopods. Possible explanations were that heterogeneity of the local magnetic field was induced by the shape of octopods or that they tend to align and/or aggregate which increase their anisotropy. Their in vivo biodistribution was followed by MRI and some accumulation in liver was noticed.

IX.3.3 Magnetic hyperthermia: SAR measurements on suspensions

Heating power of the different shapes was determined through SAR measurements. First the SAR was measured at different magnetic field amplitudes and frequencies and NP concentration. The same solution was used and diluted. To check a possible aggregation of NPs in suspension between measurements, the colloidal stability was assessed after each SAR measurement and dilution.

At first SAR measurements were performed on the different shapes at different field amplitude and frequencies. The results are given in Figure IX.3,. NS18 and NO18 were used for these experiments.

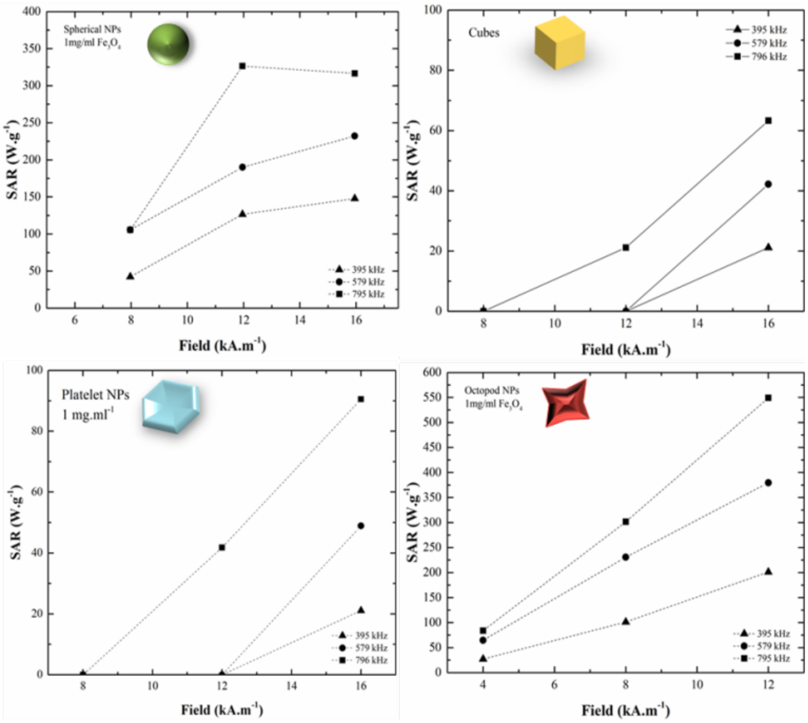

Figure IX.3 - SAR measurements for the different shapes at the same concentration but with different field amplitude and frequencies

As expected, the SAR values increased with the increase in the frequency and field amplitude for all NPs. NO18 and NS18 presented good responses to the magnetic hyperthermia with SAR values up to 550 W.g^{-1} for NO18 and 350 W.g^{-1} for NS18 at 795 kHz and 12 kA.m^{-1} (f.H = 9.54.10^{9}). NC and NPl displayed small SAR values below 100 W.g^{-1}which were expected due to their low saturation magnetization. The following trends were thus observed: SAR values increase with increasing M_s (NS18 vs NS10 or NPl,) and anisotropy (NO18 vs NS18). Furthermore, when the M_s was poor without anisotropy (NS10), no heat was released and when the M_s was poor and the anisotropy was high (NC/NPl) weak SAR values were measured. The Figure IX. 4 summarized the trends.

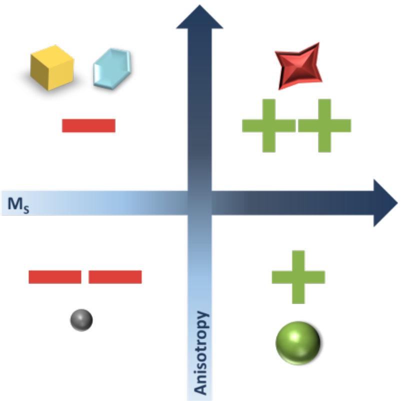

Figure IX.4 – Summary of the link between M_s and anisotropy on SAR values

Yet, magnetization and anisotropy are requirements for good SAR response but the heating power could be also greatly impacted by the collective behaviour of the NPs. It has been shown theoretically[24,25] and experimentally[26–29] that IONPs spheres could align under magnetic field improving the SAR response. But the NPs can also aggregate without control leading to deleterious effects on SAR values. Cubic morphologies are of great interest, as cubes tend to align without magnetic field. Yet, the organization of NPs does not only depend on the presence of a magnetic field. The concentration of NPs is also of great importance. Indeed, it was shown that NPs presented a non-monotonic response to the MH depending on concentration. Low concentration can favour the specific alignment boosting the SAR response.

The SAR values of NS22, NC, NPl and NO 28 were measured as a function of their concentration at 795 kHz and 12 kA.m^{-1} (15 mT). All the measurements were performed from the same suspension. DLS size distribution was measured before and after each MH treatment as well as after the dilution step in order to verify the state of aggregation. Figure IX.5 presented the evolution of SAR for all the shapes (left graph) and the corresponding DLS measurements (right graphs). Figure IX.6 showed an example of DLS measurement (in this case, for the first point of NO). As expected aggregation is observed after each MH measurement but it vanished after dilution. the re-dispersion of the dendronized NPs during the dilution is in agreement with weak interactions. Yet the aggregation was not observed the same for all.

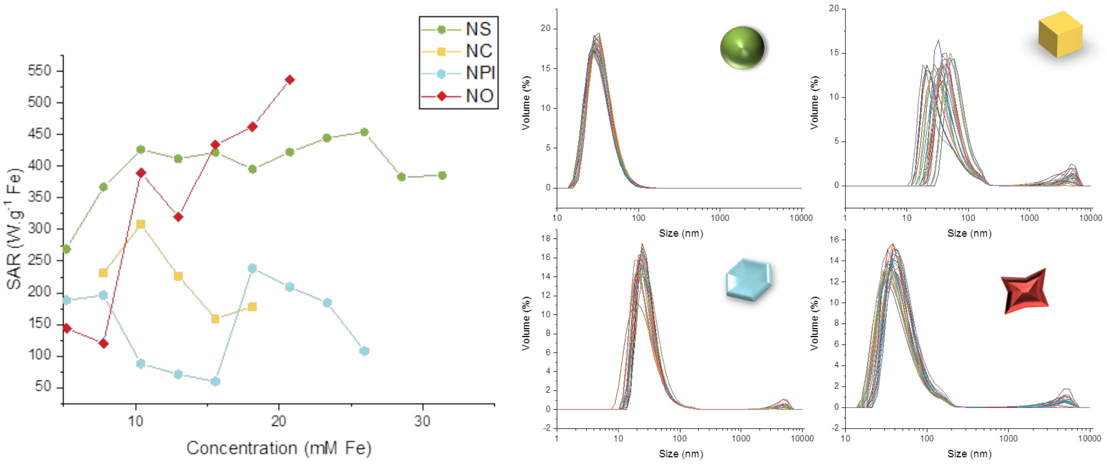

Figure IX.5 - SAR values as function of the concentration (left) and associated DLS measurements of the diluted suspensions after MH (right)

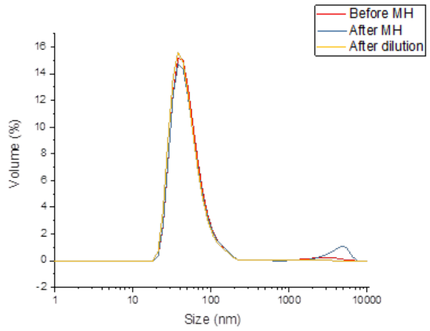

Figure IX.6 - DLS measurement before and after MH, and after dilution for NO

The nanospheres presented interesting and quite constant SAR values (*ca.* 430 W.g^{-1}) in the concentration range 10-30 mM with a decrease when the concentration decreased below 10 mM Fe. No sign of aggregation was detected with the DLS. The SAR values of nanoplates and nanocubes were observed to vary as a function of the concentration with boosted SAR values observed at specific concentration ranges (around 10 mM for NPl and NC and 20 mM for NPl) assuming thus for both the existence of a SAR maximum at a given concentration . Aggregation was detected around 5000 nm for all DLS measurements. NO presented a decrease with the decreasing concentration and aggregation was noticed on the DLS curves.

The boost of the SAR observed can originate from cooperative mechanism of the NPs through the formation of chains leading to anisotropy increase/hysteretic losses[24,28]. The formation of chains led to the unidirectional magnetization orientation along the chain that was the result of the dipolar coupling of the NPs[28]. Yet there is probably an optimal length for this chain assembly depending on the type of morphology to promote higher SAR values. Above or below the optimal value, the SAR decreases[28,30].

Considering those reports, we believe that the chain formation is responsible for the NS good and constant SAR values. The decrease occurred when the chains may not be long enough to maintain the SAR. For the anisotropic shapes, the aggregation might be the cause of the decreasing SAR. As seen in Figure IX.6 the aggregation was observed in DLS after MH application but the NPs re-dispersed after the dilution for the next measurement. Yet, we assumed that once the sample was submitted to the magnetic field it might present a tendency for aggregation. From the SAR value, this aggregation would be more unorganized and deleterious for the SAR. For some of the measurements for NC and NPl, a SAR maximum is measured. This point might be due to the cooperative alignment of the NPs.

IX.3.4 Cell studies

IX.3.4.1 NPs cell internalisation by flow cytometry and TEM

The NPs internalisation was first determined by flow cytometry. Alexa 595 amine was coupled on the carboxylic group of the D2-2P through EDC coupling. Those fluorescent NPs (NPs@D2-2P@Alexa) were incubated with Huh-7 cells for 24h and 48h at several concentrations from 0.5 to 2 mM in iron. The cells were then washed thoroughly with PBS to remove non-internalised NPs, and suspended in 2% PFA solution in PBS. Cells were analysed with FACS. In all analysis, cell debris and free particles were excluded by setting a gate on the plot of side-scattered light (SSC) vs forward-scattered light (FSC). The acquisition parameters were optimized for the Alexa 495 fluorophore with an excitation at 488 nm and detection above 505 nm. All the internalized cells were compared to a control represented by Huh7 cells that were not incubated with NPs in order to determine the base line fluorescence intensity. Curiously, instead of seeing two populations, one with fluorescence intensity comparable to the control and one showing fluorescence intensity above control, a single population was detected with fluorescence intensity above the control. As all the population showed a shift of fluorescence intensity, it would mean that all the cells internalised NPs to some extends. Thus instead of treating the % of fluorescent cell, the shift of the mean fluorescence was assessed.

Figure IX.7 showed the evolution of fluorescence shift with the NPs concentration. This shift was increasing with the NPs concentration especially above 1mM.

Yet, as the surface of each NP is different, no quantitative comparison can be done on the internalisation between different shapes. All the shapes presented shift increases in regard of concentration and time of incubation increases. At 4 hours of incubation, the shift evolution was weak. After 24 hour of incubation, fluorescence shift increased with concentration. However before 1mM, it seems to be rather limited. It could be related to a problem of threshold of detection or if these shifts are well linked to non-specific internalisation that implies the kinetic is quite low.

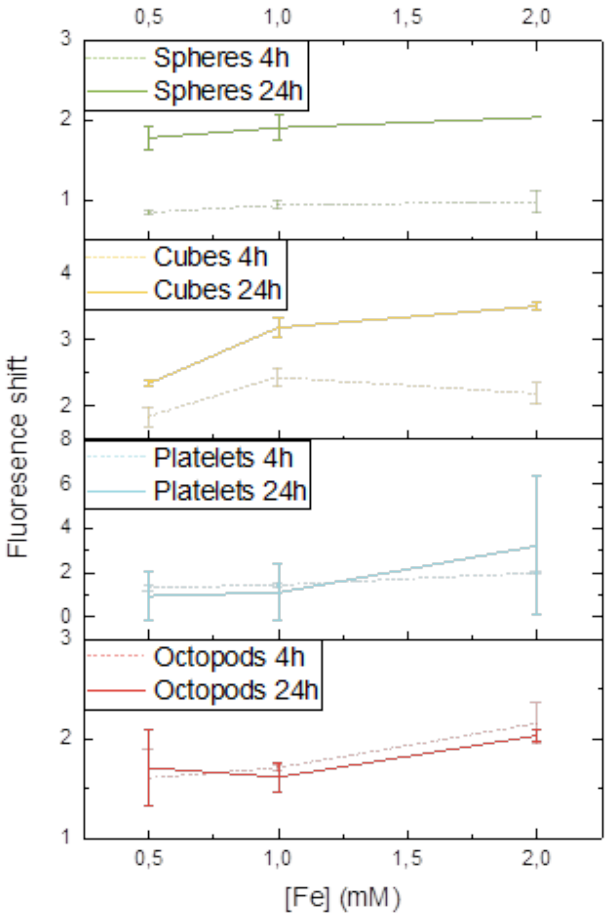

Figure IX.7 - Fluorescence shift observed in flow cytometry for the shapes depending on incubation time and concentration

To confirm that the shift of fluorescence is due to the internalisation of NPs, another method was used. To get a more quantitative insight on NPs' internalisation, the iron content of cells incubated with NPs was assessed with ICP-MS. Figure IX.8 showed evolution of the iron concentration (in pg/cell), substracted from the endogenous iron level in measured in control cells, as function of the [Fe] of the injected dose of NPs.

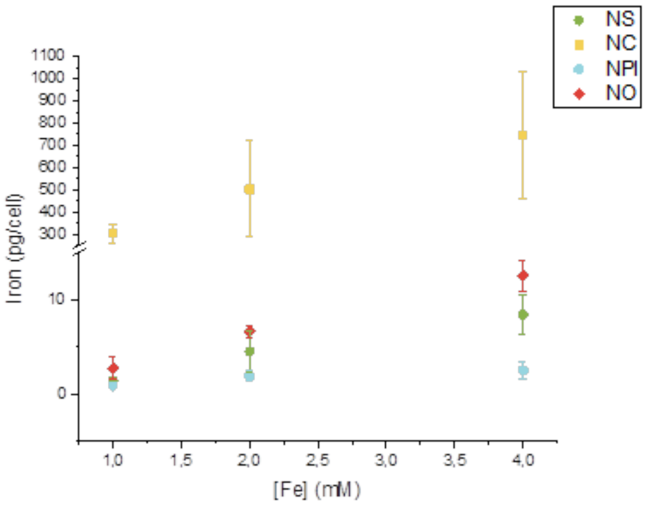

Figure IX.8 - Iron titration of cells after internalisation experiments subtracted from the endogenous level in iron in control cells.

Table IX.1 - Number of NPs per cell calculated with the titration

	Number of NPs per cell (10^5 NPs/cell)			
Concentration (mM Fe)	NS	NC	NPl	NO
4	3.9	250	4.9	6
2	2.1	170	3.8	3.2
1	1.5	100	1.8	1.1

The titration of iron confirmed that the amount of NPs internalized increased with NPs concentration in accordance with our previous results with flow cytometry. The number of NPs per cells was calculated for qualitative reasoning (the calculation considered NPs as monodisperse in size). Values are reported in table IX.1. All together it confirmed that there is a shape effect on the nonspecific internalisation. NO and NPl seemed to take advantage of their shape to get into the cells. NS presented the lowest rate of internalisation. It is in agreement with observed results of nonspecific cell internalization with 10 nm dendronized NPs: it is attributed to the low hydrodynamic size of NPs and to the dendron coating.

NC treated cells showed the highest iron content. However these NPs are less stable in aqueous solution and tended to aggregate. Thus, we can hypothesise that such NPs therefore have a tendency for sedimentation increasing the iron concentration in direct contact with cells grown in monolayer. One of the main parameter for cellular uptake is the size. The smallest, the easiest to internalize[31]. Yet here, the bigger NPs internalized better. Several reports[32] have observed the same phenomenon for anisotropic nano objetcs. It has been proposed that as the specific surface is higher for the anisotropic NPs there is more multivalent ionic interaction with the cell membrane leading to a higher internalisation.

Another question about the different shapes internalisation is the localisation of the NPs once in the cell. Cells internalized with NPs having the different shapes were imaged with TEM. Images are given in Figure IX.9.

As hypothesized before, cubes are found aggregated in the cell. This confirmed that this helped their higher internalization. For all shapes, the NPs are found to be into autophagosomes. Nevertheless, some local organisation has been observed depending on the shape. NS tended to form rings as NPl and NO preferred to align. Organisation couldn't be seen for NC as more NPs get internalized.

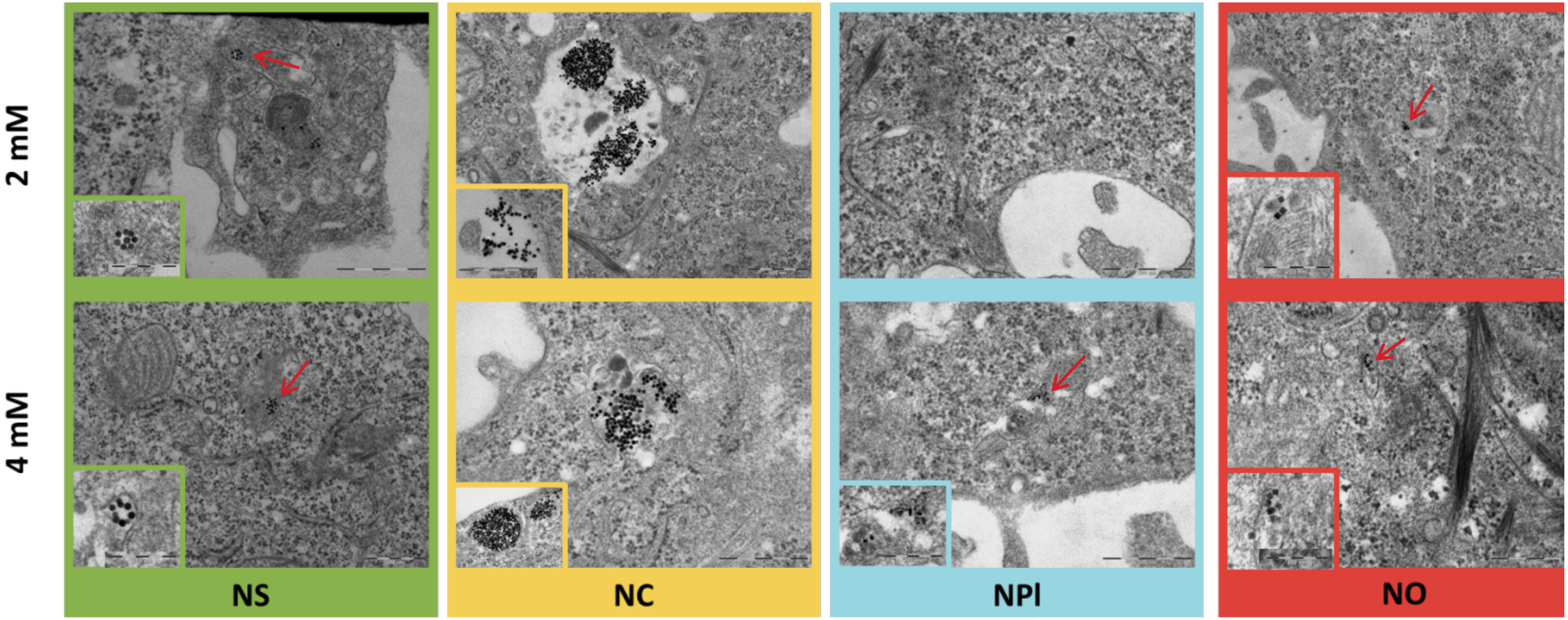

Figure IX.9 - TEM images of internalized cells as a function of the concentration, red arrow indicates the NPS

We've seen that flow cytometry could be indicative of the internalization of NPs but could it be quantitative? To answer that question, NS coupled with Alexa 595 were internalized at different concentrations (0.6 to 9 mM) in Huh7 cells in presence of a magnet to ensure the presence of NPs in the cells. After incubation and washing, the cells were counted and part of them was used to titrate the iron with ICP MS and the second part was used for flow cytometry measurements. The shift of the mean fluorescence was then plotted versus the number of NPs per cells (figure IX.10).

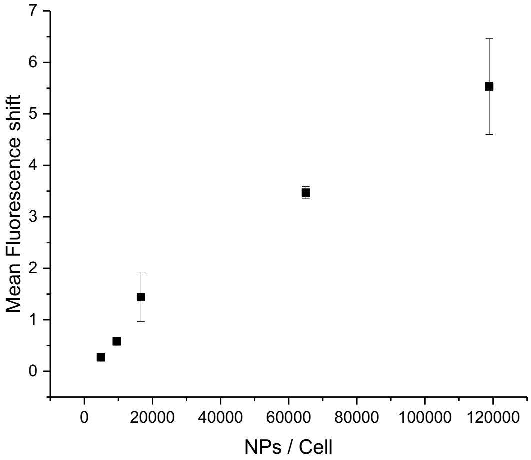

Figure IX.10 - Mean fluorescence shift versus the number of NPs per cells

We observed a nice variation almost linear of the mean fluorescence shift with the number of NPs per cells. Above 20000 NPs per cells, the variation is almost linear (R^2 = 0.9993). This result indicated that the study of the mean fluorescence shit is interesting when enough NPs are internalized (> 20000 NPs/cell, in our case for 1 mM Fe). Flow cytometry could be thus a quantitative method for the NPs internalisation on the condition that all the experiments are performed with NPs presenting the exact same fluorescence. In our case, this experiment confirmed that if the mean fluorescence shift value is higher, more NPs are internalized. Such kind of calibration curve should be hence investigated and established for each morphology in future works.

IX.3.5 In vitro magnetic hyperthermia

IX.3.5.1 Magnetic hyperthermia on cell monolayers

The efficiency towards Magnetic Hyperthermia (MH) was assessed for all shapes on Huh7 cells. NPs efficiency in hyperthermia therapy relied on two aspects; first their ability to heat, secondly their ability to enter cells. In those two aspects, size, shape and concentration mattered. In order to evaluate both, we performed hyperthermia treatment on cell incubated with NPs and on cell after magnetofection protocol to insure NP cell internalisation. On one hand, cells were incubated with NPs diluted in complete cell culture media for 24 h at 37 °C. On the other hand, the internalisation was boosted with a magnet. Cells were incubated with NPs diluted in complete cell culture media at 8 mM then a magnetic field was applied for 5 minutes by applying a magnet under the culture plate. The cells were then incubated further at 37 °C for 30 min. The rest of the procedure was the same for the two cases. Before the MH treatment, cells were washed thoroughly with PBS and medium replaced by fresh culture medium + 10 mM HEPES. Magnetic field was then applied for 50 min (400 KHz, 170 G) and incubated further at 37 °C in 5% CO_2 for 24h. After this incubation time, cells were fixed with PFA 4 % at room temperature for 15 min. Then the cells were labelled to detect apoptic and necrotic cell with annexin and ethidium homodimer III respectively. Percentage of apoptic and necrotic cells were determined on epifluorescence microscopy images (figure IX.11 and IX.12).

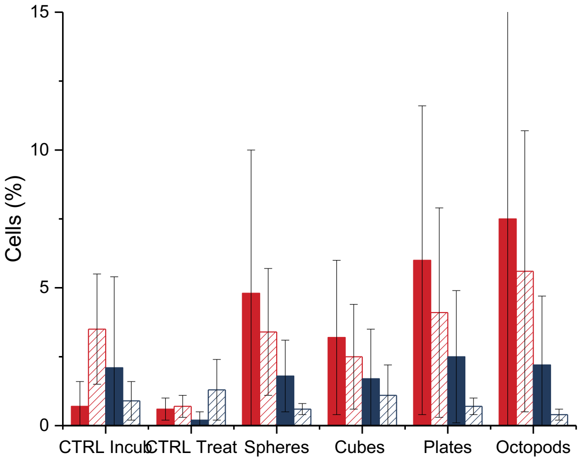

Figure IX.11 - % of Apoptic (plain) and Necrotic (stripped) cells. Red with magnetofection and blue without magnetofection

The % of necrotic and apoptic cells is quite low < 20 % and the error is big. This is due to a large heterogeneity of the transfection especially for the magnetofection whose effect is limited by the magnetic field application. The slight increase of cell mortality (apoptose and necrose) compared to the CTRL is in agreement with a poor internalisation of our dendronized NPs as it has been observed on 10 nm spheres[33]. Hence, the magnetofection experiment allowed observing an effect on the cell death through apoptosis. NO and NS seemed to be good mediator for heat generation in MH as expected from the previous characterisations. Nevertheless, NPl presented equivalent result to those shapes when the measurements in solution were weak. This might be due to the viscosity of the cell and the large surface of the NPl. However large necrotic cell death percentage was observed that would indicate that the charge of the magnetofection is leading to necrosis. That point could be confirmed with the detection of the damage-associated molecular pattern molecules (DAMPs) that could be liberated during the charge[34].

The next step would be to repeat the experiment with dendronized NPs functionalized with a targeting agent in order to internalize gently and more homogenously the NPs over the whole cell monolayer. Yet this study allowed us to rule NC out of the interesting candidates for MH.

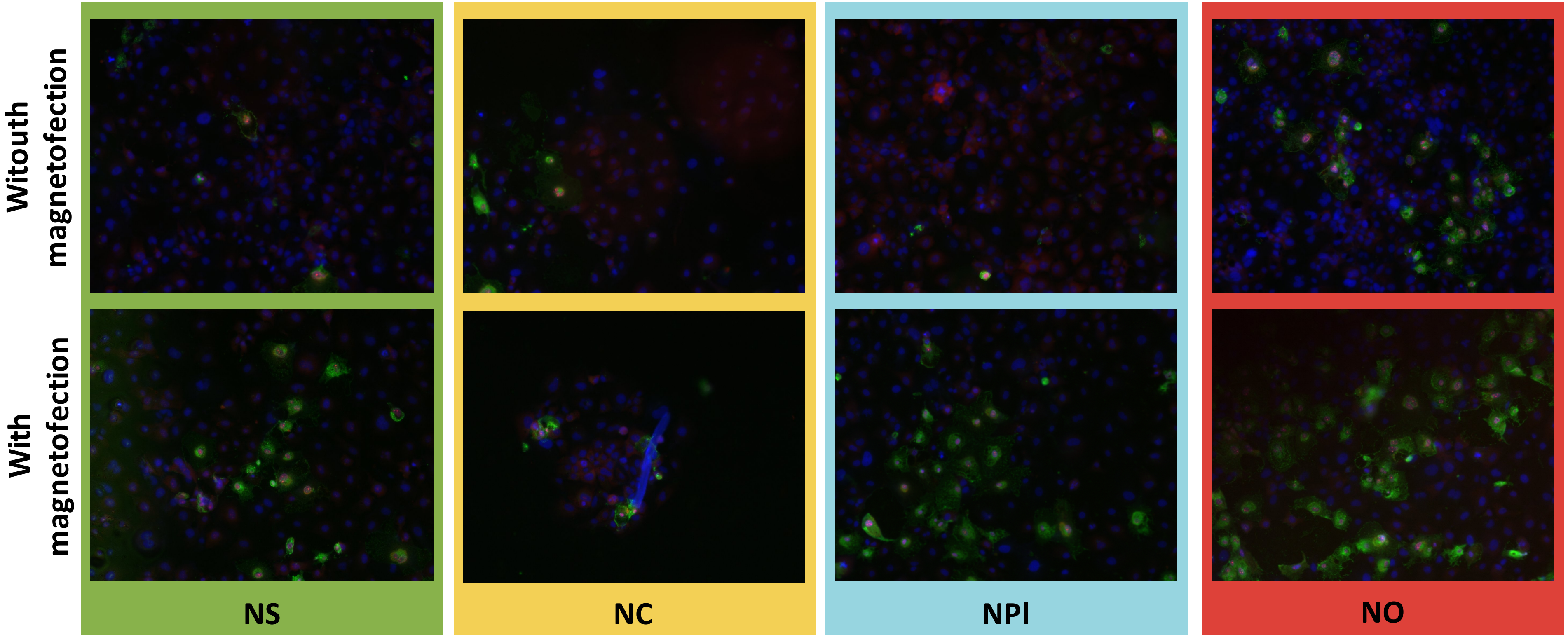

Figure IX.12 - Epifluorescence images of cells after the MH treatment, nuclei in blue, apoptic cells in green and necrotic cells in red

IX.3.6 Preliminary *in vivo* hyperthermia measurements

These preliminary *in vivo* experiments have been conducted by the team of Jesus de la Fuente ICMA-CSIC in Zaragoza (Spain).

After having performed the experiments detailed in experimental part, the tumor growth was calculated as (Tumor Volume)/(Initial Tumor Volume) and is given in Figure IX .13 . Day 2 corresponded, as can be seen in the experimental design scheme, to the measurements made after the last of the three MH treatment days. Day 4 corresponded to the measurements made 48h after the last MH treatment. The different experimental conditions are:

- BH: 4 mices with the tumor, without MNPs and with magnetic field exposure
- BNPs: 3 mices with the tumor, with MNPs and without magnetic field exposure
- HNPs: 3 mices with the tumor, with MNPs and with magnetic field exposure.

At day 4, two of the mices of the HNPs group and 1 of the BNPs group had to be sacrificed because of tumor ulceration. Although tumor volumes was not too big as the tumor growth is very fast skin do not have time to expand and is very normal to observe initial tumor ulceration even at tumor volumes not so big.

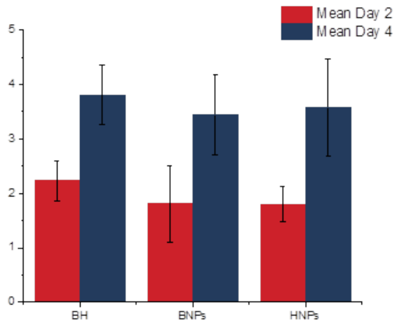

Figure IX.13 Evolution of tumor growth

PERLS staining was performed in order to detect MNPs images are given in figures IX.14-15.

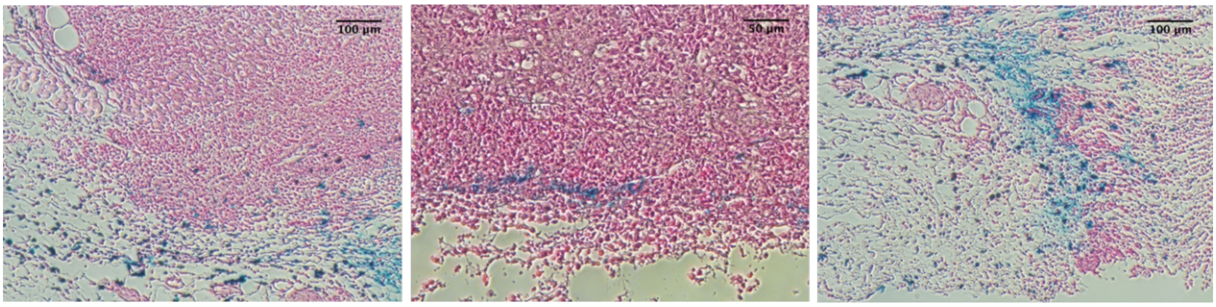

Figure IX.14 - PERLS images of tumors of the group BNPS (with NPs without AMF)

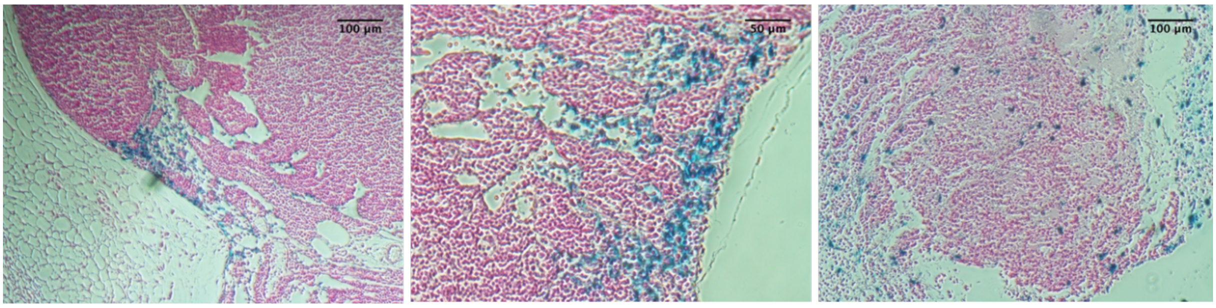

Figure IX.15 - PERLS images from tumors of the group HNPS (with NPs with AMF)

It can be seen that MNPs are mainly in the extracellular matrix but some can be detected in the tumor. However, no effect in tumor inhibition growth was evidenced in mice with NPs after AMF exposure. The NPs were very nice as they were very stable and were very easy to inject but the main problem is that they could not be internalized in the tumor but stayed in the extracellular matrix. This is not surprising as the dendron molecules were shown to prevent dendronized NPs from unspecific internalization[19,33]. The next experiments will consist in coupling glucose as a targeting agent at the surface of dendronized NPs by using the carboxylate function in dendron to improve their internalisation in tumors.

IX.4 Conclusions

The NPs with cubic, platelet, octopode and spherical shapes have been coated with dendron molecules providing them good colloidal stability in physiological media. Dendronized NPs with different shapes were shown to possess very good properties as contrast agents for MRI. High SAR values were measured for octopods and 22 nm sized nanospheres (up to 550 W/g for NO18 and 430 W/g for NS22). The SAR values have also been investigated as a function of the concentration and except for NS whose SAR values increased with the concentration up to 10 mM Fe and then stabilized at around 450 W/g, the SAR values varied with the concentration. The SAR value increased continuously with the concentration with NO up to 550 W/g. The NPl and NC SAR values showed some high value at particular concentration up to 320 W/g for NC and 240 W/g for NPls. This behavior is supposed to result from an alignment of NPs at these concentrations increasing their anisotropy. Yet, the measurements from the dilution of the same NP suspension seem to promote erratic aggregation that may spoil the SAR values. Thus this experiment should be reproduced with measurement made on “fresh” solutions at different concentrations that never saw the magnetic field.

Before testing the effect of MH on cells internalized with NPs, the NPs cell internalization was investigated by flow cytometry and TEM. For both methods, an internalization of NPs dependent on the NPs shape was observed but it was difficult to evaluate it quantitatively.

Magnetic hyperthermia performed on cells with internalized NPs showed quite low effects on cell viability attributed to a too small amount of internalized NPs. Magnectofection allowed to increase locally the amount of internalized NPs but, as this method is quite harsh, targeting would be favored for future experiments.

Non-specific internalization of NPs in cancer cells was also confirmed during preliminary *in vivo* experiments where the NPs were observed in the extracellular matrix but not inside the tumor. These experiments confirmed again the dendron effect which inhibited the nonspecific cell internalization of dendronized NPs. In future experiments, *in vitro* and *in vivo* experiments will be conducted with dendronized NPs bearing a targeting ligand to improve the NPs cell internalization.

REFERENCES

1. Liong, M. *et al.* Multifunctional Inorganic Nanoparticles for Imaging, Targeting, and Drug Delivery. *ACS Nano* **2,** 889–896 (2008).
2. Kim, J., Piao, Y. & Hyeon, T. Multifunctional nanostructured materials for multimodal imaging, and simultaneous imaging and therapy. *Chemical Society Reviews* **38,** 372–390 (2009).
3. De, M., Ghosh, P. S. & Rotello, V. M. Applications of Nanoparticles in Biology. *Advanced Materials* **20,** 4225–4241 (2008).
4. Mornet, S., Vasseur, S., Grasset, F. & Duguet, E. Magnetic nanoparticle design for medical diagnosis and therapy. *Journal of Materials Chemistry* **14,** 2161–2175 (2004).
5. Fang, C. & Zhang, M. Multifunctional Magnetic Nanoparticles for Medical Imaging Applications. *Journal of materials chemistry* **19,** 6258–6266 (2009).
6. Pankhurst, Q. A., Connolly, J., Jones, S. K. & Dobson, J. Applications of magnetic nanoparticles in biomedicine. *Journal of Physics D: Applied Physics* **36,** R167 (2003).
7. Mura, S. & Couvreur, P. Nanotheranostics for personalized medicine. *Advanced Drug Delivery Reviews* **64,** 1394–1416 (2012).
8. Choi, K. Y., Liu, G., Lee, S. & Chen, X. Theranostic nanoplatforms for simultaneous cancer imaging and therapy: current approaches and future perspectives. *Nanoscale* **4,** 330–342 (2012).
9. Maier-Hauff, K. *et al.* Intracranial Thermotherapy using Magnetic Nanoparticles Combined with External Beam Radiotherapy: Results of a Feasibility Study on Patients with Glioblastoma Multiforme. *J Neurooncol* **81,** 53–60 (2007).
10. Maier-Hauff, K. *et al.* Efficacy and safety of intratumoral thermotherapy using magnetic iron-oxide nanoparticles combined with external beam radiotherapy on patients with recurrent glioblastoma multiforme. *J Neurooncol* **103,** 317–324 (2011).
11. http://www.magforce.de/en/home.html.
12. Dennis, C. L. & Ivkov, R. Physics of heat generation using magnetic nanoparticles for hyperthermia. *International Journal of Hyperthermia* **29,** 715–729 (2013).
13. Thiesen, B. & Jordan, A. Clinical applications of magnetic nanoparticles for hyperthermia. *Int J Hyperthermia* **24,** 467–474 (2008).
14. Deatsch, A. E. & Evans, B. A. Heating efficiency in magnetic nanoparticle hyperthermia. *Journal of Magnetism and Magnetic Materials* **354,** 163–172 (2014).
15. Kolosnjaj-Tabi, J. *et al.* Heat-Generating Iron Oxide Nanocubes: Subtle ‘Destructurators’ of the Tumoral Microenvironment. *ACS Nano* **8,** 4268–4283 (2014).
16. Glöckl, G. *et al.* The effect of field parameters, nanoparticle properties and immobilization on the specific heating power in magnetic particle hyperthermia. *Journal of Physics: Condensed Matter* **18,** S2935–S2949 (2006).
17. Hergt, R., Dutz, S., Müller, R. & Zeisberger, M. Magnetic particle hyperthermia: nanoparticle magnetism and materials development for cancer therapy. *J. Phys.: Condens. Matter* **18,** S2919 (2006).
18. Gazeau, F., Lévy, M. & Wilhelm, C. Optimizing magnetic nanoparticle design for nanothermotherapy. *Nanomedicine (Lond)* **3,** 831–844 (2008).
19. Walter, A. *et al.* Mastering the Shape and Composition of Dendronized Iron Oxide Nanoparticles To Tailor Magnetic Resonance Imaging and Hyperthermia. *Chem. Mater.* **26,** 5252–5264 (2014).
20. Rosensweig, R. E. Heating magnetic fluid with alternating magnetic field. *Journal of Magnetism and Magnetic Materials* **252,** 370–374 (2002).
21. Hergt, R. & Dutz, S. Magnetic particle hyperthermia—biophysical limitations of a visionary tumour therapy. *Journal of Magnetism and Magnetic Materials* **311,** 187–192 (2007).
22. Guardia, P. *et al.* Water-Soluble Iron Oxide Nanocubes with High Values of Specific Absorption Rate for Cancer Cell Hyperthermia Treatment. *ACS Nano* **6,** 3080–3091 (2012).
23. Di Corato, R. *et al.* Magnetic hyperthermia efficiency in the cellular environment for different nanoparticle designs. *Biomaterials* doi:10.1016/j.biomaterials.2014.04.036
24. Mehdaoui, B. *et al.* Increase of magnetic hyperthermia efficiency due to dipolar interactions in low anisotropy magnetic nanoparticles : theoretical and experimental results. *Physical Review B* **87,** (2013).
25. Fu, R., Yan, Y. Y. & Roberts, C. Study of the effect of dipole interactions on hyperthermia heating the cluster composed of superparamagnetic nanoparticles. *AIP Advances* **5,** 127232 (2015).
26. Alphandéry, E., Faure, S., Seksek, O., Guyot, F. & Chebbi, I. Chains of Magnetosomes Extracted from AMB-1 Magnetotactic Bacteria for Application in Alternative Magnetic Field Cancer Therapy. *ACS Nano* **5,** 6279–6296 (2011).
27. Alphandéry, E., Chebbi, I., Guyot, F. & Durand-Dubief, M. Use of bacterial magnetosomes in the magnetic hyperthermia treatment of tumours: A review. *International Journal of Hyperthermia* **29,** 801–809 (2013).
28. Serantes, D. *et al.* Multiplying Magnetic Hyperthermia Response by Nanoparticle Assembling. *J. Phys. Chem. C* **118,** 5927–5934 (2014).
29. Saville, S. L. *et al.* The formation of linear aggregates in magnetic hyperthermia: Implications on specific absorption rate and magnetic anisotropy. *Journal of Colloid and Interface Science* **424,** 141–151 (2014).
30. Branquinho, L. C. *et al.* Effect of magnetic dipolar interactions on nanoparticle heating efficiency: implications for cancer hyperthermia. *Sci Rep* **3,** 2887 (2013).
31. Murugan, K. *et al.* Parameters and characteristics governing cellular internalization and trans-barrier trafficking of

nanostructures. *Int J Nanomedicine* **10,** 2191–2206 (2015).
32. Chen, L., Xiao, S., Zhu, H., Wang, L. & Liang, H. Shape-dependent internalization kinetics of nanoparticles by membranes. *Soft Matter* **12,** 2632–2641 (2016).
33. Bordeianu, C. *et al.* How a grafting anchor tailors the cellular uptake and in vivo fate of dendronized iron oxide nanoparticles. *J. Mater. Chem. B* **5,** 5152–5164 (2017).
34. Kaczmarek, A., Vandenabeele, P. & Krysko, D. V. Necroptosis: the release of damage-associated molecular patterns and its physiological relevance. *Immunity* **38,** 209–223 (2013).

Conclusion

This PhD work started with a central question: what are the decisive parameters for the synthesis of anisotropic iron oxide NPs?

To answer this question, we've decided to look first at the role of the precursor. Through the *in house* synthesis of iron stearate precursors with various stearate chains and hydration degree and their structural and thermal characterizations, we've been able to tie its thermal stability to its structure and more importantly to its hydration degree. Iron stearates depending on their structure and hydration degree were observed to present a distribution of precursors with different thermal stabilities. Thus iron stearates bearing the most important number of stearate chains $FeSt_3$ (hydrated or dehydrated) were observed to decompose up to 380°C when those with less chains $FeSt_2$ (hydrated or dehydrated) decomposed up to 340°C. This explains the impact of the boiling temperature of solvent on the growth of NPs. The smaller size of spherical NPs obtained with the stearate $FeSt_3$ (with the higher oleate chain number) than with the $FeSt_2$ one was explained by the fact that at the boiling point in the applied experimental conditions, more precursors were decomposed with $FeSt_2$ than with $FeSt_3$. Therefore more monomers are available with $FeSt_2$ for the growth step. The more in-depth investigation of the iron stearate evolution with temperature gave us further hints for the formation of FeO nuclei. The formation of nanocubes was thus supposed to be due to the growth of cubic FeO nuclei favoured by a higher growth than oxidation kinetics driven by the experimental synthesis conditions (Chapter III, IV & VII).

Thanks to the cutting edge characterizations, we've then revealed that the nucleation step leading to the NPs in the thermal decomposition synthesis occurred in vesicular systems. Two kinds of structures have been suggested: reverse vesicles and onion like structure. The vesicles tended to be majority in anisotropic synthesis conditions when NaOl was introduced. The formation of nuclei has been observed either inside the onion structure or in the walls of the vesicles. After this nucleation step, the vesicles disappear, the growth occurs in the reaction media and some Oswald ripenning is observed. Thus, a control of the nucleation could be operated by control of the vesicle structures. This discovery brings a new light on the LaMer theory. We suggested that what makes the nucleation possible is the fact that it takes place in confined vesicles. Indeed the vesicule confined locally the monomer/iron atoms which concentration locally increases driving thus a fast nucleation. After the nucleation the structures collapse and the growth occurs in solution. We have thus a clear separation between the nucleation and growth steps explained by a nucleation step controlled by vesicules. Investigations are still ongoing on the role of the structure of the precursor and its hydration degree.

We've then spent some time on the optimization of the thermal decomposition process. We've easily realized the scale up of the precursor synthesis by optimizing the concentration and the scale of the synthesis. We've reached the maximal amount we could produce with our equipment and ensured its quality. We've seen that we could produce NPs without ligand or solvent but the control of their size and shape is more difficult. Nevertheless, we've observed that when oleic acid was introduced and not the solvent, oxidized FeO NPs were obtained. This point would be in agreement with the formation of a FeO nucleus and with a passivation of the NPs by a shell of oleic acid that prevent the oxidation of the NPs. An alternative to the washing by centrifugation has also been developed. The simple agitation of the NPs suspensions in the right combination of warm solvent allowed removing to excess or ligand from the synthesis faster and with less solvent than the current purification process.

The precursor synthesis was also checked to be transposable to Mn and Co stearates. We have shown that these *in house* precusors led to NPs with similar shapes as those already published and reported with commercial precursors. Yet, understanding the formation mechanism of the CoO and MnO NPs is not an easy task. Nevertheless the morphologies observed with cobalt precursors are more complex than those obtained with iron stearate which led always to spherical NPs. Modeling experiments suggested that Co catalyzes the degradation of its stearate chain which is not seen for iron stearate. The cobalt atoms are thus not so free to assemble in nuclei or to participate to the NPs growth. Yet a proper study of Mn and Co structure as we realized for Fe could help to explain their synthesis mechanisms.

We have also checked the formation of core-shell $Fe_{3-x}O_4$@CoO NPs from our in house precursors but we obtained iron oxide NPs coated with a cobalt ferrite shell. The good knowledge of the precursor stability and of its thermal behavior allowed us to explain the formation of cobalt ferrite shell. This is important as controlling this kind of synthesis allowed to generate NPs displaying different magnetic properties.

After having realized the synthesis and characterization of our precursors, we've worked on the tie between the precursor structure and the synthesis of anisotropic shapes. We've agreed with the reports that showed that NaOl favoured the formation of anisotropic shape but we've demonstrated that its role can be hindered due to the presence of water. Dehydrated precursors allowed us to synthesized different shapes (cubes and plates) by tuning the ratio NaOl/OA. But we've observed that not all shapes could be obtained from all the precursors. $FeSt_2$ allowed the synthesis of nanocubes and plates when $FeSt_3$ was mostly leading to cubes. We have try to relate the formation conditions of these shapes to our previous *in situ* study showing a nucleation in vesicular structures. The vesicular process could be modified by the ligand introduced with NaOl leading to large vesicles. As a nucleation step at low temperature has been shown very important to form nanoplates,we suppose that a low temperature preserved the vesicle integrity which favours the formation of flat nuclei with a flat shape driven by the lamellar structure of the vesicle wall. The formation of nanocubes was explained as previously by the formation of FeO nuclei with a fast growth kinetics inhibiting their oxidation and preserving the cubic shape.

In the last part of this work, the synthesis conditions have been optimized to obtain NPs with nice and defined shapes and thus spheres of different sizes (18 and 22 nm) were successfully synthesized by varying the temperature. The plate morphology was not found optimisable yet. The optimisation of the cubic shape allowed obtaining much more defined cubes by playing with the heating rate but we do not succeed in obtaining nanocubes with an homogeneous spinel composition. By adapting published synthesis of such homogeneous nanocubes which involved the use of DBE as solvent, we obtained original octopod shaped NPs with a homogeneous spinel composition. The detailed structural characterization showed that the spheres were not monocrystalline but contained some defects due to their formation by oxidation of a FeO phase and their composition is that of an oxidized magnetite. Nanocubes presented core-shell structures with a core of the antiferromagnetic FeO shelled by a ferrimagnetic $Fe_{3-x}O_4$. Nanoplates were monocrystalline but very thin which make that they are strongly oxidized. Octopods are complex structures due to their elongated corners; they are also constituted of oxidized magnetite. The magnetic measurements allowed us to establish a ranking from the saturation magnetization values: octopods ≥ nanospheres ≥ nanoplates. The dipole- dipole interaction measurement was quite disappointed as they've shown none for all shapes except the cubes.

To further assess the effect of the shape on the MRI and magnetic hyperthermia properties, a functionalisation by a dendron molecule was performed. The good colloidal stability in physiological media was verified. All the shapes presented good T_2 MRI contrast agent properties with an outstanding results for the octopods as expected from the magnetic measurments and local characterization techniques. An *in vivo* biodistribution was performed by MRI showing the suitability of dendronized shaped NPs as *in vivo* contrast agent for MRI. Urinary and hepato-biliary elimination pathways were observed though some NPs accumulated in the liver. Further investigations are required to confirm these experiments and to determine if the NPs size and/or the shape may be optimized to limite the liver captation.

High SAR values were measured for octopods and nanospheres (up to 550 W/g for NO18 and 430 W/g for NS22). Nevertheless the dendron effect which help to avoid a non specific internalization of dendronized NPs in cells makes that no clear effects of hyperthermia in vitro and in vivo have been observed. The experiments have to be reproduced by coupling a targeting ligand at the surface of dendronized NPs to favour their cell internalisation.

Bien que de nombreux progrès ont été réalisés dans le traitement du cancer, de nouvelles approches sont nécessaires pour améliorer les techniques de traitement existantes ou pour développer de nouvelles techniques, ceci afin de minimiser les effets secondaires délétères et d'augmenter le taux de survie des patients. Par conséquent, il existe un réel besoin médical de développer de nouveaux nano-objets efficaces pour le traitement du cancer. Aujourd'hui, il est reconnu que la combinaison de thérapies est un moyen d'augmenter considérablement l'efficacité d'un traitement anti-cancer. Par ailleurs, le suivi de la thérapie par imagerie est également d'une importance capitale, car il apporte des informations spatiales précieuses et en temps réel permettant d'optimiser l'efficacité de la thérapie.

Le développement constant des nanotechnologies a apporté des innovations dans le domaine de la synthèse de nano-objets multifonctionnels pour la nanomédecine capable de révolutionner le diagnostic et la thérapie, notamment du cancer. En effet, la plupart des recherches sur la synthèse et la fonctionnalisation des nanoparticules inorganiques (NPs) pour des applications biomédicales visent à développer des NPs multifonctionnelles théranostiques (i.e. permettant de combiner, dans un seul nano-objet, thérapie et diagnostic). Ces NPs doivent être capables de diagnostiquer la maladie, de délivrer localement un traitement[1,2,3,4,5,6,7,8] et surtout de permettre de suivre l'effet de la thérapie par imagerie médicale.

Au sein de l'IPCMS, une collaboration entre le DCMI et le DMO a permis de développer des nanoparticules magnétiques dendronisées qui ont été démontrées être, *in vitro* et *in vivo*, de très bons agents de contraste pour l'IRM avec une capacité de ciblage *in vivo* du mélanome après leur injection intraveineuse. L'objectif de mon sujet de thèse a été de concevoir des nanoparticules dendronisées combinant des propriétés en thérapie et en imagerie multimodale.

Le développement de nouveaux agents de contraste pour le diagnostic par IRM représente un marché en plein essor. Les NPs d'oxyde de fer qui sont déjà commercialisées comme agent T_2 (agent noircissant) pour l'IRM,[9,10] sont particulièrement intéressantes car elles sont biodégradables et non toxiques comparées à d'autres familles d'agents de contraste. Pour être un bon agent de contraste, les nanoparticules d'oxyde de fer doivent présenter une aimantation à saturation la plus élevée possible et être fonctionnalisées par une biomolécule contrôlant leur agrégation et permettant une bonne diffusion de l'eau à proximité du cœur magnétique.

---

[1] ACS Nano 2008, **2**, 889-896

[2] Chem. Soc. Rev. 2009, **38**, 372-390

[3] Adv. Mater. 2008, **20**, 4225-4241

[4] J. Mater. Chem. 2004, **14**, 2161-6175

[5] J. Mater. Chem. 2009, **19**, 6258-6266

[6] J. Phys. D: Appl. Phys.2003, **36** R167-R181

[7] Advanced Drug Delivery Reviews 2012, **64**, 1394

[8] Nanoscale 2012, **4**, 330-342.

[9] Chem. Rev. 2008, **108**, 2064-2110

[10] Adv. Mater. 2009, **21**, 2133-2148

Les NPs d'oxyde de fer sont également développées pour la thérapie par hyperthermie magnétique. Quand elles sont exposées à un champ magnétique alternatif d'une intensité et fréquence précises, ces NPs libèrent localement de la chaleur là où elles se concentrent réduisant de ce fait la viabilité des cellules cancéreuses. Le potentiel de cette méthode a été démontré avec les résultats favorables de l'étude « nanothermotherapy » qui est actuellement en phase clinique II à l'hôpital Charité à Berlin[11,12,13]. Son efficacité pour augmenter la sensibilité des cellules tumorales à la chemio- ou radiotherapie, pour délivrer localement des molécules médicamenteuses ou pour agir sur les membranes cellulaires[14] laisse à penser que cette méthode pourrait révolutionner la biomédecine. De plus, les NPs d'oxyde de fer sont de plus en plus considérées comme de potentiels agents radiosensibilisants, la combinaison d'HM avec une radiothérapie externe exacerbée par la présence des NPs est un bon moyen d'augmenter l'efficacité du traitement du cancer.

Intégrer une multithérapie et un multidiagnostic dans un composé unique en utilisant des approches nanotechnologiques est le challenge de cette thèse et comprend les principaux enjeux suivants :

- La conception de NPs dendronisées permettant un très bon contraste en imagerie médicale (IRM et/ou imagerie optique) combiné à une thérapie par hyperthermie magnétique combinée ou non à de la radiothérapie (effet radiosensibilisant de l'oxyde de fer). Pour obtenir de bons agents de contraste T_2 en IRM, il est important d'avoir des NPs avec une aimantation à saturation élevée et pour l'hyperthermie magnétique, un paramètre majeur est l'énergie d'anisotropie qui doit être élevée. Un moyen pour optimiser les propriétés magnétiques des NPs pour ces applications est la synthèse de NPs de différentes morphologies avec une taille moyenne autour de 20 nm [15,16,17] ou des NPs de ferrite dopées ou des NPs cœur coquille présentant des interactions d'échanges magnétiques. Cependant si les méthodes de synthèse actuelles permettent de moduler la taille, la forme et la composition des NPs, la morphologie des NPs ainsi que l'élaboration de NPs dopées ou cœur-coquille restent complexes à contrôler de manière reproductible car elles dépendent de nombreux paramètres expérimentaux et sont notamment sensibles à la présence d'impuretés. Ainsi de nouvelles stratégies de synthèse ont été développées dans le cadre de ma thèse pour moduler, de manière reproductible et fiable, la taille, la forme et la composition de ces NPs pour obtenir des

---

[11] J. of Neuro-Oncology 2007, **81**, 53;

[12] J. of Neuro-Oncology 2011, **103**(2), 317

[13] http://www.magforce.de/en/home.html

[14] Int J Hyperthermia, 2013, 1–9

[15] ACS Nano, 2012, **6**, 3080

[16] Scientific reports, 2013, **3**,1652

[17] *J. Phys. Chem. C,* 2012, **116**, 15702–15712

NPs efficaces en hyperthermie magnétique et comme agent de contraste pour l'IRM. La méthode de synthèse que nous avons optimisée est la decomposition thermique de precurseurs de fer, souvent un oleate de fer ou un acetylacetonate de fer, en présence de ligands dans un solvant organique à haut point d'ébullition. La forme des NPs serait contrôlée par la nature des ligands et la rampe de chauffage mais nos études préliminaires nous ont montré que toute impureté pouvait avoir une influence importante sur la morphologie des NPs. Dans ce contexte, nous avons décidé de contrôler toutes les étapes de la synthèse des NPs en allant de la synthèse des réactifs de synthèse jusqu'à l'étude des mécanismes de formation des NPs jusqu'à leur bio-fonctionnalisation et la validation de leurs propriétés theranostiques. Les différentes étapes de ce travail sont listées ci-dessous.

- Tout d'abord la synthèse du précurseur, le stéarate de fer (FeSt), a été mise au point. En variant le degré d'oxydation du fer, des stéarates de fer II ($FeSt_2$) et de fer III ($FeSt_3$) ont été synthétisés. Leur structure a été étudiée ainsi que leur stabilité en température et leur décomposition. Le degré d'hydratation s'est révélé être un point capital et les composés déshydratés ont été également étudiés.
  Le comportement des stéarates dans les conditions de synthèse de NPs sphériques ont été étudiés par différentes méthodes. En particulier, des études par MET en cellule liquide ont permis de mieux comprendre les mécanismes de synthèse des NPs.

- Une réflexion a été menée sur le changement d'échelle de la production des NPs. Le « scale up » de la synthèse du précurseur a été validé. Des études se sont concentrées sur la suppression du ligand ou du solvant pendant la synthèse ce qui permettrait de réduire le coût et le risque.

- L'extrapolation de la méthode de synthèse a été testée par la synthèse de stéarates de manganèse et de cobalt. Les précurseurs ont été caractérisés et décomposés. Des NPs de MnO et de CoO ont ainsi été synthétisées. Une simulation de la structure du stéarate de Co a permis de mettre en évidence sa décomposition particulière par rapport à celle du stéarate de fer. Le dopage de l'oxyde de fer a pu être réalisé grâce à cette synthèse contrôlée des stéarate de Mn et de Co. Puis des nanoparticules core shell Fe_3O_4@MO (avec M = Mn ou Co) ont été synthétisées. Enfin le potentiel de ces différentes NPs pour l'IRM a été étudié. Des mesures de relatixivité sur des NPs de MnO de 5, 10 et 20 nm ainsi que NPs de [redacted]e_2O_3 de 5 nm se sont focalisés sur la mise en évidence d'un effet T1. Les mêmes mesures ont étés réalisées sur des NPs core shell Fe_3O_4@MnO et se sont intéressées à un effet « dual » combinant T1 et T2.

- Le contrôle de la morphologie de NPs de $Fe_{3-x}O_4$ a été étudié en fonction de la structure du précurseur ($FeSt_2$ ou $FeSt_3$), de son degré d'hydratation et des ligands introduits dans la synthèse. Des observations en TEM liquide ont permis de corréler les résultats obtenus.

  Différentes formes anisotropes de NPs ont été obtenues et leur synthèse fut optimisée pour améliorer leur définition. Les propriétés structurales et magnétiques ont été caractérisées.

  Les NPs ont été fonctionnalisées par la molécule dendron et leur stabilité ainsi que le greffage de la molécule ont été vérifiés.

  Des études de cytotoxité et d'internalisation cellulaire menées au sein de l'équipe du Pr Florent Meyer à l'INSERM se sont focalisées sur les mécanismes d'internalisation et la quantité de NPs internalisées. Différents paramètres ont été étudiés, notamment la concentration en NPs et l'effet d'un champ magnétique externe. Puis des mesures d'hyperthermie réalisées sur les cellules ont déterminées les conditions optimales de traitement. La compréhension de l'HM au niveau cellulaire est loin d'être complète. Il est important de mieux connaitre les interactions des NPs magnétiques avec les tissus vivants pour comprendre le transfert de chaleur dans les cellules malades.

  La validation in vivo de l'efficacité en imagerie et thérapie de ces NPs. La biodistribution des NPs a été suivie par IRM puis par dosage du fer présent dans les organes par ICP-MS. Les NPs présentant la morphologie donnant les meilleurs résultats en hyperthemie ont été testées *in vivo* sur des souris présentant des tumeurs (coll J.d. L. Fuente, Sarragosse, Espagne). Leurs propriétés en tant qu'agent de contraste pour l'IRM et leur biodistribution in vivo ont été déterminées en collaboration avce le Laboratoire de Sophie Laurent et Robert Muller à l'Université de Mons en Belgique.

I. Synthèse et étude de la décomposition thermique du stéarate de fer

Une originalité de ce travail de thèse a été la mise au point de la synthèse au laboratoire du précurseur de fer. Le stéarate de fer (FeSt). Le développement de sa synthèse s'est fait dans une optique de possibilité de changement d'échelle. Différentes voies de synthèse ont été testées et la méthode par co-précipitation a été retenue. Cette méthode est **verte, économique**, **flexible, reproductible et permet le « scale up ».**

Grâce à cette méthode, plusieurs précurseurs ont pu être synthétisés en faisant varier le degré d'oxydation du fer et le nombre de chaines stéarates insérées au début de la réaction. Les précurseurs $FeSt_2$ et $FeSt_3$ ont ainsi pu être étudiés. La co-précipitation se déroulant dans l'eau, la déshydratation de ses précurseurs a été analysée et une température de 140 °C s'est révélée être optimale pour la déshydratation sans dégradation des composés.

La caractérisation des précurseurs s'est donc faite sur les quatre produits : les deux précurseurs hydratées $FeSt_2$ et $FeSt_3$ et ces précurseurs déshydratés $FeSt_{2,d}$ et $FeSt_{3,d}$.

Avant analyse fine des précurseurs, un premier essai pour mettre en avant des éventuelles différences au niveau des caractéristiques des NPs a été réalisé en décomposant les précurseurs dans nos conditions de référence. Deux conditions ont été testées : la synthèse donnant des sphères de 10 nm et la synthèse donnant des nanocubes (Figure 1).

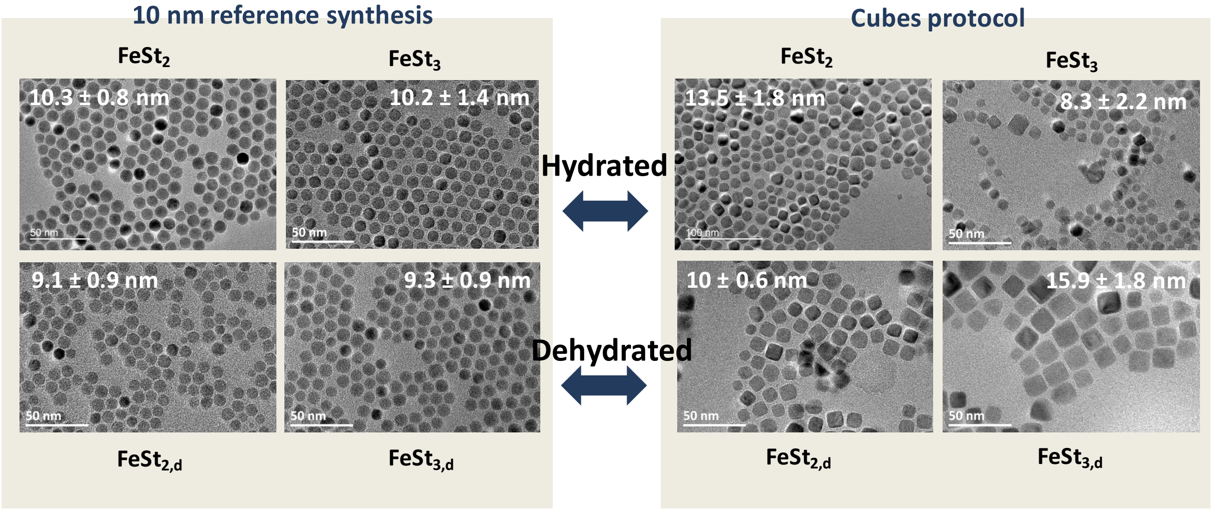

Figure 1 – Images MET des NPs résultant de la décomposition des différents précurseurs dans les conditions des sphères de 10 nm et des cubes

Les résultats présentés en Figure 1 montre que dans les conditions des sphères de 10 nm il n'y pas de différence majeure avec l'obtention de nanosphères pour tous les précurseurs. Dans la condition des nanocubes, une différence notable est observée avec l'obtention de cubes seulement avec les précurseurs déshydratés. L'analyse de ces résultats nous nous a conduits à proposer que l'eau interagirait avec l'oleate de sodium (NaOl), sensé dirigé la croissance vers la forme cubique, en formant par exemple des micelles. Cette idée est confortée par la littérature qui indique que NaOl forme des micelles pour de faibles quantités d'eau. Il n'y aurait ainsi plus assez de NaOl pour promouvoir la forme cubique en s'adsorbant sur des faces spécifiques des germes. Nous avons alors décidé d'étudier plus en détails les précurseurs synthétisés et leur décomposition thermique.

Le degré d'oxydation du fer dans les précurseurs a été déterminé par des mesures par spectroscopie Mössbauer (Col. J. M. Greneche, Université du Maine, Le MANS) et EPR (Col. N. Parizel, Université de Strasbourg). Ces mesures ont conclu à une composition en fer+III exclusive pour tous les précurseurs avec une nuance sur $FeSt_2$ qui présente un faible signal de Fe+II. Pour déterminer l'arrangement des chaines stéarates autour du cation métallique des caractérisations par spectroscopie infrarouge (IR) ont été menées.

L'arrangement des chaines stéarates va principalement dépendre de la coordination du carboxylate sur le cation fer. Différents types de coordination sont possibles comme représenté en Figure 2.

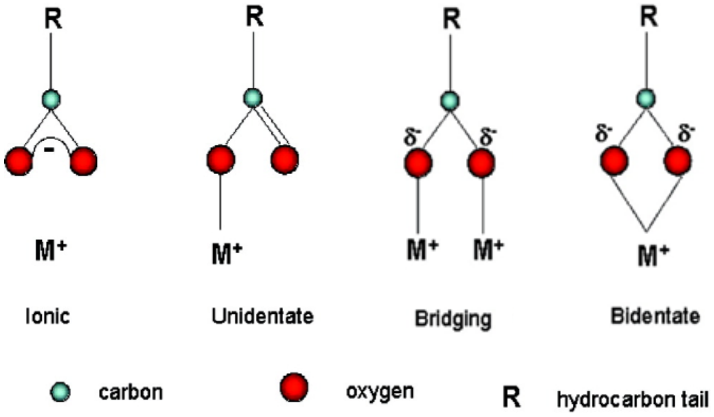

Figure 2 - Différentes coordination du groupe carboxylate sur un cation métallique

La coordination du groupe carboxylate est déterminée par IR en considérant des vibrations symétriques et asymétriques du groupe COO^- coordiné sur le cation. L'écart entre ces bandes permet de remonter au type de coordination avec une coordination chélate pour des valeurs de 40 à 100 cm^{-1} et pontante pour des valeurs comprises entre 140 à 170 cm^{-1}.

L'étude de nos composés à révélé que nos précurseurs sont assez complexes avec des bandes IR correspondant aux vibrations symétriques et asymétriques très larges qui comportent plusieurs composantes comme montré en Figure 3. Les deux types de coordinations sont présentes pour tous les composés avec une coordination chélate majoritaire pour $FeSt_2$ et pontante majoritaire pour $FeSt_3$. La déshydratation tend à favoriser la coordination chélate ce qui nous indique qu'une partie de la coordination pontante est due au phénomène d'hydratation.

Mais l'IR apporte aussi de précieuses informations sur les chaines carbonées avec l'observation du phénomène de wagging de la chaine stéarate observé pour les deux précurseurs hydratés entre 1450 et 1150 cm^{-1}. Ce wagging indique une conformation all trans des chaines carbonées et suggère une structure lamellaire. Le wagging n'est plus observé sur les composés déshydraté ce qui indique une perte de la structure lamellaire pendant la déshydratation.

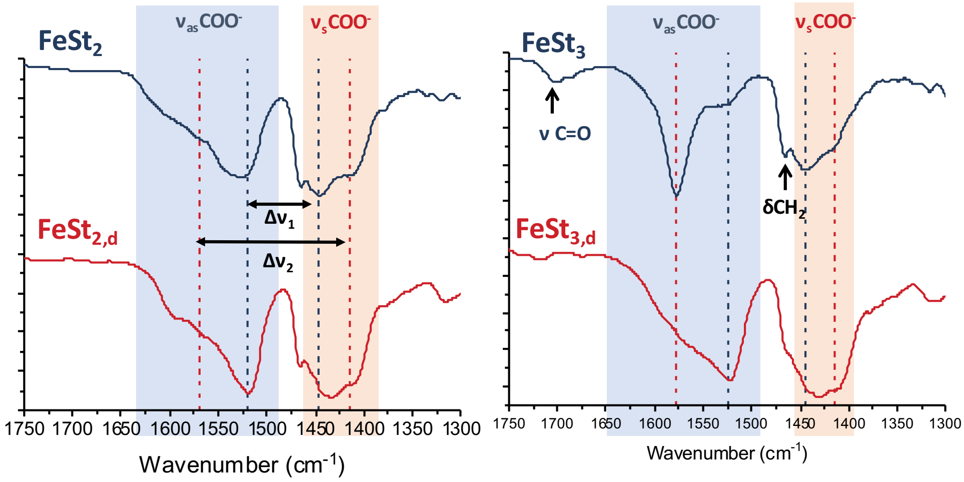

Figure 3 - Spectres IR dans la zone 1750 - 1300 cm^{-1} pour les quatre précurseurs

La structure lamellaire des précurseurs hydratés a été confirmée par diffraction des rayons X (DRX) et mesures aux petits angles SAXS (col. B. Heinrich, IPCMS, Université de Strasbourg) avec une distance inter-lamellaire d'environ 50 Å ce qui correspond à deux chaines stéarates légèrement inter digitées. De plus, les mesures SAXS montrent que les composés déshydratés sont bien amorphes à l'ambiante mais se réorganisent en structure lamellaire dès 70 °C.

L'analyse élémentaire a révélé une formule chimique moyenne présentant moins de chaines stéarates qu'attendu comme indiqué dans le tableau 1.

Tableau 1 - Formule chimique moyenne déterminée par analyse élémentaire pour les différents précurseurs

FeSt$_x$	**Coordination**		**Elemental analysis**
	Chelating	Bridging	
FeSt$_2$	++	+	FeSt1.8@6H$_2$O
FeSt$_{2d}$	+++	+	FeSt1.8@2H$_2$O
FeSt$_3$	+	+++	FeSt2.1@15H$_2$O
FeSt$_{3d}$	+++	+	FeSt2.1@5H$_2$O

Cette variation s'explique par le mélange des deux types de coordination autour de l'atome de fer qui empêchent le nombre maximal de chaines de se coordiner.

Il existe donc bien des différences structurales entres les différents précurseurs synthétisés. Les observations précédentes ont pu être complétés par une étude en modélisation (Col. M. Boero, IPCMS, Université de Strasbourg). La modélisation du $FeSt_2$ a montré que le degré d'oxydation du fer était +II seulement dans les composés anhydres. La présence de molécules d'eau autour du cation induit une élévation du degré d'oxydation vers le Fe+III. Ces mêmes molécules induisent aussi une coordination pontante entre le carboxylate, le cation de fer et une molécule d'eau.

Le travail suivant a été de mettre en évidence le lien entre ces différences structurales et la décomposition de ces précurseurs en commençant par une étude IR en température (Col. Corinne Petit, ICPEES, Université de Strasbourg) sur les différents précurseurs (Figure 4).

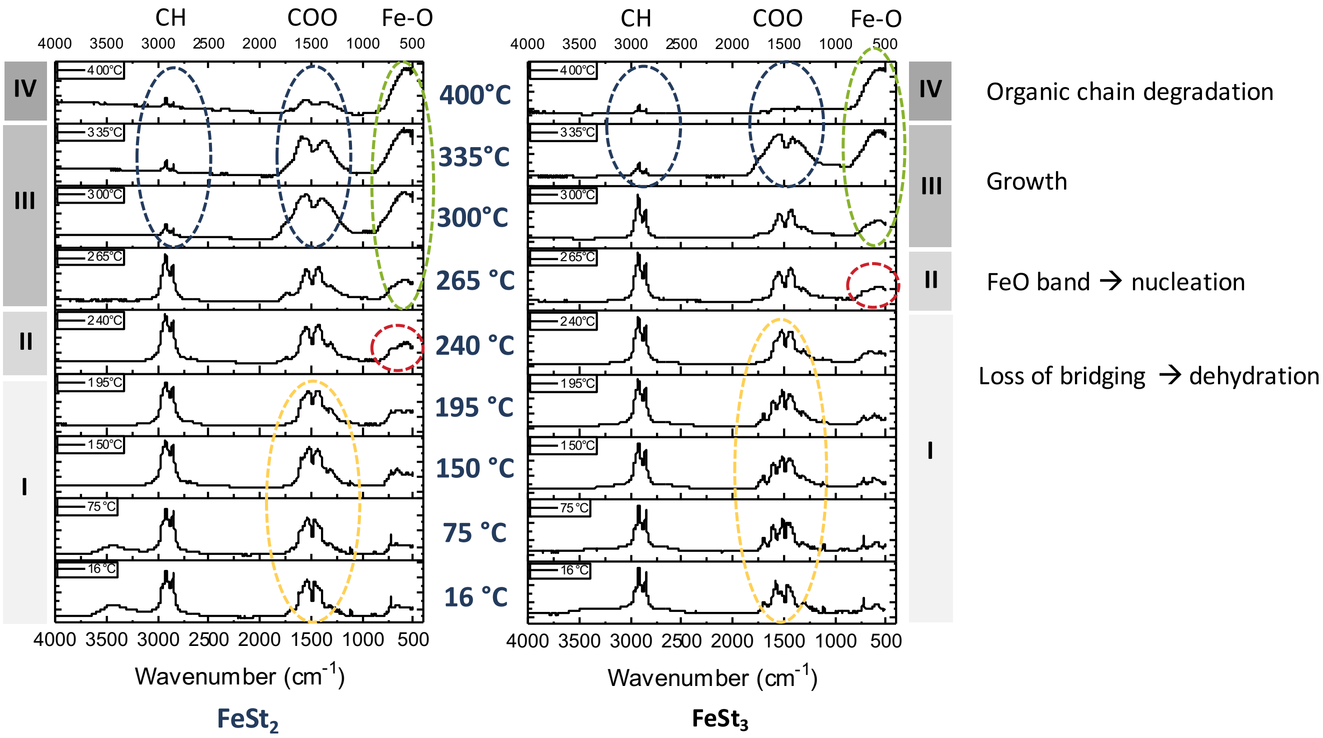

Figure 4 – Spectres IR en température des différents précurseurs entre 16 et 400 °C

Comme montré sur la Figure 4, quatre zones de température ont été identifiées avec tout d'abord une phase de déshydratation (I) puis autour de 250 °C l'apparition de la bande Fe-O (II) attribuée au phénomène de nucléation des NPs lors du procédé de décomposition thermique. Ce phénomène apparaît à plus basse température pour $FeSt_2$ que pour $FeSt_3$. Par la suite, l'intensité de la bande Fe-O augmente (III) en parallèle de la décroissance des bandes des chaines carbonées. Chaines qui sont complètement dégradées à 400 °C (IV).

Il est intéressant de noter que l'on peut retrouver ces différentes zones lors des analyses thermo gravimétriques (ATG). Ces résultats confirment les résultats de la littérature qui associent la première perte de masse à la nucléation et ceci est en accord avec l'observation de l'apparition de la bande Fe-O. La suite des évènements étant peut discernable sur les courbes ATG, l'étude des courbes DTG (Figure 5) se révèle complémentaire et démontre que $FeSt_2$ se décompose sur une plage de températures plus petite par comparaison à $FeSt_3$.

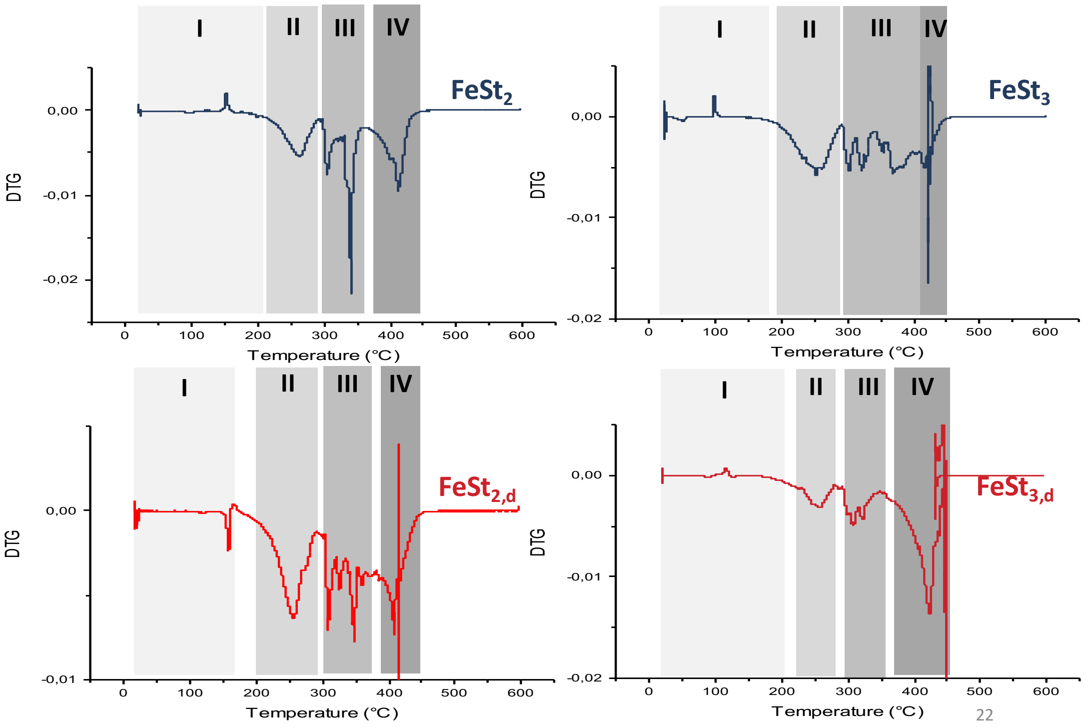

Figure 5 – Courbes DTG des différents précurseurs avec mise en évidence des zones identifiées à l'aide des spectres IR en température

Les précurseurs déshydratés présentent également une décomposition à plus basse température. Cet effet de l'eau sur la décomposition des précurseurs a également été confirmé par une étude en modélisation.

Cette étude nous a permis de mettre en évidence l'apparition de la phase oxyde de fer pendant la première perte de masse de l'ATG ce qui valide que la germination a bien lieu avant 300°C en accord avec la littérature. La décomposition thermique des différents précurseurs (figure 1) a montré des variations dans le rendement de décomposition des stéarates et ces rendements sont en cohérence avec leur stabilité thermique.

Le travail de cette partie est une première démonstration du rôle important de la structure du précurseur et se son degré d'hydratation sur la synthèse de nanoparticules. L'étude fine des composés a permis d'établir un lien entre la structure et l'hydratation sur la décomposition et le rendement en nanoparticules.

II. Etude *In Situ* de la décomposition thermique du stéarate de fer

La compréhension des mécanismes de synthèse de la décomposition thermique reste encore à élucider. En effet, les résultats de la littérature montrent clairement des difficultés pour contrôler de manière reproductible la forme ou le dopage des NPs. Des milieux réactionnels dans une condition de synthèse de référence des nanosphères de 10 nm (traitement à 120°C du milieu réactionnel pendant 1h) ont été étudiés avec les précurseurs (hydratés et déshydratés) synthétisés précédemment.

La technique originale de TEM en cellule liquide nous a tout d'abord indiqué que le milieu réactionnel des NPs présentait différents types de structure (Figure 6). Avec un seul type de structure au cœur clair et aux parois contrastées pour $FeSt_2$ et ces mêmes structures accompagnées de plus petites avec un contraste noir homogène pour $FeSt_{2,d}$.

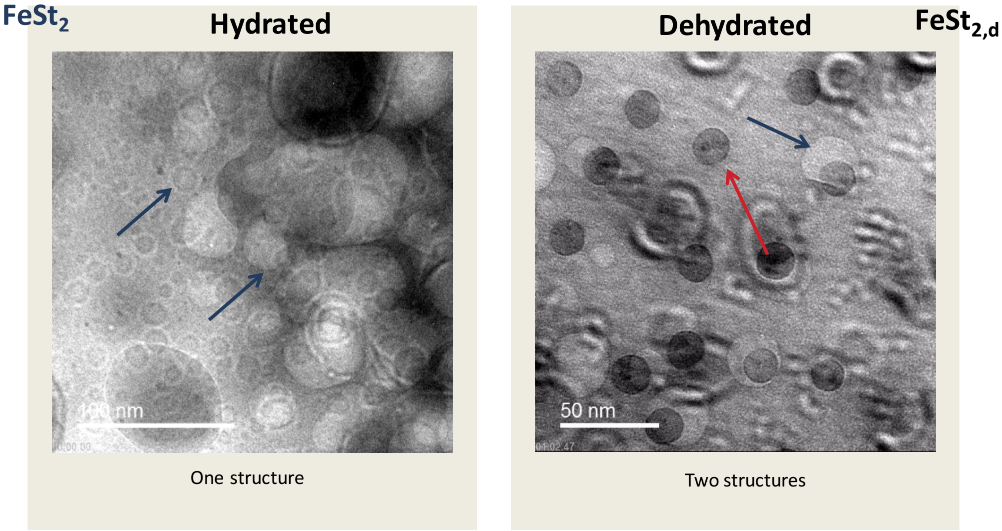

One structure

Two structures

Figure 6 - Images TEM in situ du milieu réactionnel

Différentes méthodes ont été utilisées afin de valider la présence de ces structures qui pouvaient être des artefacts du TEM.

Une étude en AFM en phase liquide a été menée (Col. G. Francius, LCPME, Université de Nancy) et a permis d'observer des structures à température ambiante. La mesure de la taille de ces structures est en accord avec les observation TEM, avec des tailles plus élevées pour les précurseurs hydratés que pour les déshydratés.

L'existence de ces structures a également été démontrée par une première étude SAXS (Col. B. Heinrich, IPCMS, Université de Strasbourg) qui doit toutefois être complétée afin d'obtenir une distribution en taille précise en fonction de la température.

Toutefois à partir de ces observations, des structures des objets observés ont pu être proposées. La quantité d'eau présente dans les précurseurs étant trop faible, elles ne peuvent pas être attribuées à des micelles. Le système serait donc vésiculaire et le milieu étant organique, les objets seraient des vésicules inverses comme représenté en Figure 7.

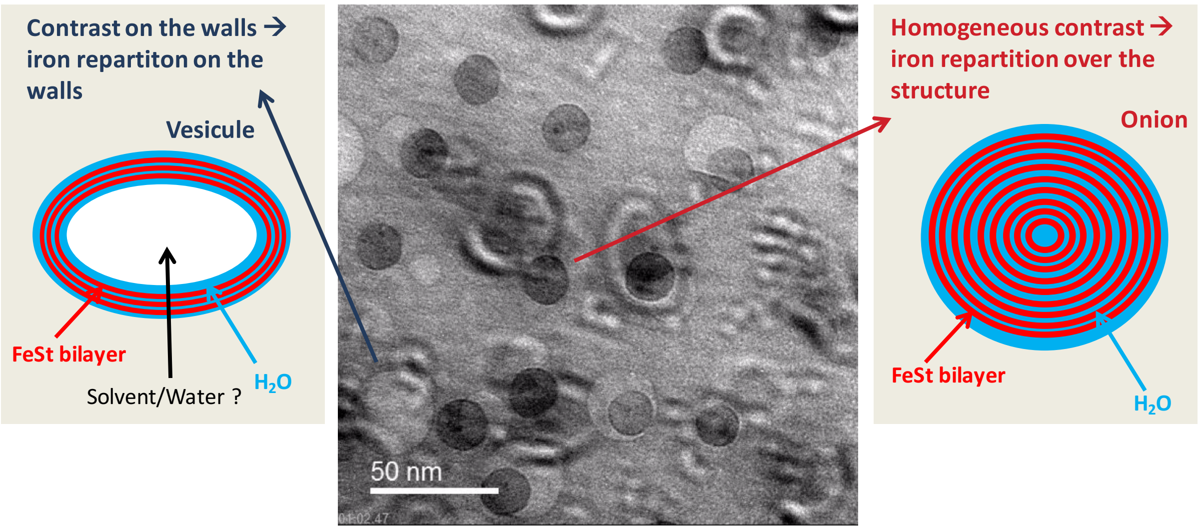

Figure 7 - Structure proposée pour les deux types d'objets observés en TEM

La première structure appelée « vésicule » serait composée de bi couches de stéarates de fer et présente une cavité. La deuxième nommée « onion », ne présenteraiet que des bicouches de stéarates de fer.

L'évolution de ces structures avec l'exposition au faisceau (qui induit une augmentation locale de température) montre la formation de point noir très contrasté qui sont très probablement des germes de nanoparticules. Le diamètre de ces germes augmente hors des structures vésiculaires ce qui tend à indiquer que la nucléation prend place dans les vésicules mais la croissance se fait en dehors (Figure 8).

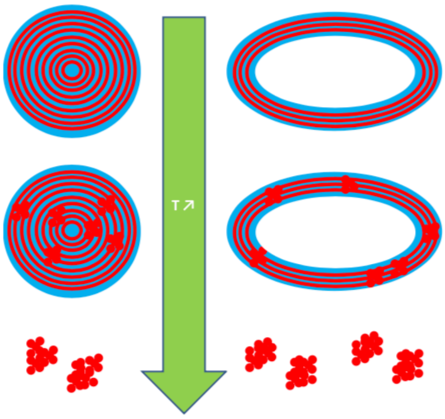

Figure 8 - Evolution des structures vésiculaires avec l'exposition au faisceau d'électrons

Cette étude est la première à montrer la formation des nanoparticules in situ. L'observation et la caractérisation de structures vésiculaires par des méthodes originales nous a permis de mettre en évidence le mécanisme peu connu de la formation de NPs par décomposition thermique. La connaissance de ce mécanisme permet de comprendre les difficultés pour contrôler la morphologie et la composition des NPs et nous permets d'imaginer de nouvelles stratégies innovantes pour le design de NPs.

III. Vers un changement d'échelle et une extrapolation de la synthèse du stéarate de fer au Mn et au Co

a. « Scale up » de la synthèse du précurseur

Un « scale up » de synthèse du précurseur a pu être mené. L'importance de l'agitation pendant la formation du complexe s'est avéré être capitale. Un changement d'échelle d'ordre 4 a pu être réalisé et pourrait être encore augmenté avec du matériel adapté.

b. Etude des paramètres de synthèse

Le ligand utilisé dans la synthèse de NPs sphériques (acide oléique) est un facteur limitant pour le changement d'échelle. Pour conserver la qualité des NPs, il lui faut être extrêmement pur ce qui implique un coût élevé (30 € le gramme). Avec plus d'1g par synthèse avant « scale up », cela fait de lui le produit le plus cher de la synthèse. Pour diminuer le coût de la synthèse, des décompositions ont étés réalisées sans la présence de ce ligand. En jouant sur la nature des solvants, le précurseur et la rampe en température des NPs sphériques de 5 et 10 nm ont pu être obtenues.

Mais le solvant organique est également un problème car faire chauffer de grands volumes à plus de 300 °C pose des questions de sécurité. Des synthèses menées sans solvant mais avec uniquement de l'acide oléique ont démontré que l'on peut synthétiser des NPs sphériques en se passant du solvant.

Pour pousser cette étude, un précurseur a été décomposé sans ligand et sans solvant. Des NPs de forme ovoïdale ont étés obtenues.

Cette étude démontre que le solvant et le ligand sont utiles dans la synthèse de NPs sphériques mais pas capitales. La synthèse des NPs en décomposant le précurseur seul pourrait être un moyen simple de synthétiser de grandes quantités. Toutefois du travail d'optimisation reste encore à réaliser.

c. La purification des NPs

Après synthèse, l'excès de ligand en surface des NPs et les sous-produits de la réaction doivent être retirés. La méthode la plus répandue est la centrifugation de NPs en suspension dans un solvant polaire (Chloroforme, THF, cyclohexane …) en présence d'un solvant apolaire (acétone, éthanol …). Les molécules de ligands très solubles dans le solvant apolaire vont donc être récupérées dans le surnageant et les NPs auront précipitées. Toutefois il faut répéter cette opération de nombreuses fois ce qui consomme du temps et prolonge l'exposition du manipulateur a des solvants CMR. Une autre méthode a été développée : la désorption contrôlée du ligand. En chauffant le précèdent mélange dans des conditions douces pendant une durée précise, des NPs « propres » ont pu être obtenues. Cette procédure va maintenant être introduite dans la laboratoire.

Concernant le changement d'échelle, la synthèse du précurseur étant bien maitrisée, les premiers résultats démontrent qu'une production à large échelle serait possible et un matériel de synthèses plus adapté devrait être acheté pour réaliser ce point. La nouvelle procédure de lavage promet un gain de temps et d'argent non négligeable. La preuve de concept étant validée, une future optimisation permettra d'implémenter cette méthode dans la routine. Les différentes pistes pour une synthèse raisonnée de NPs sont très prometteuses et ouvrent de nombreuses perspectives. Il reste toutefois un travail de recherche afin de mettre au point des protocoles implementables.

d. Synthèse du stéarate de Mn, caractérisation et décomposition

Le protocole de synthèse du stéarate de fer fut dans un premier temps étendu au stéarate de Mn. Toutefois le précurseur obtenu s'est décomposé dans des conditions de synthèse normalement isotropes en assemblage directionnel de sphères de MnO (figure 9). Une optimisation de la synthèse du stéarate de Mn ($MnSt_2$) en faisant varier divers paramètres de synthèse a été menée et a permis en augmentant le temps de réaction d'obtenir un précurseur donnant des sphères dans des conditions isotropes. Les différentes caractérisations (IR/ RX/ ATG) n'ont pas montré de différence dans la structure du précurseur mais plutôt une cinétique de réaction plus lente pour la formation de stéarate de Mn.

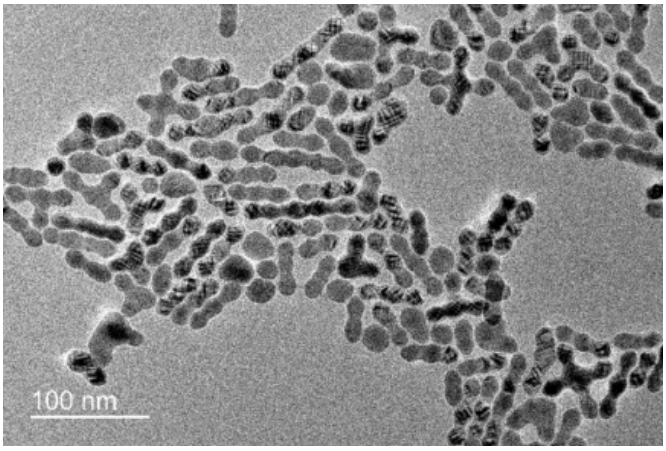

Figure 9 - Assemblage 1D de NPs de MnO

Le milieu réactionnel de la synthèse de ces assemblages a été étudié en AFM en phase liquide confirmant la présence de vésicules comme observé pour le fer. Il semblerait que cette morphologie repose sur une croissance en milieu confiné mais ce point reste à démontrer.

Différents essais ont été réalisés afin de reproduire cette morphologie en introduisant divers ligands dans la synthèse et des morphologies proches ont pu être obtenues sans pour autant reproduire cet alignement spécifique observé précédemment (Figure 10). Il a été observé la formation de structures « pods » avec l'addition de NaOl. Toutefois, la variation de la quantité de NaOl permet seulement de contrôler la tailler des NPs formant le « pods » avec des tailles de NPs qui augmentent avec la quantité de NaOl.

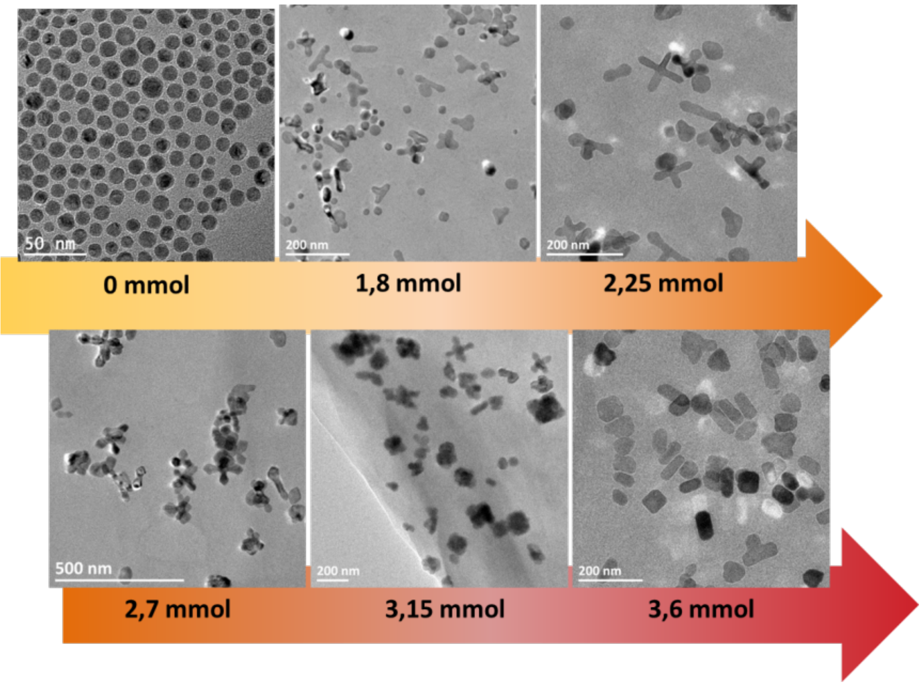

Figure 10 - Synthèse de « pods » avec différentes quantités de NaOl

La synthèse sans ligand a elle aussi été testée avec le précurseur de manganèse permettant d'obtenir des NPs sphériques de différentes tailles entre 5 et 15 nm dépendamment de la température de synthèse (Figure 11).

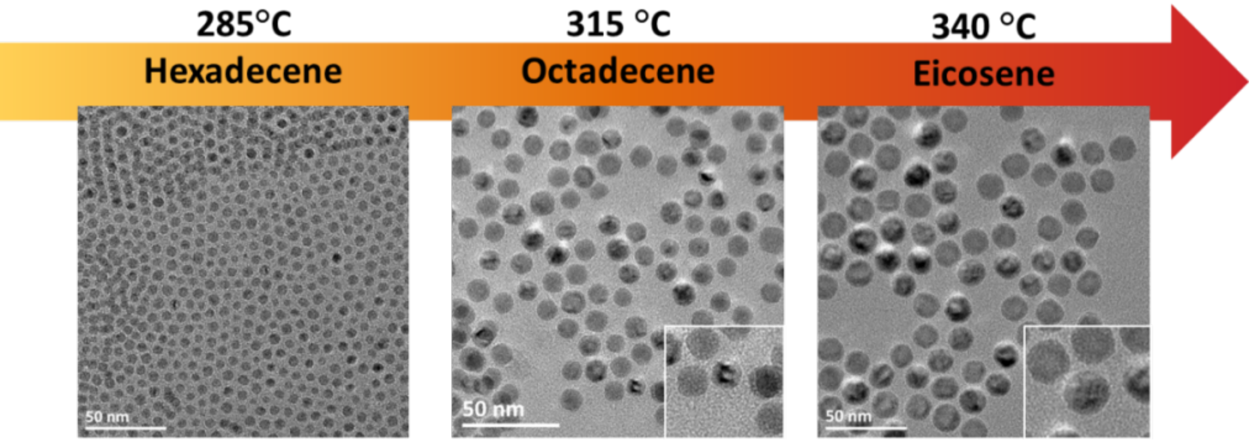

Figure 11 - Synthèses sans ligand de NPs de MnO

Le mécanisme de synthèse des NPs de MnO recèle encore quelques secrets, toutefois tout semble indiquer que la formation de structures de NPs repose sur un mécanisme de stabilisation de vésicules. La compréhension de ce mécanisme serait un atout pour la synthèse de NPs magnétiques aux propriétés optimisées.

e. Synthèse du stéarate de Co, caractérisation et décomposition

La même étude que celle réalisée sur le stéarate de M, $MnSt_2$ a été réalisé avec le stéarate de cobalt ($CoSt_2$). La synthèse à partir de $CoSt_2$ n'a pas montré la même dépendance aux paramètres de synthèse que celle utilisant $MnSt_2$ avec l'obtention de structures agrégée dans tous les cas. Toutefois, la décomposition d'un $CoSt_2$ dans différentes conditions déjà publiées a conduit aux mêmes morphologies exotiques variés déjà rapportées dans la littérature (Figure 12).

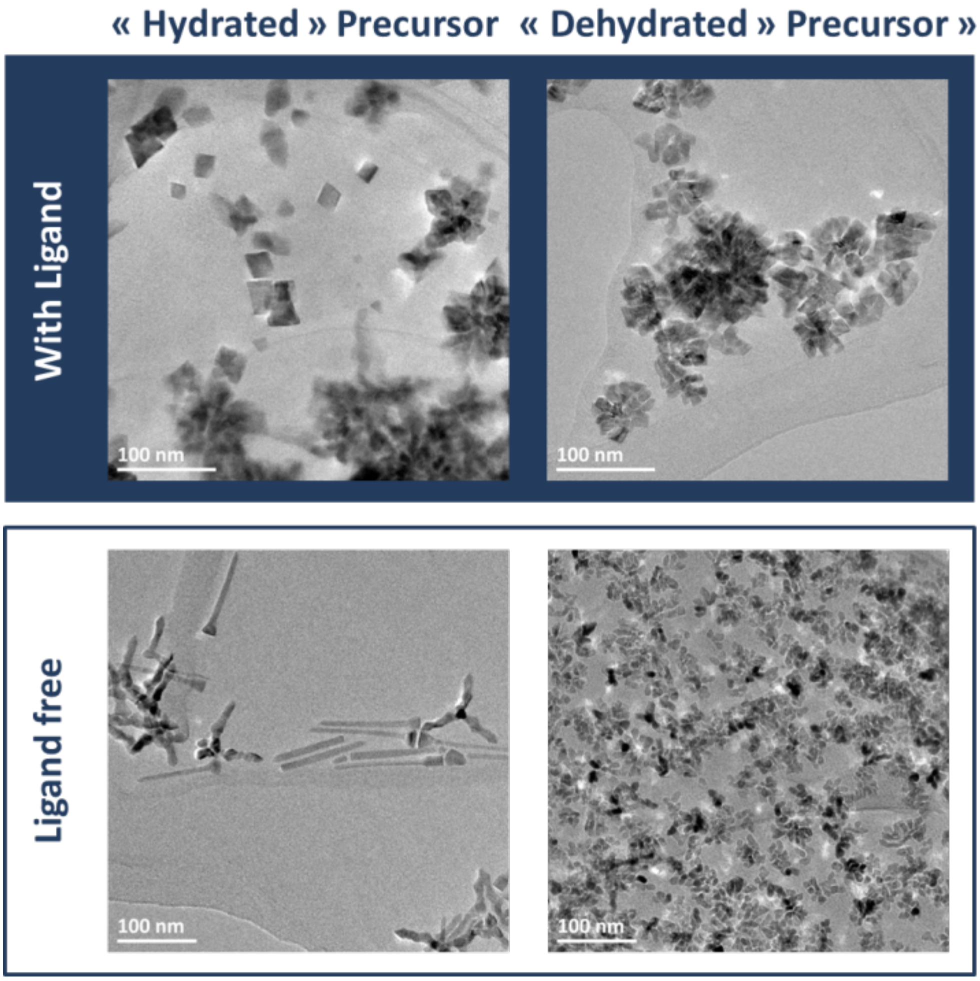

Figure 12 - NPs de CoO obtenues dans différentes conditions de décomposition

La décomposition du CoSt2 avec la température a été modélisée (Col. C. Massobrio, IPCMS, Université de Strasbourg) démontrant une décomposition et une dégradation de la chaine stéarate catalysées par le cobalt atomique ce qui pourrait expliquer les morphologies variées obtenues.

f. Synthèse de NPS cœur-coquille Fe_3O_4@MO

Une méthode pour moduler les propriétés magnétiques est la synthèse de systèmes cœur-coquille avec des matériaux constituant le cœur et la coquille avec des propriétés magnétiques différentes. Le cœur@coquille, $Fe_{3-x}O_4$@MnO, pourrait allier les propriétés IRM T_2 de $Fe_{3-x}O_4$ et T_1 du MnO. Fe_3O_4@CoO présente pour sa part un couplage d'échange bias qui augmente l'anisotropie et le champ coercitif des NPs.

La synthèse de $Fe_{3-x}O_4$@MnO a été réalisée avec une décomposition en deux temps (figure 13). Tout d'abord le cœur de $Fe_{3-x}O_4$ fut synthétisé puis $MnSt_2$ fut introduit dans le milieu réactionnel et décomposé afin de générer la couche de MnO en surface du coeur.

Des NPs Fe_3O_4@CoO furent synthétisées de la même manière. Différentes épaisseurs de CoO purent être obtenues en modulant la quantité de CoSt2 ajoutée dans la deuxième étape de la synthèse.

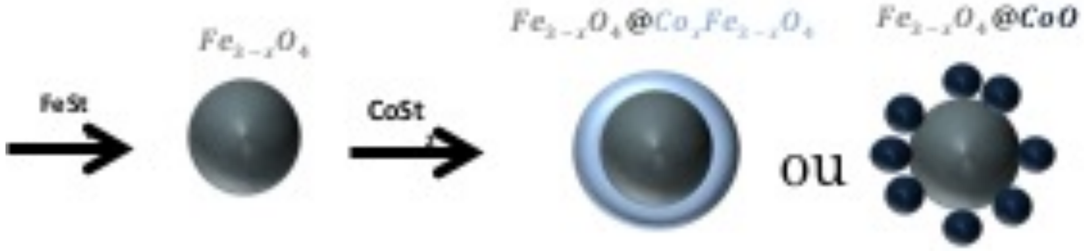

Figure 13 - Principe de synthèse des NPs coeur coquille

Des caractérisations structurales ont été menées (IR/RX/TEM) afin de valider la structure des objets synthétisés. Des mesures magnétiques ont permis de mettre en évidence l'augmentation du champ coercitif avec l'épaisseur de CoO de la coquille . Des mesures XMCD ont permis d'affiner la structure des NPs et de montrer la présence de ferrite de cobalt quand la quantité de CoSt2 introduite était assez faible.

La synthèse et la décomposition des stéarates de manganèse et de cobalt nous a permis de confirmer l'importance de contrôler la fabrication du précurseur afin de pouvoir contrôler la synthèse de nanoparticules. Les NPs d'oxydes de MnO et de CoO sont rapportés dans la littérature avec de nombreuses morphologies intéressantes pour des applications variées. Le développement de notre méthode de synthèse nous a permis de synthétiser toute un panel de ces morphologies. Cette partie démontre que le travail effectué sur le stéarate permet de travailler avec une boîte à outils chimique, véritable atout pour le design de NPs.

IV. Conception de nanoplateformes combinant des propriétés en IRM et hyperthermie magnétique

a. Influence de la structure et du taux d’hydratation sur le contrôle de la morphologie

L’étude précédente a démontré l’effet de la structure du précurseur sur sa décomposition. Au niveau de la synthèse de NPs, la différence entre les stéarates s’est montrée cruciale pour la synthèse de NPs anisotropes. Afin de mettre en évidence le rôle de la structure et du degré d’hydratation sur le contrôle de la forme, les différents précurseurs ont été décomposés en présence de différentes quantités de NaOl. NaOl est un ligand très utilisé pour la synthèse de NPs anisotropes. La définition de NPs anisotropes s’est révélée dépendant majoritairement du précurseur plus que de la quantité de NaOl introduite (figure 14).

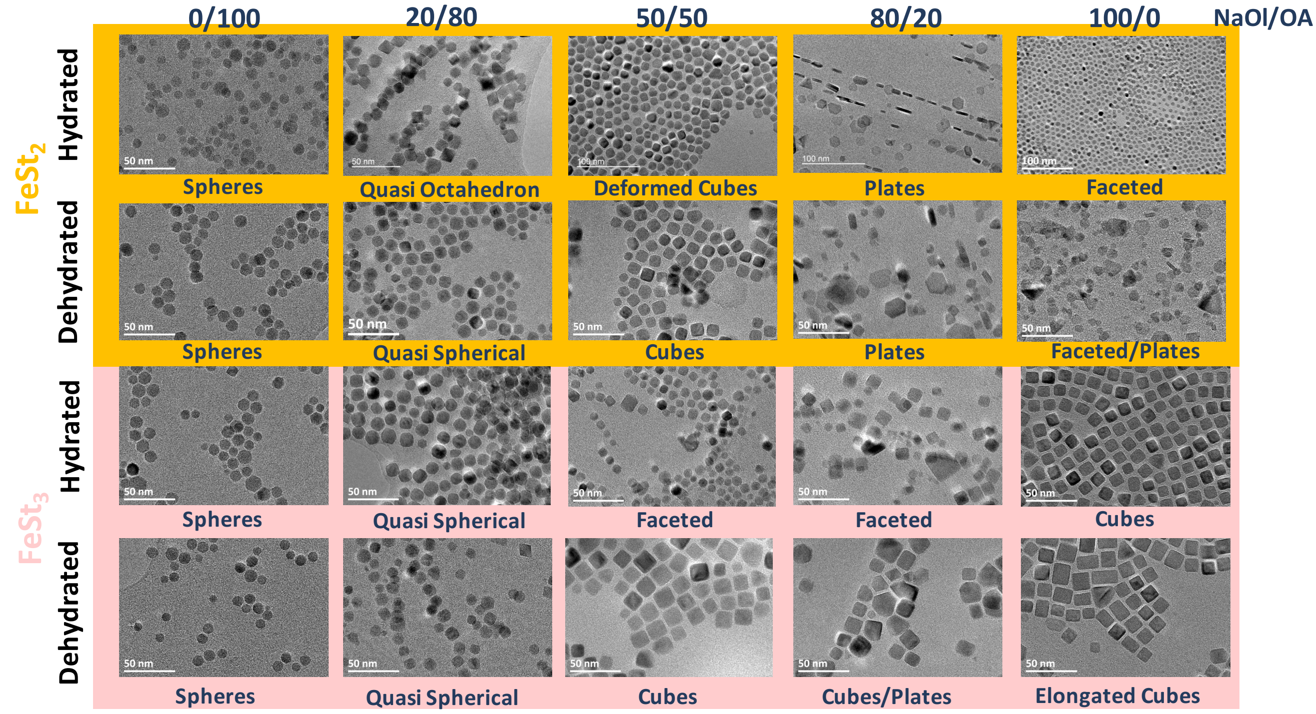

Figure 14 - Décomposition des 4 précurseurs avec différentes quantités de NaOl

Une étude du mécanisme de formation des NPs anisotropes a permis de mettre en évidence un effet capital de la phase de nucléation et de la structure du germe qui sont en lien direct avec le précurseur. Le taux d’hydratation joue un rôle seulement si la quantité d’eau présente est assez importante pour perturber les phénomènes de formation des NPs. Le rôle principal du NaOl s’est révélé d’être un agent de contrôle de la nucléation. Dans un second temps, son interaction avec la surface du germe permet une orientation de la forme. EN présence d’eau NaOl formant des micelles est moins disponible pour diriger la croissance anisotrope des NPs et différentes morphologies sont ainsi obtenues. Cette vision de la synthèse est très originale et se détache de la littérature où seules les conditions de synthèse (température, concentration …) sont étudiées. Nous verrons par la suite que ce contrôle de la synthèse du précurseur permet de mieux contrôler le « design » des NPs. L'étude des paramètres thermiques de la synthèse ont permis de confirmer le rôle de la nucléation comme central et de mettre en lumière le rôle de l'énergie thermique qui peut aussi favoriser ou non une certaine forme. Cela a été confirmé par TEM liquide où le contrôle de la dose d'électrons (donc d'énergie) a permis dans les mêmes concentrations de ligands et de précurseur de former des NPs isotropes ou anisotropes.

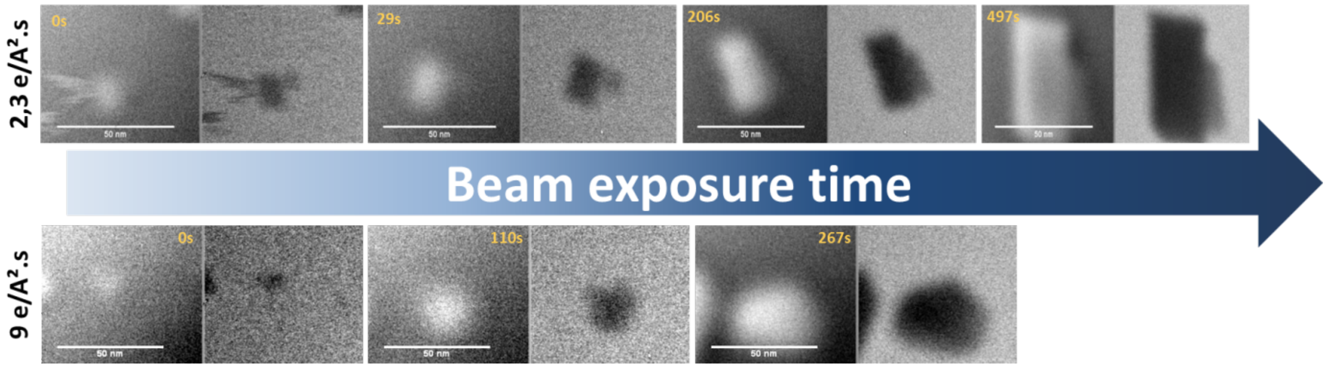

Figure 15 - Contrôle de la morphologie en TEM in situ par la dose d'électrons sur un milieu réactionnel anisotrope

Les différentes formes obtenues ont été caractérisés structuralement (IR/RX).

Cette partie montre un résultat majeur de la thèse : le précurseur et sa décomposition sont liés à la morphologie des NPs obtenues dans des conditions précises. Cela a permis d'obtenir un meilleur contrôle de la morphologie anisotrope des NPs cubiques ainsi qu'une morphologie originale les plaquettes dont l'anisotropie de forme est plus élevée que celle des NPs cubiques.

b. Optimisation de la forme pour l'optimisation des propriétés magnétiques

L'étude précédente a permis la synthèse de NPs anisotropes autour de 10-15 nm en taille. Or il a été demontré que la taille optimale pour les applications en HM est autour de 20 nm. Il a donc fallu synthétiser ces objets avec une taille plus proche de 20 nm pour espérer observer une efficacité en HM satisfaisante. La synthèse des sphères et des cubes a donc été reproduite dans des solvants à plus haut point d'ébullition (squalane et eicosène respectivement) donnant des NPs avec un diamètre moyen proche de 20 nm. Les cubes présentant une structure coeur-coquille $FeO@Fe_{3-x}O_4$ leurs aimantations à saturation sont plus faibles comparées à des NPs homogènes. Différents essais ont été menés pour obtenir des nanocubes de composition homogène (effet de la rampe en température, introduction d'un oxydant dans la synthèse) mais sans succès. En adaptant la méthode de Pellegrino et al qui ont montré que les produits de la décomposition du benzylether permettaient d'obtenir une morphologie cubique, des NPs cubiques aux faces creuses (octopods) de composition homogène ont été synthétisées en introduisant du benzylether comme seul solvant de synthèse (Figure 16).

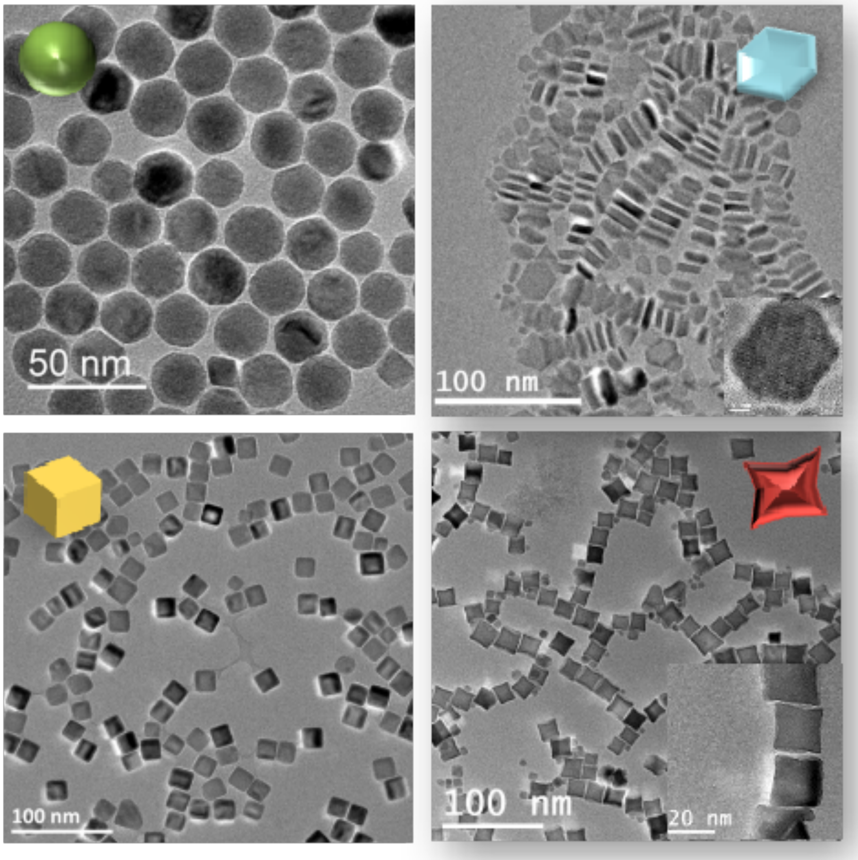

Figure 16 - Nanoparticules d'oxyde de fer de différentes morphologies (sphères, cubes, octopodes et plaquettes)

Les NPs anisotropes obtenues ont été caractérisées en commençant par leur caractérisation morphologique (TEM et Tomographie TEM pour les plaquettes [collab Ovidiu Ersen, IPCMS]), et structurale (Tableau 2) par DRX et spectroscopie IR et par la mise en évidence de leur stabilité colloïdale en suspension (DLS) montrant que l'on obtient bien des NPs d'oxyde de fer avec une structure spinelle inverse stables en suspension.

Tableau 2 - Caractérisations structurales des différentes morphologies

NPs	Mean TEM size (nm)	Crystallites size (nm)	Lattice parameter (Å)		Composition
			Spinel phase	Wüstite phase	
NS22	22.2 ± 1.8	13	8.391	X	$Fe_{3-x}O_4$
NC	15.9 ± 1.8	8	8.392	4.237	$Fe_{3-x}O_4$@FeO

NO28	27.8 ± 4.2	25 <400> /23 <511>	8.370	X	$Fe_{3-x}O_4$
NPl	16.7 ± 5.2	17 <222>	8.384	X	$Fe_{3-x}O_4$

Le savoir développé précédemment nous a donc permis d'optimiser nos différentes morphologies afin de maximiser les propriétés magnétiques de nos différents objets en vue de leur utilisation pour des applications théranostiques.

c. Dendronisation des différentes NPs

Les NPs ont ensuite été fonctionnalisées par une molécule dendron développée à l'IPCMS (Col. D. Felder, IPCMS, Strasbourg). La fonctionnalisation a été validée par spectroscopie IR (Figure 17) et par Mesures HRMAS (Col. S. Laurent, UMons).

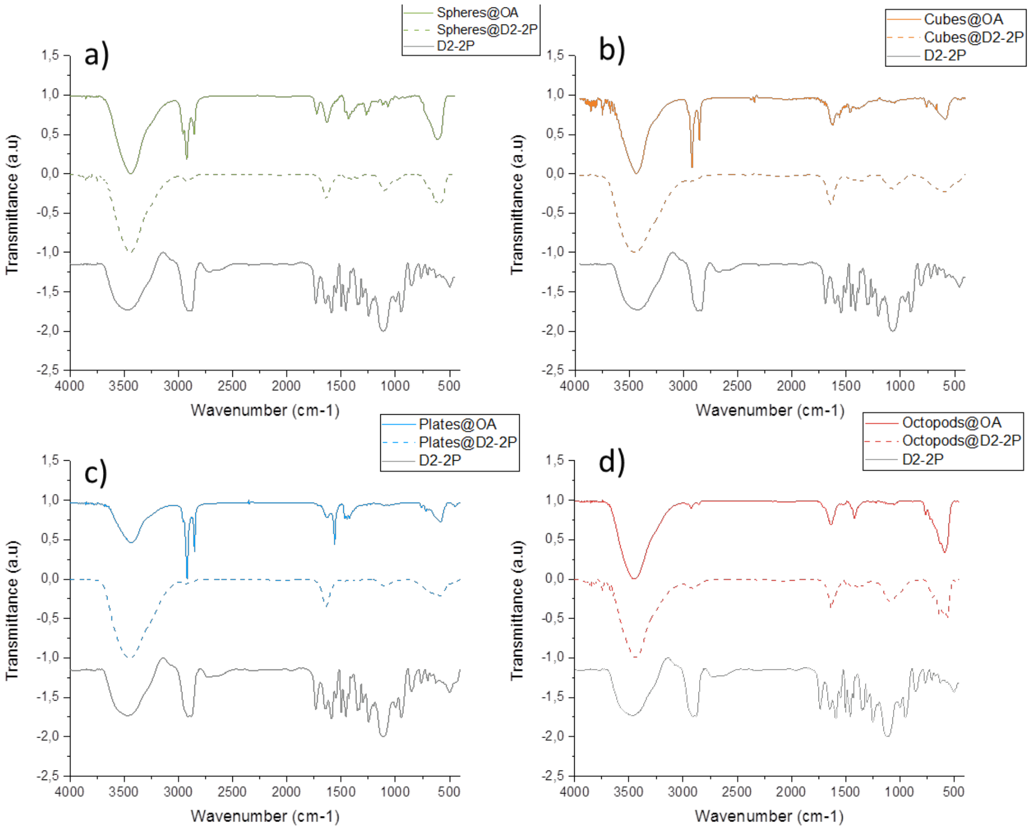

Figure 17 Validation de la fonctionnalisation par la molécule dendron par spectroscopie IR pour les différentes morphologies

La fonctionnalisation validée, la stabilité colloïdale a été vérifiée par des mesures granulométriques par DLS dans l'eau et dans différents milieux proches du milieu physiologique. Toutes les morphologies présentent une bonne stabilité colloïdale dans tous les milieux exceptés les cubes qui présentent une légère agrégation observée pendant leur fonctionnalisation. Ceci peut être expliqué par les surfaces planes qu'ils présentent qui favoriseraient les interactions entre molécules d'acide oléique et défavoriserait leur remplacement par la molécule dendron.

Une analyse originale a été menée par TEM-EELS afin d'étudier le degré d'oxydation du fer en surface des NPs (Col. G. Botoon, McMillan Univeristy, Canada). Les acquisitions EELS suggèrent un degré d'oxydation réduit du fer en surface des octopodes et des plaquettes (Figure 18) ce qui est inattendu car généralement la surface des NPs est oxydée en surface en maghemite qui ne comporte que des cations Fe^{3+}.

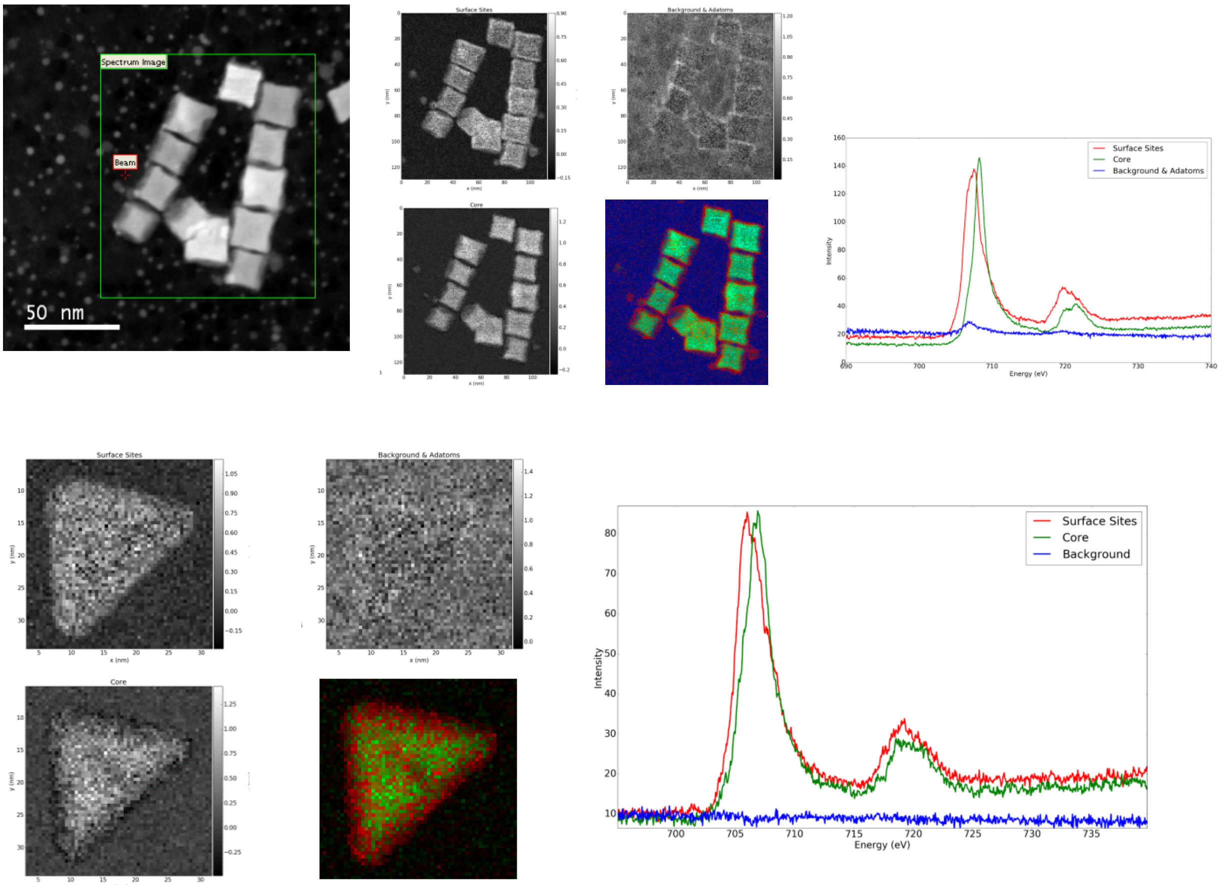

Figure 18 - Analyses EELS des ocotopodes (haut) et des plaquettes (bas)

La spectroscopie Mössbauer (Col. J. M. Greneche, Université du Maine, Le Mans) a permis de déterminer finement la composition avec : pour les sphères une composition proche de celle de la magnétite ($Fe_{2.8}O_4$), des plaquettes ($Fe_{2.68}O_4$) et des octopodes ($Fe_{2.74}O_4$) .

La spectroscopie Mössbauer sous champ suggère des distributions de degrés d'oxydation du fer plus importantes avce les octopodes et les plaquettes qu'avec les nanosphères qui pourrait être reliée aux résultats de EELS-TEM. Les deux méthodes convergent vers le fait que la surface des octopodes et des plaquettes est différente de celles des sphères.

La deuxième partie de la caractérisation s'est portée sur les propriétés magnétiques (SQUID, Col.D. Ortega, IMEDIA, Madrid). Les NPs anisotropes synthétisées sont superparamagnétiques avec des aimantations à saturation Ms différentes (de 108 à 31 $A.m^2/kg_{Fe}$ à 300 K) laissant présager des résultats différents en Hyperthermie magnétique. Les nanocubes présentent une Ms faible car le cœur FeO antiférromagnétique ne contribue pas magnétiquement. Les nanoplaquettes présentent une aimantation plus faible qu'attendue et attribuée à leur faible épaisseur.

Des mesures d'interactions entre particules ont été menées grâce à l'acquisition d' « Henkel plots ». Ces mesures permettent de calculer le champ d'interaction H_{int} qui donne une indication de la force des interactions dipolaires entre nanoparticules. Le champ d'interaction est défini selon l'équation suivante :

$$H_{int} = \frac{1}{2}|H_r' - H_d'|$$

Avec H_r' et H_d' les valeurs obtenues du fitting des courbes de Henkel plots.

Le tableau 3 présente les valeurs calculées pour les différentes formes.

Tableau 3 - Valeur du champ d'intéraction pour les différentes formes

	H_{int}	Morphology	Composition	Mössbauer spectroscopy
NC	69.2	Cubes	$FeO@Fe_{3-x}O_4$	
NS18	27.6	Spheres	$Fe_{3-x}O_4$	
NO28	18.7	Octopods	$Fe_{3-x}O_4$	$Fe_{2.74}O_4$
NPl	17.1	Platelets	$Fe_{3-x}O_4$	$Fe_{2.68}O_4$
NO18	15.6	Octopods	$Fe_{3-x}O_4$	
NS22	14.5	Spheres	$Fe_{3-x}O_4$	$Fe_{2.8}O_4$

D'après ces mesures, les interactions entre NPs seraient faibles pour toutes les formes exceptées pour les cubes où la valeur du champ d'interaction est élevée.

Nos différentes morphologies de NPs anisotropes présente donc des différences structurales mais aussi magnétiques. Cela permet de s'attendre à des résultats variables selon la morphologie dans les applications theranostiques.

d. Caractérisation *theranostic in vitro* et *in vivo* des NPs

Dans un premier temps, les propriétés des NPs en tant d'agent de contraste IRM ont été testées par des mesures de relaxométrie à différent champs (Col. S. Laurent, UMons, Belgique). La Figure 19 présente les valeurs de r_2 mesurées pour les différentes morphologies à 1.41 T. Toutes les morphologies présentes de bonnes valeurs bien au-dessus de la valeur d'un produit anciennement commercialisé.

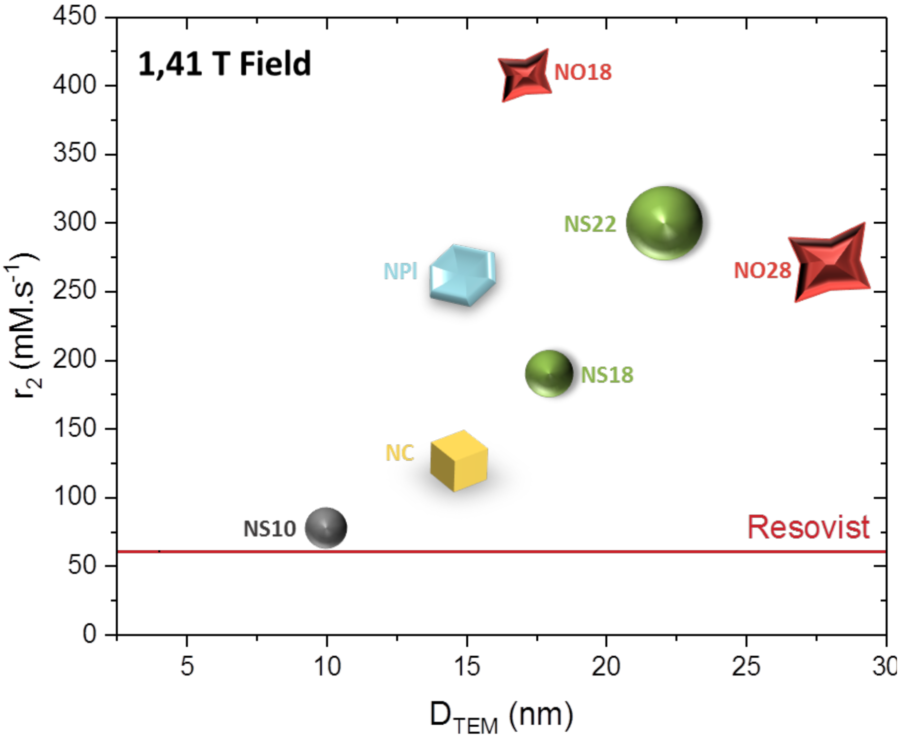

Figure 19 - Valeurs de r_2 mesurées pour les différentes NPs dendronisées à 1.41 T

On note toutefois des différences entre morphologies avec les octopodes qui se détachent du reste des autres NPs. Des mesures de NMRD ont également mis en avant un comportement unique des octopodes.

Avant de continuer vers des essais *in vivo*, la biocompatibilité des NPs dendronisées a été testée sur des cellules humaine du cancer du foie (hepatocarcinome). Un test de cytotoxicité MTT après 24h d'incubation a été réalisé montrant aucune toxicité jusqu'à 440 mg/L en fer.

Une étude de la biodistribution *in vivo* des NPs a ensuite été réalisée (Col. S. Laurent, UMons, Belgique) sur des souris dans un IRM à 9.4 T.

La biodistribution menée sur les quatre morphologies a permis de d'observer un fort contraste noir dans le foie des souris dès l'injection. Ce contraste reste constant jusqu'à 24 h après l'injection (Figure 20), ce qui suggère une captation des NPs par le foie. Un hyposignal est également observé dans la vessie ce qui indique une élimination par les voies urinaire et hépato biliaire.

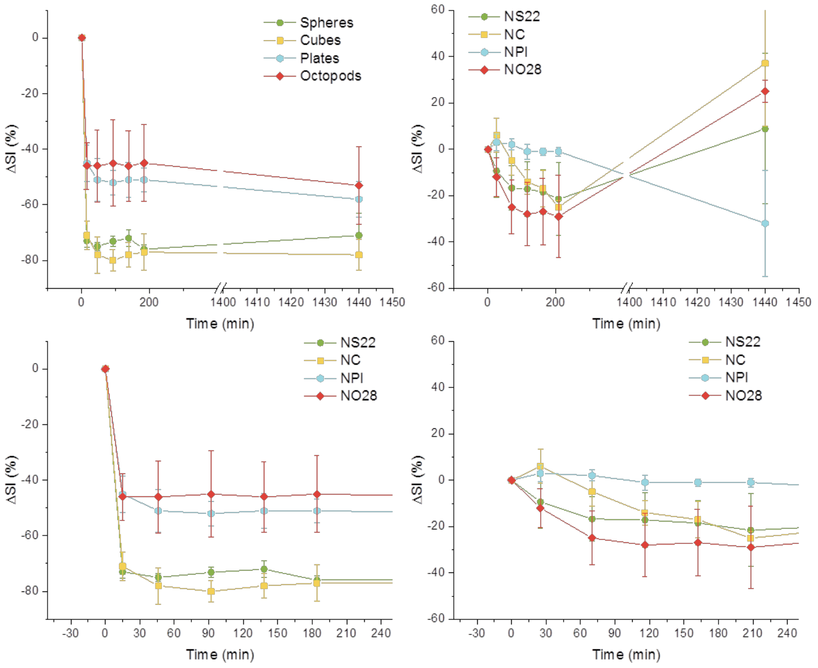

Figure 20 - Variation du signal IRM dans le foie et la vessie pour les différentes morphologies

La détermination de la quantité de fer dans les organes après 4 et 24 h par analyse élémentaire n'a pas permis de clarifier les mécanismes d'élimination ou de captation. Et des expériences complémentaires sont nécessaires afin de mieux mettre en évidences ces mécanismes en fonction de la morphologie.

Les nano-objets développés sont donc très intéressant pour l'amélioration du contraste en IRM. Une peu plus de données *in vivo* permettrait de s'assurer de leur bon comportement en circulation dans l'organisme.

Par la suite, les propriétés pour le traitement par hyperthermie magnétique ont été étudiées. Le pouvoir chauffant (SAR) des NPs a d'abord été mesuré en solution et des valeurs élevées ont été mesurées pour les octopodes et les sphères et des valeurs plus basses pour les cubes et les plaquettes comme attendus d'après les mesures magnétiques (Figure 21).

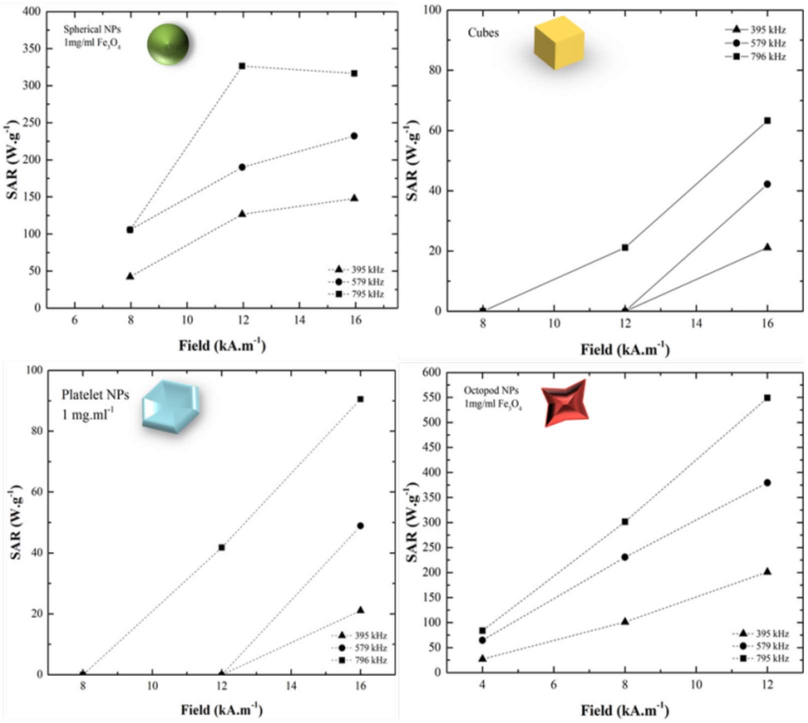

Figure 21 - Mesures du pouvoir chauffants des NPs

Les mesures d'hyperthermie en solution montrent que les sphères de 20nm ont en effet un pouvoir chauffant élevé et les cubes homogènes/octopodes présentent un pouvoir chauffant deux fois supérieur au meilleur produit commercial (ferrucarbotran). Le pouvoir chauffant des cubes cœur coquille et des plaquettes est quant à lui très décevant cela étant dû au plus faible volume magnétique disponible. Ces mesures indiquent que l'anisotropie induite par la forme aide bien à booster les valeurs de SAR mais seulement si l'aimantation à saturation est assez élevée (Figure 22).

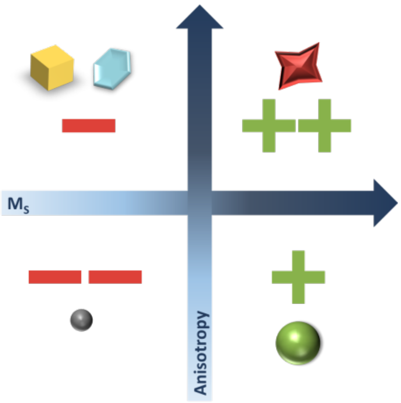

Figure 22 - Résumé du lien anisotropie de forme/ aimantation à saturation sur les valeurs de SAR

Une autre étude a été menée afin de déterminer l'évolution de la SAR en fonction de la concentration (Figure 23).

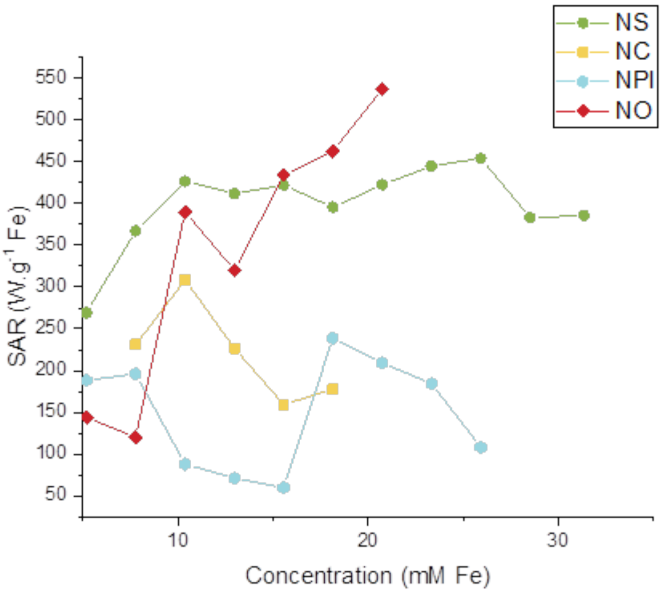

Figure 23 - Evolution de la SAR en fonction de la concentration en fer

Ces mesures réalisée à partir de la même solution en NPs ont permis d'observer des comportements variables selon les formes avec une SAR presque constante pour les sphères et une SAR qui décroit avec la concentration pour les octopodes. Ce point peut s'expliquer par une interaction inter particules diffèrente en fonction de la forme qui peuvent mener à l'alignement des NPs ce qui promeut la SAR ou une agrégation non contrôlée qui induit une décroissance de la SAR.

La question de l'internalisation cellulaire des NPs s'est ensuite posée. Les NPs ont alors été marquées avec un fluorophore puis mises en contact avec les cellules pendant 4 ou 24h à différentes concentrations. Les cellules ont ensuite été récupérées et leur fluorescence individuelle a été testée par cytométrie de flux. Les résultats montrent que l'internalisation cellulaire augmente avec le temps et la concentration. Des variations sont toutefois notées selon les formes des NPs mais afin de conclure, des mesures plus quantitatives du taux de NPs internalisées sont nécessaires. Une étude a été réalisée en comparant la quantité de fer dosée par ICP-MS et le signal de fluorescence mesurée par la cytométrie pour valider cette méthode comme montrant l'internalisation des NPs.

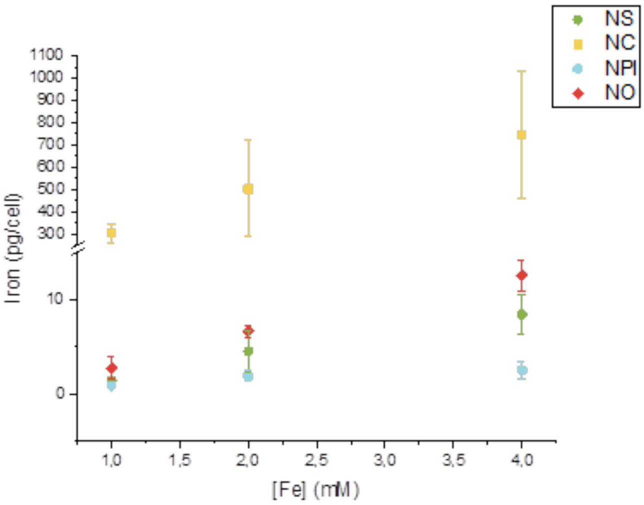

Figure 24 - Quantité en fer mesurée par ICP-MS dans les cellules

Des images TEM (Figure 25) ont été réalisées sur des cellules internalisées et il ressort que l'on retrouve les NPs dans des autophagosomes mais en qualtité assez faible à part les nanocubes qui étaient plus agrégés en suspension.

L'ensemble de ces résultats suggèrent un internalisation cellulaire assez faible des nanoparticules dendronisées avce une taille hydrodynamique moyenne inférieure à 50 nm et ceci est en accord avec les résultats obtenus avec les NPs de 10 nm dendronisées. La fonctionnalisation par les dendrons préserve d'une internalisation cellulaire non spécifique.

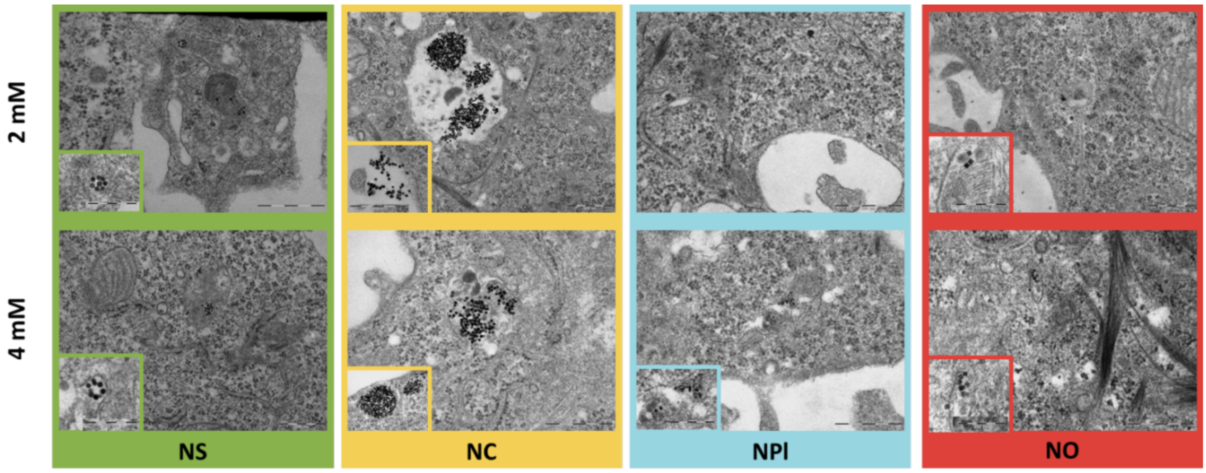

Figure 25 - Images TEM de cellules internalisées avec des NPs

Malgré des résultats variables en solution, toutes les formes ont été testées en Hyperthermie Magnétique sur cellules car elles pourraient montrer de bonnes performances dans un milieu plus visqueux. Les différentes formes ont été testées en HM sur des monocouches de cellules cancéreuses.

Mais dû à la faible internalisation passive des NPs et aux conditions expérimentales de frequence et amplitude de champ plus faibles de l'appareil *in vitro* seul les octopodes ont montré un effet satisfaisant (Figure 26). En utilisant un champ magnétique pour favoriser l'internalisation cellulaire, un signal encourageant d'apoptose a été mesuré pour les sphères, les ocotopodes et les plaquettes.

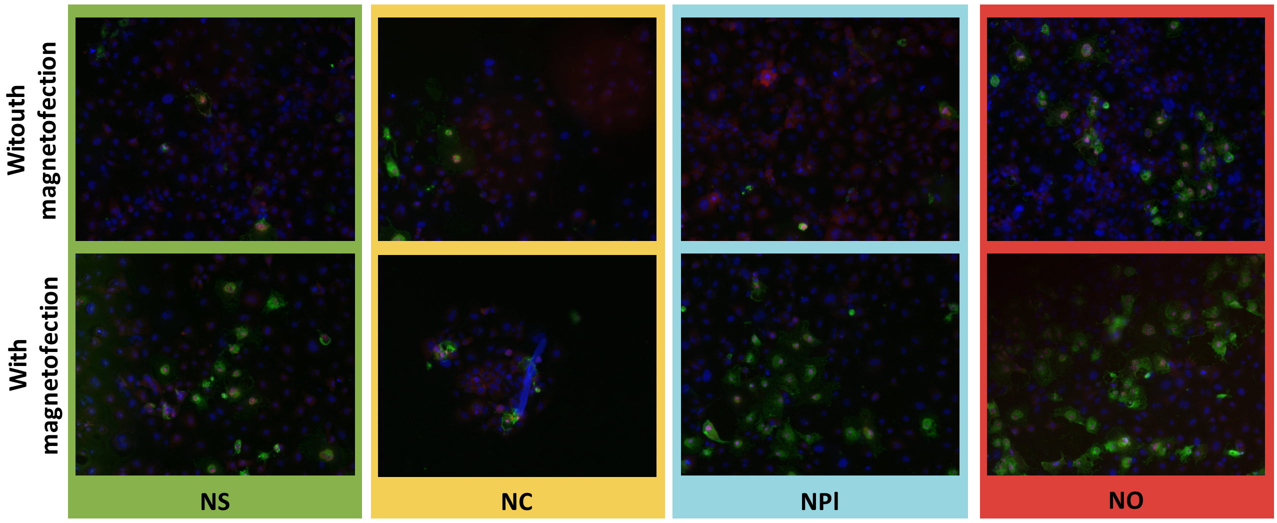

Figure 26 - Images en epifluorences de tapis cellualires traités par HM. Le bleu marque le noyau, le rouge la nécrose et le vert l'apoptose

Les octopodes avec un ligand de ciblage spécifique ont été testés *in vivo* sur des souris porteuses de tumeurs cancéreuses. Les essais in vitro et in vivo ont montrés une très faible internalisation des NPs sans ligand de ciblage. Ceci est très positif car cela signifie que les NPs ne s'internaliseront que dans les tumeurs desquelles elles portent le ligand de ciblage.

Malgré une bonne performance de tous les objets en tant qu'agent de contraste IRM, les performances en hyperthermies varient grandement. Toutefois les tests préliminaires in vitro démontrent que trois de nos formes (octopodes, sphères et plaquettes) sur les quatre sont de bons candidats en tant qu'agent d'hyperthermie magnétique.

V. Conclusion

Ce travail de thèse a mis en lumière plusieurs points. Tout d'abord, la synthèse « maison » du précurseur et son étude fine permet un contrôle de sa stabilité avec la température. Cette stabilité s'est avérée capitale pour le rendement de la synthèse de NPs d'oxyde de fer. L'effet majeur du degré d'hydratation a été mis en évidence. L'étude des milieux réactionnels à permit la visualisation du procédés de formation des NPs à travers de vésicules. Ce résultat est majeur car il permet de comprendre pourquoi le dopage et le contrôle de la forme est rapporté comme difficile dans la littérature.

Des premières solutions pour un changement d'échelle de la production de NPs sont apportées. Là encore elles confirment que le point central est la stabilité du précurseur. Le ligand ou le solvant peuvent être retirés en adaptant les conditions de synthèse. Ceci permet de contrôler le risque et le coût d'une production à plus grande échelle. Une solution à également été trouvée au lavage qui est le principal point noir pour la production en grande quantité par décomposition thermique.

L'extrapolation de la synthèse du précurseur à d'autres éléments fut possible. Toutefois le protocole n'est pas universel et peut nécessiter une optimisation. Les stéarates ne sont également pas universels. Et leur décomposition peut fortement varier comme ce fut observé pour $CoSt_2$. Malgré le contrôle du précurseur le dopage reste non facilité. Le mécanisme vésiculaire est incriminé. Mais cette identification permettra à l'avenir de définir de nouvelles stratégies pour le dopage. Toutefois le contrôle de la synthèse du précurseur a permis la synthèse de NPs cœur coquilles dont les propriétés magnétique sont pu être ajustées. Aussi la synthèse de NPs de différentes tailles a permis la synthèse de NPs présentant un effet T1.

La connaissance des différentes structures de précurseurs de fer a permis de mettre en évidence le rôle capital de la germination dans la synthèse de NPs de forme contrôlées. La stabilité et l'effet d'hydratation sont ici majeurs pour l'obtention de NPs de différentes formes.

Ces formes ont pu être optimisées et l'étude de leur propriétés magnétiques à mis en évidence l'influence de la morphologie.

Enfin le rôle de la forme sur les propriétés theranostiques a démontré que l'on peut optimiser ces propriétés.

Geoffrey COTIN

Nouvelles stratégies vers la synthèse de nanoparticules magnétiques multifonctionnelles innovantes combinant imagerie par IRM et/ou thérapie par hyperthermie magnétique

Résumé

Bien que de nombreux progrès aient été réalisés dans le traitement du cancer, de nouvelles approches sont nécessaires afin de minimiser les effets secondaires délétères et d'augmenter le taux de survie des patients. Aujourd'hui de nombreux espoirs reposent sur l'utilisation de nanoparticules (NPs) d'oxyde de fer fonctionnalisées permettant de combiner, en un seul nano-objet, le diagnostic (agent de contraste en IRM) et la thérapie par hyperthermie magnétique (i.e. « theranostic »).

Dans ce contexte, la stratégie développée est la synthèse de NPs à propriétés magnétiques optimisées par le contrôle de leurs taille, forme et composition, leur biofonctionnalisation et la validation de leurs propriétés théranostiques.

Une démarche d'ingénierie des NPs a été mise en place allant de la synthèse du précurseur de fer et de l'étude fine de sa décomposition en passant par l'étude *in situ* de la formation des NPs jusqu'à leur fonctionnalisation et la détermination de leurs propriétés theranostiques.

Mot clés : nanoparticules d'oxyde de fer, theranostic, décomposition thermique, précurseur, IRM, hyperthermie magnétique

Résumé en anglais

Despite numerous advances in cancer treatment, new approaches are necessary in order to minimize the deleterious side effects and to increase patient's survivals rate. Nowadays, many hopes rely on functionalized iron oxide nanoparticles (NPs) that combine, in a single nano-objects, diagnosis (MRI contrast agent) and magnetic hyperthermia therapy (i.e. "theranostic").

In this context, the strategy is to develop the synthesis of optimized magnetic properties NPs through the control of their size, shape, composition, biofunctionalization and the validation of their theranostic properties.

A process of NPs engineering has been developed starting at the iron precursor synthesis and the fine study of its decomposition passing through the *in situ* formation of the NPs to their functionalization and the determination of their theranostic properties.

Key words : iron oxide nanoparticles, theranostic, thermal decomposition, precursor, MRI, magnetic hyperthermia